Xuzhu Dong
Li Cai Cai   *Editors*

The Proceedings of 2023 4th International Symposium on Insulation and Discharge Computation for Power Equipment (IDCOMPU2023)

Volume II

Springer

Lecture Notes in Electrical Engineering

Volume 1101

Xuzhu Dong · Li Cai Cai

Editors

The Proceedings of 2023 4th International Symposium on Insulation and Discharge Computation for Power Equipment (IDCOMPU2023)

Volume II

Editors
Xuzhu Dong
School of Electrical Engineering
and Automation
Wuhan University
Wuhan, China

Li Cai Cai
School of Electrical Engineering
and Automation
Wuhan University
Wuhan, China

Paper in this product is recyclable.

Contents

Mixed Three-Parameter Weibull Breakdown Distribution Model and Breakdown Mechanism of Metalized Films

Jing Lan, Hua Li, Guohao Zhang, Fuchang Lin, and Gang Liu

Abstract The breakdown characteristics of the metallized film significantly affect the reliability of self-healing capacitors. Traditional two-parameter Weibull distribution can be well described breakdown distribution of metallized film, but it is difficult to describe its early failure intuitively. Metallized film breakdown under low field strength has important influence on the reliability of the capacitor. In this paper, a mixed three-parameter Weibull distribution model is established to describe the breakdown characteristics and to analyze the mechanisms of metallized film. Metallized polypropylene films with different electrode thicknesses are chosen as the object to study the breakdown characteristics and mechanisms. The paper has shown there are three apparent breakdown peaks in the breakdown field strength of 400–500, 500–600 and 600–700 V/μm, which correspond early failure breakdown, low-field defects breakdown, near-intrinsic breakdown. The metallized film with electrode thickness d_1 has been used as an example to state that three-parameter Weibull model can well describe different breakdown mechanisms. Moreover, the paper has shown that near-intrinsic breakdown is the main breakdown mechanism for metallized films.

J. Lan · H. Li (✉) · G. Zhang · F. Lin
State Key Laboratory of Advanced Electromagnetic Engineering and Technology, Huazhong University of Science and Technology, Hubei 430074, Wuhan, China
e-mail: leehua@hust.edu.cn

J. Lan
e-mail: jinglan@hust.edu.cn

G. Zhang
e-mail: guoh_zhang@hust.edu.cn

F. Lin
e-mail: fclin@hust.edu.cn

G. Liu
Electric Power Research Institute China Southern Power Grid (CSG), Guangdong, Guangzhou 510080, China

National Engineering Research Center of UHV Technology and Novel Electrical Equipment Basis, Guangdong, Guangzhou 510080, China

1 Introduction

Owing to the self-healing characteristics, the insulation can be recovered after the local breakdown in the metallized film capacitors, which make them can work under high field with high reliability [1, 2]. Metallized film capacitors have been widely used as DC-link capacitors in VSC-HVDC and other fields [3, 4].

Metallized film capacitors are generally made by the polypropylene films with evaporated metal electrode winding around a mandrel [5]. Impurities or defects are introduced in the metallized films during the production process, which lead to the electrical weak points. Breakdown event will occur first at the weakest point and a discharge channel will form under an external electrical field. Then the metal electrode will be evaporated and ionized to form an arc as a result of Joule heat of the breakdown current. As the electrode evaporation area increases, the input electrical energy will be not enough to maintain the arc burning so that the shrinkage and extinguishment happens. After that the insulation recovers. The whole process is called "self-healing" [6–9]. The self-healing performance is affected by the breakdown performance directly, which affects the reliability of the capacitor. Therefore, it is necessary to study the breakdown distribution characteristics and mechanisms of the metallized films.

The breakdown strength of the metallized film is generally described by the two-parameter Weibull distribution [10–14]. The two-parameter Weibull distribution is a simplified form in fact when the position parameter of the three-parameter Weibull distribution is set as zero [11]. Although the parameter estimation for the two-parameter Weibull distribution is simplified, it cannot describe the minimum breakdown strength of the metallized film. The three-parameter Weibull distribution can also describe data better. Additionally, some studies have shown that the data in the region of low breakdown probability deviates from a single distribution. It indicates that there are several breakdown mechanisms for metallized films [10, 13, 14]. The mixed Weibull distribution can describe the breakdown data better and provide a method for analyzing the breakdown characteristics and influencing factors caused by different breakdown mechanisms [13, 14]. Therefore, it is necessary to establish a mixed three-parameter Weibull breakdown distribution model for metallized films.

In this paper, a mixed three-parameter Weibull breakdown distribution model for metallized films has been established. And the metallized polypropylene film with different electrode thickness has been taken as the object for the breakdown experiments. Then the breakdown mechanisms of the metallized films and the effects of the electrode thickness have been studied.

2 Mixed Three-Parameter Weibull Distribution Model

The breakdown events of metallized films occur at the weakest points, which satisfy the extreme value distribution physically. The distribution also has the characteristics of large dispersion and wide distribution so that described by Weibull distribution generally. The cumulative distribution function (CDF) and probability density function (PDF) of the three-parameter Weibull breakdown distribution are expressed as [15]

$$F(E_b) = 1 - \exp\left[-\left(\frac{E_b - E_{\min}}{\alpha}\right)^{\beta}\right] \tag{1}$$

$$f(E_b) = \frac{\beta}{\alpha}\left(\frac{E_b - E_{\min}}{\alpha}\right)^{\beta-1} \exp\left[-\left(\frac{E_b - E_{\min}}{\alpha}\right)^{\beta}\right] \tag{2}$$

where E_b is the breakdown field strength; E_{min} is the position parameter, known as the characteristic breakdown field strength, which represents the minimum breakdown strength of the metallized film; α is the scale parameter; β is the shape parameter, which represents the breakdown field strength of dispersion. The maximum likelihood estimation (MLE) method can be used to estimate the parameters of the three-parameter Weibull distribution, which is more difficult than the two-parameter form [15, 16]. The position parameter E_{min} sometimes needs to be estimated in advance [17]. Some studies about metallized films breakdown have shown that the estimated position parameter E_{min} is close to the lowest experimental breakdown strength [11]. Therefore, E_{min} is determined as the lowest experimental breakdown strength in this paper.

The parameters E_a and E_m are defined to describe the breakdown field strength of the metallized film. E_a represents the breakdown strength when the cumulative probability is 63.2%, defined as

$$E_{\alpha} = E_{\min} + \alpha \tag{3}$$

E_m represents the breakdown strength corresponding to the peak value of the probability density curve, which represents the breakdown strength corresponding to the maximum probability. The derivative of the probability density function is expressed as

$$f'(E_b) = -\frac{\beta\left(\beta\left(\frac{E_b - E_{\min}}{\alpha}\right)^{\beta} - \beta + 1\right)}{(E_b - E_{\min})^2}$$
$$\times \left(\frac{E_b - E_{\min}}{\alpha}\right)^{\beta} e^{-\left(\frac{E_b - E_{\min}}{\alpha}\right)^{\beta}} \tag{4}$$

Let Eq. (4) be equal to zero and then the expression of E_m can be obtained as

$$E_m = E_{\min} + \alpha \left(\frac{\beta - 1}{\beta} \right)^{\frac{1}{\beta}} \tag{5}$$

As mentioned above, there may be multiple breakdown mechanisms for the metallized films. Assuming that the ith breakdown mechanism has its corresponding distribution $F_i(E_b)$ and $F_i(E_b)$ which are independent of each other. If there are n breakdown mechanisms totally for the metallized film, then the CDF of mixed three-parameter Weibull distribution can be expressed as [18]

$$F(E_b) = \begin{cases} m_1 F_1(E_b) & E_{\min 1} \leq E_b < E_{\min 2} \\ \sum_{i=1}^{2} m_i F_i(E_b) & E_{\min 2} \leq E_b < E_{\min 3} \\ \dots \\ \sum_{i=1}^{n} m_i F_i(E_b) & E_{\min n} < E_b \end{cases} \tag{6}$$

$$F_i(E_b) = 1 - \exp\left[-\left(\frac{E_b - E_{\min i}}{\alpha_i} \right)^{\beta_i} \right] \tag{7}$$

where m_i represents the proportion of each sub-distribution to the total distribution and also represents the impact of the breakdown caused by the ith breakdown mechanism; α_i, β_i and E_{mini} respectively represents the scale parameter, shape parameter and position parameter of each sub-distribution. In addition, each $F_i(E_b)$ has its $E_{\alpha i}$ and E_{mi}. According to the changing laws of m_i, $E_{\alpha i}$, and E_{mi}, the influencing factors for different breakdown mechanisms can be analyzed.

For the estimation of Weibull distribution parameters, maximum likelihood estimation (MLE) method was used in this paper. Statistical analysis was performed in MATLAB and ORIGIN software.

3   Experiment Setup

In this paper, metallized polypropylene films were used as the object and an experimental platform was established for studying the breakdown under DC voltage. The experimental circuit is shown in Fig. 1. The DC voltage was supplied by a DC source. A high-voltage probe was used to measure the voltage waveform during breakdown processes. The experimental sample were single-sided metallized polypropylene films. The electrode thickness of the metallized polypropylene film was d_1, d_2 and d_3 from high to low. The film thickness is 6 μm and the capacitance of samples was controlled as a constant. The experimental temperature and external pressure on films were also controlled as the constants by the platform. In the experiment, a DC voltage of 100 V/s has been applied on samples until the breakdown events occurred. Then the breakdown voltages were recorded.
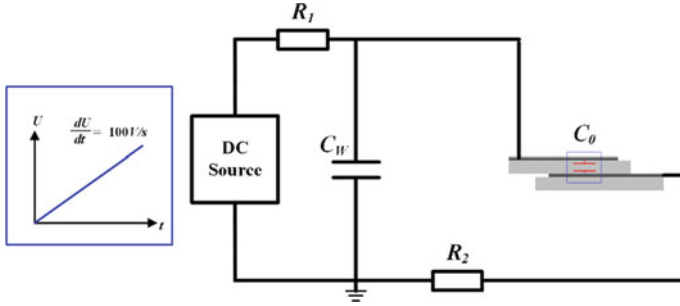
Fig. 1 The experimental platform for metallized films breakdown

(a) Single breakdown   (b) Continuous breakdown
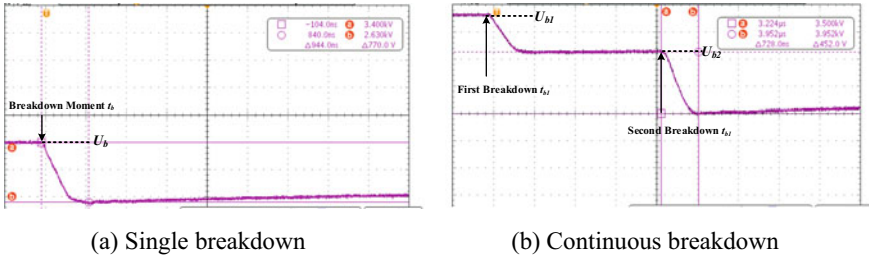
Fig. 2 Typical breakdown voltage waveforms

The typical breakdown voltage waveforms for metallized films are shown in Fig. 2. In the experiment, single breakdown events and continuous breakdown events occurred. Continuous breakdown events usually occurred at the same breakdown points a few microseconds after the first breakdown event. The single breakdown events dominated the experimental breakdown events. In the following analysis, the breakdown voltages of continuous breakdown events were taken as the first breakdown voltages U_{b1}.

4 Results and Discussion

Firstly, the breakdown strength distribution of metallized film with electrode thicknesses d_1, d_2 and d_3 were estimated in the form of Eq. (1), in which the position parameter Emin was taken 400 V/μm according to the lowest experimental breakdown strength. The breakdown PDF curves are shown in Fig. 3 and the parameters are shown in Table 1.

As shown in the graphs, the breakdown strength of the metallized film increases as the electrode thickness decreases. When the electrode thickness decreases from d_1 to d_3, E_α and E_m increases by 4.9 and 5.2%. The numbers of breakdown data above 600 V/μm for films with electrode thicknesses of d_1, d_2 and d_3 are 40, 45 and

(a) Electrode thickness d_1

(b) Electrode thickness d_2

(c) Electrode thickness d_3
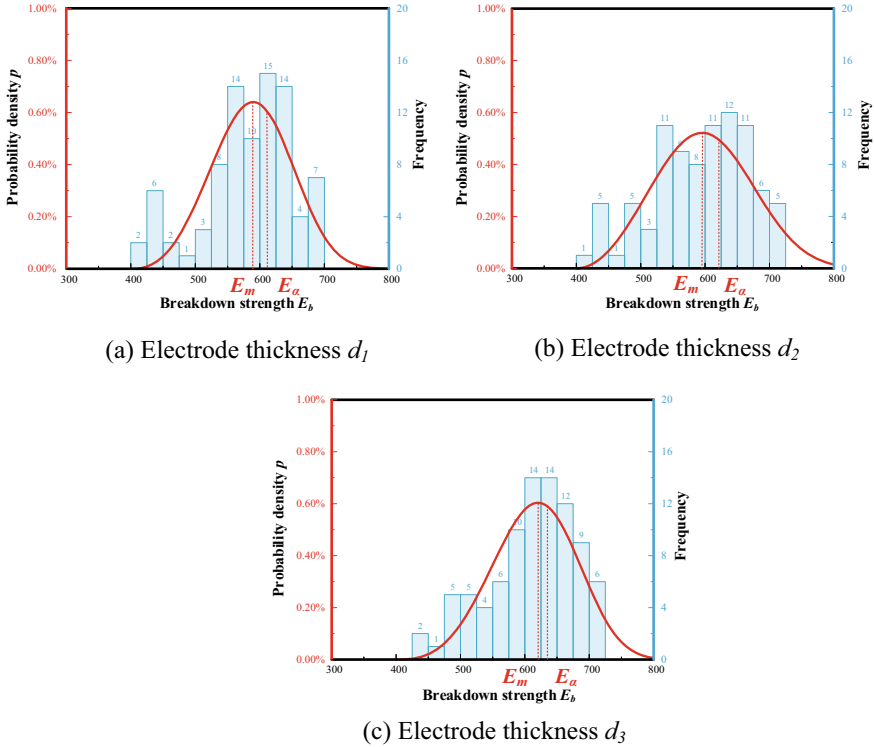
Fig. 3 Three-parameter Weibull distribution for metallized films with different electrode thickness

Table 1 Three-parameter Weibull distribution parameters

Electrode thickness	E_{min} (V/μm)	α (V/μm)	β	E_α (V/μm)	E_m (V/μm)
d_1	400	209.2	3.5	609.2	590.0
d_2	400	222.0	2.9	622.0	591.9
d_3	400	239.2	3.8	639.2	620.7

55 groups. It indicates that the probability of breakdown in high fields increases for films with low electrode thicknesses. The breakdown probability density distribution curve generally shifts toward high field strengths. It indicates that the defects in the film are less when the electrode is thinner so that the overall breakdown strength is higher. It can be concluded that the electrode vaporization process is closely related to the number of defects. The lower electrode thickness means the shorter vaporization time, which leads to the less damage for films.

Moreover, the breakdown strength data of metallized polypropylene films show three apparent breakdown peaks in each of the three intervals 400–500 V/μm, 500–600 V/μm and 600–700 V/μm. It indicates that there are three breakdown mechanisms for metallized polypropylene films. The three breakdown mechanisms are defined as early failure breakdown, low-field defects breakdown and near-intrinsic breakdown according to the breakdown strength from low to high. The breakdown strength distribution is fitted with a mixed three-parameter Weibull distribution containing three sub-distributions to further analyze the different breakdown mechanisms, with the cumulative distribution expressed as

$$
F(E_b) = \begin{cases} \sum_{i=1}^{1} m_i F_i(E_b) & E_{\min 1} \le E_b < E_{\min 2} \\ \sum_{i=1}^{2} m_i F_i(E_b) & E_{\min 2} \le E_b < E_{\min 3} \\ \sum_{i=1}^{3} m_i F_i(E_b) & E_{\min 3} < E_b \end{cases} \tag{8}
$$

where $F_1(E_b)$, $F_1(E_b)$ and $F_1(E_b)$ are the cumulative probability distribution functions of early failure breakdown, low-field defects breakdown, and near-intrinsic breakdown respectively. The sub-distributions of the three failure types are linearly summed to form the total distribution of cumulative breakdown probability. A typical mixed three-parameter Weibull breakdown PDF curve is shown in Fig. 4.

As shown in Fig. 4, there are overlapping regions between the sub-distributions of different breakdown mechanisms, which is as expected. If there is no overlap region, there will be a breakdown strength point with probability density of zero. The position parameters E_{min1}, E_{min2} and E_{min3} for early failure breakdown, low-field defects breakdown and near-intrinsic breakdown are 400 V/μm, 483 V/μm and 562 V/μm respectively. And the breakdown strength E_{m1}, E_{m2} and E_{m3} are 452.4 V/μm, 573.5 V/μm and 640.2 V/μm respectively, which fit the positions of breakdown

Fig. 4 Typical mixed three-parameter Weibull distribution
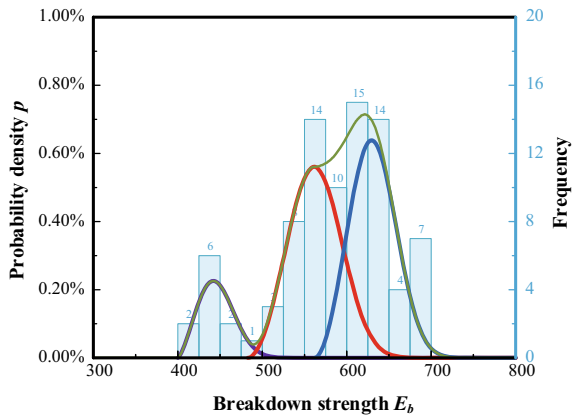
peaks. It indicates that the mixed three-parameter Weibull distribution model of metallized films can describe the different breakdown mechanisms efficiently.

Furthermore, the proportions of sub-distribution to total distribution for early failure breakdown m_1, low-field defect breakdown m_2 and near-intrinsic breakdown m_3 increases in order. It indicates that the breakdown is mainly caused by near-intrinsic breakdown, followed by low-field defect breakdown and early failure breakdown has the least effect. Although early failure is not the main breakdown mechanism, it characterizes the lowest breakdown strength of the metallized film and is closely related to the reliability of the metallized film capacitors. Therefore, it is necessary to further analyze the characteristics and influencing factors of each mechanism in the subsequent studies.

5   Conclusion

In this paper, a mixed three-parameter Weibull distribution model for metallized films was established and the influence of electrode thickness on breakdown distribution was investigated. The breakdown mechanisms of metallized polypropylene films were analyzed and the following conclusions were obtained:

(1) The breakdown strength of metallized film increases with decreasing electrode thickness. The number of defects in films is lower for lower electrode thickness metallized film. These defects are closely related to vaporization. The lower electrode thickness means the shorter vaporization time, which leads to the less damage for films.

(2) There are three different breakdown mechanisms in metallized films, which are early failure breakdown, low-field defects breakdown and near-intrinsic breakdown. Near-intrinsic breakdown is the main breakdown mechanism. The mixed three-parameter Weibull distribution model for metallized films can well describe the different breakdown mechanisms of metallized films and can be used to analyze the influencing factors of different breakdown mechanisms efficiently.

References

1. Sandström GÖ, Tingström J (2008) Management of radical innovation and environmental challenges: development of the dry Q capacitor at ABB. Eur J Innov Manag 11(2):182–198
2. Zhao Z, Davari P, Lu W, Wang H et al (2021) An overview of condition monitoring techniques for capacitors in DC-Link applications. IEEE Trans Power Electron 36(4):3692–3716

3. Tang Y, Chen M, Ran L (2016) A Compact MMC submodule structure with reduced capacitor size using the stacked switched capacitor architecture. IEEE Trans Power Electron 31(10):6920–6936

4. Qin S, Ma S, Boggs SA (2012) The mechanism of clearing in metallized film capacitors. In: Proceedings of the IEEE international symposium on electrical insulation, pp 592–595

5. Belko VO, Emelyanov OA (2016) Selfhealing in segmented metallized film capacitors: experimental and theoretical investigations for engineering design. J Appl Phys 119(2):024509

6. Kammermaier J, Rittmayer G, Birkle S (1989) Modeling of plasma-induced self-healing in organic dielectrics. J Appl Phys 66(4):1594–1609

7. Belko VO, Emelyanov OA, Ivanov IO (2021) Self-healing processes of metallized film capacitors in overload modes-part 1: experimental observations. IEEE Trans Plasma Sci 49(5):1580–1587

8. Belko VO, Emelyanov OA, Ivanov IO et al (2020) The diagnostics of metallized film capacitors under soft training test. In: 2020 international conference on diagnostics in electrical engineering, pp1–4

9. Kerwien CM, Malandro DL, Broomall JR (2016) Large area DC dielectric breakdown voltage measurement of BOPP and PTFE thin films. In: 2016 IEEE conference on electrical insulation and dielectric phenomena (CEIDP), pp 486–489

10. Laihonen SJ, Gäfvert U, Scjiutte T et al (2004) Influence of electrode area on dielectric breakdown strength of thin poly(ethyleneterephthalate) films. In: The 17th annual meeting of the IEEE lasers and electro-optics society, pp 563–567

11. Laihonen SJ, Gäfvert U (2007) DC breakdown strength of polypropylene films: area dependence and statistical behavior. IEEE Trans Dielectr Electr Insul 14(2):275–285

12. Rytöluoto I, Lahti K (2015) Large-area dielectric breakdown performance of polymer films—part I: measurement method evaluation and statistical considerations on area-dependence. IEEE Trans Dielectr Electr Insul 22(2):689–700

13. Rytöluoto I, Lahti K (2011) Effect of film thickness and electrode area on the dielectric breakdown characteristics of metallized capacitor films. In: Nordic insulation symposium, pp 33–38

14. Bain LJ (1978) Statistical analysis of reliability and life-testing models: theory and methods,1st. Marcel Dekker, New York

15. Denis C (2009) Fitting the three-parameter weibull distribution: review and evaluation of existing and new methods. IEEE Trans Dielectr Electr Insul 16(1):281–288

16. Li X (2012) Research on estimation for the three-parameter Weibull distribution. Beijing Jiaotong University, Beijing (in Chinese)

17. Hauschild W, Mosch W (1992) Statistical techniques for high-voltage engineering, 2nd edn. Institution of Engineering and Technology, Philadephia

18. Liu F (2018) Three-parameter Weibull distribution FMM and its application. Stat Decis 15:14–17 (in Chinese)

Risk Assessment of DC Bias in Multi DC Projects Under Different Operating Conditions

Renbin Su, Jianming Zou, Wei Wang, Bochao Yang, Hailiang Lu, Zhihui Zheng, and Xishan Wen

Abstract With the continuous expansion of the power grid, large-scale AC/DC hybrid transmission systems are currently facing greater pressure on DC exceeding the standard. By collecting historical operating data of various DC grounding electrodes in Central China, this paper determines the possible operating conditions of multiple DC grounding electrodes, proposes equivalent models for substations and transmission lines, and establishes a DC current model for Central China power grid. Based on the developed DC bias simulation software, the ground potential, grounding current, and DC bias current of substations near the grounding electrode under different operating conditions are calculated. The study found that the impact of the combined action of multiple DC projects on DC bias in substations can be equivalent to the vector superposition of the respective effects of a single DC ground electrode. When multiple DC ground electrodes with the same polarity operate in a relatively close monopolar earth loop, it may further exacerbate the DC bias risk in nearby substations. The research conclusions can provide a reference for DC bias risk assessment and management in areas where multiple DC projects are located.

Keywords Multi DC engineering · Different working conditions · DC bias · Risk assessment

1 Introduction

Facing the opportunities and challenges of the rapid development of new energy under the "double carbon" target, the power grid will promote the clean and low-carbon efficient use of energy through supply-side structural adjustment and demand-side response [1, 2]. However, the population distribution and energy distribution in

R. Su · J. Zou
Central China Branch of State Grid Corporation of China, Wuhan 430077, China

W. Wang (✉) · B. Yang · H. Lu · Z. Zheng · X. Wen
School of Electrical and Automation, Wuhan University, Wuhan 430072, China
e-mail: weiwang@whu.edu.cn

China are highly uncoordinated, and the vigorous development of clean energy will put a higher demand on energy transmission in China, and large capacity and long distance energy transmission is indispensable. DC transmission has the advantages of large transmission capacity, easy and fast control of power magnitude and direction, and saving line corridors, which are widely used in long-distance electric energy transmission [3–5].

The DC grounding electrode is an important component of the DC transmission system, and the operating current flows back through the earth via the grounding electrode during the operation of the DC transmission system with a single earth return [6–8]. The DC current flowing through the earth will cause the earth potential around the grounding pole to be unequal and produce a DC potential difference between two substations that are far apart. Since the DC resistance of the transmission line between the two substations is much smaller than the earth resistance, the DC current will flow back through the transformer winding directly grounded at the neutral point with the transmission line, thus producing a serious DC bias effect, which makes the transformer core severely saturated and the excitation current increases to distortion, generating a large number of harmonics in the system [9–11].

With the continuous expansion of power grid scale, large hybrid AC-DC transmission systems are now facing higher pressure of DC overruns, and the increased number of DC transmission projects will lead to more serious risk of DC bias of power grid. Luo et al. proposed a critical site identification method for biased DC under the joint action of multiple grounding poles, and established criticality indexes that have an important influencing role on biased DC distribution considering uncertainty of influencing factors to provide useful references for improving the early warning capability of DC bias of grid transformers [12]. Sun et al. studied the DC bias problem of $\pm$ 1100 kV Changji converter station and $\pm$ 800 kV Tianshan converter station acting together, and found that when two double grounding poles are injected into DC simultaneously, the plant station which originally has no risk of DC bias is also at risk; finally, the preventive methods and strategies for DC bias management were proposed [13]. Yang et al. simulated and compared various suppression measures such as capacitor isolation method and resistance-capacity combination method for the DC bias impact on the receiving power grid after the access of the Junto-Wannan EHV DC transmission project, and proposed a comprehensive management strategy for DC bias [14]. Duan et al. found that the current on one line does not flow back through the other lines when multiple DC lines operate unipolarly, and the DC current in the EHV substation is equal to the algebraic sum of the single line when multiple lines operate unipolarly at the same time [15].

Scholars at both China and abroad have conducted a lot of research on the risk of DC bias under multiple DC systems, and fruitful research results have also been achieved. However, when single-pole earth return operation occurs, the operation mode of grounding poles also has an impact on DC bias [16–18]. In this paper, we consider the risk of DC bias under different operation modes of multiple DC grounding poles in Central China, and propose the corresponding solution measures in a targeted manner.

There are nine DC grounding poles in central China, and the DC bias risk problem is very representative. In this paper, we obtain soil resistivity data of a large area in Central China through field survey, investigate the historical operation data of each DC grounding pole, calculate the probability of simultaneous operation of multiple DC grounding poles with a single earth return, build a simulation model of DC biomagnetism in Central China power grid, and propose a cross-region DC biomagnetism risk assessment and management method for Central China power grid, which can not only fundamentally solve the DC biomagnetism hazard in Central China power grid, but also provide a solution for other regions. The proposed method can not only solve the DC bias hazards in Central China Power Grid, but also provide reference for the DC bias management in other regions.

2   DC Bias Simulation Model

2.1   General Overview of Central China Power Grid

DC transmission is an important technical means for large-scale energy transmission. The geographical distribution of DC transmission grounding poles in different regions of China is shown in Fig. 1, which is the largest DC transmission power in the world in terms of total installed capacity, accounting for about 80% of the total installed DC transmission capacity worldwide. For the Central China Power Grid, four provinces including Henan, Hubei, Jiangxi and Hunan have the most dense DC transmission delivery points in China. Hubei grid currently has 5 DC transmission project grounding poles, Henan grid has 2, Jiangxi grid and Hunan grid has 1 each. There are 9 DC grounding poles in the whole Central China Power Grid, and the information about each DC grounding pole is shown in Table 1.

In order to further evaluate the DC bias risk of the Central China Power Grid, it is necessary to build a DC bias simulation model to evaluate the DC bias risk. In this paper, DC bias simulation software is designed and developed for modeling, and the DC bias results calculated by the simulation software are compared with the actual measurement results to verify the reliability of the software. The modeling using the software mainly consists of two aspects: firstly, the geographic information modeling, i.e., the establishment of the topological map of the central China power grid; secondly, the DC current modeling, i.e., the establishment of the equivalent circuit diagram based on the distribution of each component in the AC power grid.

Fig. 1 Geographical distribution map of DC transmission grounding electrode

Table 1 Overview of DC grounding electrode in central China power grid

DC grounding pole	Grounding current during monopole earth operation (A)	Operation time	Number of monopole geodesic runs since operation
Qingtai grounding pole	3000–300	2002	33
Yidu converter station old town grounding pole	3000–300	2006	28
Cao Bu lake grounding pole	3000–300	2004	44
Songjia dam grounding pole	1200–120	1989	173 times since 2005
Wugang grounding pole	3000–500	2021	22
Chenjia grounding pole	2875	2014	1
Yaosai grounding pole	6000	2020	3
Shangweizi grounding pole	5000–3000	2017	20
Lian lake grounding pole	3000	2021	5

2.2 Geographic Information Modeling

The geographic information topology of the AC power grid in Central China was created with transmission lines connected in single-loop operation, double-loop operation, and in some areas, triple- or quadruple-loop connections. The modeling of all

1000 kV, 500 kV and 220 kV grids corresponding to the main wiring diagram of the Central China Power Grid network requires consideration of three factors:

(1) Substation information, which includes the station's geographical location, grounding resistance, station transformer parameters, busbar and neutral point information;
(2) Line information, including information on line type, number and length of return lines;
(3) Earth model considering resistivity distribution.

According to the planning of the operation mode of Central China Power Grid, its geographic information model is established. The total number of substations is 2385, among which 1516 are 110 kV substations, 737 are 220 kV substations, 127 are 500 kV substations and 6 are 1000 kV substations.

2.3 DC Current Modeling

Among the DC network models, the substation model is the most complex and can be subdivided into above-ground part and underground part. The electrical wiring diagram of a 500 kV substation with dual autotransformer medium voltage side bus segment operation is shown in Fig. 2a, and the equivalent DC model of the substation is shown in Fig. 2b.

The model of the above-ground part of the substation belongs to the pure circuit problem, and the model mainly includes the substation node, transformer model, and neutral series equipment model. The transformer model includes transformer winding type, winding DC resistance, and transformer busbar. In the DC current distribution calculation, it is only necessary to distinguish whether the transformer is an autotransformer or not.

(a) 500kV substation with double autotransformer medium voltage side bus section operation

(b) Equivalent DC model of the substation
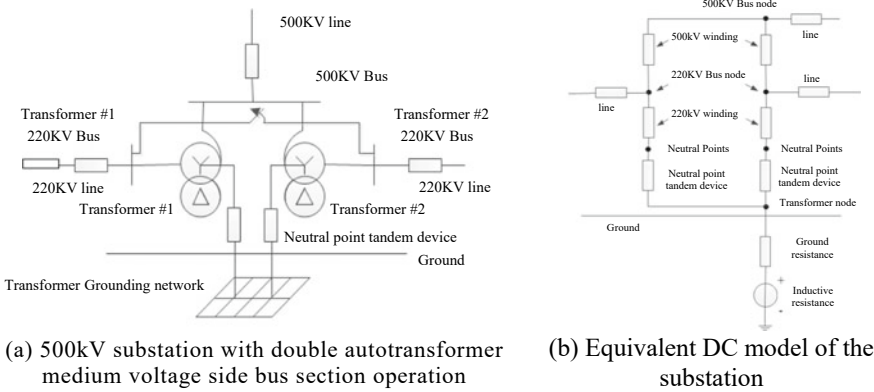
Fig. 2 DC model of AC power grid

3 Risk Analysis of DC Bias Under Different Operating Conditions

As shown in Table 1, the number of times of single earth return operation of each DC grounding pole in Central China since its commissioning was obtained through research in the early stage, and it is known through calculation that the probability of single earth return operation of a single DC grounding pole is about 1%, then the probability of single earth return operation of two DC grounding poles at the same time will drop to about 1/10000, so in the actual engineering context In this paper, we do not consider the case of three DC projects with single earth return operation at the same time.

According to the distribution of the nine DC grounding poles in Central China, the four DC grounding poles of Songjiaba, Yidu, Caofuhu and Qingtai are close to each other, which together constitute a grounding pole group and have the greatest impact on the DC bias of the surrounding substations when a single earth return occurs at the same time. Therefore, this paper takes Songjiaba and Yidu grounding poles as examples to analyze the DC bias magnetization risk under different operating conditions.

3.1 Risk Analysis of DC Bias Magnetization Under the Action of a Single DC Project

Songjiaba DC Grounding Pole Single Pole Operation

The DC grounding electrode of Songjiaba occurs in single-pole earth return operation with a rated incoming current of 1200 A. By building a simulation model, the DC current distribution in the central China power grid is calculated as shown in Fig. 3. From the calculation, it can be seen that there are 8 substations with DC bias current over 0.2 A, among which the DC bias current of Chaoyang 500 kV substation reaches 1.35 A.

The current principles for selecting the DC bias current limit of transformers are as follows: ① for 1000 kV transformers, the DC bias current limit is 2 A; ② for 500 kV transformers, the DC bias current limit is 5 A; ③ for 220 kV transformers, the DC bias current limit is 7 A; ④ for 110 kV transformers, no requirement for the time being. 220 kV transformer, the DC bias current limit is 7 A; ④ for 110 kV transformer, no requirement for the time being. By comparing with the DC bias current limit value of transformer, it is considered that the DC bias current of the nearby substation meets the safety limit value when the DC grounding pole of Songjiaba is operated in single pole earth return mode.

Fig. 3 DC bias current in substations near Songjiaba
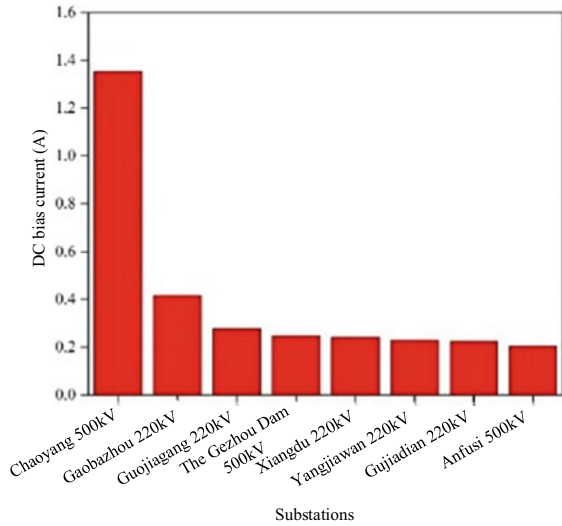
Yidu DC Grounding Electrode Single Pole Operation

The Yidu DC grounding pole occurs with a single earth return operation with a rated incoming current of 3000 A. The DC current distribution of the central China power grid is calculated by building a simulation model as shown in Fig. 4. According to the calculation, there are 13 substations with DC bias current over 0.2 A. Among them, the DC bias current of Zhijiang 220 kV, Gujiadian 220 kV, Li Zhou 500 kV and Chaoyang 500 kV substations exceeds 0.5 A. According to the requirement of transformer DC bias current limit, the DC bias current of substations near grounding electrodes also meets the safety limit. It means that the risk of DC bias magnetization in substations is small when a single DC grounding electrode occurs in the earth return operation.

3.2 Risk Analysis of DC Bias Under the Action of Multiple DC Projects

The operation mode of DC grounding electrode is mainly divided into two types when single earth return operation occurs: anode and cathode. From the previous analysis, it can be seen that three DC grounding poles occur simultaneously in the case of single-pole earth return operation mode can be disregarded in the actual project, so this paper analyzes the risk of DC bias magnetization under the same polarity of two DC grounding poles as well as the different polarity.
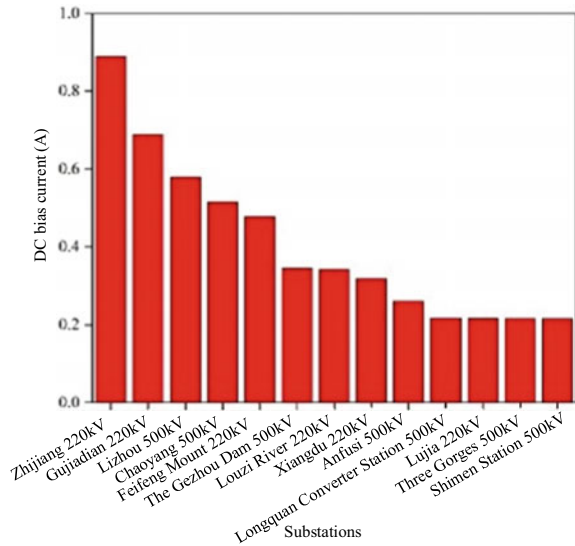
Songjiaba, Yidu Grounding Electrode with Anode Operation

When the single-pole earth return is in operation, the rated grounding current of Songjiaba DC grounding pole is 1200 A, and the rated grounding current of Yidu DC grounding pole is 3000 A. From the calculation as shown in Fig. 5, it can be seen that there are 7 substations with DC bias current over 0.5 A, among which the DC bias current of Chaoyang 500 kV substation reaches 1.87 A. According to the requirement of transformer DC bias current limit, the DC bias current of Chaoyang 500 kV substation meets the safety limit.

Different Polarity Operation

In single-pole earth return operation, Songjiaba DC grounding pole is rated at 1200 A with anode operation; Yidu DC grounding pole is rated at 3000 A with cathode operation. From the calculation as shown in Fig. 6, it can be seen that there are 9 substations with DC bias currents exceeding 0.2 A, among which the DC bias current of 220 kV substation in Zhijiang reaches 0.89 A. By further calculation, the DC bias currents of the remaining substations also meet the safety limit.

Fig. 5 DC bias current in substations operating in the same polarity
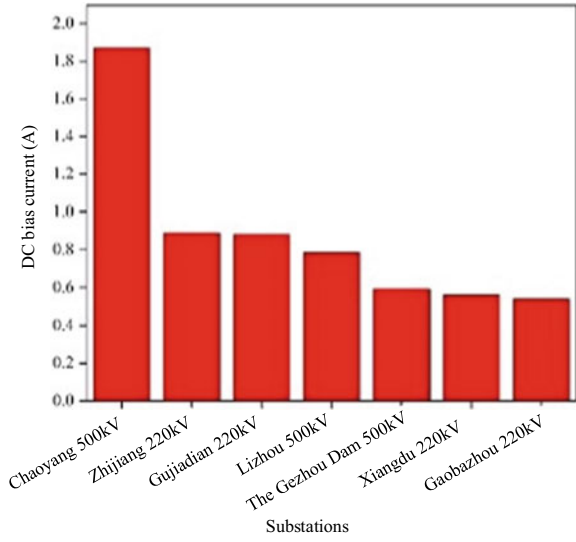
Fig. 6 DC bias current in substation with different polarity operation
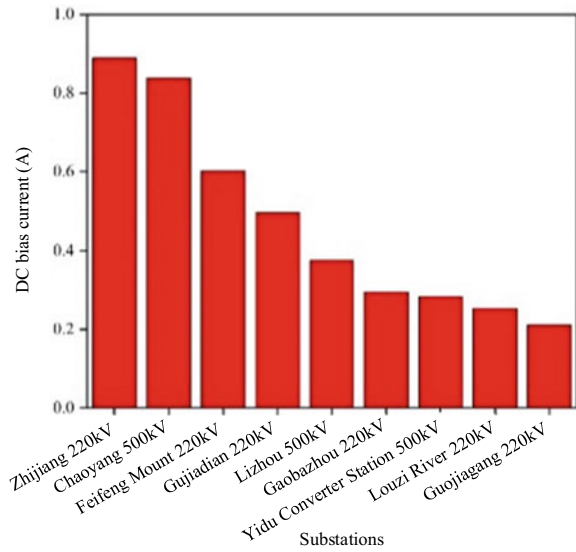
Fig. 7 DC bias current of
grounding electrode under
different operation modes
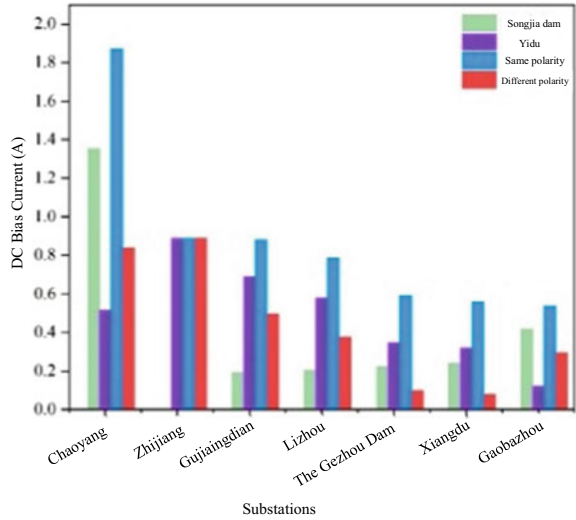
4 Risk Analysis of DC Bias Magnetization Under Different Operation Modes

4.1 DC Bias Current

The DC bias current of the substation is further analyzed based on the ground potential and the total incoming current of the DC grounding electrode under different operation modes. The DC bias currents of DC grounding electrodes under different operation modes are shown in Fig. 7.

From Fig. 7, it can be seen that when the DC grounding poles operate in the same polarity, the current fields in the ground will superimpose on each other, leading to a further increase in the risk of DC bias in the substation; while when the DC grounding poles operate in different polarity, the current fields formed in the ground by the incoming low currents in the ground will cancel each other out, which will instead reduce the risk of DC bias.

4.2 DC Bias Risk Theory for Superimposed Multiple DC Projects

In fact, there is a certain operating probability of DC bias operation after considering the superposition of multiple DC projects. Generally, the probability of unipolar earth return operation in DC projects will be around 1%, and if two DC transmission projects occur at the same time, the probability of unipolar earth return operation will

drop to around 1/10000, so generally in the actual engineering background, three DC projects will not be considered to occur at the same time, the unipolar earth return operation.

The risk of DC bias under the action of two DC projects can be equated to the vector superposition of ground potential and incoming current after the action of two DC grounding poles alone, and the risk of DC bias of transformer can be evaluated by the superposition value of DC current at neutral point. In this case, the neutral DC currents of the transformer can be linearly superimposed as follows:

$$\tilde{I}_{DC} = \sum_{i=1}^{p} I_{DC}(P_i) \tag{1}$$

in which p is the number of DC transmission projects, P_i is the specific DC transmission project, and I_{DC} is the transformer neutral DC current due to P_i.

5   Conclusion

This paper takes the central China power grid as the research object, and evaluates the DC bias risk in central China through field research, field test, simulation calculation and theoretical analysis, and proposes the DC bias risk analysis method under the action of multiple DCs, the main conclusions are as follows:

(1) Through the operation data of nine DC grounding poles put into operation in central China, the probability of single earth return operation of general DC grounding poles is obtained to be about 1%, and it is clear that the situation of single earth return operation of three DC grounding poles at the same time will not occur in actual projects basically;

(2) When multiple DC grounding electrodes occur simultaneously in single earth return operation, the ground potential, neutral point ground current and transformer DC biomagnetic current can be equated to the vector superposition of a single DC grounding electrode acting alone;

(3) Multiple DC grounding electrodes in close proximity to each other in the same area can be adjusted to achieve effective reduction of DC bias risk in DC grounding electrode attached substations by adjusting the operation of DC grounding electrode single earth return.

References

1. Wu L, Zhang L, Zhou Q, Li C (2022) Research on microgrid energy dispatching optimization strategy based on reinforcement learning. Control Eng 29(07):1162–1172 (in Chinese)

2. Li Q (2022) Research on Shanxi's energy transformation and development under the goal of carbon peak and carbon neutralization. Electric Age 12:6–9 (in Chinese)
3. Li L (2004) Development of DC transmission technology and its role in China's power grid. Electr Equipment 5(11):1–3 (in Chinese)
4. Chen J, Li G, Tong X, Li W, Tan W, Lu H (2022) Study on the electroosmosis effect and overflow density limit of high-voltage DC grounding electrode. High Voltage Technol 1–9 (in Chinese)
5. Wang W, Lu H, Wang Y et al (2022) Study on the temperature rise characteristics and calculation method of vertical DC grounding electrode. Smart Power 50(12):7–12 (in Chinese)
6. Zhang L, Wu G, Fan J et al (2013) Research on DC magnetic biasing characteristic of converter transformer for AC/DC corridor-sharing power transmission system. Power Syst Technol
7. Zhang Y, Pu Y, Lu Y, Gong X, Wu F (2021) Study on the control and protection strategy of mutual grounding poles for the two circuit UHVDC project in Meilishan, Brazil. Grid Technol 45(03):1223–1230 (in Chinese)
8. Zhou X, Zhou Z, Ma Y (2012) Research on DC magnetic bias of power transformer. Procedia Eng 29:452–455
9. Zhiq, Yan W, Yang Q et al (2000) Study of the DC-biased magnetization and estimation of magnetic field and iron loss of DC-biased electromagnetic systems. In: International conference on electromagnetic field problems and applications
10. Wu C, Li X, Ruan L, Tan B, Lu Z, Zhou T (2022) Evaluation and suppression of DC bias for UHV DC grounding nearby new energy access to the grid. High Voltage Technol 48(10):4172–4180 (in Chinese)
11. Chen J, Wang D et al (2019) Influence of DC-biased magnetic induction on magnetic property of silicon steel. IEEE Trans Magn
12. Luo L, Zhao H, Yang Z, Ma J, Zhu Y, Wu W (2020) Critical site identification method for bias DC distribution under multi DC monopole operation. Electr Meas Instrum 57(23):54–62 (in Chinese)
13. Sun B, Luo Z, Yu Y et al (2020) Study on DC bias of $\pm$ 1100 kV Changji converter station and $\pm$ 800 kV Tianshan converter station. High Voltage Apparatus 56(08):121–127 (in Chinese)
14. Yang N, Chen Y, Pan Z et al (2018) Prediction and treatment of the DC bias effect on the receiving terminal power grid of the Zhundong Wannan $\pm$ 1100 kV UHV DC transmission project. Power Grid Technol 42(02):380–386 (in Chinese)
15. Duan L, Jiang A, Fu Z et al (2014) The impact of single-pole operation of multiple DC grounding systems on DC bias in Huxi UHV substation. Power Grid Technol 38(01):132–137 (in Chinese)
16. Liu Y, Fu C, Zhao W, Wu X (2021) Research on the influence of DC grounding electrode operation mode adjustment process on transformer DC bias. High Voltage Apparatus 57(12):110–116+124 (in Chinese)
17. Zhou Y (2021) Study on the operation status of DC grounding pole of Tianguang project. Kunming University of Science and Technology (in Chinese)
18. Guo Q (2015) Influence of DC Bias on AC-DC hybrid system operation and power system active response countermeasure research. Huazhong University of Science and Technology (in Chinese)

Molecular Simulation of ZnBDC Adsorption for C_4F_7N/CO_2 and Its Decomposition Products

Keli Gao, Wei Liu, Yin Huang, Xianglian Yan, Taiyun Zhu, Menglei Jin, Song Xiao, and Yi Li

Abstract The gas mixture of C_4F_7N/CO_2 is considered as a leading choice and environmentally conscious solution for gas insulation. To maintain the stability of gas insulating equipment and ensure the safety of operation and maintenance personnel, it is crucial to choose suitable materials for treating C_4F_7N mixture and its decomposition products. One potential material for adsorption is ZnBDC, which belongs to the metal organic frameworks. Therefore, studying the interaction mechanism between ZnBDC and C_4F_7N mixture and its decomposition products can provide a theoretical basis for selecting suitable adsorbents for C_4F_7N/CO_2 gas insulating equipment. In this study, we utilized GCMC simulation to investigate the adsorption process of C_4F_7N/CO_2 gas mixture and its nine decomposition products in ZnBDC. By conducting a simulation of competitive adsorption with equal proportions, we derived the distribution of adsorption density, adsorption isotherm, and isosteric heats. Furthermore, a schematic diagram of CO molecules adsorbed inside the ZnBDC cage was demonstrated. The results suggest that ZnBDC has good adsorption performance for decomposition products with little effect on C_4F_7N. Therefore, it is a potential candidate for an adsorbent in C_4F_7N/CO_2 gas insulating equipment.

Keywords C_4F_7N/CO_2 · Decomposition products · ZnBDC · Molecular simulation

K. Gao · Y. Huang · X. Yan
China Electric Power Research Institute Co., Ltd., Beijing 100192, China

W. Liu · T. Zhu
Electric Power Research Institute of State Grid Anhui Electric Power Co., Ltd., Anhui 230601, China

M. Jin (✉) · S. Xiao · Y. Li
School of Electrical Engineering and Automation, Wuhan University, Hubei 430072, China
e-mail: 1277407676@qq.com

1 Introduction

Sulfur hexafluoride (SF_6) is a synthetic gas that has been widely used in high-voltage electrical equipment due to its excellent insulation and arc extinguishing properties [1]. The power industry accounts for more than 80% of approximately 10,000 tons of SF_6 produced worldwide each year [2]. Despite its effectiveness, SF_6 is known to be the greenhouse gas with the highest global warming potential to date. The long atmospheric lifetime of SF_6 and its strong ability to absorb 10.5 μm infrared radiation means that each kilogram of SF_6 emitted has a greenhouse effect equivalent to 23.9 tons of CO_2. The lack of effective measures to treat and recover SF_6 gas released into the atmosphere leads to a gradual accumulation of its global warming effect, which poses a permanent threat to the atmospheric environment. As the SF_6 industry grows rapidly, the pressure on environmental protection is increasing. As a result, finding new insulating gases that can replace SF_6 has become a critical topic in the interdisciplinary fields of electrical and chemical science.

Perfluoroisobutyronitrile (C_4F_7N) is a gas insulation material renowned for its remarkable insulation capabilities and low impact on global warming. Despite its high liquefaction temperature of 4.7 °C, C_4F_7N can be combined with CO_2 or other compatible buffer gases. This combination allows for its efficient application in gas insulation devices [3–5]. However, prolonged operation of gas-insulated switchgear can lead to decomposition of the insulating medium as a consequence of local over-heating and discharge phenomena. When C_4F_7N mixtures are involved, the decomposition can generate hazardous and corrosive gases, some of which can adversely affect the insulating characteristics of the mixtures. To address this, adsorption materials are commonly installed within the switchgear chamber. These materials serve to absorb the decomposition products, enabling the gas insulation equipment to maintain stable operation for a longer duration [6–9]. This study focuses on the investigation of nine decomposition products (CO, CF_4, C_2F_6, C_3F_8, C_3F_6, CF_3CN, C_2F_5CN, C_2N_2 and COF_2).

Currently, gas-insulated equipment commonly employs porous materials like molecular sieves and activated alumina as adsorbents [10, 11]. Nevertheless, previous studies have indicated that the adsorption efficiency of decomposition products in C_4F_7N mixtures is not optimal, and these adsorbents can also impact the primary gas C_4F_7N. One potential solution lies in the utilization of a metal–organic framework (MOF) called zinc benzene dicarboxylate (ZnBDC). ZnBDC is a porous material renowned for its remarkably high internal surface area, rendering it suitable for various applications related to gas separation, storage, and adsorption. This research paper aims to employ GCMC simulations to predict the performance of ZnBDC in the treatment and detection of decomposition components present in C_4F_7N/CO_2 gas mixtures. The outcomes of this study can provide valuable theoretical support for future endeavors. Furthermore, we examine the interaction characteristics between ZnBDC and C_4F_7N/CO_2, as well as its decomposition products.

Fig. 1 Optimized ZnBDC
supercell structure
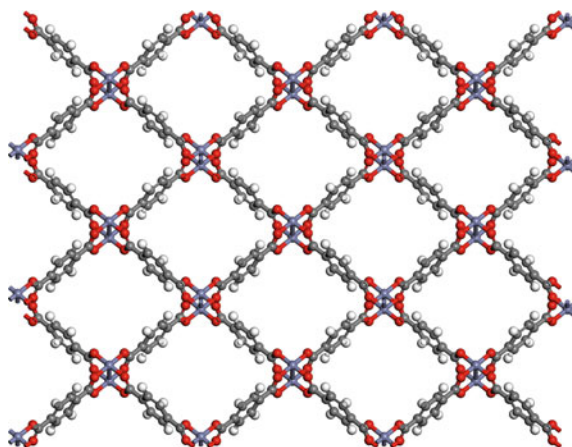
2 Simulation Details

2.1 Adsorption Model

The adsorption investigations were conducted in Materials Studio, utilizing structures constructed based on the Cambridge Crystallographic Data Centre (CCDC). Prior to performing Grand Canonical Monte Carlo (GCMC) simulations, the C$_4$F$_7$N/CO$_2$ gas mixture and its nine decomposition products (CO, CF$_4$, C$_2$F$_6$, C$_3$F$_8$, C$_3$F$_6$, CF$_3$CN, C$_2$F$_5$CN, C$_2$N$_2$ and COF$_2$) underwent geometric optimization using the Forcite code. Additionally, the guest molecules underwent the application of electrostatic potential (EPS) charges. To ensure simulation precision and satisfy the condition that the length of the three spatial dimensions was greater than twice the cutoff radius, a 5 * 3 * 3 supercell model was employed for ZnBDC. The Universal force field was employed to describe the MOF parameters, and geometry optimization was achieved using the forcite module to attain a stable geometry, as depicted in Fig. 1.

2.2 GCMC Simulation

In the study, both solid structures of the adsorbate molecules and ZnBDC were taken into consideration. The electrostatic interactions were treated using the Ewald method, while the van der Waals interactions were treated using the Atom-based method. Prior to running the sorption module, the symmetry of ZnBDC was changed to P1. The simulation consisted of 1×10^5 steps to achieve equilibrium. Subsequently, 1×10^6 production steps were performed to sample thermodynamic properties. To simulate equal proportion competitive adsorption, the sorption module was employed, utilizing the Universal forcefield and the Metropolis method. The

temperature was set at 298 K and the fugacity of both the C_4F_7N mixture and its decomposition products were maintained at the same level, ranging from 10^{-15} to 100 kPa.

3   Results and Discussion

Through the implementation of equal proportion competitive adsorption simulations, significant findings were obtained, including the distribution of adsorption density, adsorption isotherm, and isosteric heats.

Figure 2 displays the adsorption density distribution, which provides insights into the distribution of adsorption sites and the corresponding density distribution of the adsorbate at those sites. The analysis of the data reveals that the gas molecules are primarily concentrated within the ZnBDC pore cage.

Figure 3 presents the adsorption isotherm for the equal proportion competitive adsorption simulation. It is evident from the figure that ZnBDC demonstrates a notable capability for adsorbing the decomposition products of the C_4F_7N mixture during equal proportion competitive adsorption. The adsorption behavior of different decomposition product molecules in ZnBDC significantly varies in response to pressure. CO molecules exhibit low initial adsorption efficiency but rapidly increase with increasing pressure. In contrast, CF_4 exhibits relatively high initial adsorption efficiency but decreases sharply with pressure, indicating weaker interaction strength between CF_4 and the active sites of ZnBDC when compared to other C_4F_7N decomposition components. Overall, CO, CF_3CN, C_2N_2, C_2F_6, and COF_2 are more dominant in competitive adsorption, exhibiting higher adsorption capacity. The obtained results provide conclusive evidence that ZnBDC exhibits a preference for adsorbing the decomposition products of the C_4F_7N mixture, while exerting minimal influence on the primary gas insulation medium within the equipment.

Fig. 2 Adsorption density distribution of ZnBDC
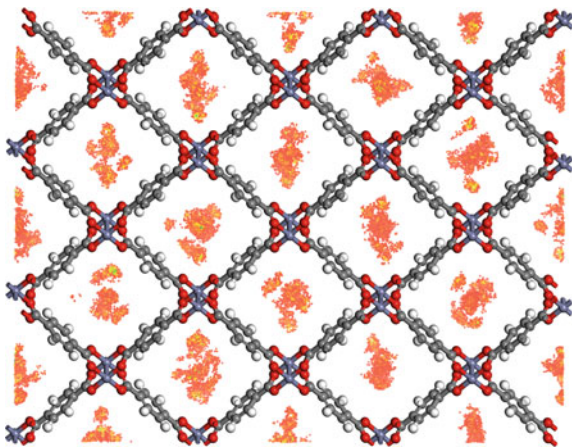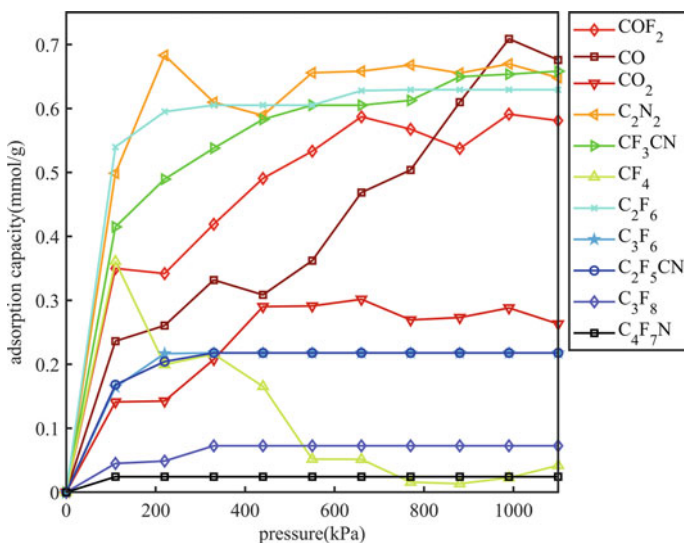
Fig. 3 Adsorption isotherm of ZnBDC

Figure 4 displays the isosteric heats obtained from the simulation of equal proportion competitive adsorption. The range of adsorption heats observed falls within the range of 30–100 kJ/mol, suggesting that physical interactions predominantly drive the adsorption process. The high adsorption heat of molecules such as CF_3CN suggests a strong adsorption effect, which explains their high adsorption capacity. However, molecules such as C_2F_5CN and C_4F_7N exhibit high adsorption heat but low adsorption capacity, implying that adsorption performance is influenced not only by adsorption heat but also by other factors, such as molecular volume, polarity, and functional groups.

In addition, CO with the greatest adsorption capacity was chosen to simulate its distribution within ZnBDC. The simulated pore structure of ZnBDC and the distributions of guest gas molecules are presented in Fig. 5. The figure illustrates that CO is effectively adsorbed inside the ZnBDC pore cage, and that each pore cage can accommodate multiple small-volume gas molecules similar to CO.
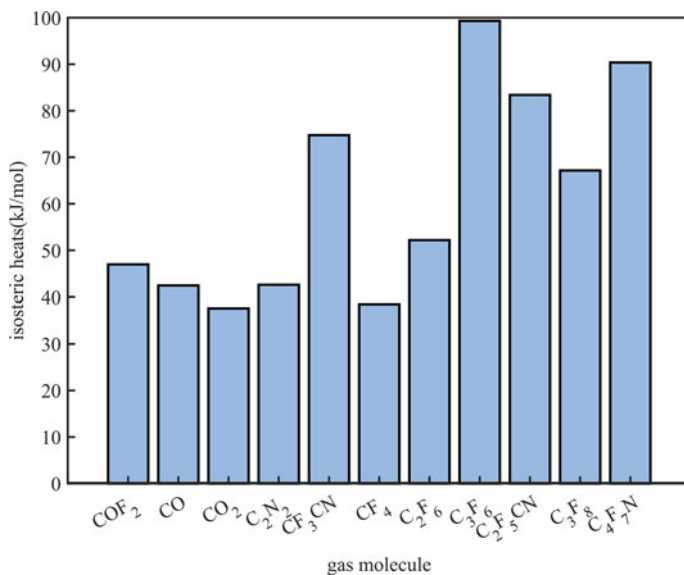
Fig. 4 Isoteric heats of ZnBDC
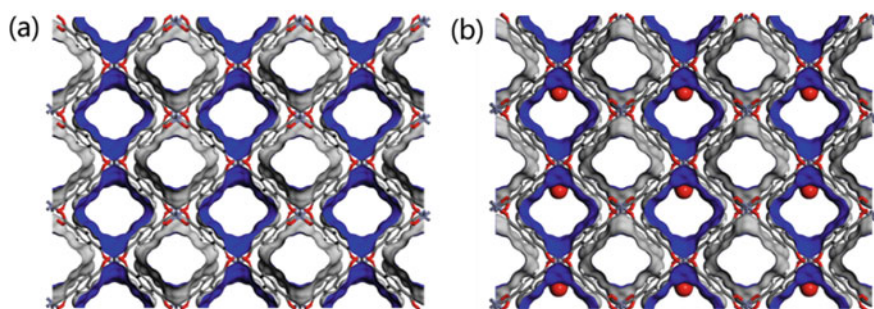
Fig. 5 **a** Pore structure of ZnBDC **b** GCMC simulations of guest inclusion structure for ZnBDC

4 Conclusion

In this study, we conducted a simulation of equal proportion competitive adsorption for the C_4F_7N mixture and its decomposition products to evaluate the adsorption characteristics of ZnBDC. The adsorption density distribution, adsorption isotherm, and isoteric heats were obtained. Additionally, we displayed the simulated pore structure of ZnBDC and the distributions of guest gas molecules. Our analysis reveals that the gas molecules are predominantly distributed within the ZnBDC pore cage. The outcomes of our research provide evidence that ZnBDC has a minimal influence on the primary gas insulation medium utilized in equipment. Additionally, ZnBDC

exhibits a notable adsorption capacity for the decomposition products derived from the C_4F_7N mixture. The adsorption capacities of CO, CF_3CN, C_2N_2, C_2F_6, and COF_2 are relatively high, and they perform well in competitive adsorption. Furthermore, we found that adsorption performance is influenced not only by adsorption heat but also by other factors, such as molecular volume, polarity, and functional groups. Moreover, our study suggests that the pore cages of ZnBDC can accommodate multiple small-volume gas molecules similar to CO. Further experimental studies can help elucidate the adsorption performance of ZnBDC, and other potential adsorbents should also be explored.

References

1. Boggs S (1989) Sulphur hexafluoride—a complex dielectric. IEEE Electr Insul Mag 5(6):16–21
2. Kieffel Y, Irwin T, Ponchon P et al (2016) Green gas to replace SF_6 in electrical grids. IEEE Power Energy Mag 14(2):32–39
3. Li Y et al (2019) Experimental study on the partial discharge and AC breakdown properties of C_4F_7N/CO_2 mixture. High Volt 4(1):12–17
4. Gao K et al (2020) Progress of technology for environment-friendly gas insulated transmission line. Trans China Electrotech Soc 35(1):3–20 (in Chinese)
5. Wang Y et al (2022) Research on infrared spectrum characteristics and detection technology of environmental-friendly insulating medium $C_5F_{10}O$. Vib Spectrosc 118:103336
6. Simka P et al (2017) Decomposition of alternative gaseous insulation under partial discharge. In: Proceedings of the 20th international symposium on high voltage engineering. Buenos Aires, Argentina, pp 28
7. Li Y et al (2020) Influence regularity of O_2 on dielectric and decomposition properties of $C_4F_7N–CO_2–O_2$ gas mixture for medium-voltage equipment. High Volt 5(3):256–263
8. Wang C et al (2019) Decomposition products and formation path of C_3F_7CN/CO_2 mixture with suspended discharge. IEEE Trans Dielectr Electr Insul 26(6):1949–1955
9. Yang T et al (2021) Experimental study on decomposition products of C_4F_7N/CO_2 mixture under different fault conditions. High Volt Eng 47(12):4216–4228 (in Chinese)
10. Su Z, Zhao Y (2013) Experimental investigation into effects of adsorbent on detection of SF_6 decomposition products in SF_6 equipment. High Volt Appar 49(6):26–37 (in Chinese)
11. Tang J et al (2013) Experiment and analysis of two adsorbents on the adsorption of characteristic components of SF_6 decomposition. Proc CSEE 33(31):211–219 (in Chinese)

Study on the Surface Charge Accumulation and Dispersion Process of Polyimide for New Cables

Yanru Wang, Yi Tian , Xinbo Huang , Haonan Shi, Guixin Zhu, Zhiwei Li, and Shuai Wang

Abstract High voltage cables are key factors that determine the quality and capacity of power transmission. Polyimide has been widely concerned for its excellent thermal stability and electrical insulation properties, and has been used in the development of cable insulation materials. The surface charge of insulating material has an important influence on the performance of the material. It can not only distort the electric field around itself, but also provide a discharge channel for surface discharge, which affects the safe and stable operation of power system. In this paper, the surface of polyimide for new cables is subjected to voltage treatment by needle-plate electrode, the surface potential is measured by electrostatic probe method, and the surface charge is calculated by inverse mathematical method. The surface charge accumulation distribution characteristics of the polyimide under different applied voltage times and amplitudes and the surface charge dissipation distribution characteristics under different dissipation time under DC high voltage are obtained. The experimental results show that increasing the time and amplitude of voltage applied to the polyimide can promote the accumulation of electric charges. The surface electric charges take on the form of charge patterns and are unevenly distributed. On the whole, compared to the edge position of the material, the charge density at the center position is greater, and in this case, the surface electric charge distribution does not have similarity. In the decay process, the surface potential of the center of the material decays faster than the surrounding, forming a bell shape. Under the action of the electric field, the surface charge pattern presents a positive and negative alternating phenomenon.

Keywords Surface charge · Polyimide · Charge accumulation · Charge dissipation · Inversion calculations

Y. Wang · Y. Tian (✉) · X. Huang · H. Shi · G. Zhu · Z. Li · S. Wang
Xi'an Polytechnic University, Xi'an 710600, China
e-mail: tianyi@xpu.edu.cn

1 Introduction

With the development of the national economy, the power users have higher requirements for the security and reliability of the power system. Power cables have high reliability in transmission lines, so they are widely used in transmission and distribution, electric power and other fields [1, 2]. With the rapid development of cable, the insulation performance of polymer materials in DC electric field has been paid great attention by researchers. In recent years, researchers have found that when a certain electric field is applied around the polymer material, a certain charge will accumulate on the surface of the material, which is called surface charge [3, 4]. The existence of surface charge has an important impact on the performance of the material, for the transmission cable in the power system, it will cause the surface insulation strength to reduce, causing surface flashover, is an important cause of line failure [5, 6]. Studying the mechanism of surface charge generation and attenuation, and mastering the influence of surface charge on the insulation performance of insulating materials, is helpful to further provide basis and guidance for the modification treatment and insulation optimization of insulating media [7]. Therefore, it is of great theoretical significance and scientific and technological value to study the charge accumulation and dissipation on the surface of polyimide dielectric under DC high voltage to ensure the safe use of power system.

In recent years, scholars have carried out a large number of experimental studies on the surface charge accumulation phenomenon of polymer dielectrics, and have achieved significant research results. Cherukupalli et al. conducted a study on the surface charge distribution of polytetrafluoroethylene insulators under DC voltage, and found that, under other conditions that remain unchanged, the surface charge of the insulator will undergo polarity reversal due to the increase in the pressurization amplitude [8]. Nakanishi et al. studied the relationship between the surface charge accumulation and the polarity of the applied voltage, and measured it by dust diagram method and electrostatic probe method. Finally, it was found that only negative charge accumulated on the surface of the material when the negative voltage was applied to the material. When a positive voltage is applied to the material, both positive and negative charges accumulate on the surface of the material, but the positive charges are more than the negative charges [9]. Wang Dibo conducted an experimental study on the dynamic accumulation and dispersion process of surface charges on insulators. The distribution characteristics of surface charges after accumulation and dissipation were measured under different conditions. The results showed that the speed of charge dissipation would be different due to different pressurization methods. At the same time, the influence of temperature on the distribution of surface charge after aggregation and dispersion is also studied. The results show that the distribution characteristics of surface charge accumulation will be different according to the increase in the time and amplitude of the applied voltage. The longer the voltage is applied, the faster the surface charge accumulation. Similarly, the larger the voltage amplitude is applied, the faster the surface charge accumulation. The polarity of the applied voltage will also affect the charge distribution [10]. Zhou Wu carried

out research and analysis on the reasons for the different distribution of surface charge accumulation of insulators and also studied their dissipation characteristics, through the dissipation process of surface positive charge under different applied voltages [11]. Gremaud et al. found through experimental studies that temperature can affect the surface charge dissipation rate, and the surface charge dissipation rate will accelerate with the increase of temperature [12].

Polyimide has extremely high heat resistance, can withstand high temperatures above 500 °C, and has good dielectric insulation and radiation resistance. Due to these good properties, polyimide materials in the microelectronics industry insulation has a wide range of applications. Therefore, in this paper, polyimide polymer insulation material is selected as the sample, and the needle-plate electrode is used to pressurize the surface of the specimen, and the surface charge is measured by the electrostatic probe method, and the distribution characteristics of the surface charge under different conditions are obtained, which lays a good foundation for the application of subsequent polyimide new cables.

2 Method for Calculating Surface Charge of Polyimide Polymers

The measurement system of this experiment can only measure the size of the surface potential, cannot directly obtain the surface charge distribution. To obtain the surface charge distribution results, it is necessary to convert them through mathematical methods. Currently, researchers commonly use the inversion calculation method.

The inversion calculation method is based on the theory of electrostatic field, and its basic idea is to first measure the surface potential of the material, and then divide the surface of the insulating material into a grid, find the correlation matrix of each small grid charge, and invert this correlation matrix to obtain the potential-charge conversion matrix. Finally, the surface charge distribution of the insulating material is obtained through the mathematical process of inverse calculation [13]. According to the idea of finite element division, the surface of the insulating material is divided by finite elements, and the total number of divisions is N. When N is large enough, the surface of the insulating material is divided into small enough surface charge cells, at which point the charge of each finite element surface can be considered uniformly distributed [14]. According to the principle of potential superposition, the electrostatic probe measures each potential and then stacks it in a linear combination.

First, the experimental device model is established, the model is meshed, and then the divided grid is numbered in turn, a total of 100 grid elements. Set the charge density of the upper surface of one of the grids to unit 1 and the rest to 0 to obtain the potential distribution of the surface of the medium at this time, which is equal to the first column of the matrix H^{-1}. H^{-1} depends on the physical structure of the sample and does not change with the change of surface charge distribution, therefore, according to the same calculation principle, the second grid is calculated. The surface

charge density is also set to be unit 1, and the rest is 0, and the potential distribution of the surface of the medium at this time is obtained. The vector is equal to the second column of the matrix H^{-1}. And so on, repeat 100 times, and finally get the complete matrix H^{-1}.

The potential—charge conversion matrix [H] can be obtained by inversing the matrix H^{-1}. The surface charge distribution can be obtained by multiplying the matrix with the surface potential data. To facilitate the calculation, the surface charge density will be calculated by joint programming of COMSOL and MATLAB.

3 Surface Charge Measurement Experiments

3.1 Preparation of Test Sample

The thin film polyimide is used as the sample, with a length of 28 mm, a width of 28 mm, and a thickness of 0.125 mm. Apply a conductive film to one side of the sample to accumulate surface charges. Before the experiment starts, roughly clean the dust on the surface of the sample for use.

3.2 Charge Measurement System

To achieve the measurement of the surface potential of polymer materials, a set of measuring system was built. Firstly, a voltage is applied to the surface of the material through a high-voltage power supply system connected with a needle-plate electrode. Secondly, the surface charge is measured by an electrostatic probe method. Therefore, Calvin probes were chosen as the tool for measuring surface potential. It works by moving the Calvin probe above the dielectric to be tested, and the Calvin probe measures the resulting potential as U_1. Assuming the actual potential of the dielectric is U_2, there is a constant potential difference between the Calvin probe and the dielectric, so there is an equivalent capacitance C between the two. Since distance has a certain relationship with C, when the distance changes, C also changes. Since the potential difference remains constant, the amount of charge q caused on the probe must be increased or decreased to accommodate the change in C, so that the probe's power circuit has a corresponding current.

According to the measuring principle of Calvin probe, the oscillator is used to oscillate back and forth in a fixed position of the probe, and when the probe output current is 0, the probe potential is equal to the dielectric potential $U_1 = U_2$. In this way, the probe potential can be regarded as the surface potential of the material.

To ensure the accuracy and validity of the measurement results, a motion control system is used to control the movement of the specimen to facilitate potential measurement at each point. The measured data is connected to the computer through

a digital multimeter, and the measured data is exported to Excel for subsequent data processing.

3.3 Surface Charge Accumulation and Dissipation Experiments

Place the sample in the center of the electrode plate, measure its surface potential to ensure that there is no accumulated charge on its surface, and perform the experiment at room temperature of 25 °C. The corona charged method is used to pressurize the surface of the sample, the needle electrode is connected with high-voltage DC power supply. The plate electrode is grounded, and 4, 5, 6, 7 kV voltage is applied between the needle plate electrodes. After pressurization for different time, the voltage was removed, and the needle electrode was removed to make it far away from the sample. According to the specification of the tested product, determining the motion track of the measuring probe, and compiling the related motion program to control the measuring probe to complete the measurement work. During measurement, the probe shall move linearly to approach the surface of the test article, adjust the distance when facing the surface of the test article, and keep it about 3 mm away from the surface for measurement. During the whole measurement process, the measuring probe shall be right and perpendicular to the test article, and keep a certain distance. In the charge dissipation experiment, the voltage of 4, 5, 6 and 7 kV were applied to the sample, and the center point position was measured after 30 min of dissipation, and the dissipation law was obtained. After the measurement process, the data is recorded and the surface potential information of the obtained sample is stored, and then converted by mathematical methods to finally obtain the distribution map of the surface charge density of the insulating material. After the whole experiment, sort out the experimental instruments and treat the surface of the tested product to facilitate the smooth progress of the next experiment.

4 Measurement Results and Analysis

In the surface charge measurement experiment, the amplitude of the voltage applied to the polymer material was 4–7 kV at room temperature of 25 °C, and the charge distribution during accumulation and dissipation was measured, respectively. When a DC high voltage is applied between the needle-plate electrodes, the air near the tip of the needle is ionized to form a corona discharge, and the charged particles migrate to the surface of the specimen under the action of electric field forces to form a surface charge.

4.1   Surface Charge Accumulation

Figure 1 shows the surface charge accumulation when pressurized 6 kV at different times. (a) Shows 30 min pressurization, due to the short pressurization time, the area of the central red area is not very large, showing that the potential amplitude in the middle position of the specimen surface is greater than the distribution state of the edge position of the specimen. (b) Shows that the surface potential increases for 1 h with increased surface potential and increased area in the center red area. Similarly, the potential amplitude is greater than the edge of the specimen surface. (c) Shows the surface potential of the specimen after 2 h of applied voltage, when the red and green parts occupy most of the area, and the amplitude of the center potential of the specimen surface reaches nearly 2400 V. This is because during the corona charging process, the electric field line under the tip of the needle is the densest, and more charge is easy to accumulate here under the action of electric field force.

In summary, due to the large number of measured data, the line chart is drawn from the intermediate potential data under different pressurization times, which is easy to analyze the surface potential change characteristics. As shown in Fig. 2, the middle position potential size is 928.57 V when pressurized for 30 min, the middle position potential size is 2180.29 V when pressurized for 1 h, and the intermediate position

(a) Applied voltage for 30min   (b) Applied voltage for 1h

(c) Applied voltage for 2h
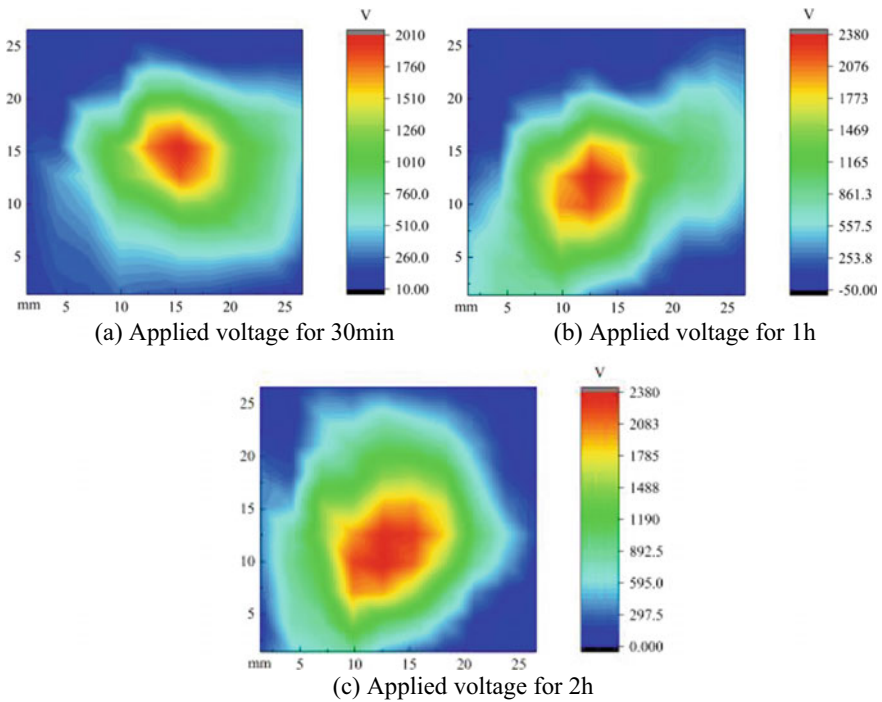
Fig. 1   Simulation results of charge accumulation at different pressurization times

Fig. 2 Variation trend of surface potential under different voltage application times
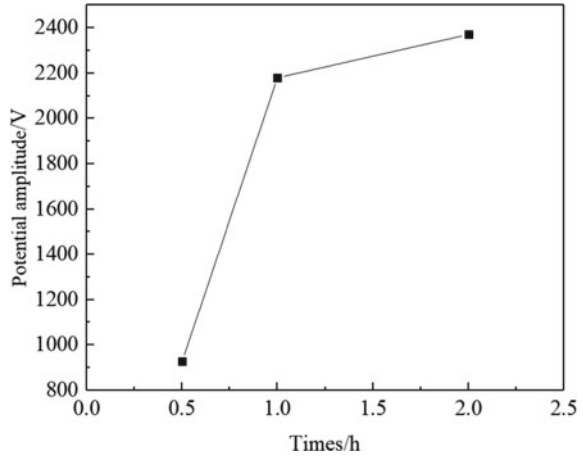
potential size is 2370.79 V when pressurized for 2 h. According to the experimental data, the increase in voltage application time causes the surface potential to increase under corona charging conditions. The potential growth rate is first fast and then slow, indicating that the potential size does not increase with the increase of pressurization time, but gradually tends to saturation.

4.2 Surface Charge Dissipation

Figure 3 shows the surface charge distribution characteristics when dissipated at different times after applying the same voltage. (a) Shows the surface potential after 0.5 h of pressurization. (b) Shows the surface potential after 1 h of dissipation, and the dissipation rate is very fast. (c) Shows the surface potential distribution after 4 h of dissipation. The surface potential of the test sample is significantly slower than the previous two hours, and there are still most areas where the surface charge is not completely dissipated, which indicates that the charge accumulated on the surface of the polymer material cannot be completely dissipated for a long time. During the dissipation process, the shape of the charge distribution remains basically unchanged, indicating that the rate of charge dissipation at each point is basically the same.

There are many data on the surface potential change in the dissipation process, so the line chart is drawn by taking the potential value of the same position at different dissipation times, which is easy to observe the potential dissipation characteristics. As shown in Fig. 4, the surface charge dissipation results at the center point of the sample surface. In the first 2 h, the surface potential dissipation rate is faster, after which the surface potential dissipation rate gradually slows and approaches 0 potential, but does not completely dissipate. Figure 5 shows the potential change trend under the same dissipation time for different applied voltage amplitudes, and the potential change trend in the figure is linear function attenuation.

(a) Dissipate for 0min

(b) Dissipate for 1h

(c) Dissipate for 4h
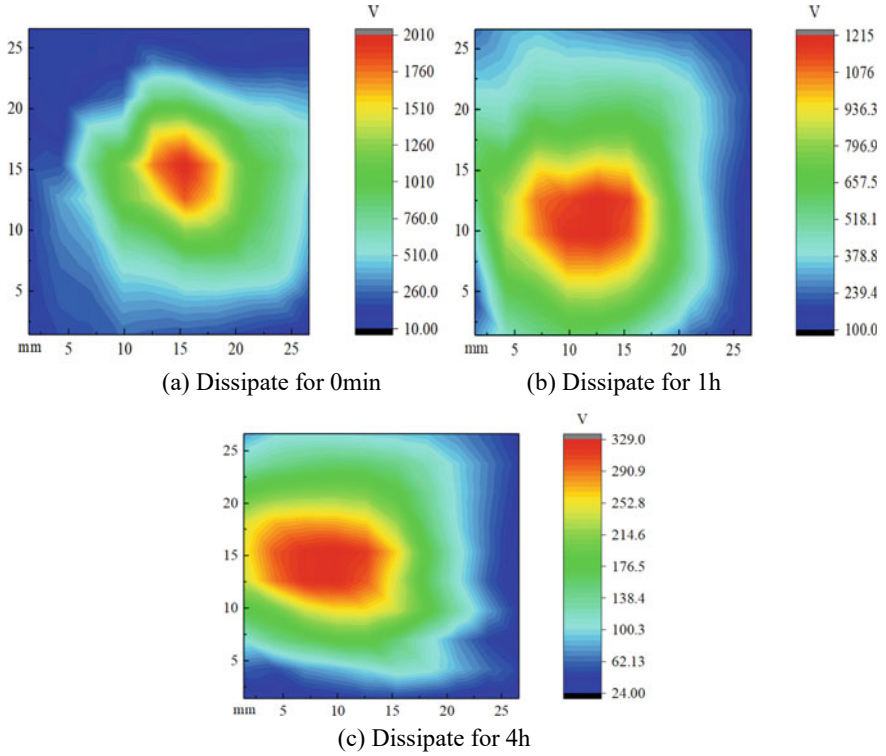
Fig. 3 Charge distribution characteristics at different dissipation times

Fig. 4 Potential attenuation
trend under dissipation of the
same applied voltage
amplitude at different times
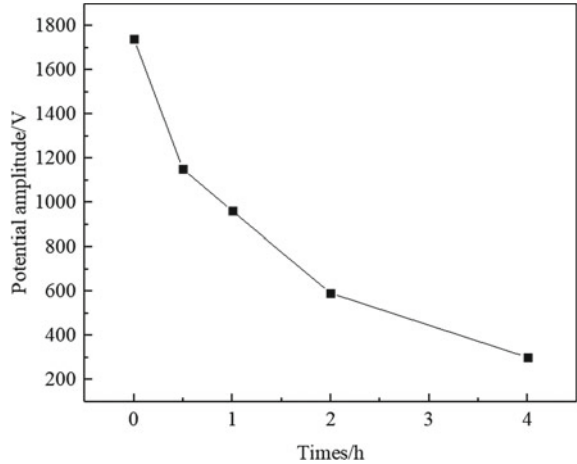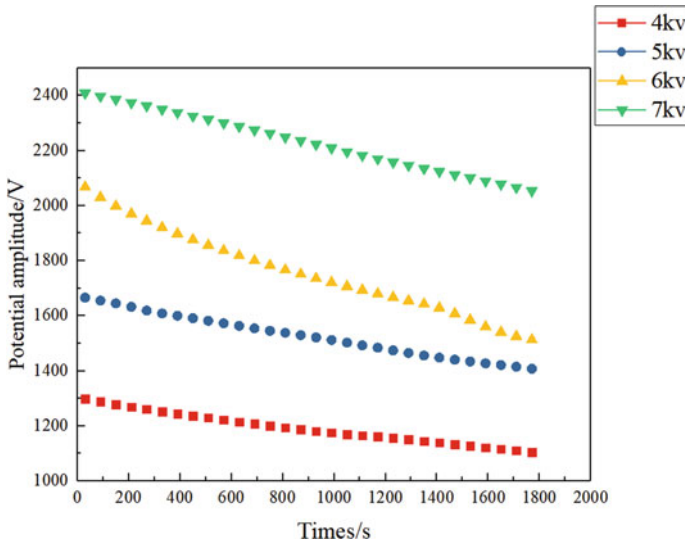
Fig. 5 Potential attenuation at different amplitudes dissipation

According to Kindersberger et al., when the surface charge is mainly dissipated through the gas side, the area with high charge density is easy to absorb the heterogeneous charge due to the large field strength. Therefore, the charge decay at the peak of the cone curve is the fastest, so that the charge distribution pattern changes to the bell shaped distribution, as shown in Fig. 6. Therefore, the gas side dissipation belongs to the main dissipation path in this experiment.

Fig. 6 Potential attenuation at different times
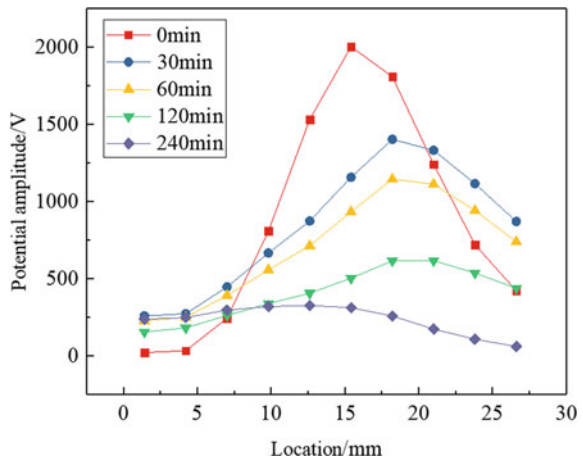
4.3 Surface Charge Distribution

Through the above charge density conversion method and the measured surface potential size, the surface charge density distribution is calculated as shown in Fig. 7. A voltage of 6 kV is applied to the surface of the material, and the density gradually increases with time, and the surface of the material presents a state of high intermediate density and small edge density.

During dissipation, the surface charge dissipates rapidly during the first two hours, slows down after two hours, and does not dissipate completely for a long time, as shown in Fig. 8.

(a) Applied voltage for 30min   (b) Applied voltage for 2h
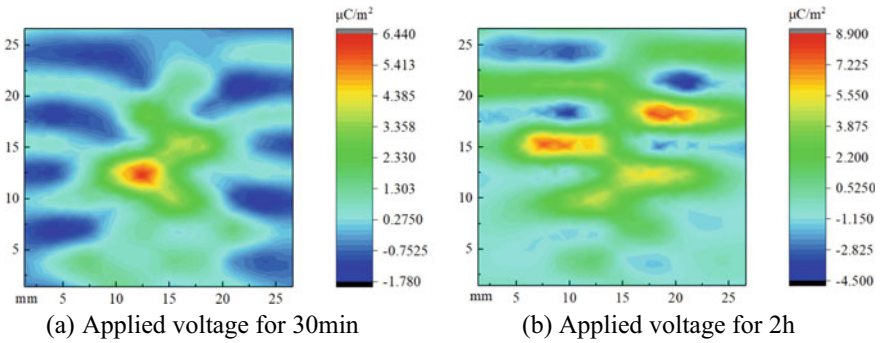
Fig. 7   Charge density distribution at different applied voltage times

(a)Dissipate for 30 min   (b) Dissipate for 2h
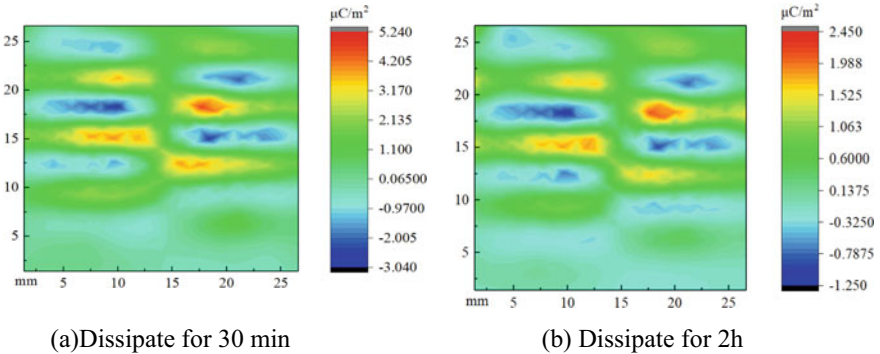
Fig. 8   Charge dissipation surface charge density distribution plot

5 Conclusion

The existence of surface charges on polyimide used for new types of cables has an important impact on the performance of materials. In this paper, an experimental study on the accumulation and dissipation of surface charges has been carried out on a constructed surface charge experimental measurement platform. A needle plate electrode structure is mainly used to apply voltage to the surface of the test object. After applying the voltage, the surface charges are quickly measured. As the measured potential needs to be converted into surface charges through mathematical methods, The effects of different voltage amplitudes and applied voltage times on surface charge accumulation and dissipation are analyzed, and the following main conclusions are obtained:

(1) Polyimide is a kind of polymer material, whose molecular structure contains a large number of repetitive imide groups, which can form linear or cross-linked structures during the polymerization process. When polyimide materials have charges on their surfaces, these charges repel each other, leading to the aggregation of molecular chains on the surface to form a certain shape. Under DC high voltage, with the same voltage amplitude, the potential amplitude and charge density of the surface area of polymer materials become larger and higher as the voltage application time increases. At the same time, as the voltage amplitude increases, the potential amplitude of the surface area of polymer materials becomes larger and larger, and the charge density becomes higher and higher. Increasing the time and amplitude of voltage applied to polymer materials can promote the accumulation of electric charges. Surface charges take the form of charge patterns and are unevenly distributed. On the whole, the charge density at the center is higher than that at the edge of the material, and in this case, the surface charge distribution is not similar.

(2) During the attenuation process, the potential of the central surface of the material decays faster than the surrounding area, forming a bell shape. Under the action of the electric field, the surface charge pattern exhibits a positive and negative alternating phenomenon. The reason for the positive and negative alternation is that the polyimide group contains two adjacent carbon groups and a central nitrogen atom, and their electron cloud distribution causes some hydrogen atoms on the molecular chain to be positively charged and some nitrogen atoms to be negatively charged. Therefore, on the polyimide surface, these positive and negative charges attract each other, causing the molecular chains to form an alternating aggregation shape on the surface. This alternating shape can make the surface of the polyimide material more stable, and has good resistance to contamination and chemical corrosion. The surface charge dissipates rapidly in the first two hours of attenuation, and gradually slows down in two to four hours, and its surface charge does not completely dissipate and cannot be completely dissipated for a long time.

References

1. Ju T, Cheng P, Dibo W et al (2017) Development of studies about surface charge accumulation on insulating material under HVDC. Trans China Electrotechnical Soc 32(8):10–21 (in Chinese)
2. Wang T, Li X, Zhang B et al (2022) Basic reason for the accumulation of charge on the surface of polymer dielectrics. Sci China Mater 65(10):2884–2888
3. Zhang B, Qi Z, Zhang G (2017) Charge accumulation patterns on spacer surface in HVDC gas-insulated system: dominant uniform charging and random charge speckles. IEEE Trans Dielectr Electr Insul 24(2):1229–1238
4. Tu Y et al (2018) Effect of nano-TiO_2/EP composite coating on dynamic characteristics of surface charge in epoxy resin. IEEE Trans Dielectr Electr Insul 25(4):1308–1317
5. Xue JY et al (2020) Surface charge transport behavior and flashover mechanism on alumina/epoxy spacers coated by SiC/epoxy composites with varied SiC particle size. Phys D Appl Phys 53(15):155503 (16 pp)
6. Haq IU, Wang F, Akram S, Yan Y (2022) Effects of ion beam treatment on DC flashover characteristics of epoxy. IEEE Trans Dielectr Electr Insul 29(6):2064–2071
7. Gao Y, Li Z, Wang H, Yuan X (2020) Metal particle encouraged surface charge accumulation on epoxy insulator with multi-arc surface profile under DC voltage. IEEE Trans Dielectr Electr Insul 27(3):998–1006
8. Cheng P, Ju T, Dibo W et al (2017) Decay characters of charges on an insulator surface after different types of discharge. Plasma Sci Technol 19(7):97–105
9. Pan Z, Pan C, Tang J, Hu B, Luo Y, Serdyuk YV (2022) Influence of SiC/epoxy coating on surface charging phenomenon at DC voltage—part II: charge dissipation. IEEE Trans Dielectr Electr Insul 29(4):1343–1352
10. Wang T, Liu C, Li D, Hou Y, Zhang G, Zhang B (2020) Nano ZnO/epoxy coating to promote surface charge dissipation on insulators in DC gas-insulated systems. IEEE Trans Dielectr Electr Insul 27(4):1322–1329
11. Han Y, Li S, Min D (2017) Nonlinear conduction and surface potential decay of epoxy/SiC nanocomposites. IEEE Trans Dielectr Electr Insul 24(5):3154–3164
12. Sima W, Cai B, Peng Q, Sun P, Jiang X (2018) Effects of electric field and temperature on space charge characteristics in double-layered polytetrafluoroethylene films. IEEE Trans Dielectr Electr Insul 25(4):1518–1525
13. Li J, Wang Y, Dong J, Liang H, Du B, Xu Y, Li X (2022) Surface charging affecting metal particle lifting behaviors around epoxy spacer of HVDC GIL/GIS. IEEE Trans Dielectr Electr Insul 29(4):1546–1552
14. Donglai W, Tiebing LU, Yuan W, Bo C, Xuebao LI (2018) Measurement of surface charges on the dielectric film based on field mills under the HVDC corona wire. Plasma Sci Technol 20(5):55–64

Improvement of Flashover Voltage of Epoxy Resin by Large-Area Dielectric Barrier Discharge

Shijia Guo, Jialiang Huang, Yu Zhu, Liang Guo, Weicheng Yu, and Zhi Fang

Abstract Insulation materials are widely used in various fields such as high voltage insulation, power electronics and aerospace. However, as the voltage level increases and the application area expands, the surface of the insulation material will have the phenomenon of flashover along the surface, which will lead to the aging of the insulation and thus reduce the stability of the power system. The current methods to enhance the flashover voltage along the surface of insulating materials generally have the disadvantages of high cost and environmental pollution. However, most of the existing plasma-modified devices focus on small-area materials. In this paper, we proposed a dielectric barrier discharge device for large-area insulating materials, which uses a water-net electrode structure to solve the problem of large-area discharge uniformity while limiting the temperature rise of the electrode so that it can operate stably for a long time. A 30 cm × 40 cm epoxy resin plate is used as the target, and the surface modification of the designed electrode is used to enhance the flashover voltage along the surface. The results show that the surface of the sample modified by the device with water repellent deposited a silica-like film, which increased the surface conductivity by an order of magnitude and increased the flashover voltage uniformly from 8.4 to 9.2 kV. The results of this paper are a guide to the deposition of thin films on large-area flat materials by DBD.

Keywords Insulating material · Flashover voltage · Plasma · Large area DBD

S. Guo · J. Huang (✉) · Y. Zhu · L. Guo · W. Yu · Z. Fang
College of Electrical Engineering and Control Science, Nanjing Tech University, Nanjing 211816, China
e-mail: hjl@njtech.edu.cn

1   Introduction

Polymer insulating materials have been widely used in mechanical, electrical, aerospace, and other fields due to their excellent insulation, mechanical, and thermal properties. They are often used as insulating components for electrical and mechanical equipment and vacuum electronic equipment [1–3]. However, due to long-term high voltage operation, ultraviolet radiation, dust accumulation, and other conditions, free charges tend to accumulate on the surface of solid insulating materials, and the accumulation of surface charges can distort the surface electric field, resulting in surface flashover [4, 5]. Therefore, insulating materials need to have excellent surface withstand voltage performance. Surface flashover and insulation aging directly threaten the safe and reliable operation of power systems. Therefore, exploring effective methods to improve the surface withstand voltage performance of solid insulation materials is of great value to ensure the safe and stable operation of electrical and electronic equipment and power systems.

The performance of insulating materials is closely related to their surface properties. By modifying the surface of materials and improving their surface properties as required, the application range of insulating materials in industry can be expanded. Research has shown that the surface roughness, surface polarity, wettability, and other characteristics of insulating materials can be changed through surface modification, which affects the surface withstand voltage level of the material. Currently, the surface modification methods applied to insulating materials include nano modification, blending modification, chemical modification, and plasma modification [6]. Nanomodification methods can improve the uniformity of particle dispersion on the surface of insulating materials, thereby improving the electrical conductivity of materials. However, nanocomposite polymer materials are difficult to prepare in large quantities, and their modification effects have poor long-term performance. Blending modification modifies materials by adding different types of fillers, which can change the microscopic morphology of polymer materials. However, the processing process of blending modification is relatively complex and the processing conditions are relatively harsh. Chemical modification laws have the problem of high processing costs and environmental pollution. Plasma modification method is a new surface modification method, which modifies materials through surface etching, surface crosslinking, introduction of active groups, and other methods. The modification depth is only within the range of 100 nm of the material surface, and does not affect the characteristics of the material itself [7]. Compared to other methods, plasma modification has the advantages of high energy efficiency, low pollution, simple formation method, and low cost [8]. Nowadays, the method of using low-temperature plasma to modify the surface of insulating materials, change their surface characteristics, and improve their surface insulation performance has become a leading direction.

The main methods used for surface modification of plasma insulating materials include atmospheric pressure plasma jet, sliding arc discharge, and dielectric barrier discharge (DBD). Among them, DBD has a wide operating voltage and frequency range, simple operating conditions, and can generate large volume, high energy

density, low-temperature plasma at atmospheric pressure, making it easy to achieve large-scale continuous operation. Černák proposed a coplanar dielectric barrier discharge electrode (1.5 mm × 1 mm × 50 μm) embedded in aluminum oxide, with a dielectric layer thickness of 0.4 mm [9]. This electrode plate can produce 21.5 cm × 8 cm plasma region . The researchers successfully activated polypropylene fabric using this electrode structure. Boselli et al. proposed a treatment area of 32 cm × 22 cm flat plate DBD electrode and polyethylene was hydrophilic modified using this electrode [10]. He et al. proposed a flat plate DBD electrode that can produce 30 cm × 10 cm plasma zone with a movable platform, the processing area can reach 30 cm × 60 cm. The team used this electrode to deposit amorphous silicon hydride films on glass [11].

Although researchers have designed several plate to plate DBD electrodes suitable for processing flat plate materials, relevant design research to meet the needs of thin film deposition is still relatively scarce. There are still problems in electrode design, such as insufficient processing area, small processing gap, and lack of medium addition. In this paper, based on the application requirements for surface modification of insulating materials, a large area water grid DBD electrode was designed and implemented. The operating conditions for large area uniform discharge were determined through discharge characteristic diagnosis. On this basis, epoxy resin was selected as the modification object, and the impact of operating parameters on the modification effect was studied and the optimal modification conditions were obtained, The modification mechanism was discussed by analyzing the electrode discharge characteristics and the physicochemical properties of the sample surface before and after modification.

2 Experimental Section

2.1 Material

The epoxy resin board sample (thickness: 1 mm) was purchased from Shanghai Liangfei Trading Co., Ltd.; Argon (99.999% concentration) was purchased from Nanjing Special Gas Factory Co., Ltd.; The hydrophobic medium hexamethyldisiloxane (HMDSO, concentration 99%) was purchased from Shanghai Aladdin Biochemical Technology Co., Ltd.

2.2 DBD Plasma Experimental Platform

In order to diagnose the characteristics of the large area DBD electrode designed in this article, an experimental platform for diagnosing the discharge characteristics is built as shown in Fig. 1a. The experimental platform consists of a large area water

network DBD electrode, a nanosecond pulse power supply, an airflow control system, an electrical characteristic detection system, and an optical characteristic detection system. According to the previous simulation results of electric field and flow field, the large area water grid DBD electrode uses a metal mesh plate with an aperture of 3 mm and a spacing between holes of 2 mm, and a 4-channel gas path with an inner diameter of 4 mm. The nanosecond pulse power supply can continuously output a voltage amplitude range of 0–15 kV, a repetition frequency range of 0–15 kHz, and a pulse width range of 50 ns–1 μs. The time range of the rising and falling edges of the pulse is 50–500 ns. The air flow control system is controlled by a mass flowmeter with four channels, with a control accuracy of 1 mL/min. The working gas is high purity argon (99.999% Argon, Ar). The hydrophobic medium hexamethyldisiloxane (HMDSO) is mixed with Ar in the main airway by bubbling method and then brought into the discharge air gap space. The electrical characteristic measurement system measures the voltage amplitude applied to both ends of the high and low voltage electrodes through a Tektronix P6015A high-voltage probe, measures the current flowing through the low voltage terminal through a Pearson current coil, and records the experimental data through a Tektronix MDO34 oscilloscope. The optical property measurement system consists of a Canon EOS 6D digital camera for capturing side and top luminescent images, and an Ocean Optics HR4000CG spectrometer for measuring the intensity of active particles.
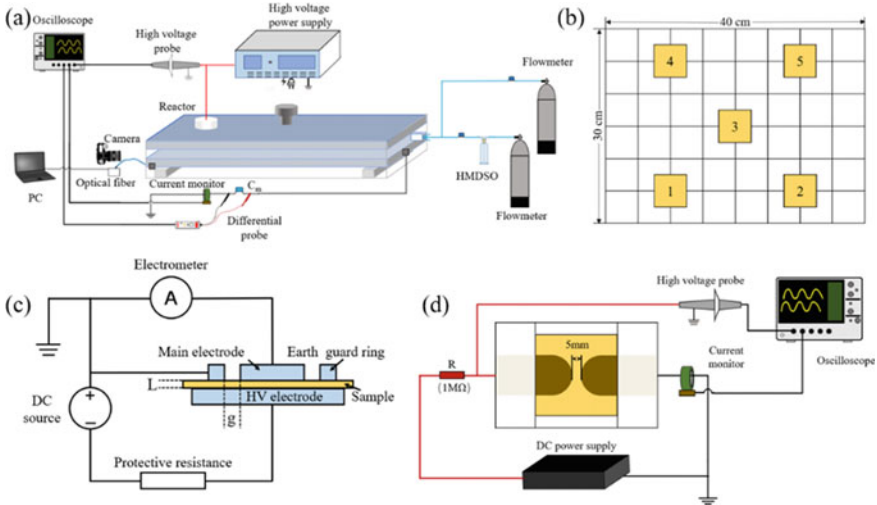
Fig. 1 **a** Large area DBD electrode discharge characteristics testing experimental platform. **b** Five-point method sample location diagram. **c** Surface conductivity test platform. **d** Flash voltage test platform

2.3 Surface Electrical Performance Testing Platform

The "five point method" [11] was used to detect the surface conductivity and surface flashover voltage of the sample to characterize the effect of modification on the electrical properties of the sample at different locations. Figure 1b is a schematic diagram of the placement position of the "five-point method" sample, with a sample size of 5 cm × 5 cm epoxy resin sample.

The electrical properties of the surface of a material are crucial for insulating materials. The uniformity of sample surface treatment and the improvement effect of electrical properties are evaluated by measuring the surface conductivity of the sample and the surface flashover voltage. The surface conductivity is measured by a HEST300 type high resistance meter. Figure 1c is a schematic diagram of a three-electrode megger used in this article. By applying a voltage of 1.0 kV to the three electrodes, a stable surface resistance value is obtained after applying a voltage to the surface of the sample for 2 min, and the surface conductivity is obtained by taking the reciprocal value. The surface conductivity calculation formula [12] is shown in Eq. (1):

$$\sigma = \frac{I}{V} \cdot \frac{4t}{\pi(L + g)^2} \tag{1}$$

In this formula, V is the applied DC voltage, L is the sample thickness, t is the main electrode diameter, and g is the ground protection ring gap.

The surface flashover voltage is the applied voltage when a DC voltage is applied to the finger electrode until a flashover occurs on the sample surface. The measurement platform for the surface flashover voltage is shown in Fig. 1d. When measuring the flashover voltage, the spacing between the finger electrodes is 5 mm, and the measurement result is the average of five flashovers per sample point.

2.4 Material Characterization

The micro physical morphology of EP was characterized by thermal field emission scanning electron microscopy (FE-SEM) and atomic force microscopy (AFM). AFM can obtain the microscopic imaging morphology and roughness changes within the three-dimensional surface range of the sample. Using the tap mode, the scanning range for testing is 10 μm × 10 μm.

Changes in chemical properties were detected by Fourier transform infrared spectroscopy (FTIR) (Thermo Nicolet iS50 FTIR, American) and X-ray photoelectron spectroscopy (XPS) (Thermo ESCALAB 250XI, America). FTIR can detect the change of chemical groups on the surface of the sample before and after modification, and the measured waveform is in the range of 500–4000 cm^{-1}. XPS is used to detect changes in elements before and after surface treatment of materials. Use

monochrome Al K α XPS of (1486.6 eV) X-rays obtained a detailed spectrum of 100 eV transfer energy and 1 eV resolution. XPSpeak41 software is used to perform peak fitting on the XPS detection results to obtain the ratio of each chemical bond.

3 Results and Discussion

3.1 Effect of HMDSO on Discharge Characteristics

There are many factors affecting the discharge characteristics, including electrode structure, gas flow rate in the main gas channel, excitation power parameters (such as voltage amplitude, repetition frequency, etc.), working gas type and flow rate, etc. In addition, for the hydrophobic modification, a reaction medium is usually required under the conditions, and the addition ratio of the reaction medium also has a significant effect on the discharge characteristics. Figure 2a shows the discharge images under argon environment with different content of HMDSO addition.

The filamentary discharge and glow discharge coexist in the luminescence image under argon conditions. After HMDSO addition, a stable discharge is formed in the dark region, but the luminescence brightness is significantly reduced. At the HMDSO flow rate of 20 mL/min, the discharge area basically covered the whole electrode, and further increase of HMDSO content had less effect on the discharge area. From
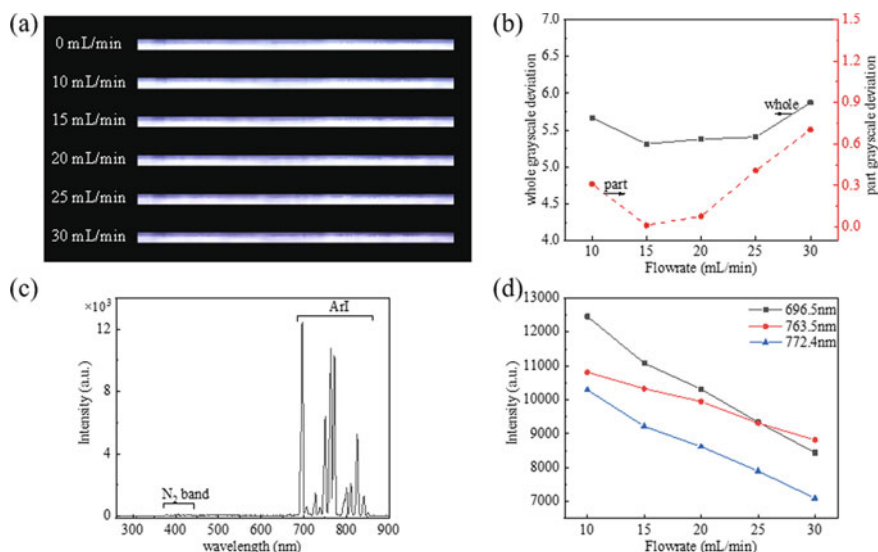
Fig. 2 **a** Discharge images at different HMDSO flow rates. **b** Grayscale deviation at different HMDSO flow rates. **c** Emission spectra at 5 mL/min HMDSO. **d** Intensity of change of major active particles

the grayness deviation variation curves in Fig. 2b, it can be seen that a small amount of HMDSO addition has less effect on the uniformity of argon DBD discharge, and the uniformity is best in the range of 15–25 mL/min of HMDSO gas channel flow rate.

Figure 2c shows the argon DBD emission spectra at the HMDSO flow rate of 5 mL/min. The N_2 second positive band system spectral line in the range of 300–400 nm and the ArI spectral line in the range of 680–850 nm were detected. 696.5, 763.5 and 772.4 nm ArI spectral lines with higher intensity were selected to characterize the variation of the intensity of the active particles, and the trend with the concentration of HMDSO addition is shown in Fig. 2d, which shows that the addition of HMDSO has a weakening effect on the intensity of the main particles.

3.2 Physical Morphology and Chemical Composition Characterization of Epoxy

Figure 3a, b show the SEM images of the untreated and water-repellent modified epoxy plates, respectively. As can be seen from the figures, the surface of the sample before treatment is relatively smooth, and the surface of the sample after plasma water-repellent modification is covered with a layer of hundred-nanometer cluster-like particles, which indicates that a micrometer-thick film is formed on the surface of EP.

The AFM surface analysis method can obtain three-dimensional three-dimensional morphological images of the sample surface at the atomic level, which are used to quantitatively analyze the changes in the physical morphology of the EP surface. The AFM images before and after the EP treatment are shown in Fig. 4c, d. It can be seen that the untreated EP surface is relatively smooth and the roughness
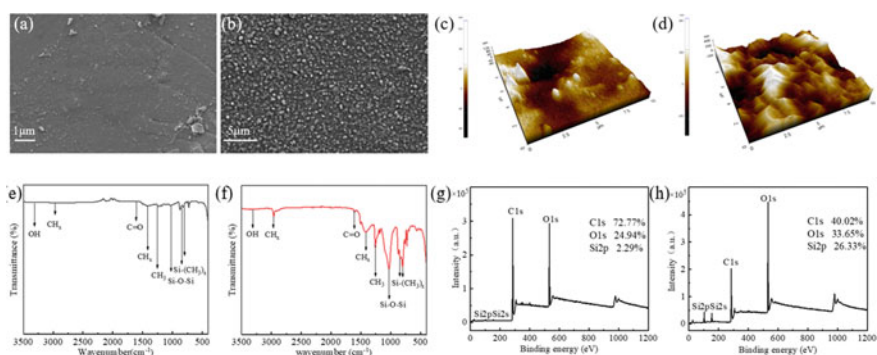
Fig. 3 **a** SEM images of untreated EP and **b** treated EP under 5.0 kV, 6.0 kHz **c** AFM images of untreated EP and **d** treated EP under 5.0 kV, 6.0 kHz **e** FTIR of untreated EP and **f** treated EP under 5.0 kV, 6.0 kHz **g** XPS of untreated EP and **h** treated EP under 5.0 kV, 6.0 kHz

of the treated EP surface is greatly increased, and the observed changes in surface roughness further prove that a hundred-nanometer-scale film is deposited on the EP surface.

The epoxy resin includes the chemical composition $(C_{11}H_{12}O_3)n$, which contains mainly C, H, and O elements and consists of C–C, C–H, C–O, and C=O bonds. The FTIR results of the water-repellent modified samples in Fig. 3e, f show that the –OH absorption peaks, C=O vibrational peaks, and CHx functional groups in the range of 2840–2960 cm^{-1} were detected, and the original C-H vibrational peaks were replaced by Si–O–Si, Si–(CH$_3$)x and other silicon-containing groups, which are the main functional groups of the deposited films.

In order to quantify the chemical element ratios on the surface of the samples before and after the modification treatment, the ratios of C, O, and Si on the surface of the samples were further examined by X-ray photoelectron spectroscopy (XPS). Figure 3g, h shows the results of XPS full spectrum scans before and after the water-repellent modification. Compared with the untreated sample, the composition
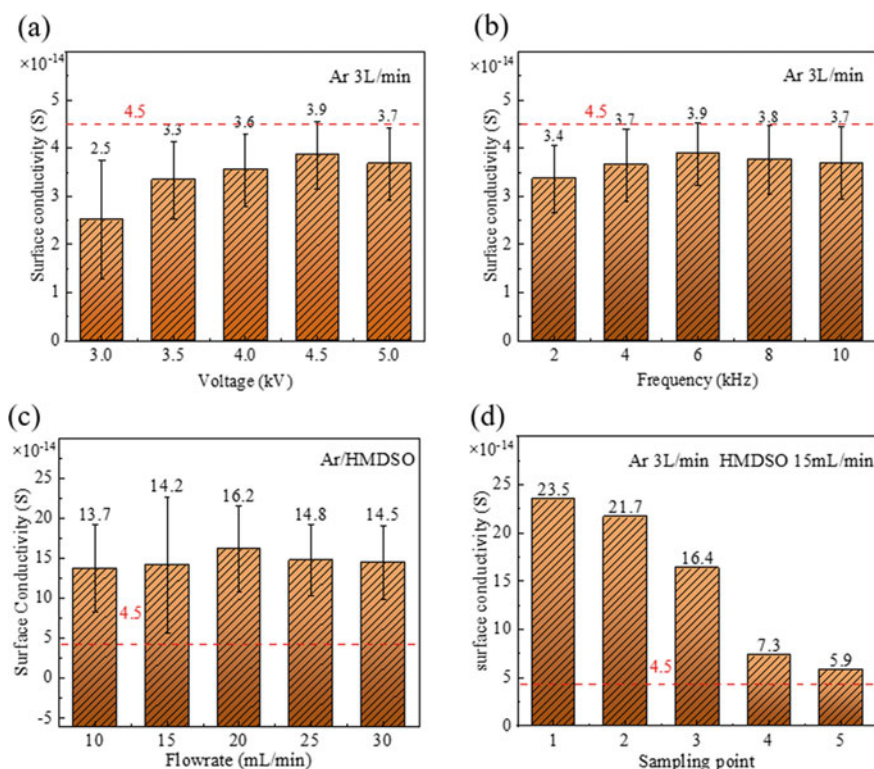
Fig. 4 **a** Trend of surface conductivity of epoxy resin under different voltage conditions **b** trend of surface conductivity of epoxy resin under different frequency conditions **c** trend of surface conductivity of epoxy resin under different HMDSO flow rate conditions **d** trend of surface conductivity of epoxy resin under different test point locations

Table 1 Chemical element ratio before and after treatment

Sample	C1s, %	O1s, %	Si2p, %	O/C, %
Untreated	72.77	24.94	2.29	34.27
Treated	40.02	33.65	26.33	84.08

and intensity of the elements on the surface of the water-repellent modified sample changed significantly, and the intensity of C1s peak (284 eV) decreased rapidly from 72.77 to 40.02%, which was 32.75% lower than that of the untreated sample, and the intensity of O1s (532 eV) spectral line increased from 24.94 to 33.94% in the untreated sample. The intensity of the O1s (532 eV) spectrum increased from 24.94 to 33.65% in the untreated sample, while a significant Si2p peak was detected on the surface of the treated sample, accounting for 26.33%, which is consistent with the FTIR detection results.

Table 1 shows the ratio of major elements before and after the hydrophobic modification, and it can be seen that the Si2p content and O/C ratio of the hydrophobically modified samples were significantly increased.

3.3 Surface Conductivity Testing and Analysis

Figure 4a, b shows the effect of the supply voltage amplitude and repetition frequency on the surface conductivity of the sample before the passage of the water-repellent medium HMDSO, respectively. As can be seen from the figures, the conductivity of the sample surface after plasma treatment is slightly decreased compared to the untreated sample surface conductivity of 4.5×10^{-14} S. Figure 4c shows the trend of surface conductivity with different flow rates of HMDSO under Ar working conditions, after water-repellent modification, the surface conductivity of the sample is significantly increased compared to the untreated one, with a maximum value of 1.62×10^{-13} S. Figure 4d shows the results of surface conductivity measurements at different positions, as seen from the figure, the surface conductivity of the sample at the inlet (positions 1 and 2) is significantly larger than that at the outlet (positions 4, 5), and the surface conductivity of the sample at the inlet is 3.4 times of that at the outlet.

3.4 Flashover Voltage Testing and Analysis

For the measurement of the electrical properties of the samples, the area of the test specimens was 5 cm × 5 cm, and the measurements were made on the epoxy resin specimens before and after the treatment. The results in this paper are the average values of the measured values under three treatments with the same modification

conditions. The effect of the modification on the electrical properties was evaluated by comparing the surface flash voltage before and after the treatment, and the results of the surface conductivity test were used to analyze the reasons for the changes in the electrical properties of the samples in combination with the changes in the physical and chemical properties of the surface.

Figure 5a, b show the variation of the flashover voltage along the surface of the sample with the amplitude and frequency of the supply voltage. It can be seen that the flashover voltage obtains its maximum value at the supply voltage amplitude of 3.0 kVz, which is 10.1 kV, an increase of 20% compared to the untreated condition. By changing the power supply parameters, the flashover voltage was maintained at about 9.4 kV for the rest of the operating conditions, which was 12% higher than the untreated condition. The flashover voltage along the surface of the sample modified with HMDSO hydrophobic modification was less variable and remained basically at 9.1–9.5 kV, which was 8–13% higher than that of the untreated sample.
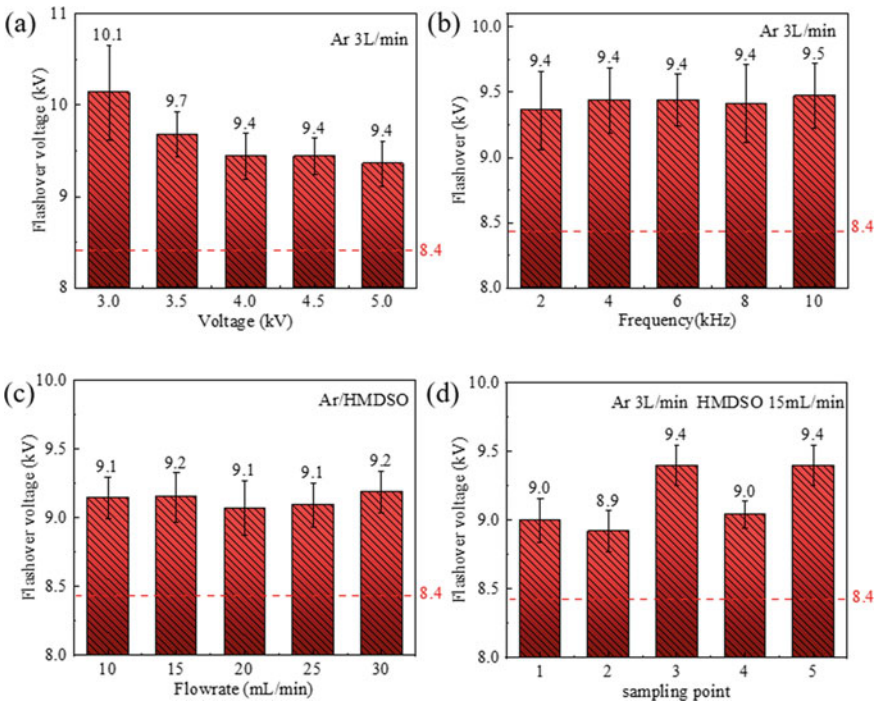
Fig. 5 a Trend of flashover voltage of epoxy resin under different voltage conditions b trend of flashover voltage of epoxy resin under different frequency conditions c trend of flashover voltage of epoxy resin under different HMDSO flow rate conditions d trend of flashover voltage of epoxy resin under different test point locations
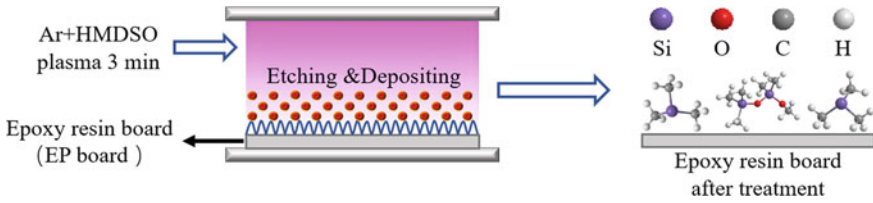
Fig. 6 Modification process of DBD and chemical structure formed after modification

3.5 Analysis of the Modification Mechanism

The above test results show that the conductivity and flashing voltage of epoxy resin treated by DBD plasma in large area water network are effectively enhanced, which is mainly due to the change of surface physicochemical properties. The process of plasma action on the polymer surface includes etching, grafting and deposition, where the hydrophobic modification of silica-containing precursors is mainly deposition, as shown in Fig. 6 Penning ionization leads to the cleavage of HMDSO molecules and the production of Si-containing groups, which is also confirmed by the XPS detection results. These cleaved HMDSO fragments are deposited on the EP surface and react to form a silicon film on the EP surface, changing its chemical structure. The silicon containing film deposited on the EP surface determines the properties of the EP surface such as electrical conductivity and flashover voltage.

4 Conclusion

(1) In this paper, a large-area water-net DBD electrode device is developed to meet the demand of large-area insulating material modification. The large-area DBD electrode designed in this paper can achieve a uniform discharge of 30 cm × 40 cm, and the designed electrode meets the demand of thin film deposition and medium addition. Meanwhile, the design of water-net electrode alleviates the problem of high electrode operation temperature, and the electrode is expected to be applied to more fields.

(2) In this paper, a 30 cm × 40 cm epoxy resin plate was treated and its surface was modified to enhance the flashover voltage along its surface using the designed electrode. The results show that the surface conductivity of the samples modified by the device increased by one order of magnitude and the flashover voltage increased uniformly from 8.4 to 9.2 kV. The results provide a guideline for DBD plasma deposition of thin films on large-area flat materials to enhance the insulation properties.

(3) A hundred-nanometer cluster-like film was deposited on the surface of the water-repellent modified sample. The film included functional groups such as $Si–CH_3$ and $Si–O–Si$, and the polarity of the deposited functional groups was lower

compared with the initial groups, and the improvement of roughness and the deposition of silica-like coating made the surface of the sample more water-repellent. The large number of shallow traps introduced by the modification to the surface accelerates the dissipation of surface charge, and its combined effect with the increase in surface roughness leads to an increase in the flashover voltage on the sample surface.

References

1. Hu Y, Dong M, Xie J (2020) Research status and development of multi-factor aging of polymeric insulation materials. Power Syst Technol 44(4):1276–1289 (in Chinese)
2. Gao Y, Wang X, Li N (2019) Characterization methods of carrier traps in polymer insulating materials and progress of research on the influence of traps on insulation breakdown. High Voltage Eng 45(7):2219–2230 (in Chinese)
3. Cai D, Tang J (2019) Overview of insulation materials, insulation structures and systems for dry-type transformers. Insulating Mater 52(11):1–8 (in Chinese)
4. Zhao Y, Zhang G, Han D (2019) Experimental study of the discharge characteristics along the face of inter-turn insulation materials for high frequency transformers. Trans China Electrotechnical Soc 34(16):3464–3471 (in Chinese)
5. Chen S, Wang S, Wang Y (2017) Surface modification of epoxy resin using He/CF4 atmospheric pressure plasma jet for flashover withstanding characteristics improvement in vacuum. Appl Surf Sci 414:107–113
6. Kong F, Chang C, Ma Y (2018) Surface modifications of polystyrene and their stability: a comparison of DBD plasma deposition and direct fluorination. Appl Surf Sci 459:300–308
7. Tynan J, Dowling DP, Byrne G (2007) Enhancing polymer adhesion through surface activation using an in-line atmospheric pressure plasma. Int J Nanomanuf 1(4):554–569
8. Sohbatzadeh F, Farhadi M, Shakerinasab E (2019) A new DBD apparatus for super-hydrophobic coating deposition on cotton fabric. Surf Coat Technol 374:944–956
9. Černák M, Kováčik D, St'ahel P (2011) Generation of a high-density highly non-equilibrium air plasma for high-speed large-area flat surface processing. Plasma Phys Controlled Fusion 53(12):124031
10. Boselli M, Colombo V, Ghedini E (2013) Parametric study on the effectiveness of treatment of polyethylene (PE) foils for pharmaceutical packaging with a large area atmospheric pressure plasma source. In: 2013 (August); proceedings of 21st international symposium on plasma chemistry
11. He H, Gao Q, Zhang X (2011) Cold deposition of large-area amorphous hydrogenated silicon films by dielectric barrier discharge chemical vapor deposition. Thin Solid Films 519(15):5038–5042
12. Du B, Yang Z, Li Z (2017) Surface charge behavior of silicone rubber/SiC composites with field-dependent conductivity. IEEE Trans Dielectr Electr Insul 24(3):1340–1348

Electric Field Simulation Analysis of Typical Defects of Main Insulation Burrs in Power Transformers

Jianwen Zhu, Jianhua Zhang, Guoliang Li, Sen Li, Yuqing Lin, Zuhui Liang, and Yongpeng Liu

Abstract With the gradual increase of the national economy's demand for electric power, power transformers are also gradually developing in the direction of high voltage level and large capacity. According to incomplete statistics, the damage of insulation structure is one of the main factors leading to the failure of transformers. Therefore, the research on the main insulation of transformers will become a top priority. In this paper, we use COMSOL finite element simulation software to simulate the electric field of the main insulation of power transformers with burr defects. The locations where the maximum field strength appears in the transformer main insulation are analyzed to investigate the effects of different sizes and locations of burr defects on the electric field distribution of the transformer main insulation. This study is of general significance to focus on detecting the main insulation devices of power transformers, avoiding partial discharges that may be caused by burrs and ensuring safe and reliable operation of power transformers.

Keywords Power transformers · Main insulation · Finite element · Burr defects · Electric field simulation

1 Introduction

The continuous development of the power industry has put forward higher requirements for power transformers, which are one of the key equipment in the power system. The operation and fault statistics of transformers in power systems show that internal insulation is the weak link of transformers, and the existence of equipment insulation defects in operation is an important factor leading to equipment failure of power transformer [1–3]. Therefore, it is important to analyze the main

J. Zhu · J. Zhang · G. Li (✉) · S. Li · Y. Lin · Z. Liang · Y. Liu
Zaozhuang Power Supply Company of State Grid Shandong Province Electric Power Company, Zaozhuang, Shandong, China
e-mail: 18369296036@163.com

insulation defects of power transformers to improve the reliability of transformer operation and ensure the safety and stability of power supply.

In order to obtain the electric field distribution of transformer main insulation under potential defects of burrs, this paper applies COMSOL simulation software to simulate a 110 kV power transformer model in China. The weak locations in the insulation structure that are highly susceptible to partial discharges are obtained through simulation and the effects of different burr locations and sizes on the electric field distribution of the main insulation of the transformer are studied.

2   Transformer Main Insulation Simulation Model

As a numerical calculation method for solving various physical problems with high efficiency, the finite element method is widely used in transformer electromagnetic field simulation analysis, which can approximate the actual structure to the greatest extent and obtain calculation results with fewer assumptions and high accuracy [4–6].

2.1   Modeling of the Main Insulation

In this paper, the main insulation simulation model is established according to the thin paper cylinder small oil gap theory between the high and low windings of the transformer, as shown in Fig. 1. To simplify the model and facilitate the calculation, the following settings are made.

(1)   The electric field is analyzed according to the steady-state, linear axisymmetric electric field [7, 8];
(2)   The iron yoke is an infinitely large flat plate perpendicular to the axis of the core column [9];
(3)   Leads and clips, etc., have no effect on the electric field at the end.

2.2   Boundary Conditions

In the COMSOL simulation platform, the transformer geometry is established, the material parameters are selected, the corresponding conditions of each boundary are specified, and the model is fine-grained mesh dissection. Among them, the dielectric constants of transformer oil and insulating paper are taken as 2.2 and 4.4 respectively [10, 11].

The left and upper boundaries of the structural model of Fig. 1 are the core and yoke, respectively, corresponding to the first type of boundary conditions [12, 13], connected to the earth and given a point position of zero. The lower and there boundaries of the model correspond to the second type of boundary conditions [14, 15].
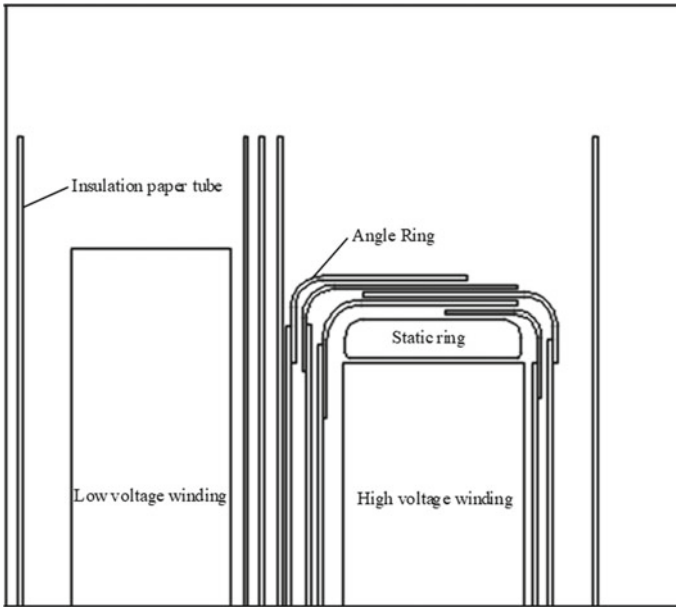
Fig. 1 Main insulation simulation model

Between the high-voltage and low-voltage windings of the transformer, an operating frequency test voltage is applied. The electrostatic ring as well as the high voltage winding is high potential, which belongs to the first type of boundary conditions. The boundary problems included above, are shown below.

$$
\begin{cases}
\dfrac{1}{r}\dfrac{\partial}{\partial r}\left(r\dfrac{\partial \varphi}{\partial r}\right) + \dfrac{\partial^2 \varphi}{\partial z^2} = 0 \\[2mm]
\varphi_1 = 0,\ \varphi_2 = 0 \\[2mm]
\dfrac{\partial \varphi}{\partial n} = 0 \\[2mm]
k_1 \dfrac{\partial \varphi}{\partial n} = k_2 \dfrac{\partial \varphi}{\partial n}
\end{cases}
\tag{1}
$$

In (1), k_1 and k_2 are the dielectric constants of the material, and φ_1 and φ_2 are the potentials.
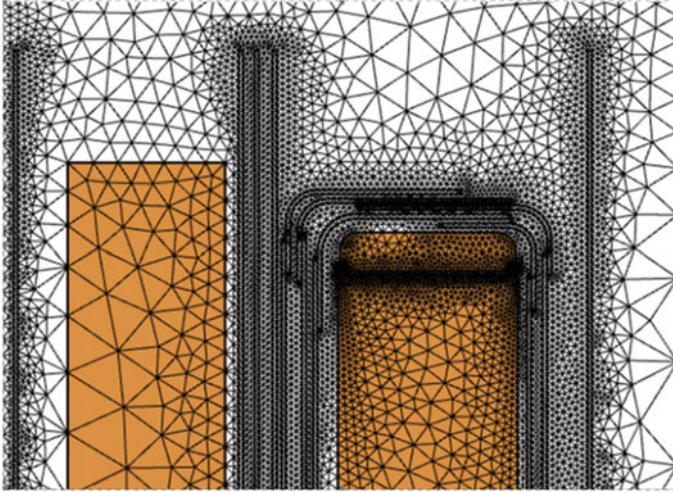
Fig. 2 Schematic diagram of the main insulation grid profile

3 Simulation Results and Analysis

3.1 Electric Field Analysis of Burr-Free Defects

The schematic mesh dissection of the main insulation structure of the power transformer is shown in Fig. 2. The electric field distribution at the winding ends is obtained in the finite element simulation software, as shown in Fig. 3. It can be seen that the maximum field strength appears at the main insulation end and the electrostatic ring, and the maximum field strength is about 4.46 kV/mm.

3.2 Burr Defects in Insulated Cardboard

The burr defects are modeled with their width instead of their curvature variation, the higher the burr curvature i.e. the more pointed the burr shape. As shown in Fig. 4, the effect of burr defects of different sizes on the insulating cardboard on the electric field distribution at the winding end is simulated in the finite element software.

From the numerical simulation analysis in Fig. 4, it can be concluded that the insulating oil in the transformer plays the main insulating role under the frequency AC voltage, and the appearance of the burr on the insulating cardboard has little effect on the electric field distribution of the transformer oil around the burr, but has a greater effect on the electric field distribution of the insulating cardboard. The maximum field strength of the main insulation of the power transformer still appears
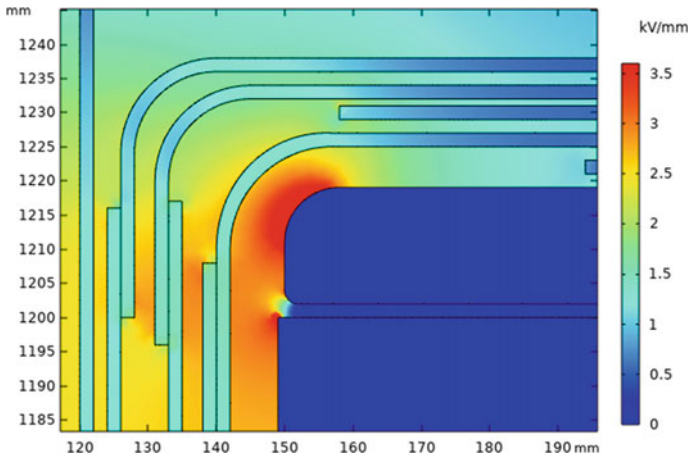
Fig. 3 Main insulation electric field distribution at the end when there is no burr

in the oil gap near the upper left corner of the electrostatic ring, with a maximum field strength of 4.43 kV/mm.

For an in-depth study of the effect of the burr on the main insulation of the transformer, the electric field distribution in the vertical direction at the insulation cardboard burr is analyzed, as shown in Fig. 5.

Figure 5 analyzes the change of electric field intensity in the vertical direction of the burr, where the vertical distance 0–2 mm is the insulating cardboard area, 2–6 mm is the burr area, and 6–7 mm is the insulating oil area. At the lower end of the burr, the more pointed the burr is, the greater its electric field intensity. At the upper end of the burr and at the insulating oil, the size of the curvature of the burr has little effect on its electric field distribution.

In the vertical direction of the burr defect area, the electric field strength as a whole tends to increase, the field strength at the tip of the burr defect is the largest in the entire burr defect area, so in the design and operation of power transformers, should focus on the burr defect, to avoid the partial discharge it may cause, to ensure the safe and reliable operation of power transformers.

3.3 Static Rings with Burr Defects

The burr defects appearing in the main insulation electrostatic ring were simulated in the finite element software, and the effects of different sizes of burr defects on the electric field distribution on the electrostatic ring were analyzed.

From Fig. 6, it can be analyzed that when the electrostatic ring has a burr defect, the maximum field strength appears at the burr tip, and the maximum field strength value of (a) is 3.55 kV/mm, and the maximum field strength value of (b) is 3.94 kV/

(a) Width 1mm, height 4mm, left side of cardboard

(b) Width 2mm, height 4mm, left side of cardboard

(c) Width 1mm, height 4mm, right side of cardboard

(d) Width 2mm, height 4mm, right side of cardboard
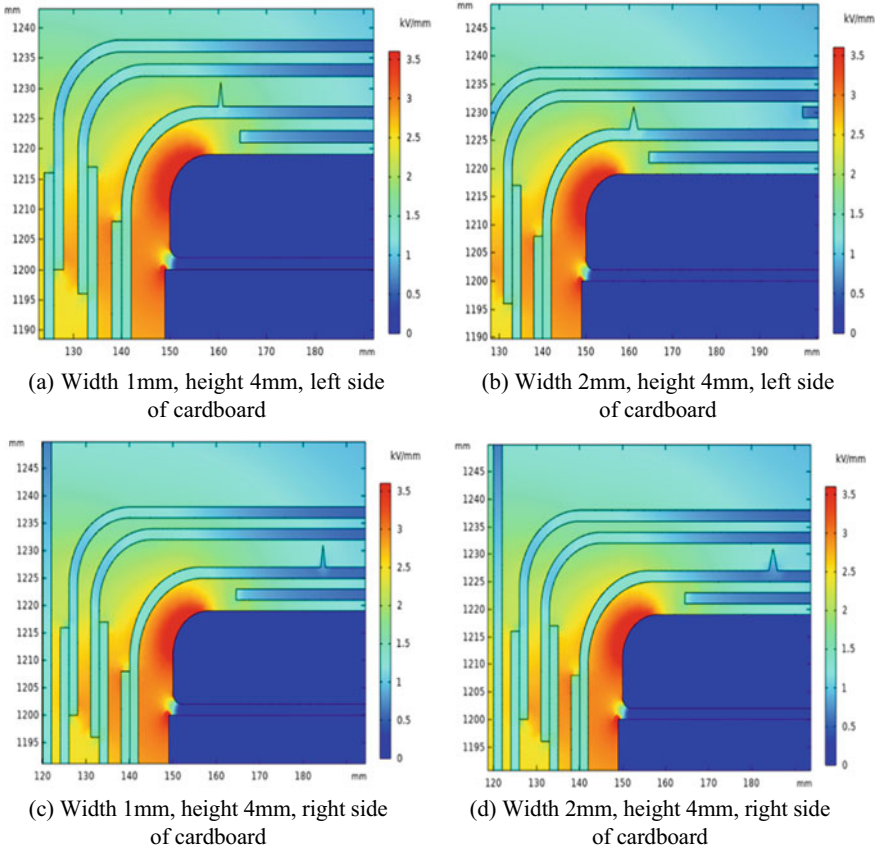
Fig. 4 Electric field distribution of burr defects of different sizes on cardboard

(a) Left side of the cardboard.

(b) Right side of the cardboard.
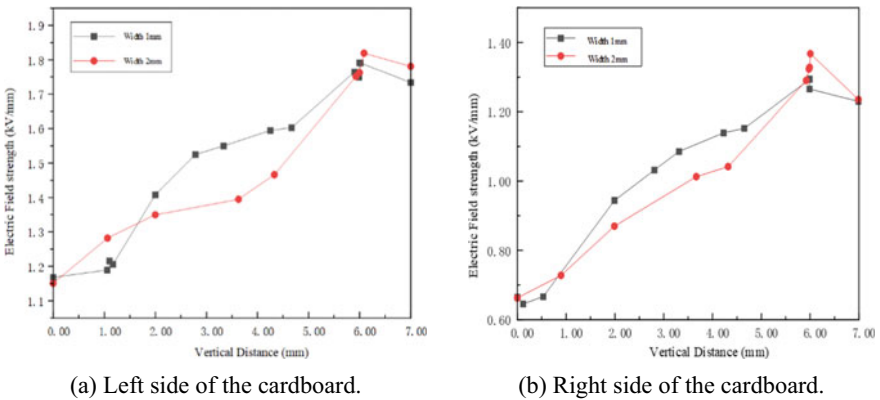
Fig. 5 Electric field intensity distribution in the vertical direction at the burr

(a) Rough burrs.   (b) Sharp burrs.
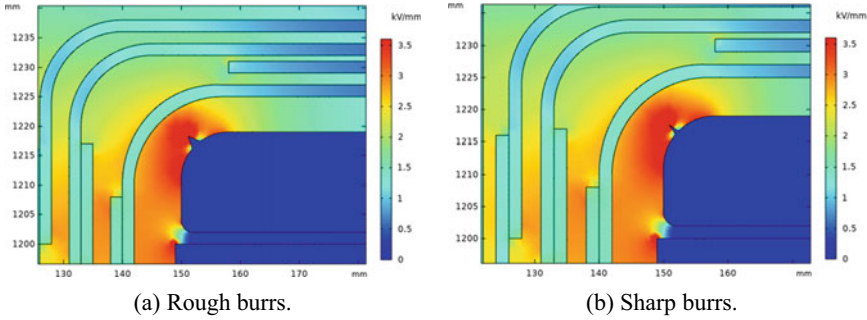
Fig. 6 Electric field distribution of burr defects of different sizes on the electrostatic ring

mm. And the comparison of (a) and (b) shows that the more pointed the burr is, the larger the field strength is compared to the appearance of burr defects on the insulating cardboard, the appearance of burr defects on the electrostatic ring has a greater impact on the distribution of the electric field around it, and the greater the curvature of the burr that is, the more pointed the burr, the higher the field strength.

4   Conclusion

In this paper, we use COMSOL finite element software to build a simulation model of the main insulation of power transformers, explore the electric field distribution when burr defects appear in the insulation cardboard and electrostatic rings, analyze the effects of different sizes and locations of burrs on the electric field of the main insulation of transformers, and obtain the following conclusions.

(1) The simulation analysis of the transformer main insulation shows that: the electric field distribution between the end of the high-voltage winding to the iron yoke is of great significance to the analysis of the transformer main insulation, and the maximum field strength appears in the upper left corner of the electrostatic ring.

(2) Numerical calculation of the electric field simulation of the burr defects on the insulating cardboard shows that: the maximum field strength of the transformer main insulation appears in the oil gap near the upper left corner of the electrostatic ring, and the burr defects on the cardboard have a greater impact on the electric field distribution of the insulating cardboard, but not on the electric field in the transformer oil. In the vertical direction, the field strength at the tip of the burr defect is much higher than in other burr areas.

(3) The simulation analysis of the burr defects on the electrostatic ring shows that: unlike the burr on the insulating cardboard, the burr on the electrostatic ring has little effect on the electric field distribution around it. The greater the curvature of the burr, the greater the field strength, so the focus should be on monitoring

the electrostatic ring parts to avoid the emergence of burr defects, triggering partial discharge.

References

1. Wang L, Hou K, Lu X, Li Q (2021) Research on electric field distribution at winding end of converter transformer considering temperature gradient. In: 2021 international conference on electrical materials and power equipment (ICEMPE), Chongqing, China, pp 1–4
2. Yong J et al (2021) Research on leakage magnetic field and electrodynamic force of large transformer windings based on finite element simulation. In: 2021 international conference on advanced electrical equipment and reliable operation (AEERO), Beijing, China, pp 1–5
3. Zhang Z, Xiao R, Wu Y, Jiang P, Deng J, Pan Z (2021) Research on multi-level feature extraction model of converter transformer vibration signal. Chin J Electr Eng 41(20):7093–7104 (in Chinese)
4. Liu FY, Han L, Zhang XL et al (2014) Numerical analysis of the electric field of the main insulation of power transformers. J Tianjin Univ Technol 33(03):75–79 (in Chinese)
5. LI Q, Wang L, Wang P, LI S (2020) A review of research on partial discharge and charge distribution characteristics of oil-paper insulation in converter transformers. High Voltage Technol 46(08):2815–2829 (in Chinese)
6. Zhang XC, Zou L, Chen X, Dai LJ (2022) Coupling and fault analysis of electro-magnetic-structural field of transformer based on COMSOL. In: 2022 IEEE/IAS industrial and commercial power system Asia (I&CPS Asia), Shanghai, China, pp 1994–1999
7. Pan Z, Deng J, Xie Z, Zhang J, Liang C, Zhou B (2020) Comparative analysis of the vibration signal characteristics of converter transformers and AC transformers. Transformer 57(03):35–40 (in Chinese)
8. Wang X, Cheng Z, Cheng L, Guo Q, Liao R (2021) Influence of oil-pressboard combination on electric field distribution of main insulation structure on valve-side winding of HVDC converter transformer. In: 22nd international symposium on high voltage engineering (ISH 2021). Hybrid Conference, Xi'an, China, pp 2245–2249
9. Wei LB, Han KJ, Li ChP (2014) Analysis and optimization of the main insulation electric field of 220 kV end-out power transformers. Transformer 51(09):6–10 (in Chinese)
10. Chen B, Shen C, Lv P, Han W, Yang Y, Li J (2020) Voltage distribution of transformer winding under the fast transient pulse. In: 2020 6th global electromagnetic compatibility conference (GEMCCON). XI'AN, China, pp 1–4
11. Pan Z, Deng J, Chu J, Zhang Z, Wu Y, Wang P (2020) A wavelet packet-based method for characterizing the vibration signal of converter transformers. Transformer 57(11):21–26 (in Chinese)
12. Liu J, Li L, Zhang M, Wang K (2020) Finite element analysis of oil-paper insulation nonuniform aging in transformer. In: 2020 IEEE international conference on high voltage engineering and application (ICHVE). Beijing, China, pp 1–4
13. Zhou F, Zhang D, Liu HJ, Hu KL, Li L, Miao W, Wu LL (2020) Study on the effect of temperature on the electric field distribution at the end of converter transformer windings. High Voltage Electron 56(01):80–86 (in Chinese)

14. Xiuke Y, Yang S, Cunzhan Y, Yanli Q (2011) Analysis of 3D electric field and insulation optimization of oil-immersed inverted current transformer. In: 2011 international conference on electrical machines and systems. Beijing, China, pp 1–4
15. Gao Y, Wang S, Gao D (2012) Effect of main insulation structure of power transformer on electric field distribution. J Shenyang Univ Technol 34(01):11–14+40 (in Chinese)

The Effect of Inlet Wind Speed on the Performance of Electrostatic Precipitation Systems and Double Rotating Venturi Systems

Wei Cheng, Chao Niu, Jing Fan, Shoufu Gu, Daxin Liang, and Da Liu

Abstract To solve the problem of atmospheric pollution caused by dust generated in the coal transportation and coal-fired processes of power plants, this article compares two common dust removal technologies, electrostatic precipitator and Venturi dust collector, and simulates electrostatic precipitators under different wind speeds using COMSOL. Simulation study of the flow characteristics of a double rotating Venturi dust collector using a k-ε turbulence model. The results show that as the inlet air velocity increases, the velocity of the flow field inside the electrostatic precipitator also increases. The maximum velocity occurs near the discharge electrode, and the particle collection efficiency is highest when the inlet wind speed is 15 m/s, but the dust removal efficiency is below 50%. The flow field inside the Venturi can be exactly simulated by the k-ε turbulence modeling. As the inlet air velocity increases, the outlet air velocity of the double rotating Venturi dust collector also increases. When the inlet liquid velocity is 0.35 m/s, the maximum flow rate of liquid inside the venturi is 40.26 m/s.

Keywords Double rotating Venturi dust collector · Electrostatic precipitator · Inlet wind speed · Particle trajectory

1 Introduction

In recent years, environmental contamination has been significantly worse, with frequent occurrences of smog in China. The chance of developing cancer in humans is increased by inhaling these cancer-causing particles [1]. At present, coal smoke is still the main source of air pollution dust in China. Coal can generate a large amount of dust during loading, unloading, transportation, screening and combustion emissions in power plants, which seriously pollutes the power plant and the surrounding atmospheric environment. With the increasing national requirements for particulate

W. Cheng (✉) · C. Niu · J. Fan · S. Gu · D. Liang · D. Liu
Tianjin Guoneng Jinneng Thermal Power Co., Ltd., Tianjin 300300, China
e-mail: cw13373180392@163.com

matter emission standards, exploring more efficient and environmentally friendly dust removal technologies has become a research hotspot.

At present, the main dust removal technologies applied domestically and internationally include water mist dust removal, mechanical dust removal, electrostatic precipitator, etc. [2]. Compared with other dust collection equipment, electrostatic precipitator dust removal efficiency is higher. The process of electrostatic precipitation involves multiple disciplines, and the charging of dust, the deposition of charged particles and the distribution of airflow can all affect the overall performance and collection efficiency of the dust collector. Through experimentation, Kasdi et al. [3] discovered that the dust collector's performance was enhanced when the number of discharge wires was increased. Although the total collection current and dust removal efficiency both decreased as a result of the narrower wire spacing. Zhou et al. [4] investigated the influence of the structure of the collecting plate on the dust collection efficiency through simulation, and the results investigated that the presence of the uneven dust collection poles would inhibit the flow close to the board, which would be conducive to reducing the enlivened particles. The collection efficiency of 5 μm particles was 6.87% higher in the triangular plate and 10.37% higher in the 10 μm particles than in the C-shaped plate. Xiong et al. [5] conducted performance experiments at different dust loading periods, and the research showed that PM2.5 was initially collected at 99.8% and 97.6% at 1.0 m/s and 2.5 m/s, respectively. After 50 days of continuous running, the PM2.5 efficiency was maintained above 90% at 1.0 m/s, while it could only be maintained at around 50% at 2.5 m/s.

According to research, the collection efficiency of electrostatic precipitators is lower when the wind speed is high. In addition, coal dust very easy to reaches the ignition point and explosion point, and under natural static electricity or human factors, it is easy to cause dust explosion safety accidents. Therefore, wet dust collectors have obvious advantages in solving the dust hazards in the coal transportation and coal-fired processes of power plants. Although water bath-type and spray-type dust collectors can handle high-temperature, flammable and explosive dust, their dust removal effect is poor. The Venturi dust collector developed using the theory of the Venturi effect has the characteristics of simple structure, high dust removal efficiency and the ability to effectively handle gases containing flammable and easily adhering dust. Among all wet scrubbers, the Venturi scrubber has the lowest power consumption and has been widely used in mining and tunnel engineering [6, 7]. The pressure drop of a Venturi dust collector is its main energy consumption. In addition to the pressure drop, the dust removal efficiency is another important parameter of a Venturi dust collector, and the distribution of liquid in the throat is the main factor affecting the dust removal efficiency [8–10]. A uniform liquid distribution can enhance the interaction between liquid droplets and solid particles and improve separation efficiency. Optimizing its structure and process to minimize energy consumption and improve dust removal efficiency is of great significance for the application of this equipment in the coal conveying system of thermal power plants.

In order to improve the dust removal efficiency of Venturi dust collectors, many scholars have conducted relevant research. Guerra et al. [11] utilized the standard k-ε turbulence model and the volume of fluid (VOF) multiphase flow model were used

to analyze the pressure loss of rectangular venturi scrubber under different liquid injection volume, injection velocity, and liquid gas ratio. Ye et al. [12] conducted numerical simulations of gas–liquid two-phase flow in a Venturi tube based on the CFD-DPM method. According to the findings, the Venturi tube's contraction portion experiences a pressure drop that makes up about 75% of the entire pressure drop, while the throat has a pressure drop that makes up about 20% of the total pressure drop. Flue gas at the pharynx had an average speed between 106 and 192 m/s. Lin et al. [13] investigated the effect of different Venturi on the dust collector pressure drop and the static pressure acting on the inner wall of the elliptical filter cartridge by numerical simulations and experiments.

The numerical simulation of the electrostatic precipitator under high wind speed is carried out by using the fluid model. In view of the harsh environment of the thermal power plant, combined with the existing dust collector, a new type of venturi dust collector is designed: double rotating Venturi dust collector. The k-ε turbulence model is established to simulate the flow field of the rotating Venturi dust collector. The influence of inlet wind velocity on the flow characteristics of the double rotating Venturi dust collector is studied and analyzed, and then the structure and configuration of the dust collector are optimized to achieve a better dust removal effect.

2　Working Principle of a New Type of Double Rotating Venturi Dust Collector

The double rotating Venturi dust collector consists of an outer cylinder, an inner cylinder, a swirling blade, a water retaining device and other parts, as shown in Fig. 1. Unlike traditional Venturi dust collectors, the new double rotating Venturi dust collector adds a swirling flow between the outer and inner barrel walls, and dust containing gas enters from the inlet of the outer barrel. Through the contraction tube, its cross-sectional area of flow gradually decreases. Due to changes in cross-section, the airflow velocity is redistributed. In the three phases of gas, liquid and solid, relative motion occurs due to differences in inertial forces, resulting in collisions between solid smoke particles of different sizes, between liquid and solid particles, and between water droplets of different diameters. The final result is the condensation phenomenon of large particles capturing small particles, and small particles hanging on large particles, thereby increasing the effective size of smoke, it is conducive to separating larger particles and then entering the inner barrel. Under the action of centrifugal force, most of the dust is caught by the liquid film formed by the droplets on the wall of the drum. The remaining small part of the dust rises with the airflow to the swirl vane to remove the finer particles, further improving the dust removal efficiency. After the water is removed by the water retaining device, the gas is discharged into the air through the induced draft fan, and the coal dust removal efficiency is higher.

Fig. 1 Working principal diagram of double rotating Venturi dust collector
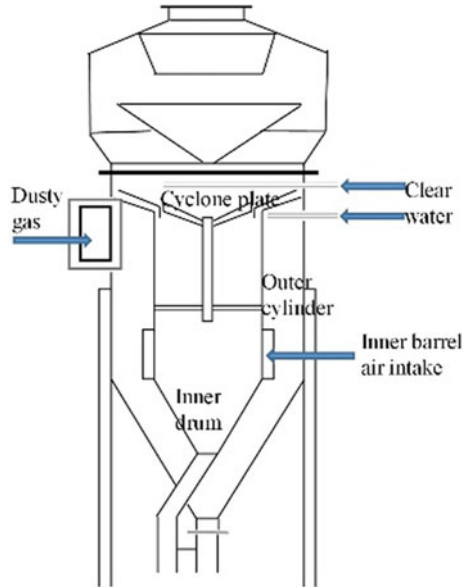
3   COMSOL Turbulence Model

In this study, the simulation steps can be roughly divided into the following steps: defining simulation-related parameters, establishing geometric models, defining materials, and setting fluid-particle related parameters, such as inlet and outlet locations, particle properties, initial airflow velocity, etc. Each step is logically related.

The flow field of the gas in the double rotating Venturi dust collector is the turbulent flow of high-speed rotation. In this paper, the k-ε turbulence modeling of COMSOL is chosen to simulate the flow characteristics of the double rotating Venturi dust collector. The "Rotating Machinery, Turbulence, k-ε" interface is used to simulate high Reynolds number flows in geometry containing one or more rotating parts, and is suitable for incompressible and compressible flows with low Mach numbers (usually less than 0.3). The interface combines the "turbulence, k-ε" interface with the "rotation domain" under the "dynamic grid", uses the Navi-Stokes equation to control momentum balance, and uses the continuity equation to control mass conservation. The turbulence effect is modeled by the typical k-ε two-equation modeling with realizable constraints, and the near-wall flow is modeled by the wall function.

The physical field interface supports two types of research. When using "transient" to study the type, rotation is achieved through the moving grid function. When studying the type with a "frozen rotor", the rotating parts remain in place and the rotation is analyzed by introducing centrifugal and Coriolis forces. In this paper, by combining using "rotating machinery, turbulence, k–ε" research on interface and frozen rotor type to establish simulation research. Because the topological structure

changes due to the relative motion between the rotating impeller and the container with baffle, the flow field has transient characteristics. In this case, the frozen rotor solution should be regarded as a quasi-steady approximation of the flow field.

4 Results and Discussion

4.1 Characteristic Analysis of Electrostatic Precipitator

In this paper, a rectangular two-dimensional model is used for simulation. The internal wire electrodes are connected to the high voltage radius of 0.5 mm, the spacing between the wire electrodes is 10 cm, and the wire electrode is 5 cm away from both the upper and lower grounding plates.

Velocity distribution. As shown in Fig. 2, by simulating the influence of 15 m/s inlet air velocity on the air speed distribution of the dust collector, it is found that the speed of the dust-containing gas decreases every time it passes through an electrode.

The maximum velocity variation of the flow field at different inlet air speeds is shown in Fig. 3. When the inlet air speed is 15 m/s, the maximum internal speed is 26.76 m/s. When the inlet air speed is 17.5 m/s, the maximum internal speed is 31.19 m/s. When the inlet air speed is 25 m/s, the maximum internal wind speed increases to 44.24 m/s. It can be noticed that as the inlet air speed increases, the maximum wind speed inside the electrostatic precipitator also increases, and the maximum wind speed occurs near the discharge electrode.

The collection of particles with different sizes at different inlet wind speeds. As shown in Fig. 4, the distribution of particle trajectories with different particle sizes at an inlet wind speed of 15 m/s. Dust particles enter from the left side of the dust collector, and during the gas diffusion process, the surface charge of the dust particles continuously accumulates. With the change of drag force and electrostatic force, the movement trajectory of the dust particles also changes, ultimately leading to the dust particles gradually moving towards the negative electrode integrated board direction.

Electrostatic dust collection simulation analysis was carried out for dust particles with particle sizes of 0.01 μm, 0.2 μm, 2 μm and 5 μm, respectively. When the
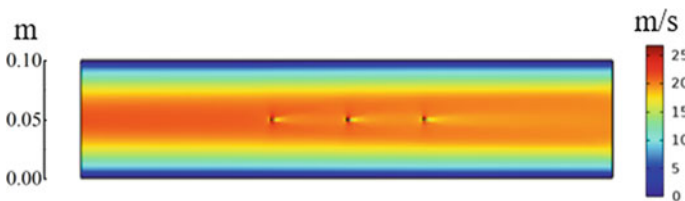
Fig. 2 Velocity distribution of flow field when inlet wind speed is 15 m/s
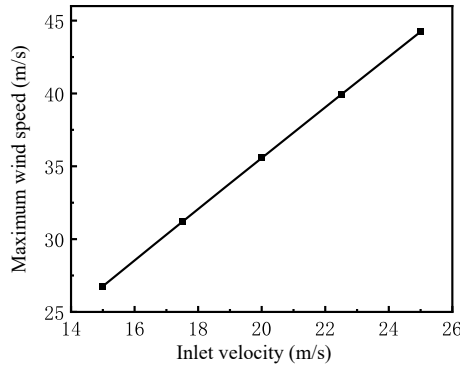
Fig. 3 The maximum wind speed in the dust collector changes with different inlet wind speed
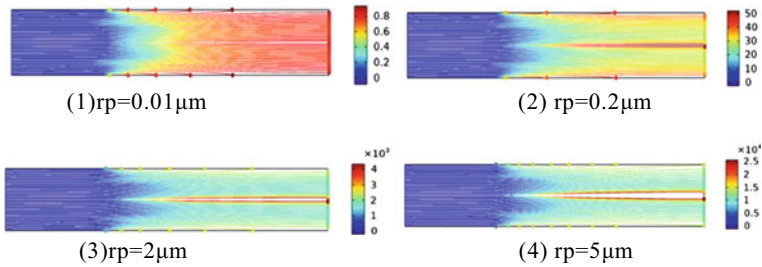
Fig. 4 Particle trajectories of different sizes are distributed when the inlet wind speed is 15 m/s

inlet air speed is 15 m/s, 17.5 m/s, 20 m/s, 22.5 m/s and 25 m/s, the efficiency of particle dust collection at different inlet air velocities is shown in Fig. 5. The smaller the inlet air velocity, the better the dust cleaning efficiency for each particle radius. When the particle radius exceeds 0.2 μm, the larger the particle size, the higher the corresponding dust cleaning efficiency. When the particle radius is smaller than 0.2 μm, the smaller the particle size, the higher the corresponding dust collection efficiency. When the particle size is 0.2 μm, the collection efficiency is minimal. The particle size in the middle, due to its drag effect, follows the air flow more in the direction parallel to the dust collector wall, resulting in low dust collection efficiency.

4.2 Characteristic Analysis of Double Rotating Venturi Dust Collector

Outlet wind speed. Dust containing gas is introduced from the outer barrel, and the overall wind speed of the outer barrel is basically the inlet air speed. The air speed of the inner barrel is higher than that of the outer barrel, but the wind speed below

Fig. 5 Dust collection efficiency of particles at different inlet wind speeds
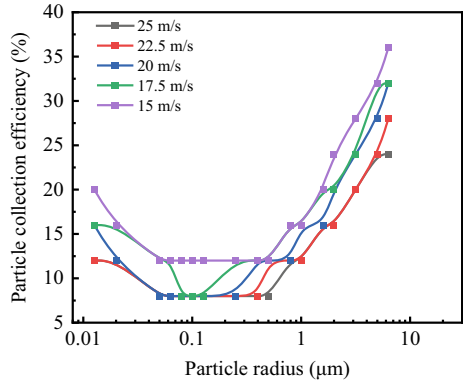
Fig. 6 Outlet wind speed at different inlet wind speeds
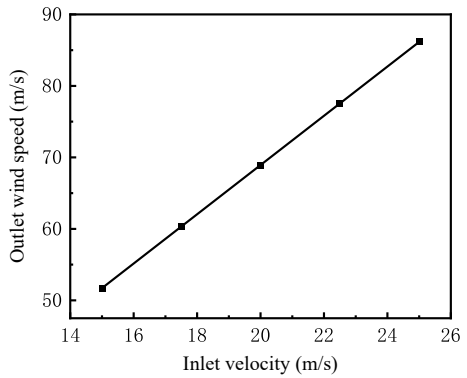
the blades is lower. The wind speed at the outlet is the highest, and the wind speed at the blades is lower than the surrounding area. The variation of outlet gas velocity of a double rotating Venturi under different inlet wind speeds is shown in Fig. 6. It can be seen that as the inlet wind speed increases, the gas outlet velocity also increases.

Liquid velocity distribution. When the inlet liquid velocity is 0.35 m/s, the liquid velocity distribution in the venturi dust collector is shown in Fig. 7. Vortex appears at the blade position, and the liquid velocity is unevenly distributed, while the velocity at the blade tail is large. In addition, below the blade, the liquid velocity near the center of the inner barrel is relatively large and evenly distributed, with a maximum internal liquid velocity of 40.26 m/s.

Fig. 7 Liquid velocity distribution when inlet liquid velocity is 0.35 m/s
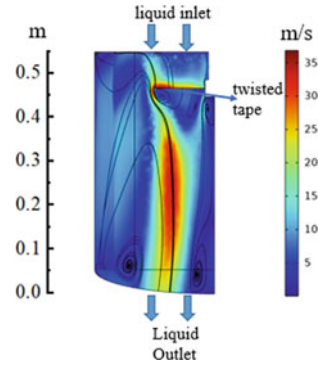
5 Conclusion

This article conducts simulation analysis on electrostatic precipitators and double rotating Venturi precipitators, and establishes fluid models and particle trajectory models.

(1) As the inlet air speed picks up, the velocity of the flow field in the electrostatic precipitator also increases, and the maximum velocity occurs near the discharge electrode. However, when the inlet wind speed increases, the efficiency of dust removal diminishes. The highest collection efficiency for all particle sizes occurs at an inlet wind speed of 15 m/s.

(2) The smaller the inlet wind speed, the better the removing dust efficiency of each particle size. When the particle radius exceeds 0.2 μm, the efficiency of dust removal increases with increasing dust particle size. When the particle radius is less than 0.2 μm, the smaller the dust particle size, the higher the corresponding dust removal efficiency.

(3) The wind speed of dust containing gas in the double rotating Venturi dust removal system reaches its maximum at the outlet, the liquid flow rate reaches its maximum below the blade, and vortex forms at the blade. As the inlet wind speed increases, the outlet wind speed of the double rotating Venturi dust collector also increases. When the inlet liquid velocity is 0.35 m/s, the maximum liquid velocity inside the venturi is 40.26 m/s.

References

1. Chen B, Li S, Guo Y et al (2022) Research on electrostatic shielding characteristics of electrostatic precipitator. J Air Waste Manag Assoc 72(4):331–345
2. Yao Q, Li SQ, Xu HW et al (2009) Studies on formation and control of combustion particulate matter in China: a review. Energy 34(9):1296–1309
3. Kasdi A (2016) Computation and measurement of corona current density and V-I characteristics in wires-to-plates electrostatic precipitator. J Electrostat 81:1–8

4. Zhou W, Jiang R, Sun Y et al (2021) Study on multi-physical field characteristics of electrostatic precipitator with different collecting electrodes. Powder Technol 381:412–420
5. Xiong W, Lin Z, Zhang W et al (2018) Experimental and simulation studies on dust loading performance of a novel electrostatic precipitator with dielectric barrier electrodes. Build Environ 144:119–128
6. Mukherjee S, Verma A, Biswas S et al (2021) Removal of cement dust particulates via fully submerged self-primed Venturi scrubber. CLEAN Soil Air Water 49(5):2000241
7. Zhang H, Zuo Z, Mørch KA et al (2019) Thermodynamic effects on Venturi cavitation characteristics. Phys Fluids 31(9):097107
8. Guerra VG, Gonçalves JAS, Coury JR (2011) Experime verification of the effect of liquid deposition on droplet size measured in a rectangular Venturi scrubber. Chem Eng Process 50(11–12):1137–1142
9. Guerra VG, Achiles AE, Béttega R (2017) Influence of droplet size distribution on liquid dispersion in a Venturi scrubber: experimental measurements and CFD simulation. Ind Eng Chem Res 56(8):2177–2187
10. Zheng G, Chen B, Li J et al (2019) Effect of liquid injection arrangements on injection flow rate of a laboratory-scale venturi scrubber. Front Energy Res 7:51
11. Guerra VG, Bettega R, Goncalves JAS (2012) Pressure drop and liquid distribution in a Venturi scrubber: experimental data and CFD simulation. Ind Eng Chem Res 51(23):8049–8060
12. Ye M, Liang M, Qian F et al (2020) The numerical simulation of gas-liquid two phase flow in annular gap Venturi of converter wet dust removal. In: IOP conference series: materials science and engineering. IOP Publishing 730(1):012051
13. Lin L, Liu T, Yuan N et al (2021) Study on the influence of venturi on the cleaning performance of elliptical filter cartridge. Powder Technol 377:139–148

Two-Dimensional Numerical Simulation of Temperature Field Distribution in Transformer Windings

Jianwen Zhu, Jianhua Zhang, Guoliang Li, Sen Li, Yuqing Lin, Zuhui Liang, and Chengzhen Li

Abstract With the rapid development of economy, modern power industry demands more and more transformer capacity. The increase of transformer capacity leads to the increase of heat production during operation and the corresponding increase of operating temperature. It is very important to analyze and calculate winding temperature rise for transformer product development and operation maintenance. In this paper, based on the heat generation and heat dissipation conditions of transformer windings, the finite element equations of temperature field and flow field are established by applying the principles of heat transfer and fluid mechanics, and the distribution of temperature field of windings is further obtained.

Keywords Temperature field · Transformer · Winding losses

1 Introduction

With the rapid development of economy, the demand for electric energy in the whole society is increasing, and the capacity requirements of transformer in the modern power industry are increasing. The increase of transformer capacity increases the loss generated in the operation process of the transformer, and also further improves the operation temperature of the transformer [1–3]. The temperature rise of the transformer winding is too high from time to time, which easily leads to the damage of the transformer and affects the normal working condition of the transformer.

The hot spot temperature of winding is one of the biggest factors limiting the load capacity of transformer, and it is also one of the main reasons leading to the aging of transformer insulation materials. Therefore, the relevant standards for transformers at home and abroad stipulate that the average temperature rise of the winding and the hot spot temperature of the transformer during operation must be controlled below

J. Zhu · J. Zhang · G. Li (✉) · S. Li · Y. Lin · Z. Liang · C. Li
Zaozhuang Power Supply Company of State Grid Shandong Province Electric Power Company, Zaozhuang, Shandong, China
e-mail: 18369296036@163.com

the specified value [4]. However, it is very difficult to accurately obtain the hot spot temperature of the transformer winding in operation, and the generation, conduction and loss process of heat inside the transformer is very complicated, so it is difficult to obtain the accurate winding hot spot temperature by analytical method. At present, there are three methods to obtain winding hot spot temperature [5]: The first is direct measurement method, which can be measured by optical fiber temperature sensor or thermocouple. However, it is difficult to ensure the accuracy because the location of winding hot spot mainly depends on experience. In addition, fiber optic sensors are expensive, so they are not widely used. The second is the prediction model based on thermoelectric analogy. The hot spot temperature is obtained by numerical calculation. However, because there are many nonlinear parameters in it, and it is difficult to determine these parameters reasonably, this method is not widely used. The third method is IEC354 and GB1094.2 standard recommended hot spot temperature analytical formula calculation method, which is more used in transformer design hot spot temperature approximate estimation method, but can't determine the distribution of temperature field.

For product development and operation, it is very important to analyze and calculate the temperature rise of transformer winding [6]. The traditional concept of average temperature rise neglects the influence of hot spot temperature on transformer and can't fully and accurately reflect the real condition of winding [7]. Therefore, based on the principles of heat transfer and fluid mechanics, the finite element equations of temperature field and insulating oil flow field of winding model are established in this paper. Through numerical calculation, the temperature of each point of the winding can be obtained, and the temperature field distribution of the whole transformer winding can be further obtained.

2   Heat Generation and Heat Dissipation Analysis

2.1   Heat Generation Analysis of Transformer Windings

In order to further explore the temperature distribution characteristics of transformer winding, we adopt a solid model of small transformer winding without iron core, in which the box is a rectangular epoxy box. The resistance loss of the winding and the eddy current loss inside the winding are the main sources of temperature rise of the transformer winding. The expression is shown as follows:

$$P = P_R + P_{WL} = I^2 R + P_{WL} \tag{1}$$

where I, R and P_{WL} are the current, resistance and eddy current loss of transformer windings respectively. The formula for calculating unit heat source used in subsequent calculation is: $q = P/V$, P is the measured active power loss; V is the volume of the winding.

2.2 Heat Dissipation Analysis of Transformer Winding

Heat dissipation of transformer windings is mainly realized through convection heat transfer, including natural convection heat transfer (for heat exchange between the outside of the transformer housing and the outside air) and forced convection heat transfer (for heat exchange between the transformer oil flow and the inside of the housing and the winding).

Natural convection heat dissipation mainly depends on the temperature difference between the two transfer, convection heat transfer coefficient and heat transfer area. Because of the regular geometry of the box, the mean value of the natural convection heat transfer coefficient α_1 has little influence on the calculation results. The formula for calculating α_1 is as follows:

$$\alpha_1 = C(\lambda/H)(Gr_m P_r)^n \tag{2}$$

where, λ is the thermal conductivity of air; H is the height of the box; Gr_m is Grashof number; P is Prandtl number; C and n are constants.

The forced convection heat dissipation of oil flow and winding is more complicated than that of natural convection heat dissipation. This is due to the influence of many factors, such as the physical characteristics and flow mode of oil, heat generation rate and geometry of winding, as well as the spatial position of each winding, etc. Therefore, the α_1 between each winding and oil is very different and cannot be approximated by average value. In addition, the oil flow mode can be divided into laminar flow and turbulent flow, which will seriously affect the heat transfer effect. The state and effect of laminar flow and turbulent flow are quite different, which can be judged by Reynolds number:

$$R_e = \rho V L_c/\mu \tag{3}$$

where, ρ is fluid density; V is the fluid velocity; L_c is the characteristic size; μ is the absolute viscosity of the fluid. When $R_e < 2300$, the oil flow mode in the transformer is laminar flow; Otherwise, it is turbulence.

It can be clearly seen that the temperature distribution of transformer winding is greatly affected by the flow field. Therefore, it is necessary to combine the temperature field of transformer winding and the flow field of insulating oil to obtain a more ideal winding temperature distribution.

3 Differential Equations and Boundary Conditions

In order to better calculate the temperature field in transformer windings, the following four assumptions are made:

1. When heating and heat dissipation reach the equilibrium state, the temperature and velocity distribution of winding and oil no longer change with time;
2. The physical characteristics of transformer oil (such as density, dynamic viscosity, specific heat, etc.) are constant and incompressible;
3. The only heat source of the transformer model is the heating of the winding, and the calorific value per unit time per unit volume is fixed, and the heat transfer coefficient is uniform;
4. Constant ambient temperature.

The temperature and velocity fields of oil flow and heat dissipation are affected by mass, momentum and energy transfer, equations are shown as follows:

Continuity equation,

$$\frac{\partial u}{\partial x} + \frac{\partial v}{\partial y} = 0 \tag{4}$$

Momentum differential equation in the x direction,

$$\rho\left(u\frac{\partial u}{\partial x} + v\frac{\partial u}{\partial y}\right) = F_x - \frac{\partial P}{\partial x} + \mu\left(\frac{\partial^2 u}{\partial x^2} + \frac{\partial^2 u}{\partial y^2}\right) \tag{5}$$

Momentum differential equation in the y direction,

$$\rho\left(u\frac{\partial v}{\partial x} + v\frac{\partial v}{\partial y}\right) = F_y - \frac{\partial P}{\partial y} + \mu\left(\frac{\partial^2 v}{\partial x^2} + \frac{\partial^2 v}{\partial y^2}\right) \tag{6}$$

Energy differential equation,

$$\rho c_p\left(u\frac{\partial t}{\partial x} + v\frac{\partial t}{\partial y}\right) = \lambda_1\left(\frac{\partial^2 t}{\partial x^2} + \frac{\partial^2 t}{\partial y^2}\right) \tag{7}$$

where, u and v are velocity components of oil per unit volume in x and y directions respectively; P is the pressure of unit volume oil; μ is the absolute viscosity of the fluid; t is the temperature of unit volume oil; F_x and F_y are the components of the force in x and y directions on the unit volume oil; c_p is the specific heat of transformer oil; λ_1 is the thermal conductivity of the winding.

Since the temperature field and the flow field need to be solved simultaneously iteratively, the boundary conditions are determined by the boundary conditions of the temperature field:

$$\begin{cases} -\lambda_1\left(\frac{\partial t}{\partial x} + \frac{\partial t}{\partial y}\right) = q \\ -\lambda_2\left(\frac{\partial t}{\partial x} + \frac{\partial t}{\partial y}\right) = \alpha_1(t - t_a) \end{cases} \tag{8}$$

and boundary conditions of flow field:

$$v = v_0, \quad P = P_0, \quad u = 0, \quad v = 0,$$

Among them, q is the heat generation rate of winding; λ_2 is the thermal conductivity of the box; α_1 is the natural convection heat transfer coefficient between the air and the outside of the box; t_a is the temperature of the outside air; v_0 is the initial speed of oil at the transformer inlet; P_0 is the pressure at the outlet of transformer oil flow; u and v are the velocity components of the unit volume oil in the x and y directions on the surface of the stationary wall (including the inner side of the box and the winding in contact with the oil).

The temperature field and flow field are discretized into degrees of freedom of several nodes, and then the four differential equations listed above are converted into the corresponding variational problems. Under the boundary conditions of temperature field and flow field, cross iteration method is used to solve the problem. First, determine the speed, temperature and winding temperature of the transformer oil. Calculate natural convection heat (heat exchange between the outside of the box and the outside air) and forced convection heat (heat exchange between the inside of the box and the windings and the transformer oil) and compare them with the total heat production. If the two are not equal, the initial value is updated and the total heat lost is recalculated until the condition is met that it is equal to the total heat produced. The temperature sequence at this point is the desired temperature field.

4 Simulation Example of Temperature Field of Transformer Winding

4.1 Two-Dimensional Finite Element Model of Transformer Winding

The solid model of small transformer adopted in this paper has no iron core in its winding, and the specific data are shown in Table 1.

Since the length of the winding is much larger than the width of the vertical oil passage, the temperature field of the transformer winding and the insulating oil flow field nearby can be regarded as uniform in length direction, thus reducing the three-dimensional problem to a two-dimensional problem for processing. Figure 1a shows

Table 1 Transformer model specific data

Component	Quantity (pcs)	Length (mm)	Width (mm)	Height (mm)
Box	1	1200	222	497
Winding	19	400	194	17.4
Horizontal oil passage	20	–	–	7.9
Vertical oil passage	2	–	10	–

(a) 2D finite element model of transformer.   (b) Grid profile of transformer.
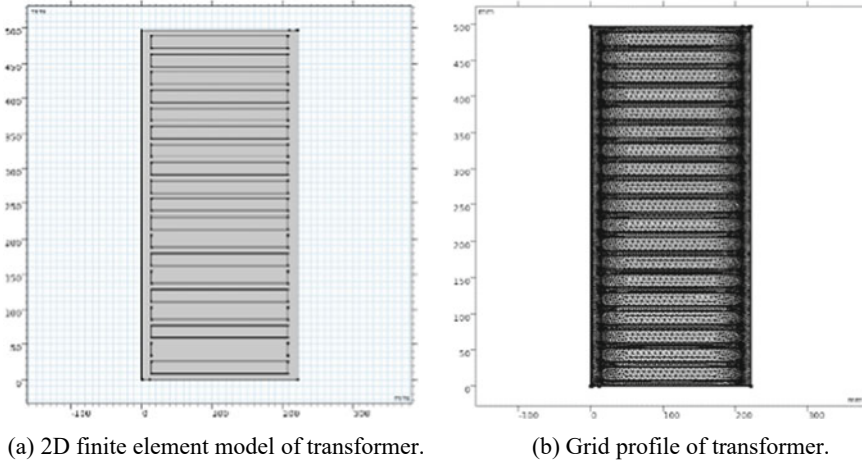
Fig. 1 In-plane displacement–time curves under single excitation

the two-dimensional finite element model of the transformer used to calculate the temperature and flow fields. The upper right corner is the oil outlet, and the lower left corner is the oil inlet.

4.2 Mesh Subdivision

The grid division of the model will affect the accuracy and efficiency of the calculation. In general, the more grids are divided, the higher the accuracy of the calculation will be, but the efficiency will be reduced [8–11]. Considering that the model used in this paper is not complicated, two meshing methods, quadrilateral and triangle, are adopted. In addition, considering the influence of the flow boundary layer, higher density of the winding and the oil flow channel near the box wall and the oil flow outlet and entrance is divided. The subdivision of this example is shown in Fig. 1b. There are 10,860 grid vertices, 14,270 triangular grids and 2552 quadrilateral grids.

4.3 Parameter Setting

For smooth simulation, parameters are set as follows: oil density is 821 kg/m^3; dynamic viscosity coefficient is 5.32829 mPa s; thermal conductivity of oil is 0.107 W/(m K); specific heat of oil is 2163 J/(kg K); The average thermal conductivity of winding is 0.78 W/(m K); the heat transfer coefficient between box wall and air is 1.2 W/(m^2 K).

The boundary conditions [12] to be introduced are:

1. The temperature of the outside air is constant at 293 K;
2. v_0 has only a y component, and $v_y = 0.297$ m/s;
3. The inlet temperature of oil is 334.25 K;
4. The relative pressure at the outlet is 0;
5. u and v at static wall surface are 0;
6. According to the loss of the transformer winding, the heat source density of the winding is 1.457×10^5 W/m^3.

4.4 Calculation Results and Analysis

After the above material parameters and boundary conditions are set, the calculated winding temperature distribution nephogram and isotherm distribution nephogram of the small transformer are shown in Fig. 2.

It can be clearly seen from Fig. 3 that the temperature of different windings is different, and the temperature of each part in the same winding is also different. The highest temperature is measured in the middle of several windings, and its position is biased to the oil outlet.

Change the positions of the oil inlet and outlet, explore the influence of the winding temperature distribution, change the positions of the oil inlet and outlet in the transformer model, move 2 mm inward, keep the material parameters and boundary conditions unchanged, and re-establish the simulation model. In this case, the winding temperature distribution cloud diagram and isotherm distribution cloud diagram are shown in Fig. 3.

By comparing the winding temperature cloud map before and after the oil inlet and outlet position changes, it can be clearly seen that the oil inlet and outlet position can

(a) Temperature distribution cloud map.   (b) Isotherm distribution diagram.
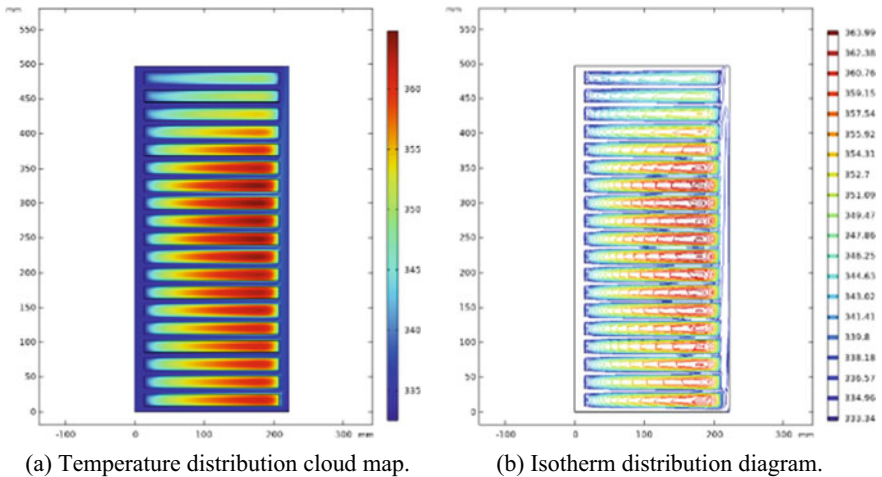
Fig. 2 Distribution diagram of winding temperature field of small transformer

(a) Temperature distribution cloud map.   (b) Isotherm distribution diagram.
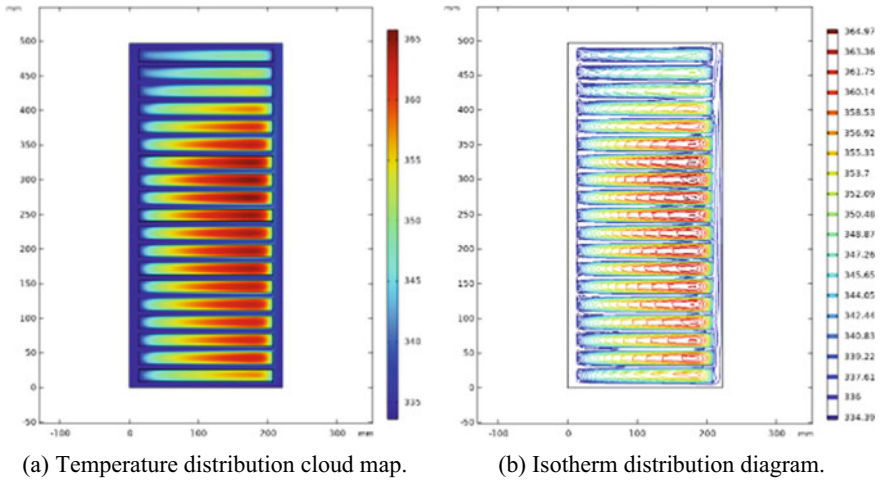
Fig. 3 The winding temperature field distribution after changing the oil passage

affect the heat dissipation of the winding. Moreover, it can be seen from the analysis that the oil flow velocity of the winding in the middle of the right side is slow, the heat dissipation is poor, and the temperature is higher than other positions. Therefore, increasing the oil flow velocity of transformer oil is also an effective method to reduce the winding temperature. In addition, the temperature of the transformer winding can be reduced by reducing the oil temperature of the oil inlet and broadening the width of the oil passage.

5   Conclusion

In this paper, the temperature field distribution of a small transformer winding model is analyzed based on the numerical method. The model comprehensively considers the influence of the internal oil channel distribution on the winding temperature field, and adopts the method of solving the temperature field and the flow field simultaneously to obtain the temperature field distribution cloud diagram of the small transformer winding. At the same time, the influence of vertical oil passage inlet and outlet position on winding temperature field distribution is also studied, and the validity of transformer two-dimensional simulation model based on finite element analysis is verified in transformer temperature field simulation. This research result can provide important basis for insulation design and life evaluation of transformer.

References

1. Li M, Wang Z, Zhang J, Ni Z, Tan R (2021) Temperature rise test and thermal-fluid coupling simulation of an oil-immersed autotransformer under DC bias. IEEE Access 9:32835–32844
2. Susa D, Nordman H (2009) A simple model for calculating transformer hot-spot temperature. IEEE Trans Power Deliv 24(3):1257–1265
3. Tian H, Sun X, Guo Y, Wang P (2015) Combustion characteristics of hybrid rocket motor with segmented grain. Aerosp Sci Technol 46:537–547
4. Liu H, Zhang D, Li W, Xu Z, Li L, Zhou F, Yang B (2019) Finite element analysis for temperature field of winding in large oil-immersed transformer. High Voltage Apparatus 55(12):83–89 (in Chinese)
5. Wang J, Zhang X, Zhang H, Shan D, Lu T, Guo Z (2013) Numerical simulation of winding temperature field of large power transformer. Electr Manufact 5:23–25+30 (in Chinese)
6. Cai C, Zhao G (2022) Calculation for temperature field of transformer winding in SF6 gas insulation test. Electr Autom 44(3):94–96 (in Chinese)
7. Islam MJ, Khang HV, Repo AK, Arkkio A (2010) Eddy-current loss and temperature rise in the form-wound stator winding of an inverter-fed cage induction motor. IEEE Trans Magn 46(8):3413–3416
8. Liu P, Zhang X, Kuang S, Guo Y, Zhang Z (2019) 3D finite element model mesh division method in motor temperature field analysis. J Electron Meas Instrum 33(8):173–178 (in Chinese)
9. Chen Y, Yang Q, Zhang C, Li Y, Li X (2022) Thermal network model of high-power dry-type transformer coupled with electromagnetic loss. IEEE Trans Magn 58(11):1–5
10. Akbari M, Rezaei A (2016) Transformer bushing thermal model for calculation of hot-spot temperature considering oil flow dynamics. IEEE Trans Power Deliv 36(3):1726–1734
11. Nie L, Yang J, Tang K (2022) Thermal network modeling of high frequency insulated core transformers. IEEE Trans Appl Supercond 32(6):1–5
12. Fu C, Ji S, Wang S, Li Y (2002) 2D numerical calculation of temperature field of winding in transformer. High Voltage Eng 5:10–12 (in Chinese)

Permeation Characteristic Comparison of the Components in the Rejuvenation Liquid of Polyethylene

Xiantao Tao, Hui Gong, Ping Fu, Kai Deng, Zihang Qin, Shize Zhang, and Fanwu Chu

Abstract Cable injection rejuvenation technology is a means to improve the insulation performance of aging cables and extend their service life. The permeability characteristics and rejuvenation effect evaluation of rejuvenation fluids are key research areas in the application of cable rejuvenation technology. The present work compares and analyzes existing cable rejuvenation fluids, and proposes a method for analyzing the infiltration characteristics that can be used in the selection of rejuvenation fluids. Molecular dynamics simulations were conducted on the main components of three rejuvenation fluids, Phenyl-methyl-dimethoxy-silane, Trimethyl-methoxy-silane, and Diphenyl-dimethoxy-silane, to obtain their diffusion coefficients in polyethylene. Furthermore, finite element simulations of chemical substance transfer were conducted to compare the infiltration characteristics of the rejuvenation fluid components in polyethylene. The results indicate that the diffusion coefficient ratios of the three organosilicon compounds in polyethylene are 1.49:5.62:1, and the concentration ratios at the same observation point on the seventh day after infiltration are 6.7:160:1. The diffusion coefficient can be used to evaluate infiltration characteristics.

Keywords Cable rejuvenation technology · Rejuvenation liquid · Diffusion coefficient · Permeation characteristics · Polyethylene

1 Introduction

With the development of power grid transformation and transmission engineering, a large number of cables, particularly those with polymer insulation, have been widely used in cable engineering due to their excellent insulation and mechanical properties. However, the complex operating environment of cables may lead to various defects, such as moisture, cracks, water trees, or electric trees, resulting in decreased

X. Tao (✉) · H. Gong · P. Fu · K. Deng · Z. Qin · S. Zhang · F. Chu
China Electric Power Research Institute, Wuhan 430074, China
e-mail: tao_xiantao@126.com

insulation performance or accidents [1]. Meanwhile, as service life of the cables gradually reaches 30 years or more, the problem of insulation aging gradually becomes apparent [2]. For cables with insulation aging, moisture or defects, direct replacement is expensive and requires excavation, which is complex and polluting. Therefore, researchers have proposed cable injection rejuvenation technology, which has gradually been promoted to the commercial application stage. The basic principle of this technology is to inject rejuvenation fluid into the cable core, and the rejuvenation fluid penetrates and reacts with water in the insulation, ultimately achieving the effect of repairing the cable [2].

Currently, the main components of the reported rejuvenation fluids include Phenyl-methyl-dimethoxy-silane (PMDMS) proposed by Corning Inc. of the United States, and Trimethyl-methoxy-silane (TMMS) added to the PMDMS formula to improve diffusion rate [3]. Hirazi and Hosseini proposed and used Diphenyl-dimethoxy-silane (DPDMS), which has good thermal and chemical stability [4].

In previous studies involving rejuvenation liquid formulas, the diffusion coefficient obtained from injection rejuvenation experiments is usually used to evaluate the penetration characteristics of the rejuvenation liquid [5, 6]. The basic operation method involves injecting the rejuvenation liquid into the cable to be repaired, and then measuring the concentration of the diffusing substance (rejuvenation liquid) at different depths using analytical methods such as mass spectrometry, radioactive tracing technology, spectrophotometry, and nuclear magnetic resonance, in order to obtain the diffusion coefficient. However, experimental methods are relatively cumbersome, and consume cable samples, consumables, and rejuvenation liquid. In order to improve this situation, Zhou Kai proposed a method based on multi-physics field coupling simulation to simulate the penetration of rejuvenation liquid, which can be used to calculate the concentration distribution at different locations and obtain the relationship between the injection time and pressure of the rejuvenation liquid in the cable [7]. However, this method is difficult to obtain accurate diffusion coefficients and further research is needed.

With the development of molecular simulation techniques, some scholars have proposed and used molecular dynamics (MD) to calculate the diffusion coefficients of substances in polymers. Yue et al. studied the diffusion mechanism of organic molecules in polyethylene films and calculated the diffusion coefficients of three organic molecules [8]. Tao et al. analyzed the adsorption and diffusion behavior of oxygen in polypropylene with different degrees of polymerization [9], while Huang et al. studied the diffusion behavior of O_2 and N_2 in rubbery polymer Polydimethylsiloxane and glassy polymer [10]. The molecular dynamics simulation method has the advantages of clear micro-scale modeling and accurate calculation, and has been widely used in the study of the microstructure and macroscopic properties of polymer composites [11]. This method can also be used to simulate the penetration of rejuvenation liquids in polyethylene materials, and to analyze and predict the permeation characteristics of rejuvenation liquids, thereby reducing the economic and time costs of repeated experiments required for rejuvenation liquid selection and optimization.

In this work, a combined method of molecular dynamics simulation and finite element simulation was used to study the diffusion behavior in polyethylene of

PMDMS, TMMS, and DPDMS, and their diffusion coefficients were obtained. Combined with finite element chemical transfer simulation, the diffusion mechanism and permeation characteristics of the three rejuvenation liquids were compared and analyzed.

2   The Components of the Rejuvenation Liquid

The commonly used formula for rejuvenation liquids in high voltage and insulation fields typically involves a mixture of several effective ingredients, among which organic silicone compounds PMDMS, TMMS, and DPDMS are the most widely used main components in rejuvenation liquids.

The chemical formula of PMDMS is $C_9H_{14}O_2Si$, and its molecular structure as shown in Fig. 1a. In the cable industry, PMDMS is commonly used as a water scavenger, which can absorb moisture and form solid substances, thereby protecting cables from damage and extending their service life [3]. In cable rejuvenation fluids, PMDMS can not only be used to eliminate water, but also serve as a repairing agent to fill in water trees or cracks and form stable silicon oxide solids, thus restoring the insulation performance of cables.

The chemical formula of TMMS is $C_4H_{12}OSi$, and its molecular structure as shown in Fig. 1b. The methoxy group can undergo hydrolysis or alcoholysis reactions [3]. In the rejuvenation of cables, TMMS functions through hydrolysis to generate silanol, which then reacts with the hydroxyl groups on the cable surface to form a silicon oxide polymer that covers the cable surface, achieving the purpose of eliminating moisture and repairing cable insulation.

The chemical formula of DPDMS is $C_{14}H_{16}O_2Si$, and its molecular structure as shown in Fig. 1c. When DPDMS comes into contact with water, hydrolysis reaction occurs, where the silicon-oxygen bonds break, producing silanols and methanol [4]. In cable rejuvenation, injecting DPDMS can be used to eliminate moisture in the cable and improve the electrical performance of the cable, such as increasing insulation resistance and reducing dielectric loss, among other indicators.

(a) PMDMS   (b) TMMS   (c) DPDMS
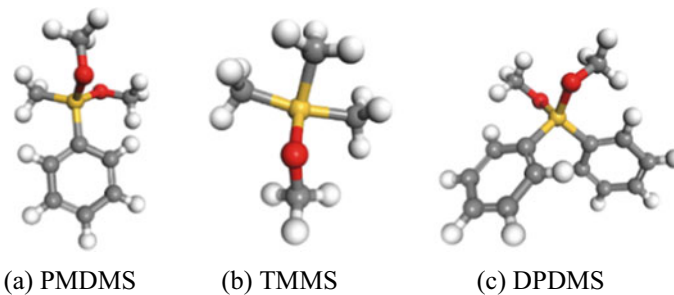
Fig. 1   Schematic diagram of molecular model

For the three components, the effective reaction is a hydrolysis reaction, and its general reaction formula is shown as Eq. (1).

$$X - PhMeSi(OMe)_2 + (X + 1)H_2O \rightarrow HO - (PhMeSiO)_X$$
$$- H + (2X) - MeOH \tag{1}$$
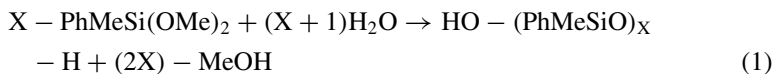
3 Molecular Dynamics Simulation

The paper uses material calculation software to construct four molecular models of rejuvenation liquids for comparative analysis. Firstly, construct the PE model, whose molecular formula is $(C_2H_4)_n$, by constructing a polyethylene chain containing 50 monomers. Secondly, construct PMDMS, TMMS, and DPDMS models as shown in Fig. 2. Thirdly, construct a 3D amorphous structure of the PE molecular chain and one rejuvenation liquid, the energy-minimizing and stable structure is selected for subsequent calculations, with an initial density of 1.0 g/cm³ and a temperature of 320 K. As shown in Fig. 2, three models are constructed, namely PE + PMDMS group, PE + DPDMS group, and PE + TMMS group.

Use the module to perform geometric optimization of the three-dimensional amorphous structure of the polymer to minimize the energy of the structure and reduce the stress generated during modeling, so that the distribution of molecules inside the model is closer to the real material. Molecular dynamics equilibrium is carried out under the NVT canonical ensemble (representing the number of particles (N), volume (V), and temperature (T)) with constant temperature and volume. The molecular dynamics simulation force field used in this study is the COMPASS II force field, with a simulation time of 150 ps, a step length of 1 fs, and a total step number of 50,000. The temperature is set at 320 K, the temperature control method is the Andersen thermostat [12], for the van der Waals interactions and electrostatic interactions, the Atom Based method [13] and Ewald method [14] were used, respectively.

After obtaining the molecular dynamics model trajectory, the diffusion coefficient can be calculated by obtaining the Mean Square Displacement (MSD). In order to

(a) PE+PMDMS   (b) PE+TMMS   (c) PE+DPDMS
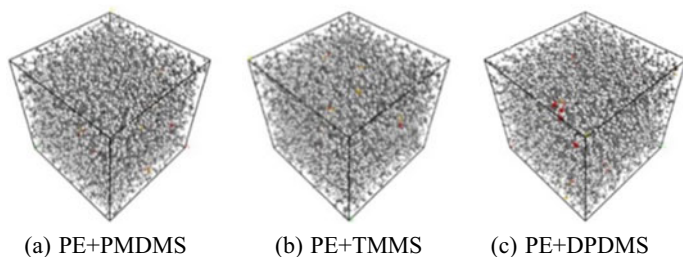
Fig. 2 Three dimensional amorphous structure after geometric optimization

calculate the diffusion coefficient of the repairing fluid in PE, the MSD-t curve should be plotted, and the slope of the best-fit straight line should be calculated. Generally, the solution to differential equations obtained by numerical methods is a numerical solution. However, to calculate the diffusion coefficient, numerical methods need to be applied to solve the differential motion equation of particles to obtain the instantaneous coordinates of particle motion, and then the diffusion coefficient is obtained by statistical averaging. In molecular dynamics, the diffusion coefficient is obtained by fitting the slope of the mean square displacement and then using the *Einstein relationship* [15].

The diffusion coefficient *D* is given by the following equation:

$$D = \frac{1}{6N} \lim_{i \to \infty} \frac{d}{dt} \sum_{i=1}^{N} \left\{ [r_i(t) - r_i(0)]^2 \right\} \tag{2}$$

In the equation above, *N* represents the number of diffusing atoms in the system, $r_i(t)$ and $r_i(0)$ represent the position vectors of the i-th atom at time t and 0, respectively.

By performing molecular dynamics simulations of three different rejuvenation liquid monomers, the MSD versus time t curves were obtained, as shown in Fig. 3. We selected a relatively smooth section for analysis and calculated the diffusion coefficient *D*. The obtained data from 5 to 105 ps were selected for linear fitting to obtain the slope.

The slope of the curves obtained by fitting for the PE + PMDMS, PE + TMMS, and PE + DPDMS groups in this study were 0.0052, 0.0197, and 0.0035, respectively, based on Eq. (2), with the units of the diffusion coefficient being $\mathring{A}^2$/ps. The diffusion coefficients of the rejuvenation liquid molecules calculated from the MSD were converted to the units of cm^2/s. The diffusion coefficients and fitting coefficients R^2 calculated from the slopes using the above method are shown in Table 1.

Fig. 3 *MSD-t* curves of polyethylene molecular chain system with rejuvenation solution
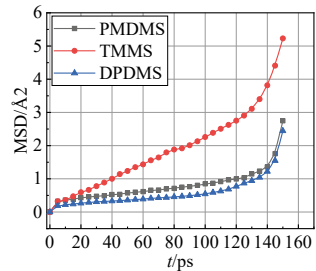
Table 1 Calculation results of diffusion coefficient

Material	Diffusion coefficient (cm^2/s)	R^2 (%)
PE + PMDMS	8.67×10^{-8}	99.59
PE + TMMS	3.23×10^{-7}	99.73
PE + DPDMS	5.83×10^{-8}	98.84

4 Finite Element Simulation of Chemical Substance Transfer

This paper uses the finite element method for simulating chemical diffusion to investigate the diffusion process of the repairing solution molecules inside the cable. The actual shape of the metal stranded wires in the core is simplified to a cylindrical channel with a radius of 23.9 mm, an inner and outer semi-conductive layer thickness of 1.3 mm, an insulation thickness of 15.1 mm, and a cable length of 260 mm. Only the penetration of repairing solution monomers is considered in the model, as shown in Fig. 4, with three observation points: observation point 1 is located in the middle of the conductor shield, observation point 2 is located in the middle of the main insulation, and observation point 3 is located in the middle of the insulation shield. The study is a transient analysis with a starting time of 0 days, a time interval of 1 day, and a total study time of 365 days. In order to investigate the short-term concentration changes in the main rejuvenation area, observation point 2 of the main insulation is studied over a short period of time with a starting time of 0 min, an interval of 720 min, and a total study time of 57,600 min.

The simulation process involves the diffusion of the repairing solution from the core to the insulation shield, with a concentration of 4.7 mol/L in the core. The diffusion passes through the conductor shield and the main insulation and flows out through the insulation shield, with a diffusion coefficient of 2.3 as calculated in Chapter 2.3.

The simulation results of each observation point at the two time nodes mentioned above are shown in Fig. 5. Figure 5a shows the concentration changes at Observation Point 1, while (b) and (c) show the concentration changes at Observation Point 2 in two separate studies. (c) Shows the concentration changes at Observation Point 3. The concentration distribution at all three observation points indicates that TMMS has a higher permeability than the other two rejuvenation fluid materials.

Fig. 4 Finite element chemical transfer simulation model
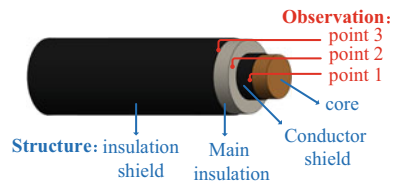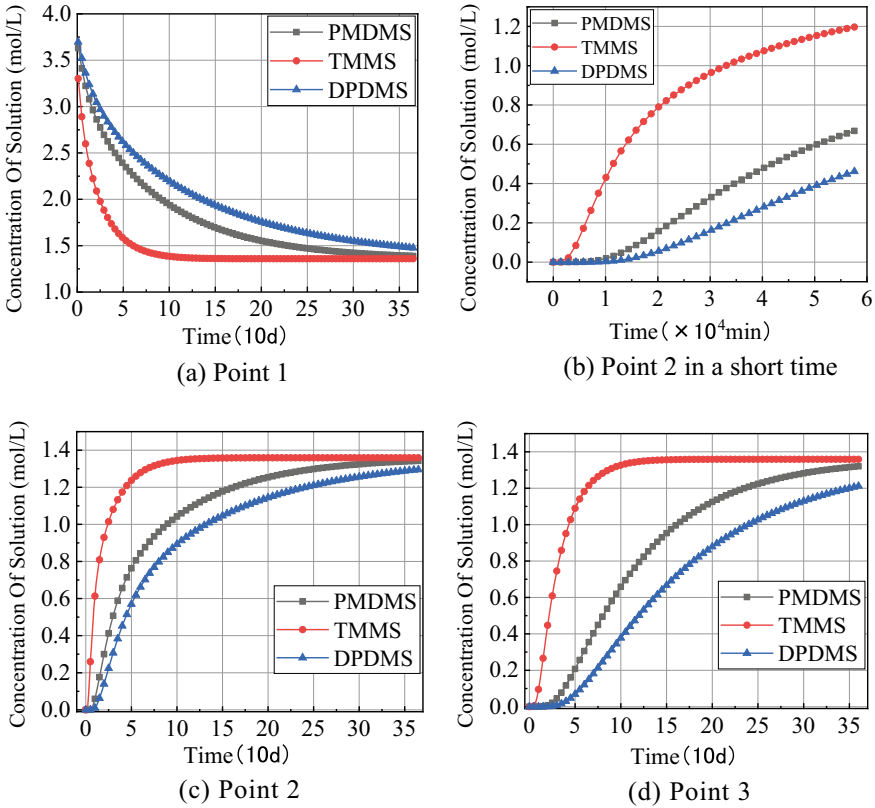
Fig. 5 Change of concentration at each observation point

5 Discussion

The molecular sizes of the three rejuvenation liquids followed the order: TMMS < PMDMS < DPDMS. Among them, TMMS had the smallest relative molecular mass of 104.22, while PMDMS and DPDMS had relative molecular masses of 182.29 and 244.36, respectively. Generally, molecules with larger relative molecular masses are also larger in size and typically contain more atoms and chemical bonds. Based on the comparison of molecular dimensions, it can be inferred that the permeability of the three rejuvenation liquids is different. Generally, smaller molecules have faster diffusion rates and better permeability in the material. TMMS has the smallest molecular size, and therefore, should have the best permeability, followed by PMDMS. The permeability of DPDMS, with the largest molecular size, may be relatively poor. However, the permeability performance is affected by multiple factors, including the material surface properties, porosity, and the substance being penetrated. Therefore, a

comprehensive evaluation of the permeability performance of the three rejuvenation liquids requires consideration of other factors.

After obtaining the concentration changes, the concentrations at the three observation points were analyzed according to Fig. 5. Point 1 can analyze the initial and steady-state concentrations as shown in Figure (a). Since the point is close to the line core, the initial concentration reaches the maximum value, which is approximately 70–80% of the injection concentration, and gradually decreases to the steady-state value over time. The concentration change gradient shows that the repairing solution with a larger diffusion coefficient reaches steady state more quickly, and the diffusion concentration changes faster in a short time. Point 2 can observe the time and concentration value of the repairing solution molecules reaching the repair area. The short-term results are shown in Figure (b), and the long-term simulation results are shown in Figure (c). The concentration change of point 2 in the short term indicates that the diffusion rate of TMMS repairing solution is much faster than the other two repairing solutions in the early stage, which presents a trend of first fast and then slow. The concentrations of PMDMS, TMMS, and DPDMS at 7 days are in a ratio of 6.7:160:1. Through concentration analysis, TMMS has much higher permeability in the short term than the other two materials. The differences in steady-state concentrations among the three repairing solutions are not significant, but the time to reach steady state is different. Point 3 can observe the outflow concentration and time as shown in Figure (d). The outflow position can observe the time when the cable is radially penetrated. From the figure, it can be seen that TMMS penetrates the cable first, which takes about 100 days, PMDMS takes about 350 days, and DPDMS still shows a slow upward trend within the simulation time range, and the penetration time is greater than 360 days.

Permeability and diffusion coefficient are two distinct physical quantities with no direct relationship between them. This paper compares the permeability characteristics of three rejuvenation fluids by establishing the relationship between diffusion coefficient and permeability through concentration changes. Higher permeability can effectively penetrate the cable insulation layer, filling cracks and voids inside the insulation layer, thereby restoring the cable's insulation performance. Based solely on the diffusion coefficient, Table 1 shows that the diffusion coefficient of TMMS is about 3.79 times that of PMDMS and about 5.63 times that of DPDMS. Based on the above conclusions, considering only the monomer, the permeability order of rejuvenation fluid molecules in polyethylene can be roughly ranked as: TMMS > PMDMS > DPDMS.

6   Conclusion

This article analyzes the permeation characteristics of rejuvenation fluids on polyethylene materials and presents the following main conclusions based on molecular dynamics simulation and finite element chemical transfer simulation of PMDMS, DPDMS, and TMMS:

(1) Under conditions of 320 K, with polyethylene as the permeated material, the diffusion coefficients of PMDMS, TMMS, and DPDMS rejuvenation fluid molecules were calculated by molecular dynamics to be 8.67×10^{-8} cm²/s, 32.83×10^{-8} cm²/s, and 5.83×10^{-8} cm²/s, respectively. The diffusion coefficient ratio of the three rejuvenation fluids is 1.49:5.62:1.

(2) Based on the results of finite element chemical transfer simulations of the three rejuvenation fluids under the same conditions, TMMS exhibits the best permeation characteristics, while PMDMS and DPDMS are relatively inferior. Based solely on the permeation characteristics of monomer rejuvenation fluid molecules in polyethylene, the permeation order is as follows: TMMS > PMDMS > DPDMS.

References

1. CIGRE Technical Brochure (2008) Remaining life management of existing AC underground lines. CIGRE Working Group, Paris, France
2. Bertini GJ, Vincent GA (2007) History and status of silicone injection technology
3. Bertini G, Vincent G. Advances in chemical rejuvenation: extending medium voltage cable life 40 years
4. Shirazi A, Hosseini SH (2018) Comparison of aged XLPE power cables restoration by injecting two various anti-failure nanofluids. Eng Fail Anal S1350630717313614
5. Mccary JL, Arigala S, Busby D et al (2010) A tale of two fluids. In: Electrical insulation conference
6. Chatterton WJ, Dionne J (2009) Chemical treatment of URD cables. In: Electrical insulation conference. IEEE
7. Zhou K, Yang D, Tao W et al (2015) Effects of diffusion activity of injected liquid on water-treeing cables' electrical properties after injection. Proc CSEE 35(019):5095–5102 (in Chinese)
8. Yue YJ, Liu QZ, Wu LY et al (2012) Molecular dynamics simulation for diffusion of organic molecules in polyethylene membranes. CIESC J 63(1) (in Chinese)
9. Tao C, Feng H, Zhou J et al (2009) Molecular simulation of oxygen adsorption and diffusion in polypropylene. Acta Phys Chim Sin 25(7):1373–1378
10. Huang Y, Liu Q, Zhang X (2007) Molecular simulation of transport behavior of penetrant through silicon-containing polymers. J Chem Ind Eng 58(6):1359–1365 (in Chinese)
11. Application of the clustering method in molecular dynamics simulation of the diffusion coefficient. J Ocean Univ China 01:43–47 (2008)
12. Andrea TA, Swope WC, Andersen HC (1983) The role of long ranged forces in determining the structure and properties of liquid water. Chem Phys 79:4576–4584
13. Karasawa N, Goddard WAI (1992) Force fields, structures, and properties of poly(vinylidene fluoride) crystals. Macromolecules 25(26):7268–7281
14. Cheatham T, Miller JL, Fox T et al (1995) Molecular dynamics simulations on solvated biomolecular systems: the particle mesh Ewald method leads to stable trajectories of DNA, RNA, and proteins. J Am Chem Soc 117(14):4193–4194
15. Allen MP, Tildesley DJ (1987) Computer simulation of liquids. Oxford University Press, Oxford

Optimization of Capacitor Core Parameters for Rubber-Impregnated Fiber Bushing of Ultra-High Voltage AC Transformer

Zhang Haojie, Sun Hanli, and Xu Xuran

Abstract The rubber-impregnated fiber high-voltage bushing boasts properties such as fire, explosion and moisture resistance, which have been widely promoted over recent years. The capacitor core is one of the core components of the Ultra-high voltage (UHV) AC rubber-impregnated fiber bushing, which is accident-prone as a result of its complex working conditions. On the basis of the initial structural parameters of 1100 kV AC transformer rubber-impregnated fiber bushing, this paper constructs a finite element model of 1100 kV AC transformer rubber-impregnated fiber bushing, which mainly focuses on the analysis of the electric field distribution of the capacitor core, analyzes the influence law of the length, thickness and spacing of the pole plate of the capacitor core on the maximum electric field strength, thereby proposing a bushing capacitor core design scheme. The results show that, in comparison with the initial scheme, the maximum Electric field strength at the end of the capacitor core pole plate is 16.886 kV/mm, which is 17.8% lower than that of the initial scheme, while the maximum electric field strength in the radial direction is 5.420 kV/mm, which is 7.6% lower than that of the initial scheme. The results can give references to the structural design of the 1100 kV AC transformer rubber-impregnated fiber bushing.

Keywords Rubber-impregnated fiber capacitor bushing · Capacitor core · Electric field · Simulation analysis · Insulation optimization

Z. Haojie (✉) · S. Hanli · X. Xuran
School of Electrica Engineering and Automation, Wuhan University, Wuhan 430072, China
e-mail: 2473510955@qq.com

1 Introduction

The ultra-high voltage transformer refers to the 1000 kV class transformer, which is an essential equipment for the construction of the ultra-high voltage transmission project. The ultra-high voltage bushing integrates electrical, thermal, force and environmental properties, which is critical to the safe, reliable and economic operation of the power system [1].

Nevertheless, subject to various influences such as complex electrical, thermal, force and operating environment, the operating conditions of UHV bushings are extremely harsh, with a number of abnormal failures of bushings having occurred in the power system, which have caused severe impact on the safe operation of the power grid. Moreover, in accordance with the statistics of the University of Hannover in Germany, the number of transformer accidents caused by bushings accounts for 45% of the number of major transformer failures. When the bushing exists structural and process defects, it is susceptible to pole plate edge discharge, even leading to bushing explosion accidents, which has gravely endangered the safe operation of power transformers and other power equipment connected to it and its vicinity [2–4]. In 2016, as a result of an internal insulation defect, a 220 kV transformer substation glass fiber reinforced plastic capacitor type bushing was eventually torn under the internal gas pressure, which led to the insulation breakdown of the lower part of the bushing, resulting in a C-phase single-phase short circuit fault on the high-voltage side of the main transformer [5]. A variety of accidents have demonstrated that the failure of the bushing is prone to cause greater safety accidents, while the quality of the bushing exerts an essential influence on the safety of electricity.

There are numerous causes of bushing failures. The pole-plate edge electric field effect is prevalent in capacitive bushings of various voltage levels. The sudden change of electric field at the pole plate edge forms a local strong field area, which provokes pole plate edge discharge, and poses a threat to the safe operation of capacitive bushings [6]. Among them, in the current power system in China, it primarily adopts foreign or joint venture products of oil paper bushing, rubber-impregnated paper bushing or SF6 gas bushing [7–10]. Through many years of technology introduction, and the development of digestion and innovation, despite the fact that some domestic bushing manufacturers have been equipped with the production capacity of ultra-high voltage bushing, there still exist technical feebleness in materials, design and processes [11, 12]. For this reason, it is imperative to study and optimize the high-voltage bushing to maintain the normal operation of the power grid, as well as to guarantee the safety of the electricity consumption in China.

The rubber-impregnated fiber bushing features the advantages of oil-free, fire and explosion-proof, high mechanical strength, moisture-proof, and less maintenance, which possesses unique advantages to resolve the above issues. Nevertheless, at the present time, there are few research contents [13, 14] for UHV transformer bushings in China, while foreign scholars, such as Shiling Z, Rokunohe T and others were primarily concentrated on the study of SF_6 gas bushings. In contrast, the research on capacitive cores of rubber-impregnated fiber transformer bushings are few and

far between. In this regard, this project is intended to examine the capacitor core and other components of 1100 kV AC transformer bushings under the conditions of temperature and electric fields in multiple situations, and to optimize the design of the capacitor core parameters, thereby enabling the electric field strength of the capacitor core to be distributed as uniformly as possible, thereby making up for the deficiencies in the domestic research on rubber-impregnated fiber bushings. In practical sense, it can facilitate the design and production level of 1100 kV AC transformer bushings in China, which is of great theoretical and practical engineering value.

2   Building a Finite Element Model

2.1   Structure and Initial Parameters of UHV Bushing

The 1100 kV AC transformer rubber-impregnated fiber bushing primarily covers the Grading ring, fixture, SF_6 gas cavity, guide rod, shed, capacitor core, flange and Grading cover, with the basic structure of the bushing shown in Fig. 1. Among them, the capacitor core stands out as one of the core components of the UHV AC rubber-impregnated fiber bushing, which is also the important part of the UHV bushing. The capacitor core consists of a multi-layer structure, which is wound by alternately spacing the insulating layer and the pole plate, with the pole plate made of graphite yarn, while the insulating layer is formed by glass fiber with high insulation performance impregnated with special epoxy resin. The initial structural parameters of the UHV bushing are shown in Table 1.

With the initial design scheme, the capacitor core adopts the design scheme of equal thickness and equal pole difference, the initial number of pole plates of the capacitor core is 99 layers, while the initial pole plate number close to the guide is

Fig. 1 Basic structure of the bushing

grading
metal fittings
SF_6 gas chamber
Guide rod
Umbrella skirt
Capacitor core
flange
Pressure equalizing cover
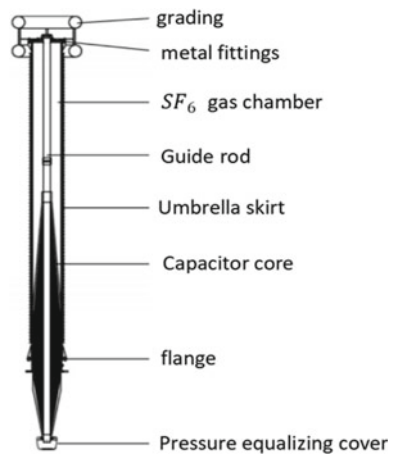
Table 1 Initial structural parameters of UHV bushing

Structural parameters	Numerical value/mm
Total length of bushing	14,343.5
Length of core	8129
Diameter of core	875
Length of flange	900
External diameter of grading ring	2200
Pipe diameter of grading ring	400
Diameter of grading cover	720
Length of grading cover	280

Table 2 Length of each pole plate

Pole plate no.	Length	Pole plate no.	Length
0	8129	7	7410
1	7770	8	7350
2	7710	9	7290
…	…	…	…
6	7470	98	1950

0. The thickness of the pole plate is 0.3 mm, the distance between the pole plates is 3.3 mm, the upper pole difference between the 0 pole plate and the 1 pole plate is 299.5 mm, the lower pole difference is 59.5 mm, the upper pole difference between the remaining pole plates is 40 mm, the lower pole difference is 20 mm, while the ratio of the upper and lower pole differences is 2:1, with the length of each plate under the initial parameters as shown in Table 2.

2.2　Establishment of Finite Element Simulation Model and Condition Loading

The actual arrangement of the UHV bushing is illustrated in Fig. 2. As can be seen from Figs. 1 and 2, the UHV bushing as a whole is an axisymmetric model, while the two-dimensional axisymmetric simplification of the UHV bushing is carried out. The simplified two-dimensional axisymmetric model is illustrated in Fig. 3, while the relative dielectric constants of each material of the bushing are presented in Table 3.

In view of its control equations and boundary conditions, the following loading methods are required for the electric field calculation of the UHV bushing:

(1) Applying 1200 kV potential to the upper and lower fixtures, the pressure equalizing ring, the zero screen and the nodal potential coupling on the surface of the guide rod;

Fig. 2 Actual arrangement of UHV bushing
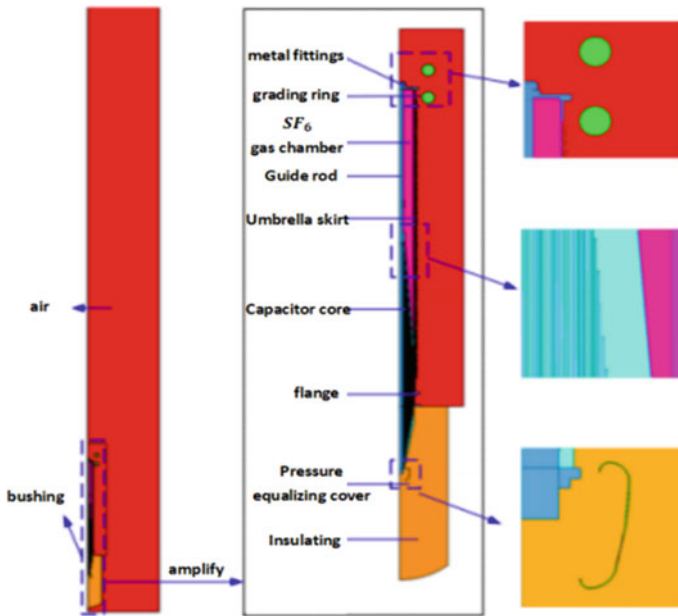
Fig. 3 Two-dimensional axisymmetric model

Table 3 Relative dielectric constant of each material

Materials	Relative dielectric constant
Rubber-impregnated fibers	4.7
Insulation oil	2.2
Silicone rubber	2.8
Epoxy resin	4.5
SF_6	1.002

Fig. 4 Potential distribution of the whole model
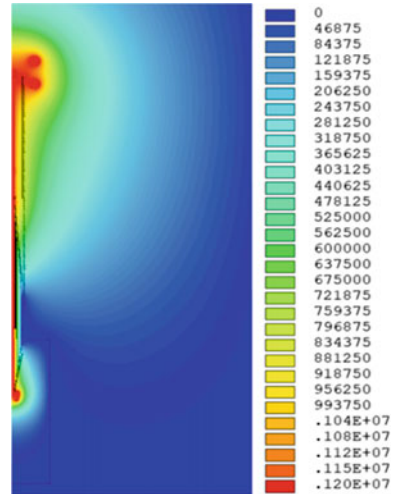
(2) Apart from the zero screen and the end screen, other capacitive screens are set to floating potential, for which the form of nodal potential coupling is adopted;

(3) The end screen ground, air boundary, the outer edges of the flange and tank are set to zero potential.

The overall potential distribution of the model is given in Fig. 4.

3 Simulation Analysis of Bushing Electric Field

3.1 Comparison of Methods

In this paper, the calculation results of the partial voltage between the pole plates of the capacitor core under the analytical method and the finite element method are compared to verify that the finite element method carries out the calculation with higher accuracy. The capacitor core of the bushing is composed of multiple layers of pole plates, where the capacitance between each two layers can be deduced from

the following equation:

$$c_1 = \frac{2\pi \varepsilon_r \varepsilon_0 l_1}{ln \frac{r_1}{r_0}}$$

$$c_2 = \frac{2\pi \varepsilon_r \varepsilon_0 l_2}{ln \frac{r_2}{r_1}}$$

$$\cdots$$

$$c_n = \frac{2\pi \varepsilon_r \varepsilon_0 l_n}{ln \frac{r_n}{r_{n-1}}}$$

Therein, ε_0 denotes the dielectric constant in vacuum, ε_r denotes the relative dielectric constant in rubber-impregnated fibers, r_n denotes the radius of the nth pole plate, and l_n denotes the length of the nth pole plate.

The total capacitance value of the capacitor core is:

$$\frac{1}{c_{总}} = \frac{1}{c_1} + \frac{1}{c_1} + \cdots + \frac{1}{c_i} + \cdots + \frac{1}{c_n} \tag{1}$$

The voltage between any two adjacent pole plates of the capacitor core is:

$$\Delta U_i = \frac{c_{总} U}{c_i} (i = 1,2,3,...,n) \tag{2}$$

According to Eqs. (1) to (3), the calculation can obtain the capacitance between the two adjacent pole plates, the total capacitance of the capacitor core and the partial voltage between the pole plates, with the calculation results and the comparison illustrated in Fig. 5.

3.2 Electric Field Distribution of Capacitor Cores

Prior to the start of optimization, the capacitor core axial, radial and end electric field strengths are first analyzed and calculated. The extracted capacitor core axial electric field strength is illustrated in Fig. 6. In view of the upper pole difference of the capacitor core gradient design is about twice as large as the lower pole difference, the axial electric field strength of the lower axis is larger. As can be observed from the figure, the axial electric field strength exhibits a trend of first decreasing and then increasing as the number of pole plates increases, where the maximum value of axial electric field strength is 0.819 kV/mm.

As can be noted from the figure, the overall radial electric field strength is characterized by U-shaped distribution, with the radial electric field strength decreasing and then increasing with the increase of the number of pole plates, in which the maximum value of radial electric field strength is 5.865 kV/mm, and the minimum value is 3.666 kV/mm.
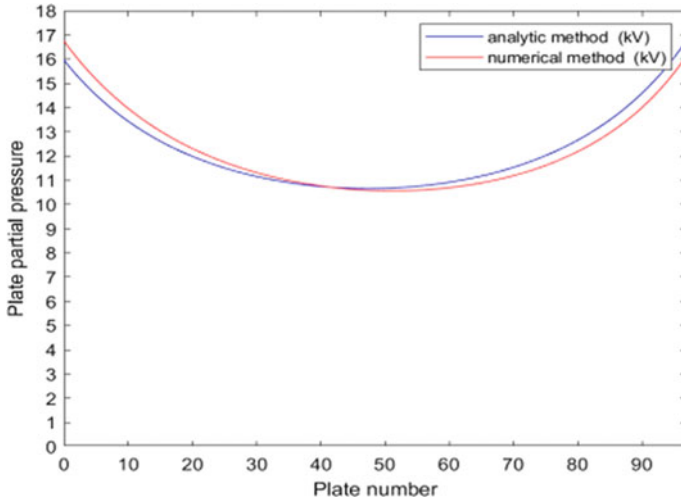
Fig. 5 Comparison of voltage distribution of each pole plate
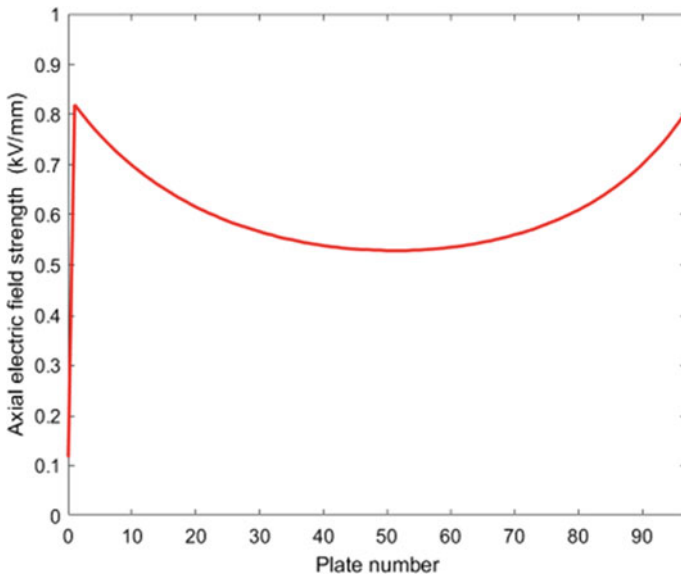
Fig. 6 Axial electric field strength of capacitor core

It can be seen from the figure, the maximum electric field strength at the end presents a trend of decreasing and then increasing as the number of pole plates increases, while the maximum electric field strength at the upper end is larger than the maximum electric field strength at the lower end. The maximum value is 20.532 kV/mm at the lower end of the capacitor core at the end of the end screen, in which the

whole capacitor core is not fully utilized for the insulation between the middle pole plates.

With the above data and electric field strength distribution graph, it is revealed that the electric field strength varies considerably with the undulation of the pole plate, while the electric field strength of the voltage in the middle part of the pole plate layers is smaller, which demonstrates that the whole capacitor core is not sufficiently utilized for the insulation between the middle pole plates, and the parameters such as the number of pole plate layers and gradient of the capacitor core need to be adjusted, thereby enabling the radial, axial and end electric field strength distribution of the capacitor core to comply with the test requirements.

4 Structural Optimization

4.1 Structural Optimization of Capacitor Cores and Electric Field Analysis

The maximum electric field strength at the end of the capacitor core is 20.532 kV/mm under the initial parameters. For the sake of improving the electric field distribution of the capacitor core, the parameters of the capacitor core of the 1100 kV AC transformer rubber-impregnated fiber bushing are optimized. The details are as follows:

(1) In the initial design scheme, the capacitor core is designed in accordance with equal thickness and equal polarization, with the ratio of upper and lower polarization being 2:1. It has been demonstrated in studies that when the capacitor core is designed with equal margin, the overall local discharge starting electric field strength of the capacitor core can be improved, with uniform electric field distribution of the capacitor core and the maximum electric field strength at the end of the capacitor core is relatively small [15]. Nevertheless, the manufacturing of capacitor cores of 1100 kV AC transformer rubber-impregnated fiber bushing still requires the processes of winding and high temperature curing of the capacitor screen, where the lengths and thicknesses of the pole plates of the capacitor cores with equal margin design vary, which is an extremely difficult task to manufacture with the current manufacturing equipment. As a consequence, the optimization idea adopted in this paper is to maintain the ratio of the upper and lower pole difference of the capacitor core on the basis of the equal thickness design scheme, while regulating the length of the capacitor core pole plates and the pole plate spacing, thereby realizing the optimization of the electric field distribution of the capacitor core.

(2) Under the initial parameters, in conjunction with Figs. 7 and 8, it can be realized that the maximum electric field strength at the end of the capacitor core appears at the end of the end screen indicated in Fig. 9, where the end electric field strength and radial electric field strength of the capacitor core are not
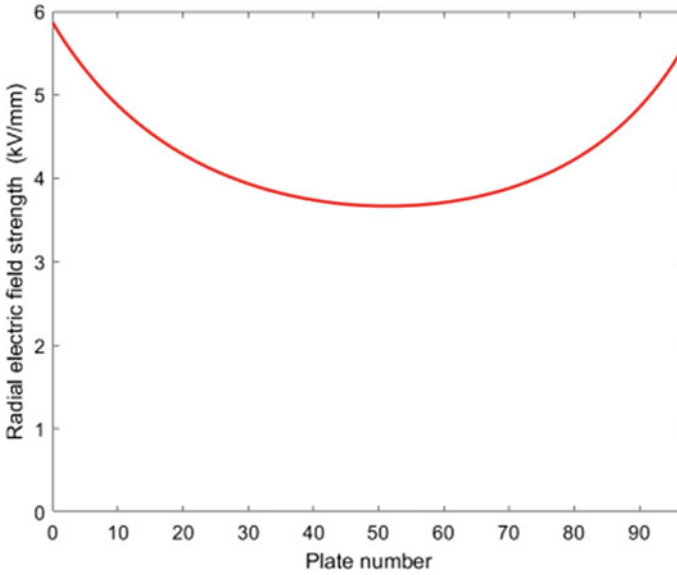
Fig. 7 Radial electric field strength of capacitor core

uniformly distributed, with an overall U-shaped distribution, while the insulation of the capacitor core on the middle pole plate is not adequately utilized. As a consequence, the length of the middle pole plate of the capacitor core and the length of the pole plate with larger electric field strength at the end have been adjusted in this paper to regulate the pole plate capacitance, thereby achieving the optimization of the electric field strength distribution of the capacitor core.

(3) In accordance with the above adjustment ideas, the pole plate lengths of the capacitor cores of the 1100 kV AC transformer rubber-impregnated fiber bushing were adjusted and recalculated for several times, which eventually led to a more superior set of optimized solutions for each pole plate length of the capacitor cores. The final optimized scheme of capacitor core is presented in Table 4, while the configuration optimization curve of each pole plate length of capacitor core and the initial pole plate length curve in the final optimized scheme are presented in Fig. 10. The final optimized solution of the capacitor core was re-calculated and presented in Figs. 11 and 12. The maximum electric field strength at the end of the capacitor core is 16.886 kV/mm, which is 17.8% lower than the maximum electric field strength of 20.532 kV/mm under the initial parameters, while the maximum electric field strength at the end of the capacitor core is 17.2 kV/mm lower than the permitted electric field strength after the optimization. The maximum radial electric field strength of the capacitor core is 5.420 kV/mm, which is 7.6% lower than the maximum radial electric field strength of 5.864 kV/mm under the initial parameters.
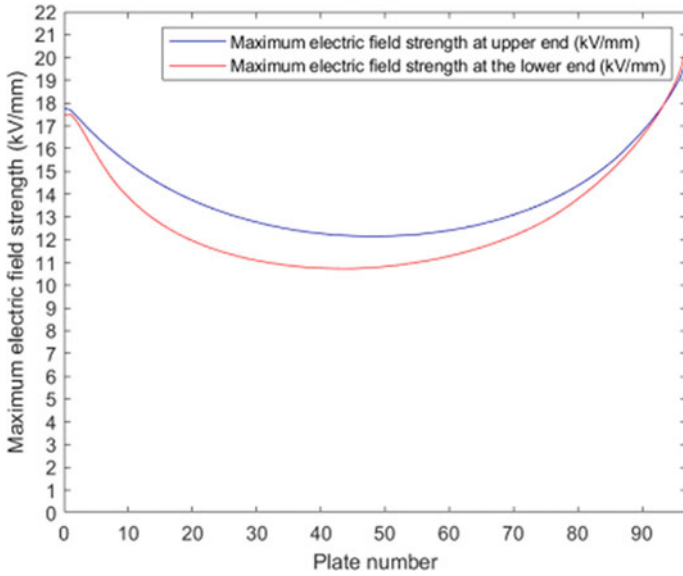
Fig. 8 The maximum electric field strength at the end of the capacitor core
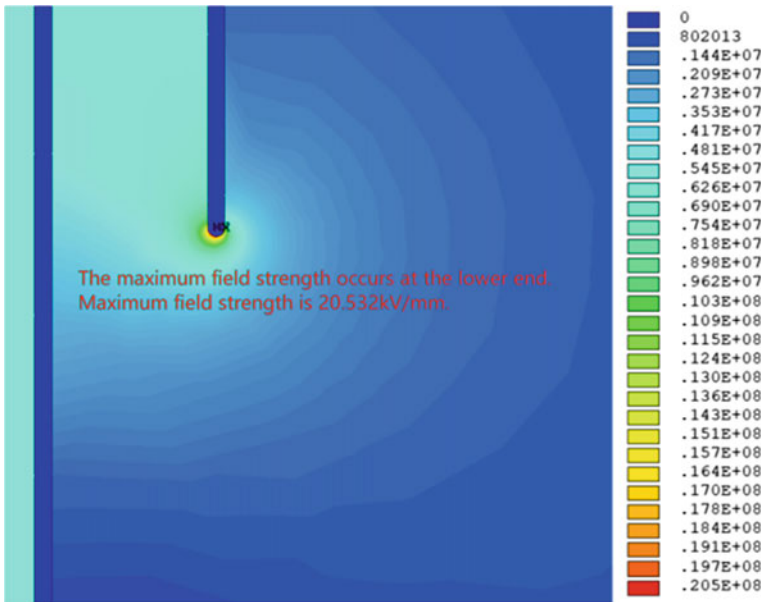
Fig. 9 Cloud chart of electric field intensity distribution at the maximum electric field strength at the end

Table 4 Final optimization
scheme of capacitor core

Pole plate no.	Length	Pole plate no.	Length
0	8230	7	5865
1	7740	8	5670
…	…	…	…
5	6345	97	2049
6	6090	98	1974
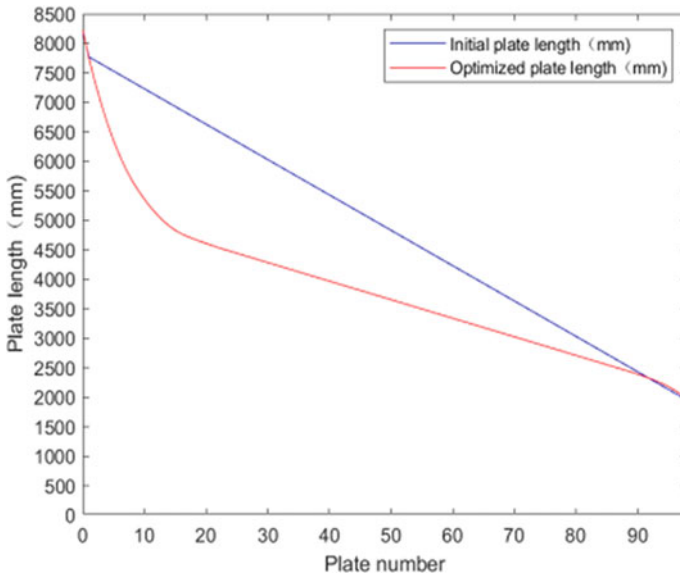
Fig. 10 Optimization curve of each electrode plate length
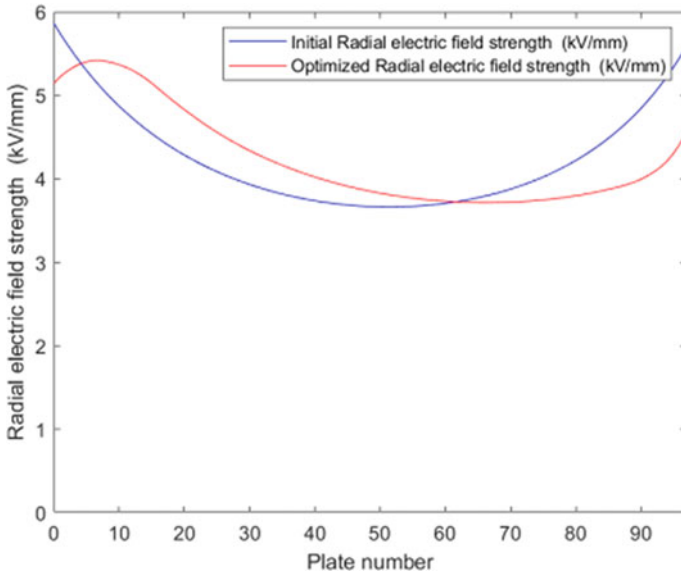
Fig. 11 Optimized radial electric field strength
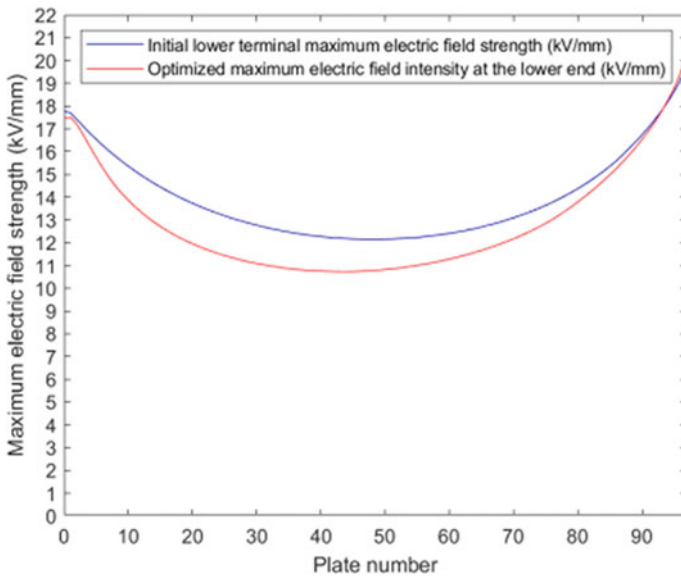
Fig. 12 Optimize rear end electric field strength

5 Conclusion

In this paper, the finite element method is adopted to examine the electric field distribution of the capacitor core of 1100 kV AC transformer rubber-impregnated fiber bushing under the initial parameters. This paper proposes a new optimized design scheme of the capacitor core on the basis of the equal thickness design scheme of the capacitor core, which keeps the ratio of the upper and lower pole difference of the pole plate of the capacitor core unchanged by adjusting the pole plate length of the capacitor core, with the following conclusions:

(1) With the initial parameters, the radial electric field strength, axial electric field strength and end electric field strength of the capacitor core are all distributed in a U-shape, with the maximum value of the radial electric field strength of the capacitor core being 5.864 kV/mm at the 0–1 layer pole plate, the maximum value of the axial electric field strength being 0.830 kV/mm at the 2–3 layer pole plate. On the whole, the electric field strength at the upper end of the capacitor core is higher than that at its lower end, while the maximum value of the electric field strength at the end of the capacitor core appears at the lower end of the end screen, with a maximum value of 20.532 kV/mm.

(2) On the basis of the above design ideas, a new optimized design scheme of the capacitor core is given, resulting in the maximum electric field strength at the end of the capacitor core being reduced to 16.886 kV/mm, which is 17% lower than the maximum electric field strength at the end of the initial parameter of 20.532 kV/mm. The maximum radial electric field strength of the capacitor core is 5.420 kV/mm, which is 7.6% lower than the maximum radial electric field strength of 5.864 kV/mm under the initial parameters.

(3) Following the optimization of the capacitor core parameters, the maximum electric field strength at the end is lower than the permissible electric field strength of 17.2 kV/mm, while the radial electric field strength is also markedly reduced, resulting in a significant improvement in the electric field strength distribution of the capacitor core.

References

1. Qiu ZX Design and application of high voltage insulators. China Electric Power Press, Beijing (in Chinese)
2. Wei Z, Qi B, Zuo J et al (2015) Diagnosis method of oil-paper insulation defects in converter transformers based on partial discharge image features. Power Syst Technol 39(4):1160–1166 (in Chinese)
3. Kuang XH, Chen WL (2007) Analysis on causes of multiple accidents of transformer high voltage incoming and outgoing bushings. Hunan Electr Power 27(3):22–24 (in Chinese)

4. Liu X, Chen M, Liang C et al (2020) Investigation on distribution of electrthermal coupled field and improved design of ±1100 kV converter valveside bushing. IET Sci Meas Technol 14(2):188–197
5. Yao WJ, Yang BH, He JH (2017) Analysis of the burnout fault of the bushing of the 220 kV fiberglass reinforced plastic capacitive main transformer. Electr Eng 2017(12):89–91 (in Chinese)
6. Dai QM, Qi B, Zhuo R, Li CR, Tian Y, Fu ML (2017) Simulation and optimization method of electric field distribution at the edge of capacitor core plate of oil-impregnated paper bushing. Electr Eng 41(5):1682–1687 (in Chinese)
7. Liu PF, Nan ZL, Li ZJ (2017) The development of ± 800 kV gas insulated DC through wall bushing. Electr Eng 18(12):42–45 (in Chinese)
8. Xie C, He P (2015) Fault analysis of 800 kV EHV DC through wall bushing. Electr Power 48(7):27–30 (in Chinese)
9. Zhang SL (2018) An analysis of I insulation performance of ±800 kV "U" type SF6 gas insulated through wall bushing. Insulators Surge Arresters (3):134–138 (in Chinese)
10. Chai YH, Zhang NN, Zhang YS (2020) Design of mechanical structure of through wall cylinder for DC through wall casing. Sci Technol Innov (14):124–125 (in Chinese)
11. Song Y, Xu Z. L Lan, Z. B, Deng JG, Ke L, Nie Y, Li HX (2021) Research on the application of 1200 kV UHV AC rubber dipped fiber through wall sleeving technology. Insulat Surge Arresters 2:40–45 (in Chinese)
12. Hopkinson P, Del Rio, Awagenaar L et al (2010) Progress report on failures of high voltage bushings with draw leads. In: IEEE PES general meeting, vol 010. IEEE, Minneapolis, USA, pp 1–15
13. Shiling Z, Siyu Z, Xialin S (2019) Multi-physics field simulation of 1100 kV GIS SF6 gas insulated composite bushing. In: 2019 IEEE conference on electrical insulation and dielectric phenomena, pp 247–250
14. Rokunohe T, Kato T, Hirose M et al (2010) Development of insulation technology in compact SF6 gas-filled bushings: development of compact 800-kV SF6 gas-filled bushings. Electr Eng Jpn 171(1):19–27
15. Chen RX (2022) A study on optimization of main insulation of oil-paper capacitor bushing based on equal margin. Ganzhou Jiangxi Univ Sci Technol 2022:20–23 (in Chinese)

Study on Factors Influencing Self-healing Energy of Metallized Film Capacitors

Fei Yan and Xiang Huang

Abstract Metallized film capacitors are widely used as low-voltage reactive power compensation devices in power systems. However, frequent self-healing breakdown seriously affects the insulation performance and life of capacitors. In order to study the self-healing characteristics of metallized film capacitors, an experimental platform was established to study the effects of voltage, temperature, shunt capacitance, film thickness, and interlayer pressure on the self-healing energy of metallized film capacitors. The results show that, the self-healing energy increases by 58.59% with increasing voltage in the range of 950–1150 V; in the range of 30–90 °C, the self-healing energy decreases by 36.08% with increasing temperature; in the range of 10–160 μF, the parallel capacitance has little effect on the self-healing energy; in the range of 6–10 μm, the self-healing energy increases by 246% with increasing film thickness and in the range of 20–800 kPa, the self-healing energy decreases by 47.11% with the increase of interlayer pressure. The results of the study can provide guidance for the optimal design of metalized film capacitors.

Keywords Metallized film capacitor · Polypropylene film · Self-healing

1 Introduction

Metallized film capacitors play an important role in power systems in terms of reactive power compensation, rectification and filtering, voltage support and energy storage [1–5]. Compared with traditional oil-immersed capacitors, metallized film capacitors have the advantages of high energy storage density, safety, environmental protection and low noise [6, 7]. Metallized film capacitors are made of micron-thick biaxial-oriented polypropylene film as the dielectric, with a nano-thick metal layer (usually

F. Yan · X. Huang (✉)
China Electric Power Research Institute, BeiJing 430074, China
e-mail: huangxiang@epri.sgcc.com.cn

F. Yan
e-mail: yanfei3@epri.sgcc.com.cn

pure aluminum or zinc-aluminum alloy) plated on one side of the film by vacuum vapor deposition as the electrode and wound around a core rod [8]. This structure provides a unique self-healing property that extends the life of the capacitor, but also brings with it a number of problems that may arise in operation, such as a decrease in capacity, an increase in leakage current, a decrease in breakdown strength and a serious heat generation due to an increase in dielectric loss as the self-healing point increases [9–11]. Self-healing failures due to poor design or other external factors also have a "snowball" effect, which can lead to bulging, integral failure or even explosion of the metalized film capacitor [12].

The self-healing characteristics of metallized film capacitors under DC voltage have been studied extensively by scholars. The main conclusions are as follows: the area of the metallized electrode to be demetallized during the self-healing process is determined by the size of the self-healing energy [13, 14]; the self-healing energy is proportional to the 2nd to 5th power of the DC voltage applied to the capacitor [15, 16]; according to the power criterion for arc extinction, the arc resistance extinction criterion is reached as the voltage rises [17]; successive breakdown of the metallized film during the voltage recovery phase after a single breakdown usually has a low self-healing energy [18]; the interlayer pressure on the metallized film increases gradually from the outer to the inner layers, and the corresponding self-healing breakdown energy decreases slowly [19], which is related to the ionization of a small number of residual air molecules during the winding process, the rapid axial expansion of the gas products of the self-healing breakdown and the difficulty of maintaining a high density plasma [20], but too high interlayer pressures may also lead to reduced dielectric strength, thermal damage to the dielectric film and self-healing failure [21]; the self-healing energy of a metallized film is approximately inversely proportional to the square of the square resistance [17], but too large a square resistance leads directly to an increase in the equivalent series resistance and economic cost of the metallized film capacitor, and may also lead to electrical explosions [22]; at the same breakdown voltage, increasing the thickness of the film increases the peak value of the self-healing breakdown current and shortens the pulse time, reducing the thickness of the film can limit the self-healing energy to less than 2 mJ [16]; When self-healing breakdown occurs, the shunt capacitor will also inject a lot of energy into the faulty component, so reducing the shunt capacity can make the capacitor self-healing breakdown when the voltage drop increases and the breakdown arc shrinks quickly, so as to reduce the peak breakdown current and self-healing energy [23]. At the same breakdown voltage, the self-healing energy increases with temperature, and at temperatures of 120 °C and above polypropylene films can suffer electro-thermal breakdown and catastrophic meltdown, resulting in severe capacity loss and self-healing failure in DC durability tests [24].

The self-healing characteristics of metalized film capacitors under pulsed discharge conditions have also been studied by some scholars: for pulsed capacitors, self-healing breakdown generally occurs during the voltage holding phase, and both charging and holding times have a significant effect on the loss of capacity [25]; as the number of charges and discharges increases, multiple self-healing breakdowns occur simultaneously, and the voltage waveform is distorted [26].

In summary, the self-healing characteristics of metalized film capacitors have been extensively studied under DC voltage and pulse discharge conditions, but there are still few reports on their self-healing characteristics under AC voltage. Only by solving the challenges posed by the self-healing breakdown problem and improving the design and manufacturing process can the application of metalized film capacitors in higher voltage power systems become possible. In this paper, an experimental platform for the self-healing breakdown of metallized polypropylene films under AC voltage is built, and the effects of voltage, temperature, shunt capacity, film thickness and interlayer pressure on the self-healing characteristics of metallized film capacitors are investigated, and the results will provide guidance for the optimal design of metallized film capacitors under AC operating conditions.

2   Experimental Platform and Experimental Protocol

In order to facilitate the observation of experimental phenomena and the measurement of experimental parameters, this experiment uses metallized polypropylene films as test specimens and simulates the actual working conditions of the capacitors by connecting capacitors in parallel at both ends of the test specimens as well as applying pressure and temperature.

The experimental circuit for the self-healing characteristics is shown in Fig. 1. T_1 is a voltage regulator; T_2 is a step-up transformer rated at 2 kV. L is a shunt reactor used to compensate for capacitive currents. C_0 is used to simulate the equivalent capacitance in parallel with the test film. C_s is the metallized polypropylene film test piece. During the experiments, the voltage across the film specimen was measured using a Tektronix P6015A high voltage probe and the current flowing through the film specimen was measured using a Pearson 110 coil.

The thin film specimen consists of two layers of metallized polypropylene film with the metal layer facing upwards and the arrangement of the specimen as shown in Fig. 2. Voltage is applied to the thin film specimen by means of copper foil electrodes. A pair of cylindrical heating electrodes made of stainless steel is used to heat and apply pressure to the specimens. The heating electrodes are temperature adjustable
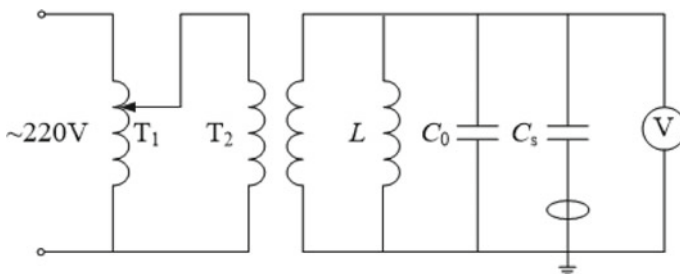
Fig. 1 Experimental circuit for self-healing characteristics

up to 200 °C, the pressure can be adjusted from 0 to 1.0 MPa and the diameter of the electrodes is 50 mm. To avoid mechanical damage to the film specimen, the heating electrodes are finely ground and eight layers of polypropylene base film with a thickness of 6.8 μm are placed on the top and bottom of the film specimen.

During the experiments, a 6.8 μm thick polypropylene base film was padded between the two metallized films to prevent flashover and shorting at the edges of the specimen to strengthen the insulation, while a 3 cm × 3 cm size experimental area was left in the middle of the specimen. The film specimens are shown in Fig. 3, where the dashed boxes represent the experimental area.

In order to investigate the factors influencing the self-healing energy, the thesis selected voltage, temperature, parallel capacitance, film thickness and interlayer pressure as experimental variables. Only one variable was changed in each set of experiments and the values of each variable were taken as shown in Table 1.

During the experiment, the voltage on the test article was raised to the set value and then held at voltage, and the self-healing phenomenon was continuously observed

Fig. 2 Arrangement of experimental electrodes and film samples
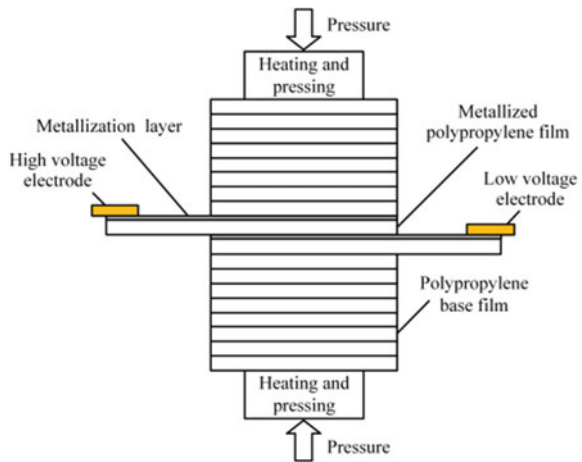
Fig. 3 Metallized polypropylene film specimens
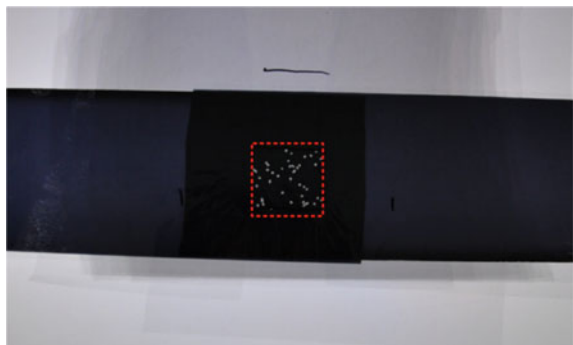
Table 1 The values of each variable taken during the test

Experimental variables	Numerical values							
Voltage U (V)	950		1000	1050		1100		1150
Temperature T (°C)	30		45	60		75		90
Parallel capacitance C_p (μF)	10		20	40		80		160
Film thickness d (μm)	6		7	8		9		10
Pressure P (kPa)		20	40	100	200	400	600	800

Fig. 4 Typical waveforms of self-healing current and self-healing voltage
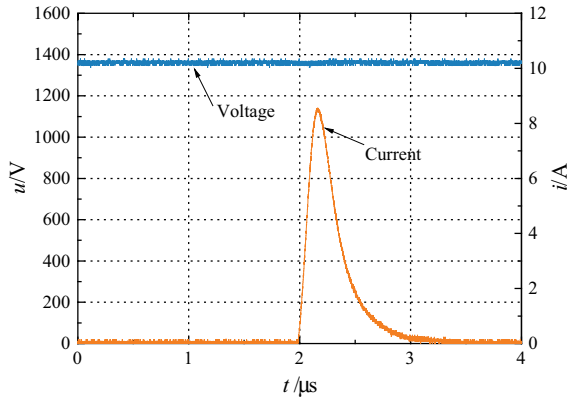
during the experiment. The voltage and current waveforms during each self-healing process were measured and recorded, and the typical experimental results are shown in Fig. 4.

From the typical waveform, it can be seen that during the self-healing process, the voltage across the specimen remains basically constant due to the presence of the shunt capacitor, and the duration of the self-healing current is about 1–2 μs. Based on the experimental waveform and Eq. (1), the self-healing energy E$_{sh}$ can be calculated.

$$E_{sh} = \int_0^{\tau_{sh}} u(t) \cdot i(t)dt \tag{1}$$

$u(t)$ is the self-healing voltage, $i(t)$ is the self-healing current and τ_{sh} is the self-healing duration.

Due to the stochastic nature of the self-healing process, the film specimens were subjected to continuous experiments under the same experimental conditions. The film specimens after the experiments are shown in Fig. 5.

Fig. 5 Self-healing points
on film specimens
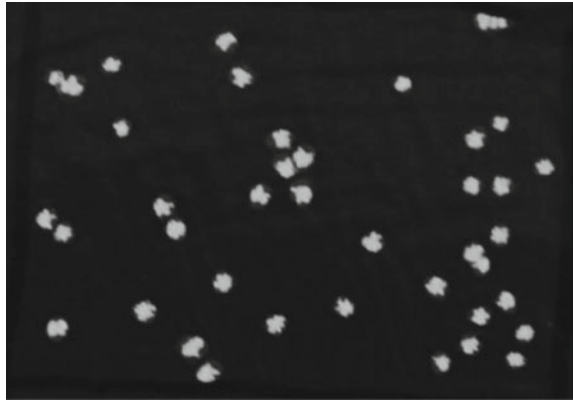
3 Experimental Results and Analysis

3.1 *Effect of Voltage on Self-healing Energy*

During the experiments, the temperature, parallel capacitance, film thickness and interlayer pressure were kept constant at 60 °C, 40 µF, 7 µm and 100 kPa respectively, and only the voltage across the film specimen was varied to carry out the experiments at different voltages. Based on the measured self-healing voltage and current waveforms, the self-healing energy was calculated and the experimental results are shown in Fig. 6.

From the experimental results, it can be seen that the average value of self-healing energy increases from 6.52 to 10.34 mJ with increasing voltage in the range of 950–1150 V, an increase of 58.59%. As most of the self-healing energy is absorbed by the polymer film, thermal damage to the film may occur when the self-healing energy

Fig. 6 Variation of
self-healing energy with
voltage
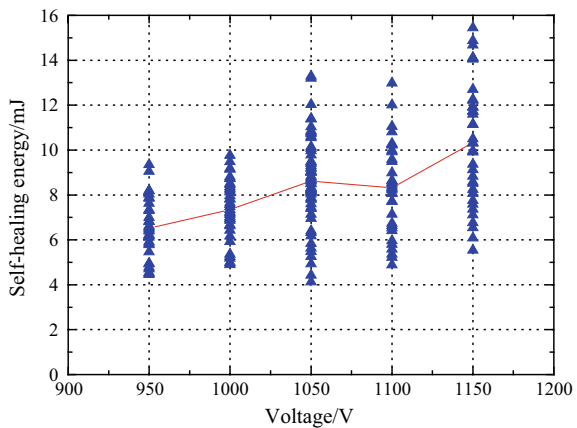
Fig. 7 Variation of self-healing energy with temperature
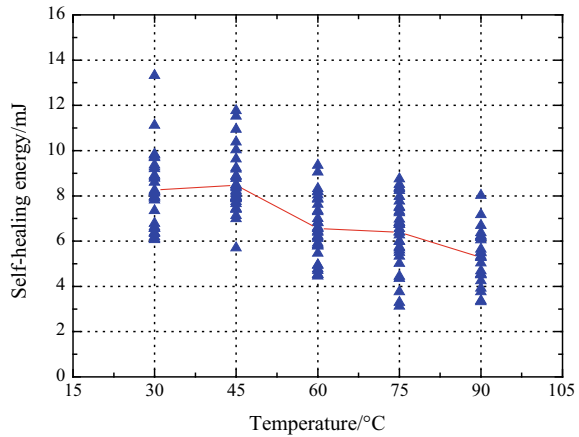
is high. Therefore, when designing capacitors, the design field strength should be chosen reasonably to avoid excessive electric field strength.

3.2 Effect of Temperature on Self-healing Energy

The voltage, parallel capacitance, film thickness and interlayer pressure were fixed at 950 V, 40 μF, 7 μm and 100 kPa respectively, and the above experiments were repeated by varying only the level of temperature. The results of the experiments are shown in Fig. 7.

The experimental results show that the average value of self-healing energy decreases from 8.26 to 5.28 mJ with increasing temperature in the range of 30–90 °C, a decrease of about 36.08%. From the experimental results, it can be seen that the increase in temperature is beneficial to reduce the self-healing energy and slow down the rate of capacity loss, while when the temperature is low, not only the self-healing energy will increase, but also the deposited graphite layer around the self-healing point will become thicker [27], which is not conducive to the recovery of the self-healing point insulation. Therefore, when designing capacitors, it is important to ensure that they are operated at the right temperature to reduce the self-healing energy and to avoid thermal ageing caused by high temperatures [28].

3.3 Effect of Parallel Capacitance on Self-healing Energy

The voltage, temperature, film thickness and interlayer pressure were fixed at 950 V, 60 °C, 7 μm and 600 kPa respectively, and the experiment was repeated by changing

Fig. 8 Variation of
self-healing energy with
parallel capacitance
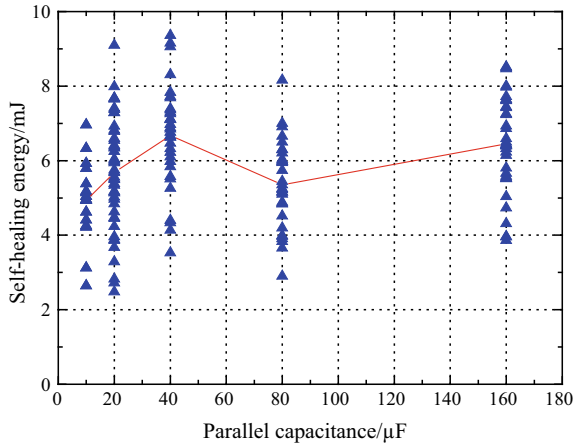
only the parallel capacitance of the film specimens during the experiment. The
experimental results are shown in Fig. 8.

The experimental results show that the parallel capacitance has little effect on
the self-healing energy when the parallel capacitance is varied in the range of 10–
160 μF, with the self-healing energy varying between 2 and 10 mJ, all with an average
value of around 6 mJ. Therefore, the number of parallel components can be flexibly
determined according to the requirements during the design of the capacitor, which
does not affect the self-healing performance of the capacitor.

3.4 Effect of Film Thickness on Self-healing Energy

The temperature, parallel capacitance and interlayer pressure were fixed at 60 °C,
40 μF and 100 kPa respectively, and only the thickness of the film specimen was
changed, keeping the field strength of the specimen constant at 136 V/μm during
the change of thickness, and the above experiment was repeated. The experimental
results are shown in Fig. 9.

From the experimental results, it can be seen that the average value of self-healing
energy increases from 3.47 to 11.99 mJ with increasing film thickness in the range
of 6–10 μm. The self-healing energy of a 10 μm thick film is 3.46 times higher
than that of a 6 μm thick film, and the film thickness has a significant effect on
the self-healing energy of the capacitor. In summary, an increase in film thickness
leads to an increase in self-healing energy, but on the other hand, an increase in
film thickness is beneficial in reducing the heat generation of the capacitor [29].
Therefore, in the design of capacitors, the choice of film thickness should take into
account both thermal and self-healing characteristics.

Fig. 9 Variation of self-healing energy with film thickness
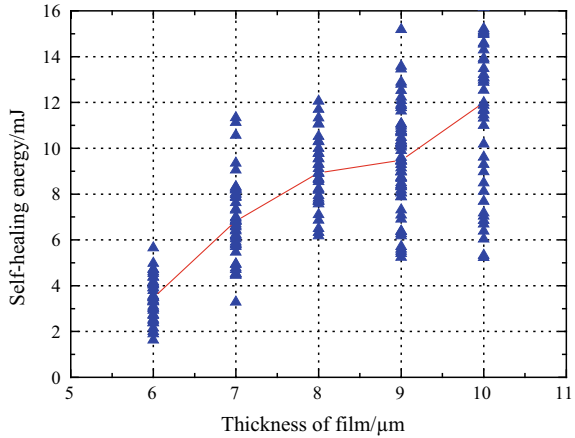
3.5 Effect of Interlayer Pressure on Self-healing Energy

An AC voltage was applied to the capacitor element (7 µm film, 52.7 µF) to cause self-healing to occur. At the completion of the experiment, the capacitor element was dissected and the experimental results are shown in Fig. 10. It can be seen that both the number of self-healing points and the self-healing area decrease from the outer layer to the inner layer, which is related to the different pressure between the film layers inside the capacitor.

To investigate the effect of interlayer pressure on the self-healing energy, the voltage, temperature, parallel capacity and film thickness were fixed at 950 V, 60 °C,
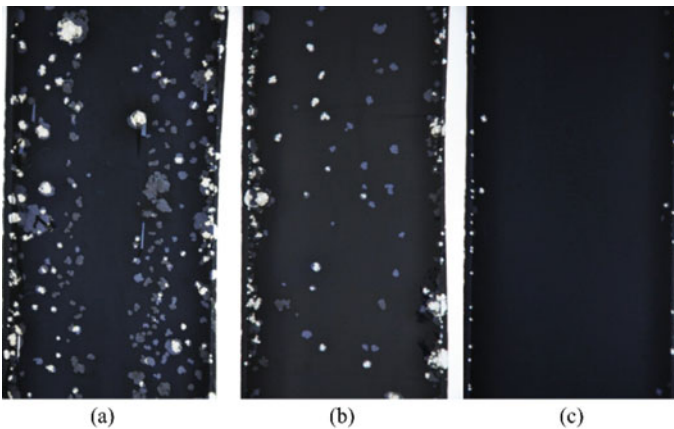
Fig. 10 Self-healing points on the metallised film after component dissection **a** outer layer **b** middle layer **c** inner layer
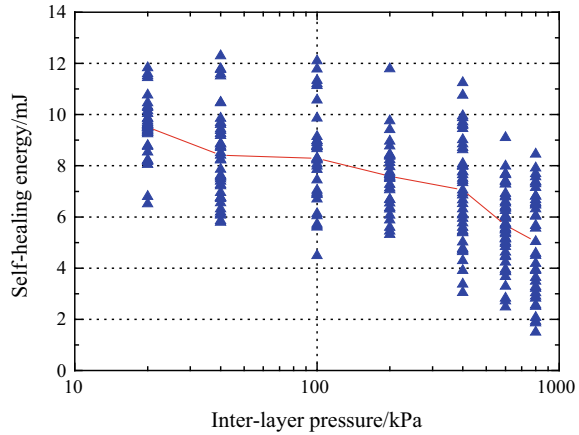
40 μF and 7 μm respectively, and the experiment was repeated by varying only the magnitude of the interlayer pressure. The experimental results are shown in Fig. 11.

The experimental results show that in the range of 20–800 kPa, the average value of self-healing energy decreases from 9.51 to 5.03 mJ with increasing interlayer pressure, a reduction of 47.11%, increasing the interlayer pressure helps to reduce the self-healing energy. The interlayer pressure of the capacitor is related to the number of winding turns, the winding tension, the winding pressure and the shrinkage of the film during the heat setting process. In practice, the interlayer pressure of the outer layer of the capacitor can be increased by increasing the number of wrapping turns to reduce its self-healing energy. In addition, a high interlayer pressure is detrimental to the diffusion of metal vapour and insulation recovery around the self-healing point, and can easily lead to self-healing failure. Therefore, during the design process of the capacitor, measures should be taken to ensure that the interlayer pressure is within a reasonable range, such as increasing the number of outer cladding turns and optimising the heat-setting process.

4 Conclusion

With the development of design and manufacturing processes, metalised film capacitors are expected to find popular application in high voltage reactive power compensation. The paper investigates the laws of voltage, temperature, shunt capacitance, film thickness and interlayer pressure on the self-healing energy of metalised film capacitors. The main conclusions of the paper are as follows:

(1) In the range of 950–1150 V, the average value of self-healing energy increases from 6.52 to 10.34 mJ with increasing voltage, an increase of 58.59%. Therefore, during the design of the capacitor, a suitable design strength should be selected to avoid excessive electric field strength.

(2) In the range of 30–90 °C, the average value of self-healing energy decreases from 8.26 to 5.28 mJ with increasing temperature, a decrease of about 36.08%. The increase in temperature is beneficial in reducing the self-healing energy, but too high a temperature can lead to a reduction in the insulation performance of the capacitor. Therefore, it is important to ensure that the capacitors are operated at the right temperature; too high or too low a temperature is detrimental to the operation of the capacitors.

(3) In the range of 10–160 μF, the shunt capacity has little effect on the self-healing energy. Therefore, the number of parallel components can be flexibly determined according to the requirements during the design of the capacitor, which does not affect the self-healing performance of the capacitor.

(4) In the range of 6–10 μm, the average value of the self-healing energy increases from 3.47 to 11.99 mJ with increasing film thickness, an increase in self-healing energy of 246%. Thicker metallised films are beneficial in reducing the heat generation and temperature rise of the capacitor, but they also increase the self-healing energy to a large extent. Therefore, when selecting the thickness of the capacitor film, the heat generation and self-healing performance of the capacitor should be taken into account.

(5) In the range of 20–800 kPa, the average value of self-healing energy decreases from 9.51 to 5.03 mJ with increasing interlayer pressure, a decrease of 47.11%. The increase in interlayer pressure can reduce the self-healing energy, but too high interlayer pressure is not conducive to the diffusion of metal vapour around the self-healing point and the recovery of insulation, increasing the risk of self-healing failure. Therefore, during the capacitor design process, measures should be taken to increase the interlayer pressure between the outer films of the capacitor, such as increasing the number of outer cladding turns and optimising the heat-setting process.

References

1. Wang Z, Qi C, Yan F et al (2022) Study on DC surface flashover at the clear edge of metallized polypropylene films. IEEE Trans Plasma Sci 50(9):3139–3147
2. Mach P, Horák M (2014) Examination of influence of electrical stress on parameters of PP film capacitors. In: 2014 IEEE 20th international symposium for design and technology in electronic packaging (SIITME). IEEE, Bucharest, pp 51–54
3. Li H, Li Z, Huang X et al (2015) Research progress on metallized film capacitors. Power Capacitor React Power Compensation 36(2):1–4 (in Chinese)
4. Fang J (2010) Development of power capacitor technology in China. Power Capacitor React Power Compensation 31(1):1–4(in Chinese)
5. Du Y, Pan L, Zhu L et al (2020) AC and DC voltage degradation characteristics of metallized film capacitors. Electric Power Eng Technol 39(6):151–158(in Chinese)

6. Chen Y, Li H, Lin F et al (2011) Effect of interlayer air on performance of dry-type metalized film capacitor in DC, AC and pulsed applications. In: IEEE transactions on dielectrics and electrical insulation. IEEE, Wuhan, pp 1301–1306

7. Kong Z, Lin F, Dai L et al (2008) Self-healing characteristics of metallized hybrid electrodes and metallized capacitors. High Voltage Eng 34(2):385–388(in Chinese)

8. Wang Y, Li H, Wang Z et al (2022) Voltage maintaining performance of metallized film capacitors based on crystallinity regulation, vol 48, issue 9, pp 3643–3650 (in Chinese)

9. Umran HM, Wang F, He Y (2022) Ageing: causes and effects on the reliability of polypropylene film used for HVDC capacitor. In: IEEE access. IEEE, Chongqing, pp 40413–40430

10. Belko V, Emelyanov O, Ivanov I et al (2020) Influence of demetallization processes on capacitor grade polymer films breakdown strength. In: 2020 IEEE 3rd international conference on dielectrics (ICD). IEEE, Petersburg, pp 166–168

11. Valentine N, Azarian MH, Pecht M (2019) Metallized film capacitors used for EMI filtering: a reliability review. Microelectron Reliab 92:123–135

12. HemesM, Spro OC, Geitner V (2016) Operability of metallized polypropylene capacitors under high pressure. In: PCIM Europe 2016; international exhibition and conference for power electronics, intelligent motion, renewable energy and energy management. VDE, Nuremberg, pp 1408–1415

13. Tortai JH, Denat A, Bonifaci N (2000) Predominance of joule heating effect on the electrode destruction due to a self-healing of a metallized film. In: 2000 annual report conference on electrical insulation and dielectric phenomena (Cat. No.00CH37132). IEEE, Victoria, pp 674–677

14. Tortai JH, Denat A, Bonifaci N (2001) Self-healing of capacitors with metalized film technology: experimental observations and theoretical model. J Electrostat 53(2):159–169

15. Walgenwitz B, Tortai JH, Bonifaci N et al (2004) Self-healing of metallized polymer films of different nature. In: Proceedings of the 2004 IEEE international conference on solid dielectrics. IEEE, Toulouse, pp 29–32

16. Wang Z, Cui C, Ma Y (2022) Experimental investigation on breakdown characteristics of metallized film capacitors under AC and DC superimposed voltage. IEEE Trans Plasma Sci 50(2):478–488

17. Qin S, Ma S, Boggs SA (2012) The mechanism of clearing in metalized film capacitors. In: 2012 IEEE international symposium on electrical insulation. IEEE, San Juan, pp 592–595

18. Rytöluoto I, Lahti K, Karttunen M et al (2015) Large-area dielectric breakdown performance of polymer films-part I: measurement method evaluation and statistical considerations on area-dependence. IEEE Trans Dielectr Electr Insul 22(2):689–700

19. Wang W, Li H, Li Z et al (2014) Lifetime improvement of metallized film capacitors by inner pressure strengthening. High Power Laser Part Beams 26(4):130–134 (in Chinese)

20. Chen Y, Li H, Lin F et al (2011) Effect of interlayer air on performance of dry-type metalized film capacitor in DC, AC and pulsed applications. IEEE Trans Dielectr Electr Insul 18(4):1301–1306

21. Wang X, Chen W, Xu M et al (2018) Study on self-healing failure process in metallized film capacitor element. Power Capacitor React Power Compensation 39(04):54–58(in Chinese)

22. Jia L, Cheng L, Liu W et al (2020) Self-healing properties of metalized polypropylene film with elevated sheet resistance. In: 2020 IEEE international conference on high voltage engineering and application (ICHVE). IEEE, Beijing, pp 1–4

23. Xin D (2002) Research on self-healing pulse capacitor with high energy storage density. Huazhong University of Science and Technology, Wuhan (in Chinese)

24. Li H (2015) Temperature dependence of self-healing characteristics of metallized polypropylene film. Microelectron Reliab 55(12):2721–2726

25. Zhonghua K (2008) Study on some problems of metallized film pulse capacitor. Huazhong University of Science and Technology, Wuhan (in Chinese)

26. Zhu MX, Li H, Shi S et al (2020) Experimental investigation of self-healing properties of metalized film capacitors. In: 2020 4th international conference on HVDC (HVDC). IEEE, Xi'an, pp 31–36

27. Heywang H (1976) Physical and chemical processes in self-healing plastic capacitors. Colloid Polym Sci 254(2):139–147
28. Wang Z, Yan F, Xu M et al (2017) Influence of external factors on self-healing capacitor temperature field distribution and its validation. IEEE Trans Plasma Sci 45(7):1680–1688
29. Wang Z, Yan F, Hua Z et al (2016) Geometric optimization of self-healing power capacitor with consideration of multiple factors. J Power Sources 323:147–157

Construction of a Novel Insulation State Evaluation System for XLPE Cable

Linyu Li, Jingsong Li, Xinyu Xu, Guofeng Li, Nianfeng Zheng, and Zhongqing Wang

Abstract The continuous rapid growth of national economy keeps improving the requirement of our electric power infrastructure. The cross-linked polyethylene (XLPE) cable with good insulation and transmission performance has become the mainstream configuration of urban electric power equipment. Based on the existing research on the causes of cable insulation aging, this paper determines the evaluation parameters reflecting the influence factors of aging, aiming at establishing a novel XLPE cable insulation evaluation model system. According to the linear regression equation, the factors that have little influence on the cable insulation are excluded, the weight vector of the main influencing factors is determined based on the entropy weight method, the weight is tested by the principal component analysis method, and the weight of the parameters affecting the insulation state of XLPE cable is calculated by the TOPSIS method. Finally, the evaluation system is formulated and the suggestions for cable stability maintenance are given.

Keywords XLPE cables · State of insulation · Evaluation model · Stability maintenance suggestion

1 Introduction

Transmission line security requirements are improving with our country, cable transmission with lower failure rate and better insulation is gradually replacing overhead line transmission. XLPE cable in all aspects of performance is significantly better than the general oil-immersed cable [1–3]. Literature [4–8] studied the influence factors of electrical and thermal aging on cable life, it is concluded that high temperature and strong electric field affect cable insulation life. Literature [9–11] adopts

L. Li · J. Li (✉) · X. Xu · G. Li
School of Electrical Engineering, Dalian University of Technology, Dalian 116024, China
e-mail: lijingsong2019@dlut.edu.cn

N. Zheng · Z. Wang
R&D, LUTE Electric Cp, Ltd., Jining 272200, China

stepwise linear regression method, based on this, a cable aging evaluation model is established. In Section 2, five cable parameter measurement methods are discussed in detail. Section 3 constructs the cable insulation evaluation system based on the measured data.

2 XLPE Cable Insulation Data Online Monitoring

The aging of XLPE cable insulation is mainly caused by water twig and electric twig phenomenon, the dielectric loss angle tangent δ, partial discharge current, cable grounding current, insulation resistance, polarized/non-polarized current and other parameters can be used to measure the content of electrical and water branches, then judge the cable aging condition.

2.1 XLPE Cable Introduce

The experimental cable model in this paper is YJW02/110 kV. In order to control different aging conditions of the cable parameters are the same, select the same cable for aging, to speed up cable aging progress, control the aging chamber temperature to 50 °C, the relative humidity is 80%, apply 110 kV AC power frequency voltage, cable parameters with different aging time are obtained.

2.2 A Subsection Sample

2.2.1 Insulation Resistance

Insulation resistance refers to volume insulation resistance. Generally, an insulation meter is used to measure the insulation resistance of a cable [12]. In this paper, high resistance meter method is used to obtain insulation resistance data of experimental cable, the measured voltage is within 100–500 V, the measured resistance ranges from 10^4 to 10^{16} Ω, the experimental schematic diagram is as shown in Fig. 1. The results are shown in Table 1.

R_x in Fig. 1 is the insulation resistance of the experimental cable, U_s stands for amplifier input resistance voltage drop, G is galvanometer.

2.2.2 Dielectric Loss Angle Tangent δ

The online detection method of ultra-low frequency cable dielectric loss used in this experiment is to set 0.1 Hz host parameters in advance before the test, apply low
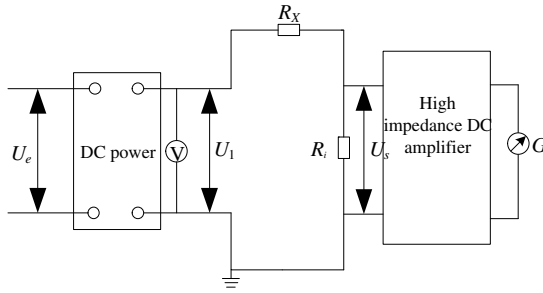
Fig. 1 Cable insulation resistance measurement experiment diagram

Table 1 Insulation resistance data obtained from the experiment

Number of measurements	Insulation resistance $R/(\times 10^9)\Omega$	Effective distance L/cm	Outer diameter of insulation/mm	Insulation inner diameter/mm
1	8.750	1016.000	8.622	6.511
2	8.970	1015.500	8.628	6.510
3	9.200	1010.700	8.621	6.527
4	10.060	1015.200	8.516	6.515
Mean value	9.382	1014.780	8.604	6.516

Table 2 Values of dielectric loss angle tangent measured at different voltage levels

Cable sample number	Voltage class	The mean of the first ten times	The mean of the last ten times
		Dielectric loss tangent δ/%	
1	$0.5U_0$	0.456	0.447
	$1.0U_0$	0.495	0.501
	$1.5U_0$	0.537	0.549
2	$0.5U_0$	0.405	0.422
	$1.0U_0$	0.482	0.516
	$1.5U_0$	0.510	0.539

frequency and high voltage to both ends of the test cable, eight cycles of dielectric loss Angle measurement were completed successively at three voltage levels of $0.5U_0$, $1.0U_0$ and $1.5U_0$, the experimental data are shown in Table 2.
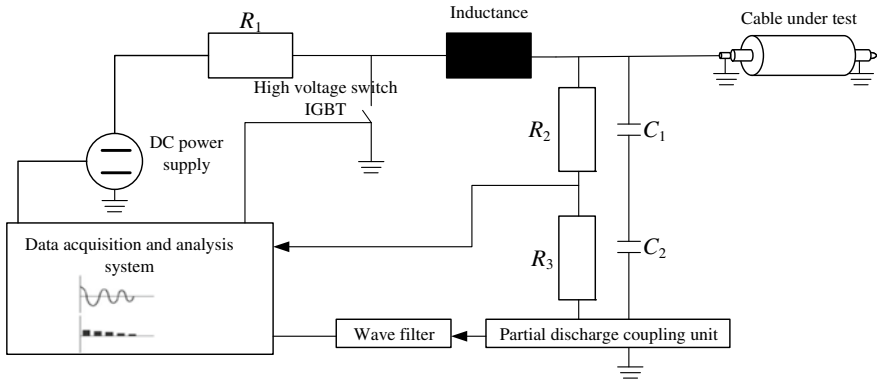
Fig. 2 Local discharge monitoring principle of cable line shock wave

Table 3 Office release data of online monitoring cable (part)

Time	0:00	4:00	8:00	12:00	16:00	20:00	24:00
I/nA	6.441	6.51	6.57	6.673	6.788	7.114	7.503

2.2.3 Partial Discharge

In this paper, OWTS MV110 local discharge monitoring device is used, the single-phase calibration was carried out by 100 nC, 50 nC and 20 nC respectively. The experimental wiring diagram is shown in Fig. 2, part of the data collected by the computer is shown in Table 3.

2.2.4 Electromagnetic Coupling Method for Online Monitoring of Grounding Wire Current

Electromagnetic coupling method uses high frequency current sensor (HFCT), the partial discharge generated on the grounding line of the cable is converted into an electromagnetic pulse, then the partial discharge pulse emitted by the grounding wire of the cable is collected by the data acquisition system and the data is collected by the computer. The flow chart of online monitoring experiment is shown in Fig. 3. The results are shown in Table 4.

2.2.5 Polarized/Non-polarized Current

The current measured in this paper is mostly polarization current caused by dipole polarization. The experimental diagram is shown in Fig. 4, switch to K_2 and apply DC voltage to polarize the experimental cable, the polarization current i_p can be
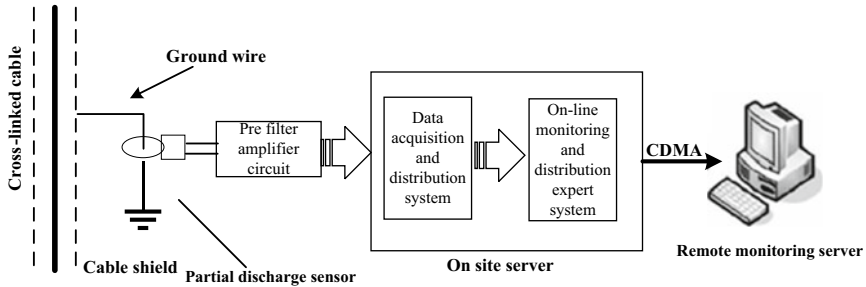
Fig. 3 Experimental diagram of on-line monitoring of grounding current of cable by electromagnetic coupling method

Table 4 Experimental data of online monitoring of grounding cable current (part)

Time	0:00	4:00	8:00	12:00	16:00	20:00	24:00
I_0/A	0.410	0.420	0.430	0.442	0.455	0.461	0.498

Fig. 4 Schematic diagram of PCD method
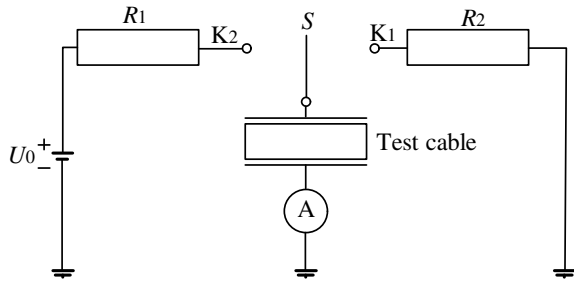
measured. After the polarization time t_c, the switch S is switched to K_1, K_2 is disconnected, the cable starts to discharge, and the non-polarized current id can be measured.

$$i_p = C_0 U_0 \left[\frac{\sigma}{\varepsilon_0} + f(t) \right] \tag{1}$$

$$i_d = C_0 U_0 \left[f(t) - f(t + t_p) \right] \tag{2}$$

3   Data Processing

3.1   Data Normalization Processing and Correlation Analysis

According to the experimental data, the original sequence data dimensionality unit of each parameter is not the same, it is necessary to normalize the original sequence data after eliminating outliers. The processed data are shown in Table 5. The calculation method is as follows:

$$x_i = \frac{x_i - x_{\min}}{x_{\max} - x_{\min}} \tag{3}$$

where, x_i is the value of the same factor at different times before normalization treatment, x_{max} and x_{min} refer to the maximum and minimum values of the original sequence data.

The establishment of multiple linear regression equation requires no multi-collinearity between indexes. The correlation calculation results of each parameter in the cable are shown in Table 6.

According to the data, the correlation between the five parameters is weak, which can be modeled by linear regression algorithm.

Table 5 Experimental data of XLPE cable (after normalization)

Time (h)	$\tan\delta$	I	I_0	$I(t)$	R
0	0.0457	0.1547	0.0614	0.0921	0.4221
20	0.0459	0.1598	0.0651	0.0857	0.4221
40	0.0514	0.1602	0.0662	0.0824	0.4221
60	0.0526	0.1679	0.0678	0.0801	0.4221
80	0.0612	0.1698	0.0687	0.0772	0.4221

Table 6 Parameters related to cable insulation influence parameters

r	$\tan\delta$	$I(t)$	I	R	I_0
$\tan\delta$	1	-0.0254	0.1625	0.4716	0.0035
$I(t)$	-0.0546	1	0.0479	0.01478	0.0549
I	-0.0464	-0.368	1	0.1246	0.0058
R	-0.7738	-0.214	0.1807	1	0.0029
I_0	-0.0797	-0.321	0.1536	0.0029	1

3.2 Multi-parameter Linear Regression Model

3.2.1 Multi-factor Linear Regression Model Based on Cable Insulation Evaluation Parameters

The multiple linear regression model involving j independent variables is:

$$\begin{cases} S_A = \beta_0 + \beta_1 x_1 + \beta_2 x_2 + \cdots + \beta_j x_j + \varepsilon \\ \varepsilon \sim N(0, \sigma^2) \end{cases} \tag{4}$$

The establishment of regression model does not exclude the possibility that some individual factors have little influence on the final results. The flow chart is shown in Fig. 5. The calculation results are shown in Table 7.

According to the judgment basis in Fig. 5, $P_2 \geq 0.05$, so it should be removed and the linear regression equation is finally obtained:

$$S_A = 9.7 \times 10^{-8} - 1.1 \times 10^{-8} x_1 + 0.83 x_3 + 2.1 \times 10^{-8} x_4 + 0.17 x_5 \tag{5}$$
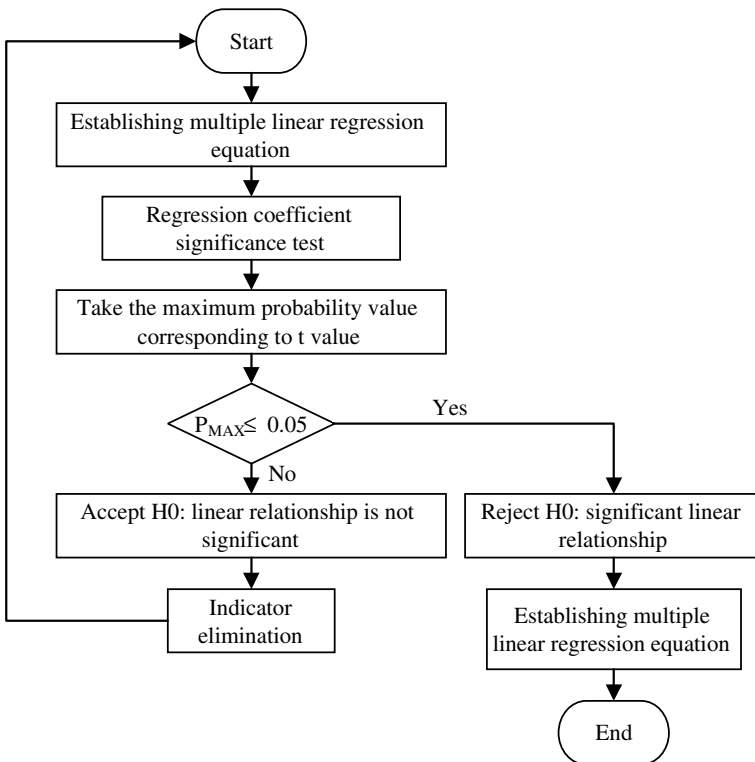
Fig. 5 Multi-factor linear regression flow chart

Table 7 Results of step-to-step linear regression

	x_0	x_1	x_2	x_3	x_4	x_5
t	2.47	-2.84	-0.067	77.40	2.80	16.20
P_{MAX}	0.014	0.005	0.947	0	0.005	0

After screening, parameters affecting cable insulation aging are determined as follows: Dielectric loss Angle tangent δ, ground wire current I_0, polarized/unpolarized current $I(t)$ and cable insulation resistance R.

3.2.2 XLPE Cable Insulation State Evaluation Model

The vector gauge method obtains the gauge decision matrix $\mathbf{B} = (b_{ij})_{m \times n}$ and constructs the weighted gauge matrix $\mathbf{C}^*$

$$b_{ij} = \frac{a_{ij}}{\sqrt{\sum_{i=1}^{m} a_{ij}^2}} \quad (i = 1, 2, ..., m \ \ j = 1, 2, ..., n) \tag{6}$$

$$c_{ij} = \omega_j \cdot b_{ij} \quad (i = 1, 2, ..., n) \tag{7}$$

where, a_{ij} is a matrix element of multifactor decision problem, and ω_j is a weight vector element.

Calculate the distance s_i between alternative d_i and positive and negative ideal solutions.

$$s_i = \sqrt{\sum_{j=1}^{n} \left(c_{ij} - c_j\right)^2} \quad i = 1, 2, \ldots, m \tag{8}$$

Calculate the evaluation index f of each scheme

$$f_i^* = s_i^0 / \left(s_i^0 + s_i^*\right) \quad i = 1, 2, \ldots, m \tag{9}$$

where, s_i^0 is the positive ideal solution distance, and s_i^* is the negative ideal solution distance.

3.2.3 Weight Vector

Establish an evaluation system of influencing factor data, The original matrix $\mathbf{D}_{zn}$ is lined with factor data, the influencing factor parameters are listed. The normalized matrix $\mathbf{R}_{zn}$ is obtained by data normalization of $\mathbf{D}_{zn}$. Then, the corresponding weight of each evaluation parameter is calculated as:

Table 8 Cable insulation evaluation range and operation suggestions

f	Evaluation	Performance	Suggestion
≤ 1.55	In good condition	Normal	Normal use
1.55–2	Mild attention	Water branches appear	Normal use
2–3.5	Moderate attention	Electrical twig	Guarded use
≥ 4	High attention	Partial discharge	Replace cable

$$\omega = [0.401, 0.29, 0.143, 0.166]^{T} \tag{10}$$

XLPE cable insulation state evaluation standards and stability maintenance suggestions are obtained by TOPSIS ideal solution, as shown in Table 8.

4   Conclusion

The correlation analysis of the five electrical parameters selected in this paper shows that the linear relationship of these electrical parameters is very weak, and the correlation between the local discharge current and the final evaluation parameters is very weak. The other four parameters are used to establish the evaluation model.

Based on the entropy weight method and principal component analysis method to determine the TOPSIS method weight vector, the XLPE cable insulation state evaluation system is constructed, and the specific evaluation interval of cable insulation is proposed.

References

1. Zhao AX, Chen X, Xu L et al (2020) Application of dielectric response in diagnoses of time and frequency domain on XLPE cable insulation. High Voltage Eng 46(1):292–302 (in Chinese)
2. Zhao SL, Zhou K, He M et al (2019) Dielectric response characteristics and insulation condition evaluation under impulse voltage for cables. High Voltage Eng 45(4):1297–1304 (in Chinese)
3. Morsalin S, Phung BT (2019) Modeling of dielectric dissipation factor measurement for XLPE cable based on Davidson-Cole model. IEEE Trans Dielectr Electr Insul 26(3):1018–1026
4. Zhang C, Li HF, Yang YB et al (2020) Research progress in ageing, evaluation and rejuvenation of XLPE cable insulation. Insulating Mater 53(07):1–11 (in Chinese)
5. Shen ZF, Liu BK, Wang GD et al (2021) Accelerated electrical ageing characteristics of 10 kV XLPE cable. Insulating Mater 54(08):60–66 (in Chinese)
6. Nie YP, Zhao XP, Li ST (2020) Research progress in condition monitoring and insulation diagnosis of XLPE cable. High Voltage Eng 46(04):1361–1371 (in Chinese)
7. Sun JS, Zhang DP, Xia JF et al (2020) Study on the regulation of cable insulation resistance in the national standard of power cable line handover test. Electrotechnics Electr (07):63–65 (in Chinese)
8. Wang W, Sonoda K, Keita S et al (2018) Current integrated technique for insulation diagnosis of water-tree degraded cable. IEEE Trans Dielectr Electr Insul 25(1):94–101

9. Hamja KJ, Illavarason P, Sridevi P (2020) Underground cable fault detection and prevention using Blynk. In: Proceedings of the first international conference on advanced scientific innovation in science, engineering and technology, ICASISET, pp 16–17
10. Ohki Y, Hirai N (2018) Detection of abnormality occurring over the whole cable length by frequency domain reflectometry. IEEE Trans Dielectr Electr Insul 25(6):2467–2469
11. Isabel L, Jean M, Akihiro A et al (2018) Frequency and time domain responses of cross-bonded cables. IEEE Trans Power Deliv 33(2):640–648
12. Babaee A, Shahrtash SM (2015) On-line partial discharge defected phase selection and localization in cross—bonded single core cables. IEEE Trans Dielectr Electr Insul 22(5):2995–3005

Fault Diagnosis Method of Impulse Impedance Characteristic Spectrum Based on Naive Bayes Classifier

Baoming Huang

Abstract The normal operation of the grounding grid is related to the safety of transmission lines and even the power grid. Due to its buried underground location, wide distribution, and harsh operating environment, the grounding body is prone to corrosion. Therefore, the corrosion problem of the grounding grid has always been a problem that troubles the power sector. Therefore, in-depth research on the methods of grounding grid corrosion diagnosis is of great significance for ensuring the safe operation of transmission lines. To effectively improve the accuracy of detecting the location and type of corrosion faults in substation grounding grids, a grounding grid fault diagnosis method based on Naive Bayes Classifier (NBC) impulse impedance feature spectrum is proposed. First, CDEGS software simulation is used to obtain the corresponding spectrum maps under various fault conditions, and then the waveform fitting degree and amplitude difference between each frequency band and the standard spectrum map are input into the Naive Bayes Classifier as characteristic parameters, and the expected results are obtained. The test results show that the identification accuracy of the model for fault types is as high as 93.33%, and can accurately distinguish Single point of failure and regional fault.

Keywords Grounding grid · Corrosion diagnosis · Naive Bayesian classification algorithm · Characteristic spectrum of impulse impedance · CDEGS

1 Introduction

With the continuous development of social economy and power grid technology, the transmission capacity of the power system is increasingly expanding, and the requirements for the dispersion performance of the grounding grid are also increasing; At the same time, the internal overvoltage caused by system faults and the potential rise of the power system caused by external overvoltage caused by lightning strikes,

B. Huang (✉)

School of Electrical Engineering, Xi'an Jiaotong University, Xi'an 710049, China
e-mail: huangbm1999@163.com

causing damage to the power system and endangering the safety of operation and maintenance personnel, are becoming increasingly serious. The requirements for the health of the grounding grid are also increasing. The main function of the grounding grid is to serve as a discharge channel for fault current. A sound grounding grid can ensure the normal operation of the power system and the safety of equipment and personnel in the substation. Due to the long-term burial of the grounding grid underground and the complex operating environment, there are many microorganisms in the soil that will corrode and decompose the grounding grid. The chemical substances such as water contained in the soil will gradually immerse into the grounding grid, and various chemical reactions such as corrosion may also be triggered when there is a large current passing through the grounding grid during operation. In addition, the breakage of grounding grids caused by factors such as poor placement and engineering construction is also one of the common faults in grounding grids. Therefore, in-depth research on methods for diagnosing grounding grid corrosion is of great significance for ensuring the safe and reliable operation of transmission lines and electrical equipment.

In recent decades, there have been five types of fault diagnosis and detection methods for grounding grids both domestically and internationally: electromagnetic field diagnosis, electrochemical diagnosis, conductor resistance diagnosis, spectrum analysis diagnosis, and non-destructive testing diagnosis technology. Document proposed to measure the distribution of magnetic flux density on the ground surface by applying a certain frequency excitation to two grounding points, and then judge the operation condition of the grounding grid, but this method has low detection accuracy and is vulnerable to electromagnetic interference from the external environment; Traditional electrochemical diagnostic methods are highly susceptible to environmental stray interference, making it difficult to accurately determine the fault situation; The conductor resistance method requires the application of excitation to multiple lead electrodes to form a fault diagnosis matrix for judgment. On the one hand, the operation process is relatively cumbersome, and on the other hand, due to the conduction resistance of m Ω level, it is difficult to identify when the corrosion situation is light; Reference defines the impact grounding impedance spectrum of grounding devices for transmission line towers, but does not form a complete spectrum diagnosis technology for grounding grids; In addition, metal detection technologies such as radar monitoring technology, eddy current testing technology, and tomography imaging technology have not yet been fully applied to the diagnosis of grounding grid faults.

This article proposes an impulse impedance characteristic spectrum method for substation grounding network fault detection based on simulation results and the theoretical foundation of spectrum diagnosis. It is expected to obtain a more accurate method for substation grounding network fault diagnosis and provide a basis for the implementation of substation grounding network status maintenance strategies [1–6].

2   Diagnostic Principle of Impulse Impedance Characteristic Spectrum Method

At present, domestic and foreign scholars' research on the impact characteristics of ground corrosion mostly focuses on the numerical value of impact impedance, and the information available is relatively single and concise, with low accuracy in fault location and identification. In fact, the impulse impedance in the time domain is not a constant value, but a variable that changes over time. Usually, the maximum value that can be reached is taken as the value of the impulse impedance, which contains low information. To fully explore the information of the impulse impedance of the grounding grid, we consider the frequency characteristics of the grounding grid and establish an impulse impedance spectrum fingerprint system similar to a fingerprint recognition system. The corresponding impulse impedance amplitude and phase angle at each frequency are equivalent to a ripple, and the entire spectrum system is a system rich in information.

Without considering the soil spark discharge, the grounding grid can be considered as a linear Time-invariant system consisting of distributed parameters such as resistance, inductance and capacitance. From the mathematical model, the linear Time-invariant system is simpler than the nonlinear system, and the parameters of the linear Time-invariant system do not change with time, especially because of the change of the signal characteristics of the impulse current. So from this property, the measurement theory of impulse impedance characteristic spectrum method can be derived.

2.1   Impulse Impedance and Frequency Response Testing Techniques

As shown in Fig. 1, a certain grounding down lead is selected as the grounding grid impulse impedance Test point, and the voltage test line and current test line are discharged according to the diagonal length of the grounding grid impulse impedance test and DL/T266-2012 Guide for Testing Impulse Characteristic Parameters of Grounding Devices. According to the research conclusion of "DLT266-2012 Guidelines for Testing Impulse Characteristic Parameters of Grounding Devices", the definition formula of impulse grounding impedance can be obtained as follows:

$$Z(f) = R_{eq}(f) + jX_{eq}(f) \tag{1}$$

Based on the voltage and current waveforms obtained from data collection, analyze the frequency domain characteristics reflected by the impulse current injected into the grounding grid from the grounding down lead, and define the impulse impedance Z in the frequency domain as follows:
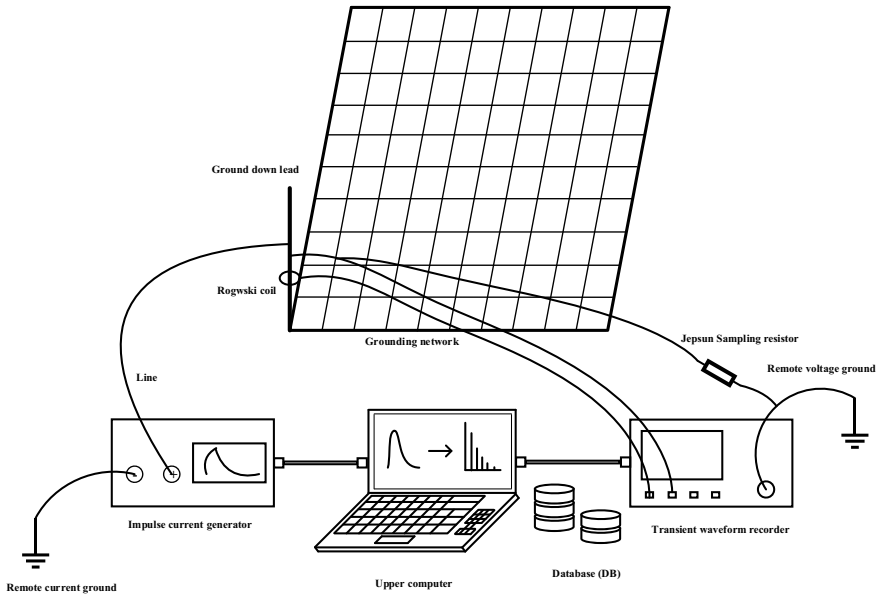
Fig. 1 Impulse impedance testing device

$$Z(f) = \frac{\text{FFT}[U(t)]}{\text{FFT}[I(t)]} \tag{2}$$

In the formula, U(t) and I(t) respectively represent the detected voltage and current signals; FFT is the discrete Fast Fourier transform of the sequence. The definition of the impulse amplitude frequency response curve Ha and phase frequency response curve H_p of the grounding grid is as follows:

$$H_a = 20lg(\text{abs}(Z(f))) \tag{3}$$

$$H_p = 20lg(\text{ph}(Z(f))) \tag{4}$$

2.2 Fault Diagnosis Technology Based on Naïve Bayes Classification

Many scholars at home and abroad use the linear correlation coefficient R to measure the similarity between the test spectrum and the standard spectrum. Due to the irregular characteristics of the impact characteristic spectrum waveform, this method can bring significant errors, low sensitivity, and poor accuracy in fault detection. To

achieve more accurate comparison of waveforms, the method of "piecewise linearization" is adopted to transform nonlinear problems into linear problems. The amplitude frequency response and phase frequency response are divided into subgraphs under several frequency bands, and the spectral response is approximately regarded as linear within each frequency band range. The waveform fitting degree under each frequency band is calculated as the feature quantity of the Naïve Bayes classification model, which can be used to evaluate the operating status of the grounding grid, i.e. the degree of corrosion. The waveform fit W is denoted as the product of the correlation coefficient R and the fitting coefficient T, where R mainly represents the trend fit between the two sets of data, and T mainly represents the waveform fit of the two sets of data.

According to the "logarithmic rule", divide the amplitude frequency and phase frequency characteristic spectra obtained from the test into n frequency intervals, denoted as $\{X_1, X_2, …, X_{2n}\}$, and take m frequency points within each frequency band as sampling points. The corresponding values are denoted as $X_i = \{X_i(1), X_i(2), …, X_i(m)\}$. Calculate the fit between the waveform and the historical database data sequence $\{Y_1, Y_2, …, Y_{2n}\}$ as follows [7–10]:

(1) Calculate the standard deviation of two sequences

$$
\begin{cases}
D_{X_i} = \frac{1}{m} \sum_{k=1}^{m} \left[X_i(k) - \frac{1}{m} \sum_{k=1}^{m} X_i(k) \right]^2 \\
D_{Y_i} = \frac{1}{m} \sum_{k=1}^{m} \left[Y_i(k) - \frac{1}{m} \sum_{k=1}^{m} Y_i(k) \right]^2
\end{cases}
\tag{5}
$$

(2) Calculate the covariance of two sequences

$$
C_{X_i Y_i} = \frac{1}{m} \sum_{k=1}^{m} \left[X_i(k) - \frac{1}{m} \sum_{k=1}^{m} X_i(k) \right] \times \left[Y_1(k) - \frac{1}{m} \sum_{k=1}^{m} Y_1(k) \right]
\tag{6}
$$

(3) Calculate correlation coefficient

$$
R_i = \frac{C_{X_i Y_i}}{\sqrt{D_{X_i} D_{Y_i}}}, i = 1, 2, \ldots, 2n
\tag{7}
$$

(4) Fitting coefficient

$$
T_i = 1 - \sqrt{\frac{\sum_{k=1}^{m} (X_i(k) - Y_i(k))}{\sum_{k=1}^{m} Y_i(k)^2}}
\tag{8}
$$

(5) Waveform Fit

$$
W_i = R_i \cdot T_i
\tag{9}
$$

The difference in amplitude is measured by the distance between two spectral lines. The difference in amplitude distribution is segmented by selecting m frequency points within each frequency range as sampling points. The calculation method for amplitude difference is as follows:

$$M_i = \sqrt{\frac{\sum_{k=1}^{m}(X_i(k)-Y_i(k))^2}{m}} \tag{10}$$

The sequence of fault characteristic parameters for the grounding grid is denoted as $I = \{W_1, W_2, ..., W_{2n}, M_1, M_2, ..., M_{2n}\}$.

2.3 Selection of Fault Categories for Grounding Grids

Record the fault category as sequence $Q = \{Q_1, Q_2, Q_3, Q_4, Q_5, Q_6, Q_7\}$, and the description of each category is shown in Table 1.

Among them, r represents the equivalent radius of the grounding body, l represents the radius of the corrosion impact area, and L represents the grid length of the grounding grid.

To avoid the situation where there is no judgment result, the Laplace smoothing coefficient is introduced to correct the problem of probability estimation being zero due to insufficient training set. As the training set becomes larger, the influence of the prior introduced by the correction process will gradually become negligible, making the estimation gradually tend to the actual probability value. Bayes based on Laplacian smoothing are as follows:

$$P(Q_i|I) = \frac{P_{Q_i}(I) \cdot P(Q_i) + \alpha}{P(I) + 2m\alpha} \tag{11}$$

In the equation, $P_{Qi}(I)$ represents Probability in class Q_i; $P(I)$ is the probability of I in all categories, which is constant for all classes; $P(Q_i)$ is the Prior probability of various grounding grid faults, that is, the ratio of the occurrence times of various faults and the total times in the sample data, which can ensure that $P(Q_1) = P(Q_2) = \ldots = P(Q_p)$; α is the Laplacian smoothing coefficient, which defaults to 1.

Table 1 Table captions should be placed above the tables

Q_1	Q_2	Q_3	Q_4	Q_5	Q_6	Q_7
Overall severe corrosion	Overall mild corrosion	Local severe corrosion	Local mild corrosion	Near end corrosion fracture occurs	Far end corrosion fracture occurs	Good
r: 0 ~ 50%	r: 50 ~ 70%	r: 0 ~ 50% $0 < l < $ L	r: 50 ~ 70% $0 < l < $ L	$0 < l < $ L	$l > $ L	

Select the Q with the highest probability as the prediction result, that is, search for the value of Q to maximize the above equation, and list the following equation:

$$f(I) = \arg\max_{Q_n} \frac{P_{Q_i}(I) \cdot P(Q_i) + \alpha}{P(I) + 2m\alpha} \tag{12}$$

It can be further simplified as:

$$f(S) = \arg\max_{Q_n} P_{Q_i}(S) \tag{13}$$

For Naïve Bayes, the distribution of characteristic attribute values conforms to Normal distribution, and the probability density function of the jth attribute value can be expressed as

$$p\left(I_{j(Q_i)}\right) = \frac{1}{\sqrt{2\pi}\sigma_{j(Q_i)}} e^{-\frac{I_{j(Q_i)} - \mu_{j(Q_i)}}{2\sigma^2_{j(Q_i)}}} \tag{14}$$

If the training sample set belongs to Q_i Number of samples is N, observe and record Q_i the *jth* attribute of each sample, $\mu_{j(Q_i)}$ and $\sigma_{j(Q_i)}$ are the mean and variance of the probability density function for the *jth* attribute value, respectively.

$$Z_{j(Q_i)} = \frac{I_{j(Q_i)} - \mu}{\sigma} \sim N(0, 1) \tag{15}$$

$$P\left(I_{j(Q_i)}\right) = \left|\Phi\left(Z_{j(Q_i)}\right) - \Phi\left(-Z_{j(Q_i)}\right)\right| \tag{16}$$

The corresponding probability can be obtained through table lookup. Naïve Bayes assumes that the sample attributes are independent of each other, so the samples to be classified $I = \{R_1, R_2, \ldots, R_{2n}, M_1, M_2, \ldots, M_{2n}\}$ in Q_i The probability of the Joint probability distribution is

$$P_{Q_i}(I) = \prod_{j=1}^{2n} P\left(I_{j(Q_i)}\right) \tag{17}$$

Compare $P_{Q_1}(I)$, $P_{Q_2}(I)$, $\ldots$, $P_{Q_n}(I)$ size, and the prediction type has the highest probability.

3 Example Analysis

Combined with thirty groups of CDEGS simulation data for training and testing, the overall model fault identification correct rate of 76.67%, in which the model for Q_1, Q_3, Q_5, Q_6 four types of fault identification is more accurate, the correct rate reached
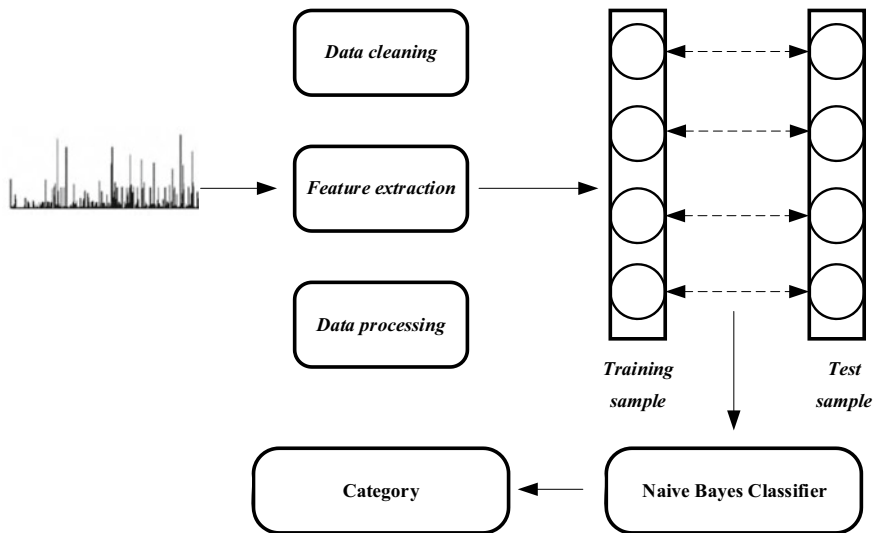
Fig. 2 Algorithm framework of Naive Bayes classifier

100%, for Q_2, Q_4 two types of discrimination rate is lower, both 25%, but observe these two types of fault misjudgment results can be seen, Q_2 misjudgment occurred more for Q_1, Q_4. Therefore, if the faults are divided into three types, i.e. overall corrosion, local corrosion and corrosion fracture, then the accuracy of the model in identifying faults will increase to 93.33%. The specific flowchart is as follows (Fig. 2).

4   Conclusion

In this paper, a new grounding grid fault diagnosis method is proposed, that is, the grounding grid fault diagnosis technology based on the impulse impedance spectrum characteristics of Naive Bayes classifier, which can more accurately identify the fault type, fault location and fault degree, and is simple to operate, without power outage maintenance, with certain application scenarios and feasibility. The main conclusion of this paper is that the impulse impedance characteristic spectrum is processed by piecewise linearization, and the characteristic parameters are the wave-form fitting degree and amplitude difference degree on each frequency band. The Naive Bayes classifier is used to judge the fault type, with an accuracy of 93.33%, and can accurately distinguish Single point of failure and regional fault.

References

1. Grcev L, Markovski B (2021) Impulse impedance and effective area of grounding grids. IEEE Trans Power Delivery 36(2):1183–1192
2. Rahman M, Ahmed M, Gutman R (1997) UPFC application on the AEP system: planning considerations. IEEE Trans Power Systems 12(4):1695–1701
3. Gupta BR, Thapar B (1980) Impulse impedance of grounding grids. IEEE Trans Power Apparatus Syst PAS-99(6):2357–2362
4. Charalambous CA, Demetriou A, Kokkinos ND (2015) Impact of photovoltaic-oriented DC stray current corrosion on large-scale solar farms' grounding and third-party infrastructure: modeling and assessment. IEEE Trans Ind Appl 51(6):5421–5430
5. Dick EP, Erven C, Harvey SM (1979) Grounding system tests for analysis of fault-induced voltages on communication cables. IEEE Trans Power Apparatus Syst PAS-98(6):2115–2125
6. Zupa FP, Laidig JF (2007) A practical ground potential rise prediction technique for power stations. IEEE Trans Power Apparatus Syst PAS-99(1):207–216
7. Eajal AA, El-Awady A, El-Saadany F et al (2021) A Bayesian approach to the reliability analysis of renewables-dominated islanded DC microgrids. IEEE Trans Power Syst 36(5)
8. Shitsi E, Boafo EK, Ameyaw F et al (2020) Investigating the effect of prior distributions on posterior estimates of common cause failure parameters using Bayesian method. J Nucl Eng Radiat Sci 6(3)
9. Lepore A, Palumbo B, Pievatolo A (2020) A Bayesian approach for site-specific wind rose prediction. Renewable Energy 150
10. Li Z, Deng Z, Sun J (2020) Extended-sampling-Bayesian method for limited aperture inverse scattering problems. SIAM J Imaging Sci 13(1)

Calculation of Temperature Distribution of GIS Bus Bar Under Multi-physical Field Coupling

Zehui Zhang, Tao Han, Zhenhua He, Shouxing Wang, and Yuanli Gu

Abstract The temperature rise of gas insulated switch-gear (GIS) bus bar is an important factor affecting its safe and stable operation. Based on the finite element method of electric-thermal-fluid multi-physical field coupling, the finite element simulation model of 252 kV GIS was established by considering the vortex loss of GIS bus bar, skin effect, heat conduction, heat convection, heat radiation and other complex heat transfer processes. The temperature distribution of GIS was calculated. The results show that when the ambient temperature is 293 K and 4 kA power frequency current is passed into the central conductor, the internal temperature of GIS distributes symmetrically along the central axis. The highest temperature in GIS is 324 K and the lowest temperature is 297 K. At the same height, the temperature of GIS decreases gradually along the radial direction from the conductor center, and the temperature difference between the top and the inside and outside is slightly larger than that at the bottom. The lower surface temperature of the basin insulator is greater than that of the upper surface, and the radial temperature difference between inside and outside is 23.5 K. Chamber height has great influence on gas temperature. The multi-physical field coupling simulation can effectively simulate the temperature rise of GIS under actual working conditions and provide theoretical support for GIS condition monitoring and maintenance.

Keywords Finite element method · Gas insulated switch-gear (GIS) · Multi-physical field coupling · Temperature rise

Z. Zhang · T. Han (✉) · Z. He · S. Wang · Y. Gu
State Grid Shandong Electric Power Company, Jinan 271100, Shandong, China
e-mail: 903364597@qq.com

Laiwu Power Supply Company, Jinan 271100, Shandong, China

1   Introduction

The gas insulated switchgear (GIS) is widely used in power transmission networks because of its small insulated area, high reliability, easy maintenance and overhaul, and so on. Its safe and stable operation is very important for power system [1–3].

However, due to its sealing property, the conductor is prone to cause the temperature rise in GIS when passing through large current. Long-term operation will lead to the reduction of bus bar current capacity, aging of insulating parts and other problems, affecting the stable operation of the transmission system [4]. The calculation of bus bar temperature rise distribution involves multi-field coupling of electromagnetic field, temperature field and flow field, which is closer to the actual condition of GIS, and has become a hot research topic in electric power industry in recent years.

In recent years, due to the rapid development of computing power, many scholars have carried out extensive research on multi-field coupling simulation. At present, most scholars consider eddy current loss, skin effect, SF_6 convection heat transfer, gravity, external environment and other factors to simulate the coupling of electromagnetic field [5–7], thermal field and flow field of GIS/GIL bus bar. The temperature rise of GIS/GIL bus bar under mixed insulating gas is considered in some literatures [8]. However, most GIS/GIL chamber models established are horizontal lying and do not include basin insulators [9, 10], ignoring the temperature rise of GIS and temperature change of basin insulators in the state of vertical placement.

The skin effect, natural convection and radiation, gravity and other factors in GIS are considered comprehensively. Based on the theories of electromagnetic field and solid heat transfer, the 252 kV coaxial single-phase GIS as the prototype is took in this paper. The finite element software is used to calculate the temperature distribution of GIS chamber under multi-field coupling and different working conditions, which provides theoretical support for GIS heat dissipation and state maintenance, and has practical significance.

2   Multiple Physical Field Coupling Mathematical Model

The operation of GIS involves many physical processes. The conductor flows into the power frequency current, resulting in Joule heat loss in the conductor, and eddy current loss in the shell. This loss will cause the temperature rise in GIS through heat conduction, heat convection and heat radiation. The process is shown in Fig. 1.

For the convenience of research, this model does not consider solar radiation and external air flow, and does not consider the absorption, reflection and heat dissipation effects of gas molecules and dust in SF_6 on conductor radiation.
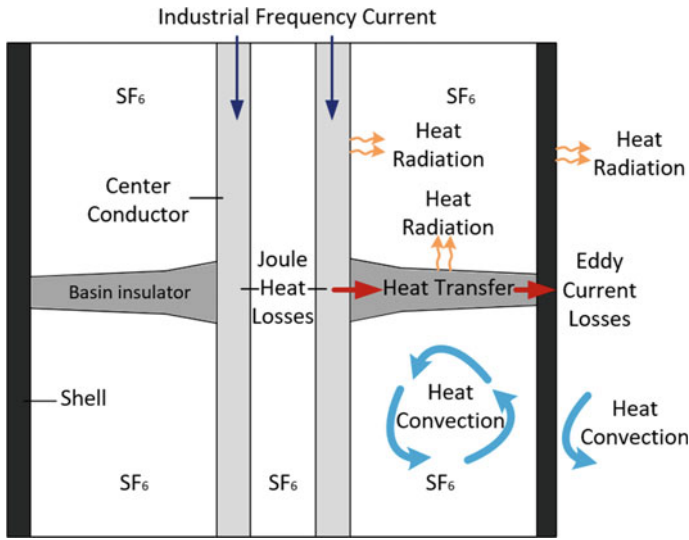
Fig. 1 GIS diagram of temperature rise process

2.1 Governing Equation of Electromagnetic Field

The governing equation of electromagnetic field is shown in Eqs. (1)–(3).

$$\nabla \times H = J \tag{1}$$

$$B = \nabla \times A \tag{2}$$

$$J = \sigma E + j\omega D \tag{3}$$

where H is the strength of the magnetic field. J is the current density. B is the flux density. E is the electric field intensity. D is the electric flux density.

The heat loss of the conductor or shell is shown in Eq. (4).

$$Q = \frac{1}{2} \int_V \frac{|J|^2}{\sigma} dV \tag{4}$$

where J is the total current density and σ is the conductivity of the conductor or shell.

The boundary conditions of the research object are set as follows.

The conductor current exists only in the z-axis direction. Magnetic insulation boundary conditions are applied to the outer boundary of GIS. Considering skin effect, the boundary of conductor and shell is divided by layers.

2.2 Governing Equation of Temperature Field and Flow Field

The governing equation of heat transfer in solids and fluids is shown in Eq. (5).

$$\rho c_p v \nabla T = \nabla \cdot (k \nabla T) + Q \tag{5}$$

where ρ is the density of materials. c_p is the specific heat capacity of materials. k is the thermal conductivity of a materials. Q is the heat source.

The governing equations of radiation heat transfer are as follows:

$$q_{net} = \varepsilon\left(G - \sigma T^4\right) \tag{6}$$

$$J_{net} = \varepsilon \sigma T^4 + (1 - \varepsilon)G \tag{7}$$

where ε is the surface emissivity of the corresponding conductor, basin insulator and housing, q_{net} is the total heat flux of radiant heat transfer into GIS internal surface, G is the surface incident radiant heat flux, σ is Stefan-Boltzmann constant.

Assume that the ideal gas is SF_6, and its density is affected by temperature and pressure, as shown in Eq. (8).

$$\rho = \frac{Mp}{RT} \tag{8}$$

where M is the molar mass of the gas, p is gas pressure, R is the gas constant of SF_6.

The boundary conditions of the research object are set as follows:

(1) For flow field setting, this model adopts wall non-slip.
(2) Keep the ambient temperature at 293 K. The heat transfer coefficient of convective heat flux is 5 W/(m^2 K).
(3) The heat sources are electromagnetic losses of conductor, insert and shell respectively. SF_6 gas adopts laminar flow model, whose pressure is maintained at 0.5 MPa.
(4) SF_6 is set as an incompressible viscous fluid with a specific heat rate of 1.1.

3 GIS Simulation Model and Parameter Setting

In this paper, the single-phase closed structure 252 kV GIS produced by a factory is used as the model for modeling and simulation. The GIS simulation model is shown in Fig. 2. Its dimension parameters are shown in Table 1. Its material parameters are shown in Table 2. GIS chamber is axisymmetric model. The GIS chamber is placed vertically, and the direction of gravity is the same as the axis.

Fig. 2 GIS simulation model
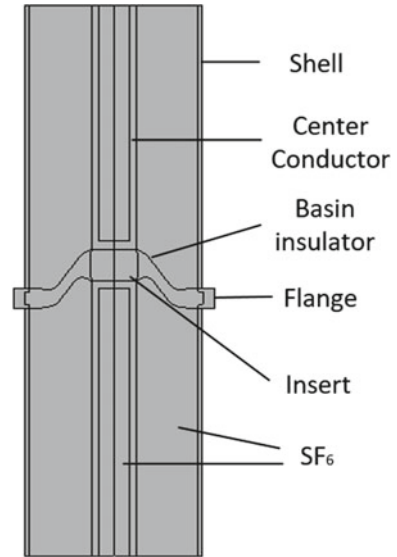
Table 1 GIS model size parameters

Parameter	Value (mm)	Parameter	Value (mm)
Inner diameter of conductor	35	Outer diameter of conductor	50
Inner diameter of shell	192	Outer diameter of shell	202
Outside diameter of flange	230	Height of flange	25
Height of basin insulator	150	Height of GIS chamber	1400

Table 2 GIS material parameters

Parameter	Center conductor and insert	Basin insulator	Shell
Thermal conductivity/(W/(m K))	218	0.7	152
Density/(kg/m^3)	2700	2300	2690
Constant pressure heat capacity/ (J/(kg K))	900	800	819
Conductivity/(S/m)	3.488×10^7	2.564×10^{-13}	3.012×10^7
Relative permeability	1.000021	1	1.000021
Surface emissivity	0.2	0.9	0.9

Fig. 3 Magnetic flux density distribution and magnetic field distribution of GIS under power frequency current

(a) Magnetic flux density distribution

(b) Magnetic field distribution
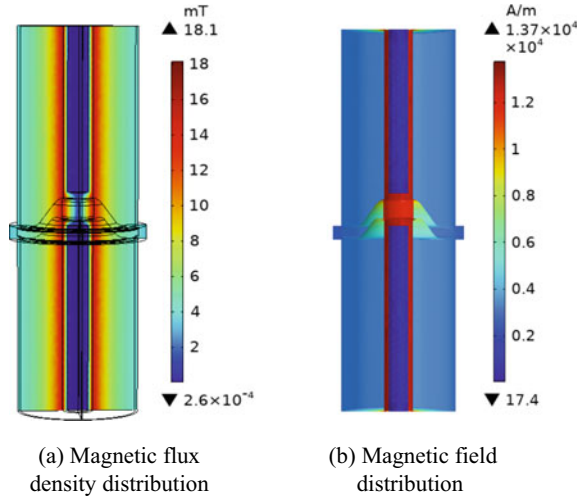
Table 3 The thermal power density of different components in GIS

Current	Conductor	Insert	Shell
4000 A	16,439 W/m^3	7358.7 W/m^3	739.62 W/m^3

4 Simulation Result

4.1 Magnetic Field Simulation

The GIS conductor is fed 4 kA power–frequency alternating current to obtain the GIS magnetic field intensity distribution, as shown in Fig. 3.

As can be seen from Fig. 3, the current frequency of GIS is small, so the magnetic flux density is small. The magnetic flux density on the conductor side is the largest and decreases along the direction of the shell. The maximum magnetic field intensity of the GIS conductor side is 13700 A/m, and that of the shell side is 3330 A/m.

At the same time, electromagnetic losses of different GIS components are calculated, as shown in Table 3. It can be seen from Table 3 that the conductor has the highest joule heat loss. The shell mainly suffers from eddy current loss and the heating power density is small.

4.2 Temperature Field Simulation

Keep the ambient temperature at 293 K and operating pressure at 0.5 MPa. The electromagnetic loss was brought into the heat flow field as a heat source to realize

Fig. 4 Temperature distribution of GIS under 4 kA current
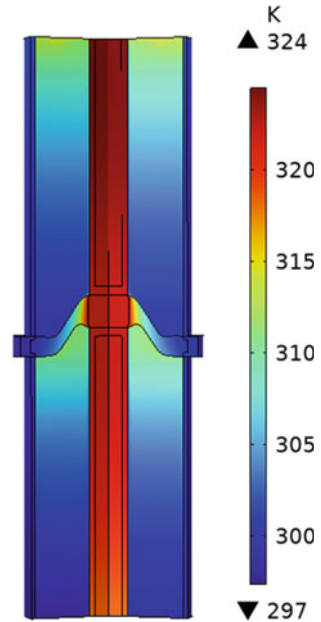
multi-field coupling of the electric heat flow, and the GIS temperature distribution under 4 kA power frequency current was calculated. The results are shown in Fig. 4.

As can be seen from Fig. 4, it will cause different degrees of temperature rise in the GIS chamber when the conductor passes a load current of 4 kA, and the temperature is distributed symmetrically along the central axis. The overall temperature decreases radially from the central conductor to the shell side, with the highest temperature rising to 31 K and the lowest temperature rising to 4 K. Due to gravity, buoyancy, conductor heating and other factors, the temperature of SF_6 distributed above the chamber is high, while the temperature at the bottom is low. The basin insulator separates the GIS chamber from the ventricle. The concave surface is located above the chamber, and the gas temperature near it is higher than that on the convex surface.

Figures 5 and 6 show the temperature distribution cloud map and graph at the top and bottom of GIS respectively. As can be seen that the temperature at the top of GIS is much higher than that at the bottom. At the same height, GIS temperature decreases along the radial direction. The temperature at the solid and gas locations changed little, but the temperature at the gas–solid junction changed obviously. The gas–solid junction of the conductor, with the bottom larger than the top. The bottom temperature plunged 20 K, the top temperature plunged about 6 K, then slowly reduced 4 K. The top of shell gas solid junction is larger than the bottom. The top temperature drops by 12 K and the bottom temperature drops by less than 1 K. The temperature difference between the upper and lower boundaries of the conductor is about 6 K, the temperature difference between the upper and lower boundaries of SF_6 is about 16 K, and the shell is about 4.3 K. It can be seen that the gas temperature

in GIS is most affected by the chamber height. The temperature difference between inside and outside the top of GIS is 23 K, and the temperature difference between inside and outside the bottom is 21 K.

Figure 7 shows the temperature distribution diagram of the inside of the conductor and the outside of the shell along the z axis. It can be seen that due to the high vertical distribution of GIS, there is a temperature difference between the top and bottom. With the height of GIS chamber, the surface of the conductor and the shell slowly heated up without sudden temperature change. The temperature variation amplitude is small, and the conductor temperature variation amplitude is slightly higher than that of the shell.

Figure 8 shows the surface temperature distribution diagram of a basin insulator. It can be seen that the surface temperature of the basin insulator decreases from the radial direction of the conductor side to the shell side, and the temperature difference
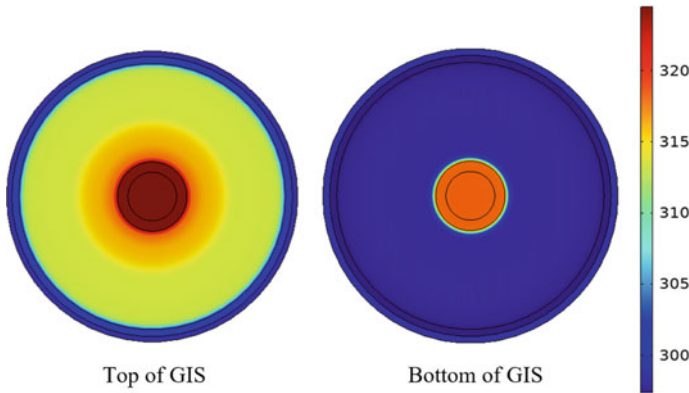
Fig. 5 Temperature distribution at the top and bottom of GIS
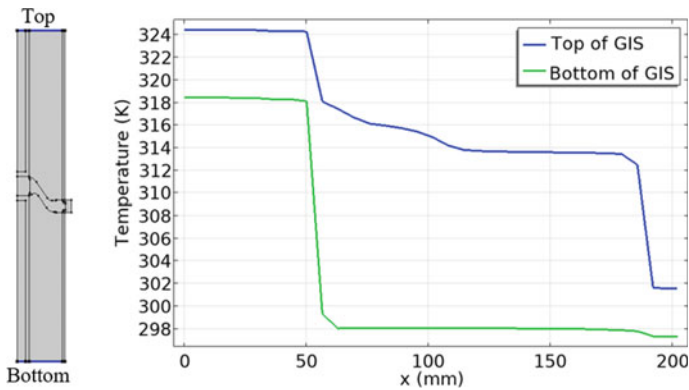
Fig. 6 Temperature distribution curve at the top and bottom of GIS
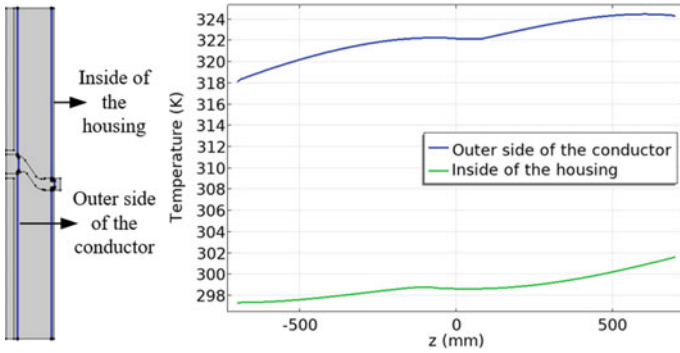
Fig. 7 Temperature distribution curve along z axis of conductor side and shell side

Fig. 8 Surface temperature distribution curve of basin insulator
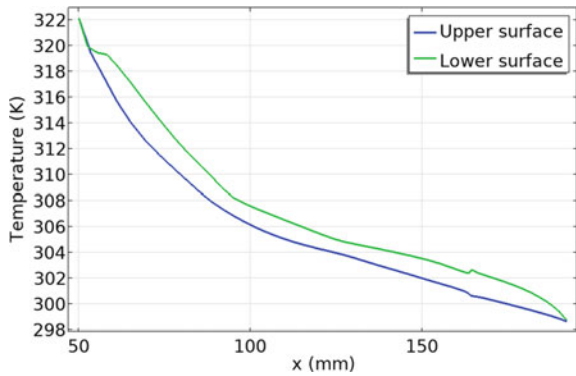
between inside and outside is 23.5 K. The lower surface temperature of the middle insulator is slightly higher than that of the upper surface.

5 Conclusion

In this paper, busbar loss, temperature distribution and flow field distribution of single-phase closed structure 252 kV GIS are calculated and analyzed, and the following conclusions are obtained:

(1) When the ambient temperature is 293 K and 4 kA power frequency current is applied to the central conductor of the GIS at 252 kV, the highest temperature of the GIS is 324 K, the lowest temperature is 297 K, the temperature of the central conductor rises to 25–31 K, and the temperature of the shell rises to 4–9 K.

(2) The temperature above the GIS chamber is higher. At the same height, the GIS temperature gradually decreases along the radial direction from the conductor center. The radial temperature difference ranges from 21 to 24 K, and the temperature difference between the top and the inside and outside is slightly larger than that at the bottom.

(3) The lower surface temperature of the basin insulator is greater than that of the upper surface. The radial temperature difference between inside and outside is 23.5 K.

(4) The gas temperature difference between the top and bottom of GIS is 16 K, the conductor temperature difference is 6 K, and the shell temperature difference is 4.3 K. The height of the chamber has a great influence on the gas temperature.

References

1. Xing Y, Wang Z, Liu L, Xu Y, Yang Y, Liu S, Zhou F, He S, Li C (2022) Defects and failure types of solid insulation in gas-insulated switchgear: in situ study and case analysis. High Voltage 7(1):158–164
2. Tang J, Li W, Liu Y (2010) Blind source separation of mixed PD signals produced by multiple insulation defects in GI. IEEE Trans Power Deliv 25(1):170–176
3. Li X, Wu M, Hu X, Jiang P, Han J, Zhao K, Li Z, Zhang Q (2022) Discharge characteristics of insulation defects in GIS under AC/LI superimposed voltage. IEEE Trans Dielectr Electr Insul 29(5):2017–2025
4. Qin Z, Zhao Y, Zhang L, Wang S, Ma Z (2021) Temperature-rise simulation and research of a new 252kV GIS disconnector based on Ansys workbench. In: 2021 3rd Asia energy and electrical engineering symposium (AEEES), Chengdu, China, pp 6–10
5. Ma B, Wu X, Li X, Ni H, Sun S, Pang P, Li J (2019) Finite element simulation of GIS temperature field distribution characteristics and influencing factor. Insulat Mater 52(3):69–73+79 (in Chinese)
6. Chen Q, Li Q, Cong H, Li J, Jin H, Peng Z (2016) Multi-field coupling calculation of temperature distribution of GIS bus bar with multiple boundary conditions and analysis of influencing factor. Trans Electrotechnical Soc 31(17):187–195 (in Chinese)
7. Wu J, Wang Z, Lu H, Wang L, Sun S, Wang Q (2020) GIS temperature rise calculation and experimental study considering the influence of airflow field. High Voltage Technol 46(3):815–823 (in Chinese)
8. Wang K, Li L, Wang J, Ren L (2021) Study on multi-physical field coupling mechanism of temperature rise of three-phase GIS bus based on mixed insulating gas. High Voltage Electron 57(04):69–75 (in Chinese)
9. Gao B, Li Z, Gao J, Liang H, Yan Z, Hu Y (2021) The simulation study on temperature field distribution of 220 kV gas insulated switchgear. J Nanoelectron Optoelectron 16(5):797–805
10. Niu H, Chen Z, Zhang H, Luo X, Zhuang X, Li X, Yang B (2020) Multi-physical coupling field study of 500 kV GIL: simulation, characteristics, and analysis. IEEE Access 8:131439–131448

The Inversion Calculation Method of Core Temperature in 110 kV Cable Inter-mediate Joint

Xiantao Tao, Lei Wang, Ying Hu, Hangrui Chang, Junhao Chen, Gang Ye, Lizhi Zhang, and Yunqi Xing

Abstract The heating of mid-joints is one of the common hidden dangers in cable systems, and temperature monitoring at the mid-joint is of significant importance for assessing cable operation status. In this paper, a method for inversely calculating the core temperature at the mid-joint of a 110 kV cable is proposed, based on the thermal circuit method for cable body from the standards IEC-60287 and GB/T-10181, as well as the temperature measurement method of distributed temperature sensing devices installed on the inner side of the outer sheath. This method aims to improve the accuracy of temperature calculations by considering the effect of contact resistance loss on core heating and comparing the results with simulation data to validate the accuracy of the proposed approach. The results show that when the cable operates under steady-state conditions and for different temperature conditions on the inner side of the outer sheath, the absolute errors between the calculated current and core temperature using the modified inversion method and the simulation results are within 5%, which basically meets the requirements for field application.

Keywords Intermediate joint · Distributed temperature measurement · Core temperature · Temperature field simulation

X. Tao (✉) · L. Wang · Y. Hu
China Electric Power Research Institute, Wuhan 430074, China
e-mail: tao_xiantao@126.com

H. Chang · J. Chen · G. Ye
School of Electronic Information, Yangtze University, Jingzhou 434023, China

L. Zhang · Y. Xing
School of Electrical Engineering, Hebei University of Technology, Tianjin 300401, China

1   Introduction

The abnormal heating of mid-joints is one of the common hidden dangers in cable system operation. Defects such as poor installation, external damage, and water ingress can all cause mid-joint heating. If not dealt with in a timely manner, these defects can cause short circuits, power outages, and even fires or explosions, leading to further expansion of the fault [1]. Therefore, temperature monitoring and temperature field calculation of cable mid-joints are of great significance for improving the safe operation of cable lines.

Currently, the main online temperature measurement methods for cable operation include thermocouple, infrared and temperature sensor surface measurements. Thermocouples are temperature sensors based on electrical signals and although they have high measurement accuracy, they are susceptible to electromagnetic interference [2]. Infrared and temperature sensor surface measurement has the advantages of a wide measurement range and flexibility in use, but its measurement accuracy is relatively low [3, 4]. In order to improve the accuracy of temperature measurement, this paper proposes a distributed temperature measurement method [5], which involves laying a device containing temperature measurement chips inside the outer sheath of cable mid-joints during their production. Compared with surface temperature measurement, this temperature measurement method has less interference from external environments and, therefore, provides more accurate measurement results.

There are mainly two methods for calculating the temperature at cable mid-joints: analytical calculation method and numerical computation method. Among them, the analytical method is the most widely used, which mainly relies on the thermal circuit model to calculate the mid-joint temperature. With known cable form and related parameters, the analytical method can conveniently calculate the core temperature of the cable through the thermal circuit model [6]. Some scholars have proposed a thermal circuit model for three-core cable mid-joints based on IEC-60287 [7] and GB/T-10181 [8]. However, this model only considers the radial heat diffusion process of mid-joint core heating but ignores the axial heat transfer process caused by the temperature difference between the mid-joint and the cable body [9]. Some scholars have also proposed the concept of axial interlayer thermal resistance for high-voltage cable mid-joint thermal circuit models, but they have not conducted specific numerical calculations for the thermal circuit model [10].

The numerical computation method mainly includes the finite element method and the finite difference method, which can simulate the actual cable operation under the coupling calculation of multiple physical fields by computer technology [11]. Relatively speaking, the analytical calculation method has a simple form and convenient calculation, but the temperature of each part of the cable is unknown during the calculation process. Some temperature process calculation values are obtained through empirical methods, which results in certain errors compared to the actual temperature [12]. The numerical computation method has high computational accuracy and can calculate the temperature of each layer structure simultaneously, which

is convenient for the temperature field analysis of the entire cable mid-joint. However, the solving process is complex and time-consuming [13].

In this paper, the analytical calculation method is selected. Based on the thermal circuit structure of the cable body calculation standards IEC-60287 and JB/T-10181, a thermal circuit model of the core temperature at the mid-joint of a 110 kV single-core cable is established [14]. Under the condition of a known external environmental temperature, the mid-joint core temperature is calculated through the temperature measurement at the inner side of the outer sheath. The accuracy of this calculation method is verified through finite element simulation. At the same time, considering the influence of contact resistance on the entire mid-joint heating, the inversion calculation method is modified to improve the calculation accuracy of the core temperature at the mid-joint, which provides a calculation and analysis method for the core temperature at the mid-joint of distributed temperature sensing methods.

2   Intermediate Joint Samples and Material Parameters

This article focuses on the YJLW03-64/110 630 mm^2 single-core cable and the corresponding YJJJI-64/110 630 mm^2 intermediate joint, as shown in Fig. 1. The materials and dimensions of the cable and the intermediate joint are shown in Table 1.
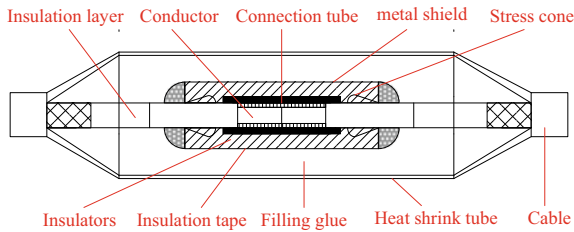
Fig. 1   The Diagram of the intermediate joint

Table 1   Dimensional parameters of the 110 kV cable

Structure	Material	Inner diameter (mm)	Outer diameter (mm)	Thermal resistance factor (K m/W)
Conductor	Copper		15.0	2.6×10^{-3}
Insulation layer	XLPE	15.0	34.5	2.5
Wrapping tape	Water barrier	34.5	36.5	6.0
Air gap	Air	36.5	38.5	43.5
Armoured layer	Aluminum	38.5	41.0	4.2×10^{-3}
Outer sheath	HDPE	41.0	44.0	3.1

3 Inversion Calculation Method for Distributed Thermometers

Referring to the thermal model of the cable body in standards IEC-60287 and JB/T-10181, a thermal model for the intermediate joint is established, considering both radial and axial heat transfer. A partial thermal resistance is combined to obtain the thermal model for the intermediate joint, as shown in Fig. 2.

Where W_c and W_c' are the heat loss of the cable joint conductor and the cable conductor (W); W_d is the dielectric loss of the cable joint insulation (W); T_1 is the thermal resistance of the cable joint insulation (K m/W); T_2 is the thermal resistance from the cable joint insulation to the outer sheath (K m/W); T_3 and T_4 are the thermal resistance of the cable joint outer sheath and the surrounding medium (K m/W); T_5 and T_6 are the axial thermal resistance of the cable joint conductor and the joint insulation, respectively (K m/W); T_7 is the thermal resistance of the cable insulation (K m/W); T_8 is the equivalent thermal resistance from the cable insulation to the outer sheath (K m/W); T_9 is the thermal resistance of the cable outer sheath (K m/W); T_{10} is the thermal resistance of the surrounding medium of the cable (K m/W); θ_c is the temperature of the cable joint conductor (°C); θ_c' is the temperature of the cable conductor (°C); θ_0 is the ambient temperature (°C). θ_s is the inner temperature of outer sheath (°C). W_1, W_2, W_3, W_4, θ_m, θ_n are all computational auxiliary parameters.

$$W_c = W_1 + W_2 \tag{1}$$

$$(W_1 + W_d)T_1 = \theta_c - \theta_m \tag{2}$$

$$W_3 T_2 = \theta_m - \theta_s \tag{3}$$

$$W_1 + W_d = W_3 + W_4 \tag{4}$$
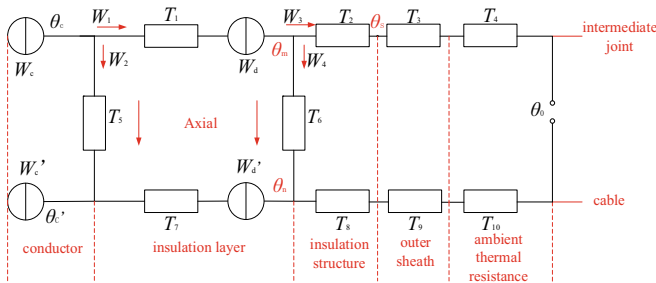
Fig. 2 The diagram of the intermediate joint thermal circuit

$$W_3(T_3 + T_4) = \theta_m - \theta_0 \tag{5}$$

$$W_4 T_6 = \theta_m - \theta_n \tag{6}$$

$$\left(W_c' + W_2\right) T_7 = \theta_c' - \theta_n \tag{7}$$

$$\left(W_c' + W_2 + W_4\right)(T_8 + T_9 + T_{10}) = \theta_n - \theta_0 \tag{8}$$

$$W_2 T_5 = \theta_c - \theta_c' \tag{9}$$

$$W_c = I^2 R \tag{10}$$

$$W_c' = I^2 R' \tag{11}$$

In the case of known cable geometry parameters and ambient temperature θ_0, the AC resistance of the cable joint conductor R, the AC resistance of the cable conductor R', and the corresponding thermal resistances T_1 to T_{10} can be directly calculated. The parameters W_1, W_2, W_3, W_4, θ_m, θ_n, θ_c, θ_c', Wc, W_c', and I are unknown, that can be determined by solving Eqs. (1)–(10) to obtain the final values of θ_c and I.

Using the above calculation method, with the ambient temperature θ_0 held constant at 25 °C, the temperature on the inner side of the outer sheath is changed, increasing from 25 °C (initial state) by equal increments to 50 °C (Table 2).

Table 2 Calculation results of the 110 kV cable

θ_s (°C)	Calculated value of I (A)	Calculated value of θ_c (°C)
25	0	25
30	691.84	56.76
35	961.34	75.82
40	1187.44	97.61
45	1385.67	124.96
50	1541.46	149.87

4 Intermediate Joint of 110 kV Cable Temperature Field Simulation

A simulation model is established based on the cable body and cable geometry parameters selected in this experiment, according to Table 1. Under the conditions of known current values and external ambient temperatures, the corresponding temperature field simulation results are obtained for different values of the inner sheath temperature.

To better reflect the temperature distribution of the cable intermediate joint under actual operating conditions, the conductivity of the connection point (compression tube) is reduced to 5×10^7 (S/m) to simulate the presence of contact resistance in the intermediate joint. The ambient temperature is set to a constant 25 °C, and the convective heat transfer coefficient is set to 6 W/(m^2 K). The temperature field distribution of the cable intermediate joint is shown in Fig. 3 (Table 3).

5 Correction of Inverse Calculation Method Considering Contact Resistance

In macroscopic calculations, it is difficult to define the specific value of the contact resistance. Currently, most scholars use a contact coefficient k to characterize the contact resistance [15]. Assuming the cable conductor has a resistivity of ρ_1 and a radius of r_1, and the compressed conductor has a resistivity of ρ_2 and a radius of r_2. The contact coefficient k is defined as the ratio of the resistance per unit length of the compressed conductor to that of the cable conductor. The corrected results are shown in Table 4.

6 Discussion

In Fig. 4 and Table 5, The relative error is represented using the standard error. The error between the calculated values and simulation values of the current obtained under the condition without contact resistance is relatively large, but the calculated values obtained by considering the contact resistance are closer to the simulation values, with a maximum error of 8.2%. In Fig. 5 the overall error between the calculated values of the core temperature before and after modification and the simulation values is relatively small.

The idealized calculation method only considers the core loss and insulation loss of the cable intermediate joint, and does not include the effect of contact resistance. However, the simulation model usually includes contact resistance, which leads to the calculated core heating being less than the simulated core heating, and as a result, the current calculated using this method is higher than the simulated current. The

(a) result for θs=25 (initial state)　　(b) result for θs=30　　(c) result for θs=35

(d) result for θs=40　　(e) result for θs=45　　(f) result for θs=50
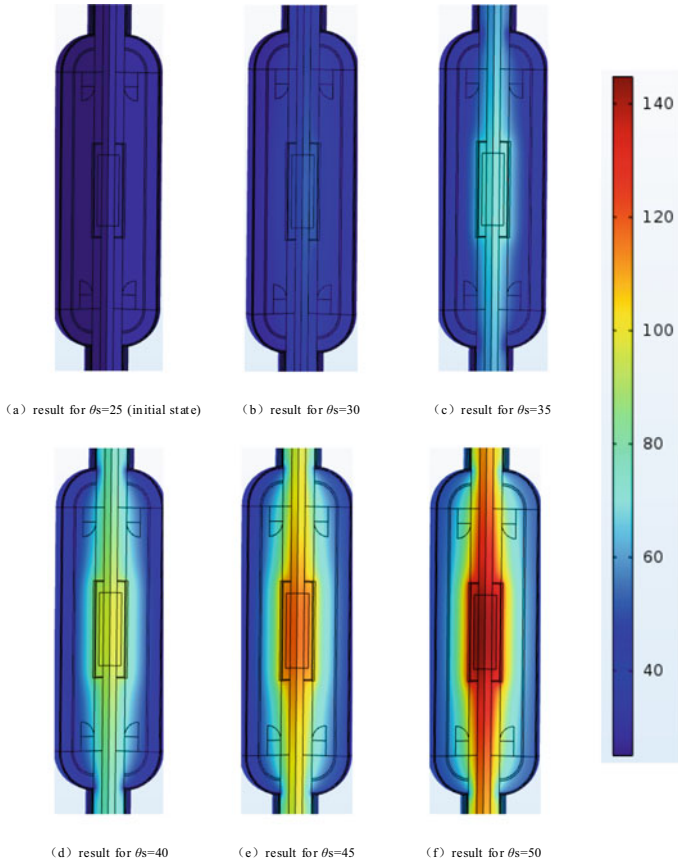
Fig. 3 Temperature field distribution of the intermediate joint

Table 3 The results of temperature field simulation

θ_s (°C)	Simulation value of I (A)	Simulation value of θ_c (°C)
25	0	25
30	619.36	48.93
35	882.37	73.21
40	1064.32	94.63
45	1229.76	118.75
50	1376.82	142.90

Table 4 Corrected calculation results of core temperature of the intermediate joint

θ_s (°C)	Calculated value of I (A)	Calculated value of θ_c (°C)
25	0	25
30	643.51	50.30
35	925.61	73.94
40	1114.47	97.76
45	1296.17	124.46
50	1489.36	151.19
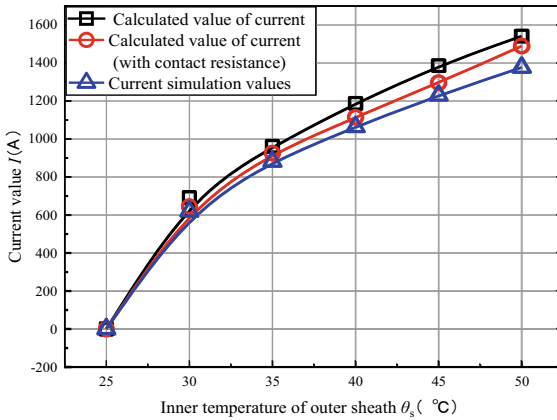
Fig. 4 The current results comparison of calculation and stimulation

Table 5 The error between the calculated results and the simulation results

θ_s (°C)	Without contact resistance				Including contact resistance			
	The error of I (A)	S.D. (%)	The error of θ_c (°C)	S.D. (%)	The error of I (A)	S.D. (%)	The error of θ_c (°C)	S.D. (%)
25	0		25		0		25	
30	72.48	11.7	7.83	16	24.15	3.9	1.37	2.8
35	78.97	8.9	2.61	3.6	43.24	4.9	0.73	1.0
40	123.12	11.6	2.98	3.1	50.15	4.7	3.13	3.3
45	155.91	12.7	6.21	5.2	66.41	5.4	5.71	4.9
50	164.64	11.9	6.97	4.9	112.54	8.2	8.29	5.8

distributed calculation method refers to the thermal method specified in standards such as IEC-60287 and JB/T-10181, and some of the calculation parameters are based on empirical values obtained from experiments, which can lead to certain

Fig. 5 The core temperature results comparison of calculation and stimulation
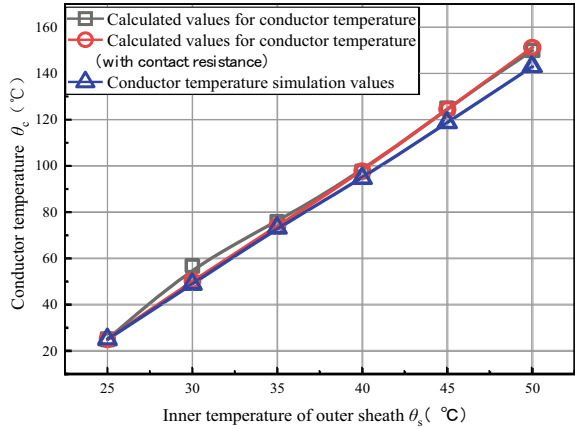
errors. Under normal steady-state operating conditions (with the core temperature below 90 °C), the calculated values of the current and core temperature obtained by the modified calculation method have an error of less than 5% compared to simulation results, indicating a certain level of accuracy of the modified calculation method.

7 Conclusion

In the present work, an inverse calculation method for the core temperature of a 110 kV cable intermediate joint is proposed. The main conclusions are as follows:

(1) The inverse calculation method can calculate the core temperature of the intermediate joint through the ambient temperature and inner jacket temperature, and the calculation process is relatively simple.

(2) The maximum error between the results obtained by the modified (including contact resistance) inverse calculation method and the simulation results is 8.2%, and the error is within 5% under normal steady-state operating conditions. This indicates that the modified inverse calculation method has good accuracy.

(3) The contact resistance is an important factor in the heating of cable intermediate joints and cannot be ignored during the calculation process. Further research is needed to investigate the impact of contact resistance and its value calculation in greater detail.

References

1. Qingsong J, Qing Y, Haonan C, Jian S, Jiaquan R (2022) Insulation state detection method of cable joint based on transient voltage transfer characteristics. High Voltage Eng 48(03):1124–1132
2. Hua J, Li X, Qin X, Wang Z et al (2018) Power cable measured device based on passive wireless sensor technology. Instrum Tech Sens (12):58–62
3. Yunpeng G, Tianyuan T, Kaipei L (2014) Discussion of power cable temperature monitoring methods. Insulating Mater 47(6):13–17
4. Deng S, Hu R, Ye W (2020) State evaluation technology of distribution network cables based on internal conductor temperature measurement. High Voltage Eng 46(12):4430–4434
5. Xiantao T, Wei Z, Hui G et al (2023) Research on inversion calculation method of cable temperature based on RFND thermometers. High Voltage Apparatus 59(4):147–155
6. Neher JH, Mcgrath MH (1957) The calculation of the temperature rise and load capacity of cable systems. IEEE Trans on Power Deliv 76(3):752–772
7. IEC 60287-1-1 (2006) Electric cables e calculation of the current rating part 1–1: current rating equations (100% Load Factor) and calculation of losses general. IEC Publication, Geneva, Switzerland
8. Cables Calculation of the Rating-Part11 (2014) Current rating equations (100% load factor) and calculation of losses-general: JB/T10181.11–2014 (in Chinese)
9. Holyk C, Liess HD, Grondel S et al (2014) Simulation and measurement of the steady-state temperature in multi-core cables. Electr Power Syst Res 116(11):54–66
10. Hanna MA, Chikhan AY, Salama MMA (1993) Thermal analysis of power cables in multi-layered soil part.1: theoretical mode. IEEE Trans Power Deliv 8(3)
11. Vaucheret P, Hartlein RA, Black WZ (2005) Ampacity derating factors for cables in short segment of conduit. IEEE Trans Power Deliv 20(2):1–6
12. Niliot CL, Rigollet F, Petit D (2018) An experimental identification of line heat sources in a diffusive system using the boundary element method. Int J Heat Mass Transf 43(12):2205–2220
13. Yang SM, Tao WQ (2006) Heat transfer. Higher Education Press, Beijing (in Chinese)
14. Horrocks DJ, Thelwell MJ, Weedy BM (1973) Reduction of cable-joint temperatures by oscillation of oil in the conductor duct a theoretical study. Proc Inst Electr Eng 120(5):593–594
15. Liu G, Wang Z, Xu T, Liu Y, Wang P (2017) Current capacity calculation and experimental analysis of 110 kV cable joint. High Voltage Eng 43(05):1670–1676

Effect of Metal Fouling on Insulator Surface on the Decomposition Characteristics of SF$_6$/N$_2$ Gas Mixture

Yinghuai Liao, Yan Luo, Weihong Yang, Chuansheng Luo, Ran Zhuo, Bing Tang, and Mingli Fu

Abstract SF$_6$/N$_2$ gas mixture applied in gas insulated equipment can reduce the greenhouse effect of pure SF$_6$ gas. This paper investigates the partial discharge decomposition of SF$_6$/N$_2$ gas mixtures under metal fouling on insulator surfaces. The results show that the decomposition products are SO$_2$F$_2$, SOF$_2$, SO$_2$, NO$_2$, NF$_3$ and CF$_4$, the generation of which increases with the increase of the discharge time, but the generation of SOF$_2$ is much higher than that of SO$_2$F$_2$. the generation of SO$_2$F$_2$, SO$_2$, NO$_2$ and NF$_3$ shows a linear saturation trend with the increase of the discharge volume. the generation of CF$_4$ increases with the increase of the PD intensity. The generation of CF$_4$ shows a linear trend with the increase of PD intensity, which can be used as a characteristic product to characterize the fault severity of insulator metal surface fouling defects.

Y. Luo · W. Yang · R. Zhuo · M. Fu
CSG Electric Power Research Institute Co., Ltd., Guangxi, China

United Laboratory of Advanced Electrical Materials and Equipment Support Technology, CSG, Guangdong, China

Y. Luo
e-mail: luoyan1@csg.cn

W. Yang
e-mail: yangwh@csg.cn

R. Zhuo
e-mail: zhuoran@csg.cn

M. Fu
e-mail: fuml@csg.cn

Y. Liao (✉) · C. Luo · B. Tang
Nanning Power Supply Bureau, Guangxi Power Grid Co., Ltd., Guangxi, China
e-mail: 1211603281@qq.com

C. Luo
e-mail: Luocs0410@gx.csg.cn

B. Tang
e-mail: b.sy@gx.csg.cn

1 Introduction

SF_6 is widely used in electrical equipment for its excellent insulation and arc extinguishing properties [1–3]. However, SF_6 is a greenhouse gas with a potential greenhouse effect of 23,500 [4, 5]. To limit the use of SF_6, a certain content of buffer gas can be added to SF_6 gas, which not only reduces the amount of SF_6, but also effectively lowers its liquefaction temperature [6, 7]. Studies have shown that the insulation strength of SF_6/N_2 gas mixture is significantly higher than that of SF_6/Air and SF_6/CO_2. When the ratio of SF_6 in SF_6/N_2 reaches 50–60%, its insulation performance can reach 85–90% of that of SF_6 [8, 9].

The current research on the decomposition characteristics of SF_6 under different fault conditions has been more comprehensive [10–12], but the research on the influence of the decomposition characteristics of SF_6/N_2 gas mixture under different discharge defects is not comprehensive enough. A certain number of metal particles are sometimes adsorbed on the insulator surface, which, due to mechanical vibration or electrostatic force, can cause their movement to a location favorable for the occurrence of discharge, thus triggering partial discharge. Some particles, due to their strong adsorption, do not move and thus become fixed metal particles on the insulator surface, i.e., forming a fouling defect on the insulator surface. Therefore, the decomposition characteristics of SF_6/N_2 gas mixture under metal fouling defects on the insulator surface need to be studied in depth.

In this paper, 96 h partial discharge decomposition experiments are conducted on SF_6/N_2 gas mixture under metal fouling defects on insulator surface, and the changes of characteristic decomposition product generation and effective gas production rate with discharge time and discharge volume are analyzed to extract characteristic quantities that can characterize the severity of insulation defect faults.

2 Experimental Setup

The partial discharge decomposition experimental platform is shown in Fig. 1, and the insulator surface metal fouling defect model is shown in Fig. 2. The breakdown voltage of the $50\%SF_6/50\%N_2$ gas mixture under the metal fouling defect on the insulator surface is measured by the step-by-step voltage addition method. Five applied voltage levels are taken at equal difference between the starting voltage and breakdown voltage, and 96 h partial discharge experiments are conducted at the above five voltage levels. The amount of discharge at different voltage levels was measured by oscilloscope. At the same time, part of the gas was taken out every 12 h for qualitative and quantitative testing. The influence of different discharge time and discharge volume on the content of each characteristic decomposition product was analyzed by
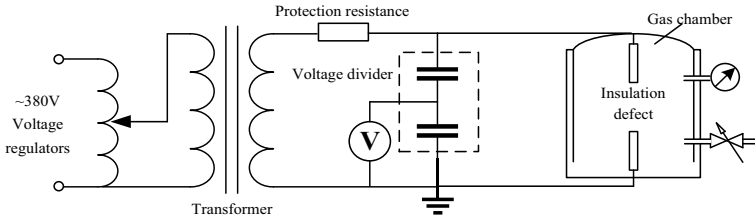
Fig. 1 Partial discharge decomposition experiment platform

Fig. 2 Insulator surface pollution defect model diagram
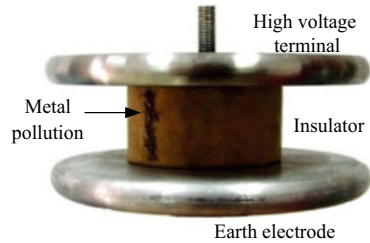
combining the content change curve with the discharge time and discharge volume, and the characteristic product suitable for characterizing the degree of fault inside the equipment was selected.

3 Result

3.1 Variation of Characteristic Component Content with Time and PD Intensity

Figure 3 shows the variation trend of characteristic product generation. The trend of SOF_2 is similar to SO_2F_2, but the SOF_2 content is much higher than SO_2F_2. SO_2 content tends to increase with the discharge time, but after 84 h, the SO_2 content starts to show saturation the NO_2 content also increases with time. The content of NF_3 increased gradually with time at the same voltage and showed the law of accelerated growth rate. The growth rate of CF_4 also increased with the increase of discharge time, CF_4 is the gas molecule at the end of the reaction, with the increase of reaction time, the large molecule product gradually began to decompose to produce CF_4 and other small molecules.

With the increase of PD intensity, the content of SO_2F_2 showed an overall increasing trend of different degrees. At low PD intensity, the SO_2F_2 content increased slowly with time, and its content increased significantly with increasing PD intensity. The growth trend of SOF_2 was similar to that of SO_2F_2, which grew more
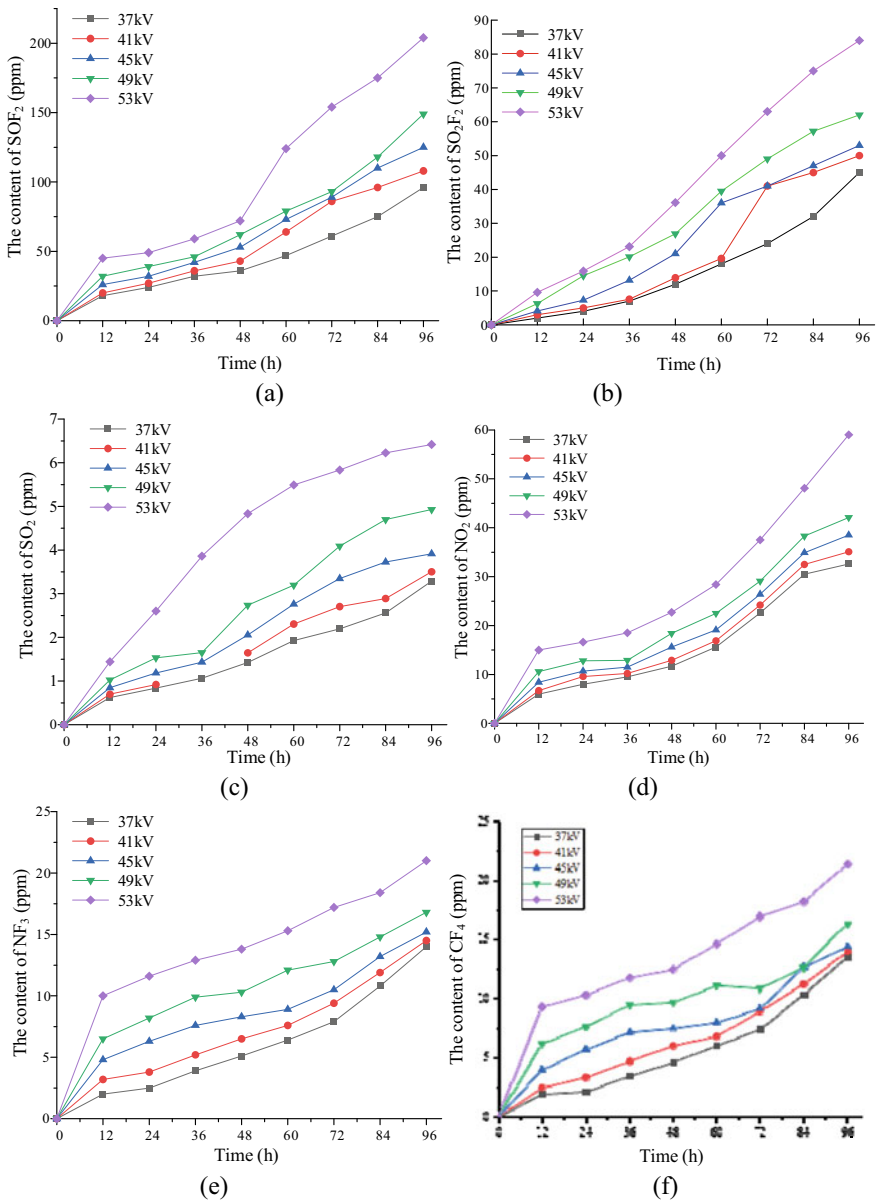
Fig. 3 Variation of each component contents

slowly at low PD intensity and increased significantly when the PD intensity was high. When the PD intensity was low, the SO_2 content showed an overall linear trend with the change of discharge. Both NO_2 and NF_3 are typical nitrogen-containing compounds. During the process of discharge decomposition, the contents of both NO_2 and NF_3 increased with the increase of PD intensity and saturated with the increase of PD intensity. The growth curve of CF_4 showed an undulating trend of growth between 138,656 and 317,376 pC, which was caused by the operation error. Overall, the content of CF_4 also increased with increasing PD intensity and showed an approximate linear growth trend.

3.2 Variation of Characteristic Component Content with PD Intensity

The variation of characteristic component content with PD intensity is shown in Fig. 4.

(1) **Variation curve of SO_2F_2 content with PD intensity**

The content of SO_2F_2 showed an increasing trend with the prolongation of discharge time under the continuous action of PD of different intensities. Meanwhile, with the increase of PD intensity, the contents of SO_2F_2 showed different degrees of growth in general. At lower PD intensities, the gas content increased more gently in general and more slowly with time, whereas when the PD intensity increased, the SO_2F_2 content all increased significantly with a clear growth trend.

(2) **Variation curve of SOF_2 content with PD intensity**

The growth trend is basically linear in a short period of time, and it takes a longer time for the saturation growth trend to appear. Moreover, the saturation trend is not obvious, indicating that the increase of PD intensity has an obvious promotion effect on the generation of SOF_2.

(3) **Variation curve of SO_2 content with PD intensity**

When the PD intensity is low, the SO_2 content shows an overall linear trend with the discharge volume. With the sharp increase in discharge, the growth trend begins to moderate and shows a saturation trend.

(4) **Variation curve of NO_2 and NF_3 content with PD intensity**

Both NO_2 and NF_3 are typical nitrogen-containing compounds. During the process of discharge decomposition, the content of both NO_2 and NF_3 increases with the increase of PD intensity, and the content tends to be saturated with the increase of PD intensity.
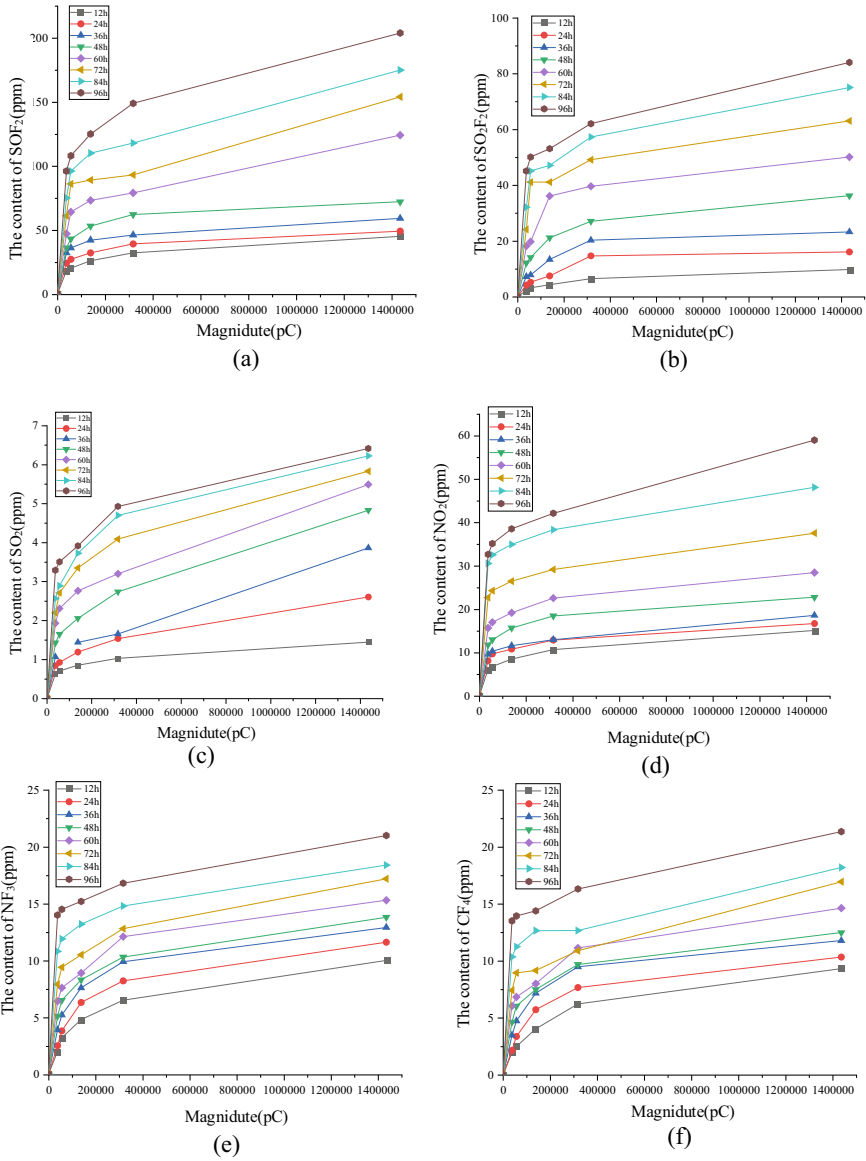
Fig. 4 Variation of each component contents with discharge

(5) **Variation curve of CF$_4$ content with PD intensity**

The growth curve of CF$_4$ has ups and downs in the growth trend between 138,656 and 317,376 pC, which is due to operational errors. Overall, the content of CF$_4$ also increased with the increase of PD strength, and the growth trend was approximately linear.

3.3 *The Effective Formation Rate of Characteristic Component*

The decomposition component mean square gas production rate RRMS is shown in Eq. 1:

$$R_{RMS} = \sqrt{\frac{\sum_{j=1}^{4} \left(\frac{c_{i2}-c_{i1}}{\Delta t}\right)_j^2}{4}} \tag{1}$$

in which, Δt denotes the time interval between the two samples analyzed, where Δt is 1 day (24 h), j is the number of days. The c_{i1} is the amount of component i measured on the first day (after 24 h). c_{i2} is the content of component i measured on the second day (after 48 h), $((c_{i2}-c_{i1})/\Delta t)_j$ is the absolute gas production rate of component i on day j.

The volumetric concentration of the decomposition components increased steadily with the extension of the partial discharge time, but their respective slope trends were different at different voltage levels, i.e., at different PD strengths, which indicated that the PD strength could be determined based on the relationship between the gas production rate of the decomposition components and the discharge volume. The mean square rates of gas production of each characteristic component are shown in Fig. 4. The mean square rates of gas production of SO$_2$F$_2$, SO$_2$, NO$_2$ and NF$_3$ show a saturation trend. The decomposition component SOF$_2$ generation process is more complicated and is a strong heat absorption process, so the increase of discharge volume can promote its generation, and the generation rate increases with the increase of discharge volume (Fig. 5).

Fig. 5 Curve of effective formation rate with discharge
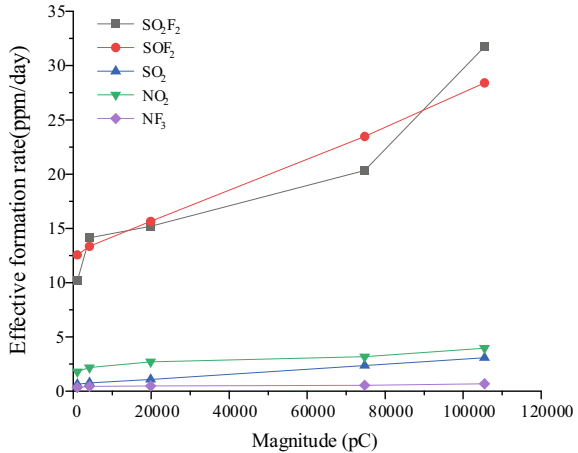
4 Conclusion

1. The results show that the main decomposition products of SF_6/N_2 gas mixture under metal fouling on insulator surface are SO_2F_2, SOF_2, SO_2, NO_2, NF_3 and CF_4.
2. The content of SO_2 and CF_4 shows an overall linear increase with the increase of discharge, where CF_4 can be used as a characteristic product to characterize the fault severity of metal fouling defects on the surface of SF_6/N_2 gas mixture insulators.
3. The gas production mean square rates of SO_2F_2, SO_2, NO_2 and NF_3 showed a saturation growth trend.

References

1. Zhang X, Wu P, Lin C et al (2021) Compatibility and interaction mechanism between EPDM rubber and a SF_6 alternative Gas-$C_4F_7N/CO_2/O_2$. ACS Omega 6:13293–13299
2. Tian S, Lan J, Rao X et al (2021) Study on compatibility between $C_6F_{12}O/N_2$ gas mixture and sealing rubber material at different temperatures. J Mol Struct 1244:130949
3. Tian S, Lan J, Rao X et al (2022) Study on compatibility between $C_6F_{12}O/N_2$ gas mixture and sealing rubber material at different temperatures. High Voltage Eng 48(11):4275–4286 (in Chinese)
4. Tian S, Liu B, Wang Y et al (2023) Adsorption performance of Cu-HfSe$_2$ on air decomposition products: a first-principles study. Mater Today Commun 34:105400
5. Tian S, Zhang X, Cressault Y et al (2020) Research status of replacement gases for SF_6 in power industry. AIP Adv 10(5):050702
6. Xiao D (2016) Development prospect of gas insulation based on environmental protection. High Voltage Eng 42(4):1035–1046 (in Chinese)
7. Yan X, Gao K, Zheng Y et al (2018) Progress of gas mixture and alternative gas of SF_6. Power Syst Technol 42(6):1837–1844 (in Chinese)

8. Malik NH, Qureshi AH (1979) A review of electrical breakdown in mixtures of SF_6 and other gases. IEEE Trans Electr Insul 14(1):1–13
9. Malik NH, Qureshi AH (1979) Calculation of discharge inception voltages in SF_6-N_2 mixtures. IEEE Trans Electr Insul 14(2):70–76
10. Coll I, Casanovas AM, Vial L et al (2000) Sparking-induced decomposition of 10% SF_6-90%N_2 mixtures: effect of a solid organic insulator, oxygen and water. J Phys D Appl Phys 33(11):1348
11. Vial L, Casanovas AM, Coll I et al (1999) Decomposition products from negative and 50 Hz AC corona discharges in compressed SF_6 and SF_6/N_2 (10:90) mixtures. Effect of water vapour added to the gas. J Phys D Appl Phys 32(14):1681
12. Vial L, Casanovas AM, Diaz J et al (2001) Decomposition of high-pressure (400 kPa) SF_6 and SF_6/N_2(10:90) mixtures submitted to negative or 50 Hz AC corona discharges in the presence of water vapour and/or oxygen. J Phys D Appl Phys 34(13):2037

Evaluation of the Arc Characteristics of High-Velocity Flows in Semi-closed Spaces Through Simulation

Shijie Fu, Jinxin Liu, Mengshi Zhao, Xiang Ji, Dan Lu, and Renbao Yan

Abstract Conventional lightning protection measures are inadequate because the lightning type is not considered, and the current flow amplitude is uncontrollable. Channel devices cannot completely overcome these drawbacks. Therefore, impact channel-arc suppression-power frequency blocking was proposed in the semi-closed space. In this study, a two-dimensional geometric model was established to develop a high-speed explosive airflow arc-extinguishing device and a self-compression multi-break arc-extinguishing device. COMSOL simulation software was used to investigate the high-speed explosive airflow arc-extinguishing device and arc physical characteristics. The simulation results revealed that the explosive high-speed airflow can quickly extinguish the flash arc and suppress the power frequency arc; the self-compression multi-break device uses the heat of the arc to form a high-speed airflow in the power frequency arc. The combination of the explosive high-speed airflow device and self-compression multi-break device can extinguish the power frequency arc with large current values. The combined device can be applied on overhead transmission lines with high-voltage grades.

Keywords High-speed explosive airflow arc extinguishing device ·
Self-compression multi-break device · High-speed airflow · Impact arc
extinguishing device · Comsol

1 Introduction

In developed countries, power grid damage because of lightning causes 50% of power outages. Thus, the lightning trip rate is a serious concern to power grid security and is exhibiting an increasing trend [1–3]. When a lightning flash occurs on an

---

S. Fu · M. Zhao · X. Ji · D. Lu · R. Yan (✉)
State Grid Jiaxing Power Supply Company, Jiaxing Zhejiang 314000, China
e-mail: fushijie91@163.com

J. Liu
State Grid Anji Power Supply Company, Anji Zhejiang 313300, China

overhead transmission line, the continuous current arc causes considerable insulator damage, which causes the power line to trip [4]. Therefore, the continuous flow arc has received considerable research attention for power failure mitigation. Japanese scientist Takashi Chino and his team developed a device in which the inner wall of high-temperature baking arc tube is used to produce a large amount of gas to blow the arc [5]. Russian scientist Podporkin and his team developed a multi-chamber lightning arrester device to extinguish the power frequency arc and neutralize the power frequency arc at the current over the zero point [6]. The arc was extinguished within half a power frequency cycle. The magnetic field force was used to elongate and truncate the arc [7]. However, extinguishing the arc using the aforementioned methods has numerous limitations, including a large loss of arc-extinguishing material, limited improvement space of the current over the zero arc-extinguishing mode, and insufficient number of actions of the internal electrode ablation limiting device.

To overcome the aforementioned drawbacks, shock diversion-arc suppression-power frequency blocking was proposed to mitigate lightning overvoltage, discharge power energy achieve rapid extinguishing of the arc, restore the air medium strength, and suppress arc reignition [8–11]. The arc quenching principle of the high-speed airflow was used to propose a blast flow arc extinguishing and lightning protection device (abbreviated EAAELP) and a self-compression multi-break arc-extinguishing lightning protection device (abbreviated SMAELP) [12–14]. The working principle of the EAAELP device is as follows: when the overhead line is struck by lightning, the EAAELP device triggers the arc pill to produce a high-speed explosive airflow in flashover arc and inhibits the development of a continuous flow arc. Thus, arc inhibition, insulator protection, and flashover protection were realized. In the SMAELP device, the high-speed airflow arc suppression process proceeds as follows: in the compression tube arc, the indoor air rapidly expanded because of the high temperature to form a high-speed impact air will arc. The arc resistance increased and sped up arc and air convection cooling, which disconnected the energy supply channel. The arc temperature decreased rapidly, and the arc could not maintain combustion and was extinguished. Furthermore, the power frequency arc could not form, and its development was hindered. The velocity of the blast flow and the structure of the EAAELP device play a decisive role in extinguishing the arc. Therefore, COMSOL simulation software was used to develop a two-dimensional geometric model for EAAELP and SMAELP devices based on magnetohydrodynamics theory. The inhibition mechanism of the power frequency arc of the EAAELP and SMAELP devices differed considerably. However, limited studies have been conducted to investigate the influence of the speed airflow on the arc effect. The development of the EAA–SMA device by combining the EAAELP and SMAELP devices to extinguish the larger arc is detailed in this study.

2   Movement Model of High Airflow Impact Arc

The arc plasma satisfies the Navier–Stokes and Maxwell equations. To describe the thermal motion of the arc: ① the arc is assumed to be thermal plasma, satisfying the local thermodynamic equilibrium condition; ② the arc fluid is the Newtonian fluid; ③ the arc is fully ionized, and its physical parameters are a single function of the temperature; ④ the energy loss caused by viscous dissipation in the arc process is ignored; and ⑤ airflow velocity satisfies the turbulent flow condition [15, 16].

The mass conservation equation is as follows:

$$\frac{d\rho}{dt} + \rho \, div \vec{V} = 0 \tag{1}$$

In the formula, ρ is the medium density, and $\vec{V}$ is the medium flow velocity.

The momentum conservation equation is as follows:

$$\rho \frac{d\vec{V}}{dt} = \rho g' - grad\,P + \vec{j} \times \vec{B} - \frac{2}{3} grad\left(\mu \, div \vec{V}\right) + 2 div\left(\mu \vec{S}\right) \tag{2}$$

In the formula, $\rho g'$ is the gravity term, P is the gas pressure, $grad\,P$ is the pressure gradient, $\vec{j}$ is the local current density in the arc, $\vec{B}$ is the magnetic induction strength in the arc, $\vec{j} \times \vec{B}$ is the electromagnetic force term, μ is the dynamic viscosity coefficient, $\vec{S}$ is the velocity deformation tensor, and the last two items on the right are the viscous force term.

The energy conservation equation is as follows:

$$\rho \frac{d}{dt}\left(h + \frac{V^2}{2}\right) - \rho \frac{\partial P}{\partial t} = \rho g \cdot \vec{V} + \sigma E^2 - e_{net} + div(\lambda \, gradT) + \varphi_{diss} \tag{3}$$

In the formula, h is the stagnation enthalpy, $\rho g \cdot \vec{V}$ is the work done by gravity, σE^2 is the ohmic heating term formed by the arc current, e_{net} is the arc column radiation balance, $div(\lambda \, gradT)$ is the thermal conductivity, and φ_{diss} is the viscous heat dissipation of the fluid.

Maxwell equations are as follows:

$$rot \vec{H} = \vec{j} \tag{4}$$

$$rot \vec{E} = -\frac{\partial \vec{B}}{\partial t} \tag{5}$$

Equation is the first equation of the constant magnetic field in the differential form, and Eq. (5) represents the differential equation of electric field due to a change in the magnetic field.

In the differential form, Ohm's law is expressed as follows:

$$\vec{j} = \sigma \vec{E} \tag{6}$$

The equation of state without considering the Hall effect is as follows:

$$P = P(\rho, T) \tag{7}$$

When the ambient temperature is high and the gas ionization degree is large, the ordinary rational gas state equation is not applicable. When the ionization is small, the equation of state can be expressed as follows:

$$P = \rho RT \tag{8}$$

where R is the gas constant. Equations (6) and (7) determine the conditions of the arc closure so that the state parameters of the gas and the arc can be accurately located.

3 Simulation of High-Speed Airflow Impact of the EAAELP Device

3.1 Geometrical Model and Parameter Setting

The geometric diagram of the EAAELP device of COMSOL software is presented in Fig. 1. The specific dimensions of the device of the geometric structure are as follows: arc-extinguishing cylinder length, internal diameter, and cylinder wall thickness were 25, 8, and 0.6 cm, respectively. The annular lightning pole was embedded in the arc-extinguishing cylinder, and the annular lightning electrode was 4 cm. Four monitoring points were set to measure the conductivity, temperature, and heat between the high-speed airflow and arc. The locations of each monitoring point are displayed in Fig. 2.

The Navier–Stokes equation was selected as the control equation of fluid heat transfer and the Maxwell electromagnetic field coupling according to the MHD airflow. To ensure the closure, solution, simulation reliability, and convergence of the PDE, establishing the known constants and solved variables is necessary. The parameters of each part of the simulation are set: the arc-extinguishing cylinder is an insulation material, and current circulation, slip, and convection heat dissipation do not occur. The initial conditions were set in this simulation model: the ambient temperature was $T = 293.15$ K. With the standard atmospheric pressure, no airflow, no current, and magnetic field were assumed in the initial stage space. A ring-flash graphite electrode with a density of 2330 kg/m^3, conductivity = 25,000 S/m, isobaric heat capacity cp = 850 J/(kg K), thermal conductivity = 151 W/(m K), and relative permeability and relative permittivity of 1 were assumed. The step length of the simulation iteration was 1×10^{-7} s. The Autodyn software was used to simulate the propagation velocity of the blast airflow [17]. In this study, the initial velocity of the airflow was set at 2000 m/s.
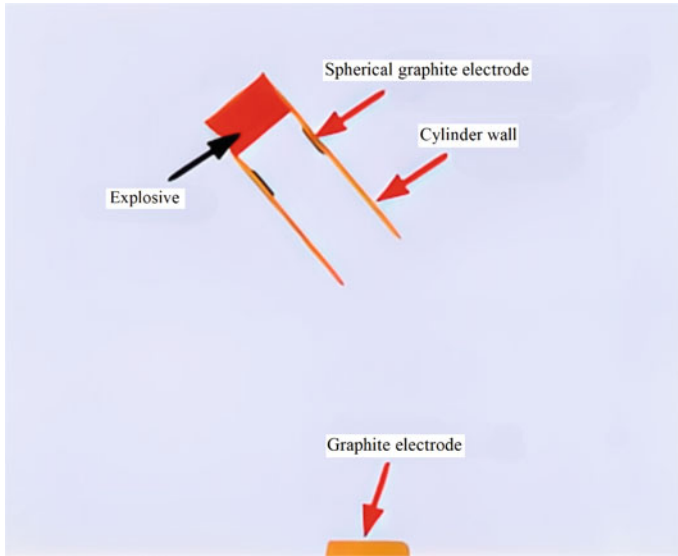
Fig. 1 Geometry of the EAAELP device

Fig. 2 Location of various
monitoring points of the
EAAELP device
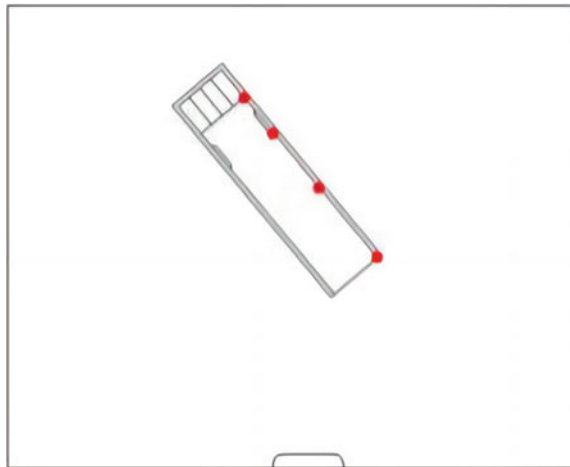
Here, the lightning flow waveform equivalent of 10/350 us with a peak of 20 kA, a power frequency current of 50 Hz, and an amplitude of 20 kA was adopted. The power frequency current is displayed in Fig. 3. The power–frequency current expression is $2 \times 10^4 \sin(100\pi t + \varphi)$ A. The lightning flow waveform expression is $2 \times 10^4 \times ((\exp(-\alpha t) - \exp(-\beta t))/\eta)$ A. The position current of 0.2 ms away from the peak power frequency current was selected as the initial value for calculation, and the lightning current was superimposed when the power frequency current reached the

Fig. 3 Power frequency
current superimposed
lightning current waveform
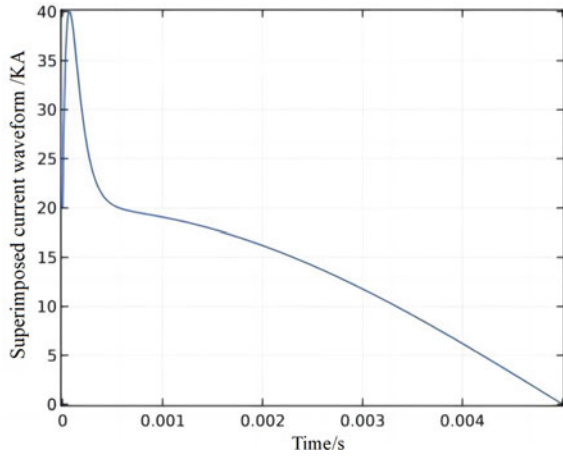
peak. Here, t is the time and φ is the phase. α is 1/10 us, β is 1/350 us, η is exp(−αt0) − exp(−βt0), and t0 is log(α/β)/(β − α).

3.2 Analysis of EAAELP Device Simulation Results

3.2.1 Temperature Change in the Arc-Extinguishing Chamber

Figure 4 displays the temperature cloud diagram for 0.35-ms arc tube process. Figure 5 displays the monitoring temperature curves of the arc tube; the temperature of the ring electrode moment was high as 16,000 K, in t = 0.25 ms arc tube continuous high temperature. The development of the explosion speed with time was monitored, and gradually, explosion and arc coupling occurred. At t = 0.3 ms, the explosion airflow and the arc were highly coupled, the arc temperature decreased rapidly, the arc also gradually moved outside the arc cylinder with the high-speed airflow, the accelerated arc energy dissipated, the arc temperature also decreased, and the arc was broken. Thus, the continuity of the arc was destroyed; at t = 0.35 ms, the arc was completely discharged from the cylinder. The arc temperature was approximately 2000 K, and the highest temperature outside the cylinder was approximately 8000 K. At t = 0.5 ms, the highest temperature outside the arc-extinguishing cylinder was approximately 3500 K. According to the AC arc temperature criterion [18], that is, when the temperature T in the arc is lower than 3000–4000 K, the ambient temperature in the arc-extinguishing cylinder was lower than 3000 K, that is, the arc was completely extinguished.

Fig. 4 Extinguishing process of the 0.35 ms arc
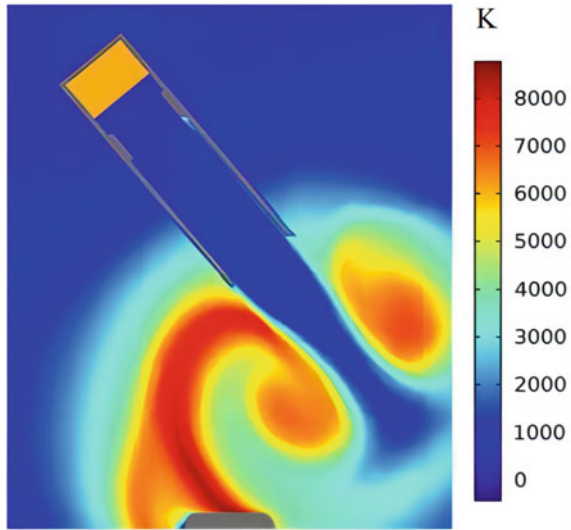
Fig. 5 Temperature change curve of the four monitoring points in the arc-extinguishing cone
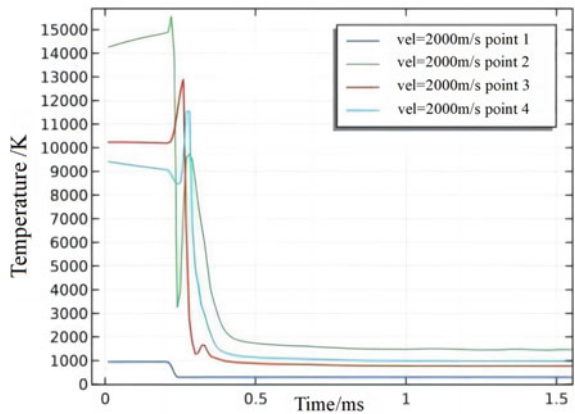
3.2.2 Changes in the Electrical Conductivity in the Arc-Extinguishing Cylinder

Figure 6 displays a cloud diagram of the conductivity change during the high-speed airflow and the arc coupling process in the 0.35-ms arc-extinguishing cylinder. Figure 7 displays the conductivity change curve during the coupling process of the high-velocity airflow and arc in the arc-extinguishing cylinder. Figures 6 and 7 reveal that when the lightning current occurs at the annular electrode, the arc-extinguishing cylinder produces the impact flashover arc. The conductivity rapidly increased from 0 to 10,000 S/m, and the conductivity was mainly distributed at the ring electrode. After t = 0.2 ms, power frequency currents generated power frequency arcs along

the lightning channel, and the ring electrode conductivity reached a maximum of approximately 10,000 S/m. At t = 0.25 ms, high-velocity flow begins coupling with the arc, and the conductivity begins to decline, t = 0.3 ms when the conductivity decreases to half, which reveals that the high-velocity flow coupled with the arc depth and accelerated the arc positive and negative ion composite, diffusion occurred, the concentration of charged ion decreased, the development of the arc was inhibited. At t = 0.4 ms, the conductivity in the arc-extinguishing cylinder was almost zero and returned to the air insulation level.

Fig. 6 Extinguishing process of the 0.35-ms arc
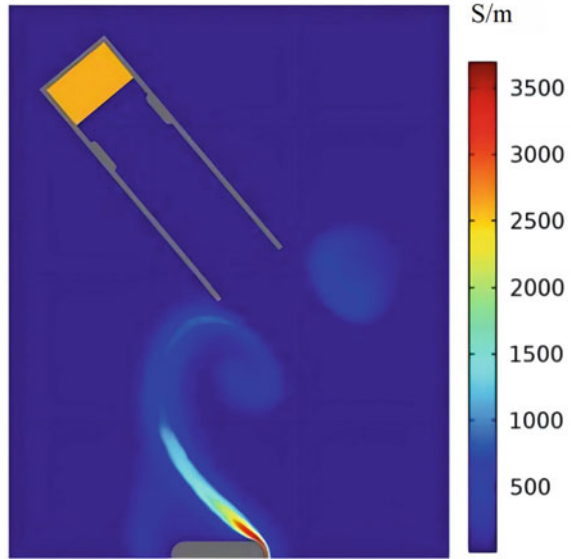
Fig. 7 Change curve of arc conductivity in the arc-extinguishing chamber
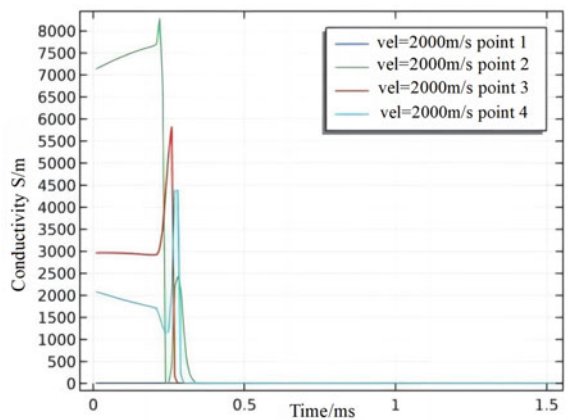
4 Simulation of the SMAELP Device

4.1 SMAELP Device Geometry Modeling and Parameter Setting

The SMAELP device has a spiral structure and a parallel gap to extinguish arcs. The multi-break arc-extinguishing structure can control the arc path. The long arc is divided into multiple small segments, and in each segment, arc flow extinguishing the arc is triggered. The self-compression arc-extinguishing mechanism is used to suppress the arc energy. The SMAELP device was composed of spherical graphite electrodes, T-type compression tubes, and other parts that are high-temperature-resistant insulation accessories. The spherical graphite electrode is located on both sides of the horizontal pipe hole of the T-type compression tube and connects each T-type compression tube, which limits the path of the arc and ensures the arc passes through the T-type compression tube. The geometric model and monitoring point setting of the SMAELP device are displayed in Fig. 8. The overall length of the unit was 150 mm, the horizontal pipe length of the internal T-type ceramic compression pipe was $L = 25$ mm, the vertical pipe length was $D = 10$ mm, and the pipe diameter was $R = 3$ mm. The specific structure is displayed in Fig. 8. The air area was set on the outside of the device to ensure that the air area did not affect the simulation results. The device was powerful to ensure the arc-extinguishing mechanism could be monitored.

In the SMAELP device, an arc building process occurs after lightning current and power frequency current superposition. In the lightning current, the lightning current waveform with the peak current of 20 kA and 10/350 us double index equivalent was
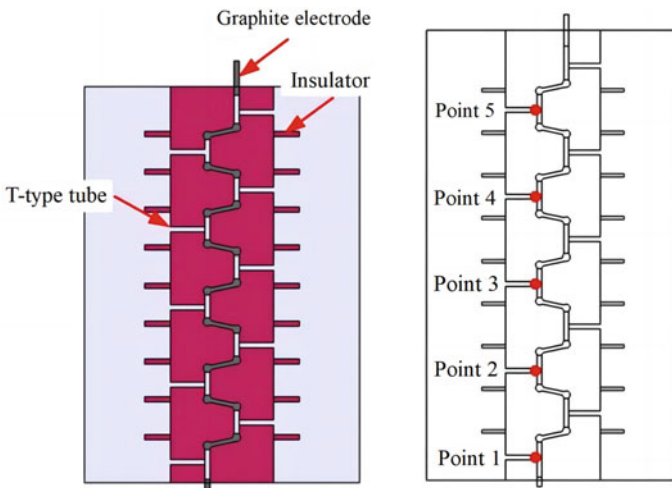
Fig. 8 SMAELP device geometry model

adopted. The power frequency current or the use frequency was 50 Hz, and the amplitude was 10 kA. The main body of SMAELP device was the insulating high-temperature-resistant material. The main body did not exhibit conduction, current flow, position sliding, and convection heat dissipation. The initial conditions in this simulation model were set as follows: ambient temperature T = 293.15 K, erical flash graphite electrode ρ = 1950 kg/m³, electrical conductivity σ = 3 × 103 S/m, heat capacity at constant pressure cp = 710 J/(kg K), and thermal conductivity λ = 150 W/(m K). With the standard atmospheric pressure, no airflow, current, and magnetic field were observed in the initial stage space. The relative permeability and the relative dielectric constant were set to 1. The iterative output time step was set as 1 us, the calculation time was 3 ms, and the time step was calculated using the backward difference formula, which was solved using the PARDISO solver.

4.2 Analysis of the Simulation Results of the SMAELP Device

4.2.1 Temperature Change of the Device

Figure 9 displays the arc-extinguishing process and temperature change cloud of the device at t = 0.2 ms, and Fig. 10 displays the device arc-extinguishing process temperature change curve. The lightning current just along the T pipe breakdown between the graphite electrodes affects flash discharge. With the stability of the subsequent arc, the temperature began to increase. At t = 0.1 ms, the arc-extinguishing indoor temperature reached 12,000 K. Because of the rising temperature of the arc chamber, the indoor air heat pressure increased, the speed of the jet increased, the arc through the compression tube was excluded, and the arc heat loss increased considerably, which reduced the temperature. With the high-speed jet flow, the arc chamber temperature decreased rapidly. At approximately t = 0.2 ms, the arc temperature decreased to approximately 7000 K. After 0.05 ms, at a monitoring point, the arc temperature decreased to approximately 3000 K. Because the arc chamber accumulation of air was limited, and the burst flow originated from air, as the arc temperature change rate decreased, the speed of airflow decreased, and arc temperature recovered. At approximately $t = 0.3$ ms, the temperature was up to 4500 K, the jet flow commenced again, competing with the arc, and finally, at approximately $t = 0.5$ ms, arc indoor temperature reached approximately 3000 K, but the heating phenomenon was not observed. The energy supply channel of the arc was disconnected, and the arc could retain energy to maintain its own form. Because after the airflow was heated by the arc waste heat, it still produced low-speed airflow, which inhibited the arc reignition.

Fig. 9 Temperature change of the arc quenching process at 0.2 ms
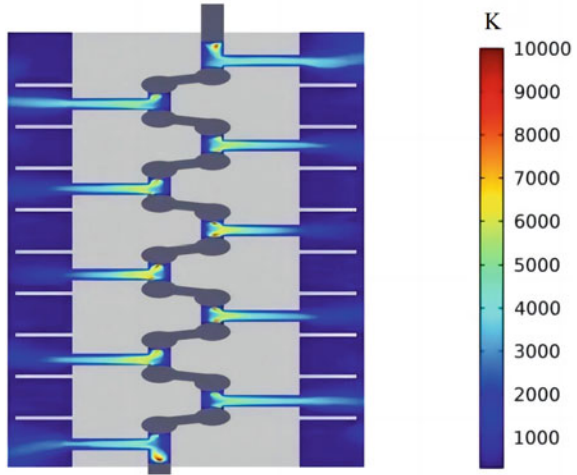
Fig. 10 Temperature change of SMAELP device
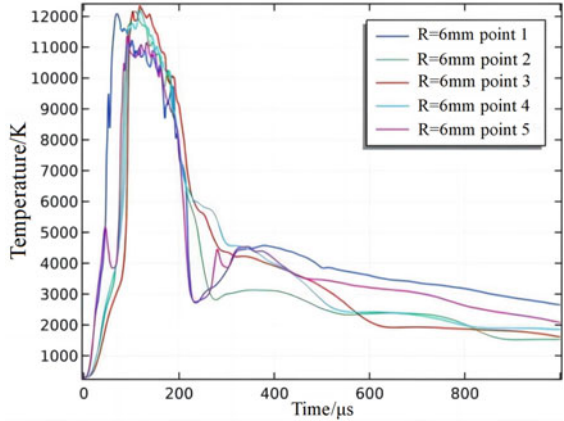
4.2.2 Airflow Change During the Arc-Extinguishing Process of the Device

When the airflow of the T-type compression pipe is constantly heated by the arc temperature, the temperature and pressure of the gas increase rapidly. Because of the wall constraint of the T-type compression pipe, the high-speed airflow changes from radial to axial development, forming the outward injection airflow velocity. Figure 11 displays the cloud map of the jet airflow speed change of the 0.2-ms device and the jet airflow velocity change curve of Fig. 12. Because the arc root temperature was the highest, the two monitoring points 1 and 5 close to the high-voltage and low-voltage electrodes first reached the highest speed. At 0.05 ms, an arc occurred between the two electrodes, and the air in the T-type compression pipe was

Fig. 11 Cloud diagram of 0.2 ms
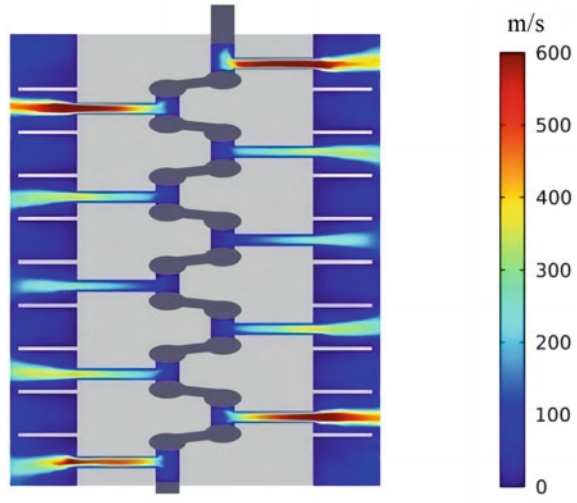
compressed and began to generate airflow. The airflow velocity rapidly increased to approximately 400 m/s. At approximately 0.2 ms, the maximum speed of the pipeline draft airflow was approximately 850 m/s after being heated by the arc. Under the continuous action of the high-speed airflow, the jet high-speed airflow elongates, cuts off, and discharges the arc between the two electrodes, which accelerates the convection and diffusion of the arc heat. The arc gap resistance of the arc increases. Thus, providing the power frequency energy to the arc becomes difficult, which accelerates arc extinguishing. Speed can be observed from the monitoring curve. The speed of the jet airflow primarily depends on the temperature change. High-speed airflow will arc discharges from the T compression pipe, the pipeline arc temperature decreases rapidly, and the airflow velocity is also low. However, the arc under the action of high-speed airflow is discharged outside the compression pipe and forms an obvious fracture, with the arc resistance continuing to increase. Because continuing the power frequency energy becomes difficult, maintaining the arc combustion becomes difficult. At approximately 0.5 ms, the arc collapsed because the airflow by the arc residual heats. However, low-speed airflow was produced, which inhibited arc rekindling.

4.2.3 Change in Conductivity of the Device

Electrical conductivity changes can be easily determined by monitoring whether the arc is extinguished. Figure 13 displays conductivity changes. Figure 14 displays the conductivity change curve of the arc quenching process. The two figures reveal that at $t = 0.05$ ms, conductivity exists in the T-type compression tube, which forms an arc. The conductivity distribution was the same as the temperature field distribution, with the highest conductivity at the high-voltage and low-voltage electrodes,

Fig. 12 Device jet flow
velocity change curve
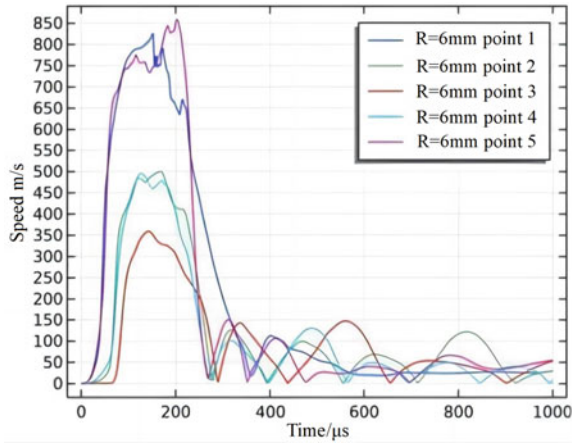
approximately 3000 S/m. With the gradual increase in the power frequency current, the electrical conductivity at the monitoring point reached a maximum value of nearly 5000 S/m at $t = 0.1$ ms. Because of the rapid development of the arc and the increase in the temperature, the flow of the air in the T-type compression pipe began to affect the arc at high speed, which gradually elongated the arc and excluded the compression pipe, forming an obvious break. At approximately $t = 0.3$ ms, the conductivity reduced to 0 S/m, which indicates that the arc was extinguished.

Fig. 13 Cloud diagram of
electrical conductivity
change of device arc
quenching process at 0.2 ms
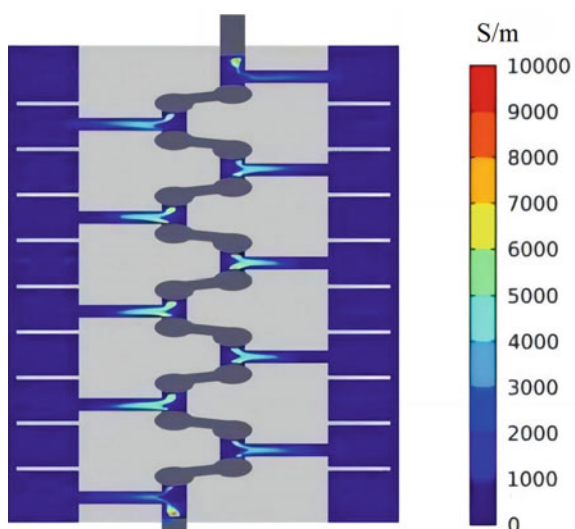
Fig. 14 Change curve of the arc quenching process
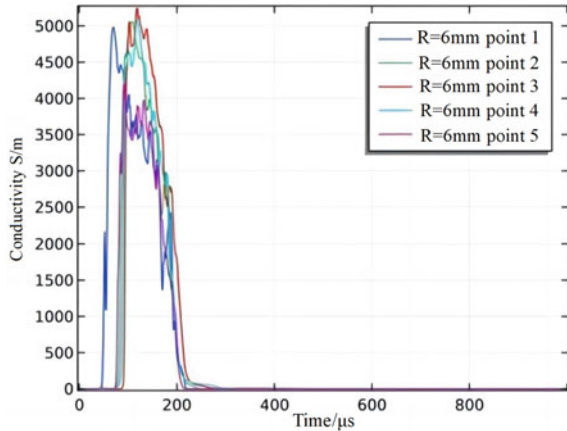
5   Simulation of Arc-Off Process of the EAA–SMA Device

5.1   EAA–SMA Device Geometry

There were a number of parameters for the EAAELP device and SMAELP device. Therefore, the interval between the two devices was 1 m. The lightning current waveform of 10/350 us exhibited a peak of 20 kA, and the power frequency current was set at 40 kA. The geometric figures and grid division graphics of the simulation of the combined device are displayed in Figs. 15 and 16. The triangle grid section method was adopted to discretize the whole calculation area. The boundary layer was added at the boundary wall of fluid and solid to ensure an accurate solution. The number of grids was 62,000, and the minimum cell grid. The mass was 0.62, and the average grid cell mass was 0.93. The iterative output time step was set to be 1 us, the calculation time was 3 ms, and the time step was calculated using the backward difference formula and solved using the PARDISO solver.

5.2   Analysis of the Simulation Results

5.2.1   Temperature Change Situation

The combined device was simulated. The arc-extinguishing process is displayed from the cloud diagram of the arc temperature change process displayed in Fig. 17. When the flash arc was formed, the combined EAA–SMA device began to produce high-speed airflow on the arc. At 0.3 ms, the arc was discharged, the temperature in the arc-extinguishing cylinder was 10,000 to approximately 5000 K, and the highest temperature at the top of the SMAELP device was only approximately 8000 K.

Fig. 15 Geometric model for the combined device simulation
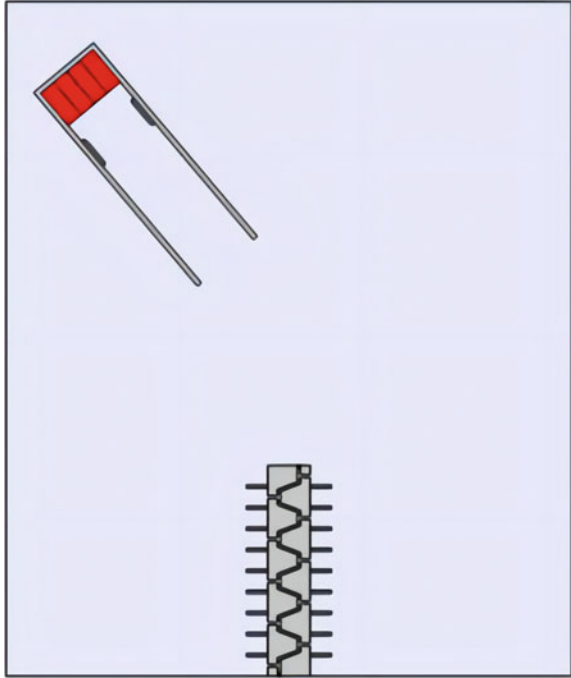
Fig. 16 Mesh division drawing of the combined device

(a) 0.1 ms   (b) 0.3 ms

(c) 0.6 ms   (d) 0.8 ms
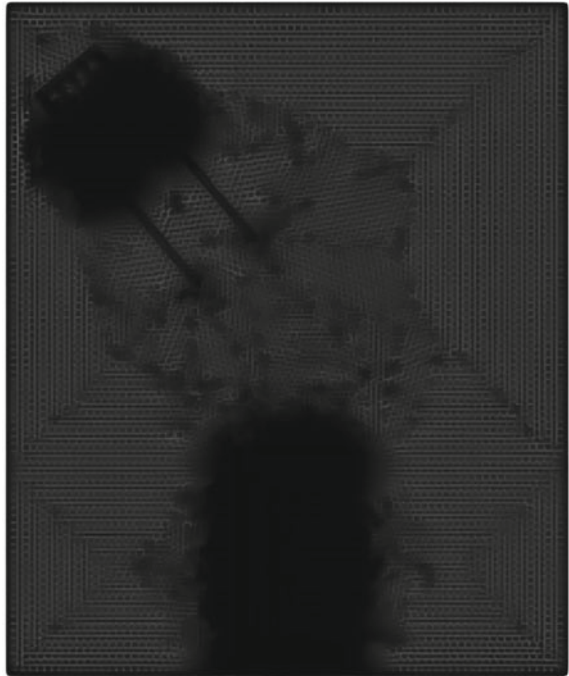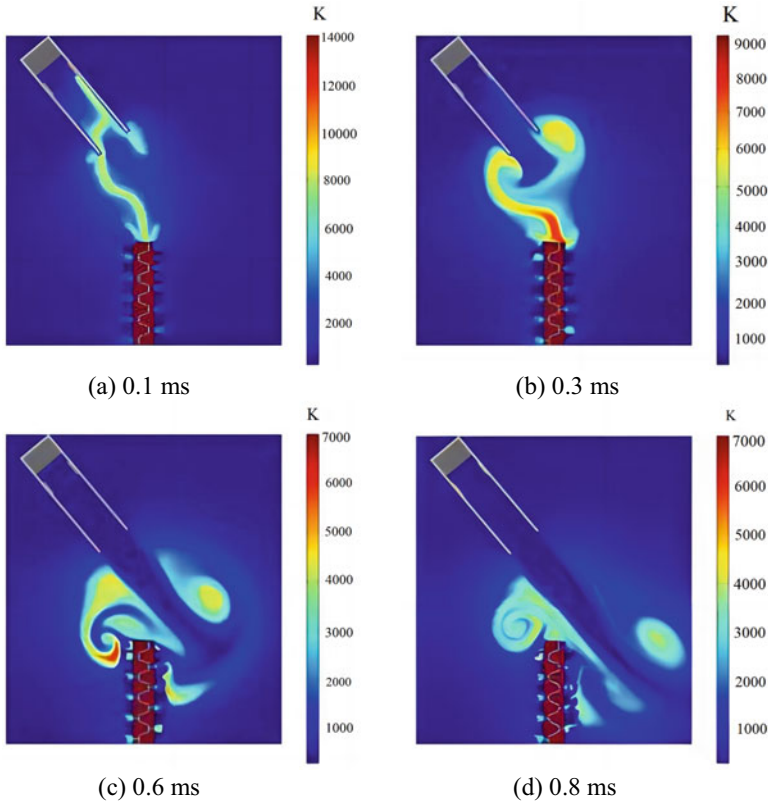
Fig. 17 Cloud diagram of the arc temperature change process

When the high-speed airflow of the two devices continued to act, the arc temperature constantly decreased. At approximately 0.8 ms, the temperature in the arc-extinguishing cylinder decreased to approximately 1000 K. The arc temperature of the whole area between the devices also decreased to approximately 3000 K. The arc was completely extinguished by the high-speed airflow of the two devices.

5.2.2 Changes in Electrical Conductivity

After the coupling of the high-velocity airflow and the arc, when the high-velocity airflow acted on the arc, the arc energy loss accelerated, the cooling accelerated, and the temperature acceleration conductivity began to change and decrease rapidly. Figure 18 displays conductivity change after high-velocity airflow and arc coupling. At 0.3 ms, with the increase in the strength of the airflow, the arc conductivity decreased from the maximum value of 6000 to 3500 S/m, and at 0.6 ms, the conductivity within both devices decreased to the range of 20–40 S/m. The conductivity

decreased to zero at 0.8 ms. The process of arc quenching becomes apparent by observing the change in conductivity. After the arc energy supply channel was removed by the rapid airflow, the arc cannot be maintained because of the lack of energy, and the air gap between the devices was fully restored to the insulation strength, which inhibited arc reignition.

The EAA–SMA device exhibits numerous advantages. First, when lightning strikes the flash network, the SMAELP device prevents arc formation. When SMAELP cannot completely destroy the arc channel and energy, the EAAELP collects the lightning flash signal and timely sprays high-speed blast impact airflow to inhibit arc development. Thus, arc rekindling is effectively prevented.
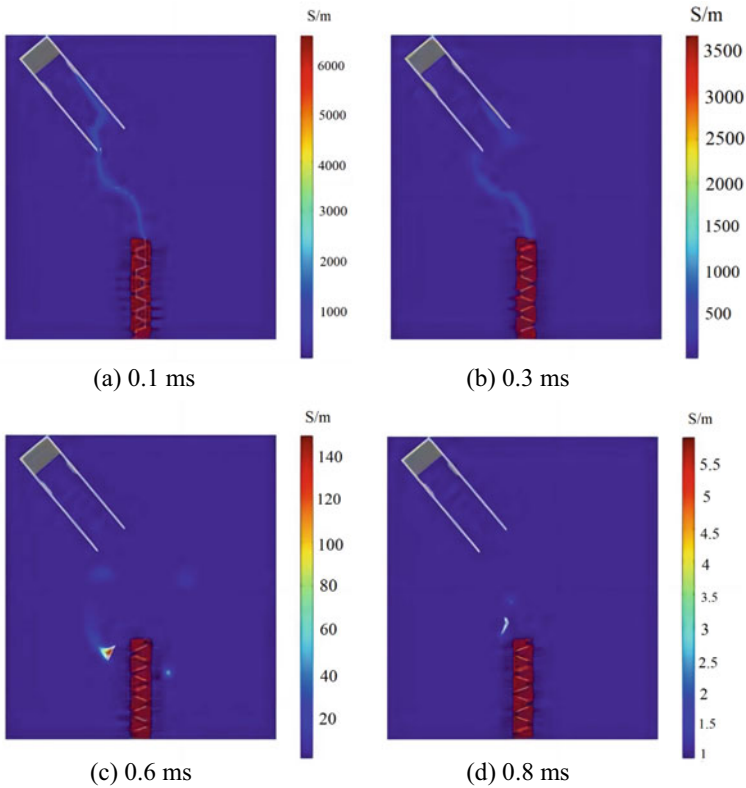
Fig. 18 Cloud diagram of conductivity change after high-velocity airflow and arc coupling

6 Conclusions

(1) High-speed airflow and arc coupling process occurred in the EAAELP device. The temperature and conductivity changed in the arc cylinder, lightning flashover. In the EAAELP device, high-speed airflow quickly affected the flashover arc, cut off the lightning channel, and prevented the power frequency current energy supply, which resulted in the arc not being able to maintain its own form and subsequently extinguishing.

(2) The coupling process of high-speed airflow and electric arc of SMAELP device is triggered when lightning strikes the flash line. The air in the compression pipe is heated to generate high-speed airflow and wash away the energy supply channel of the power frequency arc. Thus, the formation of the power frequency arc is inhibited considerably.

(3) High-speed airflow impact can extinguish the arc within 0.5 ms, without waiting until the current reaches zero. Thus, the time to extinguish the arc is shortened considerably.

References

1. Chen J, Zhao C, Gu S et al (2016) Present status and development trend of lightning detection and protection technology of power grid in China. High Voltage Eng 42(11):3361–3375
2. Shui-ming C, Jin-liang HE, Rong Z (2009) Lightning protection study of transmission line, part I: lightning parameters. High Voltage Eng 35(12):2903–2909
3. Zeng R, Zhou X, Wang Z et al (2015) State key laboratory of control and simulation of power system and generation equipments. High Voltage Eng 41(01):1–13
4. Lu G, Luo J, Liu H et al (2018) Statistics and simulation of lightning trip out of transmission lines in Guangzhou area. High Voltage Eng 44(05):1542–1548
5. Chino T, Iwata M, Imoto S et al (2005) Development of arcing horn device for interrupting ground-fault current of 77 kV overhead lines. IEEE Trans Power Deliv 20(4):2570–2575
6. Podporkin GV, Pilshikov VE, Kalakutsky ES et al (2014) Overhead lines lightning protection by multichamber arresters and insulator-arresters. In: 32th international conference on lightning prfltection (ICLP 2014), pp 1243–1249
7. Guile AE, Adams VW, Lord WT et al (1969) High-current arc in trans-verse magnetic field in atmospheric pressure. Proc IEEE 116(4):645–652
8. Yan R, Wang J, Nie Y, Li Z (2020) Suppressing arc development by arc-extinguishing and lightning-protection device. IEEJ Trans 15(1):70–77
9. Wang J, Bi J (2020) Protective effect study of solid-phase arc-quenching device on superimposed lightning strike. Electr Power Syst Res 182:106195
10. Wang J, Liu J, Wu G et al (2015) Research and application of jet stream arc-quenching lightning protection gap (JSALPG) for transmission lines. IEEE Trans Dielectr Electr Insul 22(2):782–788
11. Jufeng W, Shimin LI, Renbao Y et al (2014) Arc quenching lightning protection gap for fast extinction of power frequency arcs. High Voltage Eng 40(01):40–45
12. Huayi Z, Jufeng W, Xin Z (2019) Research and application of multi pipeline copressed gas on arc-extinguishing and lightning protection. Insul Surge Arresters 03:27–31

13. Dai Q, Wang J, Zheng C et al (2017) Research on characteristic of free arc segmented by compression effects of distribution network lightning protection. Power Syst Technol 41(07):2401–2406
14. Wang J, Li S, Guo K et al (2018) Are-extinguishing mechanism on multilateral self-expanding stream of are-extinguishing lightning protection gap. High Voltage Eng 44(12):3896–3902
15. Ghorui S, Heberlein JVR, Pfender E (2008) Thermodynamic and transport properties of two-temperature nitrogen-oxygen plasma. Plasma Chem Plasma Process 28(4):553–582
16. Boulos MI, Fauchais P, Wender E (1994) Thermal plasmas: fundamentals and applications, vol 1. Plenum Press, New York
17. YAN Renbao (2014) Research on characteristics and application of explosion shock waves with mutual coupling arc in semi-closed space. Guangxi University
18. Zengyuan G, Wenhua Z (1986) Arc and thermal plasma. Science Press, Beijing, China

Characteristics of PD Decomposition of SF_6/N_2 Gas Mixture Under Metal Protrusion Defects

Chuansheng Luo, Dibo Wang, Yan Luo, Jian Qin, Weihong Yang, Chuang Zhou, and Mingli Fu

Abstract SF_6 gas has many disadvantages such as extremely high greenhouse effect and easy to liquefy in low temperature environment. Using SF_6/N_2 gas mixture to replace pure SF_6 gas can improve the liquefaction temperature and environmental characteristics of pure SF_6 gas. In this paper, the needle-plate electrode is used to simulate the metal protrusion defects and carry out the 96 h partial discharge (PD) decomposition experiment of 50% SF_6/50% N_2 gas mixture. The results show that the content of five characteristic components, SO_2F_2, SOF_2, SO_2, NO_2 and NF_3, all increase with the increase of discharge time and external applied voltage, and the content of SOF_2 is always higher than SO_2F_2 at the same external applied voltage, and the effective gas production rate of SO_2F_2 and SOF_2 basically shows a linear growth trend with the increase of magnitude of PD, SO_2F_2 and SOF_2 can be used as the characteristic products to characterize the severity of defective metal protrusions in SF_6/N_2 gas mixture insulated equipment.

D. Wang · Y. Luo · W. Yang · M. Fu
CSG Electric Power Research Institute Co., Ltd., Guangxi, China

United Laboratory of Advanced Electrical Materials and Equipment Support Technology, CSG, Guangdong, China

D. Wang
e-mail: wangdb@csg.cn

Y. Luo
e-mail: luoyan1@csg.cn

W. Yang
e-mail: yangwh@csg.cn

M. Fu
e-mail: fuml@csg.cn

C. Luo (✉) · J. Qin · C. Zhou
Nanning Power Supply Bureau, Guangxi Power Grid Co., Ltd., Guangxi, China
e-mail: qq1920670878@163.com

J. Qin
e-mail: qin_jian@gx.csg.cn

1 Introduction

SF_6 gas is widely used as insulating gas in gas insulated equipment because of its good insulation performance and high chemical stability. However, SF_6 gas has many disadvantages such as high price, high greenhouse effect and easy to liquefy in low temperature environment, etc. SF_6/N_2 gas mixture can replace pure SF_6 gas to improve its liquefaction temperature and environmental characteristics. Therefore, SF_6/N_2 gas mixtures are widely used in gas-insulated combined appliances [1–3].

Studies related to the decomposition characteristics of SF_6 gas under different fault conditions and influencing factors and its equipment fault diagnosis and condition assessment have been relatively comprehensive [4–6]. However, there are fewer studies on the decomposition characteristics of SF_6/N_2 gas mixtures. Pang et al. simulated the partial discharge process of SF_6 gas in an extremely inhomogeneous electric field and concluded that there is a positive correlation between the gas pressure and the starting discharge voltage, while there is a negative correlation between the electric field inhomogeneity coefficient and the starting discharge voltage [7]. Hou et al. carried out physical experiments on the partial discharge of SF_6/N_2 gas mixture along the surface under DC voltage, and found that the partial discharge onset voltage increased with the increase of SF_6 gas content through comparative analysis of the experimental results. Vial et al. carried out a study on the decomposition product components and influencing factors of SF_6/N_2 (10:90) gas mixture during spark discharge [8–10].

At present, the related research on SF_6/N_2 gas mixture mainly focuses on insulation and breakdown decomposition characteristics, while less research is conducted on the variation law of partial discharge decomposition characteristic products with discharge volume and discharge time. In this paper, we adopt the needle-plate electrode to simulate the metal protrusion defects and carry out the 96 h partial discharge decomposition experiment of $50\%SF_6/50\%N_2$ gas mixture to analyze the change law of characteristic decomposition components with the discharge time and discharge volume.

2 Experimental Setup

The gas discharge experimental platform is shown in Fig. 1. We use the step-by-step pressurization method to measure the breakdown voltage of SF_6/N_2 gas mixture under metal protrusion defects. Since there is a certain uncertainty in the breakdown voltage measurement, for this problem, we measure the breakdown voltage five times and then take the average value to ensure the reliability of the data.
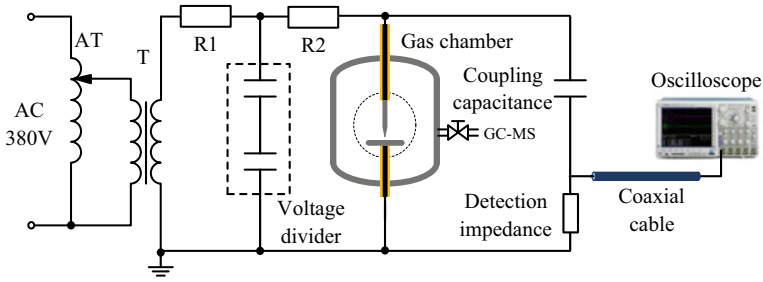
Fig. 1 Schematic diagram of gas discharge test platform

Five applied voltage levels were taken at equal differences between the starting voltage and breakdown voltage, and 96 h partial discharge experiments were performed at the above five voltage levels. The amount of discharge at different voltage levels was measured by oscilloscope. At the same time, some gases were taken out every 12 h, and the decomposition components were detected qualitatively and quantitatively based on GC-MS, and the influence of different discharge times and discharge volumes on the generation of each characteristic decomposition product was analyzed together with the variation curves of generation volume with discharge time and discharge volume, and the characteristic products suitable for characterizing the degree of fault inside the equipment were selected from them. The starting voltage of PD under metal protrusion defect is 42 kV and the breakdown voltage is 84 kV. Therefore, five applied voltages of 44 kV, 53 kV, 62 kV, 71 kV and 80 kV were selected for the experiments, and the PD parameters at different voltages are shown in Table 1.

Table 1 PD parameters of different applied voltages

U (kV)	44	53	62	71	80
Q_{MAX} (pC)	31	59	148	961	1265
Q_{AVG} (pC)	18	35	73	181	204
N_{AVG}	57	119	272	413	517
Q_{SEC} (pC)	1026	4165	19,856	74,753	105,468

3 Result

3.1 Variation of Characteristic Component Content with Time and PD Intensity

Variation of SO_2F_2 content. With the increase of time, the content of SO_2F_2 at different applied voltages increased significantly (Fig. 2a). However, the slopes of the curves of SO_2F_2 content with time were relatively similar when the applied voltage was low, and when the applied voltage was raised above 71 kV, the PD intensity was enhanced and the generation rate and content of SO_2F_2 were significantly increased, which shows that the generation process of SO_2F_2 is closely related to the PD intensity. SO_2F_2 is one of the main sulfur-containing products of SF6 under the action of PD, because the chemical nature of the low-fluorinated sulfur molecular group generated after SF_6 loses F atoms under the action of discharge is very active and strong in reduction, so it is very easy to react with O atoms, OH atoms and other products with strong oxidation inside the closed discharge chamber to generate SO_2F_2 and so on. When the discharge intensity is relatively low, the decomposition of generated low sulfur fluoride is relatively small, so the content and growth rate of SO_2F_2 are relatively small; while when the PD intensity increases, more electrons are generated by excitation, which promotes the generation of a large amount of low sulfur fluoride, thus making the content and growth rate of SO_2F_2 larger, and there is no obvious saturation trend in the experimental time.

Variation of SOF_2 content. SOF_2, like SO_2F_2, is also one of the main sulfur-containing decomposition products of SF_6 decomposition under PD. The change curve of SOF_2 content with time is relatively similar to that of SO_2F_2, with the growth of discharge time, the content of SOF_2 has increased significantly (Fig. 2b). When the applied voltage is low, the PD intensity is weak, the SOF_2 content is relatively small and the growth rate is relatively flat, while when the applied voltage is increased to 80 kV, the SOF_2 content grows more obviously and the slope of the curve has a relatively large change.

Variation of SO_2 content. When the applied voltage was relatively low, the three curves of SO_2 content with time were relatively close and the yield was relatively small. As the applied voltage increased, the SO_2 content increased significantly (Fig. 2c). SO_2 is mainly generated by the hydrolysis of SOF_2, so the SO_2 production content depends on the SOF_2 and H_2O fractional content. When the externally applied voltage is relatively low, the H_2O in the gas chamber is relatively sufficient, but the content of SOF_2 is not high, so the content of SO_2 is relatively small, and the increase rate is very slow with the growth of the discharge time. When the applied external applied voltage was increased, the content of SOF_2 grew relatively fast, and the content of SOF_2 in the confined gas chamber was relatively abundant, and the content of SO_2 was not high, and the H_2O consumed to generate SO_2 was relatively small, so there was a significant increase in the content of SO_2.
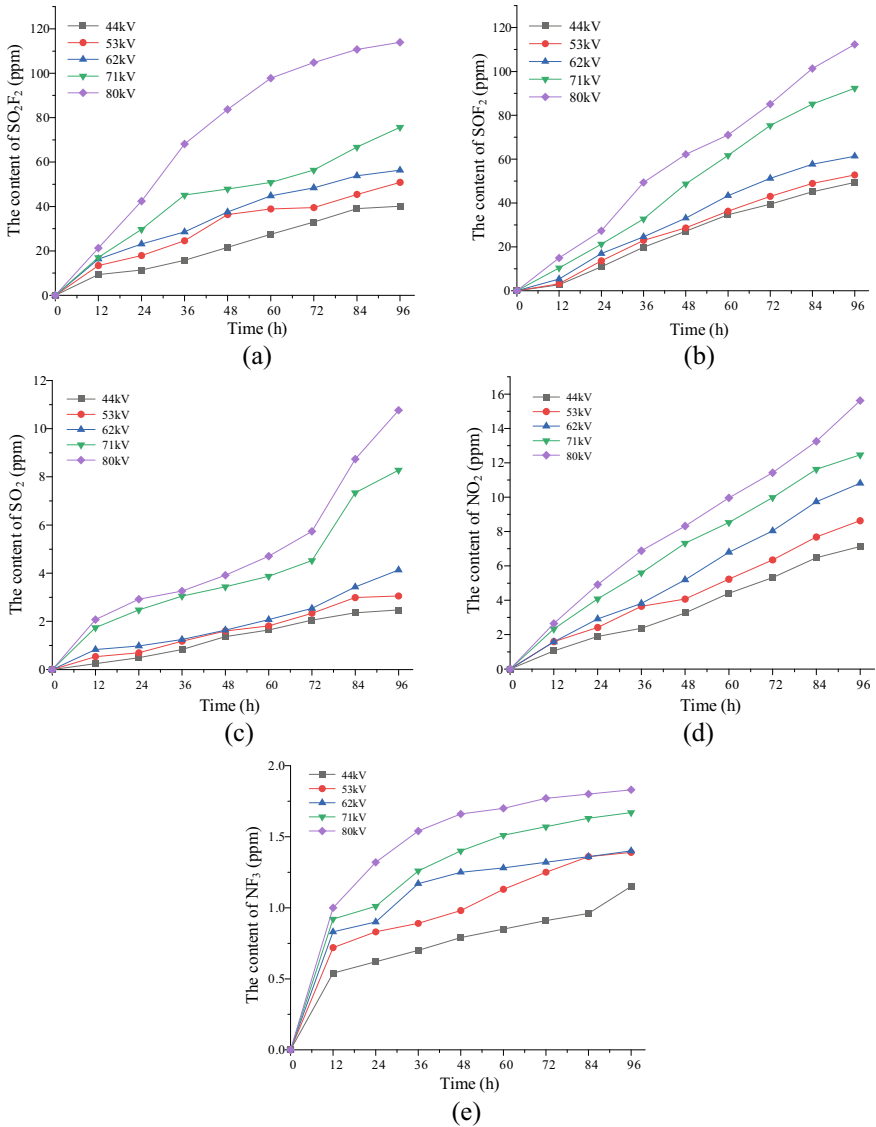
Fig. 2 Variation of each component contents

Variation of NO_2 content. NO_2 is generated by the decomposition of N_2 into N atoms after combining with O atoms under the action of PD, and the variation curve of its content with time is shown in Fig. 2d. It can be seen from the figure that the content of NO_2 has a steady increase with the growth of the discharge time, and there is no obvious saturation trend in the experimental time. This is because the O_2 in the discharge chamber was more sufficient in the pre-discharge period, so the

content of NO_2 could increase steadily, but the overall content of NO_2 was not high, so the consumption of O atoms required to generate NO_2 was not much. When the applied voltage is gradually increased, the NO_2 content also increased, but the rate of increase does not change much, and the slopes of the NO_2 content change curves under different experimental applied voltages are relatively similar. This is probably because N_2 is more stable, and the N atoms generated in the discharge chamber when the applied voltage is increased are also very small, so the overall NO_2 generation is relatively low.

Variation of NF_3 content. NF_3 is also one of the products of SF_6/N_2 gas mixture under PD, and the variation curve of its content with time is shown in Fig. 2e. It can be seen that the increase of NF_3 content with the increase of discharge time is not very large. This may be because there are fewer N atoms in the discharge gas chamber, and part of the N atoms combine with O atoms to form NO_2 and NO, so the NF_3 content does not increase much with the increase of the discharge time.

3.2 The Effective Formation Rate of Characteristic Component

Variation of SO_2F_2 effective formation rate. With the increase of Q_{SEC}, the mean square rate of gas production of SO_2F_2 increases linearly, which indicates that the mean square gas production rate R_{RMS} of SO_2F_2 has a good correlation with the average discharge per second and can reflect the size of the discharge to a certain extent. When the average discharge per second exceeds 10,000 pC, the increase of R_{RMS} of SO_2F_2 is slowed down. The average discharge per second is the apparent discharge, which corresponds to the number of active electrons transferred in the PD, and the collision of active electrons directly causes the decomposition of various ions and the formation of various products. An increase in Q_{SEC} indicates an increase in the number of active electrons, which leads to the formation of SO_2F_2 (Fig. 3).

Variation of SOF_2 effective formation rate. The gas production mean square rate of SOF_2 is similar to that of SO_2F_2, which increases basically linearly with the increase of the average discharge per second, and there is no obvious trend of slowing down, so the gas production mean square rate of SOF_2 can reflect the size of the discharge volume well. This is because the content of low-fluorinated sulfur SF_5, SF_4, SF_2, O and OH atoms groups all increase continuously with the increase of discharge time. SF_5 can react with O and OH to form SOF_2, SF_4 can react with H_2O to form SOF_2, and SF_2 can react with O to form SOF_2. Meanwhile, compared with SO_2F_2, SOF_2 requires relatively less O atoms, although the longer discharge time tends to result in lower O_2 and H_2O content, but its effect on SO_2F_2 is relatively larger. Therefore, the mean square rate of gas production of SOF_2 increases essentially linearly with the increase of the average discharge volume per second.

Fig. 3 Curve of effective formation rate with discharge
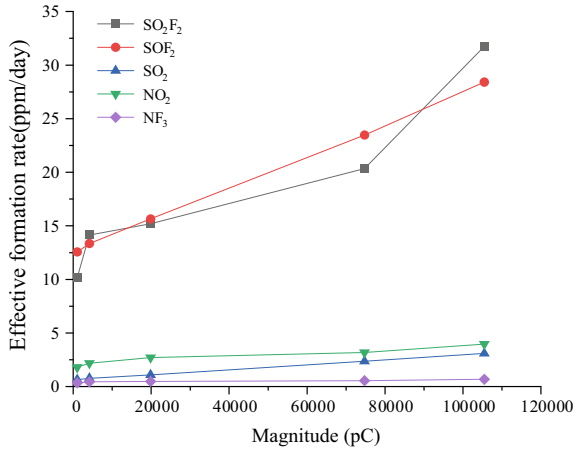
Variation of SO_2 effective formation rate. When the average discharge per second is small, the mean square rate of SO_2 production increases significantly with the increase of the average discharge per second. When the average discharge volume per second is greater than 10,000 pC, the growth rate of gas production mean square rate of SO_2 slows down. This is because SO_2 is mainly produced by the hydrolysis reaction between SOF_2 and H_2O. With the increase of discharge volume, the content of SOF_2 gradually increases, and the H_2O in the closed discharge chamber is more sufficient in the early stage of discharge, so the content of SO_2 increases faster; in the late stage of discharge, the H_2O in the chamber is gradually consumed, and the hydrolysis of SOF_2 to SO_2 slows down, so the growth trend of the mean square rate of SO_2 production slows down.

Variation of NO_2 effective formation rate. When the average discharge per second is small, the mean square rate of NO_2 production increases linearly with the increase of the average discharge per second. When the average discharge volume per second is greater than 10,000 pC, the growth rate of the gas production rms rate of NO_2 slows down. This is probably because N_2 is more stable and very few N atoms are produced in the discharge chamber when the average discharge volume per second increases, so the amount of NO_2 production is also small.

Variation of NF_3 effective formation rate. The gas production mean square rate of NF3 also increases with the increase of the average discharge volume per second, but the increase is very small. Because there are fewer N atoms in the discharge chamber, and some of the N atoms combine with O atoms to produce NO_2 and NO, the N atoms available for NF_3 production decrease as the NO_2 and NO content increases, so the gas production rms rate of NF_3 has been small overall.

4   Conclusion

1. The characteristic products of PD decomposition of SF_6/N_2 gas mixture under metal protrusion defects for 96 h are SO_2F_2, SOF_2, SO_2, NO_2 and NF_3, and the amount of these characteristic products increases with the increase of discharge time and applied voltage.
2. The amount of SOF_2 was always higher than that of SO_2F_2 at the same applied voltage, and the amount of SOF_2 increased more rapidly when the applied voltage was increased.
3. The effective gas production rates of NF_3 and NO_2 increased with the increase of the average discharge per second, but the increase was very small.

References

1. Zhou A, Gao L, Ji X et al (2018) Research and application of SF_6/N_2 mixed gas used in GIS bus. Power Syst Technol 42(10):3429–3435 (in Chinese)
2. Qiu Y, Kufffel E (1999) Comparison of SF_6/N_2 and SF_6/CO_2 gas mixtures as alternative to SF6 gas. IEEE Trans Dielectr Electr Insul 6(6):892–895
3. Zhao Y, Su Z, Qi J et al (2016) Research of the recovery key technologies for the insulating SF_6-N_2 gas in the electrical equipment. High Voltage Apparatus 52(12):151–155 (in Chinese)
4. Zeng F, Tang J, Fan Q et al (2014) Decomposition characteristics of SF_6 under thermal fault for temperature below 400 °C. IEEE Trans Dielectr Electr Insul 21(3):995–1004
5. Zeng F, Tang J, Zhang X et al (2015) Study on the influence mechanism of trace H_2O on SF_6 thermal decomposition characteristic components. IEEE Trans Dielectr Electr Insul 22(2):766–774
6. Li Z, Chen S, Gong S et al (2016) Theoretical study on gas decomposition mechanism of SF_6 by quantum chemical calculation. Comput Theor Chem 1088:24–31
7. Pang P, Sun Z, Zhang Q et al (2019) Study on partial discharge characteristics of severe non-uniform electric field in SF_6 under negative DC voltage. High Voltage Eng 45(4):1093–1100 (in Chinese)
8. Coll I, Casanovas AM, Vial L et al (2000) Sparking-induced decomposition of 10% SF_6-90%N_2 mixtures: effect of a solid organic insulator, oxygen and water. J Phys D Appl Phys 33(11):1348
9. Vial L, Casanovas AM, Coll I et al (1999) Decomposition products from negative and 50 Hz AC corona discharges in compressed SF_6 and SF_6/N_2 (10:90) mixtures. Effect of water vapour added to the gas. J Phys D Appl Phys 32(14):1681
10. Vial L, Casanovas AM, Diaz J et al (2001) Decomposition of high-pressure (400 kPa) SF_6 and SF_6/N_2(10:90) mixtures submitted to negative or 50 Hz AC corona discharges in the presence of water vapour and/or oxygen. J Phys D Appl Phys 34(13):2037

Research on Insulator Defect Detection in Power Inspection Images Based on PaddleDetection

Kai Nie, Chengzhen Li, Yongpeng Liu, Wenhao Gao, Ze Li, Xuliang Wang, and Qingquan Li

Abstract Insulators primarily support transmission lines as a shielding control in the electric power system, which exposes them to the elements over an extended period of time and forces them to contend with their severe effects, making them prone to failure. When the insulator fails, it will significantly increase regular energy use and result in significant losses in output and life. In order to safeguard the regular and steady functioning of transmission lines, insulator defect issues must be identified early on during the power inspection process. This study uses insulator images captured during the inspection process and the PP-YOLOv2 deep learning algorithm to explore insulator defect detection in the context of UAV power inspection. The PP-YOLO algorithm is found to be more accurate than the YOLOv3 algorithm while guaranteeing real-time detection and can better extract the data features of insulators in the inspection images, which has better practicability, according to simulation tests on the data set.

Keywords Deep learning · Insulators · Defect detection · YOLOv3 · PP-YOLOv2

1 Introduction

The number of power grid components constructed in complex environments has been steadily growing in recent years due to the power industry's ongoing development, which has raised the standards for the equipment's safety maintenance [1]. In order to ensure the normal operation of transmission lines, insulators must withstand a variety of harsh environmental conditions over a long period of time. These conditions include wind erosion, ice cover, and high temperatures, which can cause insulators to fail in varying degrees [2]. The normal operation of the complete power transmission system will be severely impacted by the occurrence of any of these

K. Nie · C. Li · Y. Liu · W. Gao · Z. Li · X. Wang · Q. Li (✉)
Shandong Provincial Key Laboratory of UHV Transmission Technology and Equipment, Shandong University, Jinan, China
e-mail: lqq@sdu.edu.cn

faults, which will result in severe losses to everyday life and output. As a result, the main purpose of electricity inspection is to examine and assess the state of the insulators, and if any issues are discovered, they must be resolved quickly to prevent further losses [3].

The goal of insulator defect detection is to identify insulators in an image and indicate where defects are present using the appropriate algorithms. As a result, much like the prevalent approaches for insulator target recognition, there are two general categories for insulator defect detection methods: those that recognize the image directly and those that construct models using deep learning algorithms to detect insulator defects.

In terms of image processing, the literature [4] employs the adaptive fuzzy inference system ANFIS to identify images, ascertain whether insulators are present in the recognition area, and output the location of any insulators that are present. This method can produce better recognition results, but it is computationally intensive and is not practical for situations involving many images. In Literature [5], the insulator surface features are extracted using the Gabor and standard deviation filters, respectively, and the insulator surface condition is assessed using the K-NN classifier in order to identify faults in the insulator surface ice cover. In literature [6], the identification of burn marks on insulators is accomplished by locating the burn marks using symmetric detection and localization, color, size, and shape parameters in the image candidate regions extracting features.

Deep learning algorithms are increasingly being used in research to identify insulator defects because image processing methods have high requirements for image quality and require matching pre-processing of insulator images in advance. Literature [7] trained different classifiers using the YOLOv3 model and used data augmentation techniques to prevent overfitting problems and successfully achieved insulator identification and localization under different lighting conditions. In literature [8], an online identification system for insulators is established using the YOLO algorithm, and real-time positioning of insulators during UAV flight is effectively accomplished. A full convolutional network design is used in the literature [9] to segment insulator strings and count the number of disc immutables; if there is a change, the insulator string is defective, but the precise position of the defect is not specified.

According to extensive research, deep learning has the benefits of being quick and accurate, which increases its potential for use in solving the insulator defect detection issue.

2 Insulator Defect Monitoring

2.1 YOLOv3 Algorithm

The YOLOv3 algorithm is mentioned in the literature [10] as an end-to-end single-stage detection algorithm, and this network incorporates the advantages of other networks into the original single-stage detection algorithm, which has a better performance in terms of real-time and accuracy of detection. Its network structure is shown in Fig. 1.

In contrast to other deep learning algorithms, YOLOv3 creates Darknet-53, a novel input-side network structure that completes the extraction of feature information after the input of an image. By adding a residual structure to the network, Darknet-53 successfully addresses the deterioration issue brought on by CNN models during training.

YOLOv3 uses K-means clustering in the output network to acquire three distinct anchor frames, or three target candidate frames of various sizes. In order to create prediction frames that precisely characterize the locations of the objects, yolov3 first predicts whether these candidate regions contain objects or not. It finally learns how to tell whether the candidate regions represented by the anchor frames contain objects or not by repeatedly adjusting the parameters.

The YOLOv3 algorithm improves the algorithm's ability to detect small targets by independently detecting multiple scales of fused feature maps by using the feature pyramid concept to fuse three scales of feature maps using up-sampling and merging methods.

The flow chart of the YOLOv3 algorithm training process is shown in Fig. 2.
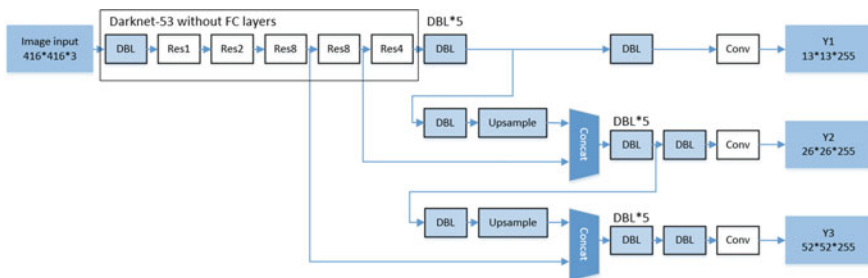
Fig. 1 The network structure of YOLOv3 algorithm
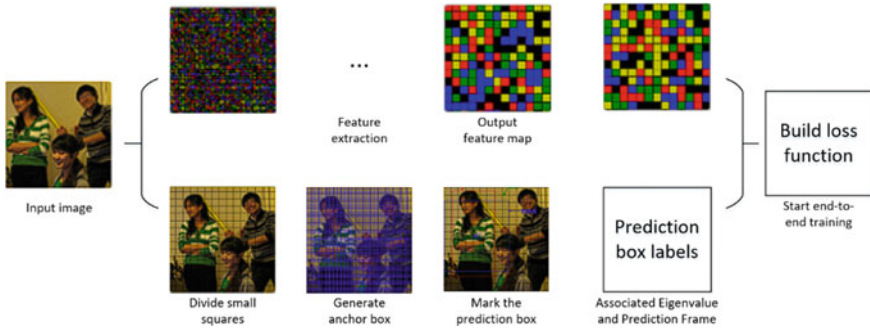
Fig. 2 YOLOv3 algorithm training flow chart

2.2 PP-YOLOv2 Based Insulator Defect Detection

Based on Baidu's flying paddle PaddlePaddle, PaddleDetection is an end-to-end target detection suite that offers a range of common target detection, instance segmentation, tracking, and key point detection algorithms. According to the literature [11], PP-YOLO, a YOLOv3 model that PaddleDetection improved and optimized, beats the YOLOv4 model in terms of accuracy (COCO data mAP) and inference speed, reaching 45.9% accuracy on the COCO test-dev2017 dataset. In this study, we apply the self-created PP-YOLOv2 algorithm by Baidu, whose network design is depicted in Fig. 3.

ResNet50-vd with deformable convolution is chosen for the entire architecture in PP-YOLOv2, and deformable convolution is used in lieu of some convolutional layers to increase network complexity and enhance feature extraction. Additionally, ResNet50-vd is more accurate and has superior feature representation capabilities than the DarkNet backbone network used in YOLOv3. PP-YOLOv2 uses a variant of FPN called Path Aggregation Network (PAN) to aggregate feature information from top to bottom and construct a high-level semantic feature map for various image sizes, in contrast to PP-YOLO, which uses FPN to build a feature pyramid from bottom to top.
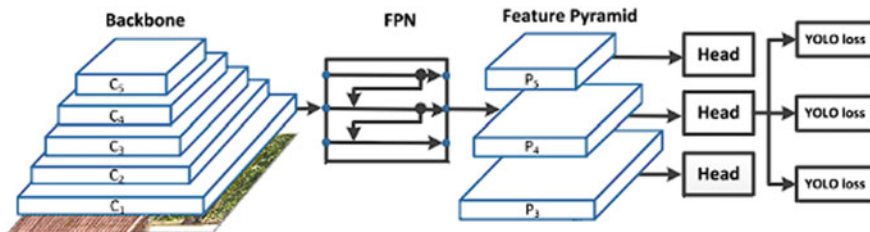
Fig. 3 Schematic diagram of PP-yolov2 algorithm network architecture

The head structure of PP-YOLOv2 employs a lightweight IoU sensing technique to more precisely anticipate the bounding box. Additionally, the PP-YOLOv2 model is optimized using loss functions like GIoU loss, DIoU loss, and CIoU loss to increase the model's precision and stability of detection.

3 Experimental Results and Analysis

3.1 Dataset Settings

The experiments in this paper are done under Win10 operating system environment, using PaddleDetection as a deep learning framework to build an experimental platform for model training.

A total of 600 insulator pictures from a public dataset, each with varying degrees of defective issues, are used in this study's power inspection insulator images. Data enhancement is applied to the images based on the original dataset because a significant number of insulator data samples are needed for model training. Examples of typical data enhancement techniques include color and geometric transformation. In order to achieve the data enhancement effect shown in Fig. 4, we flip and crop the original images in this paper using the geometric transformation technique.

The data enhancement procedure produced 1500 insulator images in total, which were divided into training sets, validation sets, and test sets in the ratio of 8:1:1.

a) Original Image   b) Image Flip

c) Image Scaling   d) Image Cropping
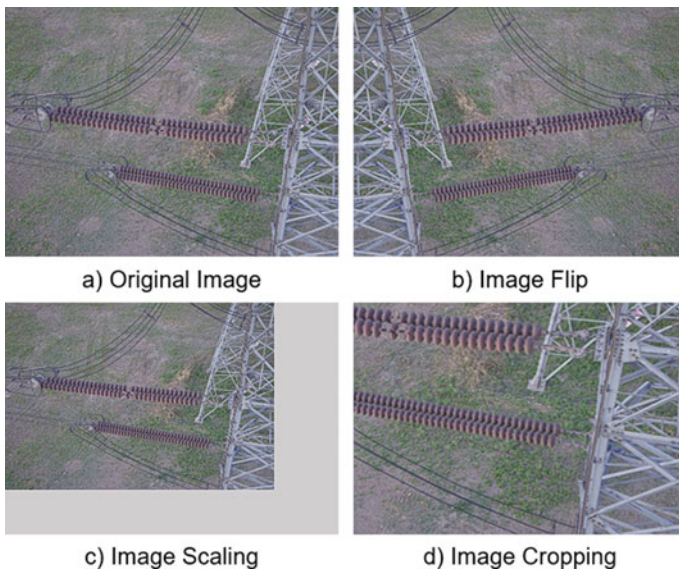
Fig. 4 Data enhancement
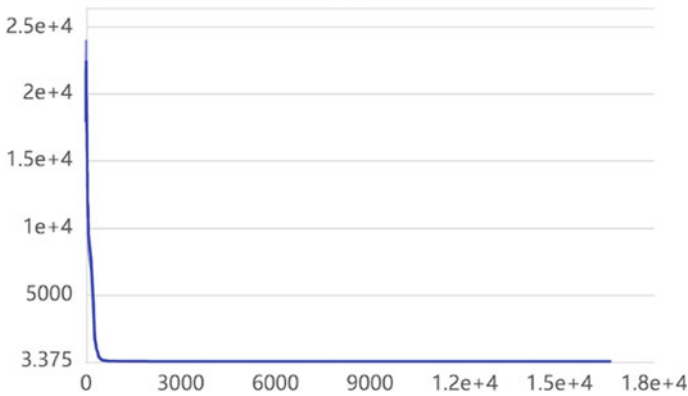
Fig. 5 Loss function

3.2 Results Analysis

The number of iterations of the PP-YOLOv2 algorithm is inversely correlated with the loss value throughout the training process, and the convergence rate is quick while the error fluctuation range progressively narrows. Before 1000 iterations, the loss function greatly shrinks, and after 1000 iterations, it tends to moderate and converge smoothly (Fig. 5).

When the training results of the PP-YOLOv2 algorithm are compared to the training results of the YOLOv3 algorithm, the effectiveness of the PP-YOLOv2 algorithm in the process of insulator defect detection is confirmed. It is clear that the YOLOv3 algorithm has lower insulator localization accuracy than the PP-YOLOv2 algorithm and exhibits a particular leakage detection phenomenon. The outcomes of the comparative test are displayed in Fig. 6.

The YOLOv3 algorithm and the PP-YOLOv2 algorithm are compared using the mean average precision (MAP) in this study, and the comparison results are displayed in the following chart. It is clear that the PP-YOLOv2 algorithm's MAP is superior to the YOLOv3 algorithm, and the accuracy of the position of the insulator and the insulator defect has significantly increased (Table 1).

Faster R-CNN, YOLO, and other popular frameworks are currently used to identify targets during power inspections. The comparative outcomes for various frameworks are displayed in Table 2. As can be seen, Faster R-CNN has an insulator MAP of up to 90%, but the detection speed is incredibly slow and is unable to meet the demand for real-time reaction to insulator defects. In addition, the speed of the YOLO algorithm is much quicker than that of the quicker R-CNN, so it should be used as the framework for power inspection detection.

a) PP-YOLOv2 detection effect diagram

b) YOLOv3 detection effect diagram
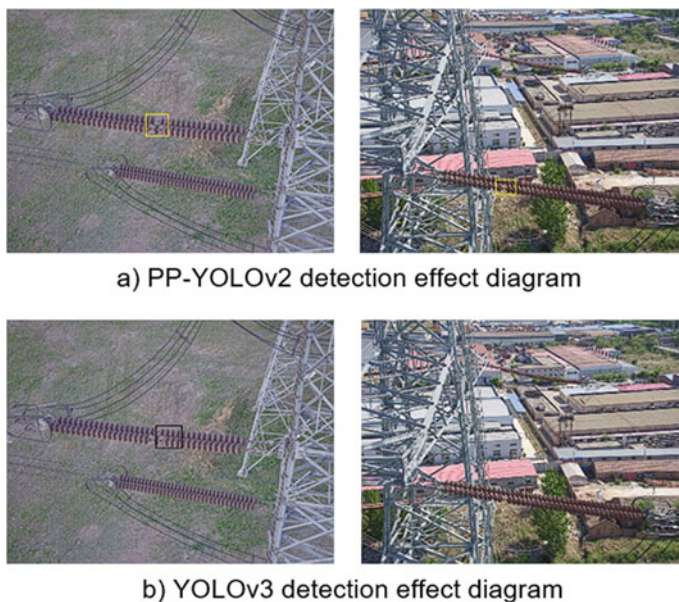
Fig. 6 Algorithm test effect comparison diagram

Table 1 Algorithm comparison results

Deep learning algorithm	MAP(%)	Accuracy rate (%)
YOLOv3	83.2	82.5
PP-YOLOv2	86.1	86.3

Table 2 Comparison of the results of various testing frameworks

Detection framework	MAP (%)	Accuracy rate (%)	Framerate/fps
Faster R-CNN	90.0	89.7	5.1
YOLOv3	89.0	88.3	24.2
PP-YOLOv2	89.4	90.2	26.3

4 Conclusion

This paper investigates deep learning-based insulator image defect detection, using the PP-YOLOv2 algorithm optimized and improved by PaddleDetection to complete defect detection, and comparing the PP-YOLOv2 algorithm with the original YOLOv3 algorithm, and verifying the effectiveness of the PP-YOLO algorithm in defect recognition with high detection accuracy and strong robustness. Insulator images captured by UAVs during power inspection are used as input for this paper.

References

1. Xia L (2022) Discussion on the development trend of power system automation and the application of new technologies. China Plant Eng 218 (in chinese)
2. Zhang Z, Huang S, Zhang Z (2020) An overview of machine vision applications in UAV patrol. Sci Technol Eng 20:13949 (in chinese)
3. Hao Y, Liang W, Pan J (2022) Review on intelligent live-line maintenance technology applied on power transmission lines. Electr Power Autom Equip 42:163 (in chinese)
4. Reddy MJB, Chandra BK, Mohanta DK (2011) A DOST based approach for the condition monitoring of 11 kV distribution line insulators. IEEE Trans Dielect Electr Insul 18:588
5. Pernebayeva D, Bagheri M, James A (2017) High voltage insulator surface evaluation using image processing. Toyohashi, Japan, 520p
6. Tudevdagva U, Battseren B, Hardt W, Troshina GV (2018) Image processing based insulator fault detection method. Novosibirsk, Russia, 579p
7. Sadykova D, Pernebayeva D, Bagheri M, James A (2020) IN-YOLO: real-time detection of outdoor high voltage insulators using UAV imaging. IEEE Trans Power Delivery 35:1599
8. Ohta H, Sato Y, Mori T, Takaya K, Kroumov V (2019) Image acquisition of power line transmission towers using UAV and deep learning technique for insulators localization and recognition. Sinaia, Romania, 125p
9. Sampedro C, Rodriguez-Vazquez J, Rodriguez-Ramos A, Carrio A, Campoy P (2019) Deep learning-based system for automatic recognition and diagnosis of electrical insulator strings. IEEE Access 7:101283
10. Redmon J, Farhadi A (2018) YOLOv3: an Incremental Improvement
11. Long X, Deng K, Wang G, Zhang Y, Dang Q, Gao Y, Shen H, Ren J, Han S, Ding E, Wen S (2020) PP-YOLO: an effective and efficient implementation of object detector
12. Huang X, Wang X, Lv W, Bai X, Long X, Deng K, Dang Q, Han S, Liu Q, Hu X, Yu D, Ma Y, Yoshie O (2021) PP-YOLOv2: a practical object detector

Influence of Micro-water on Insulation and Decomposition Characteristics of SF$_6$/N$_2$ Mixtures

Chuansheng Luo, Qiulin Chen, Mingli Fu, Zhixian Qin, Dibo Wang, Fan Fang, and Yan Luo

Abstract Mixing N$_2$ into SF$_6$ can effectively reduce the amount of SF6 used in electrical equipment. Micro-water is a common operating condition in electrical equipment, so the effect of micro-water on SF$_6$/N$_2$ needs to be considered before it is put into use. In this paper, the AC voltage breakdown experiments were performed on 0.5 MPa 30% SF$_6$/70% N$_2$ gas mixture at different concentrations and the decomposition products and breakdown voltage were quantitative analyzed. The experimental results show that when the water content exceeds 331 ppm, the content and gas production rate of SOF$_2$ and SO$_2$F$_2$ increase significantly, which can affect the safety of people and equipment. There is a linear relationship between the content of H$_2$S and the content of water inside the equipment, which can be used as a characteristic quantity to monitor the water content inside the equipment. When the water content exceeds 549 ppm, the insulation strength of the gas mixture is significantly reduced. Overall, the micro water content inside the equipment should not exceed 300 ppm.

Q. Chen · M. Fu · D. Wang · Y. Luo
CSG Electric Power Research Institute Co., Ltd, Guangxi, China

United Laboratory of Advanced Electrical Materials and Equipment Support Technology, CSG, Guangzhou, Guangdong, China

Q. Chen
e-mail: chenql5@csg.cn

M. Fu
e-mail: fuml@csg.cn

D. Wang
e-mail: wangdb@csg.cn

Y. Luo
e-mail: luoyan1@csg.cn

C. Luo (✉) · Z. Qin · F. Fang
Nanning Power Supply Bureau, Guangxi Power Grid Co., Ltd, Guangxi, China
e-mail: qq1920670878@163.com

Z. Qin
e-mail: qin_zx.nng@gx.csg.cn

1 Introduction

SF_6 is a strong electronegative gas, its stable physical and chemical properties and excellent insulation properties make it widely used in electrical equipment [1–3]. However, SF_6 is a greenhouse gas with Global Warming Potential value of 23,500 [4, 5] and was formulated as one of the six emission-limiting gases by the Kyoto Protocol. In order to limit the use of SF_6, people add natural gases to SF_6 species to form a binary mixture, which not only can reduce the amount of SF_6, but also can effectively alleviate the problem of high boiling point [6, 7]. Some studies have shown that N_2 is an ideal gas mixture, and the breakdown voltage of SF_6/N_2 mixture is significantly higher than that of SF_6/air and SF_6/CO_2. The insulation performance of the mixture can reach 85–90% of SF_6 when the percentage of SF_6 in SF_6/N_2 reaches 50–60% [8, 9].

In the process of insulating gas synthesis and filling, there are often trace amounts of H_2O mixed into the insulating medium due to technical limitations and the sealing performance of the insulating equipment. The micro-water affects the insulating properties and decomposition characteristics of the insulating gas. It has been shown that micro-water affects the content and production rate of SF_6 decomposition components under partial discharge [10], and under micro-water conditions, there is solid sulfur on the electrode surface when corona discharge occurs [11]. Micro-water also promotes the decomposition of SF_6 gas to produce stable by-products such as HF and SOF_4 [12]. All decomposition products except HF have lower electrical strength than SF_6 gas, which can lead to a decrease in the overall insulation performance of SF_6 [13]. Zhang et al. investigated the effect of micro-water on the decomposition properties of $C_5F_{10}O$. The $OH^.$ and $H^.$ produced by H_2O would promote the decomposition of $C_5F_{10}O$ to produce low ionization coefficient decomposition products such as HF, CF_2O, C_3F_7H, and C_3F_7OH, which would lead to the degradation of the insulation properties of $C_5F_{10}O$ insulating gas, in addition, HF and CF_2O would seriously affect human health and equipment safety [14]. Gao et al. studied the effect of micro-water on the insulation and decomposition characteristics of C_4F_7N/CO_2, the micro-water has an inhibitory effect on the breakdown voltage of the gas, which lead to a negative effect on the insulation properties, not only that the increase in the content of water leads to the growth of cyanogenic gases such as CNCN with a near exponential law [15]. Therefore, it is necessary to analyze the effect of micro-water on the insulating gas before putting into application.

At present, there is no comprehensive study on the insulation characteristics and decomposition characteristics of SF_6/N_2 gas mixture for micro-water. Based on it, this paper builds a gas discharge experimental platform is built to conduct AC voltage breakdown experiment on SF_6/N_2 gas mixture with different moisture in a quasi-uniform electric field. The breakdown voltage and decomposition products are

analyzed quantitatively to study the insulation properties and decomposition characteristics under different micro-water concentrations. The detection criteria of SF_6/N_2 discharge decomposition under different moisture are obtained, and the moisture standard of SF_6/N_2 gas mixture is proposed. The results from this paper can provide the theoretical basis for the application of SF_6/N_2 gas mixture in practice.

2 Experiment Platform and Method

The AC voltage breakdown experiment platform is shown in Fig. 1. The voltage regulator regulates the voltage across the electrodes by adjusting the voltage on the low voltage side, and the maximum voltage up to 100 kV. A sphere-sphere electrode with 50 mm diameter is used to simulate the quasi-uniform electric field, the electrode material is copper. The spacing between the sphere -sphere electrodes is set to 5 mm. A barometer is connected to the gas chamber to monitor the air pressure in the chamber in real time, and the decomposition products in the chamber is collect through the gas outlet to be measured by GC–MS.

To prevent external factors such as dirt, particles and moisture from the accuracy of the experiment, the gas chamber and the experimental electrodes should be cleaned with anhydrous ethanol before the experiment. The gas chamber and electrodes are then left to dry completely in a clean and dry environment for 6 h. In order to ensure the gas tightness of the experimental device, the assembled gas insulation experimental tank needs to be tested. After cleaning the gas chamber, the needle is used to fill the gas chamber with different contents of water. In order to simulate the situation that the water content inside the equipment reaches and exceeds the standard, four gradients of micro-water content are set up in this experiment. The set micro-water content and the actual micro-water content are shown in Table 1. Subsequently, a 30% SF_6/N_2 gas mixture at 0.5 MPa is charged. After completing the gas preparation work, the experimental wiring is connected. The step-up method is used to adjust the voltage in this experiment. When the gas insulation medium is broken, the regulator since the protection of the trip and record the regulator showing the breakdown voltage
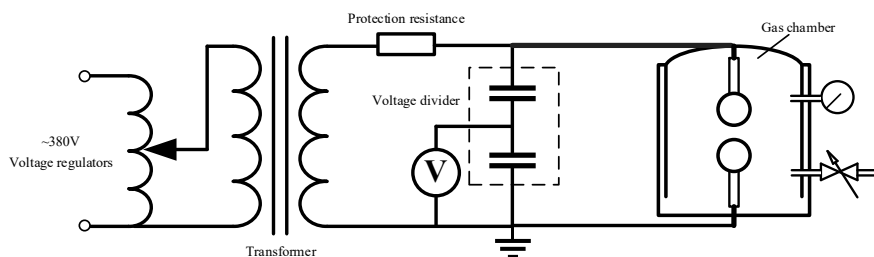
Fig. 1 Gas breakdown experiment platform

Table 1 Comparison between the set micro-water content and the actual micro-water content

Setting value/ppm	Actual value/ppm
0	96
300	331
500	549
700	763

value. Repeating the experimental operation 5 times, the breakdown voltage to take the average of five measurements.

3 Result and Discussion

3.1 Effect of Different Micro-water Content on the Decomposition Characteristics

The variation curve of SF_6/N_2 mixed gas decomposition product content with micro water content is shown in Fig. 2. The content of SOF_2 increased with the increase of water content, and the higher the water content, the faster the growth rate. When the water content exceeded 763 ppm, the growth trend shows an almost exponential function, which indicated that the water in the equipment have a significant enhancement on the SOF_2 content. The growth of SO_2F_2 is not obvious enough when the breakdown times is lower than 90, and the content of SO_2F_2 increased sharply with the rise of water content when the breakdown times is more than 90. This indicates that in the early stage of decomposition, the reactions generating SO_2F_2 are less. As the breakdown times increases, the reaction to generate SO_2F_2 increases, which may be caused by the hydrolysis of SOF_2 to produce SO_2F_2. The content of SO_2 increases with the water content, and the growth rate shows a trend of increasing and then decreasing. The reason for this trend may be that the oxygen atoms provided by the water contribute to the production of SO_2, while saturation occurs late in the reaction. The content of NO_2 increased with the increase of water content, and there is a significant increase in the content after the water content reached 549 ppm. The content of H_2S maintains a good linear relationship with the water content at different breakdown times, which can characterize the content water content inside the device well.

The gas production rate of decomposition products is an important physical quantity to describe the decomposition properties. The gas production rate (V_p) of decomposition products defined in experiment is calculated as follow:

(a)H_2S

(b)NO_2

(c)SO_2

(d)SO_2F_2

(e)SOF_2
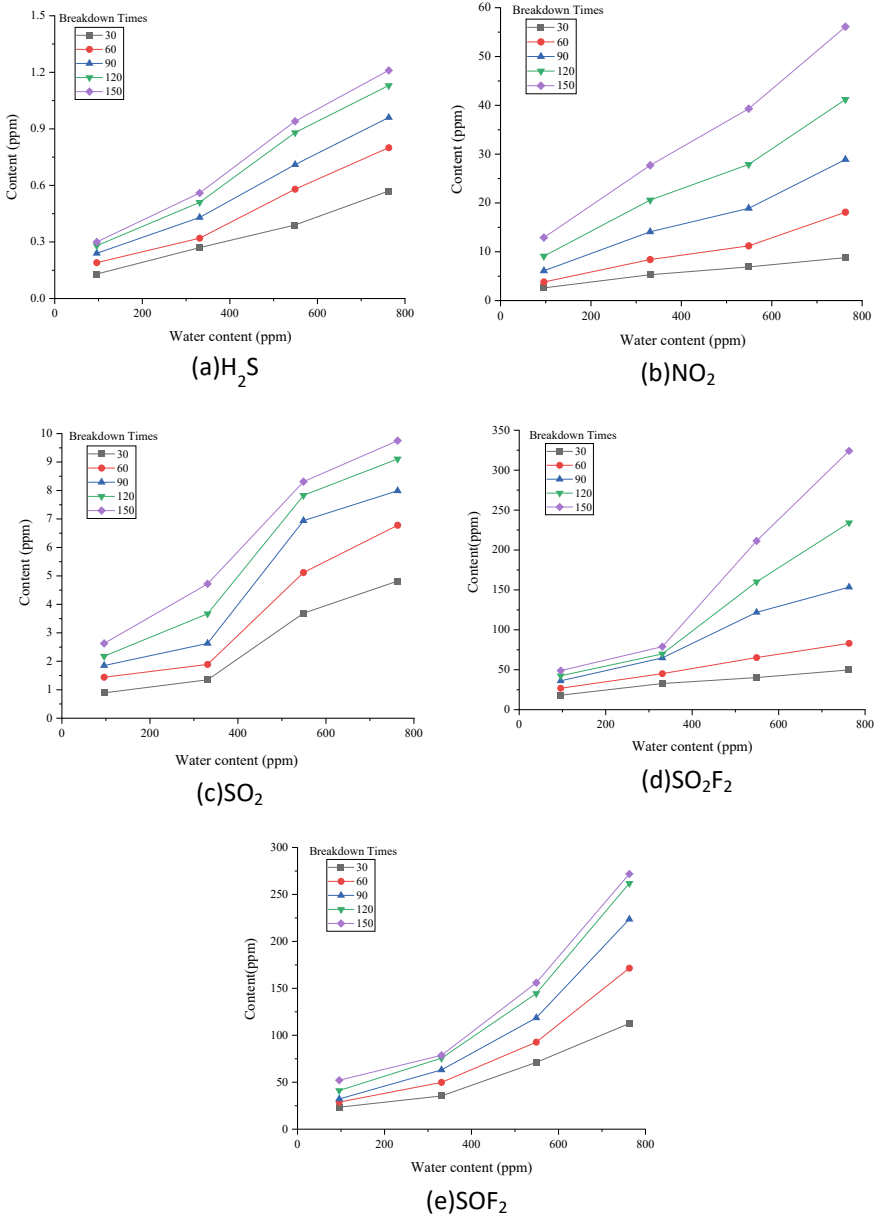
Fig. 2 Variation of each component contents with water contents

$$V_p = \left[\frac{\begin{array}{l}\left(\dfrac{V_{30}}{30}\right)^2 + \left(\dfrac{V_{60} - V_{30}}{30}\right)^2 + \left(\dfrac{V_{90} - V_{60}}{30}\right)^2 \\ + \left(\dfrac{V_{120} - V_{90}}{30}\right)^2 + \left(\dfrac{V_{150} - V_{120}}{30}\right)^2\end{array}}{5} \right]^{\frac{1}{2}} \tag{1}$$

in which, V_n is the gas content at the breakdown times of n, $n = 30, 60, 90, 120, 150$.

The gas production rate of each component with the water content is shown in Fig. 3. It can be seen that the gas production rate of each component increases when the water content increases. Especially when the water content is higher than 331 ppm, the effective gas production rate of SOF_2 and SO_2F_2 increases obviously, which is very unfavorable for the insulated equipment. The gas production rates of SO_2 and NO_2 show a good linear relationship with the content of water, while the gas production rate of H_2S is little influenced by the content of water.
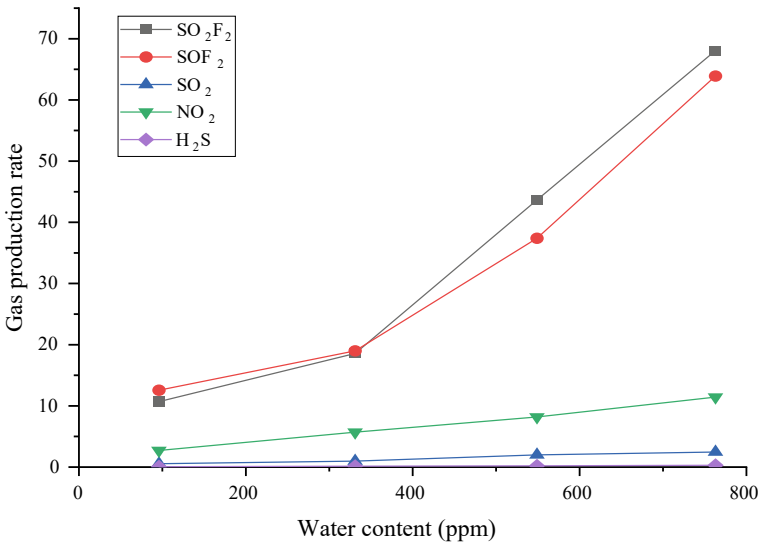
Fig. 3 Variation of gas production rate for each component with water contents
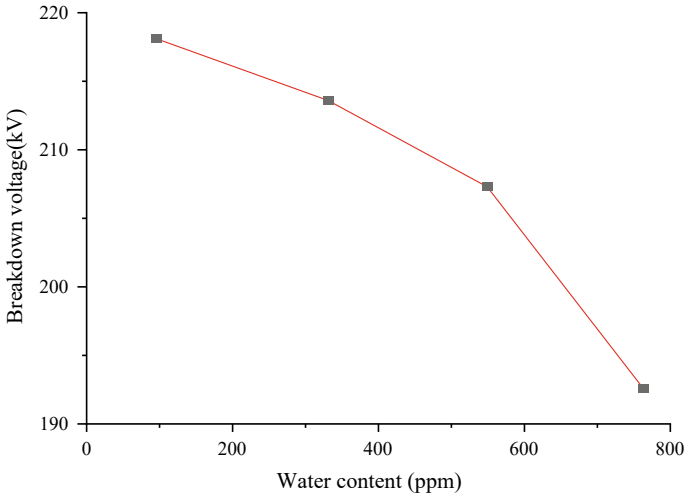
Fig. 4 Variation curve of breakdown voltage with micro water content

3.2 Effect of Different Micro-water Content on the Insulation Performance

The variation of the breakdown voltage with the water content is shown in Fig. 4. The breakdown voltage of SF_6/N_2 gas mixture decreases with the increase of water content, which indicates that the moisture inside the equipment affects the insulation performance of SF_6/N_2 gas mixture. When the content of water is 331 ppm and 549 ppm, the breakdown voltage is 97.9% and 95.0% of the breakdown voltage at 96 ppm, respectively, it shows that water has little effect on the insulation performance in this content range. When the water content is 763 ppm, the breakdown voltage of SF_6/N_2 gas mixture is 88.3% of 96 ppm, and the insulation strength appears to be reduced significantly. Therefore, during the actual operation, the water content should be monitored closely.

4 Conclusion

The AC breakdown experiment is used to study the effect of micro-water on the insulation performance and decomposition characteristics of SF_6/N_2 gas mixtures, and the following conclusions are as follow:

1. the addition of micro-water promotes the breakdown decomposition of SF_6/N_2 gas mixture. Especially when the concentration of water exceeds 331 ppm, the content and gas production rate of each components increase significantly. There

is a linear relationship between the contents of H_2S and water, which can be used to characterize the water content inside the device.

2. When the micro water content is 763 ppm, the insulation strength of SF_6/N_2 gas mixture appears to be reduced significantly. Considering all aspects, the water content in the equipment should not exceed 300 ppm.

References

1. Zhang X, Wu P, Lin C et al (2021) Compatibility and interaction mechanism between EPDM rubber and a SF_6 alternative gas-$C_4F_7N/CO_2/O_2$. ACS Omega 6:13293–13299
2. Tian S, Lan J, Rao X et al (2021) Study on compatibility between $C_6F_{12}O/N_2$ gas mixture and sealing rubber material at different temperatures. J Mol Struct 1244:130949
3. Tian S, Lan J, Rao X et al (2022) Study on compatibility between $C_6F_{12}O/N_2$ gas mixture and sealing rubber material at different temperatures. High Voltage Eng 48(11):4275–4286 (in Chinese)
4. Tian S, Liu B, Wang Y et al (2023) Adsorption performance of Cu-$HfSe_2$ on air decomposition products: a first-principles study. Mater Today Commun 34:105400
5. Tian S, Zhang X, Cressault Y et al (2020) Research status of replacement gases for SF_6 in power industry. AIP Adv 10(5):050702
6. Xiao D (2016) Development prospect of gas insulation based on environmental protection. High Voltage Eng 42(4):1035–1046 (in Chinese)
7. Yan X, Gao K, Zheng Y et al (2018) Progress of gas mixture and alternative gas of SF_6. Power Syst Technol 42(6):1837–1844 (in Chinese)
8. Malik NH, Qureshi AH (1979) A review of electrical breakdown in mixtures of SF_6 and other gases. IEEE Trans Electr Insul 14(1):1–13
9. Malik NH, Qureshi AH (1979) Calculation of discharge inception voltages in SF_6–N_2 mixtures. IEEE Trans Electr Insul 14(2):70–76
10. Tang J, Qiu Y, Zeng F et al (2012) Formation mechanism and influence rules of trace levels H_2O on SF_6 characteristic decomposition components under partial discharge. Trans China Electrotechnical Soc 27(10):13–19 (in Chinese)
11. Hergli R, Casanovas J, Derdouri A et al (2002) Study of the decomposition of SF_6 in the presence of water, subjected to gamma-Irradiation or corona discharges. IEEE Trans Dielectr Electr Insul 23(3):451–465
12. Sauers I, Harman G (1992) A mass spectrometric study of positive and negative ion formation in an SF_6 corona. II. Influence of water and SF_6 neutral by-products. J Phys D Appl Phys 25(5):774
13. Zhong J, Wang Q, Lin X et al (2020) Study on discharge decomposition mechanism of SF_6 under micro-water and micro-oxygen. High Voltage Apparatus 56(5):1–7 (in Chinese)
14. Xiao S, Li Y, Zhang X et al (2017) Effects of micro-water on decomposition of the environment-friendly insulating medium $C_5F_{10}O$. AIP Adv 7(6):065017
15. Yang Y, Gao K, Ding L et al (2022) Influence law of micro-water on insulation and decomposition characteristics of eco-friendly C_4F_7N/CO_2 gas mixture. Power Syst Technol 46(6):2402–2409 (in Chinese)

Arc Motion Behavior During Rotary Separation of Vacuum Contacts

Li Zhengbo, Yundong Cao, and Si Fu

Abstract At the moment when the contacts are separated, a metal vapor arc is generated in the gap. During the formation process, there are strong material transfer, arc root accumulation and stagnation, which causes the surface of the contact to be ablated and form a crater, resulting in the surface of the contact being broken after many times. The damage is aggravated, affecting the breaking performance. A method of contact rotation and separation is proposed to change the microscopic ionization conditions at the initial stage of arc formation, thereby affecting the motion behavior of vacuum metal vapor arc. In this paper, the influence of contact rotation on the arc characteristics is studied, and it is shown that the contact rotation promotes the transition time point of the limited arc movement in the initial stage, and the limited arc changes from bridge columnar diffusion to radial until the arc splits. The contact rotation will provide a favorable supplement to the research on the improvement of the breaking capacity of the vacuum interrupter.

1 Introduction

The vacuum switch makes high vacuum as the arc extinguishing and insulating medium. The contact and arc extinguishing system are simple, with long service life, small size, light weight, suitable for frequent operation, etc. widely used in low and medium voltage power systems. In order to respond to the national development strategy of "carbon peak, carbon neutrality" [1], Xi kai Co., Ltd. announced that it has carried out the temperature rise and flow experiment of 252 kV high voltage vacuum AC circuit breaker in Xi'an High Voltage Apparatus Research Institute, and successfully passed the temperature rise research experiment, marking a major

---

L. Zhengbo (✉) · Y. Cao · S. Fu
Institute of Electrical Apparatus New Technology and Application, Shenyang University of Technology, Shenyang 110870, Liaoning, China
e-mail: 646161325@qq.com

technological breakthrough and staged progress in the development of 252 kV high voltage vacuum circuit breaker.

A high-energy arc exists in a vacuum interrupter and requires control measures to extinguish it. From the perspective of energy, there is a temporary balance between the energy input to the arc and the energy lost by the arc. To extinguish the arc, the equilibrium state must be disrupted, and the rate of energy dissipated in the arc must exceed the rate of input arc energy. Current over zero, the main role of the vacuum is the carrier dissipation, contact gap in the dissipation of energy is much higher than the input energy. The development of vacuum breaking technology [2, 3] has experienced three periods of "simple breaking", "Transverse magnetic control" and "Longitudinal magnetic control", from the initial vacuum switch as a flat butt-contact contact, to the vacuum spiral groove, cup-shaped, and swivel-shaped structure transverse magnetic series contacts, after the vacuum arc is forced to form, the arc rotate at a high speed on the contact surface under the action of electromagnetic force, so as to reduce the ablation and space jet phenomenon caused by the arc energy on the contact surface; horseshoe-shaped, single-pole, multi-pole coil type, and cup-shaped structure longitudinal magnetic series contacts are developed in the direction of contact, limiting the escape of high-current vacuum arc plasma, avoiding the shrinkage of the arc column, and avoiding the local shrinkage and accumulation of energy on the surface of the contact. The means of magnetic field, after the arc is formed, controls the movement and transformation of the arc, so that the arc energy dissipates as soon as possible in the spatial distribution, and the vacuum arc maintains a spatial diffusion state before crossing zero, so as to achieve the purpose of extinguishing the arc. This kind of breaking method [4–6] and the existing contact structure mainly focus on the development and evolution of the magnetic field to control the arc, avoiding the retention of the arc on the contact surface to reduce the degree of contact burnout [7] and improve the arc extinguishing performance of the switch. According to the existing research, the "two-dimensional" dissipation effect of the stable combustion arc energy is close to saturation during the contact breaking process, and the improvement of the breaking capacity of the vacuum interrupter has encountered a bottleneck.

In order to further explore new measures to improve the breaking capacity of the vacuum interrupter, the institute proposed a new breaking method of the rotary arc [8, 9] of the vacuum switch contact to enhance the strong coupling between the arc and the contacts during the arc generation, arc burning and arc extinguishing process. Function, the restricted arc follows the contact rotate and moves on the surface of the contact, eventually causing the distribution and movement of the hot spots on the contact surface at the source of the vacuum metal vapor arc to change with the characteristics of rotary behavior, and this change will run through the entire vacuum arc life cycle. In the process of contacts separation, the method of adding contact rotary motion changes the arc generation conditions from the source of vacuum arc generation [10], couples the magnetic field during arc burning to control the arc, and improves the surface state of the contacts after the arc, so that the high energy between the contacts can be homogenized to the greatest extent in the whole space–time process, and the "three-dimensional" breaking of vacuum arc can be realized,

which will become a new breakthrough to improve the breaking capacity of vacuum interrupter.

2 Experiment System

The contact rotary vacuum arc platform is mainly composed of five parts: vacuum system, detachable vacuum interrupter, mechanism transmission system, high-speed camera system, and signal acquisition system. As shown in Fig. 1.

During the experiment, the vacuum system continued to work, so that the vacuum pressure of the detachable interrupter was always kept at 10-4 Pa. The detachable arc extinguishing chamber is equipped with a quartz glass observation window, which is used to directly photograph and observe the contact movement process and arc evolution process. When the main circuit is disconnected, the contact system is closed. During the experiment, the main circuit current is provided by the DC power supply. Through the load resistance, the transmission electrical control system executes the synchronous separation command, and the contact system separates in a single direct motion or synchronous rotary to generate an arc. In the experiment, the sample rate of the high-speed camera system is set to 7500 fps, and the time between frames is 133.33 µs. Voltage probes and current probes are used to measure electrical parameters such as arc current and voltage; the high-speed camera and auxiliary optical system are controlled by the main controller to ensure that the images of the vacuum arc are collected synchronously.

In order to observe the whole process of arc formation and development better, this paper adopts an asymmetric flat contact structure, the cathode contact radius is 22.5 mm, the anode contact radius is 7.5 mm, and the contact material is copper. When shooting, adjust the shooting angle to observe to the entire fracture gap and
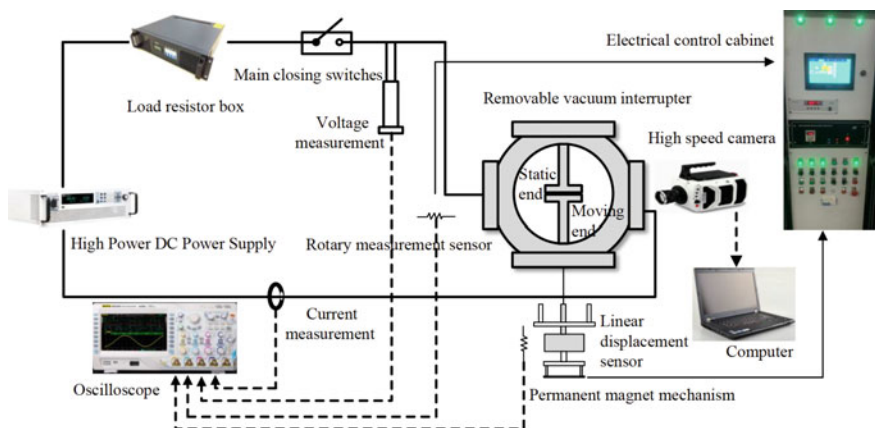
Fig. 1 Schematic diagram of vacuum arc pulling experimental system

cathode surface, the breaking current is DC 60 A, the average opening speed is set to 1.0 m/s, and the contact rotary speed is set to 3 deg/ms.

3   Results and Discussion

In order to explore the influence of contact rotation and separation on the movement behavior of vacuum metal vapor arc, a vacuum arc arcing experimental platform was built, and different separation methods of contacts in the vacuum interrupter (single direct motion separation method, synchronous rotary separation method) were established. The analysis of arc shape and motion characteristics can better compare the physical process of vacuum arc under different contact separation methods. In this paper, single direct motion separation and the contact synchronous rotary separation experiments were carried out 200 times separately. After analysis and comparison, two sets of widely representative arc images were finally selected as evidence for this research.

3.1   Arc Movement of Different Contact Separation Methods

The whole process of the arc shape evolution of breaking the 60 A DC current in different contact separation methods observed by the high-speed camera system is shown in Fig. 2. At the initial stage of arcing, the brightness of the arc generated by the two contacts separation methods is enhanced. At the moment of contacts separation, the arc images shows a temporary pause and limited arc generated near the burnt pit on the contact surface, and the arc stagnation usually results in extended break times. In the contact direct motion separation mode, when the initial separation distance is very small, the restricted arc is in the shape of a bridge column, the arc root and arc column are stable, and the arc hot spots are formed on the contact surface to inject metal vapor ionized gas into the small gap, and the images of arc light gradually becomes brighter. The restricted arc is limited by the surface of the contact with a small opening distance and hardly moves. When t = 0.800 ms, the restricted arc start move. Since the arc current is small, the arc spot moves randomly on the contact surface, and the bridge-column arc transforms into a diffuse arc until the arc is extinguished.

In the contact rotary mode, the arc movement is more active than that of the adjacent group. The contact rotary promotes the diffusion of the metal vapor jet, and at the same time increases the collision frequency between particles, which makes the arc burn violently, so that the arc burns fully at the initial stage of arc ignition. The further stretching of the column, enhance the heat exchange speed of the arc, the arc is more likely to spread outward, the particle diffusion speed is further enhanced, and the arc stagnation time is much shorter than that of direct motion separation,
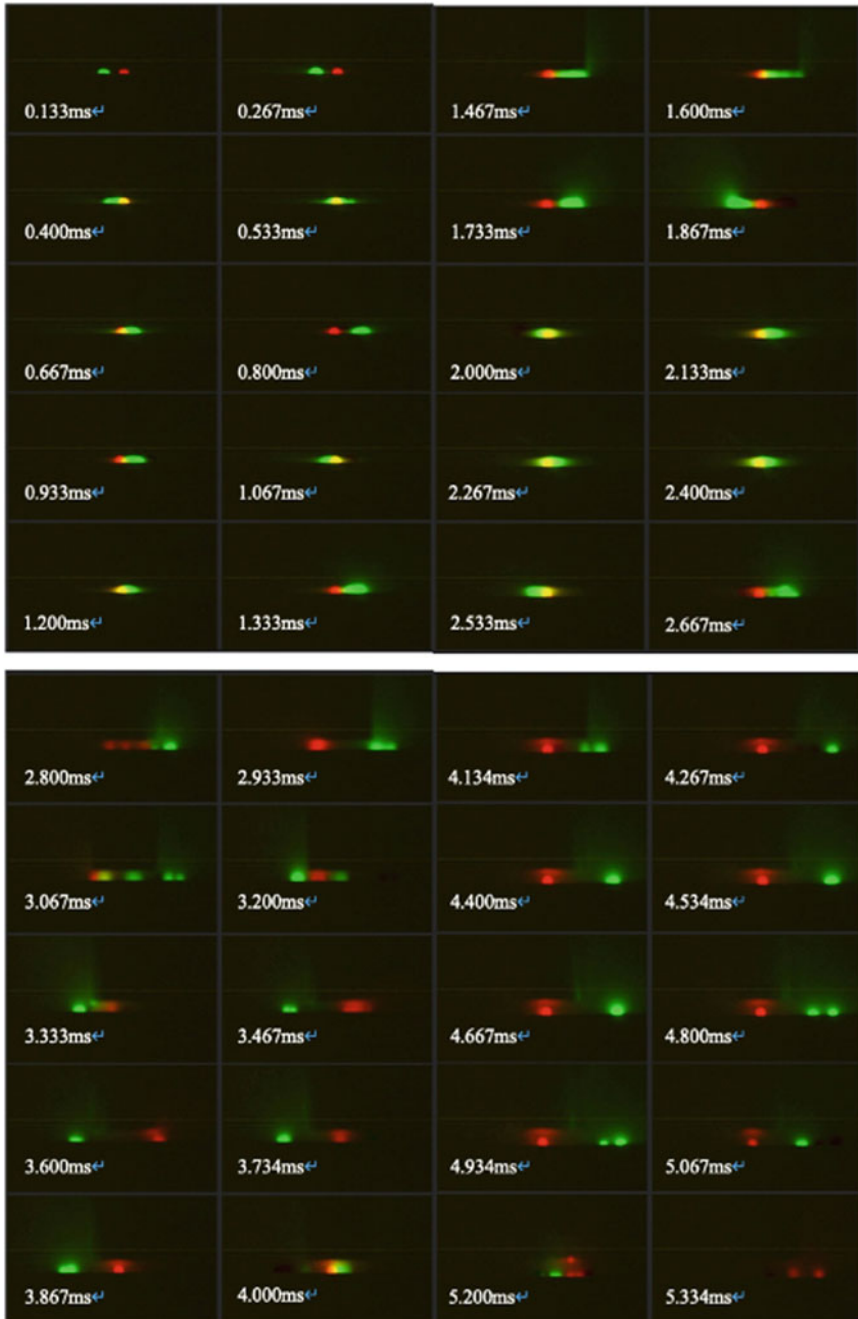
Fig. 2 Development process of arc movement under different contact separation methods (green one represents rotary method; red one represents direct method; yellow one represents overlap)

resulting in faster arc energy loss, rapid arc area growth, and the voltage rise speed in the rotary separation mode is obviously accelerated.

From the perspective of arc shape, the restricted arc under the synchronous rotary separation method is different from the bridge-column shape under the traditional and single direct motion separation methods, but presents a radial shape. The arc bright area in the arc image is much larger than the direct motion separation. This is because the rotary of the contact increases the activity of the contact during the arcing stage, the cathode emission points increase, and the metal vapor ionization gas injected from the arc spot on the contact surface into the gap increases. Due to the stronger coupling between the gap arc and the contact surface, the cathode emission point cannot exist stably, and the stability of the restricted arc is broken in advance. In the figure, the restricted arc starts to move at t = 0.800 ms, and at t = 1.600 ms the arc column splits for the first time. As the opening distance is further opened, the arc changes to a diffuse arc. From t = 2.933 ms, the arc root movement-split phenomenon obviously increased in the rotary mode.

It can be clearly seen from the figure that the radius of motion of the arc generated by the rotary separation method is much larger than that by the direct motion separation method. In addition, in the direct separation mode, the arc moves from the concentrated state to the diffuse state, and the movement of the arc is basically within the range of the cathode surface corresponding to the radius of the anode contact, while the arc generated by the rotary method can appear randomly on the cathode surface. Any position with a clear tendency to move toward the edge of the contact.

3.2 Arc Images Processing for Different Contact Separation Methods

Due to the good arc extinguishing performance of the vacuum medium, the shape of the vacuum arc will change during the combustion process, from a bridge columnar arc to a diffuse arc., the arc is on the verge of extinguishing. During the whole process, the arc energy distribution is not uniform and changes from time to time.

The digital image processing technology is used to extract the characteristic information of the arc image, draw the arc area curve, and analyze the arc shape change and energy distribution during the contact separation process. As shown in Fig. 3 at the initial stage of arcing (0–1 ms), the arc area between the contacts of the synchronous rotary separation method changes more drastically than that of the direct motion method. At this stage, the arc root diameter and the arc column brightness of the two separation methods have different The obvious increase, the interpolar metal vapor concentration increases. During the development period of the arc (1.5–4.5 ms), the arc area between the contacts of the synchronous rotary separation method changes more drastically than the direct-action method, which promotes the movement of the cathode arc root. 1.5–2.7 ms, the arc area in the rotary mode is significantly higher than that in the direct-acting mode, which shows that the rotary mode has a certain
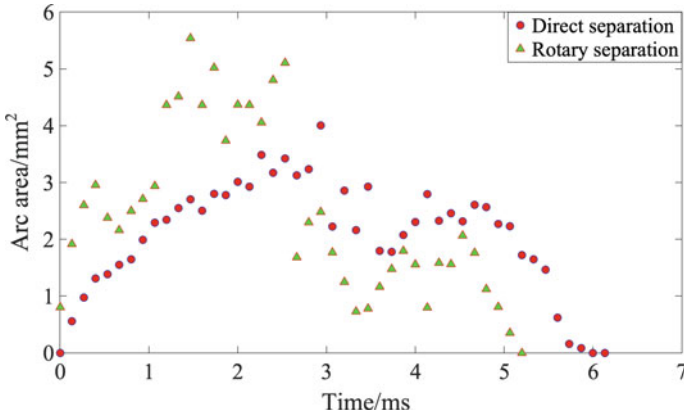
Fig. 3 Variation of arc area with time under different contact separation methods

degree of stretching of the arc between the contacts. It can be seen from the figure that the change of the arc area under the contact rotary separation method is earlier than that of the direct motion separation method, and the area change is faster. Obviously, in the arc extinguishing stage (4.5 ms—extinguishing), the phenomenon of arc root splitting occurs, which leads to the change of arc shape, accelerates the energy loss speed, and the arc area decreases more rapidly with time under the contact rotation and separation mode.

3.3 Vacuum Arc Voltage Characteristics of Different Contact Separation Methods

Vacuum switch arc combustion is a complex physical process, and its electrical, magnetic, and mechanical parameters will affect the arc shape.

Figures 4 and 5 shows the arc voltage waveforms for the contact single direct motion separation method and the contact synchronous rotation separation method. The driven contact receives the opening command and breaks the main circuit current. Under the single direct drive separation mode, the arc current and voltage waveforms show obvious fluctuations during the arc ignition process. Figure 5 shows the arc current and voltage curves when the contact rotates at a speed of 3 deg/ms synchronously rotary and separating. In this case, the arcing time is slightly shorter, 5.2 ms. At the same time, the arc voltage fluctuation is smaller than that of the single direct contact separation method, and the voltage fluctuation is small at the initial stage of arc ignition. From the analysis of the corresponding arc image, the bright part in the image is regarded as the metal vapor arc in the gap. The rotation of the contact in the first stage makes the contact more active, and the contact provides more metal vapor particles to the gap, and the arc burns more fully; in the later stage
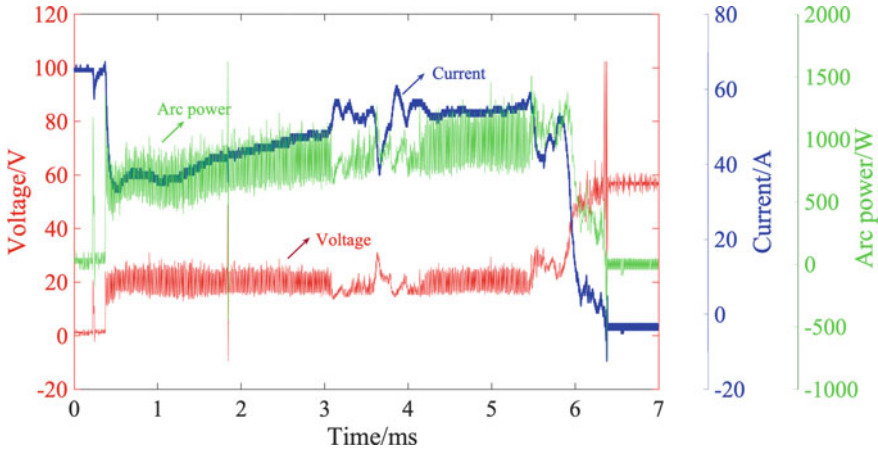
Fig. 4 Arc current, voltage and power waveforms under the contact direct separation method
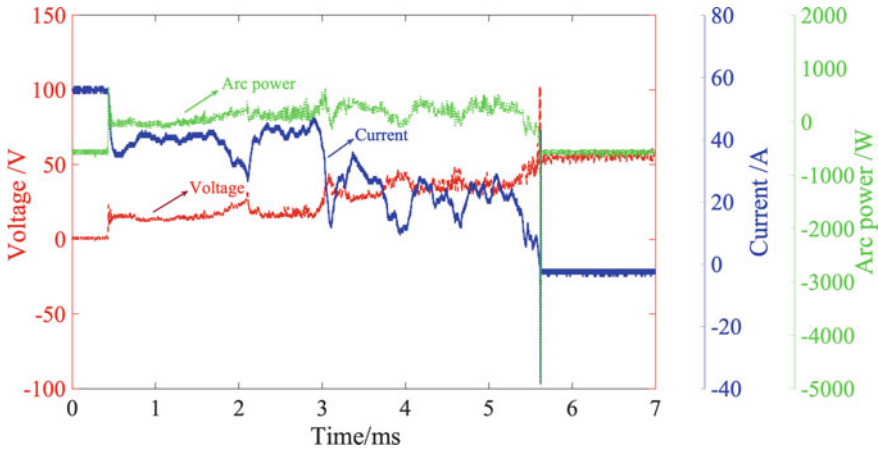
Fig. 5 Arc current, voltage and power waveforms under the contact rotary separation method

of rotary arc, the cathode spot on the contact surface is unstable, the arc voltage fluctuates greatly, and the arc more fully burned. The duration is shortened.

4   Conclusions

This paper conducts experimental research on the whole process of DC arc generation and development under different separation methods of asymmetric flat contacts (single direct motion separation method, synchronous rotary separation method).

The restricted arc is generated, the arc moves to the restricted arc and transforms into a diffuse arc, and then extinguishes. Concluded as follow:

1. For the small current of 60 A for direct separation of contacts, the arc is basically in a stagnant state after the arc is generated, and the diffusion movement is relatively late. The entire arcing process is 6.16 ms, and the arc is in a state of aggregation. Unstable anode spots appear at 5.20 ms; arcing Initially, the arc root diameter and arc column brightness increased. In the middle and late stages of arc burning, the arc root splits more frequently, the arc energy loss rate is slower, and the arc form changes to a diffuse state later.

2. For a small current of 60 A with synchronous rotary of the contacts, the arc diffuses very quickly after formation, and the entire arc is nearly 5.2 ms, and there is no stable anode phenomenon; at the early stage of arc ignition, the diameter of the arc root and the brightness of the arc column increase, there is a brief stagnation phenomenon, and then the arc moves very actively between the contacts. In the middle and late stages, the arc splits frequently, the energy loss rate is faster, the area diffusion rate in the middle and low temperature areas of the arc is faster, and the arc form is transformed into a diffuse state in a shorter time.

3. In the case of breaking a small current without a magnetic field, according to the arc behavior analysis, the contact rotary mode intensifies the coupling degree between the vacuum arc and the contact during the arc drawing process, and the arc stagnation time is greatly reduced. Restricted arcs appeared in the initial stage of arc formation in different contact separation methods. In the case of synchronous rotary separation method, the restricted arc diffused to a radial shape. The arc light area in the arc image was much larger than that of the direct separation method. The transition time point of the limited arc at the initial stage is advanced, the efficiency of the transition from the arc to the diffuse arc is improved, the duration of the arc is shortened, and the arc is easier to extinguish.

References

1. Zhang J, Zhou Q, Wang D et al (2021) Research on the development path of new power systems under the "dual carbon" goal. Huadian Technol 12:46–51 (in Chinese)
2. Zou J, Chen J, Liu X et al (2021) Vacuum switching technology. Mechanical Industry Press, Beijing (in Chinese)
3. Lafferty JM (1980) Vacuum arcs theory and application. John Wiley$Sons Inc., New York
4. Ren WB, Xue SJ, Zhao YY (2014) Test technology and experimental research on electrical contact behavior of new contact materials. Electr Appliances Energy Effi Manage Technol 19:38–42 (in Chinese)

5. Haug R, Koukaou T, Doremieux JL (1991) Phenomena preceding arc ignition between opening contacts: experimental study and the oretical approach. IEEE Trans Compon Hybrids Manuf Technol 14(3):14–19
6. Liu L, Zhuang J (2014) DC vacuum arc morphology and voltage characteristics during plate contact separation. Chin J Electr Eng 34(6):934–940
7. Chen J, Han H, Wang Z et al (2021) Analysis of discharge mechanism of electric spark surfacing under different electrode motion forms. Surf Technol 50(6):281–287. (in Chinese)
8. Fu S, Cao Y, Liu K et al (2017) Investigation on arcing behaviors in high-voltage switchgear with a rotary interruption technology. In: Proceedings of the 4th international conference on electric power equipment-switching technology. Xi'an, pp 619–619
9. Fu S, Cao Y, Li J et al (2020) Simulation of vacuum metal vapor arc formation process at the moment of contact separation. J Electr Technol 35(13):2922–2931 (in Chinese)
10. Ren WB, Wang H, Chang C, Xue SJ, Chen Y (2016) Experimental investigation and understanding of the intermittent molten bridge phenomena and mechanism of contacts with super-low opening speed. IEEE Trans Compon Packag Manuf Technol 6(3):418–423

Research on Full-Circuit Model of Damping Busbar for VFTO Suppression

Han Wang, Ning Lu, Xixiu Wu, and Xiaotong Feng

Abstract Using spiral tube damping busbar is a promising method for VFTO suppression due to its effectiveness and ease of installation. To optimize the suppression effect, it is crucial to deeply understand the suppression mechanism and related factors. Thus, a complete circuit model of the damping busbar is established, including all stray parameters and impedance. The method to calculate stray inductance and capacitance between the shell and busbar under high frequency VFTO is introduced. The completely circuit model is established based on SF6 breakdown criterion. The model is applied to a 550 kV GIS platform, and the effect of circuit parameters on suppression is analyzed. Results indicate that the stray capacitance between the busbar and shell also significantly affects VFTO rejection, in addition to coil inductance and shunt capacitance.

Keywords VFTO suppression · Damping busbar · Stray capacitance · Full-circuit model

1 Introduction

Very fast transient overvoltage (VFTO) is generated during operation of gas insulated substation (GIS) disconnectors and it has the characteristics of high amplitude and fast rise time in the range of nanoseconds [1–3]. Generally, VFTO stress on the insulated system in GIS, which seriously threatened the safety and reliability of GIS. Furthermore, VFTO can also produce electromagnetic interference effects and results in mal-operation of the control circuitry as well as the secondary equipment connect to it. Therefore, it necessary to suppress VFTO. VFTO suppression consists of three aspects [4]: reduce amplitude, flatten the steepness of the front wave and reduce number of re-strikes. There are two main approaches to VFTO suppression:

H. Wang · N. Lu · X. Wu (✉) · X. Feng
Wuhan University of Technology, WuhanHubei Province 430070, China
e-mail: wuxixiu@whut.edu.cn

(1) To suppress VFTO, the discharge energy of SF6 re-breakdown should be absorbed. A common method is to install a breaking resistor in the isolation barrier [5, 6].

(2) To inhibit the spread of SF6 and suppress VFTO amplitude, the wave impedance in the propagation path can be adjusted. This is often done using the "Inductor + Resistor" method, which flattens the wavefront and reduces amplitude. The oxy-magnetic ring method and high frequency resonator method also use this principle, with their respective advantages and disadvantages described in [7].

The damping busbar also uses the "inductor + resistor" method to suppress VFTO, it has the characteristics of simple structure, installation method and good suppression effect compared with other methods. The suppression effect of damping busbar has been verified by tests and simulations [8], and our group has also investigated the relationship between the optimal suppression effect of the VFTO and the matching of the resistance and inductance of damping busbar [9]. However, the lack of a complete full-circuit model considering the spurious parameters has made the research on damping busbar suppression mechanism not deep enough. So, this paper is dedicated to a full-circuit model study of damping busbar, discussing the effect of full-circuit parameters on the VFTO suppression effect and laying the foundation for a deeper understanding of suppression mechanism.

2 Establishment of Full-Circuit Equivalent Model of Damping Busbar

Figure 1a shows a schematic diagram of the damping busbar installation structure, it consists of spiral tubular suppression busbar body, damping resistor, epoxy support and number of connecting parts, which is held in place by a basin insulator. According to its structural characteristics, this paper builds a full-circuit equivalent model of the damping busbar shown in Fig. 1b.
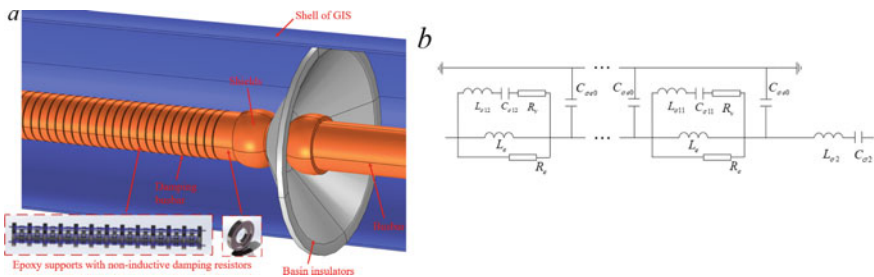
Fig. 1 **a** Schematic diagram of the damping busbar installation. **b** Full-circuit equivalent model

3 Calculation of Full-Circuit Parameters for Damping Busbar

3.1 Calculation of Inductance Parameters

(1) Principle of Inductance Calculation

① Coil Inductance Calculation

The essence of solving for coil inductance is to solve for magnetic flux density. However, due to the high frequency of the VFTO, the solution of the damping busbar coil inductance under VFTO conditions is different from low frequency.

In low frequency, the current can be seen as uniformly distributed due to the insignificant skin effect which is the opposite of the situation at high frequencies. The effective cross-sectional area of current in a conductor at high frequencies can be expressed according to the skinning depth:

$$
\begin{aligned}
s &= \pi \left[R^2 - (R - \delta)^2 + (r+\delta)^2 - r^2 \right] \\
&= 2\pi (R + r)\delta = 2\pi (R + r)\sqrt{\frac{1}{\pi f \mu \sigma}}
\end{aligned}
\tag{1}
$$

In Eq. (1) R and r stand for inner and outer diameter of the conductor, m; δ is skinning depth, m; f is the frequency of the current, Hz; μ is the magnetic permeability, H/m; σ is the conductivity, S/m. Thus the inductance L of the coil at high frequencies can be expressed by the following equation.

$$
L = \frac{\int \left[\int B ds \right] di}{i^2} = \frac{2\pi (R + r)}{i^2 R} \int \left[\int B \cdot \frac{1}{\sqrt{\pi f \mu \sigma}} dr \right] di
\tag{2}
$$

② Stray Inductance Calculation

Under VFTO conditions, the magnetic chain of the conductor is divided into an external magnetic chain closed outside the conductor and an internal magnetic chain where the magnetic field inside the conductor intersects with part of the current. The calculation of the damping busbar coil inductance only takes into account the internal magnetic chain, while the stray inductance at high frequencies is caused by the external magnetic chain of the intersecting chain of the circuit loop which can be expressed by the following equation.

$$
L_\sigma = \frac{\psi_o}{i}
\tag{3}
$$

(2) Calculation of Damping Busbar Coil Inductance
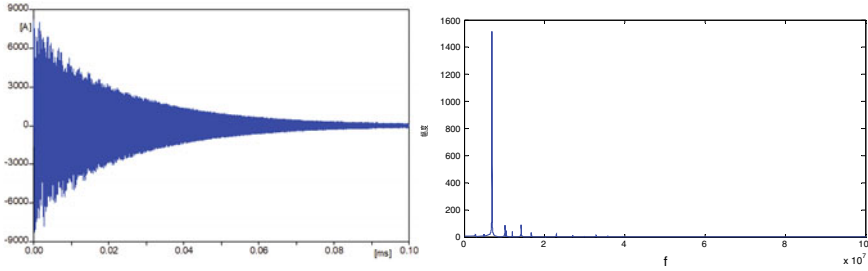
Fig. 2 Schematic and spectrum of VFTC waveform

In this paper, by establishing a multi-physics field coupling model of GIS disconnect switches, the variation of air gap breakdown voltage during contact opening is obtained and brought into a typical GIS circuit simulation model as an arc reignition criterion to obtain a typical VFTC waveform. Here the calculation process is omitted due to space limitation. The VFTC waveform as well as the spectrum diagram is shown in Fig. 2. In order to obtain the VFTC distribution characteristics, consider the effect of frequency, the VFTC waveform fitting, as the excitation of the damping bus inductance calculation, as shown in Eq. (4).

$$
\begin{aligned}
I = [&1517\sin(2\pi \times 6.9 \times 10^6 t) + 90\sin(2\pi \times 14.17 \times 10^6 t) \\
&+ 1pt88\sin(2\pi \times 10.16 \times 10^6 t)] \cdot e^{-500000t}
\end{aligned}
\tag{4}
$$

This paper uses the field calculation method to calculate the high frequency inductance of damping busbar, establishing a model for calculating the high frequency inductance of the damping busbar. Bringing in the VFTC excitation shown in Eq. (4), the final calculated damping busbar coil inductance is 10.8uH.

(3) Calculation of Stray Inductance

Stray inductance is caused by the external magnetic chains of the intersecting chains of the circuit loops. The location where the external magnetic chain is generated is shown in Fig. 3. The external magnetic chain at this location is calculated to obtain the stray inductance parameters for the different locations and the results are shown in the Table 1.
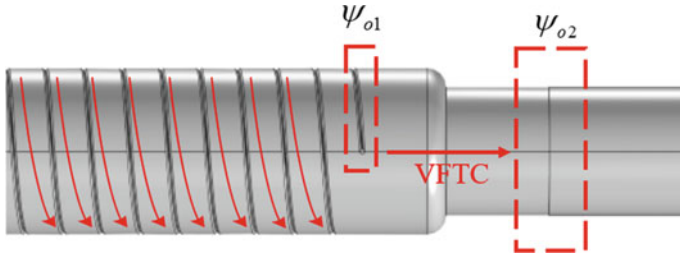
Fig. 3 Calculation of stray inductance

Table 1 Stray inductor parameters

Stray inductance	$L_{\sigma11}$	$L_{\sigma12}$	$L_{\sigma2}$
Value (pH)	40.2783	18.4562	18.4636

3.2 Calculation of Capacitance Parameters

As the damping busbar uses the "R + L" method to suppress the VFTO, this paper focuses on the calculation of the stray capacitance of the damped busbar.

(1) Principle of Stray Capacitance Calculation

For n conductors, it follows from the potential superposition theorem that:

$$\begin{pmatrix} Q_1 \\ Q_2 \\ . \\ . \\ Q_n \end{pmatrix} = C \begin{pmatrix} V_1 \\ V_2 \\ . \\ . \\ V_n \end{pmatrix} = \begin{bmatrix} c_{11} \, c_{21}...c_{n1} \\ c_{12} \, c_{22}...c_{n2} \\ . \\ . \\ c_{1n} \, c_{2n}...c_{nn} \end{bmatrix} \begin{pmatrix} V_1 \\ V_2 \\ . \\ . \\ V_n \end{pmatrix} \tag{5}$$

where, Q_i represents the charge of the i-th conductor; C is Maxwell's capacitance matrix which describes the relationship between the charge of the i-th conductor and the voltages of all conductors in the system. Thus, for n conductors, Maxwell's capacitance matrix can be expressed as:

$$C = \begin{bmatrix} \sum_{i=1}^{n} c_{m1i} & -c_{m12} \, ... & -c_{m1n} \\ -c_{m21} & \sum_{i=1}^{n} c_{m1i} \, ... & -c_{m2n} \\ . & & \\ . & & \\ -c_{mn1} & -c_{mn2} \, ... & \sum_{i=1}^{n} c_{mni} \end{bmatrix} \tag{6}$$

where, C_{mni} is the stray capacitance resulting from the accumulation of charge between the n conductor and the i conductor. Therefore, in this paper, the relationship between Maxwell's capacitance matrix and the mutual capacitance matrix will be used when solving for the stray capacitance of the damping busbar.

(2) Calculation of Stray Capacitance

Based on the principle of calculating stray capacitance, this paper has calculated $C_{\sigma 1}$, $C_{\sigma 2}$ and $C_{\sigma e0}$ in turn which is shown in Fig. 4. Equation (7) represents the mutual capacitance matrix of the 3-conductor system formed by the busbar connector, first and second turns; Eq. (8) represents the mutual capacitance matrix between the damping busbar and the conventional busbar; Eq. (9) is the mutual capacitance matrix between the damping busbar and the shell, and the stray capacitance parameters are obtained from the above mutual capacitance matrix as shown in the Table 2.

$$C_{m1} = \begin{bmatrix} 1.6103 \times 10^{-4} & 0.1871 & 1.0712 \times 10^{-2} \\ 0.1871 & 4.346 \times 10^{-5} & 0.1800 \\ 1.0712 \times 10^{-2} & 0.1800 & 1.1578 \times 10^{-4} \end{bmatrix} nF \tag{7}$$

$$C_{m2} = \begin{bmatrix} 2.1662 \times 10^{-4} & 5.1989 \\ 5.1989 & 1.6535 \times 10^{-4} \end{bmatrix} nF \tag{8}$$

$$C_m = \begin{bmatrix} 6.9767 \times 10^{-2} & 8.1486 \times 10^{-2} \\ 8.1486 \times 10^{-2} & 7.4527 \times 10^{-4} \end{bmatrix} nF \tag{9}$$
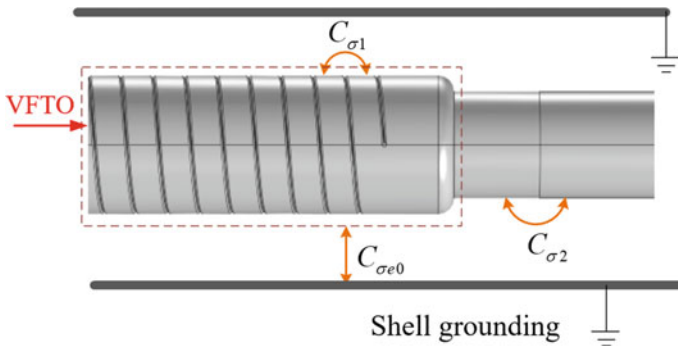
Fig. 4 Calculation of stray capacitors

Table 2 Stray capacitor parameters

Stray capacitance	$C_{\sigma 11}$	$C_{\sigma 12}$	$C_{\sigma 2}$	$C_{\sigma e0}$
Value (nF)	0.1800	0.1871	5.1989	3.2594×10^{-3}

3.3 Calculation of Breakdown Impedance

(1) Principle of Breakdown Impedance Calculation

Figure 5a shows the flow chart of the damping busbar breakdown impedance calculation. In order to obtain the electric field strength inside the GIS air chamber under VFTO conditions, VFTO shown in Fig. 2 is required as an excitation to analyze the transient electric field in each turn of the busbar air gap shown in Fig. 5b. Our group has carried out research on the breakdown criteria for SF_6 [10]:

$$E_d = E - E_{cr} = E - 1.467\rho \tag{10}$$

where: E is the electric field strength, kV/mm; E_{cr} is the gas critical breakdown field strength, kV/mm; ρ is the gas density, kg/m^3. When $E_d > 0$, the air gap is broken and SF_6 breakdown process can be considered as an arc model, and an exponential time-varying resistance model can be used to reflect the change in resistance in the channel during the whole process of a single discharge of SF_6 gas at high frequency discharge current:

$$R_v = R_0 e^{-\left(t/\tau\right)} + R_a, t \le t_0 \tag{11}$$

where, R_a is the static arc ignition resistance, $R_a = 0.5$ Ω; R_0 is the high resistance state when the disconnector is gap insulated, $R_0 = 10^{12}$ Ω; τ is the time constant, $\tau = 1ns$; t_0 is the SF_6 gas breakdown and stable combustion phase time, $t_0 = 1$ μs.
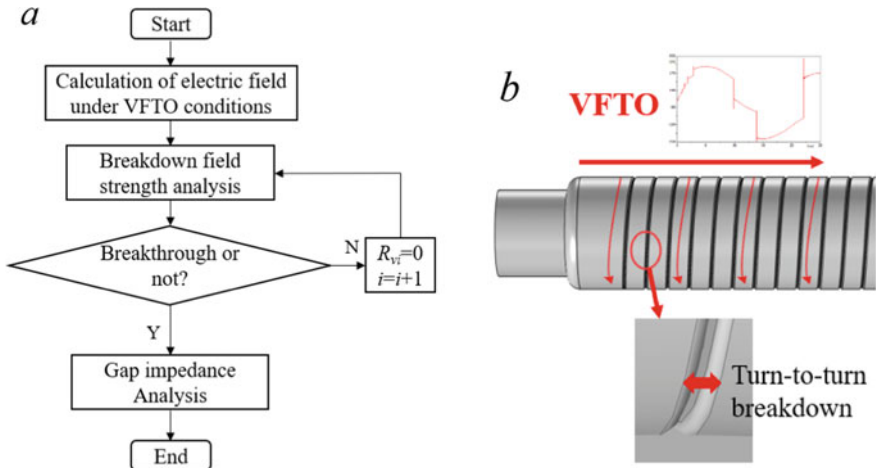
Fig. 5 a Calculation of damping busbar breakdown impedance. **b** Turn-to-turn breakdown of damping busbar
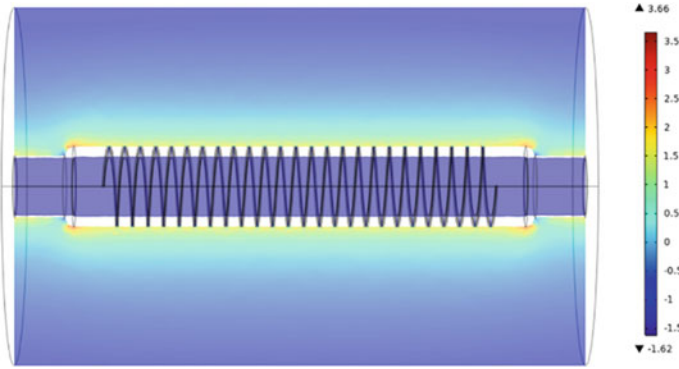
Fig. 6 Distribution diagram of E_d

(2)   Calculation of Breakdown Impedance Calculation

The VFTC excitation shown in Fig. 2 is applied to the damping busbar, and the vortex field-temperature field-flow field multi-physical field coupling simulation model is carried out for its SF_6 gas chamber. SF_6 breakdown margin E_d distribution of the gas chamber is obtained as shown in Fig. 6. Combined with Eq. (10), it can be judged that the gap breakdown occurs in the 1st, 5th, 19th, 23rd and 25th gaps of the busbar, so the damping busbar inter-turn breakdown resistance R_v can be expressed as Eq. (12).

$$R_v(i) = \begin{cases} 0 & i \neq 1, 5, 19, 23, 25 \\ R_0 e^{-\frac{t}{\tau}} + R_a & i = 1, 5, 19, 23, 25 \end{cases} \qquad (12)$$

3.4   Full-Circuit Model of Damping Busbar

Based on the results of the previous circuit parameter calculations, a full-circuit model of the damping busbar is constructed as shown in Fig. 7, with the specific parameter values shown in Table 3.
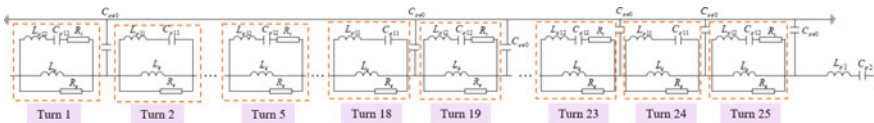
Fig. 7 Full-circuit model of damping busbar

Table 3 Full-circuit parameters

Parameters	L_e	R_e	$C_{\sigma 11}$	$L_{\sigma 11}$	$C_{\sigma 12}$	$L_{\sigma 12}$	$C_{\sigma 2}$	$L_{\sigma 2}$	$C_{\sigma e0}$
Value	0.432 uH	4 Ω	0.1800 nF	40.2783 pH	0.1871 nF	18.4562 pH	5.1989nF	18.4636 pH	3.2594×10^{-3}nF

4 Analysis of Effect of Full-Circuit Parameters on VFTO Suppression

Taking a typical 550 kV GIS circuit as an example shown in Fig. 8a, the VFTO suppression effect after the addition of damping busbar is analyzed by varying each parameter of the full circuit model of the damping busbar to obtain the amplitude U_m, maximum wavefront steepness K_{max} and waveform energy Q of the VFTO as shown in the Table 4.

According to the Table 4, L_e mainly affects K_{max}, R_e can weaken the VFTO energy Q; while the stray capacitance $C_{\sigma e0}$ between the damping bus and the GIS shell will have a greater impact on the VFTO suppression effect, in Fig. 8b, as the shell stray capacitance increases, the amplitude, energy and maximum wavefront steepness of the VFTO will be reduced. On the contrary, the remaining stray parameters have less influence on the VFTO suppression effect. This is because they are essentially part of the damping busbar body parameters and their values are negligible compared to the damping busbar coil inductance.
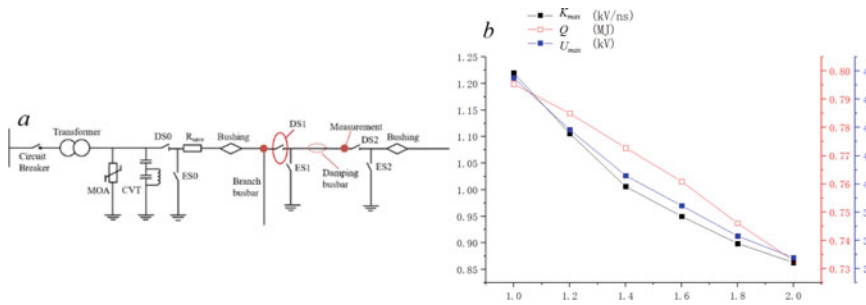
Fig. 8 **a** The simulation model. **b** Effect of shell stray capacitance on VFTO suppression

Table 4 Results of VFTO suppression with different parameters

Parameters	Full-circuit model	$2*R_e$	$2*Le$	$2*C_{\sigma e0}$	$2*C_{\sigma 2}$	$2*C_{\sigma 1}$	$2*L_{\sigma 1}$
U_{max}	475.21	473.6	472.6	347.7	475.21	475.27	475.21
K_{max}	1.22	1.20	0.67	0.863	1.22	1.22	1.22
Q	0.7954	0.7236	0.7953	0.7328	0.7953	0.7954	0.7954

In summary, when designing the damping busbar and analyzing its effect, the full-circuit model of the damping busbar should be used to study it, and in addition to considering the value of the damping busbar body inductance and shunt resistance, the shell stray capacitance should also be considered when designing the damping busbar to improve the suppression effect of the VFTO.

5 Summary

This paper develops a full-circuit parameter model for damping busbars and calculates all parameters. The effect of these parameters on VFTO suppression is analyzed, revealing the importance of considering various stray capacitances and inductances when building the equivalent model. Specifically, the stray inductance between the damping busbar and GIS shell is found to affect the amplitude, wavefront steepness, and energy of VFTO, highlighting the need for greater attention to stray parameters during subsequent design.

References

1. Sheng M, Ding D, Li Q (2022) Construction of VFTO measurement system and waveform analysis for switching test duty 1 of short busbar by GIS disconnector. High Voltage Apparatus 58(7):0207–0213 (in Chinese)
2. Li B, Zhao G, Ke X (2023) Simulation study on the damped bus equivalent device in GIS. Insulators Surge Arresters 311(1):199–207 (in Chinese)
3. He T, Gao Y, Liu X (2022) Numerical simulation and suppression measure for VFTO in 550 kV GIS substation. Proc CSU-EPSA 34(2):65–69 (in Chinese)
4. Nan B, Liu X, Lei F (2017) Review of research on VFTO protective measures in GIS. Insulators Surge Arresters 6:81–85 (in Chinese)
5. Yamagata Y, Tanaka K, Nishiwaki S et al (2002) Suppression of VFT in 1100 kV GIS by adopting resistor-fitted disconnector. IEEE Trans Power Delivery 11(2):872–880
6. Almenweer RA, Su Y, Wu X (2019) Numerical analysis of a spiral tube damping busbar to suppress VFTO in 1000 kV GIS. Appl Sci
7. Zhang W, Hu Y (2022) Research progress on suppression of fast transient overvoltage VFTO in GIS. High Voltage Eng (in Chinese). https://doi.org/10.13336/j.1003-6520.hve.20211725
8. Lin H, Zhang Z, Liu H et al (2022) Interference to the secondary cable caused by a very fast transient overvoltage in a gas-insulated switchgear substation. Math Probl Eng 2022
9. Wu X, Feng X, Hu Y (2021) Research on inductor characteristic of spiral tube damping busbar based on optimal VFTO suppression effect (in Chinese). https://doi.org/10.13335/j.1000-3673.pst.2021.1033
10. Pang W, Wu X, Wu S (2020) Compact design of 330 kV SF6/N2 mixed gas insulated busbar. High Voltage Eng 46(3):1043–1050 (in Chinese)

Sampling Inspection Method of Power Grid Materials Based on Analytic Hierarchy Process

Jing Lei, Jian Lu, Shitao Li, Bin Tai, Cuiru Yang, Jia Li, Yaru Zheng, and Yingshan Wu

Abstract Daily sampling inspection is crucial for identifying and eliminating hidden dangers in power grid materials. However, traditional sampling inspection methods that rely on experience often lead to a wastage of resources and manpower. Hence, there is a need to find a suitable method for sampling inspection of power grid materials. This paper proposes a mathematical model to evaluate the quality level of power grid materials in the sampling inspection process. The model involves data cleaning of the original data of power grid materials to obtain the standard data of operational quality. The analytic hierarchy process is then used to analyze the standard data of material quality, enabling the determination of the quality level of each supplier's materials. Based on the theory of Acceptance Quality Limit, the foundation of the sampling inspection method for each supplier's materials is established.

Keywords Power grid materials · Sampling inspection · Analytic hierarchy process · Acceptance quality limit

1   Introduction

In recent years, the development of an effective sampling inspection method for power grid materials has become a pressing issue, as it greatly influences their quality. The selection of appropriate sampling standards is a critical part of the materials' full life cycle quality. Given that the management and control levels of power grid materials are subject to various factors, the selection of standards must be tailored to

J. Lei (✉) · S. Li · B. Tai · C. Yang · J. Li · Y. Zheng
Electric Power Research Institute of Guangdong Power Grid Co., Ltd., Guangzhou 510080, China
e-mail: weijuntao@gddky.csg.cn

J. Lu
CSG Digital Enterprise Technology (Guangdong) Co., Ltd., Guangzhou 510080, China

Y. Wu
Guangdong Power Grid Co., Ltd., Guangzhou 510080, China

the specific material in question. Factors such as the equipment cost and inspection complexity, as well as their importance in the power grid, must be considered.

At present, different power grid companies use varying standards for sampling inspection, but many of these standards are not based on scientific approaches. These companies often select small sample sizes randomly, which can lead to high risks of future failure. Researchers are actively seeking scientific methods to evaluate the standards of sampling inspection for power grid materials. The Acceptance Quality Limit (AQL) is a scientifically recognized measurement for sampling inspection. Lower AQL values indicate more stringent inspection requirements. Many international standards, including MIL-STD-1916, ISO/TS 16949, GB2828, among others, use AQL for selecting the sampling scheme.

Several studies have focused on the scientific determination of Acceptance Quality Limit values for sampling inspection. For example, Huang [1] discusses the basic principles that must be followed when determining AQL and explores the application of different methods, such as the process average method, reference method, back-stepping method, and product qualification rate. Xie [2] proposes an AQL design method based on improved inductive classification, which takes into account the specific situations of materials and equipment in power supply enterprises. Jing [3] presents an optimized AQL numerical computer system that can determine the AQL value. The system's five functions are described and studied in detail. While these studies provide a basis for this work, the determination of AQL values requires further investigation.

In this paper, a novel method is proposed for analyzing the quality of power grid materials and determining the Acceptance Quality Limit. While the cost of equipment and inspection, the number of inspection items, and their importance are known, determining the historical quality level of suppliers is often challenging due to the lack of scientific sampling inspection. To overcome this challenge, a data cleaning model is employed to obtain the standard data of operational quality from the original data of power grid materials. Subsequently, the analytic hierarchy process is utilized to analyze the standard data of material quality and obtain the quality level of each supplier's materials. Using the AQL theory, a sampling inspection method can be established for each supplier's materials.

2 Data Cleaning

2.1 Text Matching

The non-standard quality operation data, which includes sampling, defects, and failure, presents a challenge in directly analyzing the quality level of each supplier's materials. One of the main issues is the lack of uniformity in supplier and material name identification. To address this problem, text-matching tools based on Fuzzy-Wuzzy [4] can be used. Fuzzy-Wuzzy calculates the similarity between two strings
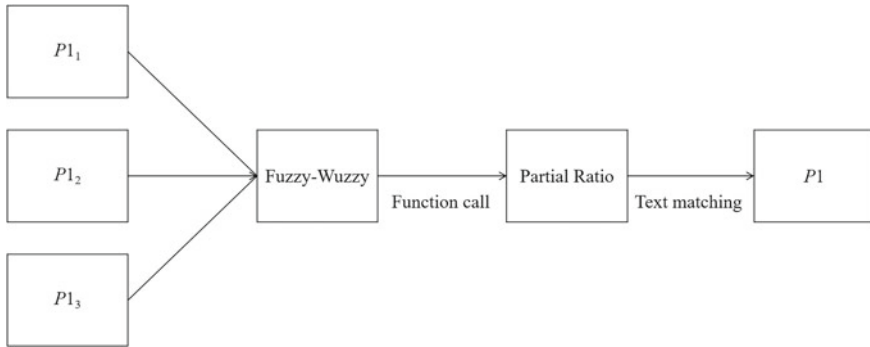
Fig. 1 Text matching process

based on the Levenshtein Distance algorithm, which measures the minimum number of editing operations required to convert one string to another. Permitted editing operations include character replacement, insertion, and deletion. The smaller the edit distance, the higher the similarity between the two strings.

Using Fuzzy-Wuzzy and the Partial Ratio function, we can fuzzily match different names of the same supplier and the same material. Suppose $P1$ is the original name, and $P1_1$, $P1_2$, and $P1_3$ are its derivatives. We can use Fuzzy-Wuzzy to calculate the similarity between $P1$ and its derivatives. If the similarity score is above the critical value, we can match $P1$'s derivatives to $P1$. This ensures that all the names of derivatives are changed to standard forms. Figure 1 illustrates the text-matching process.

2.2 Database of Quality

Following the text matching process, the resulting database of quality provides more accurate statistics. The quality level is reflected by seven key factors, including the number of contracts ($C1$), sampling number ($C2$), number of conforming products ($C3$), percent of passes ($C4$), number of failures ($C5$), average outage time (hour) ($C6$), and number of defects ($C7$). These factors are used to assess the quality level of each supplier's materials. Table 1 illustrates the quality data for 10 kV vacuum column circuit breakers from three different suppliers ($P1$, $P2$, and $P3$).

Table 1 Quality data of 10 kV vacuum column circuit breaker

Supplier	$C1$	$C2$	$C3$	$C4$	$C5$	$C6$	$C7$
$P1$	411	8	7	0.875	1	4.42	9
$P2$	180	4	3	0.75	1	12.55	8
$P3$	99	4	1	0.25	4	21.24	15

Once the data is collated, an appropriate method is needed to analyze the results and evaluate the suppliers' historical quality level. The same method is also applicable to other power grid materials.

3 Analytic Hierarchy Process

After collating the data, it is necessary to choose the appropriate method to analyze the data. The main purpose is to evaluate the suppliers' historical quality level.

3.1 Model Establishment

The analytic hierarchy process (AHP) is a decision-making method consisting of three levels: objective, criterion, and plan, which allows for both qualitative and quantitative analysis [5–7]. This hierarchical weight decision analysis method utilizes network system theory and a multi-objective comprehensive evaluation method developed by Saaty [8, 9].

3.2 Establish Hierarchical Structure Model

In AHP, decision-making objectives, criteria, and plans are categorized into the highest level, middle level, and lowest level based on their interrelationships, and a hierarchical structure diagram is created. The highest level denotes the decision-making objective and the problems to be addressed, the lowest level pertains to the plans in decision-making, and the middle level corresponds to the criteria considered for decision-making. The high level is referred to as the target level, and the low level is the factor level for the adjacent two levels [10]. Figure 2 presents the specific hierarchical structure.

The objective of our study is to determine the quality level of different suppliers, and the criteria considered are used to evaluate each supplier.

3.3 Constructing Judgement Matrix

To ensure the acceptance of the weights assigned between factors at different levels, the consistent matrix method is used [11]. This involves comparing all factors with each other, and a relative scale is used to minimize the difficulty of comparing factors with different properties to improve accuracy. For a given criterion, its elements are compared with each other and graded according to their importance. a_{ij} is the
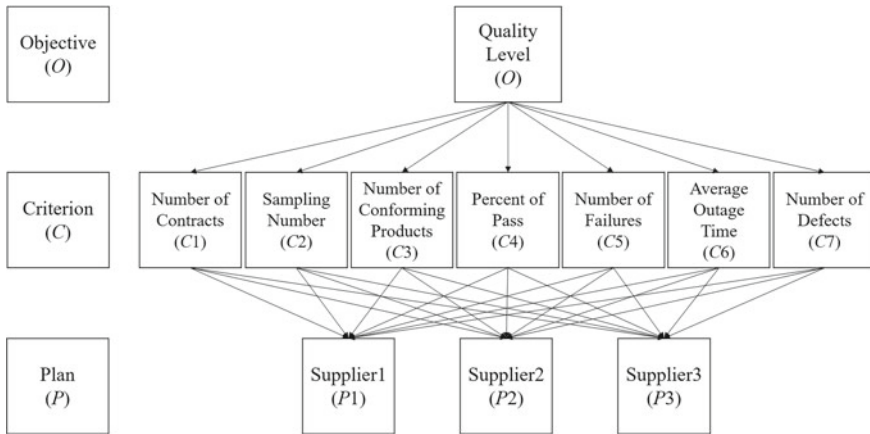
Fig. 2 Hierarchical structure

comparison result of factor *i* and factor *j*. The matrix formed by pairwise comparison results is called the judgment matrix, which has following properties:

$$a_{ij} = \frac{1}{a_{ji}} \tag{1}$$

Saaty's method assigns nine importance levels to the elements of a judgment matrix, which is formed by pairwise comparison results. The pairwise comparison scale for AHP preference is shown in Table 2. In Table 3 (judgment matrice 1), power grid experts' opinions on the relative importance of the seven criteria for evaluating suppliers' historical quality level are shown. Each criterion is assigned a value based on its importance compared to other criteria, and a reciprocal value is assigned when one criterion is less important than another. A value of 1 is assigned to all elements on the diagonal of the pairwise comparison matrix since each criterion is equally important when compared against itself.

To compare suppliers based on different factors, judgment matrices 2–8 are created. For example, the judgment matrice 2 is shown in Table 4, using the original

Table 2 Pairwise comparison scale for AHP preference

Numerical rating	Verbal judgment of preference
1	Equally preferred (or important)
3	Moderately preferred (or more important)
5	Strongly preferred (or more important)
7	Very strongly preferred (or more important)
9	Extremely preferred (or more important)
2, 4, 6, 8	Intermediate value

Table 3 Comparison of criteria concerning the supplier's historical quality level

Factor	C1	C2	C3	C4	C5	C6	C7
C1	1	3	0.2	3	0.25	0.25	0.25
C2	0.33	1	0.2	3	0.2	0.2	0.2
C3	5	5	1	3	0.33	0.33	0.33
C4	0.33	0.33	0.33	1	0.25	0.25	0.25
C5	4	5	3	4	1	2	1
C6	4	5	3	4	0.5	1	0.5
C7	4	5	3	4	1	2	1

Table 4 Comparison of suppliers concerning the number of contracts

	C1	P1	P2	P3
P1	1		2	4
P2	0.5		1	2
P3	0.25		0.5	1

quality data. And judgment matrices 3–8 are comparison of suppliers concerning other criteria which are omitted due to space limitation.

3.4 Consistency Checking

Suppose an $n \times n$ judgment matrix is called A. If Ax is a scalar multiple of the non-zero vector x, λ is the eigenvalue of A, that is, $Ax = \lambda x$. It can be proved that if the judgment matrix is a consistent matrix, then the judgment matrix has an eigenvalue equal to n. If the judgment matrix is inconsistent, then the maximum eigenvalue $\lambda_{\max} > n$. The deviation from consistency is represented by the consistency index, as follows:

$$CI = \frac{\lambda_{\max} - n}{n - 1} \tag{2}$$

The consistency index (CI) represents the degree of deviation from perfect consistency, and a lower CI indicates a more consistent evaluation. A CI of zero indicates perfect consistency. To assess the consistency of each decision maker's evaluation, we use the critical ratio (CR). After calculating the eigenvalues, the corresponding random index RI needs to be determined. T.L. Saaty has established the following random indices in Table 5 for this purpose.

The next step involves calculating the critical ratio CR. A CR value below 0.1 indicates an acceptable consistency of the judgment matrix, whereas a higher value suggests that the judgment matrix requires modification. The critical ratio is defined

Table 5 Random index *RI*

n	RI
1	0
2	0
3	0.52
4	0.89
5	1.12
6	1.26
7	1.36
8	1.41
9	1.46
10	1.49

Table 6 Consistency checking of judgment matrices

Judgment matrix	CI	CR
Judgment matrix 1	0.12	0.09
Judgment matrix 2	-4.44×10^{-16}	-8.54×10^{-16}
Judgment matrix 3	-4.44×10^{-16}	-8.54×10^{-16}
Judgment matrix 4	-0.0036	-0.007
Judgment matrix 5	0.0028	0.0053
Judgment matrix 6	-4.44×10^{-16}	-8.54×10^{-16}
Judgment matrix 7	0.00028	0.00053
Judgment matrix 8	-4.44×10^{-16}	-8.54×10^{-16}

as follows:

$$CR = \frac{CI}{RI} \tag{3}$$

Table 6 presents the consistency indices (*CI*) and critical ratios (*CR*) of all the judgment matrices. As all the *CR* values are less than 0.10, the consistency of the judgment matrices can be considered acceptable.

3.5 Geometric Mean Method to Calculate Weight

According to Aczél and Saaty [12], the geometric mean method is an appropriate rule for combining judgments in the AHP model as it maintains the reciprocal property in the combined pairwise comparison matrix. The results of the factor weight are shown in Table 7, and the calculation method of the factor weight is as follows:

Table 7 Factor weight

Factors	Weight	P1	P2	P3
C1	0.0658	0.5714	0.2857	0.1429
C2	0.0436	0.5	0.25	0.25
C3	0.1263	0.6158	0.2925	0.0917
C4	0.0376	0.4581	0.4162	0.1256
C5	0.2649	0.4444	0.4444	0.1111
C6	0.1968	0.6488	0.2291	0.1221
C7	0.2649	0.4	0.4	0.2

$$A = \begin{pmatrix} a_{11} & \cdots & a_{1n} \\ \vdots & \ddots & \vdots \\ a_{n1} & \cdots & a_{nn} \end{pmatrix} \tag{4}$$

$$\omega_i = \frac{(\prod_{j=1}^{n} a_{ij})^{\frac{1}{n}}}{\sum_{k=1}^{n} (\prod_{j=1}^{n} a_{kj})^{\frac{1}{n}}}, \quad i = (1, 2, \ldots, n) \tag{5}$$

4 Results of Quality Level and AQL

Once the factor weights have been calculated, quality level scores can be obtained for different suppliers. These scores are used to classify suppliers into three quality levels. The quality level can then be utilized to determine the AQL for each supplier.

4.1 Quality Level

The quality level scores of different suppliers can be calculated using Table 7. To calculate the score, we multiply the weight of the supplier in each factor by the weight of the factor itself, and then add them up. The score of $P1$ is defined as follows:

$$score_{P1} = \sum_{i=1}^{7} \omega_{Ci} \cdot \omega_{P1i} \tag{6}$$

ω_{Ci} is the weight of factor $Ci(i = 1, 2, \ldots, 7)$, and ω_{P1i} is the weight of $P1$ in factor Ci. The quality level scores are listed in Table 8.

Table 8 Quality level scores of different suppliers

Supplier	Score
P1	0.50576362
P2	0.35105937
P3	0.14304676

Table 9 Quality level of different suppliers

Supplier	Level
P1	High
P2	Middle
P3	Low

The results of quality level scores reveal that supplier *P*1 has the highest quality score, whereas supplier *P*3 has the lowest. Based on these scores, suppliers can be classified into three different quality levels, which are presented in Table 9.

4.2 Determine the Value of AQL

The value of AQL is determined based on several factors including the cost of equipment and inspection, the number of inspection items, importance, and quality level. Figure 3 presents the determination rule for AQL.

Using the factors of cost of equipment and inspection, number of inspection items, importance, and quality level, we determined the value of AQL for the 10 kV vacuum column circuit breaker. We utilized the quality levels of the three suppliers to calculate the AQL values, which are presented in Table 10.

With the obtained AQL values, sampling schemes can be selected according to the chosen standard.

Number of inspection items	Importance	Cost	Quality level	Adviced AQL value
				0.65
				1.0
				1.5
				2.5
				4.0
				6.5
Low	High	High	Low	
			Middle	
High	Low	Low	High	

Fig. 3 Determination rule of AQL

Table 10 AQL of different suppliers

Supplier	AQL
P1	2.5
P2	1.5
P3	1.0

5 Conclusion

Based on the results of this study, a sampling inspection method for power grid materials has been proposed. The data cleaning process effectively removed non-standard data, ensuring the accuracy and reliability of the subsequent analysis. The AHP model was applied to obtain the quality level scores of the suppliers, which allowed us to determine their quality levels. By using the determination rule of AQL, the AQL values of the suppliers were calculated, which can be used to search for the appropriate sampling schemes in sampling inspection standards.

The proposed method provides a practical solution for power grid materials inspection, allowing for efficient and effective sampling of materials while maintaining high levels of quality assurance. This method has the potential to be applied in various industries, where quality control is essential, and can contribute to improving the overall quality and safety of products.

References

1. Huang H, Xue L, Zeng Z, Yi X, Liang X (2005) The confirmation of acceptance quality limit in product sampling scheme. China Wood-Based Panels 11:26–28 (in Chinese)
2. Xie J (2014) Application of acceptance quality limit in quality control of power supply enterprises. Technol Market 21(4):187–188+190. (in Chinese)
3. Jing G, Jing H, Jing Y, Hao L (2007) Research on the design theory of numerical computer system with acceptance quality limit. Popular Stand S1:72–75 (in Chinese)
4. Rao PJ, Rao KN, Gokuruboyina S (2022) An experimental study with fuzzy-wuzzy (partial ratio) for identifying the similarity between English and French languages for plagiarism detection. Int J Adv Comput Sci Appl 13(10):393–401
5. Wang G, Dang P, Li Y (2022) Research on the evaluation system of new energy development decision in Dunhuang city based on analytic hierarchy process. Energy Rep 8(S8):129–135
6. Attajer A, Darmoul S, Chaabane S, Sallez Y, Riane F (2022) An analytic hierarchy process augmented with expert rules for product driven control in cyber-physical manufacturing systems. Comput Ind 143:103742
7. Redfoot EK, Verner KM, Borrelli RA (2022) Applying analytic hierarchy process to industrial process design in a nuclear renewable hybrid energy system. Prog Nucl Energy 145:104083
8. Saaty TL (1977) Scaling for priorities in hierarchical structures. J Math Psychol 15(3):234–281
9. Saaty TL (2008) Decision making with the analytic hierarchy process. Int J Serv Sci 1(1):83–98
10. Saaty TL (1986) Axiomatic foundations of the analytic hierarchy process. Manage Sci 32(7):841–855
11. Kandel A (1983) The analytic hierarchy process-planning, priority setting, resource allocation. In: Saaty TL (ed) McGraw-Hill, Basel (1980), 287. Fuzzy Sets and Systems 9(S1–3), 216–217
12. Aczél J, Saaty TL (1983) Procedures for synthesizing ratio judgments. J Math Psychol 27(1):93–102

Analysis of Damage Expansion and Mechanical Strength in End Insulation for High-Power AC Motor with Initial Defects

Bangwei Zhang, Haijun Zhang, Mingjie Zhang, and Haifeng Kong

Abstract With the rapid development of modern industry, the demand for stable operation of high-power AC motors is increasing. The insulation performance of the stator end winding of the motor directly affects whether the motor can operate reliably. There is a multi-physical field environment inside the high-power AC motor, and the complex physical environment affects the insulation failure of the stator end winding. In this paper, the finite element analysis of the non-destructive stator end winding insulation layer is carried out by coupling electromagnetic power and mechanical force. The analysis results show that the insulation layer at the slot outlet and the nose end is most vulnerable to damage, and then three-dimensional arbitrary cracks are added to analyze the insulation damage. Finally, the stress strength factor theory is used to analyze the propagation law of insulation cracks. Through the analysis results, it is found that the crack at the notch is easier to expand than the nose crack in the multi-physical field environment. In this paper, the failure behavior of insulation damage of high power AC motor is studied, which provides a reliable theory for the production of AC motor in the early stage and the fault maintenance and prediction in the later stage.

Keywords AC motor · Insulation damage at stator end · Stress intensity factor · Finite element analysis

1 Introduction

AC motor is the most important driving device in industry, and it is also a common electromagnetic mechanical equipment. In industry, AC motor is an important part of ensuring the normal production capacity of factories [1–3]. Because in industrial production, the traction motor is required to have sufficient kinetic energy and to

B. Zhang · H. Zhang (✉) · M. Zhang · H. Kong
Hubei Superior and Distinctive Discipline Group of "New Energy Vehicle and Smart Transportation", Hubei University of Arts and Science, Xiangyang 441053, China
e-mail: hjzhang0515@163.com

work continuously for a long time, the demand for stable and reliable AC motors in the factory is gradually increasing. The complex multi-physical field working environment inside the AC motor will easily lead to generator failure when it is overloaded for a long time. Statistics show that end winding failure is one of the main causes of high-power AC motor accidents directly or indirectly [4, 5]. Figure 1 is the health and insulation failure diagram of stator end winding of high-power AC motor. Because the end winding of the AC motor works in a variety of complex physical fields such as electromagnetic field, mechanical stress field and temperature field for a long time, the end winding will be affected by unbalanced stress and strain, resulting in cracks in the insulation layer [6]. The expansion of cracks will cause insulation failure, which will lead to abnormal kinetic energy generated by generator failure, resulting in loss of production capacity and economy of the factory. Therefore, it is of great value to analyze and study the failure principle of end winding insulation damage of high-power AC motor.

Generally speaking, before the occurrence of electrical faults, early mechanical faults will first occur. For example, under the working state of the motor, the end winding is affected by the dynamic stress and strain, which will cause mechanical wear and aging of the end winding insulation layer. Normal insulation is a necessary condition to ensure the normal operation of the motor. Therefore, it is necessary to analyze and study the root cause of mechanical failure caused by end winding insulation damage. The electromagnetic force generated by the motor in the working state is one of the important reasons for the stress and deformation of the insulation layer. Because the structure of the stator end winding is very complex, the leakage magnetic field and electromagnetic field of the end winding are analyzed and studied at present, and the three-dimensional model finite element method is mainly used to accurately analyze and study it. At present, researchers have systematically analyzed the electromagnetic–mechanical coupling and vibration principle of the internal conductor part of the end winding, such as using the finite element method (FEM) to determine the natural frequency and vibration mode of the end winding of the turbine generator
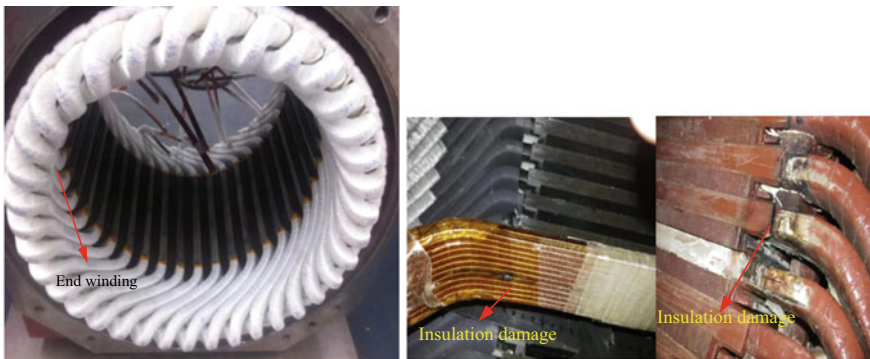
Fig. 1 End winding binding constraint graph

[7]. In addition, the research on the temperature field calculation and dynamic vibration analysis of the stator end winding has also attracted more researchers [8–10]. At present, there are few studies on the degree of stress and deformation damage and systematic mechanism of insulation damage with initial defects in end windings. In fact, due to the production process and processing defects, in the end winding production and processing stage, the insulation layer is difficult to avoid the initial crack defects and cavity defects, which is one of the important factors that cause insulation damage until insulation breakdown.

In this paper, the insulation damage fault caused by the initial arbitrary crack defect on the surface of the insulation layer is taken as the research object, and the insulation damage fault is studied by theoretical analysis and experimental verification. Firstly, the theoretical analysis of the damage and fracture behavior of the insulation layer of the end winding is carried out. According to the theoretical analysis, an effective three-dimensional analysis model is established for accurate finite element analysis to determine the magnetic flux density distribution around the internal conductor of the end winding under the working state of the motor. The calculated data are used to analyze the weak points of stress and deformation in the insulation layer of the end winding. In order to systematically study the insulation failure caused by the degree of crack propagation, the fracture analysis and stress strength factor theory are used to systematically analyze the degree of crack propagation.

2 End Winding Force Analysis Theory

2.1 Electromagnetic Force Analysis Theory

The electromagnetic force on the end winding of the motor in the working state is complex and unevenly distributed and has alternating characteristics. The end winding is subjected to a large displacement and deformation caused by a strong electromagnetic force. Calculating the electromagnetic force of the winding is the premise of analyzing the winding displacement.

Based on the equations of Maxwell, the electromagnetic field control equation for solving the magnetic potential vector A is can be expressed as follows:

$$\nabla \times (\frac{1}{\mu} \nabla \times \boldsymbol{A}) = \frac{i(t)}{s} \tag{1}$$

In the formula: $i(t)$ is the current in windings; μ denotes the permeability; s denotes the cross-sectional area of the conductor.

The magnetic flux density is calculated by combining the magnetic vector potential. According to the Lorentz force law, the electromagnetic force generated at a certain point on the end winding can be expressed as:

$$F = J \times B \tag{2}$$

In the formula: F is electromagnetic power; J is the current density; B is the magnetic flux density.

2.2 Analysis Theory of Dynamic Mechanical Stress

The end winding of the motor is subjected to a changing electromagnetic power in the working state, the conductor and insulation layer of the stator end winding produce internal stress and strain. The equilibrium differential equation of the relationship between internal stress and external electromagnetic force in space problem is given:

$$\begin{cases} \frac{\partial \sigma_x}{\partial x} + \frac{\partial \tau_{yx}}{\partial y} + \frac{\partial \tau_{zx}}{\partial z} + f_x = 0 \\ \frac{\partial \tau_{xy}}{\partial x} + \frac{\partial \sigma_y}{\partial y} + \frac{\partial \tau_{zy}}{\partial z} + f_y = 0 \\ \frac{\partial \tau_{xz}}{\partial x} + \frac{\partial \tau_{yz}}{\partial y} + \frac{\partial \sigma_z}{\partial z} + f_z = 0 \end{cases} \tag{3}$$

In the formula, $\sigma_x, \sigma_y, \sigma_z$ are normal stress components respectively: $\tau_{xy} = \tau_{yx}, \tau_{xz} = \tau_{zx}, \tau_{zy} = \tau_{yz}$ are shear stress components, respectively. For insulating materials, the force that causes stress and strain is the action of the conductor. The complete electromagnetic power in the electromagnetic field is introduced into the structural field of the workbench for magnetic-solid coupling analysis.

The geometric equation expresses the relationship between strain and displacement in space:

$$\begin{cases} \varepsilon_x = \frac{\partial u}{\partial x} \quad \gamma_{xy} = \frac{\partial u}{\partial y} + \frac{\partial v}{\partial x} \\ \varepsilon_y = \frac{\partial v}{\partial y} \quad \gamma_{xz} = \frac{\partial u}{\partial z} + \frac{\partial w}{\partial x} \\ \varepsilon_z = \frac{\partial w}{\partial z} \quad \gamma_{yz} = \frac{\partial v}{\partial z} + \frac{\partial w}{\partial y} \end{cases} \tag{4}$$

In the formula: u, v and w represent the displacement components, respectively.

2.3 Fracture Analysis

The paper suppose that there are primal crack defects on the surface of the winding insulation layer for research and analysis. The influence of the conductor on the crack of the insulating layer under the magnetic-solid coupling. By using the stress strength factor theory, the crack propagation of the insulating layer with primal crack defects is analyzed [11, 12].

Table 1 Arguments of AC machine and stator end-windings

Parameter	Value	Unit
Core inner diameter for stator	445	mm
Core outer diameter for stator	850	mm
Rated power	2800	kW
Rated voltage	10	kV
Insulation Poisson's ratio	0.41	–
Elastic modulus value for insulation	1.1	Gpa
Ratio of conductor Poisson	0.326	–
Elastic modulus of conductor	119	Gpa

$$\begin{cases} K_{\mathrm{I}} = \sqrt{2\pi}\,\frac{2G}{1+k}\,\frac{|v|}{\sqrt{r}} \\ K_{\mathrm{II}} = \sqrt{2\pi}\,\frac{2G}{1+k}\,\frac{|u|}{\sqrt{r}} \\ K_{\mathrm{III}} = \sqrt{2\pi}\,2G\,\frac{|w|}{\sqrt{r}} \end{cases} \tag{5}$$

In the formula, K_{I}, K_{II}, K_{III} are the stress strength factors corresponding to three different variant forms of open crack, shear crack and tear crack, respectively, and r is the coord of the partial coord system. The stress strength factor is an important arguments representing the stress and strain near the crack tip. The stress strength factor can describe the fracture of the insulating layer and determine whether the crack is easier to expand.

3 Numerical Examples and Results Analysis

3.1 Motor and End Winding Parameters

Taking a three-phase AC traction motor as an example, the main parameters of the end winding structure constraint simulation model are revealed Table 1.

3.2 Three-Dimensional Finite Element Electromagnetic Force Calculation

Figure 2 is the magnetic flow thickness distribution map of the stator end winding range. The nonlinear B-H curve of the core material is used to analyze the magnetic equilibration characteristics of the stator core. Set the boundary conditions, assuming that the magnetic flow thickness in the atmosphere and round the end winding is zero.
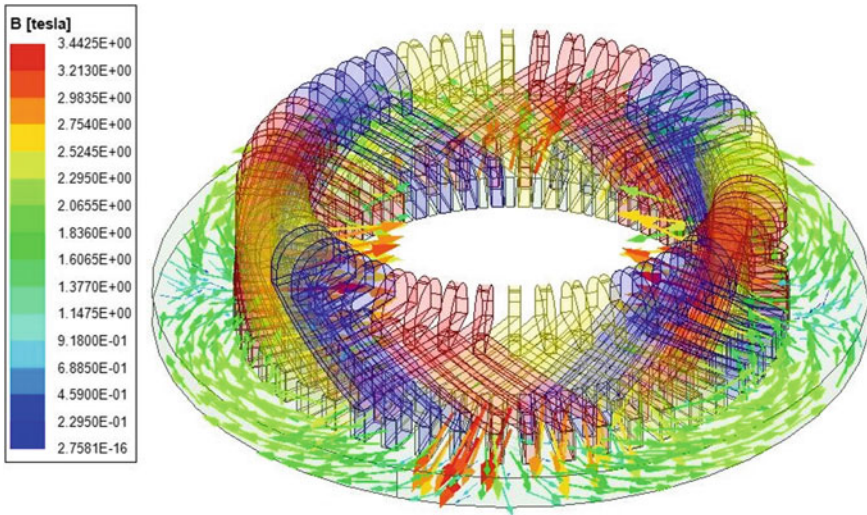
Fig. 2 Magnetic flow thickness allocation on stator end region

It can be concluded from Fig. 2 that the allocation of magnetic flow thickness in the stator slot is different, and the allocation of magnetic flow thickness along the end winding is not uniform. The uneven allocation of magnetic flow thickness density affects that the electromagnetic force on the end winding is unbalanced. In turn, the unbalanced strain of the end winding is caused, which makes it easier for any cracks in the insulation layer to expand, which directly reduces the theoretical service life of the motor.

3.3 Mechanical Calculation of Insulating Layer

The three-dimensional finite element analysis model is analyzed, mainly for the analysis of the end winding. In order to improve the analysis efficiency and accuracy, this paper only selects a single end winding for the analysis of the insulation layer characteristics of the end winding. The single end winding model is composed of copper conductor and insulation layer. It is assumed that the performance of the insulating layer is in a completely healthy working state, and the inner surface of the insulating and the external surface of the cuprum conductor are in complete link with each other. Through the finite element analysis of the electromagnetic power of the interior conductor and the mechanical stress coupling of the end winding obtained from the previous calculation, the deformation and stress of a single end winding under multiple physical fields can be determined. Figure 3a–d shows the variant and stress distribution of the conductor and insulation along the end winding respectively.

(a) Conductor displacement (b) Insulation layer displacement

(c) Conductor stress (d) Insulation layer stress
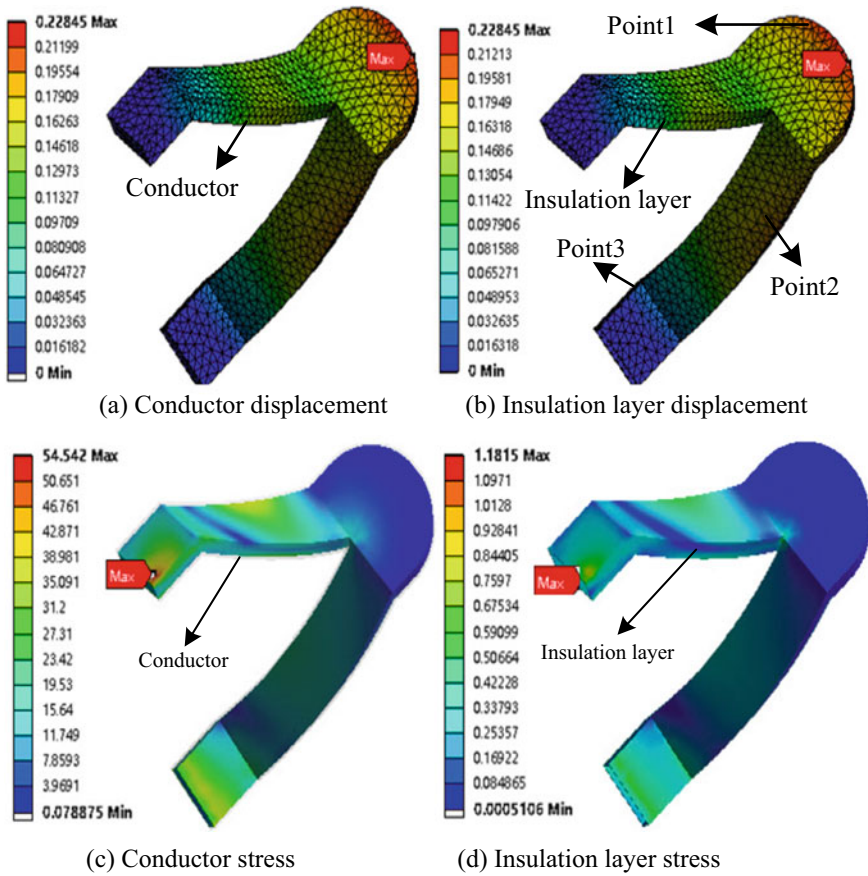
Fig. 3 Deformation and stress distribution of the end winding (t = 0.026s)

By comparing the results of (a) and (b), The insulation and conductor have roughly the same variant apportion. Through the comparison of (c) and (d) results, it can be seen that the stress apportion in the insulation is different from that of the conductor, but the largest part of the concentrated stress is mainly distributed near the outlet of the slot, which indicates that the end winding insulation layer may be more prone to damage or crack propagation.

3.4 Insulation Layer Crack Calculation and Analysis

In the practical application of the motor, the beginning crack defects lead to by vibration friction may occur at different positions of the end winding. Based on the results of variant and stress apportion feature of electromagnetic–mechanical coupling finite
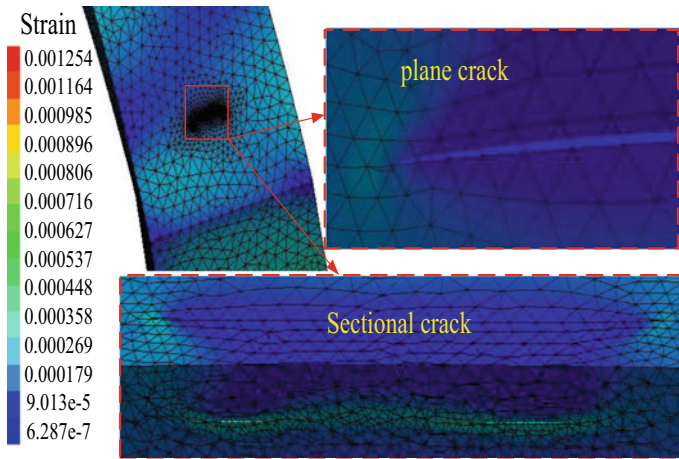
Fig. 4 Strain distribution of arbitrary crack

element analysis, the influence of crack location is analyzed to discover the unsubstantial position of crack propagation. This study only considers any crack form corresponding to the K_I type on the surface of the insulating layer, which is used to quantitatively evaluate the mechanical propagation of crack failure, as shown in Fig. 4.

It can be seen from Fig. 4 that there is obvious deformation at the crack when the crack appears at the outlet position. After the crack is divided, it can be seen that the strain at the crack is greater than the strain near the crack.

Figure 5 is the stress strength factor calculation results of cracks at different positions. Comparing the values of these two curves, it can be found that the stress intensity factor at the crack near the knee joint is much larger than the stress intensity facto strength r at the tip of the nose. The results show that the beginning crack defects at the knee joint are most likely to extend under the impact of electromagnetic force and mechanical stress in the actual work.
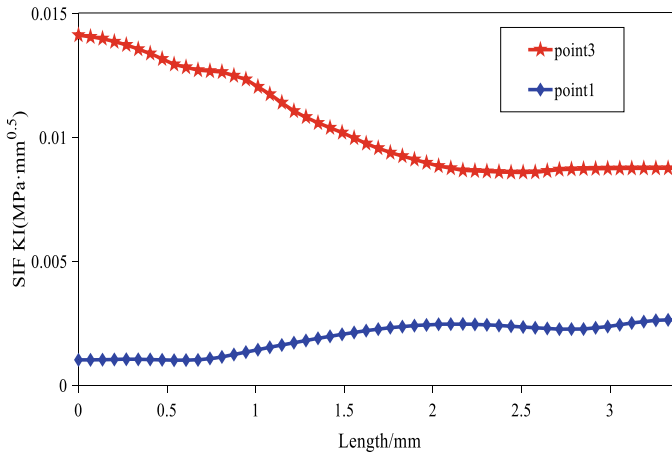
Fig. 5 Crack strength factor values at different locations

References

1. Singh M, Shaik AG (2020) Incipient fault detection in stator windings of an induction motor using stockwell transform and SVM. IEEE Trans Instrum Meas 69(12):9496–9504
2. Fernando MARM, Naranpanawa WMLB, Rathnayake RMHM, Jayantha GA (2013) Condition assessment of stator insulation during drying, wetting and electrical ageing. IEEE Trans Dielectr Electr Insul 20(6):2081–2090
3. Stone GC, Gupta BK, Kurtz M, Sharma DK (1984) Investigation of turn insulation failure mechanisms in large AC motors. IEEE Trans Power Apparatus Syst PAS-103(9):2588–2595
4. Lin R, Arkkio A (2008) 3-D finite element analysis of magnetic forces on stator end-windings of an induction machine. IEEE Trans Magn 44(11):4045–4048
5. Weiers T (2010) Symptoms of winding insulation aging after 37 years of service life in a hydrogenerator. IEEE Trans Energy Convers 25(1):20–24
6. Takeuchi K, Matsushita M, Makino H (2021) Finite-element analysis for magnetic flux in end region of synchronous machine using end-winding model. IEEE Trans Magn 57:7400506
7. Yetgin AG (2019) Effects of induction motor end ring faults on motor performance. Experimental results. Eng Fail Anal 96:374–383
8. Han J, Zheng P, Sun Y, Ge B, Li W (2020) Influence of electric shield materials on temperature distribution in the end region of a large water–hydrogen–hydrogen-cooled turbogenerator. IEEE Trans Industr Electron 67(5):3431–3441
9. Zhao Y, Yan B, Chen C, Deng J, Zhou Q (2014) Parametric study on dynamic characteristics of turbogenerator stator end winding. IEEE Trans Energy Convers 29(1):129–137
10. Letal J, Satmoko B, Manik N, Stone G (2020) Stator end-winding vibration in two-pole machines: avoiding generator failure. IEEE Ind Appl Mag 26(6):29–39
11. Tanaka S, Htut TT, Maeda K, Yagi K, Osawa N (2022) Fracture mechanics investigation of crack coalescence in a steel tubular T-joint specimen. Eng Fail Anal 139:106504

12. Zhou N, Wei H, Jiang H, Cheng Y, Yao Y, Huang P, Zhang W (2023) Fatigue crack propagation model and life prediction for pantographs on high-speed trains under different service environments. Eng Fail Anal 107065

The Influence Mechanism that Micro Grain-Boundary Structure Parameters of ZnO Varistor to the Macroscopic Electrical Characteristics

Pengfei Meng, Jingke Guo, Xiao Lei, Hengzhi Zhang, Bingbing Zhang, Kai Zhou, Zheng Liu, and Jun Hu

Abstract ZnO varistors have excellent nonlinear voltage-current characteristics, are widely used in overvoltage protection of electrical equipment. The nonlinear behavior of ZnO varistors is attributed to the double Schottky barrier structure of their grain boundaries. However, few studies have investigated the influence of micro grain-boundary structure parameters on the macroscopic electrical properties of ZnO varistors. In this paper, we utilized the Voronoi network and an improved grain boundary partitioning model to simulate and calculate the impact of micro grain-boundary parameters, such as double Schottky barrier and grain boundary partitioning parameters, on the macroscopic electrical properties of ZnO varistors. By classifying and optimizing grain boundary characteristics based on their effects on classification variables and targets, we effectively simplified the complex multi-variate and multi-objective problem. These findings provide insight into improving the performance of ZnO varistors, and are of significant importance for the production of high-performance ZnO varistors.

Keywords ZnO varistor · Materials computation · Micro grain-boundary · Electrical characteristics · Influence mechanism

P. Meng · J. Guo · K. Zhou
College of Electrical Engineering, Sichuan University, Chengdu 610065, China

X. Lei
State Grid Sichuan Electric Power Research Institute, Chengdu 610041, China

H. Zhang
Tibet Electric Power Research Institute of State Grid, Lhasa 850000, China

B. Zhang
Zhongke Tianji Technology Co., LTD, Ningxia Yinchuan 750002, China

Z. Liu (✉)
Northwest Institute of Nuclear Technology, Xi'an 710024, China
e-mail: xitulz94@163.com

J. Hu
Department of Electrical Engineering, Tsinghua University, Beijing 100084, China

1 Introduction

Zinc oxide (ZnO) varistor has excellent nonlinear characteristics and is often used for overvoltage protection. Varistor is made of ZnO as the main material, mixed with Bi_2O_3, MnO_2, Co_2O_3 and other metal oxides, and fabricated by typical ceramic materials process [1]. Previous studies shown that the nonlinear characteristics of ZnO varistor were caused by its special grain boundary structure, and the double Schottky barrier conduction model could be used to describe the grain boundary conduction mechanism of ZnO varistor. Bartkowiak et al. introduced Voronoi network to study the influence of grain boundary characteristics on the performance of ZnO varistor. Bartkowiak et al. also divided grain boundaries into three different types of "good", "bad" and "ohmic" to explain the nonlinear characteristics [2]. Eda et al. theoretically analyzed the conduction model of the intercrystalline phase part of ZnO varistor, and proposed the bypass effect model. Each grain boundary was divided into three segments: thick intercrystalline region, thin intercrystalline region and no intercrystalline region to explain the electrical characteristics of ZnO varistor [3]. Hu Jun et al. improved the partition model and divided the grain boundary layer into three segments: thick intergrain phase region, double Schoetky barrier region and grain direct contact region, which better explained the "ohm" linear grain boundary phenomenon.

The electrical performance of varistors is affected by many factors. The research process can be seen as multi-variable and multi-objective optimization problem. The corresponding sintering temperature, sintering time and other production processes were studied on the performance of Varistors in Ref. [4, 5]. The effect of double Schottky barrier on the electrical characteristics of Varistor was studied in Ref. [6, 7]. However, it takes a lot of time and resources to study varistors by experiment. With the improvement of computing power, it is possible to study Varistor by means of material calculation. A grain boundary electric network model in 3D space was established to approximate the nonlinear voltammetry characteristics of varistor in Ref. [8], and a calculation model with high agreement with the real results was obtained. The effects of Varistor diameter, resistivity and other parameters on the macroscopic electrical properties of Varistor were calculated based on Voronoi simulation in Ref. [9]. However, few previous studies summarized the effects of influencing factors on macroscopic electrical characteristics.

The special grain boundary of varistors is the fundamental reason for their nonlinear characteristics. However, there are few researches on the effects of the microscopic grain boundary characteristics of varistors on their electrical properties. In order to obtain high performance varistors, this paper studies the effects of grain boundary parameters on electrical properties through simulation calculation from the perspective of material calculation. Furthermore, the influence mechanism between the microscopic grain boundary parameters and the electrical properties of varistors is revealed, which provides a theoretical basis for the production of high performance varistors.

2   Model and Parameter Selection

2.1   Model of Gain Boundary

In the research process of Varistor, Voronoi grid introduced by Bartkowiak is generally adopted by researchers. In this study, Voronoi network research method is adopted. The improved grain boundary zoning model is adopted. Through the calculation model of Varistor, the voltage and current data of different double Schottky barrier parameters and grain boundary partition parameters corresponding to each node and branch in the equivalent circuit under the action of external power supply can be calculated. On this basis, the macroscopic electrical performance parameters of Varistor can be comprehensively analyzed.

2.2   Performance Parameters and Equivalent Model

Various indexes of Varistors need to be coordinated to meet the requirements of overvoltage protection. The most concerned macro-electrical performance parameters are the energy capacity I_{2ms} and energy absorption density Q, voltage gradient E_{1mA}, leakage current I_L, residual voltage ratio K, grain boundary current maximum K_{Igbmax}, grain boundary current mean square error K_{Igbstd} and nonlinear coefficient α_{1mA}. The voltage gradient E_{1mA}, leakage current I_L, residual voltage ratio K and nonlinear coefficient α_{1mA} need to be simply calculated according to the voltammetry characteristic, while the current capacity I_{2ms} and energy absorption density Q need to be obtained according to the perforation damage mechanism of the pressure-sensitive resistor under the action of 2 ms square wave current.

The selection of ZnO grain quantity is a key problem in studying the macroscopic electrical performance parameters of varistor by using ZnO computational simulation model. According to the study on the consistency of actual data of samples of actual size simulated by small computational scale model, the larger the grain size, the smaller the change rate of the electrical parameters of Varistors, the closer the simulation results are to the actual electrical parameters of Varistors, and the 50 × 50 grain size has a good performance in terms of calculation time and calculation error. Based on this, 50 × 50 ZnO grain sizes were used in this study as the basic scale for subsequent calculation simulation, as shown in Fig. 1.
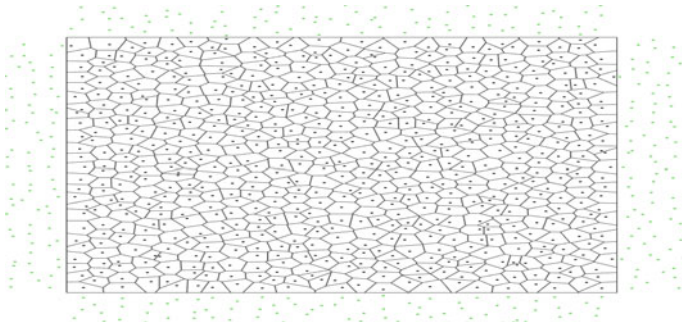
Fig. 1 Voronoi network model of ZnO varistors adopted

3　Effect of Double Schottky Barrier on Electrical Properties

In the microstructure of Varistors, two adjacent ZnO grains and their intermediate grain boundary constitute a basic barrier unit. There are a large number of surface states and internal electron traps in the grain boundary layer formed by various additives, which can trap free electrons from ZnO grains and produce negative space charge layer, so that the energy bands of ZnO grains on both sides of the adjacent grain boundary curve upward, thus forming two back-to-back grain boundary barriers, namely double Schottky barrier. ZnO grain boundary barrier height and depletion layer width are mainly determined by ZnO grain donor density N_d and grain boundary surface state density N_i. In this section, the effects of N_d and N_i on the electrical properties of Varistors are calculated by simulation and analyzed.

In the simulation model, N_d and N_i are parameters that can be changed manually. By changing the value of grain donor density N_d, the macroscopic electrical performance parameters of Varistors with different grain donor density N_d are obtained by simulation, equivalent to the cylindrical with thickness of 1 cm and diameter of 10 cm, as shown in Table 1 (The following results were treated in the same way).

Table 1 The effects of the donor density

N_d (10^{17} eV^{-1} cm^{-3})	5	3	2	1	0.5
E_{1mA} (V/mm)	13	115	259	743	1803
I_L (μA)	546.50	19.39	4.34	1.73	1.20
α_{1mA}	1.4	15.5	29.0	57.8	95.2
K	10.42	2.32	1.70	1.34	1.19
I_{2ms} (A)	13,415	8272	4984	1540	396
Q (J/cm^3)	603	601	560	376	208
K_{Igbmax}	4.67	5.11	5.75	8.52	15.42
K_{Igbstd}	1.35	1.39	1.40	1.50	2.01

According to Table 2, the influence of grain donor density N_d on macroscopic electrical performance parameters is plotted, as shown in Fig. 2. The results showed that the grain donor density N_d had a significant influence on each region of the overall voltammetry (V-I) characteristic curve of Varistor, and the macroscopic electrical performance parameters of Varistor also had a significant change. With the increase of grain donor density, the voltage gradient and the nonlinear coefficient decrease rapidly, the leakage current and residual pressure ratio increase significantly. The phenomenon of uneven concentration of grain boundary current is improved to some extent, and the corresponding energy absorption density and energy capacity of varistor increase accordingly.

Table 2 The effects of the surface state density

N_i (10^{12}eV^{-1} cm^{-2})	2	2.5	3.5	4.5	6
E_{1mA} (V/mm)	0	54	259	570	1231
I_L (μA)	737.21	106.56	4.34	2.03	1.37
α_{1mA}	1.0	7.6	29.0	49.0	77.5
K	432.81	3.53	1.70	1.40	1.24
I_{2ms} (A)	16,888	10,904	4984	2176	737
Q (J/cm^3)	657	609	560	428	276
K_{Igbmax}	4.11	4.87	5.75	7.46	11.58
K_{Igbstd}	1.14	1.39	1.40	1.46	1.69
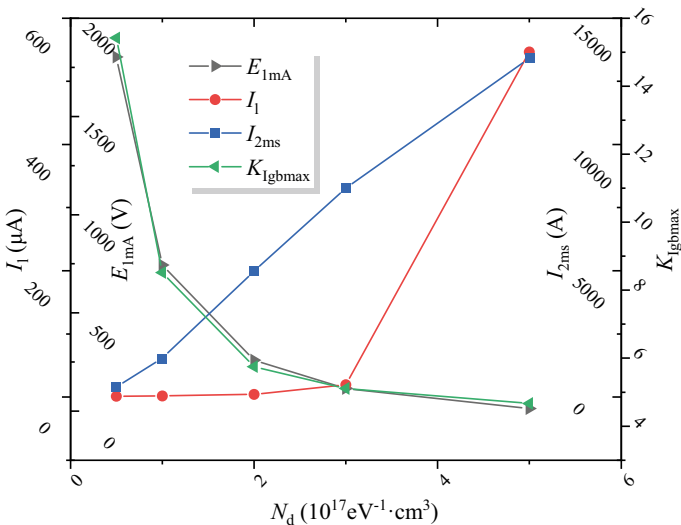
Fig. 2 Effect of donor density N_d
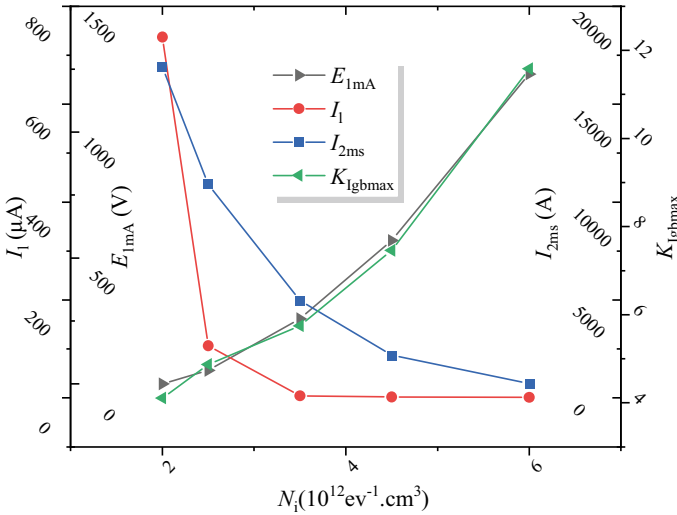
Fig. 3 Effect of surface state density N_i

The effect of Varistor grain boundary surface state density N_i on the macro-electrical performance parameters of the valve plate is shown in Table 2. Similar to the N_d, N_i has a significant impact on each region of the overall *V-I* characteristic curve of Varistors, and the various macroscopic electrical performance parameters of varistor also have a significant change. Compared with Figs. 3 and 2, the change trend is opposite, that is, with the increase of the grain boundary surface state density, The voltage gradient and the nonlinear coefficient of varistor increase rapidly, while the leakage current and residual voltage ratio decrease significantly, and there is an obvious saturation phenomenon. The phenomenon of uneven concentration of grain boundary current tends to be aggravated, and the corresponding energy absorption density and energy capacity of varistor decrease accordingly. The variation of macro-scopic electrical properties of varistor under the influence of grain boundary surface state density is basically opposite to that under the influence of grain donor density.

4 Influence of Different Grain Boundary Zoning

As shown in Fig. 4, in addition to the double Schottky barrier, grain boundary forms a non-linear conductive mainstream channel, and there are also thick intercrystalline regions and regions where ZnO grains contact directly, forming a small current leakage bypass channel, which has a significant effect on the macroscopic electrical performance of Varistors.

Various existing test data show that various characteristic parameters of varistor grain boundaries are basically normally distributed. Therefore the normal distribution

Fig. 4 Grain boundary partition model of ZnO varistor
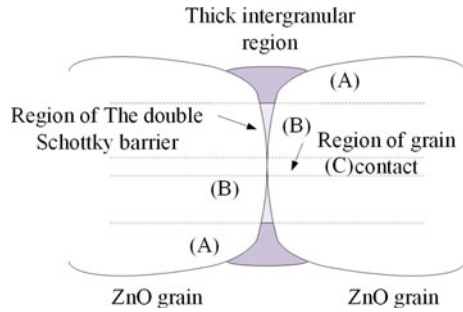
model of parameter P_A of the thick intergranular phase region is defined by

$$P_A = \overline{P}_A + \sigma_{PA} \cdot \text{randn}()$$

$\overline{P}_A$ is the arithmetic mean, and is the standard variance of the parameter distribution. randn() is a standard normally distributed random number constructor. The direct contact region of grains also adopts the same definition and is represented by $\overline{P}_C$ and σ_{PC}.

4.1 Influence of Regional Ratio of Thick Intercrystalline Phase

By changing the normal distribution parameters $\overline{P}_A$ and σ_{PA} corresponding to the area ratio P_A of thick intercrystalline phase region in the simulation model of ZnO varistor. The effect of simulated thick intercrystalline phase area on the macroscopic electrical performance parameters of varistor was calculated. The simulation results were shown in Table 3.

Table 3 The effects of the thick intergranular region has on the calculation results

$\overline{P}_A$	0	0	0	0	0	0	0.1	0.2	0.3	0.4
σ_{PA}	0	0.1	0.2	0.3	0.4	0.5	0.5	0.5	0.5	0.5
E_{1mA} (V/mm)	259	260	261	262	263	264	264	265	265	266
I_L (μA)	4.3	6.6	9.3	11.7	14.0	15.8	16.5	17.3	18.1	18.9
α_{1mA}	29.0	28.7	28.2	27.9	27.5	27.3	27.2	27.1	26.9	26.8
K	1.70	1.71	1.72	1.74	1.76	1.78	1.79	1.81	1.82	1.84
I_{2ms} (A)	4984	4871	4651	4242	3528	3370	3145	3145	3003	2803
Q (J/cm^3)	560	550	528	484	403	389	363	366	350	328
K_{Igbmax}	5.75	5.77	5.81	6.35	6.18	6.55	8.26	7.86	6.60	6.83
K_{Igbstd}	1.40	1.40	1.40	1.41	1.42	1.43	1.46	1.45	1.44	1.44

The thick intercrystalline region mainly affected the small current region *V-I* characteristic curve. With the increase of the proportion of thick intergranular area in the grain boundary, the overall voltage gradient increased slightly, but the leakage current increased significantly. This trend was completely consistent with the effect of thick intergranular region on the bypass channel of grain boundary current leakage.

The thick intergranular region had some influence on the high current region. The nonlinear coefficient decreased slightly with the increase of the area ratio of thick intercrystalline phase, while the residual pressure ratio increased with a larger range.

In addition, the increase of the area proportion of thick intercrystalline phase played a role in exacerbating the phenomenon of uneven concentration of grain boundary current. The energy absorption density and energy capacity showed a trend of continuous decline on the whole.

4.2 Effect of Grain Contact Region Proportion

By changing the distribution parameters $\overline{P}_C$ and σ_{PC} corresponding to the proportion of the direct contact area, the effect of the direct contact area of simulated grains on the electrical performance parameters of ZnO varistor was calculated. The simulation results were shown in Table 4.

The direct grain contact region appearing in the grain boundary of ZnO varistor had a serious impact on the small current region of the overall *V-I* characteristic curve. As a result, various parameters of the electrical performance of ZnO varistor were seriously deteriorated, the voltage gradient and the nonlinear coefficient were decreased, while the leakage current and residual voltage ratio were increased. The grain contact region had no obvious effect on the inhomogeneous concentration of grain boundary current.

Table 4 The effects of the grain contact zone

$\overline{P}_C$	0	0	0	0	0	$\overline{P}_C$	0	0	0	0	0
σ_{PC}	0	10^{-9}	10^{-8}	10^{-7}	10^{-6}	σ_{PC}	0	10^{-9}	10^{-8}	10^{-7}	10^{-6}
E_{1mA} (V/mm)	265	264	239	38	4	I_{2ms} (A)	2935	3073	3003	3218	3073
I_L (μA)	17.3	79.0	521.9	737.2	737.2	Q (J/cm^3)	339	356	347	375	356
α_{1mA}	27.0	11.6	1.2	1.0	1.0	K_{Igbmax}	6.92	7.25	7.13	7.38	6.52
K	1.81	1.82	2.00	12.53	123.03	K_{Igbstd}	1.44	1.45	1.45	1.45	1.44

5 Discussion on Influence Mechanism

In conclusion, there is a certain influence mechanism between the microscopic grain boundary parameters and macroscopic electrical performance parameters of ZnO varistors.

In this study, the influence of the grain boundary microstructure of ZnO varistor on its macroscopic electrical properties is considered as a multi-variable, multi-objective optimization problem. The optimization variables are the micro-grain boundary structural parameters of ZnO varistors, and the optimization objectives are the electrical parameters of ZnO varistors. According to the relationship between variables and objectives, the classification can be based on whether any variable has the same influence on all kinds of objectives. The optimized variables are classified according to whether they have the same effect on the electrical performance parameters.

As shown in Table 5, the optimization objectives can be divided into two categories. The first category is the voltage gradient E_{1mA}, the leakage current I_L, the nonlinear coefficient α_{1mA}, and the residual voltage ratio K. The second category is the energy capacity I_{2ms} and the energy absorption density Q. Changes in the variables have opposite effects on the two types of objectives. Then the variables are classified according to whether they have the same effect on the two types of objectives. The first type of variables are the donor density N_d and the surface density of states N_i, which have exactly opposite effects on the above two types of objectives. The second type of variables are the ratio P_A of thick intercrystalline phase region and the ratio P_C of grain contact region. These variables have the same effect on the two types of objectives. The classified objectives and variables have obvious characteristics. Therefore, according to the influence relationship between variables and objectives, a series of measures can be obtained. The simplest measure is to adjust the first type of variables in the direction of a certain type of objective, so that this type of objective far exceeds the required scope of indicators. Then, the related variables were reversed to improve the other type of objective until both types of objectives met the requirements. The second type of variables are used to adjust the related characteristic parameters as much as possible in the direction that is beneficial to all objectives.

Table 5 The correlation mechanism between grain-boundary parameter and electrical performance parameters

Influence factor		Electrical performance parameters					
		$E_{1mA}\uparrow$	$I_L\downarrow$	$\alpha_{1mA}\uparrow$	$K\downarrow$	$I_{2ms}\uparrow$	$Q\uparrow$
N_d	↓	√√	√√	√√	√√	××	××
N_i	↑	√√	√√	√√	√√	××	××
P_A	↓	—	√√	√	√	√√	√√
P_C	↓	√√	√√	√√	√√	—	—

Marginal data: ↑ parameter increase, ↓ parameter decrease, √ positive effect, √√ significant positive effects, × negative influence, ×× significant negative influence, — No significant effect

6 Conclusion

This study established the Voronoi network calculation model of varistor, studied the influence mechanism of grain boundary characteristics on the electrical performance, obtained the optimization method of varistor, and obtained the following conclusions:

1. The improved grain boundary partition model of ZnO varistor was established, and the influence law of different grain boundary parameters on macroscopic electrical performance was obtained, which provided a low-carbon and efficient method for the development of high-performance varistor.
2. The mechanism of the influence between the micro-grain boundary characteristics and the macro-electrical performance of ZnO varistors is revealed, and the research process of the micro–macro mapping association is transformed from a multi-variable and multi-objective optimization problem to a problem with only two types of objectives and two types of variables.
3. Based on the established micro–macro influence mechanism of ZnO varistor, a two-step optimization strategy for the variant-target influence characteristics is proposed, which is of great significance for the design and preparation of ZnO varistor.

References

1. Hembram K (2020) Influence of CaO doping on phase, microstructure, electrical and dielectric properties of ZnO varistors. J Alloys Compd 817
2. Bartkowiak M (1995) Nonlinear currents in Voronoi networks. Phys Rev B 51(16):10825–10832
3. Eda K (1982) Electrical properties of ZnO-Bi$_2$O$_3$ metal oxide heterojunctiona clue of a role of intergranular layers in ZnO varistors. In: Grain boundaries in semiconductors proceedings of the materials research society annual meeting. pp 381–392
4. Frigura-Iliasa FM (2019) New technical parameters and operational improvements of the metal oxide varistors manufacturing process. Processes 7(1)
5. Roy TK (2021) High nonlinearity in 0.1 mol.% In$_2$O$_3$ added ZnO-V$_2$O$_5$ based varistors prepared at different sintering temperatures. Ceram Int 47(24):35152–35159
6. Kaufmann B (2021) Observation of an electrical breakdown at ZnO Schottky contacts in varistors. J Eur Ceram Soc 41(3):1969–1974
7. Wang Y (2021) Simultaneously enhanced potential gradient and nonlinearity of ZnO Varistor ceramics by MnO doping with nano-sized ZnO powders. Materials 14(24)
8. Benjamin K (2021) A modelling approach to describe the DC current-voltage behaviour of low-voltage zinc oxide varistor. Open Ceram 6:100113
9. Kuan C (2023) Influence of micro parameters of ZnO Varistor on its electrical properties based on Voronoi grid simulation. Guangdong Electr Power 36(01):102–113

Numerically Investigating Interturn Arcing Faults Inside a UHV Converter Transformer

Dong Liang, Jianhua Zhu, Peng Zhang ⓘ**, Cui Zhang, Zhangshun Ma, Jiaxu Guo** ⓘ**, and Chenguang Yan** ⓘ

Abstract A succession of ultrahigh-voltage (UHV) converter transformer interturn arcing faults have recently emerged, eventually giving rise to catastrophic fire accidents. For a long time, modeling and analyzing transformer interturn faults have been well-known challenges in both academia and industry, while such a dilemma turns out to be intractable in the face of those in UHV converter transformers. In this study, a coupled field-circuit model is presented for numerically investigating converter transformer interturn faults. In the circuit domain, a black box model is chosen for a quantitative description of the nonlinear conductance of the fault arc. As study cases, representative line-side winding (LSW) interturn arcing fault scenarios within a typical single-phase converter transformer are analyzed. The specific results reveal that an interturn fault causes the internal flux distribution to be seriously distorted and leakage flux lines to concentrate around the faulty turns. The LSW interturn fault witnesses a high-amplitude circulating current flowing in the fault loop, and a certain increase in the LSW current, while no apparent fault features can be observed on the

D. Liang · J. Zhu · C. Zhang · Z. Ma
Xi'an Xibian Components Co., Ltd, Xi'an 710077, Shaanxi, China
e-mail: liangdong_xdxb@foxmail.com

J. Zhu
e-mail: tech@xdxb.com.cn

C. Zhang
e-mail: 164392003@qq.com

Z. Ma
e-mail: 15029216224@163.com

P. Zhang · J. Guo · C. Yan (✉)
State Key Laboratory of Electrical Insulation and Power Equipment, Xi'an Jiaotong University,
Xi'an 710049, Shaanxi, China
e-mail: chgyan@xjtu.edu.cn

P. Zhang
e-mail: jshazp990528@stu.xjtu.edu.cn

J. Guo
e-mail: gg1270564498@stu.xjtu.edu.cn

271

valve side. This investigation sheds light on the complex characteristics of interturn arcing faults inside a converter transformer and is expected to offer an alternative to dangerous and costly short-circuit experiments in the field.

Keywords Interturn arcing fault · Coupled field-circuit analysis · Numerical simulation · Ultrahigh-voltage (UHV) converter transformer

1 Introduction

Ultrahigh-voltage (UHV) converter transformers, as core power equipment in converter systems, constitute the connecting hub of the AC and DC system in conjunction with converter valves [1]. With continuous increases in the transmission capacity and voltage level, the manufacturing operation requirements of converter transformers have been greatly improved. In the meantime, the fault risks of critical equipment during operation have increased accordingly. Since 2018, several interturn arcing faults in UHV converter transformers have occurred, some of which finally gave rise to explosions and fires. These accidents have brought about economic losses amounting to billions of yuan and have seriously affected the safety of power systems [2].

In the occurrence of an interturn fault in a converter transformer, the high-energy electric arc violently vaporizes and decomposes the surrounding insulating oil, producing large amounts of flammable gases over a very short time. The high-temperature high-pressure gas bubble thus generated shows a pulsating growth behavior and continuously compresses the surrounding insulating oil, resulting in oil pressure rises and fluctuations [3]. Once internal steady-state pressure exceeds the mechanical strength of the oil tank, converter transformer rupture and explosion will be inevitable to occur.

Fault analysis is considered as a prerequisite for conducting fault characterization and relay protection studies. In [4], an *L-M* transformer winding fault model with linear splitting of the leakage inductance matrix is proposed on the basis of the electrical parameters obtained from nameplate data. With the rapid development of computational capability and numerical theory, in Ref. [5], a two-dimensional finite element (FE) model was established for transformer winding internal faults, and ANSOFT Maxwell simulation was applied to calculate the internal leakage distribution and short-circuit circulating current. Thereafter, a simplified leakage inductance calculation method ignoring the radial leakage component was proposed in Ref. [6]. Detailed structure geometry parameters of the transformer are not necessary for this model, but the long-standing and intractable challenge of calculation accuracy is still a major concern. Recently, more effective transformer interturn fault models with integration considerations of the influence of both the magnetic field and the circuit topology [7, 8] have yielded meaningful results and provided references for converter transformers. It is worth noting that the external circuit system and load conditions of UHV converter transformers show more complexity, and an interturn

fault tends to produce a short-circuit current with higher amplitude due to larger capacities compared to common transformers.

To this end, a coupled field-circuit model for UHV converter transformer interturn arcing fault studies is developed, where the improved Mayr-type black box arc model was directly integrated using a user-defined formula module in the domain of circuit systems. With the corresponding numerical methodology, typical interturn arcing fault scenarios of a ZZDFPZ-415000/500-600 UHV converter transformer have been simulated and examined on the ANSYS platform.

2 Theoretical Modeling

2.1 Internal Electromagnetic Field

For the calculation of the magnetic flux distribution inside a converter transformer, the windings are always assumed to be stranded coils with a certain number of turns. Since the stranded conductor consists of fine wires lacking eddy current behavior, and current densities are in a uniform distribution over the solution region, the same current flows through each wire. Therefore, the electromagnetic field for stranded windings within the converter transformer will be governed by the following equation [9]:

$$\nabla \times \left(\frac{1}{\mu} \nabla \times A \right) = J_s \tag{1}$$

where μ is the magnetic permeability, J_s represents the impressed current density, and A represents the magnetic vector potential.

For transient field analysis in two-dimensional xOy coordinates, if the magnetic field is approximated to be uniformly distributed in the axial direction, the magnetic vector potential A and the current density vector J_s retain only the z-axis components, namely A_z and J_z. By neglecting the nonlinearity of the core material, the magnetic potential A_z satisfies:

$$\begin{cases} \Omega : \frac{\partial}{\partial x}\left(\frac{1}{\mu} \frac{\partial A_z}{\partial x} \right) + \frac{\partial}{\partial y}\left(\frac{1}{\mu} \frac{\partial A_z}{\partial y} \right) = J_z \\ \partial_D \Omega : A_z = 0 \end{cases} \tag{2}$$

where Ω denotes the solution domain and $\partial_D \Omega$ is a Dirichlet boundary condition.

The induced voltage of the winding u_f can be expressed as:

$$u_f = \frac{d_f N_f l}{a \cdot S_f} \int \int \frac{dA_z}{dt} \cdot d\Omega \tag{3}$$

where t denotes the time, d_f is the circuit polarity usually taken as -1 or $+1$, N_f denotes the total amount of fine wires in the winding, l denotes the depth in the two-dimensional simulation model along the z-axis direction, a denotes the parallel branch number in the winding, and S_f denotes the winding cross-sectional area.

2.2 External Electric Circuit

For the external circuit of the coils in a certain section of the winding, the expression for the input voltage u_s can be established based on Kirchhoff's voltage law (KVL) as follows:

$$u_s = u_f + (R_{\text{ext}} + R_{\text{end}} + R_{\text{d}}) \cdot i_s + (L_{\text{ext}} + L_{\text{end}}) \cdot \frac{\mathrm{d}i_s}{\mathrm{d}t} \qquad (4)$$

where i_s denotes the current flowing into the winding; L_{end} and R_{end} are the inductance and resistance, respectively, at the end of the winding; L_{ext} and R_{ext} are the inductance and resistance, respectively, of the external circuit connected to the winding; and R_{d} is the total direct-current resistance.

When an interturn fault occurs, the physical process is manifested as a low-impedance arc in oil, which connects two adjacent turns along the winding. By filming the arcing faults in the insulating oil [10], the conclusion is drawn that an arc in oil is actually that in gas. In our work, the improved Mayr-type arc model developed in Ref. [11] was selected for the acquisition of the arc conductance for a detailed description of arc at both high and low current stages. The differential equation for this model is:

$$\frac{1}{g_{\text{arc}}} \cdot \frac{\mathrm{d}g_{\text{arc}}}{\mathrm{d}t} = \frac{1}{\tau}\left(\frac{u_{\text{arc}} i_{\text{arc}}}{\max\{U_{av}|i_{\text{arc}}|, P_0 + P_1 \cdot u_{\text{arc}} i_{\text{arc}}\}} - 1\right) \qquad (5)$$

where i_{arc} and u_{arc} are the current and voltage, respectively, of the arc; g_{arc} denotes the arc conductance; τ denotes the time constant; U_{av} is the average voltage; P_1 represents a dissipated power coefficient; and P_0 represents the dissipated power constant.

2.3 Coupled Field-Circuit Analysis

In the previous two sections, the governing equation for the internal magnetic field, the constraint equation for the external circuit system, together with the differential equation for the fault arc conductance are provided. With the combination of (2), (3) and (4) and applying the standard Galerkin approach [12], the direct coupled field-circuit equation is obtained and written in block matrix form:

$$\begin{bmatrix} K & C \\ 0 & R \end{bmatrix} \begin{Bmatrix} A_z \\ i_s \end{Bmatrix} + \begin{bmatrix} 0 & 0 \\ C^T & L \end{bmatrix} \frac{d}{dt} \begin{Bmatrix} A_z \\ i_s \end{Bmatrix} = \begin{Bmatrix} 0 \\ u_s \end{Bmatrix} \tag{6}$$

Equation (6) indicates that the coupled field-circuit model for the converter transformer interturn arcing fault is essentially reflected in the complex correlations among the winding leakage flux, the winding input current and the input voltage. To be specific, as to the winding two-dimensional cross section, the excitation current i_s is first substituted into the governing equation of the magnetic field to compute A_z. Thereafter, the input voltage u_s can be acquired with the solution of the circuit constraint equation. In addition, the nonlinear arc conductance g_{arc}, serving as a vital part in the resistance matrix, is solved simultaneously with the rest of the electric circuit system.

3 Simulation and Discussion

In this section, the developed coupled field-circuit model is utilized to numerically investigate the interturn fault behaviors of an actual 415 MVA UHV converter transformer within a $\pm$ 800 kV UHV converter station. Through transient co-simulations thus conducted, typical results regarding the arc waveforms, terminal behaviors and other electromagnetic characteristics are presented and analyzed.

3.1 Simulation Setup

To lower the operating temperature and reduce transport size, the cores for UHV converter transformers are generally in a single-phase four-limb design, and the windings around the two main limbs are in parallel connection. In this paper, a ZZDFPZ-415000/500-600 converter transformer is employed as a study case and Fig. 1 illustrates a cross-sectional view of its internal structures.

The external circuit system for the UHV converter transformer refers to a pole I converter system of the $\pm$ 800 kV UHVDC sending-end network. It contains two twelve-pulse units in the high-end part and low-end part, and each unit contains two transformer groups in the Y/Y and Y/D connections. On the basis of the internal two-dimensional FE model along with the external circuit model for the UHV converter transformer, transient cosimulation of interturn arcing faults is conducted with the Maxwell transient solver and Simplorer transient simulator in ANSYS software to achieve two-way data transfer at the coupling pins.
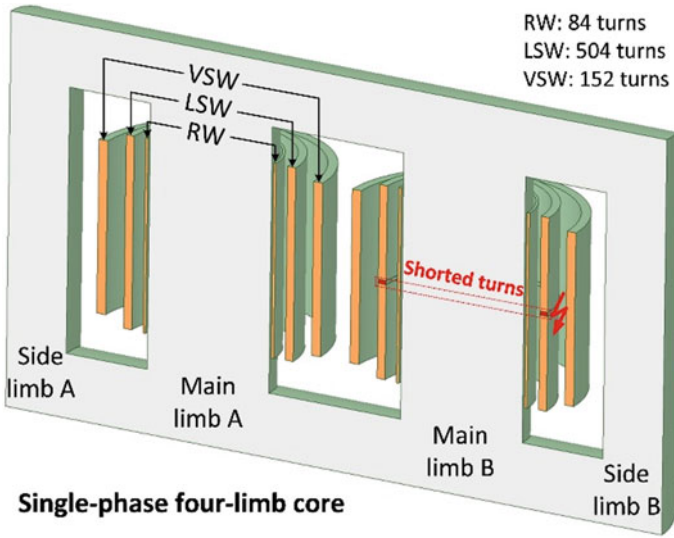
Fig. 1 Cross-sectional view of the windings and core structures

3.2 Typical Results

Case 1: 1.98% Interturn Arcing Fault. As a typical case, the converter transformer in phase A is simulated subject to an interturn fault involving 10 turns (1.98%) in the axial center of the LSW around main limb B. The moment of the fault trigger is $t = 40$ ms, before which the transformer operates normally with RW tap positions at $+ 18$. Figures 2 and 3 present the simulated results in the field and circuit domains, respectively.

As shown in Fig. 2, the interturn fault brings about a large degree of leakage flux distortion with a great number of flux lines concentrated near the faulty point. Different from that on the healthy limb, many radial components appear in the middle region on the faulty limb, and the peak value of flux density achieves 3.99 T at 5 ms after fault emergence. Such a distorted flux distribution and a high density result from

(a) Flux lines   (b) Flux density vector
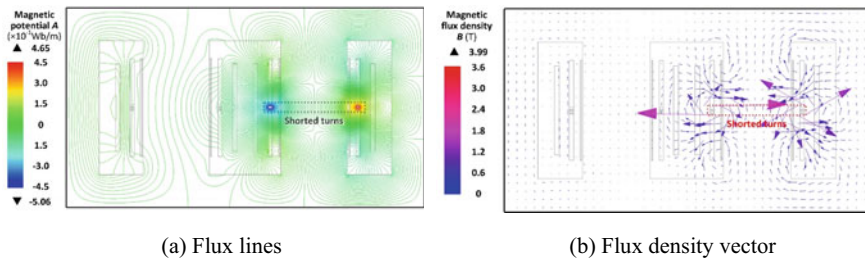
Fig. 2 Flux distribution within the transformer at $t = 45$ ms in case 1
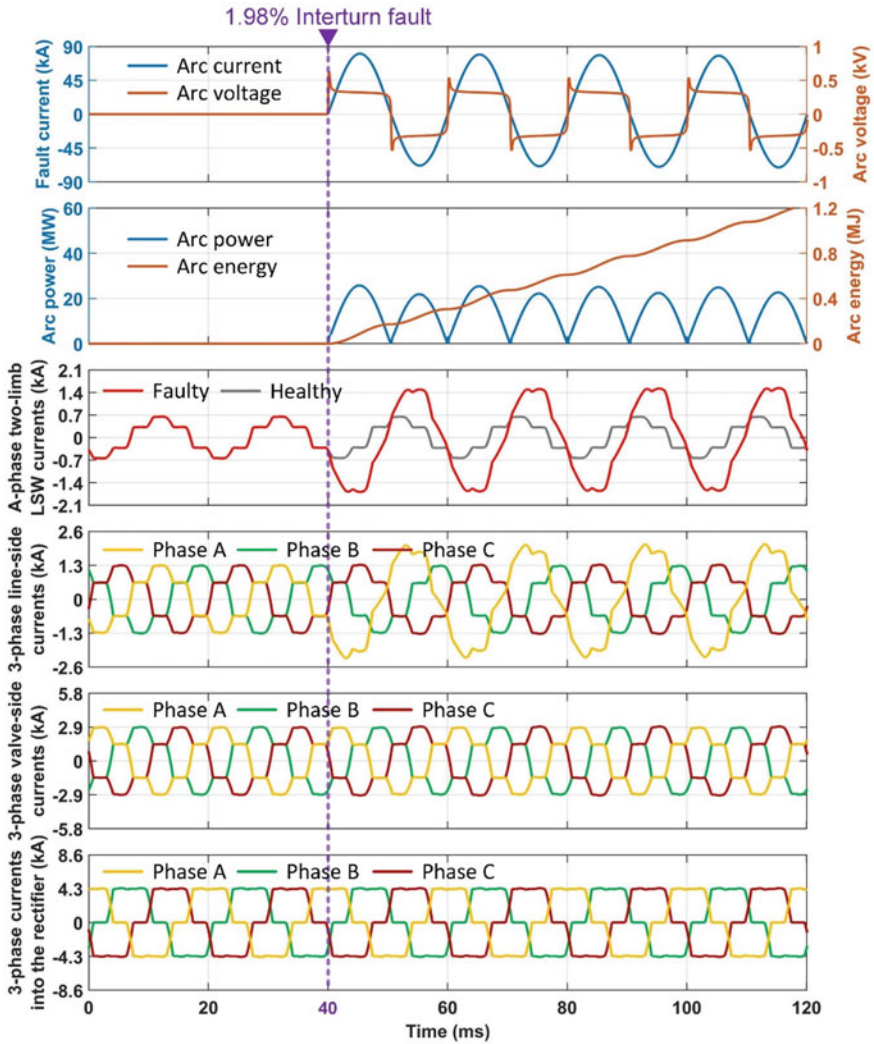
Fig. 3 Computed results from the circuit domain in case 1

the huge circulating current induced in the fault loop, with a root-mean-square (rms) value equal to 52.7 kA. The waveform of the voltage drop across the arc column exhibits a typical saddle-like shape, with an average value calculated to be 321.4 V. With the arc power fluctuating, the energy variation shows a stepped-up trend, and ultimately achieves 1.2 MJ in four cycles. For terminal behaviors, the A-phase B-limb LSW current has a remarkable rise, with a rms value from 0.44 to 1.2 kA, while that of the healthy limb is little affected. Due to the increase in the fundamental

component, the A-phase line-side current waveform is more nearly sinusoidal than that in normal operation.

Case 2: 5.95% Interturn Arcing Fault. The second case introduces an interturn arcing fault involving 30 turns (5.95%) in the axial center of the LSW around main limb B, and the converter transformer operating parameters, fault location and duration are all consistent with those in the previous case. Figure 4 presents the simulated results in the circuit domain, and it can be observed that the rms value of the circulating current turns out to be only 21.4 kA. By contrast, the average arc voltage is 965.8 V, which is approximately three times that of case 1. For this reason, more arc energy is released in the fault duration, 21.6% greater than that in the former case. In addition, the terminal behaviors under a 5.95% interturn fault exhibit similar characteristics. The current in the LSW around the faulty limb witnesses more than a twofold increase, while the currents in healthy windings remain virtually unchanged.

4   Conclusion

The transformer interturn fault model has been pursued for decades whereas recent UHV converter transformer fire accidents highlighted the necessity and urgency of this study. This article provided a coupled field-circuit model for UHV converter transformer interturn fault studies, where arc conductance was taken into account and simulated by applying the improved Mayr-type black box model. A real 415 MVA/ 500 kV UHV converter transformer was modeled and simulated to subject interturn arcing faults with different turns. The results demonstrated that severe flux distortion emerged near the faulty point, characterized by a sharp increase in radial components in flux density. Meanwhile, the arc continued to burn with a high-amplitude circulating current passing through and released a large amount of energy. In addition, no apparent characteristics were found in the terminal behaviors, except for a certain increase in LSW current. This developed numerical methodology and representative results can enrich the research on transformer interturn fault analysis and serve as an effective alternative to risky and expensive short-circuit experiments inside UHV converter transformers in the field.
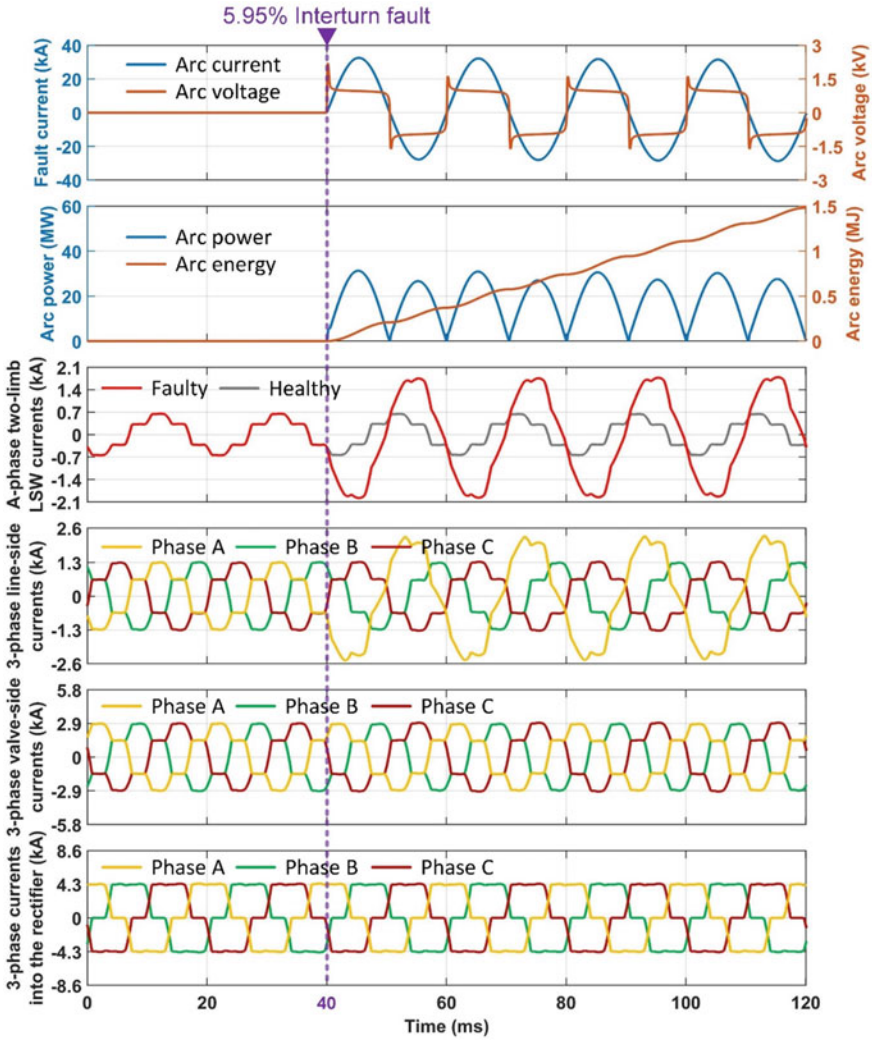
Fig. 4 Computed results from the circuit domain in case 2

References

1. He S, Li J, Wang Y (2022) Analysis of electromagnetic transient characteristics on the winding of UHVDC converter transformers based on an improved broadband model. IEEE Trans Magn 58(8):8401505
2. Yan C, Zhang P, Guo J, Liu H, Yang H, Zhang B (2023) An improved coupled FE–circuit model for turn-to-turn short-circuit faults inside converter transformers. IEEE Trans Magn 59(5):8400205
3. Yan C, Xu C, Liu H, Guo J, Zhang P, Xu Y, Zhou X, Zhang B (2023) Research on oil pressure rise and fluctuation due to arcing faults inside transformers. IEEE Trans Power Delivery 38(2):1483–1492
4. Bastard P, Bertrand P, Meunier M (1994) A transformer model for winding fault studies. IEEE Trans Power Delivery 9(2):690–699
5. Wang H, Butler KL (2001) Finite element analysis of internal winding faults in distribution transformers. IEEE Trans Power Delivery 16(3):422–428
6. Oliveira LMR, Cardoso AJM (2010) A permeance-based transformer model and its application to winding interturn arcing fault studies. IEEE Trans Power Delivery 25(3):1589–1598
7. Wiszniewski A, Solak K, Rebizant W, Schiel L (2018) Calculation of the lowest currents caused by turn-to-turn short-circuits in power transformers. Int J Electr Power Energy Syst 95:301–306
8. Yan C, Wang W, Zhang P, Liu Z, Zhang B (2023) Investigation on interturn short-circuit faults in an onboard traction transformer for high-speed railway. IEEE Trans Magn 59(11):8401706
9. Yan C, Zhang P, Xu Y, Liu S, An T (2022) Bidirectional field–circuit coupling analysis of converter transformer inter-tap short-circuit faults in on-load tap changers. IET Gener Trans Dist 16(23):4750–4760
10. Yan C, Xu Y, Zhang P, Kang S, Zhou X, Zhu S (2022) Investigation of the gas bubble dynamics induced by an electric arc in insulation oil. Plasma Sci Technol 24(4):044003
11. Schavemaker PH, Sluis LVD (2000) An improved Mayr-type arc model based on current-zero measurements. IEEE Trans Power Delivery 15(2):580–584
12. Yang W, Pan Y, Qiu Z, Zhai G (2023) Electromagnetic transient model and field-circuit coupling numerical calculation of Sen transformer based on finite-element method. Electr Power Syst Res 214:108941

A Numerical Study on Oil Pressure Rise Caused by Arcing Faults Inside a Converter Transformer

Jianhua Zhu, Dong Liang, Jiaxu Guo , Zhiming Hui, Cui Zhang, Peng Zhang , and Chenguang Yan

Abstract Oil pressure rise caused by internal faults in converter transformers and the possible resulting tank rupture have long been a serious concern for the power industry. This paper presents a numerical method to study overpressures inside a converter transformer tank during an arcing fault. Specifically, an arc-driven bubble dynamics model is established to quantitatively describe the gas bubble behavior with the release of arc energy and the overall variations in oil pressure. Meanwhile, a fluid model and the bubble-fluid interaction model are utilized to simulate the complex fault effects within the converter transformer. In addition, a simulation model of a full-scale 415 MVA/500 kV converter transformer is established, and representative results of the dynamic evolution of the gas bubble and oil pressure fluctuations under internal faults with arc energy of 1.2 MJ are obtained and analyzed. The simulation results show that the oil pressure rise inside the faulty converter transformer tank depends on the gas bubble, and exhibits an obvious uneven spatial distribution.

J. Zhu · D. Liang · Z. Hui · C. Zhang
Xi'an Xibian Components Co., Ltd, Xi'an 710077, Shaanxi, China
e-mail: tech@xdxb.com.cn

D. Liang
e-mail: liangdong_xdxb@foxmail.com

Z. Hui
e-mail: 120341957@qq.com

C. Zhang
e-mail: 164392003@qq.com

J. Guo · P. Zhang · C. Yan (✉)
State Key Laboratory of Electrical Insulation and Power Equipment, Xi'an Jiaotong University, Xi'an 710049, Shaanxi, China
e-mail: chgyan@xjtu.edu.cn

J. Guo
e-mail: gg1270564498@stu.xjtu.edu.cn

P. Zhang
e-mail: jshazp990528@stu.xjtu.edu.cn

1   Introduction

Converter transformers, as critical equipment that links AC and DC systems, play a critical role in energy conversion and transmission in high-voltage direct current (HVDC) systems. When an arcing fault occurs inside the oil-filled converter transformer, the ignited fault arc will vaporize and decompose the surrounding oil and generate a rapidly expanding gas bubble, leading to significant oil pressure rise inside the tank [1]. Once the overpressure exceeds the mechanical strength of the tank, it will rupture, explode and even cause a fire. Since 2018, several ultra-high voltage converter transformer explosion accidents caused by fault-induced overpressure have occurred, leading to equipment rupture, catastrophic fire, and enormous economic losses [2, 3].

The internal fault-induced overpressure is the basis for the analysis of converter transformer rupture. Numerical simulation methods have been pursued since the 1970s as important alternatives. In [4], a significant contribution was presented by developing an empirical equation for the pressure amplitude due to an arc in the gaseous space inside an oil-filled pole-type distribution transformer, which mainly relies on the available current, arc duration, arc length and geometric parameters of the tank. In [5], an important expression was proposed for estimating the instantaneous pressure rise in a tank by considering the tank expansion coefficient and the arcing gas generation rate, which is widely used even to this day. In the same year, a simplified 2-D model was presented to study the overpressure inside a transformer and was compared with the specialized software PISCES-2DELK [6]. In [7], an empirical equation was developed to estimate the overpressures caused by arcs inside different pole-type distribution transformers.

Taking advantage of the increasing computational capabilities of microprocessors, a three-dimensional numerical tool was proposed in [8] for investigating the complex physical phenomena occurring during transformer internal faults, which made use of the simplified 5-equation model presented in [9]. In [10], a numerical method on the basis of explicit dynamic analysis was presented for modeling the mechanical effect of arcing faults. Under the assumption of an adiabatic gas generation process and the simplification of the model using shell elements, the process of tank rupture caused by internal arcing faults was modeled. In [11], a static finite element method was presented to analyze a transformer tank under overpressure using various material models. In [12], two main methods of nonlinear static and explicit dynamic finite element analysis were compared for assessing the capability of a reactor tank to withstand the overpressures caused by low-impedance faults. In [13], the design of a transformer tank that can withstand high energy arcing faults was presented, which was based on nonlinear explicit finite element analysis. In the same year, the internal overpressure and the stress in the tank were analyzed in [14] and it

was found that the ascending flanged base was more prone to experience a higher pressure. In [15], by means of coupling the pressure, fluid and solid field, the fault-induced pressure wave inside a 110 kV power transformer was investigated with the aid of the commercial software COMSOL. In recent years, field arcing fault tests were performed inside transformers, and the testing images confirmed that the gas bubble generated by the fault arc exhibits an obvious pulsation behavior [16, 17]. Over the past several decades, extensive investigations have been reported on topics including but not limited to arc-induced pressure buildup, transformer tank rupture and mitigation. These studies have yielded encouraging and representative results that are meaningful for arc-induced overpressure analysis and tank structural design. However, current studies on the arc-induced overpressure inside a converter transformer rarely involve the modeling of the indispensable pulsating gas bubble.

Given this background, a dynamic model for the gas bubble in a finite fluid domain involving the continuous injection of the arc energy is developed. Meanwhile, a fluid model and the bubble-fluid interaction were used to numerically calculate the overpressure driven by the gas bubble. In addition, a simulation model of an actual full-scale ZZDFPZ-415000/500-600 converter transformer was developed. Based on the ANSYS Fluent environment, the simulation results of gas bubble evolution and overpressure distributions under a 1.2 MJ arcing fault were obtained and analyzed.

2 Theoretical Modeling

2.1 The Dynamics Model for Gas Bubble

When an arcing fault occurs inside a converter transformer, the high-energy arc will instantly vaporize the surrounding insulation oil and produce an initial gas cavity. In a finite fluid domain, the dynamic behavior of a gas bubble can be described as follows [1]:

$$\ddot{R}R^2\left(\frac{1}{R} - \frac{1}{r_d}\right) + \dot{R}^2\left(\frac{3}{2} - \frac{2R}{r_d} + \frac{R^4}{2r_d^4}\right) = \frac{1}{\rho}\left[p_b - \frac{4\mu\dot{R}}{R} - \frac{2\sigma_{\text{oil}}}{R} - p_d\right] \quad (1)$$

where R represents the radius of the gas bubble, and dots represent derivatives with respect to time, r_d is the distance from the gas bubble to the liquid boundary, ρ is the liquid density, μ is the viscosity coefficient of the liquid, p_d is the pressure at the liquid boundary and p_b is the inner pressure of the gas bubble.

Based on the first law of thermodynamics and the assumption that the vapor within the bubble is an ideal gas, the inner pressure of the gas bubble p_b can be expressed as follows:

$$p_b = \frac{(\gamma - 1)}{V_b} \left[\alpha W_{\text{arc}} - 2\pi\rho \dot{R}^2 R^3 + \frac{2\pi\rho}{r_d} \dot{R}^2 R^4 - 4\pi \int_{t_0}^{t} p_d(\tau) R(\tau)^2 \dot{R}(\tau) d\tau \right.$$

$$\left. - 8\pi\sigma_{\text{oil}} \int_{t_0}^{t} R(\tau)\dot{R}(\tau) d\tau - 16\pi\mu \int_{t_0}^{t} R(\tau)\dot{R}(\tau)^2 d\tau + U_0 \right] \tag{2}$$

where t denotes the time, t_0 denotes the initial fault time, γ denotes the specific heat ratio of the vapor, σ_{oil} represents the surface tension coefficient, U_b represents the internal energy of the gas bubble, V_b denotes the gas bubble volume, α is a transfer coefficient and W_{arc} represents the arc energy.

By combining (2) and (1), the complete gas bubble dynamics equation considering continuous arc energy injection can be obtained.

2.2 Fluid Model

To model the oil flow within the converter transformer tank, the transient form of the compressible Reynolds-averaged Navier–Stokes (RANS) equations was used.

$$\rho\left(\frac{\partial \overline{u}_i}{\partial t} + \overline{u}_k \frac{\partial \overline{u}_i}{\partial x_k}\right) = -\frac{\partial \overline{p}}{\partial x_i} + \frac{\partial}{\partial x_j}\left(\mu \frac{\partial \overline{u}_i}{\partial x_j}\right) + \frac{\partial R_{ij}}{\partial x_j} \tag{3}$$

where i and j represent the ith and jth components of a vector, x is the position vector, $\overline{u}$ denotes the time-averaged velocity and p denotes the kinematic pressure of the fluid. R_{ij} is the Reynolds stress as follows:

$$R_{ij} = -\rho\overline{u_i' u_j'} = \mu_T\left(\frac{\partial \overline{u}_i}{\partial x_j} + \frac{\partial \overline{u}_j}{\partial x_i}\right) - \frac{2}{3}\mu_T \frac{\partial \overline{u}_k}{\partial x_k}\delta_{ij} - \frac{2}{3}\rho k \delta_{ij} \tag{4}$$

where k denotes the turbulence kinetic energy, μ_T denotes the turbulence viscosity and δ_{ij} represents the Kronecker delta.

2.3 Bubble-Fluid Interaction

The expanding gas bubble produced by an arc compresses the surrounding oil and leads to fluid field variations throughout the whole tank. In this study, the specific motions governed by the aforementioned equations are assigned to nodes on the bubble boundary, which was realized by means of (user-defined functions) UDFs on the ANSYS Fluent platform. For transient simulations based on diffusion-based smoothing, the mesh is updated at the start of each step. With respect to a control

volume whose boundary ∂V is moving, the conservation equation for a general scalar ϕ on the volume V can be described as [18]:

$$\frac{\mathrm{d}}{\mathrm{d}t} \int\limits_{V} \rho\phi\mathrm{d}V + \int\limits_{\partial V} \rho\phi(\boldsymbol{u} - \boldsymbol{u}_g) \cdot \mathrm{d}\boldsymbol{A} = \int\limits_{\partial V} \Gamma\nabla\phi \cdot \mathrm{d}\boldsymbol{A} + \int\limits_{V} S_\phi\mathrm{d}V \qquad (5)$$

where $\boldsymbol{u}$ denotes the velocity vector of the fluid, Γ is the diffusion coefficient, $\boldsymbol{A}$ is the face area vector, S_ϕ denotes the source term of ϕ, and $\boldsymbol{u}_g$ denotes the velocity of the moving mesh.

3 Simulation and Discussion

In this section, the developed numerical method is utilized to investigate the behavior of the gas bubble produced by the arc and distributions of the arc-induced over-pressure in a ZZDFPZ-415000/500-600 converter transformer. As study cases, the transformer was simulated to be subjected to an arcing fault with energy of 1.2 MJ in the middle of the winding.

3.1 Simulation Model

The converter transformer studied in this paper is an actual ZZDFPZ-415000/500-600 converter transformer within a $\pm$ 800 kV UHV converter system. Based on the geometric parameters and dimensions of the converter transformer, a corresponding three-dimensional model is established, where some structures are simplified, as shown in Fig. 1a. Three points located near the front wall, the sidewall and the cover are selected as measurement points for oil pressure. In addition, a finite element model is established on the ANSYS Fluent platform, as shown in Fig. 1b. Discretizing the three-dimensional model into finer meshes will result in a more accurate calculation results at the expense of computational time. To balance the computation time and the numerical accuracy, the mesh of the insulation oil used in the computational fluid dynamics model is created with 236,942 elements and 49,262 nodes, with a higher grid density in regions with curvature.

3.2 Typical Results

In this case, the converter transformer is simulated to suffer from an arcing fault of 1.2 MJ with a duration of four cycles, which corresponds to a 10-turn (1.98%) short-circuit fault in the middle of the winding. The dynamic growth of the gas bubble
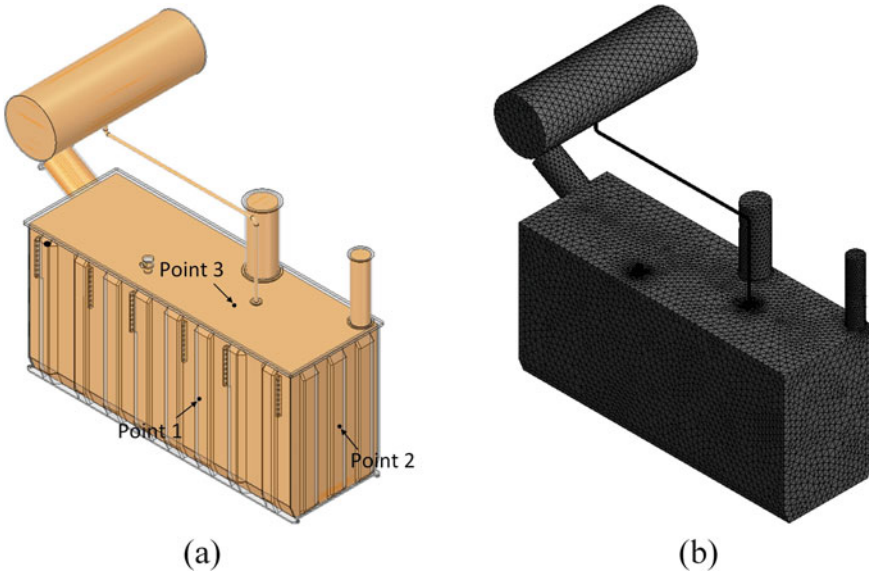
Fig. 1 **a** 3-D model and **b** finite element model of the converter transformer

produced by the arc during the whole arcing fault was calculated, as shown in Fig. 2. Meanwhile, the overpressure distributions within the tank and the pressure history curves at specific locations are presented in Figs. 3 and 4, respectively.

The gas bubble shows a slight pulsation under the arcing fault of 1.2 MJ, which is attributed to the continuous energy injection and the large size of the converter transformer tank. With the continuous arc energy injection, the gas bubble rapidly expands within the first 30.0 ms at a growth rate of 3.5 L/ms. Then, its radius reaches
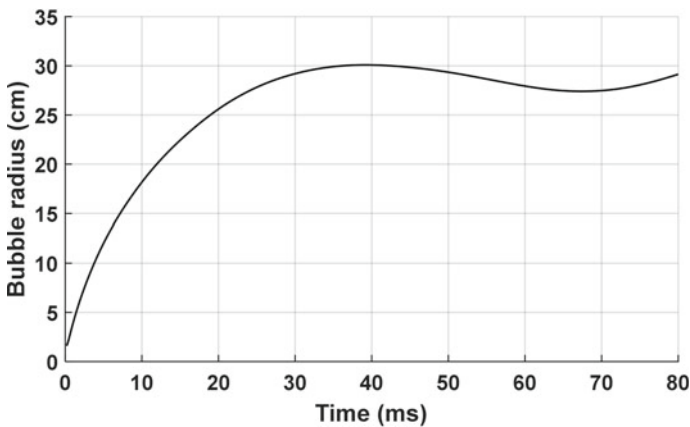
Fig. 2 Calculated gas bubble radius
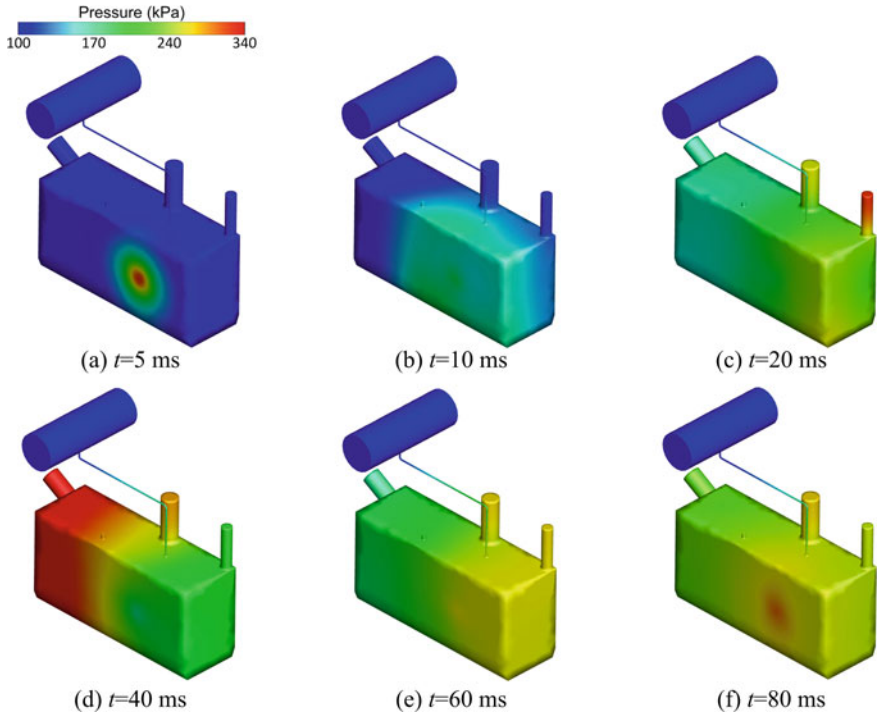
Fig. 3 Oil pressure distributions inside the converter transformer
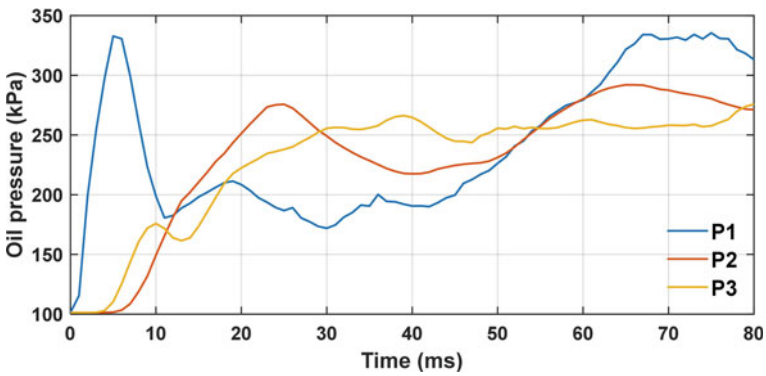
Fig. 4 Oil pressure history curves at different locations

a maximum value of 30.1 cm at $t = 39.2$ ms. Thereafter, although the arc energy is continually injected, the gas bubble begins to contract, and its minimum radius value of 27.4 cm appears at $t = 67.4$ ms. Finally, the gas bubble re-expands again and the radius reaches 29.1 cm at $t = 80$ ms.

When the turn-to-turn short circuit fault occurs, the continuously burning arc instantaneously evaporates the insulating oil, generating a rapidly expanding bubble and dynamic overpressures. As can been seen from Figs. 3 and 4, the area around point 1 first experience high-amplitude dynamic overpressure. Specifically, the oil pressure at point 1 reaches its first peak value of 332.8 kPa at $t = 5$ ms, which corresponds to a rising rate of 46.3 kPa/ms. Due to the reflection of the pressure wave, the oil pressure at point 1 drops to 180 kPa at $t = 11$ ms. At $t = 20$ ms, a significant pressure rise was found in the line side winding terminal bushing, with an amplitude of nearly 340 kPa. Thereafter, the oil pressure near the line side winding terminal bushing declines while the oil pressure near the valve side wingding terminal bushing increases sharply. As the bubble starts to contract, the oil pressures inside the tank correspondingly drop. Finally, the oil pressure near point 3 shows a slight increase due to the re-expansion of the gas bubble.

4   Conclusion

Fault-induced overpressures in oil-filled equipment have long been a challenging issue for the power industry, which is essentially a complex multifield coupling phenomenon involving the dynamic behavior of fault-induced gas bubble growth. Recently, a series of converter transformer explosion accidents urgently increased the need for research on this issue. This paper presents a numerical method for the calculation of oil pressure rise inside the converter transformer tank during an arcing fault where the dynamic behavior of the gas bubble is considered. The simulation results indicate that the oil pressure fluctuation depends on the pulsation of the gas bubble. In addition, the distributions of oil pressure exhibit an uneven nature. The oil near the fault location first experience the dynamic overpressure with peak pressure values of 332.8 kPa. The proposed method and representative findings enrich fundamental studies on the dynamic effects of arcing faults on the pressure rise inside converter transformers. They can also serve as effective tools for replacing costly and high-risk field tests and further investigation of explosion-proof and mitigation methods.

References

1. Yan C, Xu C, Liu H, Guo J, Zhang P, Xu Y, Zhou X, Zhang B (2023) Research on oil pressure rise and fluctuation due to arcing faults inside transformers. IEEE Trans Power Delivery 38(2):1483–1492

2. Yan C, Zhang P, Guo J, Liu H, Yang H, Zhang B (2022) An improved coupled FE–circuit model for turn-to-turn short-circuit faults inside converter transformers. IEEE Trans Magn 59(5):8400205

3. Yan C, Zhang P, Xu Y, Liu S, An T (2022) Bidirectional field–circuit coupling analysis of converter transformer inter-tap short-circuit faults in on-load tap changers. IET Gener Trans Dist 16(23):4750–4760

4. Mahieu WR (1975) Prevention of high-fault rupture of pole-type distribution transformers. IEEE Trans Power Appar Syst 94(5):1698–1707

5. Kawamura T, Udea M, Ando K, Maeda T, Abiru Y, Watanabe M, Moritsu K (1988) Prevention of tank rupture due to internal fault of oil-filled transformer. In: Proceedings of the CIGRE 1988 Session. CIGRE, Paris, France

6. Foata M, Iordanescu M, Hardy C (1988) Computation methods for the analysis of explosions in oil-insulated electrical equipment. IEEE Trans Power Syst 3(1):286–293

7. Dastous JB, Hamel A, Foata M (2003) Estimating overpressures in pole-type distribution transformer part II: prediction tools. IEEE Trans Power Delivery 18(1):120–127

8. Perigaud G, Muller S, de Bressy G, Brady R, Magnier P (2008) Contribution to the study of transformer tank rupture due to internal arcing development of a computer simulation tool. In: IEEE power and energy society general meeting (PESGM). IEEE, Portand, OR, USA

9. Allaire G, Clerc S, Kokh S (2002) A five-equation model for the simulation of interfaces between compressible and fluids. J Comput Phys 181(2):577–616

10. Dastous JB, Lanteigne J, Foata M (2010) Numerical method for the investigation of fault containment and tank rupture of power transformers. IEEE Trans Power Delivery 25(3):1657–1665

11. Hackl A, Hamberger P (2012) Predict the rupture of transformer tanks with static FEM analysis. In: XXth international conference on electrical machines. IEEE, Marseille, France

12. Dastous JB, Taschler E, Belanger S, Sari M (2017) Comparison of numerical methods for modeling overpressure effects from low impedance faults in power transformers. Procedia Eng 202:202–223

13. Brodeur S, Lê VN, Champliaud H (2021) A nonlinear finite-element analysis tool to prevent rupture of power transformer tank. Sustainability 13(3):1048

14. Li B, Hao Z, Ding G, Zhang Y, Xue Z, Wu X (2021) Modeling and analysis of tank rupture due to internal electrical fault in oil-filled power transformer. In: International conference on advanced electrical equipment and reliable operation (AEERO). IEEE, Beijing, China

15. Li J, Yang X, Wang S, Jiang X, Ma Y (2022) Research on fault pressure variation characteristics of oil-immersed power transformers. In: IEEE 5th international conference on electronics technology (ICET). IEEE, Chengdu, China

16. Yan C, Zhou X, Xu Y, Wu Y, Liu H, Xu C, Wei Y, Zhang B (2021) Experimental study on the gas bubble temperature around an arc under insulation oil. IEEE Trans Power Delivery 36(2):1245–1248

17. Yan C, Xu Y, Zhang P, Kang S, Zhou X, Zhu S (2022) Investigation of the gas bubble dynamics induced by an electric arc in insulation oil. Plasma Sci Technol 24(4):044003

18. Hinze JO (1975) Turbulence. McGraw-Hill Publishing Co., New York, USA

Thermal Characteristics of 10 kV Cable Joints Under Defects in the Crimping Process

Ting Jiao

Abstract In order to study the impact of crimping defects caused by excessive contact resistance on the temperature distribution of cable joints, based on the contact resistance theory of equivalent conductivity, a multi-physical field coupling simulation model of 10 kV high-voltage cable joints with crimping defects was established using finite element software, and the variation of thermal stress characteristics under the condition of crimping defects in cable joints was studied. The results show that, taking $k = 5$ as an example, the temperature at the conductor junction of the cable joint with crimping defects is the highest, reaching 58.5 °C, which is 19.9% higher than without defects. As the contact coefficient k increases, the temperature of the connector increases, but the influence of the change in k on the cable core temperature at 2500 mm from the center of the connector can be ignored. The research results of this paper can provide theoretical support for monitoring heating faults caused by crimping defects in 10 kV cable joints.

Keywords Crimping defects · 10 kV cable joints · Contact resistance theory

1 Introduction

With the rapid development of urban power grids in China, the demand for power cables of various voltage levels in power systems is increasing daily [1–3].

Under the influence of the external environment, some latent faults inevitably occur during the operation of cable lines, even serious accidents such as insulation breakdown and explosion. In the past, statistical analysis has been conducted on cable accident data in major cities across the country, and the results show that the manufacturing quality of the body, the quality of laying and installation, the manufacturing quality of accessories, and external force damage are the four major types of causes for cable failures [4–6].

T. Jiao (✉)
State Grid Shanghai Electric Power Research Instituute, Shanghai 200437, China
e-mail: jiaoting92@163.com

During the manufacturing or installation process of cable connectors, it is easy to cause contact resistance (i.e., crimping defects) between the crimping tube and the cable core conductor, making the failure rate of the intermediate cable connector much higher than that of the cable body [7, 8].

However, current research on cable joint defects mainly focuses on insulation interface creep, internal air gap, insulation moisture, and other aspects. For example, In literature [9] has studied the distribution characteristics of electric field and temperature field of T-type cable terminal joints with air gap defects at the insulation interface. The variation rules of electric field and temperature field amplitudes under defect conditions are analyzed. The characteristic quantities and monitoring locations that can effectively reflect the air gap defects in T-type cable terminal joints are proposed. In literature [10] typical artificial particles, including air particles, metal particles, were added to the cable's insulation.

Therefore, studying the impact of crimping defects on cable joints is significant. This paper established a multi-physical field coupling simulation model of 10 kV high-voltage cable joints with crimping defects using finite element software based on the contact resistance theory of equivalent conductivity. The variation of thermal stress characteristics was also established under the condition of crimping defects in cable joints was studied.

2   Thermal Characteristic Calculation Model

2.1   Principles of Thermal Characteristic Calculation

To study the electrothermal coupling problem of cable joints, a magnetic vector potential $\dot{A}$ is introduced based on Maxwell's Equation. The control equation for the magnetic vector potential in the current region with an excitation source is Eq. (1), and the control equation for the magnetic vector potential in the non-current region without an excitation source is Eq. (2).

$$\left(\nabla \cdot \frac{1}{u} \nabla\right)\dot{A} = -\dot{J}_s + j\omega\sigma\dot{A} \tag{1}$$

$$\left(\nabla \cdot \frac{1}{\mu} \nabla\right)\dot{A} = 0 \tag{2}$$

where, ω is the angular frequency, μ is the magnetic permeability, σ is the conductivity, and $\dot{J}_s$ is the applied current density. The magnetic field problem of cable joints can be summarized as a solution to Eqs. (1) and (2).

For the cable joint temperature field calculation, the cable joint belongs to a solid medium, and the thermal conductivity differential Equation satisfied by its temperature field can be written into Eq. (3) in a rectangular coordinate system. Here, ρ represents the density of the microelement, c is the specific heat capacity, T is the temperature, t is the time, q_v is volumetric heat production rate, and λ is thermal conductivity. The cable joint temperature field studied in this article belongs to a steady-state temperature field. Therefore, the steady-state heat conduction differential Equation can be simplified to Eq. (4).

$$\rho c \frac{\partial T}{\partial t} = \frac{\partial}{\partial x}\left(\lambda \frac{\partial T}{\partial x}\right) + \frac{\partial}{\partial y}\left(\lambda \frac{\partial T}{\partial y}\right) + \frac{\partial}{\partial z}\left(\lambda \frac{\partial T}{\partial z}\right) + q_v \tag{3}$$

$$\frac{\partial^2 T}{\partial x^2} + \frac{\partial^2 T}{\partial y^2} + \frac{\partial^2 T}{\partial z^2} + \frac{q_v}{\lambda} = 0 \tag{4}$$

The coupling between the electromagnetic field and the temperature field in the air of a cable joint requires that the heat source term in the equation be known first when solving the temperature field distribution through the heat conduction control equation. The heat source term is determined by the electromagnetic loss density calculated in the electromagnetic field, and belongs to the source coupling relationship category. The electromagnetic loss density of the cable joint conductor is related to the conductivity of the metal conductor material, and the conductivity is a function of temperature, As it belongs to the category of attribute coupling, the calculation of electromagnetic field and temperature field of cable joints is a two-way coupling process.

2.2 Calculation Model

The electromagnetic, thermal coupling field modeling calculation was conducted for the cold shrinkable straight-through XLPE power cable connectors. The axial sectional view of the cable connector was obtained by taking the axial direction of the cable connector as the z-axis and the radial direction as the x-axis, as shown in Fig. 1a. The cable joint geometric model and joint cable grid division are shown in Fig. 1b and c.

The material physical parameters required for calculating the intermediate cable joint's electromagnetic, thermal coupling field are shown in Table 1.
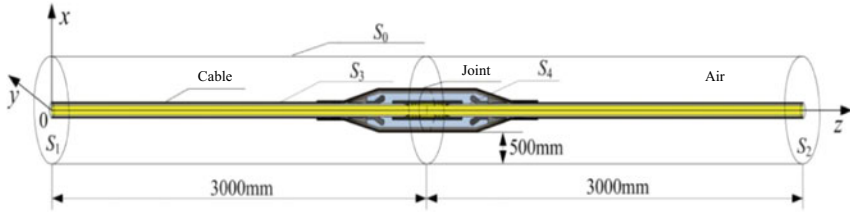
(a) Overall model
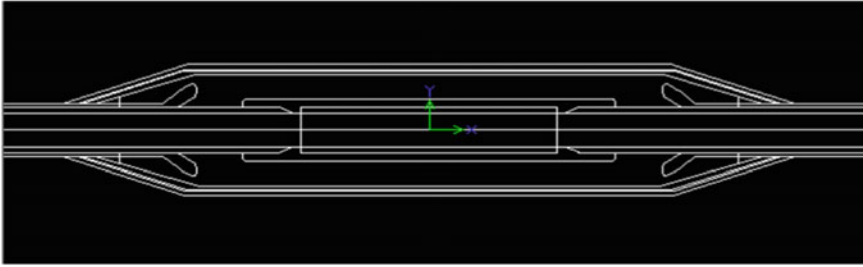
(b) Cable joint geometric model
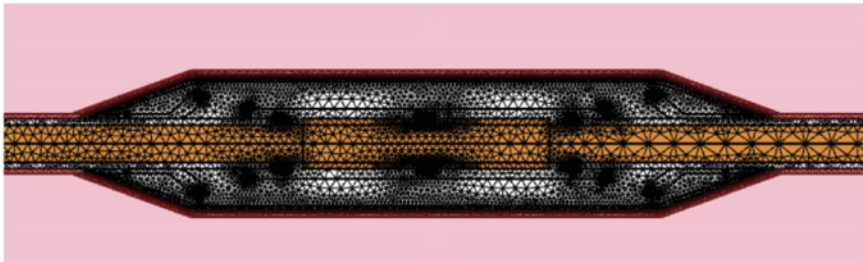
(c) Cable joint grid division

Fig. 1 Simulation model and meshing

Table 1 Parameters

Position	Medium material	Thermal conductivity W/m k	Resistivity Ω m	Relative dielectric constant
Conductor	Copper	401	1.75e−8	/
Insulating layer	XLPE	0.29	1.36e13	2.25
Stress cone	Semiconductive body	0.286	0.002	30
Silicone cap	Silastic	0.27	1.42e13	2.8

3 Calculation Results and Analysis of Thermal Characteristics

3.1 Temperature Distribution Characteristics

Setting the cable load current of 645 A, contact coefficient k = 5 (The calculation method is shown in Eq. 5), and ambient temperature of 25 °C, the temperature distribution of the cable joints can be calculated as shown in Fig. 2. Figure 3 shows the temperature radial distribution curve on the central cross-section of the cable connector at z = 3000 mm and the temperature radial distribution curve on the cross-section of the cable body at z = 5500 mm.

$$k = \frac{\frac{1}{\sigma_2} \cdot \frac{l}{\pi \cdot r_2^2}}{\frac{1}{\sigma_1} \cdot \frac{l}{\pi \cdot r_1^2}} = \frac{\sigma_1}{\sigma_2} \cdot \left(\frac{r_1}{r_2}\right)^2 \tag{5}$$

As shown in Fig. 2, the temperature at the conductor connection of the cable joint is the highest, reaching 58.5 °C, which is 19.9% higher than the calculated result without considering the contact resistance (48.8 °C).

As can be seen from Fig. 3, the temperature of conductor at the cross sections of z = 3000 mm and z = 5500 mm is 58.5 °C and 53.4 °C, respectively. The temperature of the cable core conductor at the center of the joint is 9.6% higher than that at the body. The corresponding surface temperatures are 41.8 °C and 48.2 °C, respectively, and the central surface temperature of the joint is 13.3% lower than that of the body. The reason for this phenomenon is that due to the large outer diameter of the cable connector, the heat dissipation area is large, and the convective heat dissipation ability is also relatively strong.

Figure 4 shows the axial distribution curves of cable core and surface temperatures, respectively. As can be seen from the figure, when k = 5, the temperature of the cable

Fig. 2 Temperature distribution
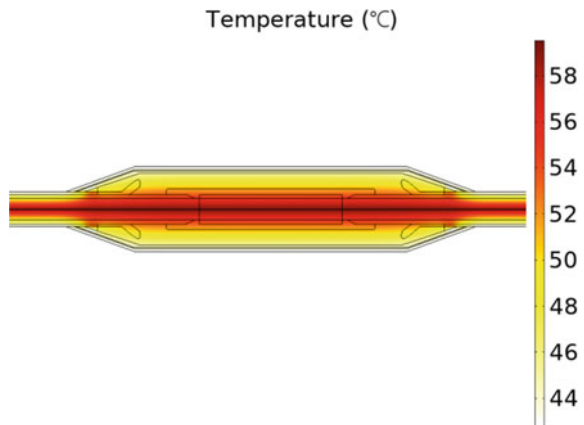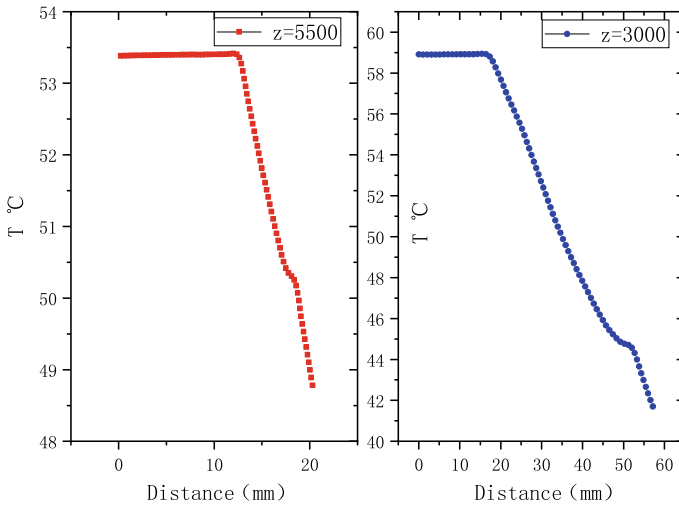
Temperature (°C)

Fig. 3 Radial temperature distribution characteristics

core conductor exhibits an exponential downward trend in the axial (z = 3000 mm) to both ends of the cable body (z = 0 mm and z = 6000 mm). In addition, the cable core temperature at the joint is higher, but its surface temperature is lower due to the cable joint surface's strong heat dissipation ability.

When $k = 1, 5, 9$, and 11, the calculated temperature distribution is shown in Fig. 5. As can be seen from the figure.
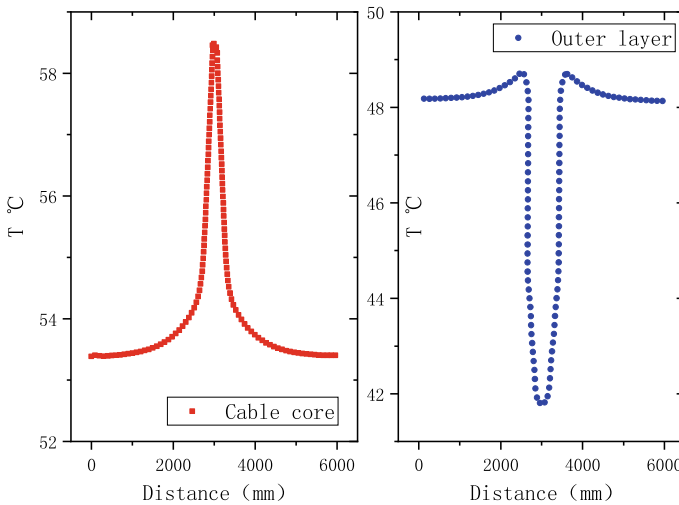
Fig. 4 Axial temperature distribution characteristics
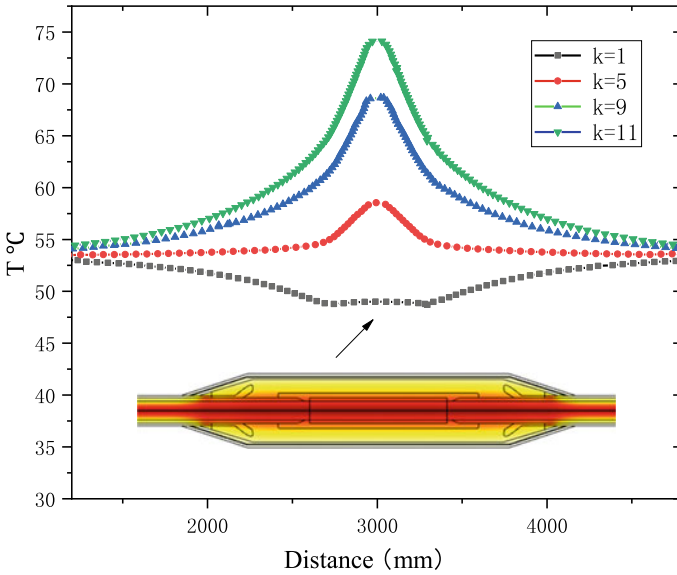
Fig. 5 Effect of contact resistance on temperature distribution

1. As k increases, the temperature of the core conductor at the center of the joint at z = 3000 mm increases. For example, when k increases from 9 to 11, the temperature increases from 69.18 to 74.74 °C, increasing by 5.56 °C. The core conductor temperature of the cable body at z = 5500 mm remains almost constant as the contact coefficient k increases. This is because the axial heat conduction effect of cable cores within the range of z < 500 mm and z > 5500 mm has become very weak, making the temperature of the cable body core at 2500 mm from the center of the connector negligible due to the change in the connector contact coefficient k.

2. As k increases, the volumetric heat generation rate of the equivalent conductor at the joint increases. However, the dominant heat dissipation at the joint when the contact coefficient k is less than 2.5 and the temperature of the cable body is higher than the temperature of the cable joint. When the contact coefficient k is greater than 2.5, the heat generation at the joint is dominant. The temperature of the cable joint is higher than the temperature of the cable body.

4 Conclusions

This paper established a multi-physical field coupling simulation model of 10 kV high-voltage cable joints with crimping defects using finite element software based on the contact resistance theory of equivalent conductivity. The main conclusions of the paper are as follows.

1. Taking $k = 5$ as an example, the temperature at the conductor junction of the cable joint with crimping defects is the highest, reaching 58.5 °C, which is 19.9% higher than without defects.
2. The temperature of the cable core conductor exhibits an exponential downward trend in the axial distance from the center of the cable joint (z = 3000 mm) to both ends of the cable body (z = 0 mm and z = 6000 mm). The cable core temperature at the joint is higher, but its surface temperature is lower due to the cable joint surface's strong heat dissipation ability.
3. As the contact coefficient k increases, the temperature of the cable core the connector increases, but the influence of the change in k on the cable core temperature at 2500 mm from the center of the connector can be ignored.

References

1. Wu RN, Chang CK (2011) The use of partial discharges as an online monitoring system for underground cable joints. IEEE Trans Power Delivery 26(3):1585–1591
2. Jiang J, Ge Z, Zhao M et al (2018) A capacitive strip sensor for detecting partial discharge in 110-kV XLPE cable joints. IEEE Sens J 18(17):7122–7129
3. Chang CK, Chang HH, Boyanapalli BK (2022) Application of pulse sequence partial discharge based convolutional neural network in pattern recognition for underground cable joints. IEEE Trans Dielect Electr Insul 29(3):1070–1078
4. Yunpeng Z, Shuai H, Mingli F et al (2022) Electric field simulation analysis of typical defects of 220kV molded joints of polypropylene cable. In: IEEE 5th international electrical and energy conference (CIEEC), pp 2309–2313
5. Metwally IA, Al-Badi AH, Al-Hinai AS et al (2016) Influence of design parameters and defects on electric field distributions inside MV cable joints. In: 18th mediterranean electrotechnical conference (MELECON), pp 1–6
6. Khamlichi A, Adel M, Garnacho F et al (2017) Measuring cable sheath currents to detect defects in cable sheath connections. In: 52nd international universities power engineering conference (UPEC), pp 1–6
7. Liang Y, Qi Y (2022) Research on the defects and improvement of the manufacturing process of YJYD and DYJY cable connectors for civil aviation airport navigation lighting. China Equip Eng 498(10):3–7. (in Chinese)
8. Fang Y (2018) Detection method and application of cable joint crimping defects based on temperature measurement. Chongqing University. (in Chinese)
9. Liu G, Xu Q, Shi C et al (2022) Study on the influence of insulation interface air gap defects and their dampness on the electric field of T type cable joints. Insulating Mater 55(09):107–115 (in Chinese)
10. Bhatti AA, Yang B, Peng X et al (2021) Simulation of temperature distribution behavior of high voltage cable joints with typical defects. In: 6th Asia conference on power and electrical engineering (ACPEE), pp 1139–1143

Simulation of Mechanical Characteristics of Contact Group During the Switching Process of On-Load Tap Changer

Zhiqin Ma, Danyu Jiang, Dan Zhou, Linglong Cai, Ziyang Hong, and Zihao Liao

Abstract The contact group is the core component of the on-load tap changer, which has a crucial impact on the mechanical life of the tap changer. In this section, the dynamic and static simulation models of the transition contact of the on load tap changer are established, and the static and dynamic simulation analysis of the contact process of the contact is carried out using the COMSOL finite element software, and the motion characteristics of the dynamic contact bridge of the transition contact are analyzed. Through the simulation analysis, the mechanical characteristics of the Contact process of the transition contact of the on load tap changer are obtained. The greater the stiffness coefficient of the spring behind the static contact, the greater the contact pressure on the contact surface, and the greater the degree of spring bounce; The curvature radius of the moving contact is different, and the degree of spring bounce is different, which needs to be selected and analyzed according to the actual situation; The higher the initial speed of the moving contact, the longer the bounce time, and the more intense the bounce.

Keywords Mechanical characteristics · Contact group · On-load tap changer · Switching process

1 Introduction

On-load tap-changer (OLTC) is the key component of transformer which can adjust the output voltage under load condition, through switching the tap of transformer winding to change the turn ratio [1–3]. Due to the lack of effective online monitoring methods, the internal state of the tap changer during the switching operation is difficult to be directly obtained [4]. The core of on-load tap changer is the switching

Z. Ma (✉) · D. Jiang · L. Cai · Z. Hong · Z. Liao
Guangdong Electric Power Equipment Reliability Key Enterprise Laboratory,
Guangzhou 510080, China
e-mail: mzhqcqu@163.com

Electric Power Research Institute of Guangdong Power Grid Co., Ltd, Guangzhou 510080, China

core, and the most important part of the switching core is the contact group [5]. According to data statistics, mechanical faults of OLTC account for more than 25% of total transformer faults in recent years, which are mainly in contacts and driving components [6]. One example of the contact group failure in a 500 kV substation is that the 4C moving contact and the fixed contact of the selected part of the on-load tap changer are not in good contact, causing internal spark discharge and intermittent growth of acetylene in the oil [7]. For on-load tap changer, the mechanical life of the contact has a direct impact on the mechanical life of the on-load tap changer, and the key indicator to measure the mechanical life of the contact is its mechanical characteristics [8, 9]. This paper analyzes the mechanical characteristics of the contact group by studying the static and dynamic contact process of the on load tap changer contact.

2 Modeling Methods

This paper needs to establish a static contact model for the contact process of the dynamic and static contacts. Because the contacts on both sides of the contact bridge are symmetrical contacts, the simulation model is simplified to facilitate calculation. The simulation model of the contact process is established using the software Solidworks, where the fixed constraint fit is adopted between the dynamic contact bridge and the dynamic contact, and a virtual spring is added with the static contact to simulate the compensation spring assembled with the static contact [10] (Fig. 1).

Import the model into the simulation software COMSOL, establish a three-dimensional simulation environment, study solid mechanics and current physical field, set the material as copper, fix the fixed parts of the static contact, set the spring stiffness coefficient as 100 N/mm, set a specified displacement of the moving contact bridge, ensure full contact between the moving contact and the static contact, apply corresponding voltage on the contact bridge, so that the static contact is grounded,
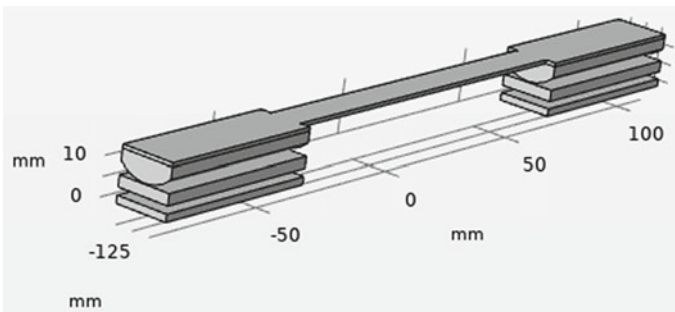
Fig. 1 Simulation model of the contact group

Test and simulate the solid mechanics characteristics and current and voltage characteristics of the entire simulation process. The stress nephogram is shown in Fig. 2. It can be seen from the contact resistance stress nephogram that the contact pressure and the contact area between the moving and static contacts increase with the increase of the displacement of the moving contact.

For the contact pressure and contact resistance in the contact process of dynamic and static contacts, the spring will have a greater impact on the numerical changes in the simulation process. Without changing other conditions, change the stiffness coefficient of the spring, simulate the changes in the contact pressure and contact resistance, set the spring stiffness coefficient as k. The experimental results are shown in Fig. 3.

For the contact process of moving contacts, the influence of the curvature of moving contacts on the contact process of moving contacts also needs to be studied. Under other conditions, the contact process of moving contacts and stationary contacts with different curvature is simulated, and the curvature is set as ρ. The variation curve of contact resistance is shown in Fig. 4. The curvature of the moving contact mainly affects the contact area between the moving and stationary contacts. The larger the curvature, the smaller the contact area under the same displacement, but the faster the rate of change in the contact area.

After being impacted by a fast mechanism, the dynamic contact bridge mechanism can be simply regarded as simple harmonic motion within a certain time period due to the action of the tail push spring. However, in practical situations, there must be damping during the motion process. The damping of the motion of the dynamic
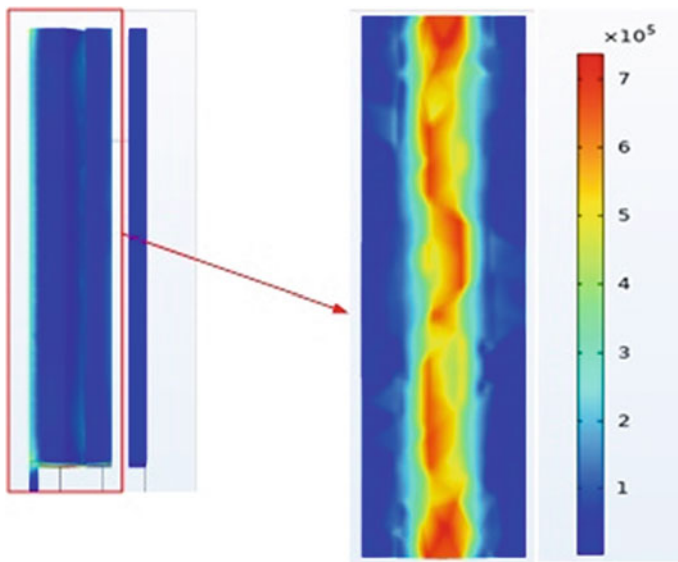
Fig. 2 Surface stress cloud of the static contact
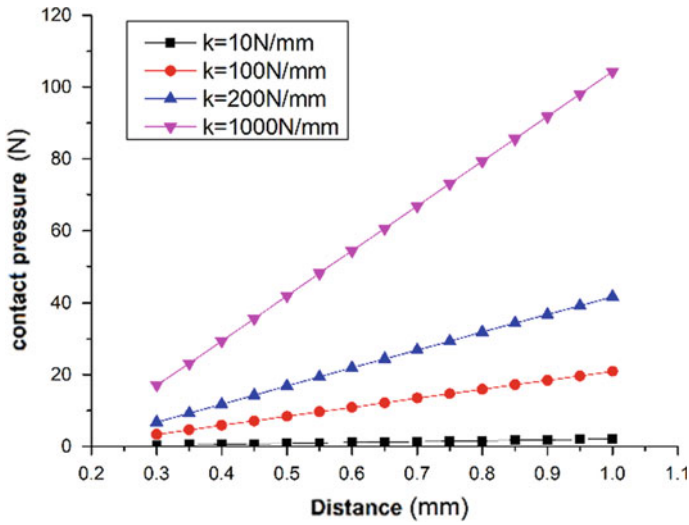
Fig. 3 The change of contact pressure with displacement under different stiffness coefficients
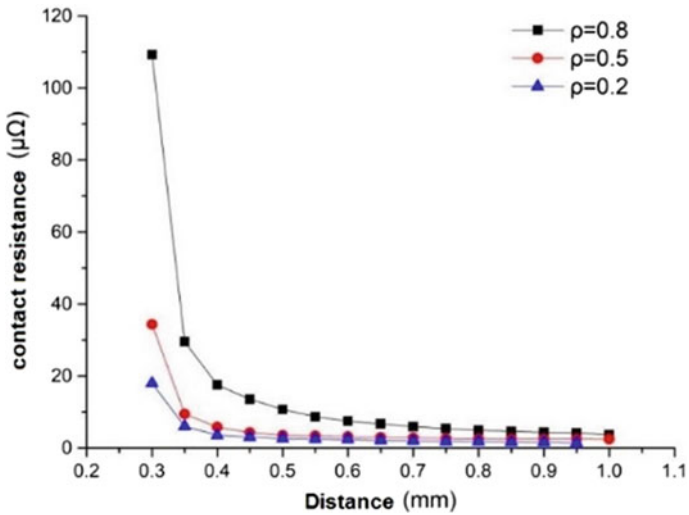
Fig. 4 Contact resistance between moving and stationary contacts under different curvature conditions

contact bridge system should be less than the critical damping. At this point, we can consider the motion as a low damping vibration system. The motion pattern can be represented by the following equation.

$$v(t) = \left[G_1 \exp(i\omega_D t) + G_2 \exp(-i\omega_D t) \right] \exp(-\varepsilon\omega t) \qquad (1)$$

By analyzing the dynamic contact bridge system of the transition contact, a dynamic simulation model of the transition contact of the on-load tap changer is established. Based on calculation, analysis, and research, the contact time of the dynamic and static contacts of the transition contact is 28–30 ms. This article only analyzes the mechanical characteristics of the contact at the moment of contact. At this time, the distance between the contact and the gap is about 1 mm, the stiffness coefficient of the tail push spring is 100 N/mm, and the contact curvature is 0.5. Given the initial velocity of the moving contact, a dynamic motion model of the transition contact is constructed. Through mechanical calculations of surface integration on the contact surface, the contact pressure curve is obtained as shown in the following Fig. 5.

From the above figure, it can be seen that when the dynamic and static contacts of the transition contact come into contact, the surface contact pressure continuously increases with the increase of movement time. However, due to the effect of the spring behind the static contact, the contact between the dynamic and static contacts is not completely rigid body contact, and the contact pressure is small. However, due to the presence of the spring, the dynamic and static contacts undergo significant bouncing before stable contact. However, due to the fixed effect of the fan-shaped component, the degree of contact bouncing is relatively small, two bounces occurred, and after the second bounce, the moving and stationary contacts made stable contact.
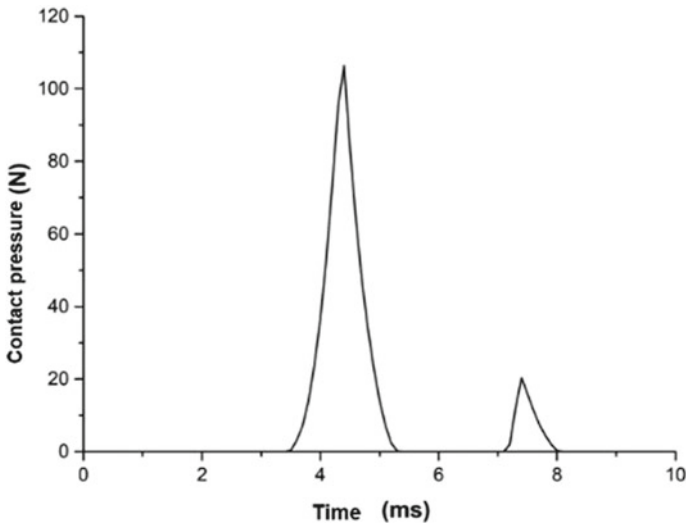
Fig. 5 Surface contact pressure of transition contact in dynamic contact process

3   Simulation of Action Characteristics

3.1   The Influence of Spring Stiffness Coefficient

From the figure, it can be seen that under the same other conditions, the larger the spring stiffness coefficient behind the static contact, the higher the contact pressure, and the higher the peak value. However, it also reaches the peak value later. This is because at the same initial speed, the larger the spring stiffness coefficient, the harder it is to compress the spring, the greater the resistance the dynamic contact faces, the higher the surface contact pressure, but the longer the movement time, and the more difficult it is to reach the peak value of the contact pressure, Due to the higher contact pressure on the contact surface, the greater the reverse force on the moving contact, the more severe the bounce, and the longer the bounce time, as shown in the Fig. 6, the longer the interval between two contact times. When the stiffness coefficient of the spring reaches a sufficient size, it is extremely difficult for the spring to be compressed, similar to a rigid body. Even if the stiffness coefficient of the spring increases further, it is difficult for the contact to compress the spring again, and the peak contact pressure will hardly change. The dynamic and static contacts are in close contact with the rigid body, making it difficult for the spring to play a buffering role. The spring rebounds and grows, causing significant wear and tear between the contacts, making it difficult to fully contact, It is not conducive to the normal operation and mechanical life of the on-load tap changer. Therefore, at the beginning of the design, it is necessary to consider the relationship between the spring stiffness coefficient to ensure that the transition contact is in full contact, reducing rebound and contact wear as much as possible, which is conducive to extending the service life of the on-load tap changer.

3.2   The Influence of Contact Curvature Radius

Under the same other conditions, different curvature radii of the contact will have different effects on the collision process of the moving and stationary contacts. The following Fig. 7 shows the impact of different curvature of the transition contact on the contact pressure. In general, the smaller the curvature of the contact, the larger the curvature radius of the contact, and the larger the contact pressure, which is more likely to cause bounce. However, when the curvature radius of the contact reaches a certain degree, due to the effect of the compensation spring of the static contact, the dynamic and static contacts do not have direct contact, and the static contact appears a slight tilt in the contact process, which makes the contact collision occur torsional vibration, increasing the contact pressure and bounce time after the contact collision.
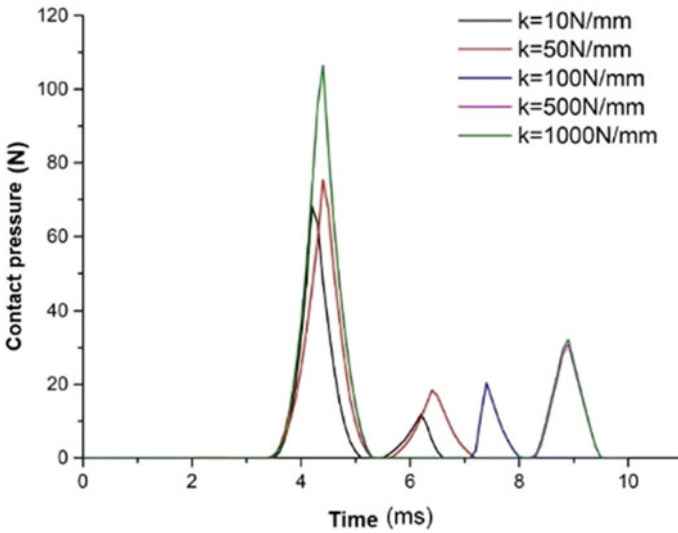
Fig. 6 The contact pressure with movement time under different spring stiffness
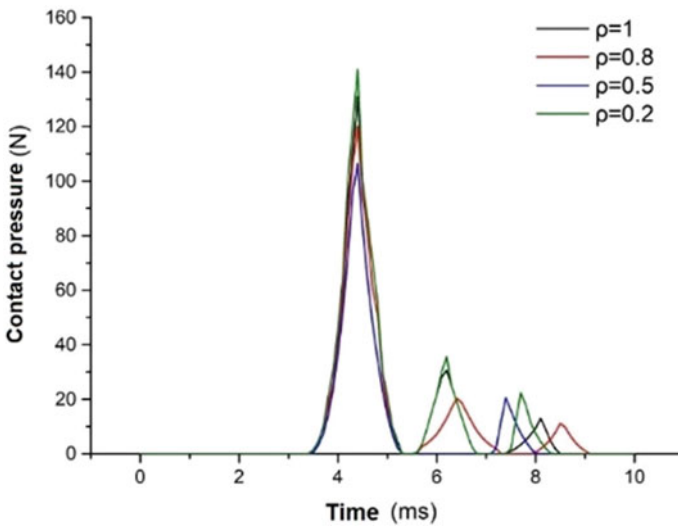
Fig. 7 The variation of contact pressure between contacts with different curvature radii during movement time

3.3 The Influence of Different Initial Velocities

As shown in Fig. 8, under different initial velocities, according to the law of conservation of energy and the law of momentum, the larger the initial velocity of the moving
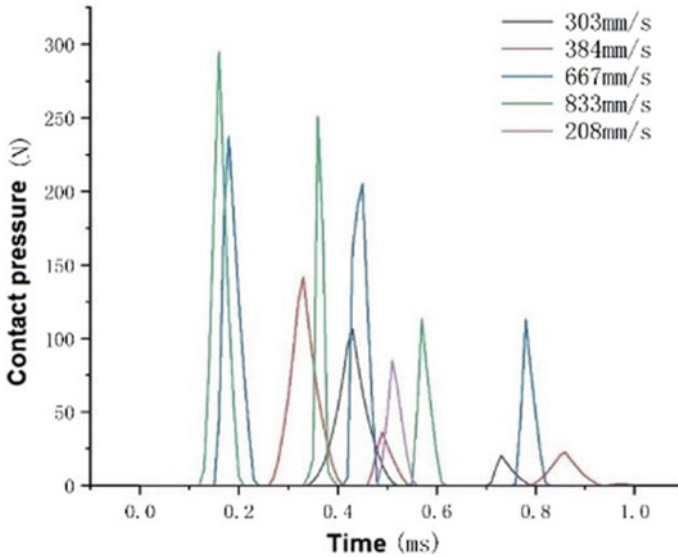
Fig. 8 The variation of contact pressure with time under different initial velocities

contact, the greater the contact pressure between the contacts. At the same time, the degree of contact bounce is proportional to the initial velocity of the moving contact. The larger the initial velocity of the contact, the longer the contact bounce time and the more bounce times. Therefore, the degree of contact bounce can be reduced by controlling the initial velocity of the contact.

4 Conclusion

In this section, the dynamic and static simulation models of the transition contact of the on load tap changer are established, and the static and dynamic simulation analysis of the contact process of the contact is carried out using the COMSOL finite element software, and the motion characteristics of the dynamic contact bridge of the transition contact are analyzed. Through the simulation analysis, the mechanical characteristics of the contact process of the transition contact of the on load tap changer are obtained. The greater the stiffness coefficient of the spring behind the static contact, the greater the contact pressure on the contact surface, and the greater the degree of spring bounce; The curvature radius of the moving contact is different, and the degree of spring bounce is different, which needs to be selected and analyzed according to the actual situation; The higher the initial speed of the moving contact, the longer the bounce time, and the more intense the bounce.

References

1. International Electrotechnical Commission (2004) IEC 60214-2 tap-changers-part 2: application guide. Standard Press of International Electrotechnical Commission, Switzerland
2. Cao H (2020) Identification of the operation state of transformer on-load tap-changer based on time-frequency characteristic analysis. High Voltage Apparatus56(4):215–221 (in Chinese)
3. Tojo S (2004) Loading guide for individual transformers with on-load tap-changer facility and the comparison of calculation results with established loading guide and the consideration. IEEE Trans Power Energy 124(9):1161–1168
4. Lei Y, Zhao L, Zhu Q, Bao L, Cheng J, Yang J (2023) Analysis and simulation study on a fault of service duty test of vacuum on-load tap changer. J Phys: Conf Ser 2433:1–7
5. Seo J, Ma H, Saha TK (2017) A Joint vibration and arcing measurement system for online condition monitoring of on-load tap changer of the power transformer. IEEE Trans Power Delivery 32(2):1031–1038
6. Geng J, Zhang Z, Wang X, Gao S, Wang P (2022) On-load tap-changer fault mode recognition based on the singular value of Hilbert energy spectrum time-frequency matrix and spectrum entropy. IET Gener Trans Dist 16:3256–3266
7. Lan D (2021) Research on 500 kV transformer on-load tap changer fault treatment and physical properties testing. J Phys: Conf Ser 2083:1–7
8. Gao T, Zhao H, Li X et al (2019) Mechanical fault recorgnition of on-load tap-changer based on s-transform and singular value decomposition. Guangdong Electr Power 32(10):111–118 (in Chinese)
9. Pan Z, Zhang J (2020) Mechanical condition detection of vacuum on-load tap-changer for converter transformer based on time-frequency domain characteristics of vibration signal. High Voltage Apparatus 56(6):232–237 (in Chinese)
10. Pan Z, Deng J, Peng X et al (2022) Research on arc test in oil chamber of vacuum on-load tap-changer of converter transformer. Guangdong Electr Power 35(12):76–83 (in Chinese)

Structural Dynamic Analysis and Static Stability Analysis of Drum-Type Self-Standing Power Transmission Towers

Chengyang Yan, Lijun Wang, and Wenzhe Zhang

Abstract Power transmission towers are the support point of transmission lines in power system. With the increase of voltage level and the development of UHV transmission, the stability and safety of power transmission towers has been paid more attention. At present, it is an effective method to design and verify power transmission towers by analyzing structural and mechanical characteristics of power transmission towers with finite element analysis software. The characteristic analysis of power transmission towers is mainly divided into static analysis and dynamic analysis. The two bases are buckling analysis and modal analysis respectively. In this paper, aiming at drum-type self-supporting power transmission towers, finite element simulation model of power transmission towers is established by using finite element software ANSYS. Further more, Modal analysis and buckling analysis of strong wind load under different wind directions are carried out. The results show that the first-order natural frequency of power transmission towers is 2.02, which is close to the result of empirical formula 2.05. The low-order vibration modes of power transmission towers are mainly flat bending, while the high-order vibration modes are mainly local torsion. The main materials and adjacent auxiliary materials in the lower section of the tower body are weak parts, so reinforcement and improvement are required. Eigenvalue buckling analysis and nonlinear buckling analysis both show that the tower structure is most likely to destabilize when the wind direction angle is 90°, and the results of Eigenvalue buckling analysis are more conservative, which must be based on the results of nonlinear buckling analysis.

C. Yan · L. Wang (✉) · W. Zhang
State Key Laboratory of Electrical Insulation and Power Equipment, Xi'an Jiaotong University, Xi'an 710049, China
e-mail: lijunwang@mail.xjtu.edu.cn

C. Yan
e-mail: yanchengyang@stu.xjtu.edu.cn

W. Zhang
e-mail: zhangwenzhe@stu.xjtu.edu.cn

1 Introduction

According to statistics, most of the collapse accidents of power transmission towers are caused by strong wind [1, 2]. Wind load can be divided into static wind and pulsating wind. The research on response of wind load to power transmission towers is also divided into static analysis and dynamic analysis [3, 4]. Static stability analysis of power transmission towers under strong wind is the basis of static analysis of wind load of power transmission towers. Buckling analysis is the core method to study static stability, which can determine the critical destabilization load of structure under specific load [5]. Modal analysis of power transmission towers is the basis of dynamic analysis of wind load of power transmission towers, which can get the vibration frequency and mode [6].

After the model of power transmission towers is established, the dynamic characteristics of the structure need to be analyzed, and the modal analysis needs to be carried out by means of finite element analysis software to get its natural frequency and corresponding vibration mode. Liang et al. [7] takes the power transmission tower line system as the research object and considers the influence of multi-directional vibration. The self-vibration frequency of tower line system is obtained by modal analysis. It is found that the self-vibration frequency of tower line system is mainly affected by lines. Gao et al. [8] established a steel tube composite tower model with mixed poles and beams, and obtained the first modes of the model using subspace iteration method. Buckling analysis is a typical method to study the static stability of power transmission towers, which has been studied by many scholars at home and abroad. Liu and Kang [9] takes the unstable cable-stayed portal tower as the research object, carries out the static stability analysis under the multi-load condition by the finite element method. Liu et al. [10] analyzed the non-linear buckling of power transmission towers by ABAQUS finite element analysis software and combined with Budiansky-Roth criterion, and obtained the critical instability wind speed.

In this paper, the 1W2C9 drum-type self-standing power transmission tower applied in Guangdong area is taken as the research object, and a refined finite element model of the power transmission tower is established by using ANSYS software. First, the first ten modes of the power transmission tower are extracted, their vibration modes and frequencies are analyzed, and the first vibration modes obtained are verified by theoretical calculation. Then considering the influence of wind load on the condition of power transmission towers, static stability analysis of power transmission towers under different wind direction angular wind load is carried out. Eigenvalue buckling analysis and non-linear buckling analysis are used to obtain the critical load of power transmission towers under wind load, and the differences between the two analysis methods are compared. Through modal analysis and buckling analysis, the weak parts of power transmission towers are found.

Fig. 1 Finite element
modeling diagram of the
power transmission tower
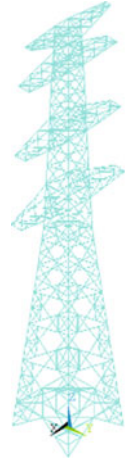
2 Establishment of Finite Element Model for the Power Transmission Tower

The research object of this article is the 1W2C9 drum type self-supporting power transmission tower. This article uses a spatial steel frame model to model power transmission towers, treating all members as beam structures, and simulates each member using the BEAM188 element in ANSYS software. Consider the center of the iron tower as the coordinate origin, the X-axis as the vertical wire direction, the Y-axis as the parallel wire direction, and the Z-axis as the positive direction. In addition, the model ignores the influence of bolted connections and simplifies each node as a rigid node. The final established power transmission tower model is shown in Fig. 1.

3 Principles of Modal Analysis and Buckling Analysis

3.1 Principles of Modal Analysis

Modal analysis of power transmission towers is the foundation of all structural dynamics analysis, which means extracting modal parameters (frequency, damping ratio, vibration mode, etc.) from dynamic response measurement results [11]. The inherent mode of power transmission tower structures is related to their own mass and stiffness, and it will determine the behavior of the structure under dynamic loads (such as fluctuating wind loads and seismic loads).

The dynamic balance equation of the overall structure is [12]:

$$[M]\{\ddot{u}\} + [C]\{\dot{u}\} + [K]\{u\} = \{F(t)\} \tag{1}$$

where, $[M]$ is the mass matrix, $[C]$ is the damping matrix, $[K]$ is the stiffness matrix, $\{F(t)\}$ is the load function changing with time, and $\{u\}$ is the displacement vector of the node.

The BlockLanczos method of ANSYS software can perform modal analysis well.

3.2 Principles of Buckling Analysis

Buckling analysis is used to study the static stability of a structure under specific loads and determine the critical load when the structure transitions from a stable equilibrium state to an unstable equilibrium state. At present, buckling analysis is mainly divided into two types: eigenvalue buckling analysis and nonlinear buckling analysis, both of which can be completed using ANSYS software.

3.2.1 Principle of Eigenvalue Buckling Analysis

Eigenvalue buckling analysis is mainly used to predict the theoretical buckling strength of ideal linear structures. Its main feature is that the critical load of the structure can be obtained without the need for nonlinear analysis.

This article uses the Block Lanczos method to solve the first-order eigenvalue of the structure, and its equation is:

$$([K_\beta] + \lambda[K_\sigma])\{\varphi\} = 0 \tag{2}$$

where, λ is the eigenvalue, $\{\varphi\}$ is the characteristic displacement vector, $[K_\beta]$ is the small displacement stiffness matrix of the structure, and $[K_\sigma]$ is the reference initial stress matrix.

3.2.2 Principles of Nonlinear Buckling Analysis

Nonlinear buckling analysis is a more accurate analysis method than eigenvalue buckling analysis. Its principle is based on static analysis, which only needs to consider nonlinear effects such as large deformation to analyze the ultimate load that the structure can withstand.

This article uses the cylindrical equal arc length method to track the nonlinear equilibrium path. In the iterative process of nonlinear buckling analysis, the load convergence criterion is selected as the criterion for convergence [13], namely:

$$\sqrt{\{g\}^T\{g\}} \leq \beta\sqrt{\{q\}^T\{q\}} \tag{3}$$

where, $\{g\}$ is the node imbalance vector; $\{q\}$ is the reference load vector; β is a parameter and can be taken 10^{-5}. If the number of iterations has exceeded a predetermined maximum or the displacement vector is getting larger, it is considered divergent.

In this paper, the sparse matrix method is used for nonlinear buckling analysis.

4 Modal Analysis Results of the Power Transmission Tower

The first ten natural frequencies are shown in Table 1, and the vibration modes of the first ten are shown in Fig. 2.

From Fig. 2, it can be seen that the first vibration mode is bent in the X direction, that is, there is a significant displacement of the tower body along the X direction and the displacement increases with the increase of the tower height; The second mode of vibration is bending in the Y direction; The third to sixth vibration modes are all local torsion, that is, the main material and some auxiliary materials of the tower body closest to the tower legs produce torsion around the Z-axis, with the difference being that the four main materials turn differently; The seventh to tenth mode shapes are also local torsion, but it is the upper section of the third to sixth order torsion main material and some surrounding auxiliary materials that produce torsion around the Z-axis.

The results of modal analysis indicate that:

1. The natural frequencies of adjacent vibrations of drum type self-supporting power transmission towers are not significantly different, and the frequencies are very dense, which is in line with the characteristics of the tower body being arranged in a square shape; The frequencies of the third to sixth orders and the seventh to tenth orders are very similar, and the overall vibration mode exhibits the characteristic of local torsion. The first two modes of the power transmission tower exhibit bending in the X direction and bending in the Y direction, which are in line with the actual situation of overturning failure.
2. The experimental study on power transmission towers conducted by China's power sector [14] obtained an approximate calculation formula for the natural vibration period of the power transmission tower structure as $T_1 = 0.034 \frac{H}{\sqrt{bB}}$, where b is the width of the tower head and B is the width of the root opening. The calculated first order natural frequency is 2.05. The first order natural frequency

Table 1 Table of the first ten natural frequencies and amplitudes of the power transmission tower

Order	Frequency/HZ	Amplitude/mm
1	2.0217	17.3
2	2.0442	17.1
3	2.5123	66.1
7	2.9497	98.3

(a)
(b)

(c)
(d)
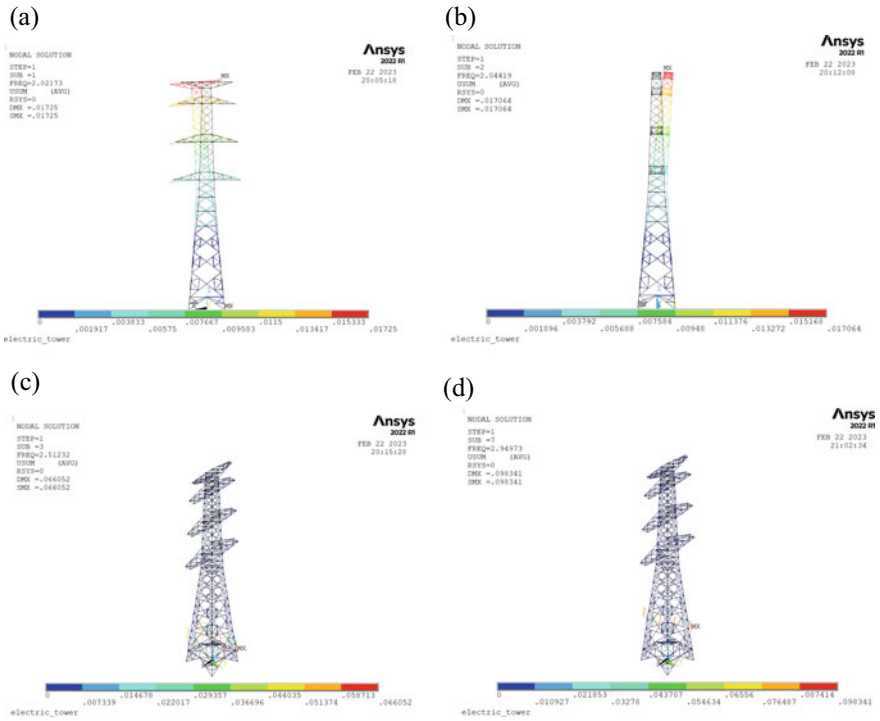
Fig. 2 The first ten vibration modes of the power transmission tower, **a** represent 1, **b** represent 2, **c** represent 3, **d** represent 7

result 2.02 of ANSYS modal analysis is very close to the empirical formula calculation result 2.05, with an error of only 1.5%.

5 Buckling Analysis Results of the Power Transmission Tower

5.1 Eigenvalue Buckling Analysis Results

The minimum buckling eigenvalues of the power transmission tower structure under various wind directions obtained through simulation calculation are shown in Table 2.

Table 2 Eigenvalue buckling analysis results table

Wind direction angle	0°	30°	45°	60°	90°
Minimum buckling characteristic value	6.863	6.401	6.236	6.093	5.991

From the table, it can be seen that as the wind direction angle increases, the impact of wind load on the power transmission tower structure becomes greater, resulting in a decrease in the minimum buckling characteristic value, reaching its lowest point at a 90° wind direction angle.

5.2 Nonlinear Buckling Analysis Results

The instability curve of the load multiple and the horizontal displacement of the tower top at each wind direction angle is shown in Fig. 3.

From Fig. 3, it can be seen that the instability curves have horizontal segments approximately at the abscissa 0.3. According to the Budiansky-Roth criterion, the structure undergoes severe response changes under small load increments, indicating that the structure has undergone static instability. The critical load at each wind direction angle and the horizontal displacement of the tower top node during instability are shown in Table 3.

Fig. 3 Instability curve of the power transmission tower
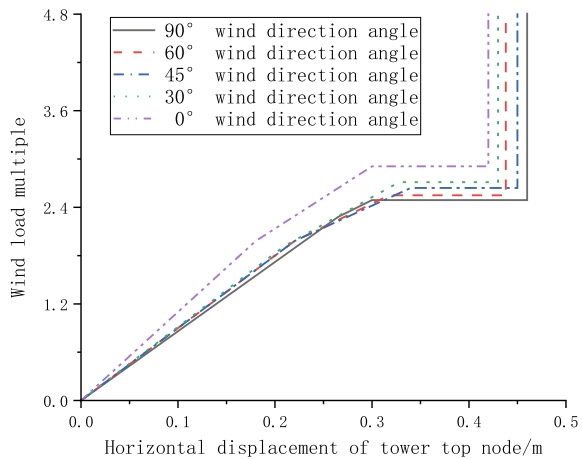
Table 3 Table of critical load and horizontal displacement of tower top nodes during instability of power transmission towers under different wind angles

Wind direction angle	Critical wind load multiple	Horizontal displacement of tower top joint during unstability (m)
0°	2.91	0.293
30°	2.70	0.332
45°	2.65	0.341
60°	2.58	0.318
90°	2.52	0.275

It can be seen from Fig. 3 and Table 3 that with the increase of wind direction angle, the greater the influence of wind load on power transmission tower is, the smaller the critical wind load multiple of nonlinear buckling analysis is. With the increase of wind load gradually, the tower structure will first destabilize when the wind direction angle is 90°.

Based on the results, it can be seen that the maximum axial stress of the power transmission tower is located on the four main tower legs, with maximum axial compressive stress of 278 Mpa.

6   Conclusion

1. The low order vibration mode of the power transmission tower is mainly translational bending; The higher-order vibration mode is mainly localized torsional deformation, and the main material of the lower section of the tower body belongs to the weak part of the structure; The first-order frequency results of modal analysis are highly consistent with empirical formulas.
2. Under the action of strong winds, the weak position of the power transmission tower is the four main materials of its tower legs. When the axial compressive stress of the main materials of the tower legs reaches 278 MPa, the overall structure begins to lose stability.
3. Regardless of the buckling analysis method, when the wind direction angle is 90°, the power transmission tower structure first experiences instability. As the wind direction angle decreases, its critical load multiple increases, making it less likely to experience instability.

References

1. Zeng M (2014) Study on static and dynamic response of high-voltage power transmission tower and tower line system. Lanzhou University (in Chinese)
2. Ozono S, Maeda J (1992) In-plane dynamic interaction between a tower and conductors at lower frequencies. Eng Struct 14(4):13–20
3. Haan FL Jr, Sarkar PP, Gallus WA (2008) Design, construction and performance of a large tornado simulator for wind engineering applications. Eng Struct 30(4):1146
4. Karen A, Kosiba P (2014) Wind field of a nonmesocyclone anticyclonic tornado crossing the Hong Kong international airport. Adv Meteorol 14(1):1–7
5. Yang Y et al (2023) Global/local buckling analysis of thin-walled I-section beams via hierarchical one-dimensional finite elements. Eng Struct 280
6. Huang X (2017) Study on the correction of natural vibration period and corrosion overall safety performance of bucket power transmission tower. South China University of Technology (in Chinese)
7. Liang S, Zhu J, Wang L (2003) Dynamic characteristics analysis of long-span power transmission tower-line system. Earthq Eng Eng Dyn 06:63–69 (in Chinese)

8. Cao M, Xu Z, Liu Z (2005) Theoretical analysis of dynamic characteristics of long-span transmission steel tube composite tower. Power Constr 12:51-54 (in Chinese)

9. Shutang L, Liping K (2007) Analysis of static and natural vibration characteristics of long and short leg tension power transmission tower. Guangdong Electric Power 117(10):24–28 (in Chinese)

10. Chun L, Yong J, Hongdong C (2007) Buckling analysis of the second loop guyed portal tower of Fusha 500 kV transmission line. Electric Power 463(06):45–47 (in Chinese)

11. Chen S (2021) Wind-induced response and stability analysis of transmission lines. Changsha University of Science and Technology (in Chinese)

12. Bao Y, Dong C (2020) Modal analysis of power transmission tower steel structure based on Ansys. J Lanzhou Inst Technol 27(01):20–23 (in Chinese)

13. Lu J (2019) Wind-induced response analysis of high-voltage power transmission tower-line system. Changsha University of Science and Technology (in Chinese)

14. Fu P, Deng H, Wu J (2005) Modal analysis of dynamic characteristics of power transmission tower structure. Spec Struct 22(1):47–49 (in Chinese)

Identification of Construction Defects in 10 kV Cable Intermediate Joints Based on Canny Algorithm

Yuhe Cheng, Chunhua Fang, and Zhi Chen

Abstract The construction defects of 10 kV cable intermediate joint is easy to cause insulation fault. In order to detect and identify the construction defects of cable intermediate joint quickly and accurately, an edge detection method of Canny operator is proposed. Firstly, the Canny algorithm is used to remove the false edge and highlight the edge information, and the edge information of different parts of the intermediate joint is obtained. The experimental results show that the stains and scratches in the cable main insulation surface defect image detected by the Canny edge detection algorithm have high purity and integrity, and the accuracy of the defect algorithm is more than 90%. The Canny edge detection algorithm improves the intelligence of defect detection and can effectively control the construction quality.

Keywords 10 kV cables · Construction defects · Defect identification · Canny operator

1 Introduction

The intermediate joint of 10 kV cable is the weak link in the cable operation process. Intermediate joints are installed by workers, and the varying technical levels and unregulated construction habits of construction personnel can easily cause the installation quality to be substandard [1]. These hidden problems can lead to large scale power outages and huge losses in the event of a failure.

At present, the main method for detecting defects during the construction of cable intermediate joints is human monitoring, which is time-consuming and unreliable

Y. Cheng
China Southern Power Grid, Zhongshan Power Supply Company, Guangdong 528400, China

C. Fang · Z. Chen (✉)
School of Electrical and New Energy, China Three Gorges University, Yicang 443000, China
e-mail: 572451367@qq.com

[2]. The edge detection algorithm has the advantages of high recognition rate, accurate position of edge points and single edge point response. Image processing techniques based on edge detection are currently mostly used in industry and agriculture, including the detection of cracks using multiscale edge detection [3]; the discrimination of fruit stalks using image morphology as well as edge detection methods [4]. A Canny algorithm for the identification of defects in 10 kV cable intermediate joints is proposed to address the characteristics of slender and small color differences in the main insulation defects of the cables that are the subject of this paper. This method can avoid the secondary damage of cable, providing technical means for the control of construction quality and processes, and effectively improving the operational reliability of the power system [5–7].

2   10 kV Cable Defect Types and Characteristics

Most of the 10 kV cables are urban distribution cables, where the intermediate joints are in an uncrimped state. The parts to be tested are the main insulation, the semiconducting layer, the junction between the core and the main insulation and the crimped joints [8].

The surface of the main insulation will get scratched, when the builder uses too much force on the outer semi-conductor of the cable, if not dealt with in time, insulation breakdown will occur at the scratched area after a long period of operation, as shown in Fig. 1a.

Installers who fail to clean up the semi-conducting mass on the insulator surface or contaminate the main insulation surface during the cutting process will create a 10 kV cable intermediate joint stain defect, as shown in Fig. 1b.

Fig. 1 Defects of main insulation

(a) Scratch defects   (b) Stain defects
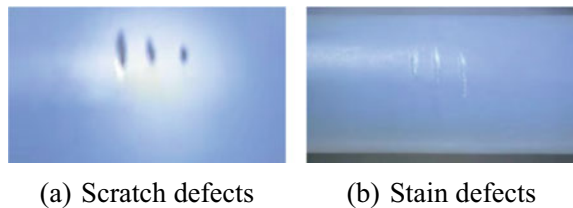
3 Canny-Based Edge Detection and Part Segmentation

3.1 Algorithm Flow

The Canny operator calculates the grey-scale partial derivatives in different directions for each pixel point to obtain the grey-scale gradient information of the image. In cable intermediate joint images, the image grey scale values change at the locations of various types of construction defects, representing the movement of image gradient information from one local area into another local area, i.e. generating edge information. The method can be roughly divided into four steps: (1) image pre-processing; (2) calculation of the intensity and direction of the gradient; (3) non-extreme value detection; (4) double threshold detection [9].

3.2 Gaussian Filtering of Cable Defect Images

Before analysing the defects in the image of the cable main insulation surface, the image quality needs to be enhanced to eliminate the noise interference in the image, thus improving the detection accuracy of the algorithm. The original image of the cable main insulation is set as $f(x, y)$ and the $f(x, y)$ is smoothed and filtered by a Gaussian function component filter $G(x, y, \sigma)$, the Gaussian function taken in this paper is expressed using Eq. 1:

$$G(x, y, \sigma) = \frac{1}{2\pi\sigma^2}\left(x^2 + y^2\right) \tag{1}$$

where x, y are the coordinate positions of the main insulated 2D image and σ is taken as 14, the standard deviation of the Gaussian curve. The filtered image is obtained by Eq. (2):

$$I(x, y) = G(x, y, \sigma) * f(x, y) \tag{2}$$

3.3 Cable Defect Image Gradient Amplitude and Direction

The components in the intermediate joint image have well-defined boundaries and the grey scale values of these parts are different from the adjacent areas, the edge information of the joint is obtained by calculating the gradient amplitude and direction of the main insulation defect image.

Using a domain with a specification of 2 * 2, the Canny operator calculates the filtered image $I(x, y)$ to obtain the gradient as well as the orientation. The expressions

for the different arrays are Eqs. (3) and (4):

$$P_x[i, j] = \frac{I[i + 1, j] - I[i, j] + I[i + 1, j + 1] - I[i, j + 1]}{2} \tag{3}$$

$$P_y[i, j] = \frac{I[i, j + 1] - I[i, j] + I[i + 1, j + 1] - I[i + 1, j]}{2} \tag{4}$$

where i takes values in the range $[0, N - 2]$ and j takes values in the range $[0, M - 2]$. If M and N take odd values, the last sequence in the corresponding $\theta(i, j)$ and y directions is not considered. Let the gradient mode $\theta(i, j)$, the direction $\theta(i, j)$, compute the difference in the horizontal and vertical directions, i.e.:

$$H(i, j) = \sqrt{P_x[i, j]^2 + P_y[i, j]^2} \tag{5}$$

$$\theta(i, j) = a \tan(P_y[i, j]/P_x[i, j]) \tag{6}$$

3.4 Non-extreme Value Suppression

The magnitude of $H(i, j)$ represents the magnitude of the gradient value of the main insulation defect point, and pseudo-edges may appear in gradients of different strengths in the same direction. The interpolation method is used to determine whether a point is the main insulation defect point, and to suppress non-extreme point information and highlight edge points.

The adjacency of pixels can be divided into four regions, where each region contains upper and lower parts. If the central pixel point x has a gradient intensity in the x-direction of $g_x(i, j)$, the y-direction gradient intensity is $g_y(i, j)$ and the gradient intensity is $g_{xy}(i, j)$, its gradient direction is judged by the positive and negative and size of $g_x(i, j)$ and $g_y(i, j)$, and then according to the pixel gradient direction and the linear interpolation of the pixel gradient of the adjacent points, the two gradient intensities $g_{up}(i, j)$ and $g_{down}(i, j)$ involved in the comparison of the positive and negative gradient directions are obtained. The formula is as follows.

$$g_{up}(i, j) = (1 - t) * g_{xy}(i, j + 1) + t * g_{xy}(i - 1, j + 1) \tag{7}$$

$$g_{down}(i, j) = (1 - t) * g_{xy}(i, j - 1) + t * g_{xy}(i + 1, j - 1) \tag{8}$$

The other three regions are calculated in a similar way. If $g_x(i, j) = 0$, it means that the pixel point has no pixel gradient and it is a non-edge.

3.5 *Double Threshold to Solve for Image Edges*

The algorithm in this paper divides the image into two main parts, foreground and background, both of which form peaks on the grey scale histogram, which is where the extreme values in the interval are located. The very small value is then the threshold for edge detection pre-processing the middle joint image. The pixel histogram is obtained specifically using the grayscale image, and the detected peaks, which are the locations in the background that present the most pixel values. The sequence of waveforms is traversed to obtain the first waveform that satisfies the following conditions [10]:

A Detecting the size of the number of pixels adjacent to the luminance value and generating a valid very large and very small value if there is a change;
B The number of pixels at the adjacent trough to the right of the wave crest is smaller than the average number of pixels in the image, otherwise filter out this trough and the wave crest to its right;
C The cumulative sum of pixels taken up from the left trough to the crest and then to the right trough is less than 30% of the pixels of the whole picture.

The threshold value obtained above is the low threshold c1, and the histogram with the most pixel points is found using the same method to obtain the high threshold c2 in the double threshold, and the set of pixel points within [c1, c2] is called the pixel edge. In order to prevent the algorithm from misjudging the double threshold value obtained in isolation, the corresponding pixel edge set is set to $f(z)$, and if elements of the pixel edge set $f(z)$ exist around an edge pixel point $f(i)$, it will be judged as a pseudo-edge and ignored; if elements of the pixel edge set $f(z)$ do not exist around an edge pixel point $f(i)$, it will be judged as a true edge. When the edge pixel grey level > k1 && > k2, it is specified that the edge pixel at this point is a strong edge pixel point.

4 Experimental Analysis

The previous chapter describes the detection of all types of defects in 10 kV cable intermediate joints, i.e. the detection of edge information in intermediate joints based on Canny. This step provides a good representation of the image information of the intermediate joint to be detected and is an indispensable preparation for defect detection in this chapter.

4.1 Identification of Defects in the Main Insulation Stains and Scratches

As the collection device closes the connector and is illuminated by the LED strip, then the color of the strip cannot be ignored in terms of its effect on the test results. As shown in Fig. 2, (A) is the original light illumination, (B) is the blue light illumination. In practice the defects in the stain type are often very subtle and the effect of the algorithm is better in this paper by zooming in on the process.

Edge detection experiments were conducted on Fig. 2a, b respectively, where the algorithm identifies stains on the main insulation of the cable intermediate joint at different thresholds. The experimental data was taken from real cable images, where stains were artificially added to generate stain defects, and the Canny edge detection operator was used for edge detection, where the size of the Canny detection threshold had a very significant impact on the experimental results.

When the main insulation is free of defects, the main insulation detection result map should not have any edge information. It can be seen through the experiment, natural light irradiation, when the edge detection threshold interval is [10–200], the stain defects on the surface of the main insulation all appear to be missed, with the threshold value gradually increasing, the leakage phenomenon is gradually serious; blue light irradiation under the main insulation stain image defect details are more abundant, more complete information retention, the best threshold area is [30–80].
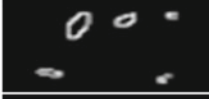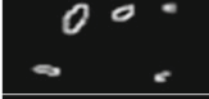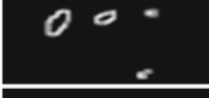
It was obtained experimentally that when the threshold is chosen small, many interfering items are detected and when the threshold is chosen large, obvious stains are filtered out. Experimentally, better results were obtained when blue illumination was selected and the size range of the Canny detection threshold was [30–80], and the presence of stains was determined by whether the number of pixel points for a specific pixel value after detection was greater than the set threshold.

The main insulation scratch defect is shown in Fig. 1a, with more obvious scratches. For the main insulation scratch defect detection, the same edge detection algorithm is used. After edge detection, a clear area of scratches can be seen. The specific pixel values in the image are then counted to determine if a scratch defect is present. In order to be able to detect the different levels of scratches, experiments are required to select the best edge detection threshold. The specific experimental procedure is shown in the detection diagram within Table 2.
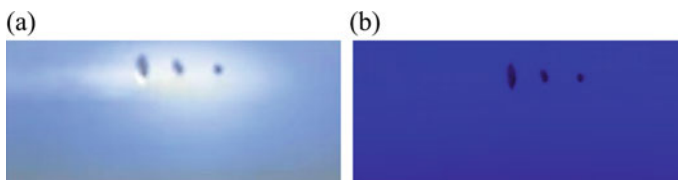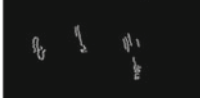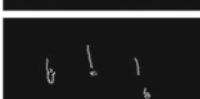
Fig. 2 Image of main insulation stain

Table 1 Stain threshold test table

Serial number	Threshold value	Natural light	Blue light
1	10		
2	30		
3	50		
4	80		
5	100		
6	200		

Table 2 Experimental table of scratch threshold

Serial number	Threshold value	Natural light	Blue light
1	10		
2	30		
3	50		
4	80		
5	100		

Table 3 The recognition rate of various types of defects by different algorithms

Algorithm type	Scratch recognition rate (%)	Stain recognition rate (%)	Average recognition rate (%)
Canny	95.83	95.00	95.42
Laplace	71.67	73.33	72.55
Roberts	91.67	90.00	90.84
Sobel	80.83	78.33	79.58
Prewitt	83.33	85.83	84.58

Similar to stain-like defects, the detection information is lost as the threshold increases under natural light irradiation, while under blue light irradiation, the threshold between [10–100] retains the scratch information well.

The experimental results show that, the detection intensity is strong and many unwanted features are detected, when the threshold is set too small. The features of the scratches are screened out again, when the threshold is set too large. The experiments show that the scratches can be detected more completely without other unwanted feature information when the selected threshold ranges of [30, 80].

4.2 Comparison of Different Algorithms

The sample of this paper adopts 10 kV intermediate joint, imitating defects during construction by fabricators, to obtain the closest possible approximation to the state of defects in actual construction situations. All types of defects have a very high degree of similarity to the field operation to produce defects and are universal. The Canny, Laplace, Roberts, Sobel and Prewitt detection algorithms were also used to detect the edges of the intermediate joint images under the same conditions respectively.

In accordance with the above defect determination criteria, different algorithms were used for edge detection of the main insulation, with 110 groups of each type of defect, as shown in Table 3. Comparing the recognition rate and average recognition rate of each defect with different algorithms, it was concluded that the edge detection based on Canny algorithm had the highest recognition rate and average defect recognition rate for each type of defect, with an average recognition rate of 95.42%.

5   Conclusion

In this paper, the Canny algorithm is used to identify typical construction defects in order to solve the problem of 10 kV cable intermediate joints that produce various types of defects due to substandard construction quality and difficult control. The Canny defect detection algorithm has a recognition rate of more than 90% for various

defects of 10 kV cable intermediate joints. The defect recognition rate is much higher than other detection operators, and has high practical value.

References

1. Jiang XJ, Liang WG, Xia JF et al (2015) Electric field calculation and fault analysis of typical defects of 35 kV power cable shrink- type intermediate joints. Insul Mater 49(11):59–63 (in Chinese)
2. Yuan JQ (2016) Analysis of fault causes of power cable intermediate joints and improvement of production process. Sci Technol Innovation 33(13):141–142 (in Chinese)
3. Yang YB, Lu MJ, Liu C (2021) Research on monitoring and identification of concrete cracks in assembled subway station node test. J Railway Sci Eng 18(12):3303–3310 (in Chinese)
4. Ning ZD, Luo LF, Liao JX, Wen HJ, Wei HL, Lu QH (2021) Grape stem identification and optimal picking location based on deep learning. J Agric Eng 37(09):222–229. (in Chinese)
5. Woods RE, Gonzalez RC (2007) Digital Image processing. In: Ruan QQ (ed) Transl 2th. Electronic Industry Press, Beijing, pp 152–158
6. Yücel MK, Legg M, Kappatos V, Gan T-H (2017) An ultrasonic guided wave approach for the inspection of overhead transmission line cables. Appl Acoust 122:23–34
7. Huang Q (2016) Study on partial discharge of typical defects in 10 kV cable joint. South China University of Technology. (in Chinese)
8. Liu QW, Wang YS, Wang ZK (2014) Common construction defects and countermeasures of cross-linked cable. Autom Appl 6:109–110 (in Chinese)
9. Harini S, Abhiram V, Hegde R et al (2017) A smart driver alert system for vehicle traffic using image detection and recognition technique. In: IEEE International conference on recent trends in electronics, information and communication technology. IEEE, pp 1540–1543
10. Kim SW, Kim NS (2013) Dynamic characteristics of suspension bridge hanger cables using digital image processing. NDT E Int 59(7):25–33

Identification of Typical Construction Defects of 10 kV Cable Intermediate Joints Based on SIFT Algorithm and Canny Algorithm

Sichen Dong, Qiao Yu, Chunhua Fang, and Zhi Chen

Abstract The uneven cutting of the main insulation and the outer semi-conductive layer and the burr of the pressure pipe are easy to lead to insulation failure. The image recognition technology can be used to intelligently control the construction defects. Aiming at the construction defects of cable intermediate joint, an edge detection method based on Canny operator is proposed. Firstly, the image of segmented cable joint is spliced by using Scale-in-Variant Feature Transform (SIFT) algorithm, and then the false edge can be removed and the edge information can be highlighted by using Canny operator, and the edge information of different parts of the intermediate joint can be obtained. The experimental results show that the cable detected by the algorithm in this paper can also accurately detect the defects of uneven peeling of semi-conductor and burr, and the accuracy of defect algorithm can reach more than 90%, which verifies the effectiveness of the algorithm.

Keywords 10 kV cable · Construction defects · Defect identification · Feature extraction · Canny operator

1 Introduction

The installation of power cable accessories has high requirements on the construction environment and process quality, the uneven technical level of construction personnel and irregular construction habits cause burrs on the crimp tube, which will lead to insulation failure [1].

At present, the research on the construction defects of cable main insulation mainly lies in the simulation of partial discharge characteristics of power cable construction

S. Dong · Q. Yu
China Southern Power Grid, Zhongshan Power Supply Company, Guangdong 528400, China

C. Fang · Z. Chen (✉)
School of Electrical and New Energy, China Three Gorges University, Yicang 443000, China
e-mail: 572451367@qq.com

defects, the analysis of characteristics in time domain and frequency domain and the fault diagnosis of power cable accessories [2]. These diagnosis methods can only be implemented if the cable is electrified, and they can't prevent the occurrence of transmission faults. Reference [3] proposes a method to detect the construction defects of 10 kV cable joints based on image recognition. Using image processing method to detect surface defects of main insulation of power cable can avoid secondary damage and achieve the purpose of non-interference detection of main insulation [4, 5]. For example, Song and others [6] use color information to identify the scratches of mobile phones, and put forward the scratch detection of mobile phone accessories based on Gabor and texture suppression; Li et al. [7] used morphological knowledge to compare and analyze the morphological characteristics of surface scratches of parts. Still, these methods can only be used for defects with large color contrast or damage on the surface of the workpiece. In this paper, the main insulation scratches and stains have the characteristics of inconspicuous color contrast and subtle defects, and the above methods are ineffective for the research object of this paper.

In this paper, the edge detection method in image processing is applied to the detection of cable main insulation defects [8], and a 10 kV cable accessory main insulation defect identification method based on Canny algorithm is proposed. Compared with other edge algorithms, Canny algorithm has the advantages of low error rate, more accurate edge point location and single edge point response characteristics for cable main insulation defects.

2   10 kV Cable Image Acquisition and Features

In order to obtain a large field of view and high resolution image of the main insulation of a 10 kV cable, multiple macro cameras need to be segmented due to the long and thin cable insulation and the wide angle of view required.

Due to irregularities in stripping and cutting by the builder, the outer semiconductor was not stripped flush, as shown in Fig. 1.

If the builder has not polished the crimped tube, or if the polishing is not careful, leaving a metal tip burr on the connecting tube, a typical defect of a connecting tube burr will be formed, as shown in Fig. 2.
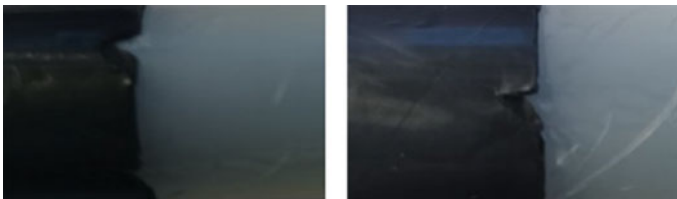
Fig. 1 Semi-conductive stripping irregularities

Fig. 2 Pressure nozzles burr
defects

3 Image Stitching Based on SIFT Algorithm

Cable accessories and cable main insulation are large in size and the defects in each category are subtle and not easily detectable. Conventional filming methods do not provide a complete high-resolution image of the defects. The image is obtained by segmented shooting, and then the complete main insulation image is obtained based on SIFT algorithm. The algorithm mainly includes image acquisition, image preprocessing, image matching and image fusion [9].

3.1 Construction of the Scale Space

The scale space is constructed by a Gaussian kernel function, thus preserving more image features, and the 2D Gaussian function is defined as in Eq. (1):

$$G(x, y, \sigma) = \frac{1}{2\pi\sigma^2} e^{\frac{-(x^2+y^2)}{2\sigma^2}} \tag{1}$$

$G(x, y, \sigma)$ is the scale-variable Gaussian function and σ is the scale-space factor

$$\sigma \nabla^2 G = \frac{G(x, y, k\sigma) - G(x, y, \sigma)}{k\sigma - \sigma} \tag{2}$$

$G(x, y, \sigma)$ denotes the Gaussian kernel; k is a positive constant.

3.2 Positioning of Feature Points

To extract valid feature points, the pixel points in the image are compared with all points in their adjacency, and if the pixel points being compared are extremely large or small, they are considered potential feature points. Then these potential feature points are processed twice to remove the points with insignificant features and obtain more stable feature points.

3.3 Calculation of Gradient Amplitude and Angle

The algorithm obtains stable feature point coordinates with scale invariance after these steps. By calculating the gradient modes and gradient angles around the image feature points, each feature point is assigned a corresponding orientation to achieve rotational invariance.

The primary direction of the cable feature corner points constitutes a cable image stitching feature point. The histogram is used to count the gradient and amplitude corresponding to the feature pixels, with the highest amplitude being the primary direction, and the direction exceeding 80% of the peak being the secondary direction in order to enhance the robustness of the matching.

3.4 Stitching Effect of Images

A set of vectors is used to express the position and scale direction of the feature points between the images of the intermediate cable joints, i.e. Take a set of feature vectors of the target cable image, find the key point with the smallest Euclidean distance, and connect the corresponding points into a line to achieve the stitching between the images, as follows Fig. 3a and b:

(a)

(b)
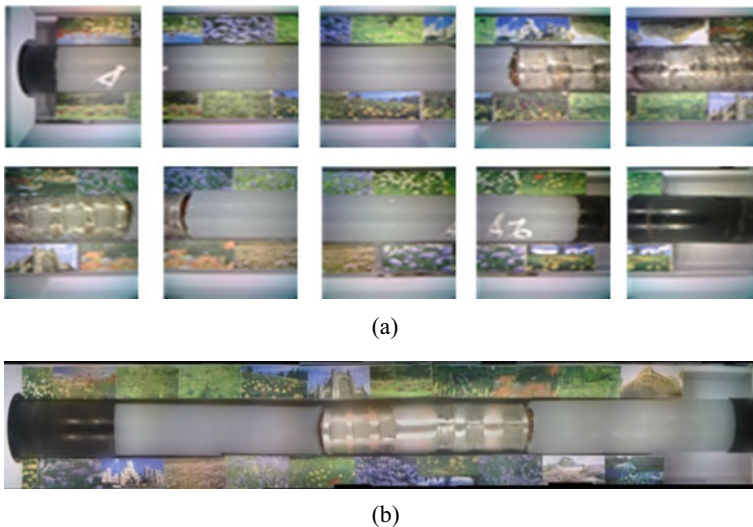
Fig. 3 **a** Sample of cable accessories to be spliced. **b** Sample of cable accessories to be spliced

4 Canny-Based Edge Detection and Part Segmentation

4.1 Algorithm Flow

The method can be roughly divided into four steps: (1) image pre-processing; (2) calculation of the intensity and direction of the gradient; (3) non-extreme value detection; (4) double threshold detection [10].

4.2 Gaussian Filtering of Cable Defect Images

In the process of image acquisition, due to the interference of the environment, the image will produce noise. The noise interference is eliminated by Gaussian filtering to improve the detection accuracy of the algorithm.

The original image of the cable main insulation is set as $f(x, y)$ and the $f(x, y)$ is smoothed and filtered by the Gaussian function component filter $G(x, y, \sigma)$.

$$G(x, y, \sigma) = \frac{1}{2\pi\sigma^2}(x^2 + y^2) \tag{3}$$

where x, y are the coordinate positions of the main insulated 2D image and σ is taken as 14, the standard deviation of the Gaussian curve.

$$I(x, y) = G(x, y, \sigma) * f(x, y) \tag{4}$$

4.3 The Gradient Amplitude and Direction of the Image

The gray value of the defect part is different from that of the non-defect area. In the process of obtaining the edge information of the joint, it is necessary to calculate the gradient amplitude and direction of the main insulation defect image.

Using a domain with a specification of 2 * 2, the Canny operator calculates the filtered image $I(x, y)$ to obtain the gradient as well as the orientation. The expressions for the different arrays are Eq. (5) and (6):

$$P_x[i, j] = \frac{I[i + 1, j] - I[i, j] + I[i + 1, j + 1] - I[i, j + 1]}{2} \tag{5}$$

$$P_y[i, j] = \frac{I[i, j + 1] - I[i, j] + I[i + 1, j + 1] - I[i + 1, j]}{2} \tag{6}$$

Let the gradient mode $H(i, j)$, the direction $\theta(i, j)$, compute the difference in the horizontal and vertical directions, i.e.:

$$H(i, j) = \sqrt{P_x[i, j]^2 + P_y[i, j]^2} \tag{7}$$

$$\theta(i, j) = a\tan(P_y[i, j]/P_x[i, j]) \tag{8}$$

4.4 Non-extreme Value Suppression

Pseudo-edges may appear in gradients of different strengths in the same direction, the local optimum method is used to determine whether a point is the main insulation defect point, and to suppress non-extreme point information and highlight edge points.

The gradient intensity in the *x-direction* is $g_x(i, j)$, the y-direction gradient intensity is $g_y(i, j)$ and the gradient intensity is $g_{xy}(i, j)$, its gradient direction is judged by the positive and negative and size of $g_x(i, j)$ and $g_y(i, j)$, and then according to the pixel gradient direction and the linear interpolation of the pixel gradient of the adjacent points, the two gradient intensities $g_{up}(i, j)$ and $g_{down}(i, j)$ involved in the comparison of the positive and negative gradient directions are obtained. The formula is as follows:

$$g_{up}(i, j) = (1 - t) * g_{xy}(i, j + 1) + t * g_{xy}(i - 1, j + 1) \tag{9}$$

$$g_{down}(i, j) = (1 - t) * g_{xy}(i, j - 1) + t * g_{xy}(i + 1, j - 1) \tag{10}$$

The other three regions are calculated in a similar way. If $g_x(i, j) = 0$, it means that the pixel point has no pixel gradient and it is a non-edge.

4.5 Double Threshold to Solve for Image Edges

When using a single threshold to determine the defect edge, setting the threshold too high or too low can result in pseudo-edges and loss of true defect points. This paper uses double threshold method, the Canny algorithm uses hysteresis threshold to set the threshold values for strong and weak edges, effectively solving the problem [11].

5 Experimental Analysis

The experimental object is the 10 kV cable. The Win10 computer and the cable photographing device used for the experiments, with Microsoft VisualStudio 2012 as the development platform, are tested under the above hardware and software conditions to realize the main insulation defect recognition algorithm for 10 kV cable accessories based on the Canny algorithm proposed in this paper and verify its effectiveness.

5.1 Identification of Crimp Tube Burr and External Semi-conductive Defects

See Table 1.

In this paper, the edge of the crimp tube is extracted using edge detection. The edge of a smoothly polished crimp tube is generally a straight line, but when the burr is not polished or polished in place, the curvature of the crimp tube edge increases, i.e. there are extreme points in the curved section of the crimp tube boundary line,

Table 1 Fitting image and curve equation of intermediate joint

Fitting image	Fitting equation peak
	87.08
	223.37
	66.89

and the extreme points differ significantly from the polished and smooth crimp tube boundary.

The edge of the crimping pipe can be regarded as a function curve, and the quadratic function is used for fitting. When there are burr defects, the surface boundary of the crimping pipe will be uneven. The function extreme error between the flatness and unevenness of the crimping pipe is calculated, and the size of the error is used to determine whether the boundary is uneven.

This paper compares the magnitude of the absolute value of the peak value of the fitting function of the crimp tube with and without burr defects. Through several tests and analyses, when there are burrs in the crimp tube of the 10 kV cable intermediate joint, the curvature of the fitting curve will be greater and the extreme value of the fitting equation will be too large or too small. When the extreme value is at [80, 100], it can be considered that the crimp tube burr is polished and there are no defects such as burrs (Table 1).

In order to judge whether the outer semi-conductive and the main insulating layer are peeled off unevenly, it is necessary to intercept the image at the boundary, extract the boundary of the image based on edge detection, and then fit the boundary. Calculate the mean square error of the stripping neat and the stripping uneven fitting function, and judge whether the boundary is uneven by the error size.

Table 2 Fitting image and curve equation of external semiconducting

Fitting image	mean square deviation
$y=0.001898x^2+0.3871x+92.73$	0
$y=0.0005855x^2+0.08083x+67.38$	2214
$y=0.002672x^2-0.4058x+107.7$	449

By fitting the image, the mean square difference of all points on the fit function is found, and the mean square difference is used to determine whether the peel is not flush or not. Through the experiment, it is clear that the mean squared difference of the peeled uneven image is significantly larger than the mean squared difference of the peeled neat image, and when the mean squared difference belongs to [0, 200], it is considered that there is no defect, and if it is larger than this interval, it is judged that the outer semi-conducting peel is uneven. It is practical and reasonable to follow this criterion.

5.2 Defect Quantification Accuracy

For different types of defects, a large number of samples are made by imitating the construction site. For example, the pressure nozzle is not polished or not polished enough to cause burrs. All kinds of defects are highly similar to the defects produced by field operation. In this paper, 200 defect samples are repeated by using the algorithm in this paper. The detection results are shown in Fig. 4, and a result picture has multiple defect recognition results.

The results of the experiments to identify the number of defects for different types of defects were counted and the data are shown in Table 3.

Fig. 4 Diagram of repeated test results

Table 3 All kinds of defect recognition rate statistics

Defect type	Detection times	Number of successful recognition	Recognition rate (%)
The uneven semi-conductive notch	300	288	96.00
Pressure nozzle burr	400	363	90.75

6   Conclusion

In this paper, the SIFT algorithm and Canny algorithm are used to identify typical construction defects in order to solve the problem of 10 kV cable intermediate joints that produce various types of defects due to substandard construction quality and difficult control.

The Canny defect detection algorithm has a high practical value with a recognition rate of over 90% for all types of defects in 10 kV cable intermediate joints.

References

1. Ma T, Gao Z (2015) Analysis of manufacturing process defects of 10 kV cable intermediate joint and improvement measures. Hebei Electr Power Technol 34(3):60–62 (in Chinese)
2. Fang CH, Tang SX, Pan ML (2016) Simulation analysis of typical defects of 10 kV cable intermediate joint. J Three Gorges Univ (Nat Sci Ed) 38(2):55–59 (in Chinese)
3. Lin Y (2018) Research on construction defect detection technology of 10 kV cable joint based on image recognition. Three Gorges University, Yichang, pp 16–63 (in Chinese)
4. Gonzalez RC, Woods RE (2007) Digital image processing. In: Ruan QQ, Ruan YZ (eds) Translation, 2th edn. Electronic Industry Press, Beijing, pp 152–158
5. Yücel MK, Legg M, Kappatos V, Gan T-H (2017) An ultrasonic guided wave approach for the inspection of overhead transmission line cables. Appl Acoust 122:23–34
6. Song D, Zhang DB, Liu X (2014) Mobile phone accessories scratch detection based on Gabor and texture suppression. Comput Eng 40(9):1–5 (in Chinese)
7. Li ZY, Gao M, Ma WH (2007) Research on scratch detection technology of shell and tube surface based on computer vision. Appl Opt 27(6):802–805 (in Chinese)
8. Zeng J (2011) Research on image edge detection technology and its application. Huazhong University of Science and Technology, Wuhan, pp 17–38 (in Chinese)
9. Dai JB (2013) Algorithms of image feature extraction based on visual information. Jilin University, Jilin (in Chinese)
10. Harini S, Abhiram V, Hegde R et al (2017) A smart driver alert system for vehicle traffic using image detection and recognition technique. In: IEEE international conference on recent trends in electronics, information and communication technology. IEEE, pp 1540–1543
11. Kim SW, Kim NS (2013) Dynamic characteristics of suspension bridge hanger cables using digital image processing. NDT E Int 59(7):25–33

Analysis of Lightning Activity Over Cambodia, 2021

Xiaoyan Dong, Jiajun Song, Qiming Ma, Lei Gu, Heang Vandy, Pavming Chhin, Moeung Sereivath, and Ngoun Songtheng

Abstract Based on the monitoring data from the 3-D lightning monitoring network (LMN) in the Kingdom of Cambodia (Cambodia), we analyzed the spatial and temporal distribution of lightning activity in 2021. The results show that the transitions between the dry and rainy seasons are periods with a high incidence of lightning activity, and there are very few lightning activities in the middle of the dry season. The predominant feature of diurnal lightning activity is the occurrence of lightning during the afternoon and early evening. The distribution of lightning activity is predominantly concentrated over mountainous regions and over the plateau areas, with less lightning activity over the Tonle Sap and Tonle Sap River basins.

Keywords Cambodia · Lightning activity · Flash density · Lightning intensity

1   Introduction

Southeast Asia is recognized as a "climate change hotspot," and within this region, Cambodia is regarded as one of the most susceptible countries to the effects of climate change [1, 2]. Cambodia experiences a tropical monsoon climate characterized by

X. Dong · J. Song · Q. Ma (✉)
Institute of Electrical Engineering, Chinese Academy of Sciences, Beijing 100190, China
e-mail: maqiming@mail.iee.ac.cn

X. Dong · Q. Ma
University of Chinese Academy of Sciences, Beijing 101408, China

L. Gu
Aviation Meteorological Center, Air Traffic Management Bureau, CAAC, Beijing, China

H. Vandy · P. Chhin
Aeronautical Services Department, State Secretariat of Civil Aviation, Phnom Penh, Cambodia

M. Sereivath · N. Songtheng
Deputy Chief Bureau of Technical, Civil Aviation and Air Traffic Control Authority, Phnom Penh, Cambodia

an average annual temperature ranging from 29 to 30 °C. The country has a rainy season spanning from May to October, and a dry season that extends from November to April [3–5]. The plains dominate the central and southern regions of Cambodia, whereas the eastern, northern, and western parts are encompassed by mountains and plateaus, many of which are adorned with lush forest cover [6]. In spite of a low latitude location, convective rain in the rainy season, strong airflow, and a mainly plain, flat and open terrain, lightning can easily reach the ground. Lightning plays a crucial role as a natural source of wildfires and oxynitride, exerting a substantial impact on ecological systems and atmospheric chemistry [7]. The examination of the spatiotemporal distribution of lightning has been the focus of extensive research efforts [8]. Understanding the lightning activity in a specific area is a valuable tool for meteorologists. Extensive literature exists, dedicated to exploring the diurnal variations of lightning activity in various regions [7–16].

Due to the lack of a lightning monitoring system covering the whole area of Cambodia for a long time, the analysis of lightning activity characteristics has been in a blank state. In 2019, the Institute of Electrical Engineering (IEE), Chinese Academy of Sciences (CAS) began to build lightning locators in Cambodia. LMN has been established with a total of 12 sites by the end of 2020, which can cover the whole country of Cambodia and its surrounding areas. Now, it has accumulated a large amount of real and reliable lightning data. Therefore, this paper analyzed the spatial and temporal distribution of lightning activity in Cambodia. In addition, analyzing the characteristics of lightning activities and understanding the generation of lightning and development are also of great significance to the monitoring, early warning, disaster prevention and mitigation of lightning disasters in Cambodia [17, 18].

2 Data

In this work, lightning data comes from January 2021 to December 2021 period have been extracted from the LMN website. The data were used to study temporal and spatial variations of lightning activities over Cambodia and the surrounding area. LMN has a total of 12 detection sites in Cambodia, as shown in Fig. 1. At each detection site, there are several components including a VLF/LF electric field antenna, a magnetic antenna, a GPS receiving system, and a signal processing system. The device's channel bandwidth ranges from 3 to 400 kHz, while the GPS time synchronization accuracy is maintained at less than 20 ns [19].
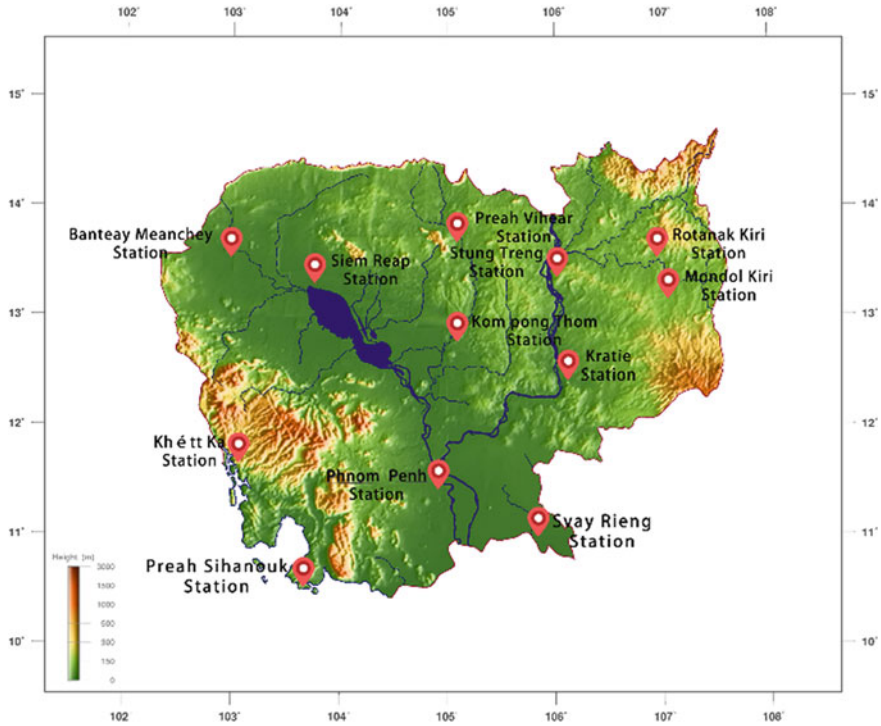
Fig. 1 Distribution map of lightning locators. Each lightning locator is marked by a red pin

3 Result

3.1 Temporal Variation of Lightning Activity Over Cambodia

3.1.1 Annual Flash Distribution

Lightning can be divided into cloud-to-ground lightning (CG) flash and in-cloud lightning (IC) flash according to its location, and also can be divided into positive (POS) flash and negative (NEG) flash by its polarity. Table 1 shows the general count of lightning flashes over Cambodia and surrounding areas in 2021 by the above two classifications.

Table 1 General count of lightning flash in Cambodia (2021)

	Total	CG	IC	POS	NEG
Count	4,293,728	3,374,644	919,084	829,891	3,463,837
Percentage of total (%)	100	78.6	21.4	19.3	80.7

3.1.2 Monthly Variation

Figure 2 shows the monthly (January–December) variation of total flash count with two peaks, the first peak in April and the second in October. Due to Cambodia's weather being categorized into two distinct seasons, namely the rainy season (May–October) and the dry season (November–April), there is a considerable disparity in monthly variations between these two seasons [11]. It can be seen that Cambodia experienced the greatest number of lightning flashes during April when a total of 1,047,177 flashes occurred over the study period. The total count of flashes remains at a high level during May. February is the least active month during the year with only 2269 flashes. The transition from the dry to the rainy season is a period of the high incidence of lightning activity, and there are very few lightning activities in the middle of the dry season. The reason may be that during the rainy season, the strong solar radiation leads to an increased water evaporation rate, which facilitates the formation of strong convective weather.

3.1.3 Diurnal Variation

Figure 3 shows the diurnal variation of lightning activity in 2021. The peak times of the diurnal variation are spreading from early afternoon to late afternoon. The lightning activity is strong from 14:00 to 20:00 and weak during 7:00–12:00. At 17:00, the lightning activity reaches its peak, and then the frequency of lightning activities gradually decreases, reaching the lowest value around 10:00–11:00 am. The reason for this situation is that the sun radiates to the ground and the lower atmosphere during the day, which leads to the development of near-surface thermal conditions from afternoon to evening, and it is easy to form strong convective weather.

Fig. 3 Diurnal variation of lightning activity over Cambodia (2021)
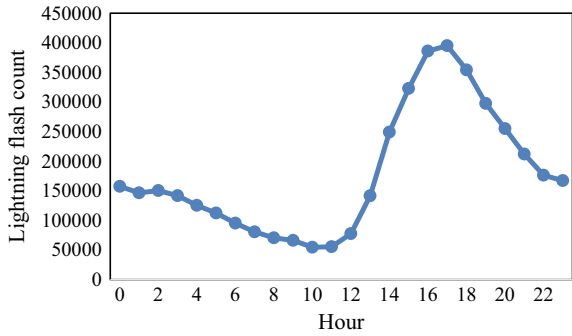
3.2 Spatial Distribution of the Lightning Flash Activities

3.2.1 Regional Distribution of Lightning Density

Figure 4 shows flash density derived from LMN in 2021 over Cambodia. A spatial resolution of $0.02° \times 0.02°$ (2.2 km × 2.2 km) was used on the map. This figure shows that the annual lightning flash density in Cambodia is generally above 4.0 flashes/ km^2/year. The main lightning activity is confined in two zones between 10.5°– 12°N, 103°–104°E, and 11.5°–13°N, 105°–107°E. Koh Kong, Kampong Cham and Kampong Thom are located within this area. These regions present a background lightning activity of 30 flashes/km^2/year and also show a spatial distribution with centres of maximum lightning activities larger than 80 flashes/km^2/year on the southeast edge of Cambodia. The capital of Cambodia, Phnom Penh (11.55° N, 104.91° E) shows less lightning activity compared to its surrounding areas. For the year analyzed, the results show that the lightning activity is largely confined over the mountainous, and over the plateau areas, with less lightning activity over the Tonle Sap and Tonle Sap River basins. The majority of lightning activity occurs over land, while only a minimal amount of lightning activity is observed over the sea and ocean.

3.3 Lightning Polarity Distribution

Figure 5 shows the density distribution of positive flash density. It can be seen that the average value of positive flash density is above 2.5 flashes/km^2/year. Different from the distribution of total flash, there is only one hot spot of positive flash near 12° N and 106° E, the Tonle Sap Lake and Tonle Sap River basins have the lowest positive flash density compared to the whole country, and other distribution laws are the same as the total flash density distribution.

Figure 6 shows the distribution of negative flash density. The average negative flash density is above 4.0 flashes/km^2/year, it shows a similar spatial flash rate distribution with the total flash.
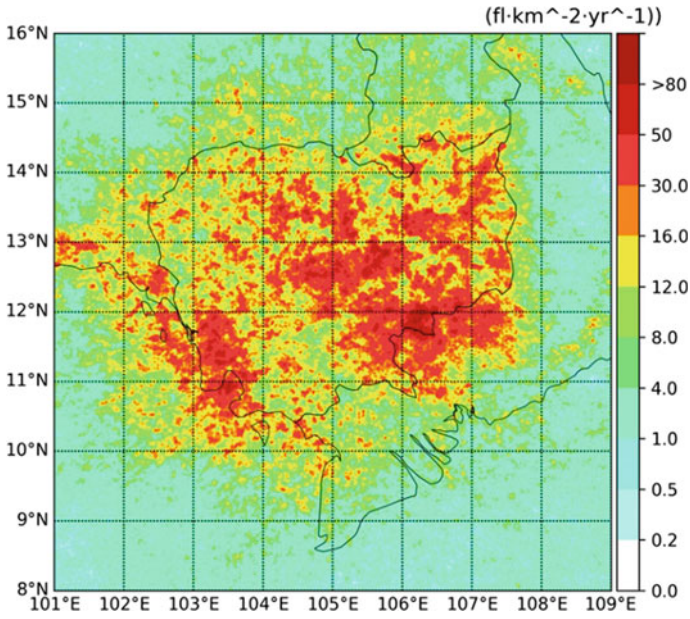
Fig. 4 Spatial distribution of the flash density (flash/km^2/year) over Cambodia (2021)
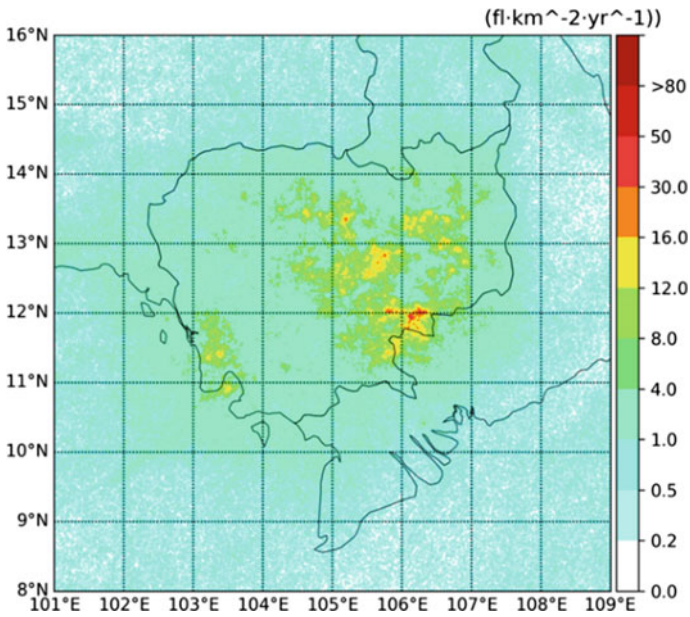
Fig. 5 Spatial distribution of the positive flash density (flash/km^2/year) over Cambodia (2021)
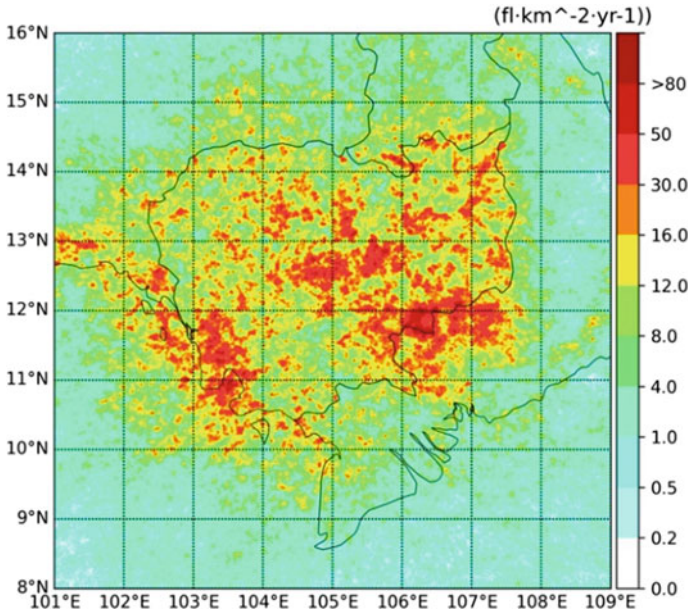
Fig. 6 Spatial distribution of the negative flash density (flash/km^2/year) over Cambodia (2021)

3.4 Characteristics of the Lightning Current Intensity Distribution

According to the statistics of lightning data in 2021, a total of 829,891 positive flashes occurred throughout the year, with an average current intensity of 53.4 kA, for negative flashes, these numbers are 3,463,837 and 36.86 kA respectively. The positive and negative flash ratio is about 1:4. As shown in Fig. 7, the lightning current intensity spectrum demonstrates that the distribution curves of negative and total flashes closely match each one, and both show a unimodal distribution. The proportion of positive flash current value above 70 kA is greater than that of negative flash. The positive flash current intensity spectrum also presents a unimodal distribution, and its spectral type is narrower than that of the negative flash. The positive flash intensity is mostly distributed in 0–30 kA, accounting for 65% of the total number of positive flashes. The peak value appears at 5–15 kA. The proportion of positive flash current value above 70 kA is greater than that of negative flash. The negative flash intensity is mostly distributed between 0 and 40 kA, accounting for 75% of the total negative flash, and the peak appears at 20–30 kA.

Fig. 7 Lightning current intensity spectral distribution
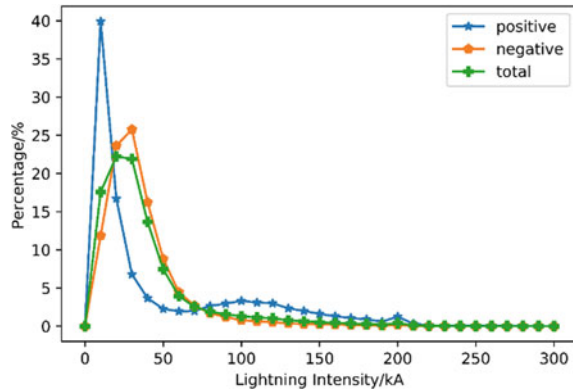
4 Conclusions

We analyzed the lightning data for the Cambodia region in 2021, main findings can be summarized as follows.

The junction of the dry and rainy seasons is a period of the high incidence of lightning activity, and there are very few lightning activities in the middle of the dry season.

General patterns of diurnal lightning activity are mainly characterized by the high occurrence of lightning activity in the afternoon and early evening.

The lightning activity is largely confined over the mountainous, and over the plateau areas, with less lightning activity over the Tonle Sap and Tonle Sap River basins.

The current intensity spectra of both positive and negative flashes showed a unimodal distribution, and the current intensity distribution curves of negative flash and total flashes were well matched. The average current intensity of positive flash is larger, and the proportion of positive flash currents above 70 kA is greater than that of negative flash.

References

1. Davies GI, Mciver L, Kim Y et al (2015) Water-borne diseases and extreme weather events in Cambodia: review of impacts and implications of climate change. Int J Environ Res Public Health 12(1):191–213
2. Sok C, Choup S (2017) Climate change and groundwater resources in Cambodia. J Groundw Sci Eng 5(1):31–43
3. Thoeun HC (2015) Observed and projected changes in temperature and rainfall in Cambodia. Weather Clim Extremes 7:61–71
4. Kazama S, Aizawa T, Watanabe T et al (2012) A quantitative risk assessment of waterborne infectious disease in the inundation area of a tropical monsoon region. Sustain Sci 7(1):45–54

5. Nagumo N, Kubo S, Sugai T (2016) Characteristics of extreme monsoon floods and local land use in the lower Mekong basin, Cambodia
6. Gupta A (2009) Geology and landforms of the Mekong basin
7. Qie K, Qie X, Tian W (2021) Increasing trend of lightning activity in the South Asia region. Sci Bull 66(1):78–84
8. Galanaki E, Kotroni V, Lagouvardos K et al (2015) A ten-year analysis of cloud-to-ground lightning activity over the Eastern Mediterranean region. Atmos Res 166:213–222
9. Dayeh MA, Farahat A, Ismail-Aldayeh H et al (2021) Effects of aerosols on lightning activity over the Arabian Peninsula. Atmos Res 261
10. Guo H, Xiong Y, Fu Z et al (2008) Temporal-spatial characteristics of lightning activity and lightning disaster over Beijing. Meteorol Monthly 34(1):12–17
11. Hamid EY, Kawasaki ZI, Mardiana R et al (2000) TRMM/LIS observations of lightning activity over Indonesia. In: Proceedings of the 2000 winter meeting of the IEEE power engineering-society, Singapore, Singapore 23–27 Jan 2000
12. Kandalgaonkar SS, Tinmaker MIR, Kulkarni JR et al (2003) Diurnal variation of lightning activity over the Indian region. Geophys Res Lett 30(20)
13. Kuleshov Y (2004) Seasonal and latitudinal variations of lightning ground flash activity in Australia. Aust Meteorol Mag 53(3):197–204
14. Tarabukina LD, Kozlov VI (2016) Spatial and temporal variations of lightning activity in North Asia in 2009–2014. In: Proceedings of the 22nd international symposium on atmospheric and Ocean Optics—atmospheric physics, Tomsk, RUSSIA, Jun 30–Jul 03 2016
15. Tarabukina LD, Kozlov VI (2017) Climatology of lightning activity in northern Asia in 2009–2016. In: Proceedings of the 23rd international symposium on atmospheric and ocean optics—atmospheric physics, Irkutsk, RUSSIA 03–07 Jul 2017
16. Wang J, Zhu B, Ma M (2017) Characteristics of lightning activity and its relationship with the atmospheric environment parameters in Southeast China. J Univ Sci Technol China 47(5):403–412, 434
17. Tran TH (2018) Modeling of LEMP propagation in the Lossy atmosphere
18. Jacobson AR, Holzworth RH, Brundell JB (2021) Using the world wide lightning location network (WWLLN) to study very low frequency transmission in the earth-ionosphere waveguide: 1. Comparison with a full-wave model. Radio Sci 56(7)
19. Wang J, Huang Q, Ma Q et al (2020) Classification of VLF/LF lightning signals using sensors and deep learning methods. Sensors 20(4)

Mechanism Analysis of Insulator Fault in Enclosed Isolated Phase Bus Caused by Vibration

Jianwen Fu, Bo Yang, Xiaomei Wang, Antao Feng, Feihong Cai, and Hailong Zhang

Abstract The conductor and shell of an enclosed isolated phase bus will be subjected to alternating electromagnetic forces, bring by alternating magnetic field environment, which causes a long time vibration. The insulator that supports these two parts may become damaged or loose under this vibration environment, which can cause some faults. In this paper, the insulator failure into air gap fault and crack defect, to reveal the mechanism of insulator failure caused by bus vibration. Through theoretical analysis and finite element simulation, the different stress and deformation manifestations of insulators under normal state, air gap and crack faults are analyzed. Thus, the influence of internal electric force on faulty insulators in isolated phase enclosed bus is revealed. The impact of air gap and crack faults on insulators should receive more attentions.

Keywords Enclosed isolated phase bus · Insulator air gap · Insulation aging · Crack

1 Introduction

In the power system, enclosed isolated phase bus (EIPB) is widely used in the outgoing of large power generation equipment and substation circuit, as a large current transmission device [1, 2]. It is responsible for transmitting and distributing electrical energy from power plants or distribution stations, which is of great significance for the reliable operation of generators and power systems. When passing through the current, it causes vibration of the busbar structure under the action of

J. Fu · B. Yang · X. Wang
Xinanjiang Hydropower Plant, State Grid Xinyuan Hydropower Co. Ltd, Hangzhou 311600, China

A. Feng · F. Cai · H. Zhang (✉)
School of Electrical Engineering and Automation, Nanjing Normal University, Nanjing 210043, China
e-mail: zhanghl@njnu.edu.cn

electric force [3]. Long-term vibration can cause loosening, fracture, insulation structure damage, busbar deformation, fatigue, etc., thus bringing serious hazards to safety [4].

The majority of EIPB failures caused by vibration are concentrated on the failure of insulators. Currently, few research and analysis on insulator failures in EIPB is reported. However, the insulators used in EIPB are very similar to those in gas insulated switchgear (GIS) and gas insulated metal enclosed transmission line (GIL) buses, regardless of material, operating conditions, and force conditions. Therefore, insulator failures in GIS and GIL busbars may also occur during the actual operation of EIPB. Scholars have conducted some researches on insulator faults in GIS and GIL busbars. Chen et al. conducted in-depth research on the abnormal condition of 110 kV GIS busbars in a 220 kV substation. It was found that the discharge issue was caused by the presence of millimeter level gaps in the support insulators [5]. Compared with insulators in GIS and GIL, the insulators used in EIPB are very similar in terms of material, operating conditions, and even stress conditions. Therefore, similar insulator failures may also occur during the actual operation of EIPB.

There are many reasons for insulator failures, of which the actual operating conditions are also a very important reason. Actually, when two parallel and in-phase double busbars are simultaneously connected with current, an electric force will be generated on each copper bus, which will cause vibration of the busbars. If the copper busbar vibrates excessively for a long time. It will damage the pillar insulator, loosen the angle steel bracket, and damage the hardware bolts [6]. In addition, if the electrodynamic force frequency of the bus is close to the natural frequency, it will cause mechanical resonance of the system. At the same time, the vibration of the busbar can also cause mechanical fatigue, mechanical strength reduction, and insulation aging of the post insulator. Jiang et al. conducted a study on the power generation failure of isolated phase enclosed busbar support insulators in hydropower stations, pointing out that the installation of the support insulators was not in place, resulting in discharge of the support insulators [7]. Li et al. analyzed the causes of internal flashover faults in 330 kV GIS busbar equipment and pointed out that the fundamental cause of the busbar tube flashover accident was due to the installation of the busbar insulation support platform not meeting the requirements [8]. Fan et al. conducted the compositive calculation and analysis of the loss and temperature of the self-cooling enclosure-isolated phase bus of a 600 MW generator. A more accurate quantitative calculation and analysis of the loss and heat of the self-cooling high-current separated-phase enclosed bus was performed, by considering more factors, like the skin effect, eddy current loss, convection and so on [9]. You et al. Studied a new co-simulation method of EIPB. The subsegments EIPB model based on FEM was established, and the temperature distribution in joint surfaces was transmitted. The dynamic stability of EIPB was calculated under short-circuit condition, based on the thermal results [10].

This work conducts a study on the mechanism of insulator failure caused by vibration for EIPB, under the support of Technology Project Funding from State Grid Xinyuan Group Co. Ltd. (SGXY-2022-129). Based on the mechanism analysis of

(a) Horizontal and Vertical Layout of EIPB   **(b) Physical Drawing of Insulator**
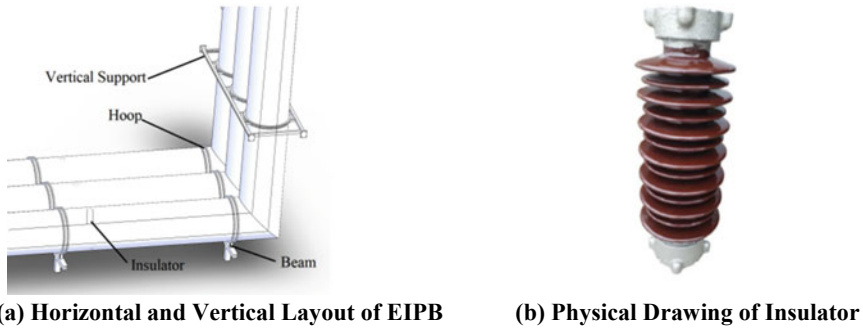
Fig. 1 Overall structure and insulator diagram

insulator vibration, the influence of air gaps and cracks on the vibration characteristics of insulators is demonstrated. The demonstration basis for identifying insulator faults of EIPB through vibration characteristic changes is clarified, laying a certain basis for the fault diagnosis and positioning in next research.

2 Structure of Enclosed Isolated Phase Bus

2.1 Structure and Layout of Insulator

EIPB is generally arranged in horizontally, vertically, and diagonally, as shown in Fig. 1. The layout of the horizontal-vertical mixed arrangement is shown in Fig. 1a, which mainly consists of bus conductors, shielding shells, I-beams, cross arms, clamping insulators, and fixed slots. The conductor and shell are mainly made of aluminum material, while support devices such as clamps are made of structural steel, and support insulators are made of epoxy resin material. The insulation is shown in Fig. 1b.

2.2 Force Analysis of Insulator

The stress condition of insulators varies under different arrangements, as shown in Fig. 2. The upper and lower insulators of horizontally arranged are subjected to significant tensile and compressive stress, due to the gravity of the shell and conductor. The left and right end insulators of vertically arranged are mainly subjected to shear forces. The stress condition at the horizontal-vertical connection is similar to that of the horizontal, but the value is greater.
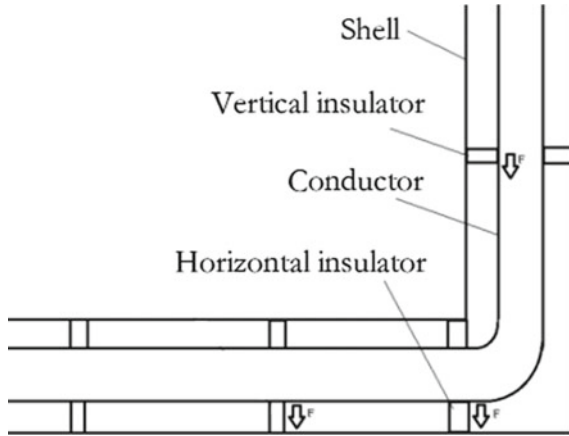
Fig. 2 The stress condition of EIPB horizontal and vertical layout structure

3 Mechanism of Vibration-Induced Insulator Failure

3.1 Vibration Characteristics of Insulators with Air Gap

EIPB is constantly exposed to external vibration environment, and slight friction can cause air gaps between the insulator, conductor, and shell, as shown in Fig. 3a.

The bottom two insulators can be partially filled by the conductor sinking, but the air gap of the top insulator will definitely increase over time. At the same time, an increase in the air gap between the top insulator and the casing will lead to a decrease in the connection strength and generate stronger vibrations. Figure 3b shows the influence curve of bolts under different degrees of tightness over time.
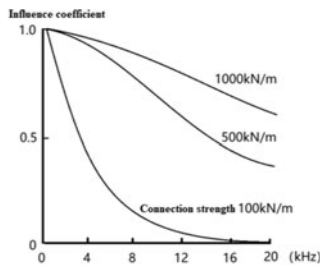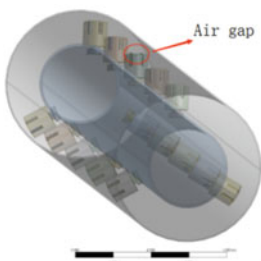
(a) Schematic of air gap   (b) Influence curve of bolts under different degrees of tightness

Fig. 3 Air gap position and influence of tightness of insulator

(a) Model with fissure   (b) Size of insulator   (c) Physical picture
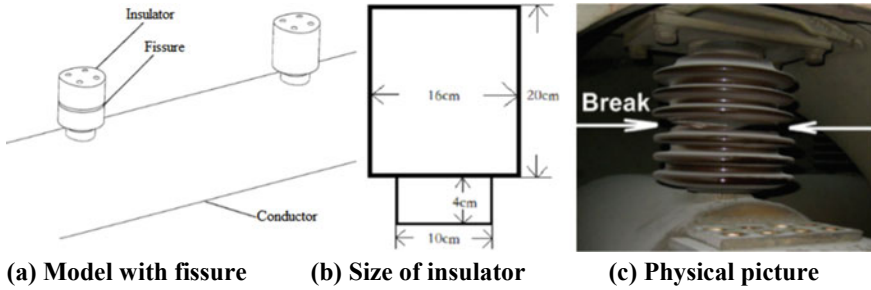
Fig. 4 Diagrams of insulator with crack

3.2   *Vibration Characteristics of Insulators with Crack*

During installation and operation, insulators often produce cracks, as shown in Fig. 4. Especially when subjected to some impact forces, such as short circuits, earthquakes, and water flow impacts, cracks can lead to stress concentration and further increase in cracks.

4   Simulation Verification

According to the theory of insulators under air gap and crack faults mentioned above, both air gap and crack will reduce the strength of insulators, thereby increasing their vibration speed. The above theory was not verified, and simulation was used to verify it. The insulator material parameters in the simulation are shown in Table 1.

4.1   *Vibration Characteristics of Insulator with Air Gap*

In Fig. 5a, the overall deformation diagram is shown when an air gap appears. The maximum deformation occurs at the edge of the air gap, which is relatively uniform from top to bottom. However, compared with the normal deformation of the insulator in Fig. 5b, the deformation at the same part increases by about 30%, and the maximum deformation occurs alternately at two opposite edges, showing a swinging trend.

Table 1 Materials parameters of insulator

	Density (kg/m^3)	Elastic modulus (Mpa)	Shear modulus (Mpa)
Epoxy resin	1200	1528	40
Structural steel	7850	1667	77
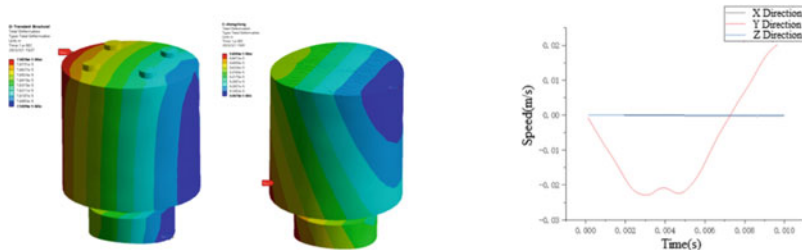
(a) Air gap condition (b) Normal condition (c) Vibration response under air gap condition

Fig. 5 Cloud diagram of insulator strain distribution

Therefore, it will reduce the connection strength of the insulator at the top of the bus. Figure 5c indicates that the velocity value in the Y-axis direction increases from 0.01 to 0.025 m/s, with a significant increase of over 150%. It can be seen that the vibration response of the insulator undergoes a significant change, which is consistent with the theoretical results.

4.2   Vibration Characteristics of Insulator with Cracks

A insulator with a 10 mm crack located in the middle is established. The comparison of normal insulator and one with cracks are extracted as shown in Fig. 6.

It can be seen from Fig. 6a that although the crack of the insulator completely separated from each other, the deformation of the upper and lower halves of the insulators in the same vertical direction is almost the same, resembling a mouth shaped shape. In addition, the left and right ends of the upper and lower parts of the insulator open and close each other alternately, which will accelerate the wear of both ends, forming a vicious cycle. As shown in Fig. 6b, the normal insulator undergoes uniform deformation from top to bottom, with a numerical value of about 70% of that of the cracked one. The deformation is characterized by overall compression, etc.
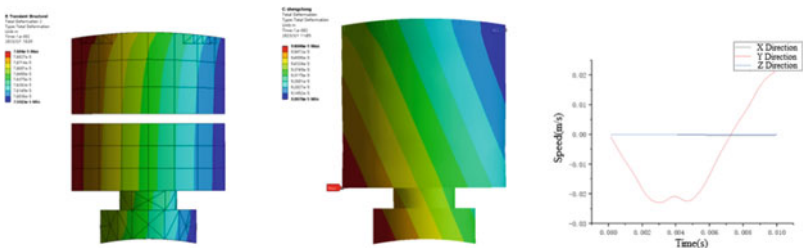
(a) Crack condition   (b) Normal condition   (c) Vibration response under crack condition

Fig. 6 Cloud diagram of insulator strain distribution

The intact insulator has good resistance to this deformation. Moreover, as shown in Fig. 6c, the vibration velocity of the cracked insulator in the Y-axis direction increases from 0.01 to 0.025 m/s, with a significant increase of over 150%. When a crack fault occurs, there is a small abnormal fluctuation in the speed of the insulator. From this, it can be seen that the vibration response of the insulator undergoes a significant change when a fault occurs, which is consistent with the theoretical analysis.

5   Conclusion

This work theoretically analyzes the connection relationship between EIPB insulators, as well as shells and conductors. The influence of air gaps and crack defects on the connection performance and strength of insulators are revealed. Subsequently, the calculated results are verified through finite element analysis, which showed that air gap failure would reduce the connection strength between the insulator and the casing, while significantly increasing the burden on the screws. Then the impact of crack fault is analyzed, and it is found that crack fault will also significantly reduce the role of insulator itself in connecting conductor and shell. What's more serious, it will increase the compression effect of top insulator on conductor, even cause serious wear, and induce partial discharge and other faults.

References

1. Xu M (2016) Research on the application of off-phase closed bus. Electr Eng (5):165, 167
2. Yu ZL, Wang J, Zhang B et al (2019) Application of micro-positive pressure system in isolated-phase bus. Mech Electr Tech Hydropower Stat 42(11):30–32
3. Zhang L, Hu TT (2012) A brief discussion on the vibration of common box closed busbar. In: Electrical academic exchange conference of the electrical committee of the Chinese society of hydropower engineering. China Hydropower Engineering Society, Chengdu, pp 190–193
4. Chen L, Zhang H, Ni H et al (2022) Analysis on abnormal busbar of 110 kV GIS at 220 kV substation. High Voltage Eng 58(12):190–198
5. Peng JQ, Pu Y, Liu J et al (2021) Analysis of a fault of supporting insulator for 110 kV outdoor gas insulated switchgear bus gas chamber. Electr Eng 22(3):61–64
6. Jiang YJ, Wang H (2017) Analysis and treatment of discharge faults of isolated phase enclosed busbar support insulators in hydropower stations. Sichuan Water Power 36(6):107–109
7. Liu SC, Chen Q, Zhang J et al (2008) Cause analysis of flashover fault in 330 kV GIS bus-bar equipment. Smart Grid 36(2):60–63
8. Guo SZ, Duan YP (2021) Reason analysis and countermeasures for GIL bus fault in nuclear power plants. Electrotechnics Electr 2021(4):75–76
9. Fan Z-N, Bian Z-Y, Xiao K et al (2021) The electromagnetic-fluid-temperature field analysis of loss and heat of self-cooling separate-phase enclosed bus of large generator. IEEE Access 2021(9):11372–11377
10. You JX, Wu Y, Wang L et al (2018) Thermal-dynamic stability analysis for the enclosed isolated-phase bus bar based on the subsegment calculation model. IEEE Trans Compon Packag Manuf Technol 8(4):626–634

Study on the Influence Mechanism of Voltage on Sulfide Corrosion in Power Transformer

Boyi Li

Abstract At present, only the deterioration effect of electric field on insulating oil under oil-sulfur corrosion has been studied, but the deterioration of insulating paper has not been studied. Therefore, two sulfides, dibenzyl disulfide and dodecyl mercaptan, were selected in this paper. The effect of electric field on insulating paper under oil corrosion was studied by measuring elastic modulus and molecular chain motion of cellulose using reaction molecular dynamics simulation technique. Then the ball plate electrode was used to apply 2 times the initial discharge voltage, and aged in a 150 °C electrothermal aging chamber for 24 h. Another group of control group was set up without electric field. The final results showed that the breakdown voltage, polymerization degree and moisture mass fraction of insulating paper decreased. This verifies the correctness of the simulation from macroscopic experiment. The results show that the addition of electric field will accelerate the process of oil sulfur corrosion, resulting in the deterioration of the performance of the oil paper insulation system.

Keywords Electric field · Insulating paper · Oil corrosion · Voltage

1 Introduction

With the improvement of our economic level, the scale of power system and grid are expanding constantly. This will further improve the reliability of transmission and distribution related devices. Once a power transformer fails, it will directly threaten the continuity of the power supply to the grid. In addition, power transformers are difficult and time-consuming to repair, which will bring huge economic losses to society. Oil-immersed power transformers are commonly used as power transformers for transmission and distribution equipment. A large number of data show that the

B. Li (✉)
Institute of Thermal Power Generation Technology, China Da Tang Corporation Science and Technology General Research Institute Co, Beijing, China
e-mail: liboyi@cdt-kxjs.com

main cause of transformer accidents is the aging or failure of transformer internal insulation [1–3]. The internal insulation of the transformer is a composite insulation. The composite insulation consists of transformer oil and insulating paper or cardboard. During the long-term operation of the transformer, the composite insulation is gradually aged by various stresses, reducing the electrical and mechanical properties of the insulation. The insulation safety of oil-immersed power transformers is a major concern due to the trace sulfides contained in the transformer insulating oil [4–6]. The active sulfides contained in the trace sulfides react with copper ions in the copper winding or transformer oil to produce copper sulfide precipitates on the surface of the copper winding and insulating paper [7]. This reduces the insulation performance of the composite insulation [8, 9]. Studies have shown that dibenzyl disulfide (DBDS) is the main sulfide causing the deposition of cuprous sulfide [10, 11], but the actual oil samples besides DBDS also contain mercaptan, thiophene, sulfoxide [12] and other sulfides. Different sulfides can be converted into each other under certain conditions [13]. The research shows that multiple sulfur corrosion is not simple linear superposition of single sulfur corrosion [14]. Numerous studies have been carried out by many scholars on the factors that influence the degree of sulfur corrosion. The factors contain the influence of active and inactive sulfides, the concentration of corrosive sulfides [15], the level of temperature [16, 17] and the electric field. The electrical stress analysis of transformer oil paper insulation under the action of sulfur corrosion was investigated in the literature [18]. It was found that the deposition of copper sulfide on the sides of the insulating paper forms a continuous conducting path for the current. The increase in current and temperature leads to rupture of the insulating paper. Yang et al. [19] explored the effect of electric fields on copper sulfide deposition by setting up experiments with purely thermal aging compared to electrothermal aging. The results showed that the electric field increased the amount of copper sulfide deposited on the copper windings. Gonzalez et al. [20] found that DBDS degradation increased through the cleavage of disulfide bonds under pressurization. From the above studies in the literature, it can be found that the electric field is an important factor affecting the degree of sulfur corrosion.

However, it only studied the effect of voltage action under oil and sulfur corrosion on the deterioration of insulating oil, not the effect on insulating paper. This project conducted experiments to study the effect of voltage action under oil and sulfur corrosion on the deterioration of insulating paper. The present study only illustrates the effect of single sulfide on insulating oil in composite insulation. Therefore, it is necessary to study the effect of multiple sulfur corrosion on insulating paper under different electric fields. Since the actual oil sample contains more than DBDS, two representative sulfides, DBDS and DDM, are selected in this paper. The reaction molecular dynamics simulation method is used to find out the microscopic degree under different electric field conditions. The changes of insulating paper molecules were observed by measuring the elastic modulus and molecular chain movement of cellulose. Then the reliability of the simulation was verified by experiments, in which the breakdown voltage, polymerization degree and other characteristic parameters of the insulating paper were measured.

2 Molecular Dynamics Simulations on the Effects of Electric Field on Sulfur Corrosion

2.1 Model Building and Simulation Process

Two typical sulfides are selected in this paper. DBDS make the most corrosive and most studied sulfide. Mercaptan may also oxidize to form another corrosive disulfide under certain conditions. The sulfur compounds were mixed with oil molecules in the ratio of DBDS and DDM sulfur atoms to 1:1 to form an oil-sulfur model (Fig. 1).

It is shown that cellulose chains of different lengths exhibit similar physical and chemical properties and are not affected by model DP values. Therefore, a single glucose molecule is drawn, and Amorphous Cell module is used to mix 25 glucose molecules into the insulating paper model (Fig. 2).

The function of "Build Layers" was used to combine the oil-sulfur model with the insulating paper model to form the oil-sulfur paper model, which was used to restore the composite insulation components in the actual transformer (Fig. 3).

Two groups of models were set, and the oil-sulfur paper models used in both groups were the above models. One group was simulated at 1 V/Å (1×10^{10} V/ m), while the other group served as a control group without any electric field. Both

Fig. 1 Oil-sulfur model
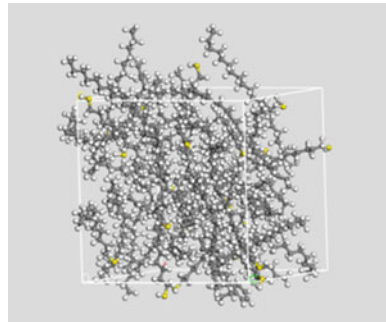
Fig. 2 Insulating paper model
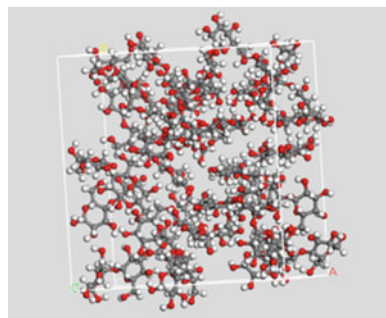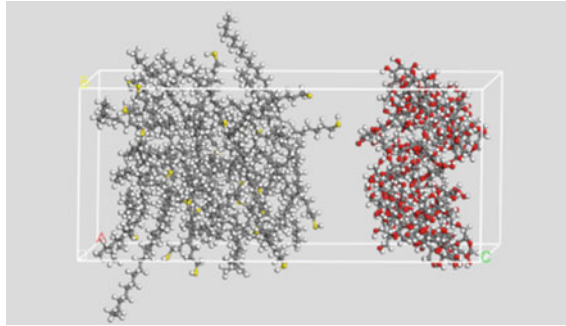
Fig. 3 Oil-sulfur-paper model

models were simulated at 100 ps using constant temperature and constant pressure (NVT) ensembles at 150 °C. The elastic modulus of cellulose and molecular chain motion (MSD) of cellulose were measured to observe the effect of voltage on the oil-sulfur paper model (Fig. 4).
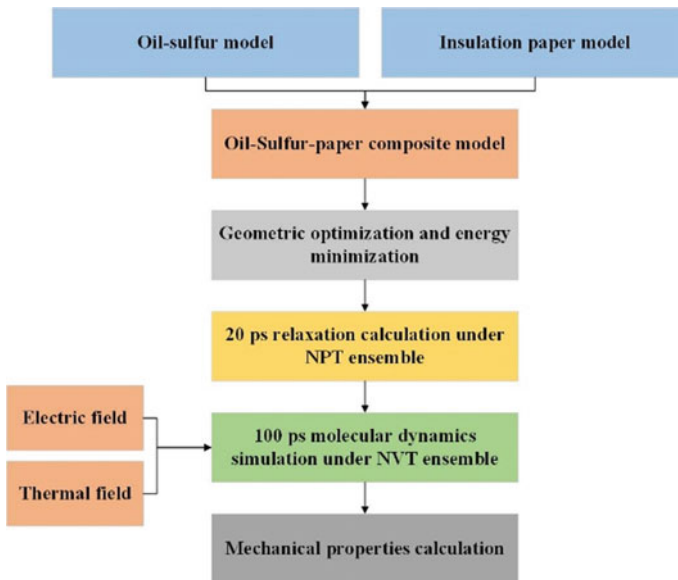
Fig. 4 Simulation flowchart

2.2 Elastic Modulus of Cellulose

The general relationship between stress and strain in solid materials can be expressed in terms of Hooke's law formula (1):

$$
\begin{bmatrix}
\sigma_x \\
\sigma_y \\
\sigma_z \\
\tau_{yz} \\
\tau_{zx} \\
\tau_{xy}
\end{bmatrix}
=
\begin{bmatrix}
C_{11} & C_{12} & C_{13} & C_{14} & C_{15} & C_{16} \\
C_{21} & C_{22} & C_{23} & C_{24} & C_{25} & C_{26} \\
C_{31} & C_{32} & C_{33} & C_{34} & C_{35} & C_{36} \\
C_{41} & C_{42} & C_{43} & C_{44} & C_{45} & C_{46} \\
C_{51} & C_{52} & C_{53} & C_{54} & C_{55} & C_{56} \\
C_{61} & C_{62} & C_{63} & C_{64} & C_{65} & C_{66}
\end{bmatrix}
\begin{bmatrix}
\varepsilon_x \\
\varepsilon_y \\
\varepsilon_z \\
\gamma_{yz} \\
\gamma_{zx} \\
\gamma_{xy}
\end{bmatrix}
\tag{1}
$$

C_{ij} is a 6 * 6 matrix of elasticity coefficients from which all the mechanical properties of the material can be derived. Each mechanical property satisfies the following formula:

$$
E = 2G(1 + v) = 3K(1 - 2v) \tag{2}
$$

where E is the Young's modulus. Young's modulus is equal to the ratio of stress to strain and can be used to evaluate the stiffness of a material. A large value indicates high stiffness and resistance to deformation. K is the bulk modulus. The bulk modulus is used to describe the elasticity of homogeneous isotropic solids. It is an expression of the incompressibility of a material and a large value indicates a high energy requirement for the material to fracture. G is the shear modulus. The shear modulus is the ratio of shear stress to strain. It expresses the ability of a material to resist shear strain. V is the Poisson's ratio. Poisson's ratio is the ratio of transverse strain to longitudinal strain. Poisson's ratio is an elasticity factor used to reflect the transverse deformation of a material. A large value indicates a high plasticity of the material.

The following Fig. 5 is the comparison of the elastic modulus of cellulose after simulation with the same oil-sulfur paper model under different electric field conditions and at 423 K temperature. It can be seen from the figure that after adding DC electric field, the elastic modulus of cellulose, namely Young's modulus, bulk modulus and shear modulus, all decrease compared with that without electric field. It can be shown that after the addition of electric field, the electric field accelerates the breaking of cellulose molecular chain, which leads to the reduction of mechanical strength of insulating paper.

2.3 Mean Square Displacement of Cellulose

The chain motion of the cellulose molecules is characterized by calculating the mean square displacement (MSD) characteristic quantities of the cellulose molecules in each model. The stronger the chain motion of cellulose, the worse the mechanical

Fig. 5 Comparison of elastic modulus of cellulose
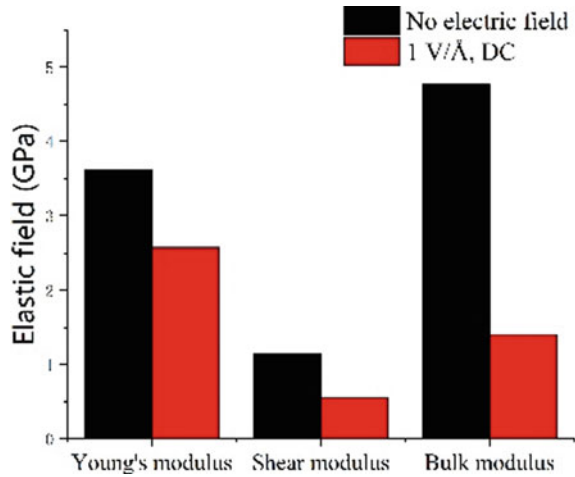
properties and thermal stability of the cellulose.

$$MSD = \langle |r(t) - r(0)|^2 \rangle \tag{3}$$

The following Fig. 6 is the comparison of molecular chain movements of cellulose after simulation with the same oil-sulfur paper model under different electric field conditions and at 423 K temperature. As can be seen from the figure, the addition of electric field makes the MSD of cellulose increase as a whole compared with that without electric field, indicating that the molecular chain movement of cellulose is more intense. It can be understood that the addition of electric field reduces the mechanical strength of the insulating paper, and the molecular chain moves violently, making it easier to break.

Fig. 6 Comparison of mean square displacement of cellulose
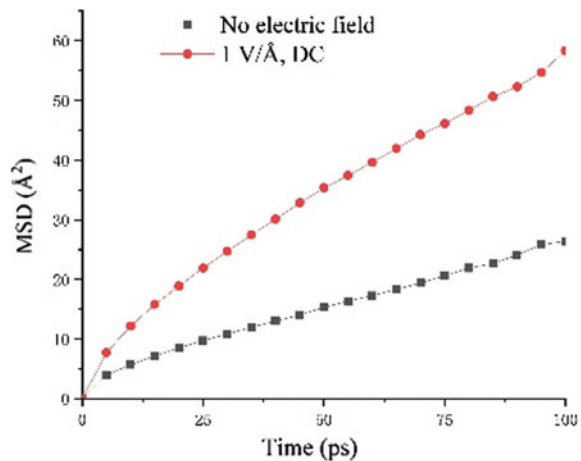
In summary, the changes of MSD and elastic modulus of cellulose are closely related to the mechanical strength of insulating paper. In the macroscopic experiment, the degree of polymerization of cardboard is also related to the mechanical strength of insulating paper. Therefore, it can be known that the changes in MSD and elastic modulus of cellulose at the micro level can be verified by the changes in the degree of polymerization of cardboard in the macro experiment.

3 Simulation Results with Experimental Verification

3.1 Experimental Materials and Test Procedures

The test material was insulated board with thickness of 0.6 mm, which was dried for 48 h at 90 °C/50 Pa. Then 25# transformer new oil was used to add 100 mg/kg DBDS and 200 mg/kg DDM and heated to 40 °C. The cardboard was immersed in insulating oil at 40 °C/50 Pa for 24 h. In the test process, group A uses the ball electrode to apply 2 times the initial discharge voltage, and ages for 24 h in a 150 °C electrothermal combined aging chamber. The physical picture of the electrodes is shown in Fig. 7a, and the electrothermal combined aging chamber is shown in Fig. 7b. Group B was simply thermally aged at 150 °C for 24 h.

The initial discharge voltage and breakdown voltage are tested using the step-up method. The initial voltage is 0, the boost step is 0.5 kV, and the residence time is 1 min. Kehaishi KH-100 M current sensor and YKDL-6000 series oscilloscope are used to collect the discharge pulse for signal acquisition, so as to judge the initial discharge voltage and breakdown voltage. The moisture content in paper was measured by Karl Fischer moisture meter, Metrohm KF831, produced by Switzerland Wantong Co., LTD., according to GB/T462-2008 "Determination of Moisture content in Paper and Board". The degree of polymerization of insulating paper was tested with the assistance of China Pulp and Paper Research Institute. Refer to GB/T 29305-2012 "Measurement of Viscotropic Polymerization of new and aged Cellulose Electrical insulation Materials" and IEC 60450: The standard "Measurement of

Fig. 7 **a** Ball electrode **b** electric heating combined aging box

(a)   (b)
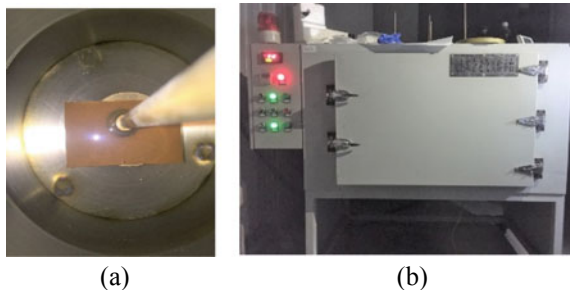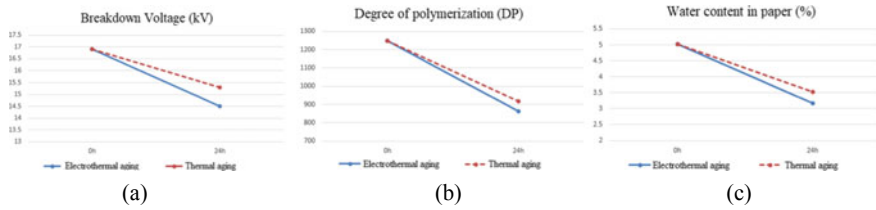
Fig. 8 Test results: **a** breakdown voltage, **b** degree of polymerization, **c** water conent in paper

the viscosity of viscohomicity of New and Aged cellulose electrical insulation Materials" was implemented in 2007. The viscosity of the solution of insulating paper dissolved in copper ethylenediamine solvent was measured to calculate the degree of paper polymerization.

3.2 Test Results and Analysis

The physical wiring diagram for testing the initial discharge voltage and breakdown voltage of the insulated cardboard is shown in Fig. 8. The measured initial discharge voltage of the insulated cardboard is 3.1 kV. Therefore, the power frequency voltage of 6.2 kV is selected for electric heating combined aging.

Figure 8 show the breakdown voltage, polymerization degree, and moisture content test results of the insulated cardboard. It can be seen that within the aging interval (24 h), the breakdown voltage, polymerization degree and moisture of insulating paper all show a downward trend, and the decline is more serious in the electro-thermal combined aging group than in the thermal aging group. It shows that the electric field can accelerate the deterioration of insulating paper and promote the oil-sulfur corrosion of transformer.

It can be seen from the above figure that the degree of polymerization of cardboard decreases after the addition of electric field, indicating that the addition of electric field will reduce the mechanical strength of insulating paper. The microcosmic manifestation is that the MSD and elastic modulus of cellulose also decrease after the addition of electric field. This verifies the correctness of microsimulation from macroscopic experiment.

4 Conclusions

The presence of voltage will accelerate the corrosion of oil and sulfur. It will not only cause the increase of oleic acid value and dielectric loss value of insulating oil, breakdown voltage and volume resistivity decrease, accelerate the deterioration of insulating oil and reduce its performance, but also cause the decrease of breakdown

voltage, polymerization degree and moisture quality fraction of insulating board, reduce the performance of insulating paper. To sum up, the existence of voltage will accelerate the corrosion of oil and sulfur, resulting in the deterioration of the performance of oil paper insulation system.

References

1. Shirasaka Y, Murase H, Okabe S, Okubo H (2009) Cross-sectional comparison of insulation degradation mechanisms and lifetime evaluation of power transmission equipment. IEEE Trans Dielectr Electr Insul 16(2):560–573
2. Lukic J et al (2015) CIGRE WG A2.40 copper sulphide long term mitigation and risk assessment
3. Ren S, Zhong L, Yu Q, Cao X, Li S (2012) Influence of the atmosphere on the reaction of dibenzyl disulfide with copper in mineral insulation oil. IEEE Trans Dielectr Electr Insul 19(3):849–854
4. Maina R, Tumiatti V, Scatiggio F, Pompili M, Bartnikas R (2011) Transformers surveillance following corrosive sulfur remedial procedures. IEEE Trans Power Del 26(4):2391–2397
5. Kato F, Amimoto T, Nagao E (2011) Effect of DBDS concentration and heating duration on copper sulfide formation in oil-immersed transformer insulation. IEEE Trans Dielectr Electr Insul 18(6):1869–1876
6. De Carlo RM, Bruzzoniti MC, Sarzanini C, Maina R, Tumiatti V (2013) Copper contaminated insulating mineral oils-testing and investigations. IEEE Trans Dielectr Electr Insul 20(2):557–563
7. Cong H, Pan H, Hu X, Li Q (2021) Deterioration degree assessment of multiple sulfides in transformer oil based on the entropy-weight method. IEEE Trans Dielectr Electr Insul 28(5):1628–1635
8. Scatiggio F, Tumiatti V, Maina R, Tumiatti M, Pompili M, Bartnikas R (2009) Corrosive sulfur induced failures in oil-filled electrical power transformers and shunt reactors. IEEE Trans Power Del 24(3):1240–1248
9. Kato F, Amimoto T, Nishiura R, Mizuno K, Toyama S (2013) Suppressive effect and its duration of triazole-based passivators on copper sulfide deposition on Kraft paper in transformer. IEEE Trans Dielectr Electr Insul 20(5):1915–1921
10. Cong H, Liu Z, Hu X, Du Y, Li Q (2022) Correlation analysis and regression fitting of multiple sulfide aging characteristic parameters. IEEE Trans Dielectr Electr Insul 29(5):2008–2016
11. Mehanna N, Jaber A, Oweimreen G, Abulkibasha A (2014) Assessment of dibenzyl disulfide and other oxidation inhibitors in transformer mineral oils. IEEE Trans Dielectr Electr Insul 21(3):1095–1099
12. Cong H, Zhang M, Li Q (2018) Study on sulfide distribution in the operating oil of power transformers and its effect on the oil quality. Appl Sci 8(9):1–12
13. Cong H, Pan H, Qian D, Zhao H, Li Q (2021) Reviews on sulphur corrosion phenomenon of the oil-paper insulating system in mineral oil transformer. High Volt 6(2):193–209
14. Li Q, Shu X, Li F, Zhou Y, Han S, Cong H (2018) Effects of multiple sulfur corrosion on transformer oil-paper insulation thermal aging properties. High Volt Eng 44(2):470–477
15. Jadim R, Kans M, Rehman S, Alhems LM (2020) A relevant condition monitoring of corrosive sulphur deposition on the windings of oil-filled electrical transformers. IEEE Trans Dielectr Electr Insul 27(5):1736–1742
16. Cong H, Wang Y, Pan H, Hu X, Li Q (2023) Multiple sulfur corrosion simulation on the oil–paper insulation system under synergistic electric and thermal fields. IEEE Trans Dielectr Electr Insul 30(2):634–642
17. Rehman S, Alhems LM, Jadim R, Al Faraj BA, Al Mutairi KS, Al-Yemni AK (2017) Experimental investigation of temperature effect on corrosive sulfur formation in transformers. IEEE Trans Dielectr Electr Insul 24(5):3201–3206

18. Flora DS, Kumari MK, Rajan JS (2014) A new approach to study the effects of copper sulphide on electric stress distribution in paper oil insulation of transformers. In: Proceedings of the IEEE electrical insulation conference (EIC), pp 198–202
19. Yang L, Gao S, Deng B, Tang J, Huang J (2017) Effects of electric fields on copper sulfide deposition and the properties of insulating oils in oil-immersed transformers. IEEE Trans Dielectr Electr Insul 24(5):2847–2853
20. Gonzalez B, Gasca O, Juarez M, Bravo F (2015) Effect of electric field at 150 °C on the formation of corrosive sulfur in mineral transformer oil. IEEE Trans Dielectr Electr Insul 22(5):2449–2454

Level Set Method Assisted Topology Optimization of Permanent Magnet Synchronous Machine

Jiaqi Wu, Bin Tian, Ziyan Ren, Dianhai Zhang, and Yanli Zhang

Abstract Aiming at improving material utilization and performance quality of electrical equipment, this paper investigates the level set method (LSM) assisted topology optimization to obtain new electromagnetic structure. The performance of LSM is validated by the magnetic actuator. Finally, the LSM topology optimization combined with size optimization is applied to improve torque properties of an interior permanent magnet synchronous machine (IPMSM). The no-load back EMF, torque ripple, and average torque of optimal design are compared with the initial design, which shows better improvement.

Keywords Level set method · Magnetic actuator · Permanent magnet synchronous machine · Topology optimization

1 Introduction

Recent years, the optimal design of electrical equipment has attracted extensive attention [1, 2]. Size optimization and shape optimization of electrical equipment mainly depend on priori experience, and cannot generate new topologies. The topology optimization (TO) does not require the preset empirical topology structure, and can provide more novel ideas for optimal design [3, 4]. The TO assisted by advanced additive manufacturing technology will take structural design to a new level [5, 6].

J. Wu · Z. Ren (✉) · D. Zhang · Y. Zhang
School of Electrical Engineering, Shenyang University of Technology, Shenyang, China
e-mail: zyren@sut.edu.cn

D. Zhang
e-mail: zhangdh@sut.edu.cn

Y. Zhang
e-mail: ylzhang@sut.edu.cn

B. Tian
Jing-Jin Electric Technologies Co., Ltd, Beijing, China

The TO is usually applied to design of continuous structure in mechanical engineering [7]. Recently, it is pained more attention by the research scholars in electrical engineering. The ON/OFF method is applied to the TO design of synchronous motor for obtaining practical topological shapes [8]. The normalized Gaussian network method is used to the TO of an interior permanent magnet motor, which shows that this method can effectively suppress abnormal topology in the optimization process, and the optimized structure is easier to be manufactured [9]. Currently, the level set method (LSM) is also used for motor TO. In the LSM, the interface is regarded as a zero-level set of a plane in a high-dimensional space called the level set function, while expanding the movement speed of the interface to a high dimensional zero level set. Based on level sets, the LSM is combined with the virtual interface energy theory, and applied to design of magnetic actuator [10]. The application of level set method for TO is applied in distributed compliant mechanisms [11]. The modified TO by the LSM is applied to the core design of magnetic levitation system [12]. The obtained topology is similar to the existing solid isotropic material with penalization method and converges faster than traditional LSM.

The TO of electromagnetic device starts relatively late, which has more problems needed to be solved. Therefore, the level set method for electromagnetic problems is studied in this paper. The effect of grid distribution on searching performance of TO is investigated. Finally, the TO and size optimization are combined to improve the torque characteristics of an interior permanent magnet synchronous machine.

2   Level Set Topology Optimization Algorithm

In the LSM, the interface formed by the material boundary of the design domain is equivalent to a two-dimensional closed curve. That is the intersection of the curved surface and the identified horizontal layer as shown in Fig. 1.

The level set equation is written as (1a):

$$\partial \Phi / \partial t + V_n |\nabla \Phi| = 0 \tag{1a}$$

$$\partial (x, y) / \partial t = V_n \cdot n \tag{1b}$$

Fig. 1 Schematic diagram of moving boundary
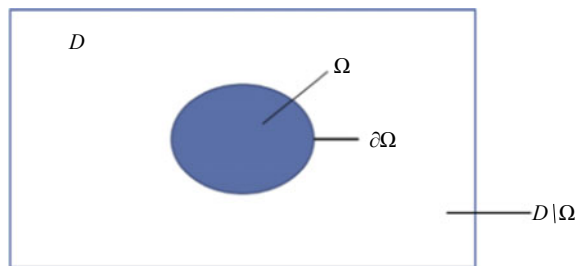
where Φ is the level set function and V_n is the normal velocity component. The curve Ω is set of all points satisfying $\Phi(x, y) = c$. The (1a) describes the variation process of level set function Φ with respect to time and normal velocity, which can be used to describe evolution process of material interface. The implementation of LSM includes initial value setting, distance initialization, velocity evolution, and expansion. The specific numerical implementation is explained as follows.

Step 1. Initial value setting and distance initialization.

The general form of initialization of level set function is:

$$\Phi(x, y, t = 0) \pm c(x, y, t = 0) \tag{2}$$

where $c(x, y, t)$ is a symbolic distance function representing the shortest distance from the coordinate point (x, y) to the level set curve at time t. The positive and negative signs in (2) indicate that when the coordinate point is inside the closed curve, it is taken as positive, and vice versa.

To ensure the accuracy of the results as much as possible, after each numerical solution of the level set equation is completed, it is necessary to correct the level set function $\Phi(x, y, t)$ as a symbolic distance function. For correction, the mature partial differential equations are applied,

$$\partial \Phi / \partial t + \text{sign}(\Phi_0)(\|\nabla \Phi\| - 1) = 0 \tag{3}$$

where Φ_0 is the level set function that needs to be corrected after each iteration calculation, and sign() is a symbolic function.

Step 2. Velocity evolution.

The evolved velocity V_n is calculated using the following formula:

$$\frac{\partial V_n}{\partial t} + \text{sign}(\Phi_0)\frac{\nabla \Phi}{\|\nabla \Phi\|} \cdot \nabla V_n = 0 \tag{4}$$

The material boundary is evolved through level set function. To ensure convergence of calculation results and meet termination condition, it is necessary to restrict the size of time step by the Courant Frideriche Lewy condition described as:

$$\Delta t \max\{V_x / \Delta x + V_y / \Delta y\} = c \tag{5}$$

where Δt is the time step of advancing the material boundary, V_x and V_y represent the velocities in the x and y axis directions, respectively, and c is a constant, $0 < c < 1$.

Step 3. Sensitivity analysis.

If there is a small variation of geometric shape of material region, the performance variation of electromagnetic device can be evaluated though sensitivity analysis. The

adjoint variable method is applied to calculate the discrete sensitivity. For magnetic problem, the objective performance to be optimized is function of design variable μ_e (material magnetic permeability) and magnetic vector potential $\mathbf{A}$. The sensitivity of objective function $F(\mu_e, \mathbf{A})$ with respect to design variables can be calculated as:

$$\frac{\mathrm{d}F}{\mathrm{d}\mu_e} = \frac{\partial F}{\partial \mu_e} + \lambda^T \left(\frac{\partial F}{\partial \mu_e} - \frac{\partial \mathbf{K}}{\partial \mu_e} \tilde{\mathbf{A}} \right) \tag{6a}$$

$$\mathbf{K}^T \lambda = \frac{\partial F}{\partial \mathbf{A}} \tag{6b}$$

$$[\mathbf{K}]\{\mathbf{A}\} = \{\mathbf{Q}\} \tag{6c}$$

where $\tilde{\mathbf{A}}$ is the solution of system Eq. (6c), $\mathbf{K}$ and $\mathbf{Q}$ are stiffness matrix and forcing vector respectively.

If the objective function of practical problem is to be maximized, the sensitivity of eth element in design space is negative ($\mathrm{d}F/\mathrm{d}\mu_e < 0$). $F(\mu_e, \mathbf{A})$ will decrease with increment of μ_e so that the material of corresponding element can be set air. For positive $\mathrm{d}F/\mathrm{d}\mu_e$, the objective performance will increase as μ_e is increased so that the element e can be set as a magnetic material.

Step 4. Topological sensitivity.

Topological sensitivity randomly generates a small hole in the design domain. If objective function is $F(\Omega)$, a small hole with radius a and centered at point x in design domain Ω. Ω_a represents the design domain after opening pore; Γ represents boundary; The topological derivative is expressed as:

$$D_T(x) = \lim_{a \to 0} \frac{F(\Omega_a) - F(\Omega)}{\mathrm{meas}(C_a)} \tag{7}$$

where $\mathrm{meas}(C_a)$ represents the measure of pore C. The above formula describes the variation of objective function when material property in a certain area is changed.

If there are holes in the original design domain, only the topology will be changed. A small hole C with a radius of already exists at a point x in the design domain Ω, a small perturbation is introduced, making the radius $a + \delta_a$, using Ω_a to represent the changed design domain changes the objective function of the design domain and generates new topological derivatives. The topological derivative is expressed as:

$$D_T(x) = \lim_{\substack{a \to 0 \\ \delta_a \to 0}} \frac{F(\Omega_{a+\delta_a}) - F(\Omega)}{\mathrm{meas}(C_{a+\delta_a}) - \mathrm{meas}(C_a)} \tag{8}$$

3 Topology Optimization of Magnetic Actuator

The magnetic actuator is composed of coil, iron yoke and armature. The optimization object is the magnetic yoke. The electromagnetic attractive force on the x-axis of the armature portion needs to be maximized. The design area of different structures is shown in Fig. 2. The current density of coil is 1 A/mm^2, and the relative magnetic permeability is set 2000.

The mathematical model for TO of magnetic actuator is described as follows:

$$\text{find} \quad \{x(t)|\Phi(x(t), t) = 0\}$$

$$\max \quad F_x = \sum_{e=1}^{m} f_x^e$$

$$f_x^e = 1/\mu_0 \cdot [(d_{nx}B_x + d_{ny}B_y)B_x - 0.5B^2 d_{nx}]$$

$$\text{s.t} \quad V = \int_\Omega H\{\Phi[x(t)]\}d\Omega / \int_\Omega d\Omega - V_{req} \le 0 \tag{9}$$

where x represents any position that changes over time in design domain, H is a step function, V_{req} is the preset volume ratio. The maximum number of iterations is set 200, and no convergence check is performed for the first five iterations. The preset volume ratio fluctuates is within a range of 0.05, and the results of the last five iterations tend to be stable, with a tolerance rate of within 2%.

For structure 1, the corresponding objective function for each topology is calculated. V_{req} is set to 0.7. The results are compared in Table 1.

(a) Structure 1   (b) Structure 2
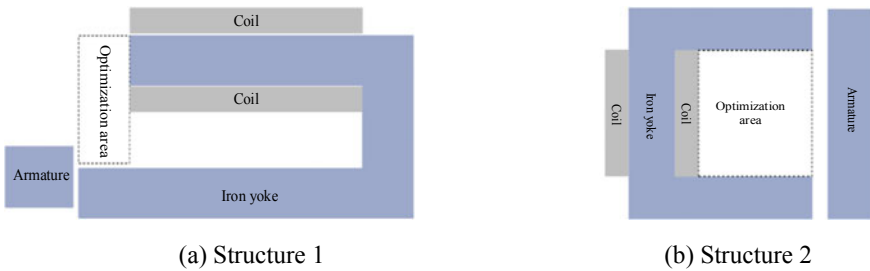
Fig. 2 Structure of magnetic actuator

Table 1 Comparison of objective functions in different cases of structure 1

No. element	F_x(N)	No. element	F_x(N)
Initial	0.66	6 × 5	12.26
3 × 2	3.32	7 × 6	12.69
4 × 3	2.50	8 × 7	12.20
5 × 4	6.85	Solid	12.60

Compared with initial situation, the optimized results have been improved to varying degrees. 6×5 compared to the solid case, under the premise that the electromagnetic attraction of the x-axis is close, the material used is saved by 35%, and the topological material is more aggregated, which is conducive to later production and manufacturing. The magnetic force line distribution diagram is shown in Fig. 3.

For structure 2, the results comparison is shown in Table 2 and Fig. 4. The optimized new topology can maximize the air gap magnetic density while suppressing the closing of magnetic lines in the yoke, thereby increasing the electromagnetic force on the armature. For 7×6 optimization units, the electromagnetic attraction of the armature increases when filling 60% of material in design space.

(a) 6×5 elements   (b) solid
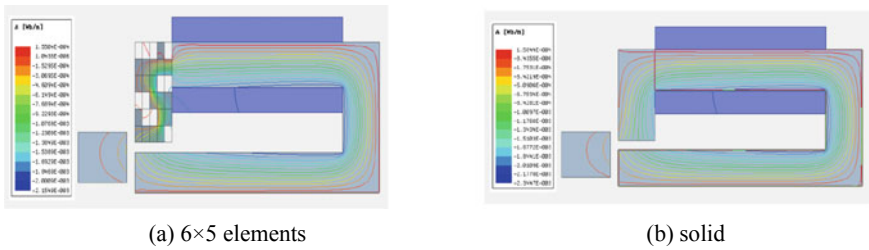
Fig. 3 Distribution of magnetic flux lines with different number of elements

Table 2 Comparison of objective functions in different cases of structure 2

No. element	$F_x(N)$	No. element	$F_x(N)$
Initial	1.6358	6×5	2.9342
3×2	2.0520	7×6	2.9746
4×3	2.5189	8×7	2.9709
5×4	2.7117	–	–

(a) Initial structure   (b) 8×7 elements
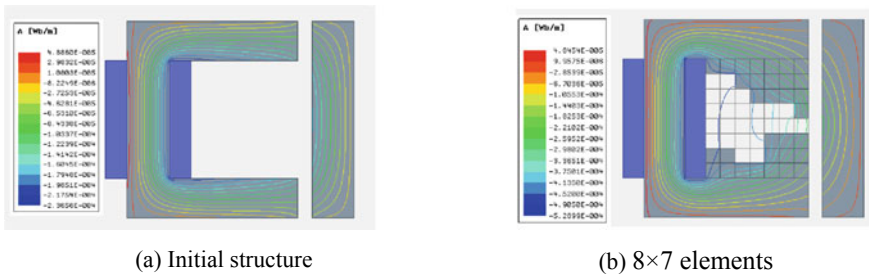
Fig. 4 Distribution of magnetic flux lines

4 TO of Permanent Magnet Synchronous Motor (PMSM)

The LSM assisted TO is applied to design of PMSM. Firstly, the size optimization is carried out for finding proper size of permanent magnet. Then the TO is applied to find optimal material distribution in the rotor region.

4.1 Size Optimization of Permanent Magnet for Reducing Torque Ripple

The motor excitation is set a current source excitation with a rated power of 35 kW. The permanent magnet material is N35, and the basic parameters of PMSM are shown in Table 3. The simulation model is shown in Fig. 5.

The length (L) and width (W) of permanent magnet with initial values of 36 mm and 4.5 mm are selected as design variables, with their design space of [35, 37] mm and [4.5, 5.5] mm, respectively. Based on initial 50 samples and their response data, a radial basis function response surface method is constructed. The particle swarm optimization algorithm with 50 particles and 300 iterations is used to search for global optimal solution. Finally, the optimal (L, W) of permanent magnet are (36.15 mm,

Table 3 Basic parameters of motor

Item	Value	Unit	Item	Value	Unit
No. poles	4	–	Rotor outer diameter	140	(mm)
No. stator slots	48	–	Rated current	180	(A)
Stator outer diameter	220	(mm)	Rated speed	3000	(rpm)
Stator inner diameter	141.6	(mm)			

Fig. 5 1/8 model of motor
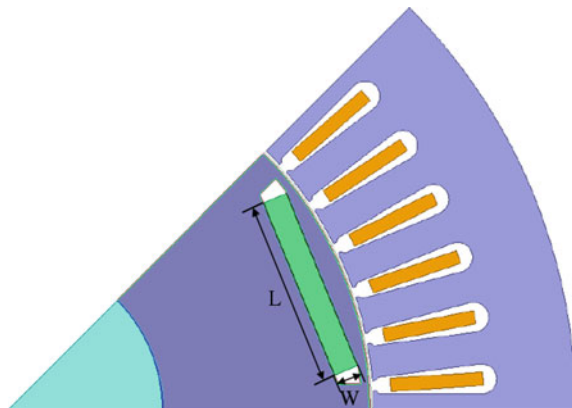
Fig. 6 Comparison of electromagnetic torque
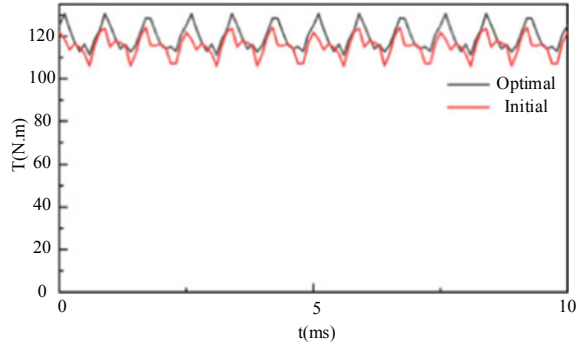
4.97 mm). As shown in Fig. 6, the average torque reaches 119.63 N m, which is improved compared to the initial design. The torque ripple is 0.0814.

4.2 Topology Optimization of Rotor Region

In TO, the design variables are magnetic permeability corresponding to location points in design region. The optimization area is divided into 6 (Case 2), 24 (Case 3), and 35 (Case 4) grids. The initial (Case 1) and optimized structures are shown in Fig. 7. The back electromotive force waveforms are compared in Fig. 8. The waveform after optimization basically has no change in amplitude with original design, and the wave peak value is weakened, with a better sine degree. The EMF with 6 elements grids is 162.45 V, with a small variation rate of original 162.07 V.

The electromagnetic torque results under different elements conditions of the motor are shown in Fig. 9. Compared to the initial scheme, the average torque of the TO scheme have been slightly decreased, but all meet the rated operating requirements. In case 3, the torque ripple decreased from original 0.081 to 0.067, a decrease of 17.9%. The torque ripple is effectively suppressed.

The EMF and its Fourier decomposition before and after optimization are shown in Fig. 10, the cogging torque is shown in Fig. 11. The amplitude of the cogging torque before and after optimization was 1.0601 N m and 0.7808 N m, respectively, a decrease of 26.3%, effectively optimizing the cogging torque. As can be seen, the sine degree of the optimized back electromotive force waveform is higher, and the fundamental wave amplitude increases by 2.3% from 145.95 V before optimization to 149.19 V after optimization.

(a) Initial design scheme

(b) 6 optimization grids

(c) 24 optimization grids

(d) 35 optimization grids
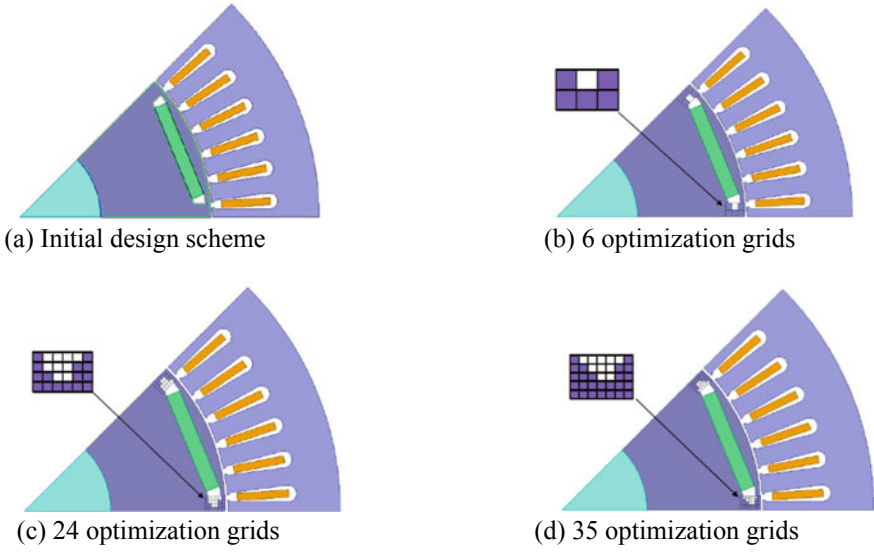
Fig. 7 Topological structure under different elements

Fig. 8 No-load back EMF waveform

Fig. 9 Electromagnetic torque

(a) Electromotive force waveform

(b) Harmonic distribution
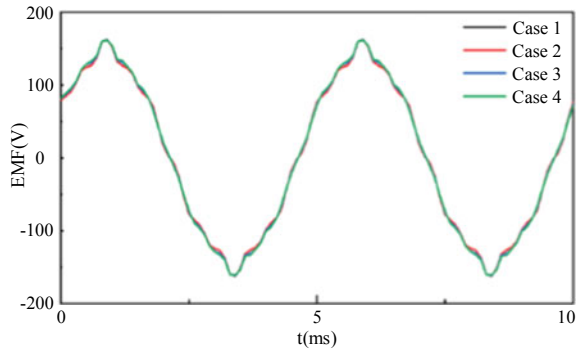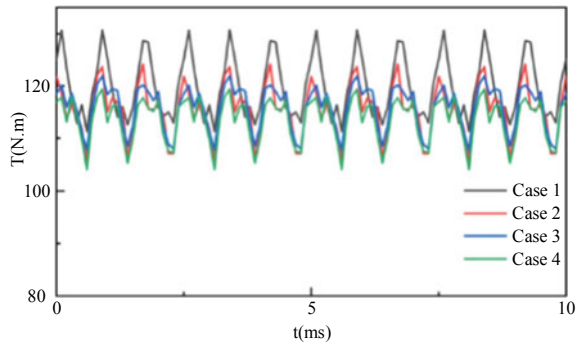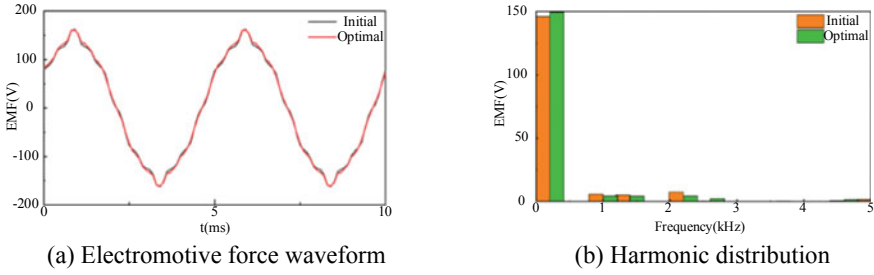
Fig. 10 Back electromotive force before and after optimization

Fig. 11 Cogging torque before and after optimization
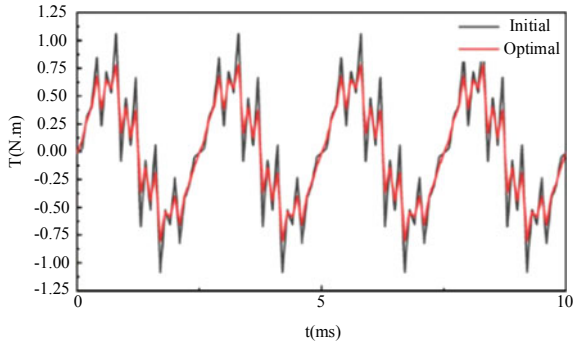
5 Conclusion

This paper studies a level set topology optimization method suitable for electromagnetic devices. The level set method topology optimization is applied to an interior permanent magnet synchronous machine for improving torque properties. During optimization process, the radial basis function assisted response surface model is constructed to predict performance analysis. Finally, comparing the main performance of motor before and after optimization, the sine degree of no-load back electromagnetic force after optimization is better, effectively suppressing higher harmonics, and weakening the cogging torque.

References

1. Zhang J, Ning L, Hao Y et al (2021) Int J Crashworthiness 26(6):651–660
2. Yamano M, Katayama K, Okamoto Y (2022) IEEE Trans Magn 58(9):1–4

3. Hidaka Y, Sasaki H (2021) J Adv Simul Sci Eng 8(1):98–113
4. Wang C, Li W, Sun P (2022) IEEE Trans Dielectr Electr Insul 29(4):1590–1598
5. Sixel W, Liu M, Nellis G et al (2020) IEEE Trans Ind Appl 56(3):2510–2519
6. Simpson N, North D, Collins S et al (2020) IEEE Trans Ind Appl 56(5):4718–4726
7. Meng Z, Guo L, Yıldız AR et al (2022) Eng Comput 38(6):5489–5505
8. Watanabe K, Suga T, Kitabatake S (2017) IEEE Trans Magn 54(3):1–4
9. Hu Y, Chen B, Xiao Y et al (2019) International conference on electrical machines and systems (ICEMS). pp 1–5
10. Lim A, Yamada T, Min S et al (2011) IEEE Trans Magn 47(5):1318–1321
11. Zhu BL (2014) South China University of Technology, Guangzhou (in Chinese)
12. Shim H, Ho V, Wang S et al (2009) IEEE Trans Magn 45(3):1582–1585

A New Method of Lithium Battery Insulation Fault Diagnosis Based on Double Kalman Filter

Liyuan Duan, Dazhi Wang, Guofeng Sun, Yongliang Ni, Keling Song, and Yanming Li

Abstract The high voltage rating of the battery pack requires that it has good insulation properties. Once an insulation fault occurs, it will not only cause a fire, but also poses a threat to equipment and personal safety, therefore, the study of insulation fault diagnosis methods for power storage systems is of great importance. This paper firstly proposes an equivalent model for battery pack insulation fault diagnosis based on the signal injection method; then uses a double Kalman filter algorithm to identify the model parameters to improve the identification accuracy, and at the same time makes an estimate of the end voltage and charge state; finally, the lithium battery pack is tested and verified using the hybrid power pulse characteristics experiment, and the results show that the maximum absolute error of the output voltage of the battery pack is 3.48 mV, and the maximum absolute value of the error in the prediction of the charge state is 0.0005 which improves the recognition accuracy and prediction accuracy of the parameters effectively.

Keywords Power battery pack · Insulation failure · Double extended Kalman filtering · SOC estimation

1 Introduction

Lithium batteries have the advantages of no memory effect and high energy density [1], applied in vehicle systems after series–parallel modification, the whole vehicle voltage is up to several hundred volts [2]. In the harsh vehicle operating environment,

L. Duan · D. Wang (✉)
Northeastern University, Shenyang 110819, China
e-mail: ProDZW@126.com

G. Sun
State Grid Shandong Electric Power Company, Yantai 264000, China

Y. Ni · K. Song · Y. Li
China North Vehicle Research Institute, Beijing 100072, China

the insulation state of the electric power battery pack is very easy to change, so that the operating state of the system and the life and safety of personnel are threatened, therefore, it is important to study the insulation condition of the power storage system [3]. In addition, the reliability of the model parameter identification results seriously affects the performance of the battery pack insulation fault, and a high-precision model parameter identification method is the primary prerequisite for battery pack insulation fault diagnosis and energy management system [4].

There are various commonly used insulation detection methods for battery packs at present. The bridge method measures the voltage across the external resistor to determine the resistance of the insulation resistance according to the law of voltage division, which is a simple topology, but requires high accuracy of the circuit, and it cannot be accurately detected when the insulation fault occurs on the positive and negative poles at the same time [5]. The current sensing method determines whether an insulation fault has occurred by detecting the leakage current, which requires the system to be in operation all the time and has certain limitations [6]. The high-voltage signal injection method can reduce the interference of electromagnetic signals to the detection circuit, but it can affect the life of the vehicle components [7], and frequent injection of high-voltage pulses will shorten the life of the battery pack. In order to improve the problems of the detection method, in this paper, voltage and current signals with low frequency are injected into the system, and the voltage value across the sampling resistor is measured to make a judgment on the insulation condition of the storage system.

Current research on battery models is divided into: electrochemical model [8], equivalent circuit model [9], thermal model [10], and supervised learning model [11]. The parameter identification results of the system have a great influence on the accuracy of SOC identification and fault diagnosis. Chen et al. used a variable forgetting factor least squares algorithm to determine the insulation status of power cells [12], and Sun Xin et al. used an improved genetic algorithm to identify the parameters of the fractional order model [13]. The battery system is highly nonlinear and the model parameters are in constant change, neural networks enable accurate insulation fault diagnosis without taking into account the internal influences of the battery system [14]. Sun et al. narrow down the number of recoverable lithium ions by estimating battery capacity through back-propagation neural networks [15], but neural networks are more demanding on data and less efficient in diagnosis.

In this paper, firstly, based on the signal injection method, an insulation fault diagnosis model is established, and considering that the circuit model parameters are always in the process of dynamic change, a double Kalman filtering algorithm is used to identify the model parameters, while the terminal voltage as the output quantity is predicted and the state of charge of the battery pack is estimated, and finally the lithium battery pack is tested by the hybrid power pulse characteristic experiment.

2 Establishment of Battery Pack Insulation Fault Detection Model

The battery model is used to understand its internal behavior and give the battery properties in the form of equations, this section focuses on the insulation fault diagnosis model based on the low-frequency low-voltage signal injection method. To improve the efficiency and accuracy of diagnosis, the Thevenin second-order equivalent circuit model is used, and its topology is shown in Fig. 1.

According to the schematic diagram of the circuit model, it is obtained that:

$$\begin{cases} \dot{U}_1 = -\dfrac{U_1}{R_{p1}C_{p1}} + \dfrac{I_L}{C_{p1}} \\ \dot{U}_2 = -\dfrac{U_2}{R_{p2}C_{p1}} + \dfrac{I_L}{C_{p1}} \end{cases} \tag{1}$$

$$U_L = U_{OCV} - U_1 - U_2 - I_L R_0 \tag{2}$$

where $U_{pi}(i = 1, 2)$ represents the polarization voltage, U_{OCV} represents open circuit voltage, R_0 represents ohmic internal resistance, R_{p1} and R_{p2} represents the polarization resistance, C_{p1} and C_{p2} represents the polarization capacitance, and represents the terminal voltage.

Plett pointed out that the open circuit voltage varies with the state of charge (SOC) of the battery [16], and the fitting function is represented by the following formula:

$$\begin{aligned} U_{ocv}(x) &= a_1 x^8 + a_2 x^7 + a_3 x^6 + a_4 x^5 + a_5 x^3 \\ &+ a_6 x^3 + a_7 x^2 + a_8 x^1 + a_9 \end{aligned} \tag{3}$$

The equivalent circuit for detecting insulation faults in battery packs is shown in Fig. 2, the first part is a battery pack model composed of battery cells, and the second part represents the insulation fault diagnosis model. Where R_1 and R_2 are the current limiting resistors of the testing equipment respectively, R_f is the sampling resistor,
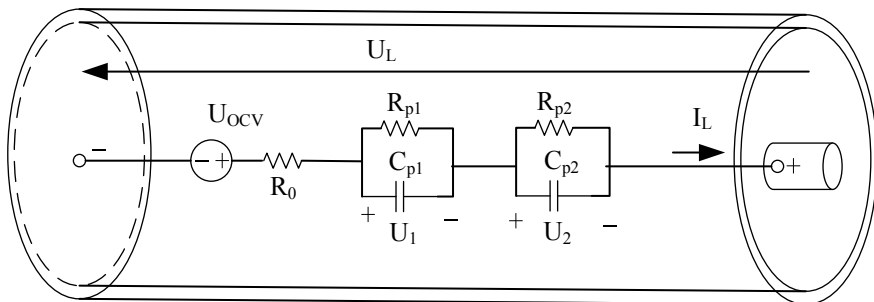
Fig. 1 Equivalent Thevenin cell model

the insulation resistance is checked in real time by detecting the voltage V_f across the sampling resistor. The equivalent model for an insulation fault occurring in the negative terminal is shown in Fig. 3. The battery pack voltage V_B is:

$$V_B = U_{ocv} - R_0 I_L - U_{p1} - U_{p2} \tag{4}$$

where V_B denotes the equivalent battery pack voltage, U_{ocv} denotes the equivalent battery pack open circuit voltage, R_0 denotes the equivalent battery pack internal resistance, U_{p1} and U_{p2} is the equivalent battery pack polarization voltage, respectively.

According to Kirchhoff's theorem, the circuit equation of Fig. 3 can be obtained as:

$$\begin{cases} V_B - I_1 R_1 - (I_1 - I_2) R_2 = 0 \\ V_s + I_2 R_N + (I_2 - I_1) R_2 + I_2 R_f = 0 \end{cases} \tag{5}$$

The positive and negative insulation resistance can be written respectively as:
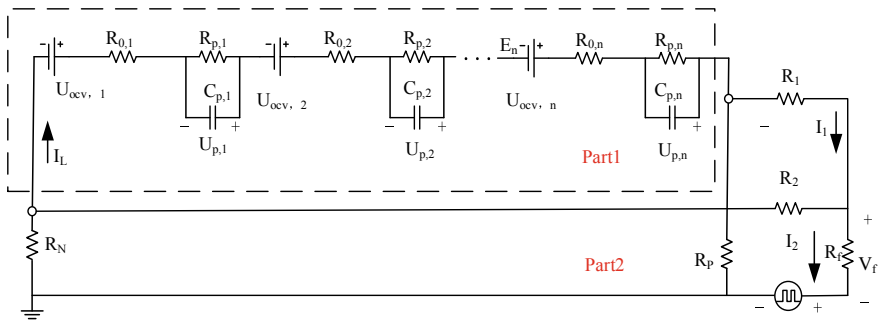
Fig. 2 Equivalent circuit for battery pack insulation detection

Fig. 3 Simplified model of negative insulation fault
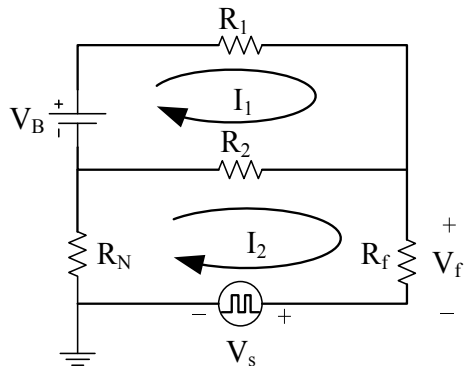
$$R_N = \frac{1}{2}\frac{R_f}{V_f}(U_{OCV} - R_0 I - U_{p1} - U_{p2}) - (1 + \frac{V_S}{V_f})R_f - \frac{R}{2} \tag{6}$$

$$R_p = -\frac{1}{2}\frac{R_f}{V_f}(U_{OCV} - R_0 I - U_{p1} - U_{p2}) - (1 + \frac{V_S}{V_f})R_f - \frac{R}{2} \tag{7}$$

3 Parameter Identification Based on Double Extended Kalman Filter Algorithm

Combining Eqs. (1) and (2), the cell model can be rewritten using the Laplace transformation as:

$$U_{OCV}(s) - U_L(s) = I_L(s)\left(R_0 + \frac{R_{p1}}{1 + R_{p1}C_{p1}s} + \frac{R_{p2}}{1 + R_{p2}C_{p2}s}\right) \tag{8}$$

Defined $E_L = U_{OCV} - U_L$, then the transfer function is:

$$
\begin{aligned}
G(s) &= \frac{E_L(s)}{I_L(s)} = \left(R_0 + \frac{R_{p1}}{1 + R_{p1}C_{p1}s} + \frac{R_{p2}}{1 + R_{p2}C_{p2}s}\right) \\
&= \frac{R_0 s^2 + \frac{1}{\tau_1\tau_2}\left(R_0\tau_1 + R_0\tau_2 + R_{p1}\tau_2 + R_2\tau_1\right)s + \frac{R_0 + R_{p1} + R_{p2}}{\tau_1\tau_2}}{s^2 + \frac{(\tau_1+\tau_2)}{\tau_1\tau_2}s + \frac{1}{\tau_1\tau_2}}
\end{aligned} \tag{9}
$$

For discretization using bilinear transformation, can be written as Eq. (10):

$$G(z^{-1}) = \frac{R_0\frac{4(1-z^{-1})^2}{T^2(1+z^{-1})^2} + \frac{1}{\tau_1\tau_2}\left(R_0\tau_1 + R_0\tau_2 + R_{p1}\tau_2 + R_{p2}\tau_1\right)\frac{2(1-z^{-1})}{T(1+z^{-1})} + \frac{R_0+R_1+R_2}{\tau_1\tau_2}}{\frac{4(1-z^{-1})^2}{T^2(1+z^{-1})^2} + \frac{(\tau_1+\tau_2)}{\tau_1\tau_2}\frac{2(1-z^{-1})}{T(1+z^{-1})} + \frac{1}{\tau_1\tau_2}}$$

$$\tag{10}$$

To simplify writing, define:

$$\begin{cases} a = R_0 \\ b = \tau_1\tau_2 \\ c = \tau_1 + \tau_2 \\ d = R_0 + R_{p1} + R_{p2} \\ e = R_0\tau_1 + R_0\tau_2 + R_{p1}\tau_2 + R_{p2}\tau_1 \end{cases} \tag{11}$$

Then

$$G(z^{-1}) = \frac{\left[\frac{4ab+2eT+dT^2}{4b+2cT+T^2}\right] + \left[\frac{-8ab+2dT^2}{4b+2cT+T^2}\right]z^{-1} + \left[\frac{4ab-2eT+dT^2}{4b+2cT+T^2}\right]z^{-2}}{1 + \left[\frac{2T^2-8b}{4b+2cT+T^2}\right]z^{-1} + \left[\frac{4b+2cT-T^2}{4b+2cT+T^2}\right]z^{-2}} \tag{12}$$

$$G(z^{-1}) = \frac{k_3 + k_4 z^{-1} + k_5 z^{-2}}{1 - k_1 z^{-1} - k_2 z^{-2}} \tag{13}$$

Reverse inference can obtain:

$$G(s) = \frac{k_3 + k_4 \frac{2-Ts}{2+Ts} + k_5 \frac{4-4Ts+T^2s^2}{4+4Ts+T^2s^2}}{1 + k_1 \frac{2-Ts}{2+Ts} + k_2 \frac{4-4Ts+T^2s^2}{4+4Ts+T^2s^2}} \tag{14}$$

$k_1 \sim k_5$ are identified through recursive formulas, and model parameters can be obtained through $k_1 \sim k_5$:

$$\begin{cases} R_0 = \dfrac{k_3 - k_4 + k_5}{4 - k_1 + k_2} \\[2mm] R_{p1}C_{p1}R_{p2}C_{p2} = \dfrac{4T^2 - k_1 T^2 + k_2 T^2}{4k_1 + 4k_2} \\[2mm] R_{p1}C_{p1} + R_{p2}C_{p2} = \dfrac{T - k_2 T + k}{k_1 + k_2} \\[2mm] R_0 + R_{p1} + R_{p2} = \dfrac{k_3 + k_4 + k_5}{k_1 + k_2} \\[2mm] R_0 R_{p1}C_{p1} + R_0 R_{p2}C_{p2} + R_{p1}R_{p2}C_{p2} + R_2 R_{p1}C_{p1} = \dfrac{k_3 T - k_5 T}{k_1 + k_2} \end{cases} \tag{15}$$

The accuracy of system model parameter identification will have an impact on the effectiveness of system condition estimation, fault diagnosis, health assessment and health management. The commonly used identification algorithm is the recursive least squares method, but as the recursion progresses, there may be data saturation and poor adaptability to operating conditions. In order to meet the constantly changing characteristics of internal parameters of batteries, it is necessary to find a method with strong real-time performance and high accuracy. The DEKF algorithm can realize the joint estimation of system state and parameters, and constantly carry out "prediction-correction", which is well applied in nonlinear systems. The structure diagram is shown in the Fig. 4.

The state space equation and observation equation corresponding to the state of the battery model are:

$$\begin{cases} x_k = e^{-\frac{\Delta t}{R_p C_p}} x_{k-1} + (1 - e^{-\frac{\Delta t}{R_{p1}C_{p1}}})R_{p1}i_{L,k} + (1 - e^{-\frac{\Delta t}{R_{p2}C_{p2}}})R_{p2}i_{L,k} + \omega_{k-1} \\ y_k = U_{OCV,k} - R_0 i_{L,k} - U_{1,k} - U_{2,k} + v_k \end{cases} \tag{16}$$
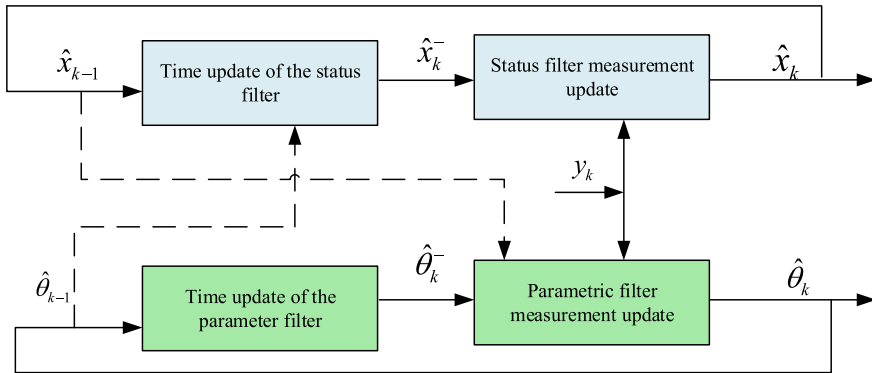
Fig. 4 DEKF algorithm structure diagram

Among them, x_k and y_k are the state and observation values of the model state, u_k is the input vector, ω_k and v_k are the process noise and measurement noise of the state, respectively, and their covariance matrices Q^x are and R^x.

In this paper, we choose U_1, U_2, Z_k the polarization voltage as the state vector, $x_k = [U_1, U_2, Z_k]^T$, the terminal voltage U_L as the observation vector $y_k = [U_L]^T$, and the input vector is $u_k = i_{L,k}$. Rewrite (16) as follows:

$$
\begin{cases}
\begin{bmatrix} \hat{U}_{1,k+1} \\ \hat{U}_{2,k+1} \\ \hat{z}_{k+1} \end{bmatrix} = \begin{bmatrix} e^{\frac{-\Delta t}{R_{p1}C_{p1}}} & 0 & 0 \\ 0 & e^{\frac{-\Delta t}{R_{p2}C_{p2}}} & 0 \\ 0 & 0 & 1 \end{bmatrix} \begin{bmatrix} \hat{U}_{1,k} \\ \hat{U}_{2,k} \\ \hat{z}_k \end{bmatrix} + \begin{bmatrix} \left(1 - e^{\frac{-\Delta t}{R_{p1}C_{p1}}}\right) R_{p1} \\ \left(1 - e^{\frac{-\Delta t}{R_{p2}C_{p2}}}\right) R_{p2} \\ -\dfrac{\eta \Delta t}{c_N} \end{bmatrix} i_k \\[3em]
\hat{U}_{L,k} = \begin{bmatrix} -1 & -1 & \partial U_{OCV,k}/\partial z_k \end{bmatrix} \begin{bmatrix} \hat{U}_{1,k} \\ \hat{U}_{2,k} \\ \hat{z}_k \end{bmatrix} - R_0 i_k
\end{cases}
\tag{17}
$$

Select the ohmic resistance, polarization resistance, and capacitance in the circuit model as the parameters to be identified. Since OCV is in the process of changing with SOC all the time, it is also necessary to identify OCV, $\theta = \left[R_0, R_{p1}, R_{p2}, C_{p1}, C_{p2}, U_{OCV}\right]^T$, The discrete state space equation of the parameter is:

$$
\begin{cases}
\theta_k = \theta_{k-1} + r_{k-1} \\
y_k = g(x_k, u_k, \theta_k) + e_k \\
g(x_k, u_k, \theta_k) = C_k^\theta \theta_k - U_{1,k} - U_{2,k} \\
C_k^\theta = [-i_{L,k}00001]
\end{cases}
\tag{18}
$$

where θ_k is the parameter value to be identified, $g(x_k, u_k, \theta_k)$ is the observation value of the parameter filter, r_k and e_k are respectively the stochastic process noise and measurement noise of the parameters, and their covariance matrices are Q^θ and R^θ respectively.

The Dual Extended Kalman filter consists of two parallel operated filters. At each sampling time, the parameters identified by the current AEKF-S are used in AEFK-P to estimate the corresponding state; At the same time, the state obtained by AEFK-P is used to estimate parameters in AEKF-S, and the two work together to jointly estimate the model parameters of the system. The equation for estimating battery status and parameters using the DEKF algorithm is shown in Table 1.

Online parameter identification of the circuit model can be realized according to the equations in Table 1, which lays the foundation for the prediction of the terminal voltage and charge state of the battery pack.

Table 1 Dual extended Kalman filter algorithm

Step 1: Initialization	When k = 0, set the initial value $\hat{x}_0 = E(x_0), P_0^x = E[(x_0 - \hat{x}_0)(x_0 - \hat{x}_0)^T]; \hat{\theta}_0 = E(\theta_0), P_0^\theta = E[(\theta_0 - \hat{\theta}_0)(\theta_0 - \hat{\theta}_0)^T]$ (19)
Step 2: Prior estimation	(1) Prior estimation of parameters: $\hat{x}_{k\|k-1} = A_{k\|k-1}\hat{x}_{k-1\|k-1} + B_{k\|k-1}i_{L,k}, P_{k\|k-1}^x = A_{k\|k-1}P_{k-1\|k-1}^x A_{k\|k-1}^T + Q_{k-1}^x$ (20) (2) Prior estimation of state: $\hat{x}_{k\|k-1} = A_{k\|k-1}\hat{x}_{k-1\|k-1} + B_{k\|k-1}i_{L,k}, P_{k\|k-1}^x = A_{k\|k-1}P_{k-1\|k-1}^x A_{k\|k-1}^T + Q_{k-1}^x$ (21)
Step 3: Calculate the Kalman gain	(1) Gain Matrix of State Filter: $K_k^x = P_{k\|k-1}^x (H_k^x)^T [H_k^x P_{k\|k-1}^x (H_k^x)^T + R_k^x]^{-1}$ (22) (2) Gain matrix of parametric filters: $K_k^\theta = P_{k\|k-1}^\theta (H_k^\theta)^T [H_k^\theta P_{k\|k-1}^\theta (H_k^\theta)^T + R_k^\theta]^{-1}$ (23)
Step 4: Measurement update	(1) Parameter measurement update: $\hat{\theta}_{k\|k} = \hat{\theta}_{k\|k-1} + K_k^\theta [y_k - (C_k^\theta \hat{\theta}_{k\|k-1} - \hat{U}_{p,k\|k-1})]$, $P_{k\|k}^\theta = (I - K_k^\theta H_k^\theta)P_{k\|k-1}^\theta$ (24) (2) Status measurement update: $\hat{x}_{k\|k} = \hat{x}_{k\|k-1} + K_k^x [y_k - (\hat{U}_{OCV,k\|k-1} - \hat{R}_{0,k}i_{L,k} - H_k^x \hat{x}_{k\|k})]$, $P_{k\|k}^x = (I - K_k^x H_k^x)P_{k\|k-1}^x$ (25)

4 Experimental Verification

In this paper, a battery test platform is established to verify the feasibility of the proposed method, and the experimental platform is shown in Fig. 5. The experimental device is mainly composed of the following parts: (1) an insulation detector that provides a detection channel for insulation resistance; (2) a power module that provides power for the low-voltage equipment of the insulation detector; (3) a bus that transmits experimental data; (4) a personal laptop that records and processes experimental data.

This paper selects the lithium iron phosphate battery produced by Zhicheng Champion for experimental verification. The specific parameters of each single battery are shown in the Table 2.

Before identifying model parameters, the polynomial coefficients of the OCV-SOC curve should be determined first. In this paper, the battery was tested for Hybrid Pulse Power Characterization (HPPC) under constant temperature conditions of 25 °C. The battery continued to discharge for 70,509 s, and the discharge current and terminal voltage were sampled every 1 s. The current curve of the HPPC experiment is shown in Fig. 6.

The OCV-SOC curve obtained under the condition of discharging the battery at a rate of 0.5C is shown in Fig. 7.

The fitting parameters of Eq. (3) are shown in Table 3.

Fig. 5 Experimental platform
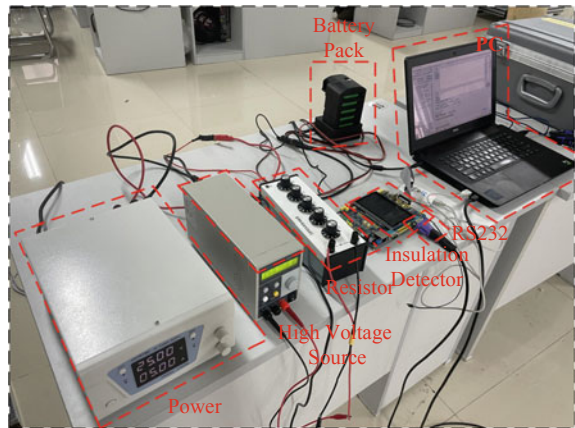
Table 2 Parameters of lithium iron phosphate battery

Rated voltage	3.2 V	Standard charging maximum voltage	3.65 V
Rated capacity	25 Ah	Standard discharge cutoff voltage	2.5 V
Maximum charging current	50 A	Charging operating temperature	0–45 °C
Maximum discharge current	75 A	Discharge working temperature	−20–60 °C

Fig. 6 HPPC experimental
current curve
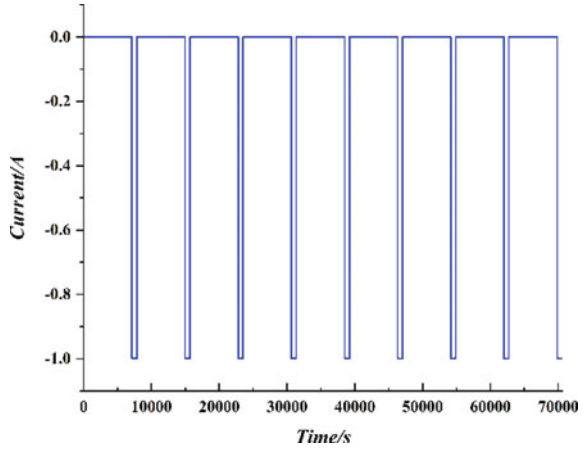
Fig. 7 OCV-SOC curve
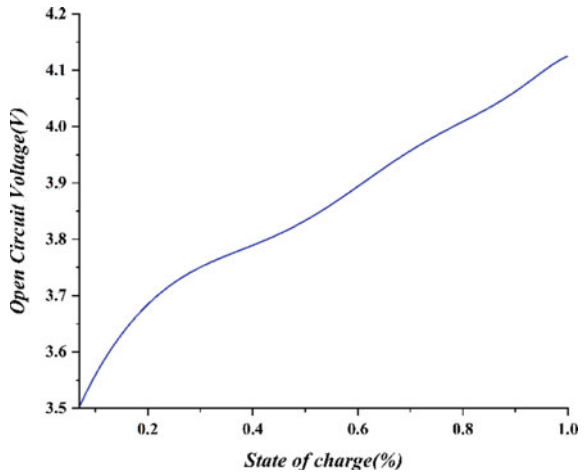
Table 3 OCV-SOC fitting coefficient

a_1	a_2	a_3	a_4	a_5	a_6	a_7	a_8	a_9
-102.2	398.9	-624.967	505.888	-232.037	67.497	-15.733	3.509	3.317

Before the model parameters of the equivalent circuit are identified, the algorithm needs to be initialized, respectively, as follows: the measurement noise covariance matrix R^x is set to 0.75×0.75, Q^x is set to a 5th order square matrix with diagonal elements of 0.05, $R_0 = 0.04\Omega$, $R_{p1} = R_{p1} = 0.4\Omega$, $C_{p1} = 400F$, $C_{p2} = 5F$.

The model parameters identified using the Double Extended Kalman filter algorithm are shown in Fig. 8.

The above identification results lead to the following:
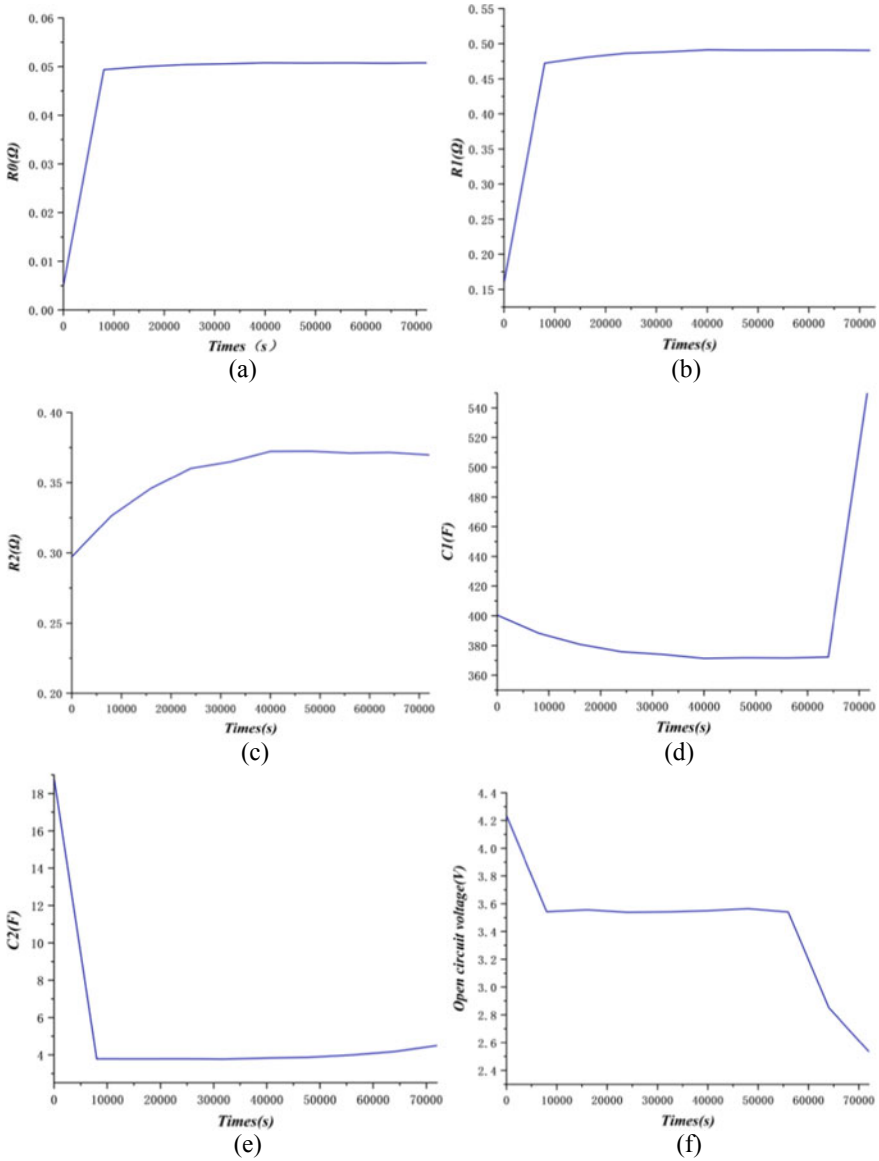
Fig. 8 Model parameters and open circuit voltage identification results: **a** Identification results of Ohmic internal resistance R0, **b** identification result of polarized internal resistance Rp1, **c** polarization internal resistance Rp2 identification results, **d** polarization capacitor Cp1 identification results, **e** polarization capacitor Cp2 identification results, **f** open circuit voltage identification results

(1) The ohmic internal resistance R_0 and the polarized internal resistance R_{p1} and R_{p2} have a similar trend of change, the identification results have a large error in the early stage of discharge, and gradually stabilize after 10,000 s.

(2) The polarization capacitance C_{p1} varies greatly at the beginning and end of discharge, and stabilizes between 15,000 and 65,000 s. The polarization capacitance C_{p2} has a large error at the beginning of discharge, and the identification result gradually stabilizes after 10,000 s as the experiment proceeds.

(3) At the beginning of the experiment, there is a large error in the identification of the open-circuit voltage, which gradually stabilizes after 8000 s as the experiment proceeds and then gradually decreases.

In practical applications, measurement noise and measurement errors in power storage systems are difficult to avoid, and the accuracy of battery pack state estimation will be affected. Taking into account the nonlinearity and estimation accuracy of the system, a Dual Extended Kalman filtering algorithm was proposed. Based on the model parameters R_0, R_{p1}, R_{p2}, C_{p1} and C_{p2} identification, the model terminal voltage and the SOC are iteratively calculated as the output quantities. Figure 9a shows the predicted values of the model terminal voltage, and Fig. 9b shows the prediction error. Figure 10a shows the predicted results of the charge state, and Fig. 10b shows its error curve. The maximum absolute error of the battery terminal voltage is 3.48 mV and the maximum absolute error of the SOC is 0.0005, so the proposed model and parameter identification algorithm can obtain accurate prediction results.
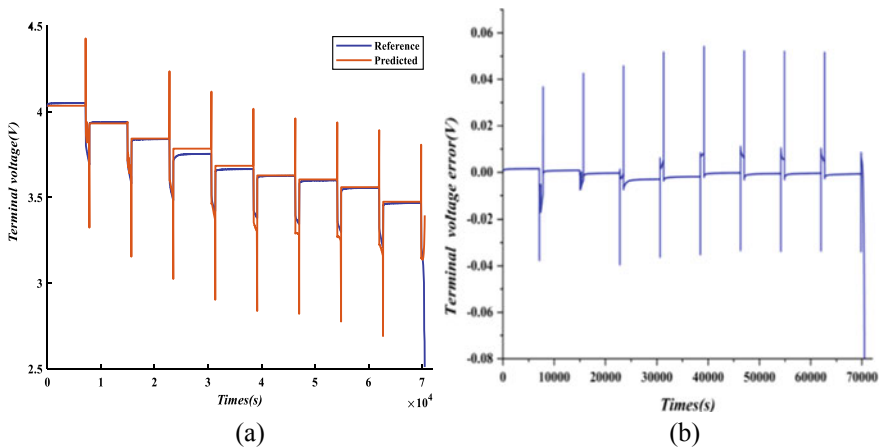
Fig. 9 Terminal voltage prediction curve: **a** Terminal voltage reference value and predicted value, **b** terminal voltage prediction error
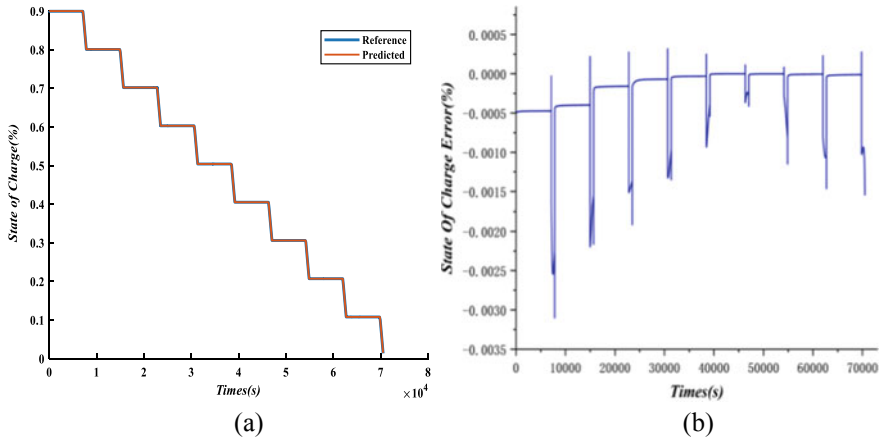
Fig. 10 SOC prediction: **a** Reference and predicted values of SOC, **b** prediction error

5 Conclusion

In this paper, a high-performance lithium battery pack insulation fault detection method is investigated. Taking into account the nonlinearity of the battery pack and the detection accuracy, an equivalent model for battery pack insulation detection is established, and the double Kalman filter algorithm is used to identify the model parameters, which solves the problem that the convergence ability of the commonly used recursive least squares method with variable forgetting factor is affected by the prediction error. The correctness and rationality of the method in this paper are verified through experimental analysis of the battery pack terminal voltage and SOC.

References

1. Lin H, Kang L, Xie D et al (2022) Online state-of-health estimation of lithium-ion battery based on incremental capacity curve and BP neural network. Batteries 8(4):29
2. Xiong R, Sun W, Yu Q et al (2020) Research progress, challenges and prospects of fault diagnosis on battery system of electric vehicles. Appl Energy 279:115855
3. Wang Y, Tian J, Chen Z et al (2019) Model based insulation fault diagnosis for lithium-ion battery pack in electric vehicles. Measurement 131:443–451
4. Ren X, Guo W (2019) RC equivalent circuit model of lumped parameters for lithium-ion batteries in electric vehicles. Energy Storage Sci Technol 8(5):930–934
5. Tian JQ, Li XY, Wang Y et al (2017) Hardware design and research of electric vehicle insulation monitoring instrument based on low frequency signal injection method. In: Proceedings of the

18th China annual conference on system simulation technology and its applications (18th CCSSTA 2017) (in Chinese)

6. Han XX (2022) Application of electrical insulation testing and monitoring methods for new energy vehicles. Autom New Power 5(5):99–101 (in Chinese). https://doi.org/10.16776/j.cnki.1000-3797.2022.05.012

7. Zhi QW (2020) Research on on-line monitoring method of insulation state of electric vehicle high voltage system. In: 2020 IEEE International conference on high voltage engineering and application (ICHVE). IEEE, pp 1–4

8. Gu R, Malysz P, Yang H et al (2016) On the suitability of electrochemical-based modeling for lithium-ion batteries. IEEE Trans Transp Electrification 2(4):417–431

9. Lai X, Zheng Y, Sun T (2018) A comparative study of different equivalent circuit models for estimating state-of-charge of lithium-ion batteries. Electro Chimica Acta 259:566–577

10. Liu P, Zhu J, Chu A, Zhou X (2015) A thermal model based thermal fault diagnosis system for power batteries. J Shanghai Jiao Tong Univ 49(04):487–493 (in Chinese). https://doi.org/10.16183/j.cnki.jsjtu.2015.04.013

11. Lipu MSH, Hannan MA, Hussain A et al (2018) State of charge estimation for lithium-ion battery using recurrent NARX neural network model based lighting search algorithm. IEEE access 6:28150–28161

12. Kumar S, Jangir P, Tejani GG et al (2021) MOPGO: a new physics-based multi-objective plasma generation optimizer for solving structural optimization problems. IEEE Access 9:84982–85016

13. Sun X, Yang H, Gu Q, Li C, Lv Y, Tang J (2022) Phased adaptive state of charge estimation for lithium-ion batteries based on fractional order models. J Wuhan Univ (Eng Ed) 55(02):183–192 (in Chinese). https://doi.org/10.14188/j.1671-8844.2002-02-010

14. Cui Z, Wang L, Li Q et al (2022) A comprehensive review on the state of charge estimation for lithium-ion battery based on neural network. Int J Energy Res 46(5):5423–5440

15. Sun X, Chen Q, Zheng L et al (2022) Joint estimation of state-of-health and state-of-charge for lithium-ion battery based on electrochemical model optimized by neural network. IEEE J Emerg Sel Top Ind Electron 4(1):168–177

16. Plett GL (2004) Extended Kalman filtering for battery management systems of LiPB-based HEV battery packs: Part 3. State and parameter estimation. J Power Sources 134(2):277–292

Study on the Temperature Rise Performance of Propellant-Assisted Interrupter Propellant Chamber

Zhou Yutao, Zhang Xietian, Wang Hongda, Jiao Zhipeng, Zhao Jiubing, and Mu Xiangjing

Abstract As a kind of passive monitoring DC short circuit protection device, propellant-assisted interrupting and arc triggered hybrid current limiting fuse is widely used in the integrated power system of ships. The closed environment temperature of warship is higher, and the temperature rise generated by rated current of device makes the propellant in high temperature environment. High temperature will accelerate the reaction of the propellant itself, weaken the power after excitation, and affect the interrupting performance of the interrupter. In this paper, the thermoelectric coupling model of the device is established to reduce the temperature rise of the propellant, and the temperature rise distribution of the propellant-assisted interrupter is analyzed. Based on the thermal resistance model, the optimal structure design of the interrupter is proposed, and the relevant temperature rise test is carried out. The test and simulation results verify that the optimized structure can reduce the temperature rise of the propellant.

Keywords Propellant-assisted interruption · Thermoelectric coupling · Temperature rise · Thermal resistance

1 Introduction

With the rapid development of current ship integrated power system [1, 2], the system capacity is further increased, and the short-circuit current level also rises sharply. The initial rise rate of short-circuit current can be as high as 50 A/μs, and the expected

---

Z. Yutao · W. Hongda (✉) · J. Zhipeng · Z. Jiubing · M. Xiangjing
Department of Supply Management, Naval Logistics Academy, Tianjin 300450, China
e-mail: 502863086@qq.com

Z. Xietian
First Military Representative Office of the Naval Equipment Department in Shanghai, Shanghai 201913, China

W. Hongda
Key Laboratory of Smart Grid Ministry of Education, Tianjin University, Tianjin 300072, China

peak value can reach 100 kA, which poses a great challenge to traditional protection devices. The hybrid current limiting fuse [3, 4] is a new type of protection equipment that integrates strong current carrying capacity, fast breaking speed, and good current limiting effect. Its basic components are current monitors, high-speed interrupters, and arc extinguishing fuses, which are currently widely used in ship power systems.

In view of the complex and changeable electromagnetic environment of ships, the commonly used electronic measurement and control current monitor has the risk of rejection and misoperation due to the dependence on external power supply, many components, complex structure and logic circuit. In this study, an arc triggered current monitor (hereinafter referred to as "arc trigger") which does not require external power supply and is not interfered by the complex electromagnetic environment of the ship is adopted [5, 6]. When the fault signal comes, the arc trigger fuses the arc, and the output arc voltage directly ignites the explosive in the high-speed interrupter to complete the function of current monitoring. The performance of the arc trigger is stable and the reliability is high, but the temperature rise is high at the rated current because the resistance of the arc trigger is directly seriated into the line.

High speed interrupters include explosive interrupters [4], electromagnetic repulsive interrupters [5], and propellant interrupters [7–9]. The explosive disconnector has problems such as large volume, large mass, complex explosive unit structure, and high price; The electromagnetic repulsive force disconnector requires an external discharge capacitor, which has a complex structure and also has issues such as electromagnetic interference. The propellant-assisted interruption selected in this study is a fast driving mechanism that utilizes propellant combustion to generate high-temperature and high-pressure gas. It has the advantages of simple structure, compact size, light weight, low noise, good economy, and fast breaking speed. However, due to the weak design of the breaking unit, the resistance is high and the temperature rise during rated flow is high.

As a chemical agent, propellant-assisted interruption is highly sensitive to the environment, and the typical naval environment presents the characteristics of high temperature, high humidity and high salt. Due to its excellent sealing performance, propellant has a good tolerance to high humidity and high salt environment, and temperature has become the most important factor affecting the performance of propellant. The higher ambient temperature combined with the rated temperature rise of the device will cause the self-reaction of the powder to attenuate the power after excitation, affect the work performance of the powder and thus affect the breaking performance of the interrupter. The main heating source of the hybrid fuse is arc trigger and interrupter. According to the specific breaking performance requirements, the melt structure of the trigger determines the detonation time, and the bridge structure of the interrupter determines the just-minute time, the arc pressure of the break and the withstand voltage of the break. Under the constraint of specific breaking performance index, the structure of arc trigger and interrupter is relatively fixed, and it is very difficult to reduce the resistance of the two places, so the temperature at the powder can only be reduced by increasing the temperature difference between the heating source and the powder, and lower the temperature of the powder.

   This article establishes a thermoelectric coupling model of the device, analyzes the influence of different structural designs on the temperature rise of the interrupter chamber, and conducts relevant temperature rise tests.

2   Composition of Propellant-Assisted Interrupting and Arc Triggered Hybrid Current Limiting Fuse

The propellant-assisted interrupting and arc triggered hybrid current limiting fuse mainly consists of three parts: an arc trigger, a propellant-assisted interrupter, and an arc extinguishing fuse. The arc trigger is similar to a single break low-voltage fuse, which uses the principle of electric heating to generate arc voltage and directly ignite the propellant. Its main function is to detect short circuit current and ignite the propellant, The characteristic of arc trigger monitoring short circuit current is that it does not require external power supply and is a pure physical melting process that is not affected by the complex electromagnetic environment of ships. It has stable performance and high reliability. The disadvantage is that the heating of the arc trigger during rated current flow affects the temperature rise performance of the device; The propellant circuit interrupter bears the rated current under normal conditions. When a short circuit occurs, the arc voltage of the arc trigger ignites the propellant to achieve rapid disconnection of the circuit interrupter. The arc voltage formed by the disconnection of the circuit interrupter quickly transfers the main circuit current to the arc extinguishing fuse; The arc extinguishing fuse mainly serves to break the short-circuit current, and the composition of the hybrid current limiting fuse is shown in Fig. 1.

   According to the principle of hybrid current limiting fuses, during normal operation, the current mainly flows through the arc trigger and the propellant-assisted interrupting. In order to ensure the monitoring performance of the arc trigger, the narrow neck design of the trigger has strict standards, that is, the adjustable range of the trigger's own resistance is very limited, and the temperature rise distribution of the interrupter components can only be analyzed from the propellant-assisted interrupting, The purpose of reducing the temperature rise of the propellant is achieved through different structural designs.

Fig. 1 Composition of propellant-assisted interrupting and arc triggered hybrid current limiting fuse
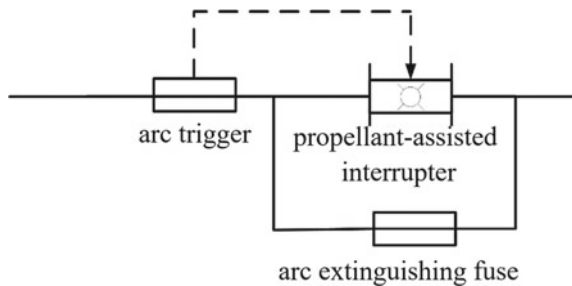
3　Modeling Temperature Rise and Analysis

3.1　Thermoelectric Coupling Model

3.1.1　Mathematical Model of Steady-State Electric Heating Field

The temperature rise problem of hybrid current limiting fuses can be abstracted as a stable electric field coupling process. Ignoring the radiation heat dissipation of the device, the steady-state electric field equation will be obtained as

$$\begin{cases} \nabla\gamma\nabla\varphi + \gamma\nabla^2\varphi = 0 \\ \gamma(\nabla\varphi)^2 = -\lambda\nabla^2 T \end{cases} \tag{1}$$

where, γ and λ are respectively the electrical conductivity and thermal conductivity of the material; φ is the potential at any point; T is the temperature.

3.1.2　Modeling COMSOL Multiphysics

The physical field selected in this study is the Thermoelectric effect module in COMSOL Multiphysics. The Thermoelectric effect physical field couples the solid heat transfer module and the current module. From the operating characteristics of the device, it can be seen that the rated current mainly flows through the arc trigger and propellant-assisted interruption. To simplify the calculation, the arc extinguishing fuse unit was omitted, with a copper bar length of 3 m and a cross-section of $800\,\text{mm}^2$, as shown in Fig. 2a. The propellant-assisted interruption is connected to a conductive bridge between the inner and outer electrodes to achieve the flow function. The propellant is placed between the aluminum base connected by bolts and the epoxy wall surface. When the short circuit signal triggers the propellant, the piston and insulation plate are pushed to break the conductive bridge, as shown in Fig. 2b.

(a) Temperature rise model of the whole machine

(b) Structure of propellant-assisted interrupter
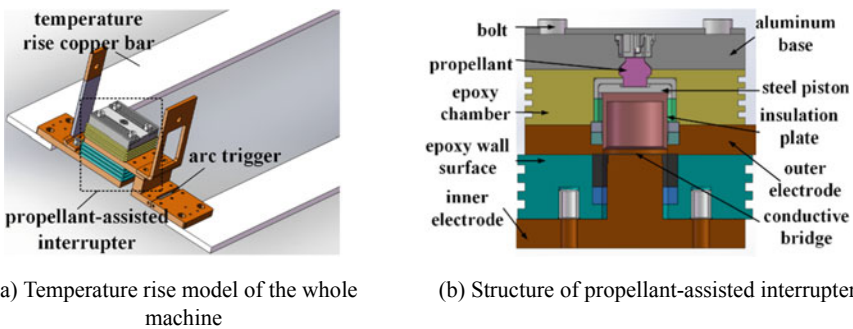
Fig. 2　Geometric model of device and temperature rise bus

Table 1 Physical parameters of temperature rise model

Parameter	T2	Pure silver	LY12	Steel	Epoxy
$\gamma_{20°C}/10^7$ S m^{-1}	5.71	6.17	–	–	–
$\gamma_{150°C}/10^7$ S m^{-1}	3.12	4.13	–	–	–
$\lambda_{20°C}/$(W (mK)$^{-1}$)	385	429	237	14.8	0.2
$\lambda_{150°C}/$(W (mK)$^{-1}$)	380	425	240	15.8	0.2
$\rho/$(kg m^{-3})	8960	10,490	2770	7950	1800
$c/$(J (kg °C)$^{-1}$)	386	232	880	460	1500

In the simulation, the material of trigger and interrupter is pure silver, the aluminum base of interrupter is LY12 aluminum, the connecting bolt is stainless steel, the conductive bar is T2 red copper, and the wall is epoxy material. The physical parameters are shown in Table 1 [10–12], ρ is the density of the material, and ς is the Specific heat capacity of the material. The upper, lower and side Natural convection heat transfer coefficients [6] are 14, 7 and 28 W/(m^2 K) respectively, the ambient temperature is set at 27 °C, and the flow is 1100 A. The model can clearly analyze the influence of parameter changes on the temperature rise of the mechanism.

3.2 Simulation Results and Analysis

3.2.1 Rated Current of Simulation Results

The temperature rise simulation results of the hybrid current-limiting fuse under the rated current condition of 1100 A are shown in Fig. 3. As this study focuses on the analysis of temperature rise around the propellant, points around the propellant-assisted interruption are selected for testing. The central part of the outer electrode A, the central part of the outer side of the epoxy chamber B, the upper surface of the bolt cap C, and the propellant D are mainly selected as measuring points. Temperature of each measuring point is shown in Table 2.

Combine Fig. 3 with Table 2, it can be observed that the temperature at point A in the middle of the outer electrode of the interruption is relatively high. Due to the epoxy chamber being cling to the outer electrode, the heat of the outer electrode is transmitted upwards through the epoxy chamber; Through further observation, it is found that the temperature of points C and D which far from point A is higher than that of point B which near point A. It is suspected that the reason for this temperature distribution is that the heat of the external electrode is transferred to the aluminum by means of the bolt. For further analysis, cut the section of the interruption along the middle section of the bolt, as shown in Fig. 4; And take the rated temperature rise simulation section at the same position, as shown in Fig. 5.

According to Fig. 4, we analysis the bolt wire sheath contacts the outer electrode, and the bolt cap contacts the aluminum base, which forms a metal medium channel

Fig. 3 Rated temperature rise and measuring point position of the device
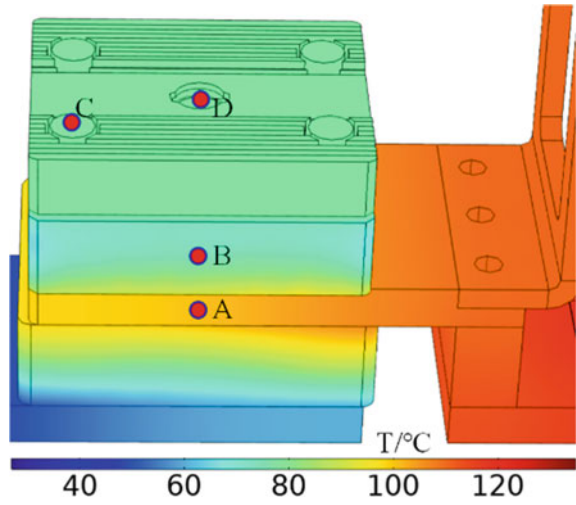
Table 2 Temperature of each measuring point

Positions	T/°C	Positions	T/°C
A	100.69	C	77.68
B	75.01	D	77.82

Fig. 4 Sectional view of the interrupter along the middle section of the bolt
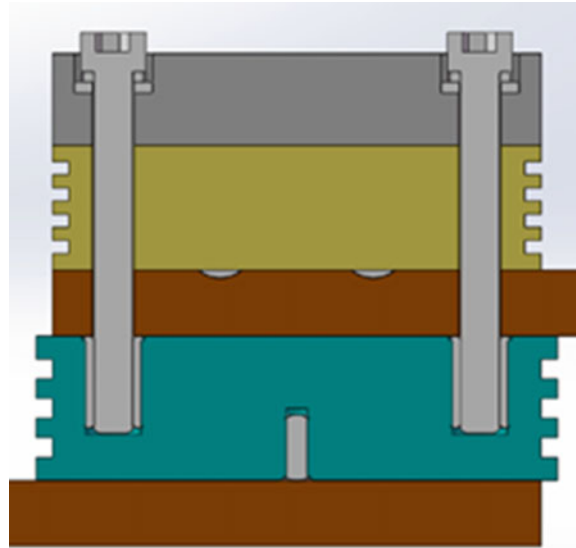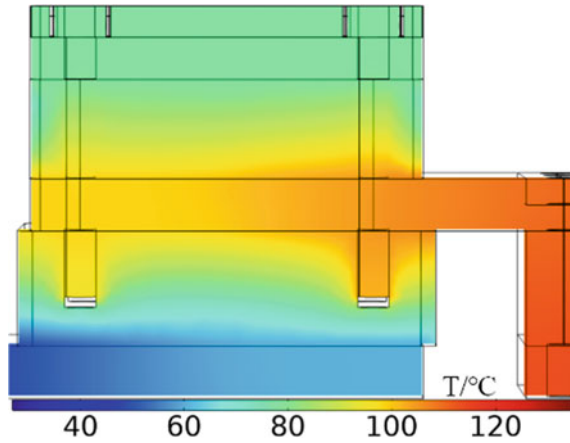
that conducts heat from the outer electrode to the base. Figure 5 further verifies the analysis, the temperature on the bolt wire sheath and bolt is higher, and it can be found that the epoxy chamber cling to the outer electrode has obvious heat transfer, and the heat conduction of these two parts from the outer electrode to the base causes the excessive temperature around the propellant.

The essence of heat transfer from the outer electrode of the interruption interrupter to propellant is a typical heat conduction problem, in which the expression of Fourier's law [13] involving heat transfer resistance is

$$
\begin{cases}
\Phi = \frac{\Delta T}{R_\theta} \\
R_\theta = \frac{l}{A \cdot \lambda}
\end{cases}
\tag{2}
$$

where, Φ is heat flow; ΔT is Temperature difference; R is Heat transfer resistance; l is the length of the material in the direction of Heat flux; A is the sectional area perpendicular to the direction of Heat flux.

Reducing the temperature of the propellant is to increase the temperature difference between the propellant and the external electrode, and under the premise that the heat flow can not be adjusted temporarily, it can only be achieved by increasing the heat resistance between the propellant and the external electrode. According to the analysis of formula (2), it is found that the R increases with the increase of l, and increase with the decrease of A and λ. Returning to the actual problem of the interruption, increasing l means increasing the distance between the propellant and the external electrode, decreasing A means reducing the contact area between the epoxy cavity and the external electrode, and decreasing λ means reducing the thermal conductivity of the bolt. A new interruption structure is designed from the above three aspects. As shown in Fig. 6.

From Fig. 6a, after optimization, the distance of propellant increased by 10 mm to the base, which enlarges the distance of propellant from the outer electrode. In the new design, the connection between the epoxy chamber and the external electrode adopts
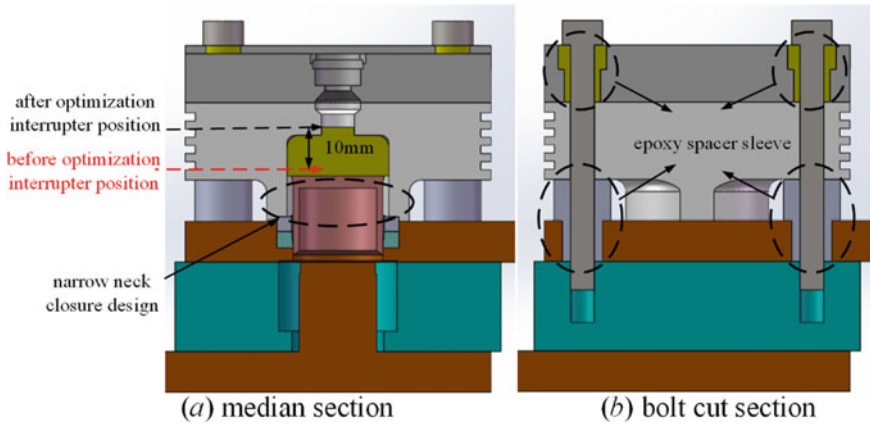
Fig. 6 Optimized structure of interrupter

a narrow neck closure design, which ensures the normal movement of insulation plate while reducing the contact area between the epoxy chamber and the external electrode, and can partly reduce the heat conduction of the external electrode through the epoxy chamber. From Fig. 6b, in the new design, epoxy spacers are used to fill the joints between the bolts and the outer electrode and the base. The metal medium conduction of the original structure in this design is epoxy conduction with low thermal conductivity between the metal and the base, which can further reduce the heat conduction of the outer electrode to the base through the bolts.

3.2.2 Simulation Results of Rated Current After Optimization

Using an analysis method similar to 3.2.1, the optimized device was simulated for a rated temperature rise of 1100 A. The simulation results are shown in Fig. 7. The outer middle of the outer electrode, the outer middle of the epoxy chamber, the upper surface of the bolt cap, and the propellant were selected as measurement points. The temperature of each measurement point and the temperature rise data of the original structure, is organized as shown in Table 3.

According to Fig. 7, the temperature of measuring point B decreased significantly relative to measuring point A. Although the temperature at measuring point C of the bolt cap was still higher than that at measuring point B, the design of the epoxy sleeve reduced the temperature at point C to a certain extent, and the temperature at the propellant of measuring point D was 60.83 °C.

From the comparison of temperature before and after optimization at each measurement point in Table 3, it can be found that the temperature at point A of the outer electrode is relatively consistent, while the temperature at the other measurement points has significantly decreased after optimization. The temperature at the
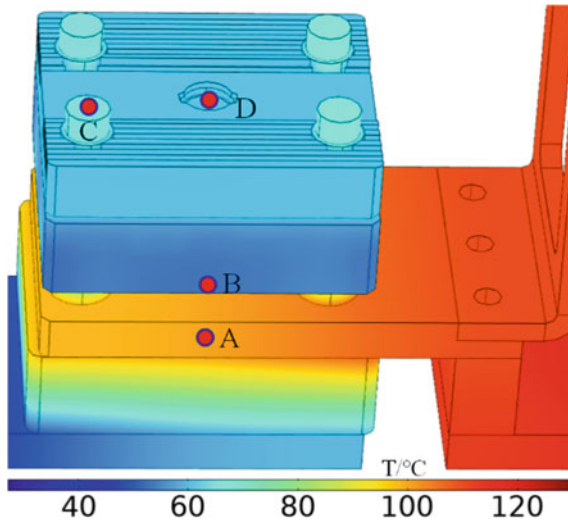
Fig. 7 Rated temperature rise and measuring point position after optimization

Table 3 Temperature comparison of each measuring point before and after optimization

Positions	Temperature after optimization/°C	Temperature before optimization/°C
A	100.23	100.69
B	53.24	75.01
C	65.00	77.68
D	60.83	77.82

propellant site has decreased from 77.82 to 60.83 °C, with a decrease of 16.99 °C, indicating that the optimized design has a certain effect on reducing the temperature of the propellant.

4 Test Verification

In order to verify the correctness of the temperature rise simulation analysis, two prototypes before and after optimization were made to carry out temperature rise test at a rated 1100 A. The prototypes were connected to the copper bar of the temperature rise platform, and the temperature monitoring instrument was used to detect and record the temperature at the same point as the simulation measurement point. Temperature rise test scenario was shown in Fig. 8, and the prototype before and after optimization was shown in Fig. 9.

Fig. 8 Temperature rise test scenario
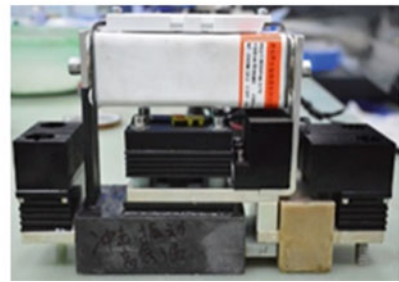
(a) before optimization　　　　　　　　(b) after optimization

Fig. 9 Prototype before and after optimization

The standard for judging the stability of temperature rise is to when the temperature change at each measuring point is less than 1 K/h, organize the temperature rise test data and simulation data of the two prototypes, as shown in Table 4.

From the analysis of Table 4, it is found that the simulation results are basically consistent with the test results, which proves the accuracy of the temperature rise simulation model.

Table 4 Comparison of test and simulation temperature of each measuring point before and after optimization

Positions	Temperature before optimization/°C		Temperature after optimization/°C	
	Simulation	Test	Simulation	Test
A	100.69	100.01	100.23	102.50
B	75.01	74.21	53.24	55.32
C	77.68	75.39	65.00	63.89
D	77.82	77.22	60.83	60.02

After optimization, the temperature at the propellant location of the prototype is 60.02 °C, and the temperature rise at the propellant location is 33.02 K. In the technical indicators, the actual average annual usage time and working temperature of the device are required to be 90 days @ 55 °C, which means that the actual working temperature of the propellant under this condition is 88.02 °C, and the required service life of the device is 12 years. Therefore, it is necessary to assess and calculate the lifespan of the propellant at specific temperatures.

5   Conclusion

The temperature rise generated by the rated current of the hybrid current limiting fuse triggered by the high temperature superposition of propellant in the marine environment will cause the propellant used in the interruption to be in a high temperature environment, and the high temperature will accelerate the reaction of the propellant itself, attenuate the power after excitation, and affect the breaking performance of the interruption. This article starts with reducing the temperature rise at the powder location of the device, establishes a thermoelectric coupling model of the device, optimizes the structure of the propellant-assisted interruption. Through simulation analysis and experimental verification, the following conclusions can be drawn:

1. The simulation of rated current temperature rise found that the temperature at the external electrode of the original interruption was high, and it was mainly transmitted to the propellant through the epoxy chamber and connecting bolts in contact with it.
2. Optimizing the structure starts with increasing the distance between the propellant and the outer electrode, reducing the contact area between the epoxy powder cavity and the outer electrode, and hindering the heat transfer from the outer electrode through the bolt. The temperature at the propellant is reduced from 77.82 to 60.83 °C, with a decrease of 16.99 °C.
3. Two prototypes were made before and after processing optimization and temperature rise test of rated current was carried out. The simulation results were basically consistent with the test results, which proved the accuracy of the temperature rise simulation model.

References

1. Gattozzi AL, Herbst JD, Hebner RE (2015) Power system and energy storage models for laser integration on naval platforms. In: IEEE electric ship technologies symposium (ESTS 2015), pp 441–445
2. (2018) IEEE Recommended Practice for 1 kV to 35 kV medium-voltage dc power systems on ships. IEEE Standard 1709

3. Sakuraba T, Ouaida R, Chen S et al (2018) Evaluation of novel hybrid protection based on Pyroswitch and fuse technologies. In: International power electronics conference (IPEC-Niigata 2018 –ECCE Asia)
4. Li F, Zhuang J, Jiang Z et al (2017) Structure analysis and optimum design on explosive chamber of explosive piston type high-speed interrupter in hybrid current-limiting fuse. High Voltage Eng 43(7):2417–2424 (in Chinese)
5. Liu J, Peng H, Mo W et al (2022) Influence of driving time on efficiency of electromagnetic repulsion mechanism and structural stress of drive system. High Voltage Apparatus 58(09):78–84+93 (in Chinese)
6. Li F, Zhuang J, Fang W et al (2017) Effect of filler material on the arc-trigger characteristic. J Huazhong Univ Sci Technol (Nat Sci Ed) (7):74–77 (in Chinese)
7. Zhou Y, Zhuang J, Wu J et al (2020) Analysis and optimum design of propellant-assisted interrupter. High Voltage Eng 46(3):939–946 (in Chinese)
8. Zhou Y, Zhuang J, Wu J et al (2020) Propellant-assisted interrupter design and its dielectric recovery characteristics. Proc CSEE 40(23):7824–7833 (in Chinese)
9. Zhou Y, Zhuang J, Wu J et al (2020) Effect of structural design on interruption characteristics of propellant-assisted interrupter. Trans China Electrotech Soc 35(05):1075–1082 (in Chinese)
10. Fang K (2002) Engineering materials manual, non-ferrous metal material book. Beijing Publishing House, Beijing, China (in Chinese)
11. Ning Y, Zhao H (2015) Silver. Central South University Press, Changsha, China (in Chinese)
12. Mills KC (2002) Recommended values of thermo-physical properties for selected commercial alloys. pp 19–25
13. Yang S, Tao W (2010) Heat transfer, 4th edn. Higher Education Press (in Chinese)

Simulation of Hot Spot Temperature Rise of Dry Bridge Reactor Based on Highly Conductive Epoxy Composites

Li Yin, Wei Yang, Kun Wang, Jie Wang, Chong Zhang, Yun Chen, Jian Qiao, and Guangke Wang

Abstract In this paper, based on the theory of multi-physical field coupling, the coupled calculation model of fluid-temperature field is established. The data of dry reactor temperature field in normal operation are calculated by means of finite element modeling, and the transient temperature change law of reactor in normal operation is obtained. On this basis, the microcosmic COMSOL simulation model of the encapsulation material is established and the thermal conductivity of the composite material is calculated. Simulation models of epoxy reactors with different thermal conductivity are established to analyze the influence of thermal conductivity on hot spot temperature rise of dry bridge arm reactors. The results show that there are obvious differences in temperature rise of hot spots between different thermal conductivity. Compared with conventional epoxy materials, the temperature of hot spots of high thermal conductivity materials is reduced by 9.5 °C, which can achieve the goal of reducing the temperature rise of hot spots by 5 K.

Keywords Dry reactor · Fluid-temperature field · Multi-physical field coupling · Hot spot temperature rise · Thermal conductivity

1 Introduction

With the advantages of good linearity, high saturation, low loss and convenient operation and maintenance, dry reactor has become an important development direction for building a new power system under the "dual carbon" strategy. However, due to its long-term outdoor work, the encapsulation material will gradually age with the increase of operating life, resulting in the mismatch between the hot spot temperature

L. Yin · W. Yang (✉) · K. Wang · Y. Chen · J. Qiao · G. Wang
State Grid Smart Srid Research Institute Co. Ltd, Beijing 102209, China
e-mail: yinlibj@163.coms

J. Wang · C. Zhang
Power Science Research Institute of State Grid, Sichuan Electric Power Company,
Chengdu 610041, Sichuan, China

rise of the reactor and the heat resistance level [1], resulting in frequent insulation breakdown accidents and becoming a safety hazard for the continuous and reliable operation of the power grid.

At present, there are many related researches on dry-type reactor temperature in China. Documents [2] establish differential equations of temperature field according to thermodynamic principles, determine local heat exchange coefficient according to structural characteristics of reactors, and reasonably deduce the change law of dry-type reactor heat dissipation at the same height. In engineering, there are test methods for the average temperature rise of reactor windings [3], and an average temperature rise calculation formula based on curve fitting and thermal balance principles is used to facilitate testing of the thermal performance of the reactor in engineering applications [4]. Some studies have shown that the empirical formula can be used to obtain the temperature data of the dry reactor [5], and the influence of the height parameters can be analyzed based on the principle of heat transfer [6], but the average temperature rise method has a large error and it is difficult to accurately locate the overheating area [7]. Relevant scholars used finite element numerical calculation methods to study the temperature field distribution of dry reactors. The literature [8] considered the effect of the ventilation structure of the rain cap on the hot spot temperature. Based on the influence of temperature on the conductivity of the conductor region, Feng analyzed the interaction between conductivity and temperature rise based on bidirectional coupling [8], and Wang and others simulated short circuit faults between reactor turns based on the finite element method [2].

It can be seen from this that there are still very few studies on the thermal conductivity of encapsulated epoxy composites, so the article uses encapsulating materials as research subjects, establishes microscopic simulation models, and calculates the thermal conductivity of composites composed of conventional and high thermal conductivity epoxy composites.

2   Dry Air-Core Reactor

2.1   Basic Structure of Dry Air-Core Reactor

The dry air-core reactor shown in Fig. 1 has no iron core and uses air as the magnetic conductive medium. Compared with the iron core reactor, the hollow reactor has high saturation resistance and good linearity. Due to the low magnetic permeability of the air, the magnetic circuit is not easy to be saturated and the degree of linearization of the magnetic circuit is high. The superposition theorem can be used for research and analysis. Dry-type hollow reactors have low inductance, constant resistance value, and stable performance. The hollow reactor has many encapsulation layers, and there is a parallel relationship between the envelopes. Since the expansion coefficient of the copper wire differs greatly from the insulating material, it is easy to crack. Most of them use aluminum wire as the winding material, and each winding branch is also

Fig. 1 Physical map of a dry-type reactor

made of multiple identical wires wound in parallel. At present, the winding of the hollow core reactor is basically based on the structure of high-strength glass fiber plus epoxy resin load insulation, using wet winding, the wire and glass fiber and other insulating filling materials are infiltrated with epoxy resin without gel curing and wound together, and after the winding is completed, it is placed into a high-temperature oven to solidify and form, and the cured has excellent electrical and mechanical properties.

When the reactor coil is wrapped, a support made of GFRP material is used as an axial heat dissipation airway support to form natural convection cooling. The reactor uses a star-shaped boom structure, and the star frame structure uses an aluminum alloy composite row, which has high mechanical strength and low eddy current loss.

2.2 Working Principle of Dry Air-Core Reactor

As the main auxiliary equipment of the long-distance AC transmission system, the dry hollow shunt reactor plays a role in compensating capacitive current, maintaining system voltage level and improving line transmission ability. Dry-type hollow reactor is an important auxiliary equipment in long-distance power transmission system, which is mainly responsible for reactive power compensation, short circuit current limitation, high order harmonic filtering and harmonic component reduction in DC system. The dry hollow shunt reactor is an axisymmetric structure composed of multiple layers of coils wound together, and each layer of coil can be equivalent to

Fig. 2 Dry-type bridge arm
reactor equivalent circuit
diagram
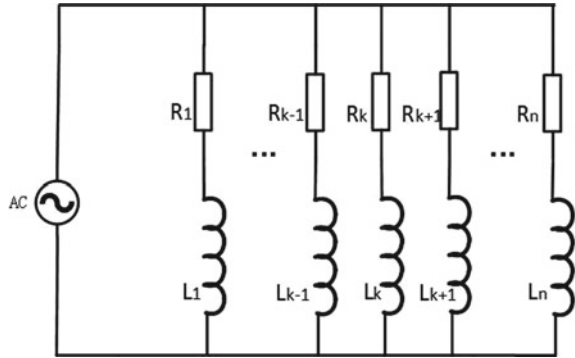
the inductive form formed by wire resistance, self-inductance and mutual inductance. The equivalent circuit built in units of each packet is shown in Fig. 2.

In a cylindrical coordinate system, the magnetic field control equation is:

$$\frac{\partial}{\partial z}\left(\frac{1}{r}\frac{\partial A}{\partial z}\right) + \frac{\partial}{\partial r}\left(\frac{1}{r}\frac{\partial A}{\partial r}\right) = -\mu_0 J \tag{1}$$

In the formula, r is the radial distance in cylindrical coordinates; z is the axial distance; A is the magnetic vector position; μ_0 is the magnetic permeability; J is the source current density.

The equation for a layer i coil constrained by an external circuit is:

$$U = R_i I_i + \frac{d\psi_i}{dt} \tag{2}$$

$$\psi_i = N_i \iint\limits_{S_i} (\nabla \times A) \cdot dS \tag{3}$$

$$J = \frac{N_i I_i}{S_i} \tag{4}$$

In the formula, U is the external constraint voltage; R_i, ψ_i, N_i, I_i and S_i respectively represent the resistances, magnetic chains, turns, currents and cross-sectional areas of the layer I coils.

By connecting Eqs. (1)–(4) and establishing a field-coupled finite element equation system, the current value and magnetic vector position A in each layer of encapsulation can be obtained, and the magnetic induction intensity is obtained from the magnetic vector bit:

$$B = \nabla \times A \tag{5}$$

The i-layer loss P_i of the winding mainly includes the resistive loss P_{ri} and the eddy current loss P_{ei}, where the loss of the i-layer winding is:

$$\begin{cases} P_i = P_{ri} + P_{ei} \\ P_{ei} = \sum_{i=1}^{m} \frac{\pi^2 D_i^4 \gamma \omega^2}{32} l_i B_i^2 \\ P_{ri} = I_i^2 R_i \end{cases} \tag{6}$$

In the formula: γ is the conductivity of the aluminum wire; ω is the angular frequency at which the excitation is applied; D_i is the line diameter of the i turn conductor; l_i is the radius of each turn of wire; B_i is the magnetic induction strength at the center of the i-turn wire.

3 Temperature Field Simulation Study of Dry-Type Hollow Reactors Under Normal Conditions

Losses in dry-type hollow parallel reactors include eddy current loss, resistor loss, and stray loss. Among them, resistance loss is greatest, eddy current loss is second, and minimal stray loss can be ignored. Based on the above analysis, this paper uses the RkgKL-10kV-600A-20MH dry-type hollow parallel reactor as a research object, A two-dimensional flow field-temperature field coupling model is established, the direct resistance loss of the dry hollow reactor is used as a heat source, and the hot spot temperature rise when the heat transfer and flow field of the reactor fluid and solid are coupled to the flow field is obtained.

3.1 Establish a Dry Air-Core Reactor Simulation Model

The finite element calculation of heat transfer and turbulence fields of fluids and solids has high requirements for the mesh, and the model needs to be reasonably simplified. As a heat source, the encapsulation exchanges heat with the air, and the air density changes with the temperature, flowing under the action of buoyancy, and the rainproof cap has an obstructive effect on it. Because the inter-airway brace and star frame structure have limited effect on air flow [10], they are omitted from the calculation. Create simulation models including rain caps, envelopes, and air. This is axisymmetric and can be simplified to a two-dimensional axisymmetric model.

The size parameters of each encapsulation of the reactor are shown in Table 1. The radial direction of the encapsulation from the inside to the outer edge is numbered 1, 2, 3, 4, 5, 6, respectively.

Table 1 Encapsulation size parameters

Encapsulation number	Inner diameter (mm)	Outside diameter (mm)	Height (mm)
1	1300	1331.77	2715
2	1381.77	1398.97	2715
3	1448.97	1466.99	2715
4	1516.99	1535.57	2715
5	1585.57	1617.65	2715
6	1667.65	1675.65	2715

3.2 Coupling Analysis of Flow Field and Temperature Field

The heat source of the encapsulation is determined by the rate of heat generation generated by the current inside the envelope.

$$q = \frac{P}{V} \tag{7}$$

In the formula: P is the loss of the reactor encapsulation, which can be obtained from (6); V is the volume of the encapsulation.

The fluid control equations include mass continuity equation, momentum conservation equation and mass conservation equation. The surrounding air fluid is considered to be an incompressible viscous fluid, the fluid is in a steady flow state, and the mass conservation equation can be expressed as the following formula:

$$\nabla \cdot (\rho u) = 0 \tag{8}$$

The momentum conservation equation can be expressed as:

$$\nabla \cdot (\rho u u) = \mu \nabla^2 u - \frac{\partial p}{\partial x} + S_u \tag{9}$$

$$\nabla \cdot (\rho v u) = \mu \nabla^2 u - \frac{\partial p}{\partial y} + S_v \tag{10}$$

$$\nabla \cdot (\rho w u) = \mu \nabla^2 w v - \frac{\partial p}{\partial z} + S_w \tag{11}$$

The energy conservation equation is:

$$\nabla \cdot (\rho u T_f) = \frac{\lambda}{c_p} \nabla^2 T_f + S_T \tag{12}$$

In the formula: ρ is the density of air; u is the fluid velocity vector; u, v, w indicate the coordinate components of the velocity vector u in the x, y, z directions of the

axes; μ is the kinematic viscosity coefficient of air; p is the air pressure; c_p is the specific heat capacity of the air; λ is the thermal conductivity of the air; S_u, S_v, S_w is the generalized source term of the fluid momentum equation, when the gravity direction is vertically downward along the z axis, $S_u = S_v = 0$, $S_w = -\rho g$; S_T is the viscous dissipation term of fluids. In addition, in order to close the fluid equation group, the air also needs to meet the gas state equation:

$$\rho = f(p, T_f) \tag{13}$$

The dry air-core reactor and the surrounding air are dissipated by natural convection and heat radiation, and the inside of the reactor is dissipated by heat conduction. At the same height all angles with equal temperatures, in cylindrical coordinates, the differential equation for heat conduction is:

$$\frac{\partial}{r \partial r}\left(kr\frac{\partial T}{\partial r}\right) + \frac{\partial}{\partial z}\left(k\frac{\partial T}{\partial z}\right) + \sum_{i=1}^{m} q_i - \rho c\frac{\partial T}{\partial t} = 0 \tag{14}$$

After thermal stabilization, the heat gain is zero, and the thermal conductivity is maximum. The differential equation of heat conduction per unit volume of each package is:

$$\frac{\partial}{r \partial r}\left(kr\frac{\partial T}{\partial r}\right) + \frac{\partial}{\partial z}\left(k\frac{\partial T}{\partial z}\right) + \sum_{i=1}^{m} q_i = 0 \tag{15}$$

In the formula, k is the thermal conductivity, T is the temperature, q_i is the heat generation rate per unit volume of the inner coil inside the package, m is the number of coils inside the package, ρ is the density, c is the specific heat, and t is the time.

The thermal convection effect between the surface of each package and the air of the dry hollow shunt reactor is natural convection heat transfer, and the calculation formula is as follows:

$$\phi = Ah(t_w - t_f) \tag{16}$$

In the formula, ϕ is the heat transferred during thermal convection, A is the surface area of the reactor encapsulation, h is the local thermal convection coefficient, t_w is the encapsulation temperature of the reactor, and t_f is the temperature of the surrounding air.

After the dry-type hollow parallel reactor starts operating, the density of the air surrounding the envelope becomes smaller after being heated, and it gradually flows upward along the encapsulation surface, creating a thermal boundary layer with a constantly changing range. The heat generated by the encapsulation flows through the air in a turbulent manner with unsteady, non-cyclical transport volume fluctuating in time and space. The generation of turbulence can be judged based on the magnitude of the Rayleigh parameter. The calculation formula for the Rayleigh parameter is:

$$R_\alpha = \frac{g\beta L^3 \Delta T}{\nu\alpha} \tag{17}$$

In the formula, ΔT is the difference between the package surface and the gas temperature, g is the acceleration of gravity, ν is the coefficient of air kinematic viscosity, α is the coefficient of thermal diffusion, and β is the coefficient of gas expansion.

The thermal radiation of the outer surface of each package of the dry-type hollow parallel reactor towards the peripheral space satisfies the following requirements:

$$q_1 = \varepsilon\sigma_b\left(T_w^4 - T_\infty^4\right) \tag{18}$$

In the formula, q_1 is the heat flow of radiant heat transfer on the radiation surface, ε is the surface emissivity, σ_b is the Boltzmann constant, T_w is the temperature of the encapsulation surface, and T_∞ is the ambient air temperature.

3.3 Temperature Field Simulation Results of Dry Air Core Reactor Under Normal Conditions

A two-dimensional axisymmetric model of a dry-type hollow reactor was established in COMSOL, and the volumetric heat source density was substituted as a heat source into the temperature field model. The grid is divided by a physical field, reasonable boundary conditions are set, and the physical properties parameters of each part of the material are set as shown in Table 2. Through verification data, the surface emissivity of thermal radiation from the encapsulated surface was determined to be 0.9 [9]. The temperature field distribution cloud at 6 h is shown in Fig. 3. The temperature of the hot spot in the calculation area was 110.33 °C, located at the upper end of the 5th package, and the hot spot temperature rose to 83.33 °C.

Table 2 Physical property parameters of materials

Material	Thermal conductivity (W · m^{-1} · K^{-1})	Constant pressure heat capacity (J · kg^{-1} · K^{-1})	Density (kg/m^3)	Kinematic viscosity coefficient (Pa · s)
Epoxy composites	0.43677	871	2719	
Aluminium	238	900	2700	
Air	0.0242	1006.43	Weak compressible, temperature dependent	1.7894 × 10–5
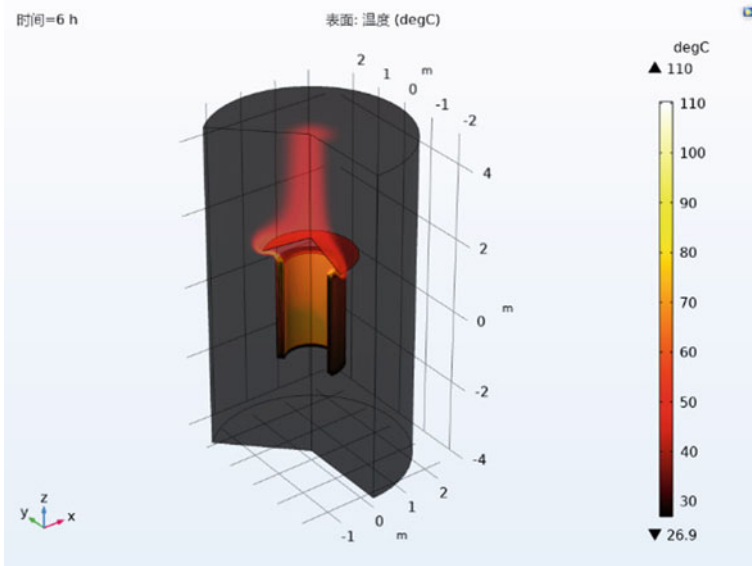
Fig. 3 The reactor solves the temperature field distribution in the

As can be seen from Fig. 4, the hottest point temperature of the dry-type hollow reactor under normal operation at room temperature is 110.32 °C. It is located at about 93.6% of the 5th layer encapsulation. Its temperature rise value is 83.33 °C. The upper area of the 5th layer encapsulation is the area where hot spots are concentrated. The innermost layer encapsulation has poor heat dissipation conditions and a high temperature rise value due to the barrier of a rain cap.

4 Simulation Study on the Effect of Conventional/highly Conductive Epoxy Materials on the Reactor Hotspot Temperature Rise

According to the thermal conductivity definition, the thermal conductivity of composite materials is calculated by simulation calculation. The thermal conductivity of a material is the amount of heat transferred through an area of 1 square meter over a period of 1 s for a material that is 1 m thick and has a surface area of 1 square meter on both sides and a temperature difference of 1 degree under stable heat transfer conditions. Units are watts per meter per degree. K here can be replaced by °C.

The volume fraction of glass fiber is 65%, and the thermal conductivity of epoxy resin is set to be 0.2 $(\mathrm{W \cdot m^{-1} \cdot K^{-1}})$, 0.6 $(\mathrm{W \cdot m^{-1} \cdot K^{-1}})$, 0.9 $(\mathrm{W \cdot m^{-1} \cdot K^{-1}})$, and 1.2 $(\mathrm{W \cdot m^{-1} \cdot K^{-1}})$, respectively.

Fig. 4 Local temperature
distribution of dry resistance
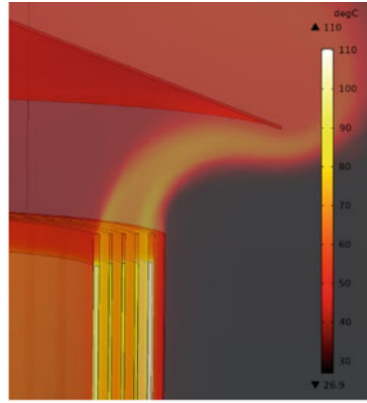
（a）Upper end temperature details
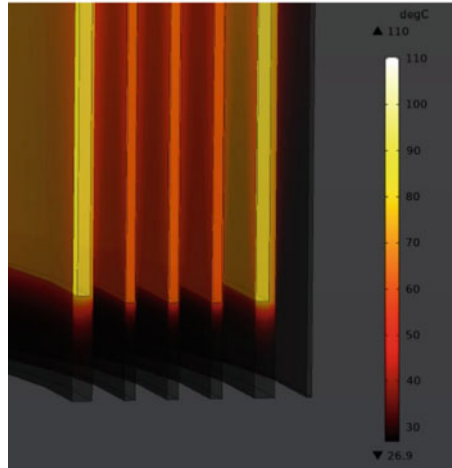
(b) Lower end temperature details

4.1 Simulation Calculation of Thermal Conductivity Performance of Conventional/high Thermal Conductivity Epoxy Composites

Using COMSOL simulation software, the thermal conductivity of the composite material was calculated as shown in Table 3.

Figure 5 of the simulation results shows that as the thermal conductivity of the epoxy resin increases, the thermal conductivity of the composite material increases linearly. When the thermal conductivity of the epoxy resin is 1.2 ($W \cdot m^{-1} \cdot K^{-1}$), the thermal conductivity of the composite material is 0.437 ($W \cdot m^{-1} \cdot K^{-1}$).

Table 3 Thermal conductivity parameters of epoxy resin

Epoxy resin thermal conductivity $(W \cdot m^{-1} \cdot K^{-1})$	Thermal conductivity of composite materials $(W \cdot m^{-1} \cdot K^{-1})$
0.2	0.091342
0.6	0.22951
0.9	0.33314
1.2	0.43677
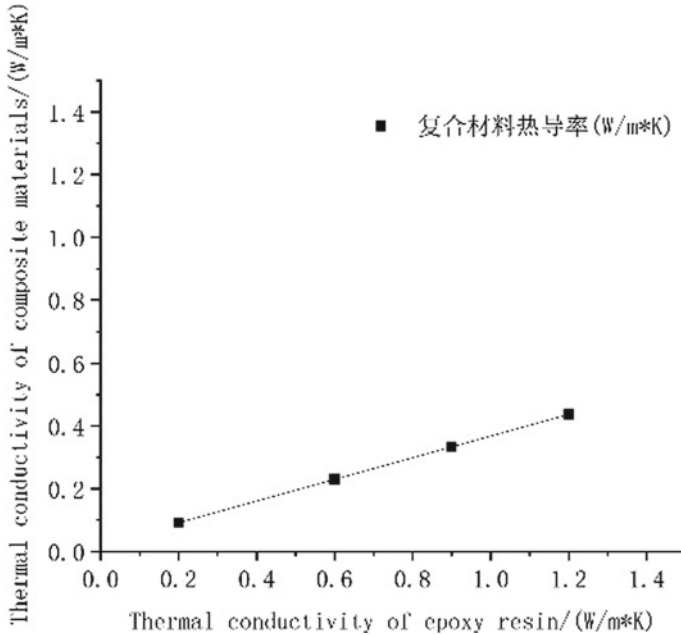
Fig. 5 Relationship between thermal conductivity of epoxy resin and thermal conductivity of clad composites

4.2 Influence of Conventional/high Thermal Conductivity Epoxy Materials on the Temperature Rise of Reactor Hot Spots

The relationship between the hot spot temperature rise and the thermal conductivity of the composite material is shown in Fig. 6.

The difference in hot spot temperature rise of encapsulated epoxy materials with different thermal conductivity coefficients was analyzed. Comparing the steady hot spot temperature rise of dry hollow reactors under normal conditions, it can be seen that when the ambient temperature is 27 °C and the thermal conductivity of
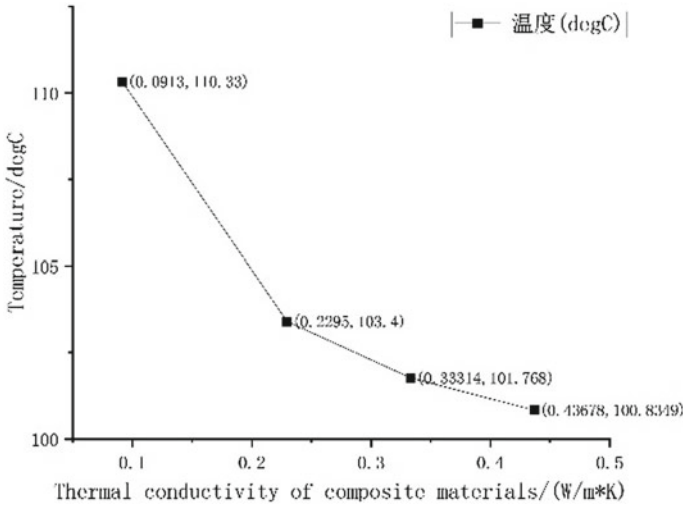
Fig. 6 Hot spot temperature rise of dry resistance of epoxy composites with different thermal conductivity

conventional epoxy materials is 0.2 (W · m^{-1} · K^{-1}), the thermal conductivity of the composite material is 0.0913 (W · m^{-1} · K^{-1}), and the hot spot temperature rise is 110.33 °C. As the thermal conductivity of epoxy materials with high thermal conductivity increased, the temperature rise of the hot spot dropped significantly. When the thermal conductivity of the epoxy material was 1.2 (W · m^{-1} · K^{-1}), the thermal conductivity of the composite material was 0.437 (W · m^{-1} · K^{-1}), the hot spot temperature was 100.83 °C, and the temperature rise was 83.33 °C. The high thermal conductivity composite reduced the temperature rise of the reactor by 9.5 °C, exceeding the expected target of 5 K, and the cooling effect was remarkable.

5 Conclusion

(1) The value of the thermal conductivity of the composite material was calculated using the COMSOL finite element simulation model, and the analysis showed that the effect of high thermal conductivity epoxy resin on the thermal conductivity of the composite material was remarkable.

(2) The maximum temperature rise of the hot spot in the area of the envelope body and the surrounding air temperature field is 110.33 °C, which appears at the upper end of the internal envelope 5.

(3) Combined with the thermal conductivity of conventional and high thermal conductivity epoxy composites obtained by simulation, it is calculated as material characteristics input fluid-temperature field simulation: high thermal conductivity composites have a significant effect on reducing the hot spot

temperature rise of dry air-core reactors, and the use of epoxy resin with thermal conductivity of 1.2 ($W \cdot m^{-1} \cdot K^{-1}$) can reduce the hot spot temperature rise by 9.5 °C, which proves the importance of the physical properties of the encapsulation material to the temperature field calculation.

References

1. Sippola M, Sepponen RE (2002) Accurate prediction of high-frequency power-transformer losses and temperature rise. IEEE Trans Power Electron 17(5):835–847
2. Wang Z, Han D, Fan X, Li J, Zhou Q, Wang Z (2022) Simulation of reactor turn to turn short circuit detection based on finite element analysis. J Guilin Univ Electron Technol 42(06):443–448 (in Chinese)
3. Fan M-Y (2021) Finite element simulation of dry resistance temperature field and measurement method based on optical fiber sensing. North China Electric Power University (in Chinese)
4. Shi C, Chen S, Wang Y, Jin S, Yu Y, He Y, Yang S, Xiong Z, Shi Q (2022) Effects of fibre orientation on thermal conductivity of epoxy/glass fibre composites. Eng Plastics Appl 50(11):108–116 (in Chinese)
5. Liang K (2021) Research on heat transfer characteristics of dry hollow reactor cladding material. Kunming University of Science and Technology (in Chinese)
6. Yu JZ, Wei NQ, Gang LW et al (2013) Analysis of temperature rise in reactors using coupled multi-physics simulations. In: 2013 IEEE International conference on applied superconductivity and electromagnetic devices (ASEMD). IEEE
7. Dong J, Shu N, Yan Q, Sun L (2018) Coupling calculation and analysis of temperature field of dry-type air-core shunt reactor during overheat fault. J Wuhan Univ (Eng Sci) 51(05):437–442 (in Chinese)
8. Feng C, Zhao Y, Ma X (2012) An efficient calculation for the temperature of dry air-core reactor based on coupled multi-physics model. In: Sixth International conference on electromagnetic field problems & applications. IEEE
9. Pfeifer N, Kizilcay M, Malicki P (2023) Analytical and numerical study of an iron-core shunt-compensation reactor on a mixed transmission line. Electr Power Syst Res 220
10. Coelho L, Guerra FA, Leite JV (2012) Multiobjective exponential particle swarm optimization approach applied to hysteresis parameters estimation. IEEE Trans Magn 48(2):283–286

Research on Short Circuit Cumulative Effect and Deformation Prediction Method of Transformer Windings

Hewei Dou, Xiufeng Dou, Weimin Xia, Shulin Liu, Zhenqin Liang, and Yuqing Zhang

Abstract Power transformer is one of the most important electrical equipment in power system operation. Therefore, the calibration of the transformer helps to prevent the abnormal operation of the transformer system timely. A method to consider the cumulative effect of short circuit windings deformation and its deformation prediction is proposed in the paper. Firstly, the mathematical expressions and influencing factors between the accumulated number of short circuit shocks and transformer windings deformation are determined. Secondly, based on COMSOL finite element analysis method, by the actual transformer basic parameters, a three-dimensional finite element simulation model of magnetic and structural coupling field of transformer core and winding is established. The accumulated winding deformation renderings under different short-circuit shock are simulated, and the law between the accumulated number of short circuits and the transformer winding deformation is obtained. Simulation and experimental results prove the feasibility of the theoretical analysis, which provides a reliable method for transformer calibration.

Keywords Transformer windings · Magnetic-structural coupling · Short circuit shocks

H. Dou
State Grid Shaanxi Electric Power Co., Ltd. Yulin Power Supply Company, Yulin 719000, China

X. Dou
State Grid Henan Electric Power Co., Ltd. Zhoukou Power Supply Company, Zhoukou 466000, China

W. Xia
Xi'an University of Technology, Xi'an 710048, China
e-mail: xiaweimin@xaut.edu.cn

S. Liu · Z. Liang (✉) · Y. Zhang
Xi'an University of Science and Technology, Xi'an 710600, China
e-mail: 2420530401@qq.com

1 Introduction

Power transformer is one of the important links of the power system. However, a large number of transformers are damaged due to the action of output short circuit current and leakage flux under multiple cumulative shocks in [1], and the resulting electromagnetic force causes transformer windings to deform in [2]. The study of accumulation effect provides an important basis for calibrating the short circuit resistance of transformers in [3]. Therefore, it can effectively reduce the probability of damage caused by winding deformation.

In recent years, domestic scholars have been actively engaged in the research on the short circuit accumulation effect of transformers. Reference [4] used an empirical algorithm and proposed the real-time short-circuit force coefficient f as an index for detecting the degree of short-circuit. The ANSYS software to build a magnetic-structural coupled-field independent model of the cumulative effect of transformer short-circuit shocks in [5], proposing the relationship between the number of transformer short-circuit shocks and winding deformation under different short circuit currents. The finite element method was used to establish the magnetic- structural field in [6], and it is found that the winding stress will suddenly change when multiple short circuit shocks. The accumulation model of plastic deformation of winding was established by finite element analysis method, and the accumulation law of transformer winding deformation and the influencing factors were analyzed in [7]. In [8], a transformer magnetic-mechanical coupling model is established, and three test results are compared with the field frequency response analysis method, short-circuit impedance method and winding capacity method. The axial stability of power transformer windings was analyzed through using the finite element method in [9], and it is concluded that the deformation of the winding can be reduced by increasing the number and width of pads around the windings. The above references for analyzing the windings deformation during short circuits are value. However, none of the above reference has been able to determine the quantitative relationship between the number of short circuit shocks and winding deformation.

In view of this, this paper determines the mathematical equation of the cumulative effect between the number of short-circuit shocks and the winding deformation at first. Then, a three-dimensional finite element simulation model of the magnetic and structural coupling fields is constructed. Finally, the accumulated winding deformation under short circuit shock is simulated and its law is obtained, which provides a basis for transformer calibration.

2 Analysis of Short Circuit Effect and Deformation Characteristics of Transformer Windings

2.1 Calculation of "Magnetic Field and Circuit"

According to the short-circuit characteristic analysis, the short-circuit current of the transformer when a short-circuit occurs [9] is

$$i' = \sqrt{2}I\left[e^{-\frac{Rt}{L}}\cos\theta - \cos(\omega t + \theta)\right] \tag{1}$$

In (1), I is the root-mean-square value of the symmetric short-circuit current; $R\,(\Omega)$ and L (mH) are the short-circuit equivalent resistance and inductance, respectively.

In order to obtain the leakage flux caused by the transformer short-circuit current, firstly, the two degrees of freedom of vector magnetic potential A and current I are introduced into the model of magnetic-structure coupling field by COMSOL. The boundary value problems of the model are as follows.

The boundary equation of the winding in the high voltage side is given by

$$\nabla^2 A_1 = -\mu_0 J_1; \quad \frac{\partial A_1}{\partial n}; \quad J_1 = \frac{N_1 i_1}{K_1 V_1} \tag{2}$$

The boundary equation of winding in low voltage side is

$$\nabla^2 A_2 = -\mu_0; \quad J_2 J_2 = \frac{N_2 i_2}{K_2 V_2}; \quad \frac{\partial A_2}{\partial n}|l = 0 \tag{3}$$

The oil boundary equation of transformer is

$$\nabla^2 A_3 = 0; \quad \frac{\partial A_3}{\partial n}|l = 0 \tag{4}$$

where J is the current density (A/m^2); N is the number of windings turns; V is the volume of the winding (m^3); i is short-circuit current (A). and the discrete form of "magnetic field-circuit" coupling equation is

$$\begin{pmatrix} 0 & 0 & 0 \\ C^{iA} & 0 & 0 \\ C^{iA} & 0 & 0 \end{pmatrix} \begin{pmatrix} \frac{\partial A}{\partial t} \\ 0 \\ 0 \end{pmatrix} + \begin{pmatrix} K^{AA} & K^{Ai} & 0 \\ 0 & K^{ii} & 0 \\ 0 & K^{ii} & K^{ie} \end{pmatrix} \begin{pmatrix} A \\ I \\ e \end{pmatrix} = \begin{pmatrix} 0 \\ V_0 \\ 0 \end{pmatrix} \tag{5}$$

In (5), A is the node vector magnetic potential matrix; J is the node current matrix; P is the node electromotive force matrix; K^{AA} is a vector bit stiffness matrix; K^{ii} is the resistance stiffness matrix; K^{Ai} is the coupling stiffness matrix of magnetic potential and current; C is the inductance damping matrix; K^{ie} is the coupling stiffness matrix of current and electromotive force; V_o is the matrix of applied voltage.

In an axisymmetric magnetic field, there are $B = \nabla \times A$, the axial leakage and radial density are expressed as

$$B = \frac{1}{r}\sqrt{\left[\frac{\partial(rA)}{\partial z}\right]^2 + \left[\frac{\partial(rA)}{\partial r}\right]^2}; \quad B_y = \frac{1}{r}\frac{\partial(rA)}{\partial r}; \quad B_x = -\frac{\partial A}{\partial z} \qquad (6)$$

2.2 Transformer Deformation Calculation

According to theoretical analysis, transformer winding is damage, due to deformation in the action of electromagnetic forces, which is the main factor. Then, assuming that the electric fluid density of a unit is J and the magnetic induction strength vector of the magnetic field is B, the electromagnetic force applied to a single unit as

$$F_j = \int J' \cdot dv \times B \qquad (7)$$

When the winding is subjected to electromagnetic forces, the deformation formula as

$$\varepsilon = \frac{F_j}{E}; \quad \Delta L = \varepsilon \cdot L \qquad (8)$$

In the above equation, E is the Young modulus; F_j is the voltage stress (N); is the strain coefficient; L is the length of the object (mm); ΔL is the deformation variable under the effect of electromagnetic force, so the deformation variable of a certain unit under the number of M short-circuit shocks can be obtained as

$$\Delta L = \sum_{m=1}^{M} \Delta L_m = \int \frac{F_j}{E} d \qquad (9)$$

In (9), the quantified relationship between transformer winding deformation and short circuit shocks is determined. It is found that the winding deformation is related to the voltage stress, the number of short circuit shocks and the windings' own performance.

Fig. 1 Schematic of the model

3 Finite Element Simulation Analysis Model of Transformer

3.1 Introduction of the Model

COMSOL is widely used in finite element calculations of mechanics, electromagnetic fields, heat transfer, chemicals, etc. The advantage of the software is that multiple physical fields can be coupled. In this paper, taking advantage of this to build a magnetic -structural coupling field model, as shown in Fig. 1.

It can be seen from Fig. 1 that when the transformer is short-circuited, the winding is deformed. This process includes the electromagnetic and the structural field. Firstly, by applying continuous and equal impulse current for several times, the analysis results of electromagnetic force is obtained in electromagnetic field, then, which is applied the structure field, and the deformation of winding occurs under the action of stress. Therefore, the quantitative description of short circuits times and winding deformation variables can be realized.

3.2 3-D Finite Element Simulation Model of Transformer

In this paper, a COMSOL 3-D finite element simulation model is established with a transformer SFSZ9-40000/110, assuming that the main parameters of the transformer are shown in Table 1.

Table 1 Main parameters of transformer

Internal Components of SFSZ9—40000/110	Main parameter
Core column diameter/mm	650
Iron core distance/mm	1390
High voltage winding (turns/turn; Winding inner, outer radius, winding height/mm)	556; 525.5, 620.5, 1042
Medium voltage winding (turns/turn; Winding inner, outer radius, winding height/mm)	195; 434.5, 496.5, 1042
Low voltage winding (turns/turn; Winding inner, outer radius, winding height/mm)	125; 325.5, 356.5, 1042
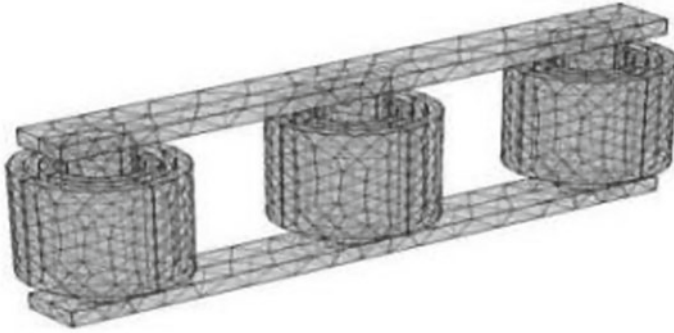
Fig. 2 Grid plan of 3-D finite element model

In order to facilitate the simulation calculations, the assumptions as follows:

Ignoring the influence of leakage magnetic field distribution under the effect of structural components such as transformer internal support, pull plate and clamp on leakage magnetic field distribution.

Ignoring the influence of displacement current which is smaller than short circuit current in transformer.

Ignoring the influence of the eddy current of the iron core and metal structural materials on the magnetic field. The higher harmonics are not considered.

Therefore, the grid plan of 3-D finite element model is shown in Fig. 2.

4   Simulation Results and Analysis of Transformer Short Circuit Shocks

In the case of new energy grid connection, the short-circuit current of 110 kV power system is kept 20 ~ 30 kA [10], when a short-circuit occurs in the power system. Therefore, 2.5 times and 6.5 times the rated short-circuit current are used to simulate the minimum and maximum values of it when the system is short circuit. In order to achieve the simulation, it is assumed that the transformer has to withstand 10 short circuit current shocks. The simulation process of cumulative deformation of windings is shown in Fig. 3.

Based on this, the transformer winding is calculated as the initial state. Regarding it as the initial state under the second short-circuit current shocks, the deformation of the winding is calculated. And so on for the 10 short circuit current shocks, and the deformation of the winding is calculated. Though this process, the cumulative effect of short circuit current impact is simulated.

When the transformer winding is subjected to 10 consecutive short circuit shocks of 2.5 times and 6.5 rated current, the relationship between the number of short circuits and the maximum winding variables is shown in Fig. 4. In the figure, the
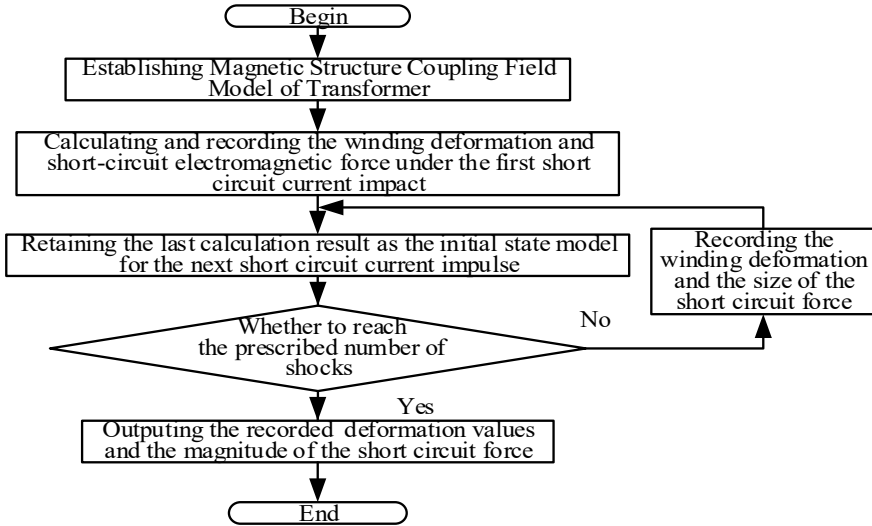
Fig. 3 Simulation of cumulative deformation of windings

black line indicates the accumulation of deformation in the high voltage winding, the red line is medium voltage, and the green line is low voltage.

It can be seen from above that the winding deformation increases with the accumulation of cumulative the number of shocks. When the winding experiences 4 shocks, the deformation of the middle and low voltage winding more obviously change. After 10 shocks, the deformation of the low voltage winding of 6.5 times reaches 10 cm, Its deformation is twice as high as that of 2.5 times. Moreover, deformation of the low voltage winding is significantly higher than those of the medium and high voltage. It is found that the transformer's ability to withstand short-circuit shocks gradually decreases with the accumulation of the number of shocks.

The winding deformation of winding under the impact of single 2.5 times and single 6.5 rated current is simulated, as shown in Fig. 5. In the figure, three bar graphs

(a) 10 times 2.5 times rated current   (b) 10 times 6.5 times rated current
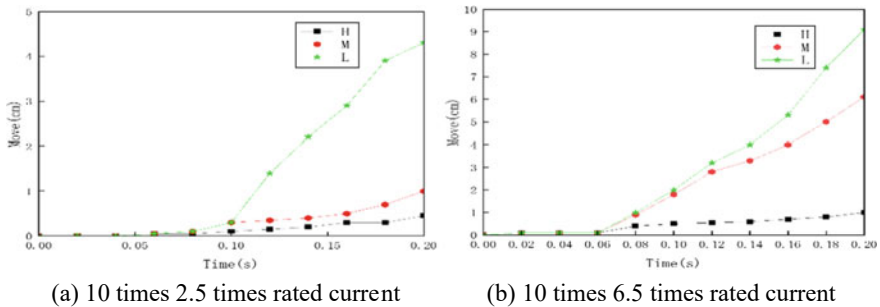
Fig. 4 Comparison of deformation conditions under different shocks

(a) single 2.5 times rated current   (b) single 6.5 times rated current
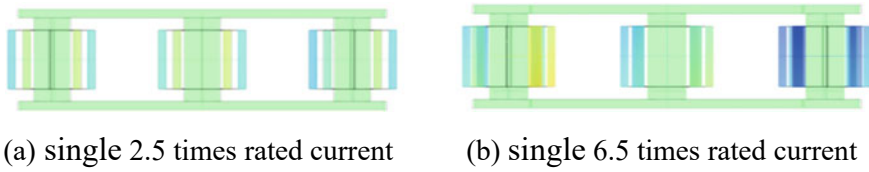
Fig. 5 Comparison of transformer model deformation conditions under different shocks

from left to right, indicate high voltage winding, medium and low. The light green color of the simulation graph means that no deformation, the darker of blue color means that the larger deformation, and the more area of the blue means that the larger area of the deformation.

As can be seen from figures and Eq. (9), show that the higher short circuit impulse current in the electromagnetic field leads to higher electromagnetic force and structural stress, resulting in the larger deformation. If the maximum stress exceeds the limit that the winding can bear, it will breakdown. And the transformer is not short circuit resistant. Therefore, the transformer deformation law is consistent with the theoretical analysis.

5   Conclusion

By deducing the mathematical equation, a definite relationship between short-circuit shocks times and transformer winding deformation is determined. Then, the finite element model of actual transformation parameters is used for simulation, under the same conditions, it is found that the low voltage winding is easier to deform than others and the ability of windings to withstand shocks gradually decreases with the accumulation of the number of shocks. Results shows that the transformer does not have the ability to resist short circuit current shocks, in order to avoid accidents and affect the normal and stable operation of power system. So it is necessary to check its ability to resist short circuit.

References

1. Ge M, Lin SQ, Chang Q et al (2019) Fault diagnosis of large-capacity transformer after short-circuit current surge in near zone. High Voltage Apparatus 55(5):7 (in Chinese)
2. Bali K, Bhalla D (2021) Coupled field method for analyzing short-circuit electromagnetic forces in power transformers. In: Dewan L, Bansal C, Kumar R, Kalla U (eds) Advances in renewable energy and sustainable environment. Lecture notes in electrical engineering, vol 667. Springer, Singapore
3. Li T, Gao SG, Sun L et al (2022) Simulation analysis of multiple short circuits of transformers considering cumulative effect. Hebei Electric Power 41(3):73–7787 (in Chinese)

4. Wang PZ, Wu T, Zhou L, Zhang CX, Wu ZF (2022) Critical transient information detection of transmission line short circuit fault based on FP-growth algorithm. Computer Applications and Software 39(8):99–104 (in Chinese)
5. Kurlaev NV, Ryngach NA, Tagoev FM et al (2021) Investigation of the free expansion of thin-walled tubular parts by pulsed-magnetic field. Journal of Physics Conference Series 1889(4):042047
6. Bao Doan T, Phi Do C (2021) Calculation of the magnetic field and inrush current in a three-phase transformer. In: 2020 applying new technology in green buildings (ATiGB). Da Nang, Vietnam, pp 94–99
7. Du GA, Xu YZ, Lan S, Chen J, Lin Y (2021) Analysis of factors of transformer winding deformation based on magnetic-structural field coupling. Electr Technol 22(1):1–746 (in Chinese)
8. Wang YG, Zhu QL, Shen Y et al (2021) Measurement analysis and judgment of a transformer winding deformation fault. Power Equipment Management 6:4 (in Chinese)
9. Li Z, Hao Z, Yan C et al (2016) Axial stability analysis and simulation of power transformer windings. In: 2016 IEEE PES Asia-Pacific power and energy engineering conference (APPEEC). Xi'an, China, pp 1665–1669
10. Viktorovich KA, Petrovich YY, Aleksandrovich MA (2021) The problem of short-circuit current limitation in energy–saving systems of transportation and electricity distribution. In: 2021 12th international symposium on advanced topics in electrical engineering (ATEE). Bucharest, Romania, pp 1–5

Scramjet Plasma Ignition and Assisted Combustion Technology Review

Qian Zhang, Xiuqian Li, Xueke Che, Tiantian Zhang, Boyuan Deng, Jiaying Ge, Yanghong Wei, and Shaopeng Zhu

Abstract The use of plasma technology to assist scramjet ignition and combustion has been a research hotspot in the field of supersonic propulsion technology. This paper summarizes the main mechanisms of plasma aerodynamic, thermal, and activity effects and their roles in enhanced fuel mixing, ignition, and combustion in scramjets, before reviewing the main research results of plasma technology applied to the above three scramjet stages, focusing on research progress related to different discharge forms of plasma ignition and combustion technologies. Research shows that plasma based on the triggering of aerodynamic disturbances and thermal effects, through interaction with shock waves, control the flow structure to promote the generation of a vortex structure, improve the thickness of the mixing layer, enhance jet instability, to achieve mixing efficiency. The plasma ignition field has matured, with short ignition time delays, flameout limits, and improved ignition efficiency. However, different conditions—such as the nature of the plasma jet working gas and ignition location—can have a considerable impact on the ignition success. Limited by the complexity of the plasma-enhanced combustion research results focused on the description of phenomena and changes in the law, the research mechanism is relatively constrained, but it has been shown to enhance the flame propagation speed, increase flame intensity, suppress combustion oscillations, and improve combustion efficiency. Finally, the difficulties and problems associated with the current research on plasma ignition and enhanced combustion are analyzed.

Keywords Scramjet · Plasma · Ignition and combustion · Flow control

Q. Zhang · X. Li · X. Che (✉) · T. Zhang · B. Deng · J. Ge · Y. Wei · S. Zhu
Space Engineering University, Beijing 101416, China
e-mail: hrche2021@163.com

1 Introduction

Scramjets have been the focus of attention and a research hotspot in the field of aerospace propulsion technology in various countries. They are supersonic and hypersonic power devices with great potential, having the advantages of high flight Mach numbers, no need to carry oxidizers, light weight, low cost, easy manufacturing, and uncomplicated maintenance [1]. However, scramjets still exhibit key technical problems—including insufficient air–fuel mixtures, long ignition delay times, and poor combustion stability [2]—these challenges determining the key research trends in the field of scramjets.

In general, most of the research is dedicated to achieving high-quality mixing of the fuel and incoming flow by changing the fuel injection methods—including coaxial injection with the help of a branch plate [3] and wall transverse jets [4]—or by changing the scramjet configuration—such as by adding ramps [5], steps [6], single cavities [7], double cavities [8], and other structures in the combustor—to achieve flame stabilization and high-efficiency combustion in the scramjet combustor.

To better exploit the working performance of the scramjet, Itsuro Kimura et al. [9] successfully used plasma jets to promote and stabilize combustion in the scramjet for the first time in 1981. To date, a large number of experiments have demonstrated the high research value of applying plasma technology to enhance fuel mixing, ignition performance, and combustion efficiency. This paper reviews the main research results on the application of plasma technology to enhance fuel mixing, ignition, and combustion in scramjets, starting from the mechanism of plasma ignition and combustion, before summarizing the role of plasma aerodynamics, and the thermal and activity effects in the above three stages. Additionally, this paper summarizes the current status of research on the use of plasma to improve mixing efficiency, compares the progress of research on plasma ignition and combustion technology in different discharge forms, and difficulties in the current research process and future research trends that should be embraced are analyzed to provide a reference for further research in the field.

2 Mechanism of Plasma Ignition and Combustion

When a high voltage is applied to a gas, a strong electric field forms, accelerating the electrons in the gas which collide with neutral particles at high speed, exciting the activated gas particles and macroscopically forming a plasma containing electrons, ions, neutral groups, excited-state atoms and molecules, and neutral atoms and molecules [10]. As shown in Fig. 1, based on the form of discharge, plasmas can be classified as arc plasma [11–14] (Fig. 1a, b, c, d), gliding arc plasma [15] (Fig. 1e), dielectric barrier discharge plasma [16] (Fig. 1f), laser plasma [17] (Fig. 1g), free microwave plasma [18] (Fig. 1h), and surface microwave plasma [19] (Fig. 1i) amongst others.
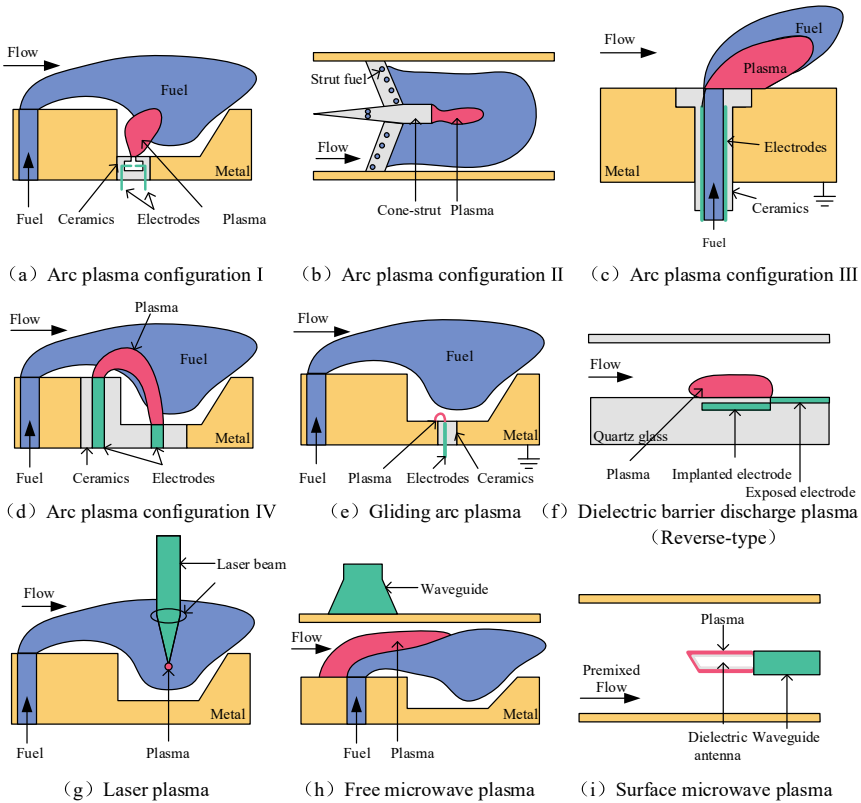
Fig. 1 Common plasma excitation method structure diagram

The green parts shown in Fig. 1 represent the plasma excitation devices, the red parts representing the locations of the initial plasma generation. The arc plasma and gliding arc plasma show filamentary flow discharge patterns when discharging, in which the gliding arc plasma flows with the airflow or periodic movements along the fixed electrode structure; when the arc discharge is generated in the semi-closed insulated cavity, the positive and negative electrodes in the cavity penetrate the air and form a high-temperature and high-pressure gas, which is entrained with the plasma generated by the discharge and ejected from the nozzle at high speed to form a jet, in this paper, this plasma generation method is called a plasma jet, which is used to distinguish it from other arc discharge methods; dielectric barrier discharge plasma excitation devices usually comprise an exposed high-voltage electrode, dielectric blocking layer, and an implanted ground electrode, which generates plasma around the ground electrode and generates induced airflow along the direction from the high-voltage electrode to the ground electrode (based on whether the direction of the induced airflow is the same or different as the incoming flow, the

process can be divided into a forward-type dielectric barrier discharge and reverse-type dielectric barrier discharge [20]); a laser plasma can be used to generate a high energy–density spot at a designated laser position to produce plasma through the air; microwave plasma belongs to the electrode-free discharge, which—based on the form of discharge—can be divided into free microwave plasma and surface microwave plasma, the former discharge using a high-power microwave beam focused in a given area, and the latter being carried out in a tube filled with a gas medium, the electromagnetic energy applied to the system being converted to surface waves, resulting in a further increase in the electron number density.

Plasma shows great potential for aerospace applications, mainly involving flow control, ignition-assisted combustion, stealth, and anti/de-icing. Since academician Li et al. [21] proposed three major mechanisms for plasma flow control, after gradual development and refinement, the current mechanisms when describing it and assisted ignition combustion can be collectively referred to as aerodynamic effects (or transport effects), thermal effects, and activity effects (or chemical kinetic effects).

Plasma aerodynamic effects include kinetic effects, energy impact effects, and physical change effects [22]. Kinetic effects refer to the movements of charged particles in a gas toward an electrode under the action of an applied electric field, resulting in an induced gas flow called "ionic wind". The initiation vortex [23] and subsequent development of wall jets [24] are evident in experiments related to dielectric barrier discharge plasma, where the maximum induced airflow velocity can reach 12 m/s [25]. The energy-shock effect refers to the rapid heating of the gas during the generation of the plasma, which causes a local rapid-expansion induced pressure disturbance, creating a micro-explosion-like shock effect [26] that propagates in the form of acoustic waves. These shock waves/acoustic waves can be used to enhance combustion—such as by controlling thermoacoustic instability [27]. However, shock waves that are too strong can also destabilize combustion. The physical change effect is due to phenomena such as interaction forces and inelastic collisions in the plasma, which macroscopically change the physical parameters—such as the fluid viscosity and frictional shear stress—subsequently having an effect on the flow field. Charged particles in the plasma are accelerated under the action of the applied electric field and collide with neutral particles, so that the internal energy of neutral particles increases and the temperature rises; high-energy electrons collide with atoms which then enter an excited state, an increase in their number also causing the temperature to rise, macroscopically manifesting as a large quantity of heat released from the plasma. Two thermal mechanisms of action exist in plasma [28]—that is, uniform and non-uniform heating of the gas caused by atomic thermal energetics, vibrations, and electron energy relaxation. Among them, homogeneous heating accelerates chemical reactions and inhomogeneous heating generates gas stream perturbations, which can promote increased turbulence and enhanced mixing effects. Although the thermal effect can effectively shorten ignition delay times and enhance combustion, it is not a case of "the stronger the better"—for example, the gas temperature in the arc discharge plasma channel can reach 5000–6000 K [29], far exceeding the temperature required for complete combustion and potentially causing unnecessary energy

waste; moreover, the large quantities of nitrogen oxides produced also cause air pollution; too high a temperature also produces electrode ablation problems, shortening the life of the igniter. By controlling the current in the plasma channel, the plasma thermal effect can be improved to avoid the generation of excessively high temperatures [30]. During the activity effect, the charged particles generated by the plasma further collide with neutral particles thus dissociating active radicals and producing long-lived active substances and catalytic intermediates, such as ozone. The large number of reactive particles and radicals in plasma can create alternative reaction paths and shorten the chain reaction time during assisted ignition and combustion. Such reaction pathway changes allow the activation energy to decrease, increasing the reaction rate by multiple orders of magnitude [31], resulting in more rapid ignition, combustion processes, and flame propagation [32].

The above three mechanisms influence and couple with one another to greatly reduce the ignition delay time, broadening the ignition boundary and extinction limit during ignition; and increase the flame propagation speed, expand the combustion boundary, enhance the combustion stability [33, 34], reduce the blow-out limit [35], and enhance the heat release rate and combustion efficiency [36] during enhanced combustion. However, experiments often require decoupling analysis to study the effect of a particular mechanism on the results, requiring some means of suppressing effects that are not within the scope of interest.

For example, aerodynamic effects caused by the "ionic wind" can be suppressed by applying ultrashort pulses; thermal effects can be greatly reduced by adding a dielectric barrier layer to avoid the formation of an arc through the dielectric; thermal effects can also be suppressed by limiting the current in the discharge channel, although it can be difficult to measure as the inhomogeneity of the temperature during the combustion process cannot be completely excluded [30]. A precise and effective decoupling process in the experiment can better demonstrate the impact of each plasma effect, playing a key role in the study of plasma mechanisms. For the convenience of readers, an overview of the experimental conditions related to ignition and enhanced combustion is summarized in Table 1. A preliminary analysis shows that current experiments have generally been conducted in the Mach 2–3 range, where the fuel cannot be spontaneously ignited and requires forced ignition. Moreover, the fuels are mostly simple compounds such as gaseous hydrogen or ethylene, and there are few liquid fuels. The energy consumption of different plasma excitation methods varies greatly, with DC arc plasma discharge and surface microwave plasma discharge methods requiring considerably more power—which can reach tens of kilowatts—while nanosecond pulse plasma discharge and dielectric blocking plasma discharge methods consume only tens of watts of power.

Table 1 Overview of the main experimental conditions

Plasma generation method	Plasma jet			Plasma jet + DBD	Arc plasma		
Research unit	South Korea Seoul National University [6]	China Harbin Institute of Technology [12, 37]	China Space Engineering University [11]	Japan Tohoku University [38, 39]	Joint Institute for High Temperatures of the Russian Academy of Sciences [13, 14, 40–44]	Russia Moscow State University [45]	United States Stanford University [46]
Plasma Power (kW) Energy (mJ)	2.49 kW	/	/	DBD 0.0041–0.01 kW Plasma jet 1.75–4.05 kW	3–18.6 kW	/	0.01–0.02 kW
Incoming flow rate (Ma)	2	2.8–3	1.8	2	1.436^* – 2	1.8	1.7–2.4
Total pressure (MPa)	0.0993	1.15	0.55	Atmospheric pressure	$0.0678–0.2607^*$	0.1–0.6	0.016–0.025
Total temperature (K)	292	1680	800	Room temperature	300–750	175	900–1300
Fuel	Hydrogen	Kerosene	Methane/ Ethylene	Hydrogen/ Ethylene	Ethylene/Hydrogen Hydrogen + Ethylene	Propane	Hydrogen + Ethylene

Table 1 (continued)

Plasma generation method	Gliding arc plasma	Multichannel plasma	Rail type electric discharge	Laser plasma			Surface microwave plasma	Microwave/microwave + gliding arc plasma
Research unit	China National University of Defense Technology [15, 47–52]	China Air Force Engineering University [53]	United States University of Notre Dame [54]	United States Air Force Research Laboratory [55, 56] University of Illinois at Urbana-Champaign [57]	China National University of Defense Technology [17, 58–61]	China National University of Defense Technology [62]	Russia Moscow State University [19, 63, 64]	China University of Chinese Academy of Sciences [18, 65]
Plasma Power (kW) Energy (mJ)	Gliding arc plasma 0.2–1.199 kW Multi-channel gliding arc plasma 1.196–1.824 kW	1680 mJ (Five-channel)	8–10 kW (Three electrode rail)	100 mJ	200–300 mJ	960 mJ	35–70 kW	Microwave 0.5–1 kW Gliding arc Plasma 0.1028 kW

(continued)

Table 1 (continued)

Plasma generation method	Gliding arc plasma	Multichannel plasma	Rail type electric discharge	Laser plasma			Surface microwave plasma	Microwave/microwave + gliding arc plasma
Research unit	China National University of Defense Technology [15, 47–52]	China Air Force Engineering University [53]	United States University of Notre Dame [54]	United States Air Force Research Laboratory [55, 56] University of Illinois at Urbana-Champaign [57]	China National University of Defense Technology [17, 58–61]	China National University of Defense Technology [62]	Russia Moscow State University [19, 63, 64]	China University of Chinese Academy of Sciences [18, 65]
Incoming flow rate (Ma)	2.52–2.92	2.52	2	2	2.52–2.92	2.1	2	2.5
Total pressure (MPa)	1.65–2.6	1.6	0.1–0.32	0.483	2.6	0.65	0.15	1.55
Total temperature (K)	1550–1650	1600	295–750	590–600	1530–1650	947	/	1249
Fuel	Ethylene	Ethylene	Ethylene	Ethylene	Ethylene	Ethylene	Propane	Ethylene

*Note: Data converted from $\frac{P_0}{P} = \left(1 + \frac{\kappa-1}{2} M_a^2\right)^{\frac{\kappa}{\kappa-1}}$, $Ma = \frac{V}{a}$

3 Plasma-Promoted Fuel Mixing

The current research on the application of plasma technology in scramjets primarily involves the ignition and combustion processes. In experimental studies, because of the overlap of the mixing-ignition-combustion time scale, the large-scale dithering of the flame itself and the mixing situation are coupled together, placing certain requirements on the decoupling analysis of the experimental results. Consequently, there are relatively few experimental studies on combustion for the mixing effect, although enhancing the mixing performance of the fuel and incoming flow has been an important means of improving the combustion efficiency. Common enhanced mixing methods in scramjets include passive methods—such as the addition of ramps, struts, tower structures, and concave cavities—and active methods—such as pulsating jets, Holmz resonators, and acoustic excitation [66, 67]. Passive methods in which components intrude into the flow field subject the combustion chamber to higher heat loads, and changing the combustor configuration can cause additional total pressure loss. Consequently, active mixing enhancement techniques are gradually gaining attention, although traditional active mixing enhancement techniques do have disadvantages—such as slow response and low energy. The plasma active flow control technique is used mostly for boosting and reducing resistance, and suppressing boundary layer separation, although recent studies have shown that it can also be used as an effective means of enhanced mixing [16].

Plasma can directly affect the flow field structure through aerodynamic and thermal effects [68, 69]. For example, the thermal effect generates a vortex similar to a Kármán vortex street to promote the mixing effect [70]. The pneumatic effect, on the other hand, releases a shock wave at the moment of plasma generation, which can affect the flow field and its structures—such as the shock wave, boundary layer, and reflow zone. First of all, the shock wave is one of the most important flow-field structures in the scramjet, contributing to the prolongation of the fuel-residence time in the supersonic flow [71]. When the shock wave acts downstream of the fuel jet, it can promote the mixing of the fuel with the incoming flow [72, 73]. By applying plasma, the shock wave can be made to act at locations more favorable for mixing, while influencing the size of the reflux zone and providing a favorable environment for subsequent steady combustion [74]. Secondly, for a scramjet with flame stabilization by means of a cavity, the use of turbulence to carry the fuel and flame from the shear layer into the concave cavity reflux zone is crucial for flame propagation and flame stabilization. Enhancing the mass exchange between the shear layer and the concave cavity reflux zone can improve ignition capability and promote flame propagation [58]. Active control of the shock wave using plasma allows more fuel to be brought into the cavity, boosting the pressure in the cavity [75]. Additionally, the Richtmyer–Meshkov instability induced by the plasma can indirectly affect the mixing [76].

There are not many teams conducting research on the effect of plasma-promoted mixing at supersonic velocities; the Institute of High Temperature Research of the Russian Academy of Sciences and the University of Notre Dame (United States)

have conducted a large number of experiments around the direction of the arc plasma; the National University of Defense Technology (China) has conducted research on plasma synthesis jets to enhance mixing; Northwestern Polytechnical University (China) has focused on the use of laser plasma to promote mixing; the Space Engineering University (China) has focused on the study of media blocking discharge to enhance mixing.

Leonov's team, who worked at the Institute of High Temperature of the Russian Academy of Sciences and the University of Notre Dame, conducted a systematic study of DC arc plasma for mixing. In terms of the discharge effect, a high-voltage sub-microsecond discharge with a fast turbulent expansion effect was evident [77–79]. The small-scale aerodynamic disturbances triggered at 50 μs after the discharge channel was established continuously amplified the diffusion laterally and improved the mixing effect in multicomponent flows with little total pressure loss caused. In terms of the effect on supersonic transverse jets, the arc plasma can induce the generation of a shock wave and interact with it in the flow field, change the position of the shock wave string in the flow field, or attenuate the downstream reflected shock wave [69], resulting in considerable changes in the pressure distribution in the combustor and achieving active control of the supersonic flow field by the plasma and promoting mixing [80]. Additionally, the team proposed an injection device that coupled the arc plasma to the fuel nozzle [70] (Fig. 1c) and found that compared to the case where the plasma was placed in front of and behind the fuel nozzle [81], the plasma changed the barrel shock wave and Mach disk structure when generated inside the fuel nozzle, leading to an increase in the jet penetration depth and ultimately improving the fuel mixing effect [82]. Additionally, the team experimentally confirmed that the arc plasma located inside the concave cavity could likewise enhance the turbulence of the fuel and improve the mixing effect [83].

The plasma synthetic jet exciter can generate a high-speed jet close to 600 m/s [84] with high penetration capability, which is an active flow control device with obvious advantages. Liu et al. [11] and Zhong et al. [85] observed that the shear interaction between the plasma jet and the main stream in a supersonic transverse jet experiment formed a large-scale vortex structure, and the resulting coiled suction contributed to mixing. The same experimental phenomenon was found by Wang et al. [86] at the National University of Defense Technology, where the plasma jet effectively increased the thickness of the mixing layer and could act up to eight times the distance of the jet diameter in the spreading range.

Liu et al. [87, 88] from Northwestern Polytechnic University found that when a high-frequency pulsed-laser plasma was applied at the center (downstream) of a parallel jet, the laser released heat with oblique excitation waves, which formed a series of large-scale vortex ring structures downstream of the jet, the vortex-ring suction effect caused by the large-scale vortex generated and local energy deposition area enhancing the mixing ability—that is, the increase of turbulent kinetic energy enhanced the longitudinal thickness of the jet by more than 30%, and the local mixing efficiency increased exponentially, although the total pressure loss caused was just 0.16%. Meanwhile, when the injection Mach number (Ma = 1.05) was low, the laser

plasma located above the jet nozzle was better able to induce the formation of a large-scale vortex ring structure; while at a high injection Mach number (Ma = 1.76), the laser plasma located at the center of the jet nozzle was better able to enhance mixing [89].

A series of dielectric barrier discharge plasma-enhanced jet mixing studies were conducted by the Space Engineering University Che et al. Firstly, the plasma control effects on a single-stranded jet of a DC-impinging nozzle and double-stranded jet of a shear nozzle under two excitation modes of forward and reverse surface dielectric barrier discharge were examined [16, 90–92]. It was evident from the large vortex simulations that the inverse type exciter was more likely to generate vortex structures and promote jet instability by interfering with the shear layer of the jet in the inverse direction. The inverse type exciter was found to have a stronger control effect than the forward-type exciter, which was able to greatly increase the range of influence of the single-strand jet vortices compared to the no-plasma case, increase the double-strand jet width by approximately 66%, shorten the mixing point location by approximately 51%, increase the mixing angle by approximately 72%, and increase the optimal pulse frequency (110 Hz), with the mixing effect being more significant under conditions of optimal pulse frequency (110 Hz) and duty cycle (50–70%). The next focus was on the control effect of two excitation methods—that is, the body dielectric barrier discharge and surface dielectric barrier discharge methods—on the coaxial shear nozzle jet [93, 94]. It was found that the aerodynamic effect produced by the reverse surface-type discharge was stronger than that of the bulk dielectric barrier discharge, increasing the jet turbulence and jet angle (Fig. 2a), extending the premixing zone above the nozzle (Fig. 2b), and better promoting fuel mixing. Finally, it was also evident that the nanosecond pulsed dielectric barrier discharge located at the trailing edge of the concave cavity in the scramjet could greatly improve the concave mass exchange capability and enhance the downstream fuel mixing efficiency [95]. However, further experimental studies are needed to determine how best to use the dielectric barrier discharge to promote the fuel mixing effect at supersonic speeds.

In conclusion, a greater mixing effect means more adequate combustion, the use of plasma to enhance fuel mixing efficiency under supersonic incoming flow proving to be feasible, with space for development. First, we need to study the relevant mechanism problems in depth and clarify the contribution of different action mechanisms to master the core key mechanism and further improve the mixing efficiency; second, for the nanosecond pulse dielectric barrier discharge, gliding arc plasma, and microwave discharge plasma methods, we need to conduct systematic "enhancement of mixing" research to determine the mechanisms and effects.

4 Ignition of Plasma

Conventional spark-plug ignition relies on local gas heating at ignition and subsequent combustion wave propagation to trigger the combustion chain reaction required to achieve ignition, which can result in a long ignition delay. Plasma can use the

(a) Comparison of jet angle variations

(b) Comparison of changes in premixed areas
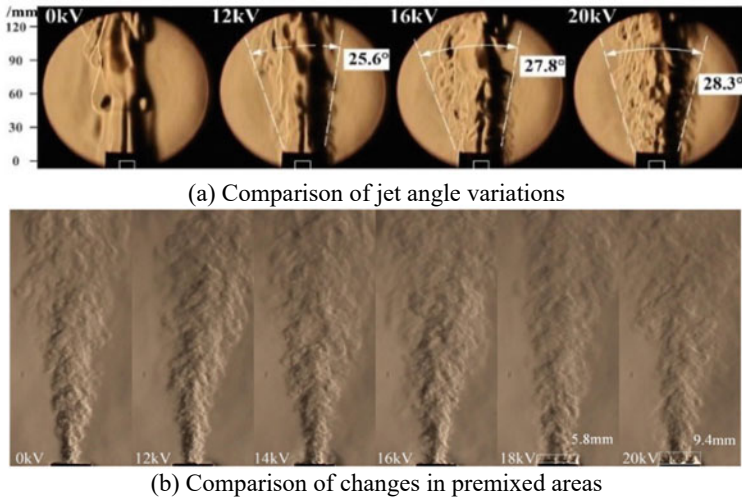
Fig. 2 Air-methane jet ripple image at different excitation voltages during surface-type discharge excitation [93, 94]

combined impact of its active and thermal effects to achieve rapid ignition, and its active effect can form a new reaction path or bypass the original path, contributing more to shortening the ignition delay than the thermal effect [96]; the aerodynamic effect of ionic wind can cause flow-field disturbances, promote fuel mixing, and improve the ignition performance of combustible mixtures, although the impact is minimal.

Although reliable ignition at supersonic velocities can be difficult [2], plasma igniters can achieve reliable ignition at high incoming velocities, under lean combustion, higher air pressure, and lower temperature conditions through multiple mechanisms [97], showing great promise for applications that improve ignition performance. Leonov's team, currently working at the Institute of High Temperature Research of the Russian Academy of Sciences and the University of Notre Dame (United States) has been deeply involved in the area of arc plasma ignition and has conducted systematic experimental research on the subject; Moscow State University (Russia) has focused on microwave discharge plasma and combined plasma ignition; the U.S. Air Force Laboratory has focused on laser-induced plasma ignition in a cavity; Tohoku University (Japan) and Virginia University (United States) have studied combined plasma ignition; and the University of Illinois (United States), Purdue University (United States), and the University of Queensland (Australia) have reported relevant research results. The National University of Defense Technology (China) has conducted a series of experimental studies on gliding arc plasma-assisted concave cavity ignition and laser-induced plasma ignition; the Air Force Engineering University (China) has researched the plasma jet, gliding arc plasma,

and multi-channel surface discharge plasma ignition; the Harbin Institute of Technology (China) has conducted experimental research on plasma jets; and the Space Engineering University (China) has explored the field of gliding arc plasma ignition.

4.1 Plasma Jet Ignition

Plasma jet ignition is one of the most mature plasma ignition methods, exhibiting the advantages of high temperatures, rapid ignition, and large jet-penetration depths. Foreign basic research in this direction was conducted earlier than domestic research, the excellent working performance [98] and high reliability of plasma jet igniters having been proved in several studies [99]. The reliable ignition of kerosene in a scramjet combustor using a central embedded plasma jet at a simulated Mach number of 6 was achieved in China [12] (Fig. 1b), and the effects of fuel injection pressure, fuel mixtures, and different plasma jet media on supersonic ignition characteristics have also been analyzed using numerical simulations, the results showing that high-temperature plasma jet injection into the fuel mixture stream can lead to an enlarged ignition area and higher ignition efficiency [100]. However, it was found that the plasma jet wake using nitrogen or argon as the working gas could have a diluting effect on the fuel concentration after mixing with the incoming flow, affecting the ignition performance [11]. The research into plasma jet ignition is more mature, but weaknesses remain—such as the more complex structure of the jet igniter and the need to provide a specific cooling system for it [101].

4.2 Arc/Gliding Arc Plasma Ignition

Arc and gliding arc plasma ignition form another of the current research hotspots, with systematic experimental studies being conducted by teams both at home and abroad. Among them, the gliding arc plasma has the advantages of both partial equilibrium plasma and nonequilibrium plasma methods, with a stronger approximate field strength, and thermal and activity effects [102], boasting great development potential.

The first secondary ignition experiments conducted at low temperatures in a concave-free cavity scramjet were performed by Leonov's team in the United States using an arc plasma coupled to a fuel nozzle injection device [13]. The plasma was found to be a critical factor for achieving ignition and stable combustion—that is, when the plasma exciter was turned off, the flame was rapidly extinguished [40]. To make the plasma deeper into the mainstream, Firsov et al. [44, 103] proposed a new branch-plate structured arc plasma igniter with the structure shown in Fig. 3, which was experimentally shown to achieve rapid ignition and stable combustion in a smaller input-power and larger fuel-flow range. To improve the conventional arc discharge energy and the number of initial fire nuclei, Huang et al. [53, 104] proposed

a multi-channel surface discharge plasma ignition method and designed a "C"-type igniter with the structure shown in Fig. 4. Experimentally, this igniter was shown to increase the size of the fire nucleus by 150%, reducing the ignition delay time by 50–70%, and expanding the poor ignition boundary by 25% compared to spark plug ignition [105].

Feng et al. of the National University of Defense Technology observed the complete evolution of the gliding arc plasma in the cavity (Fig. 1e) from the generation of the fire nucleus to the formation of the initial flame [15, 52], concluding that the gliding arc igniter at high equivalent ratios could shorten the ignition delay time and bring the flame ignition limit closer to its blow-out limit, while continuous ignition using gliding arc plasma in the cavity could produce better results with lower energy consumption. At Ma = 2.92 and an equivalent ratio of 0.07–0.326, the gliding arc plasma ignition in the cavity can be divided into two modes—that is, the reignition (Fig. 5a, c) and direct ignition modes (Fig. 5b, d) [47]. With a delay
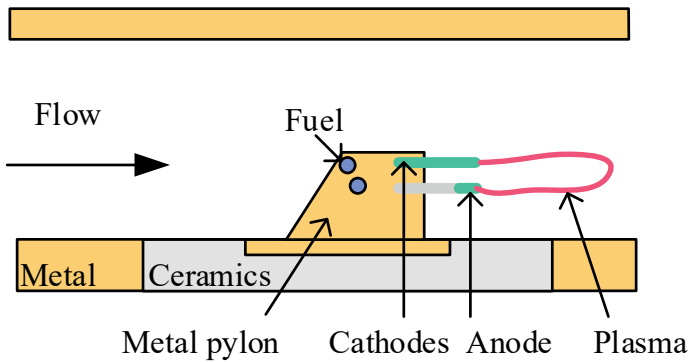
Fig. 3 Structure diagram of arc plasma igniter with pylon structure
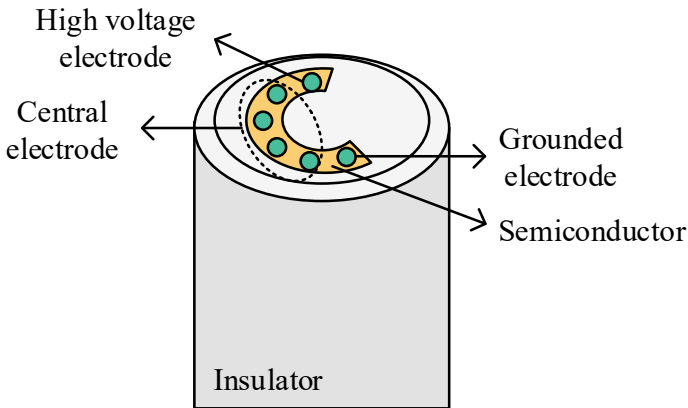
Fig. 4 Structure diagram of multi-channel surface discharge plasma igniter
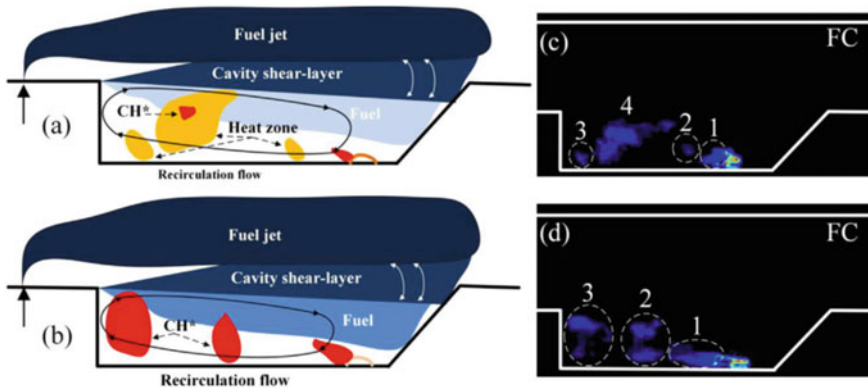
Fig. 5 Mechanism diagram of gliding arc ignition mode in cavity (left) and CH* emission diagram of fire nucleus trajectory (right), **a**, **c** for reignition mode, **b**, **d** for direct ignition mode [47]

time of hundreds of microseconds in the reignition mode, the fire nucleus is unable to generate the initial flame directly and is more likely to occur in localized poor ignition conditions. Compared to the direct ignition mode (with no delay time), the reignition mode achieved a 1.6 times longer flame propagation time and approximately 15% smaller fire nucleus size. Finally, a multi-channel gliding arc igniter comprising multiple gliding arc igniters in parallel could reduce the average power of the plasma discharge, shorten the ignition time by 61%, reduce the flame propagation time by 48%, and generate ozone with a lifetime of approximately 2 ms during ignition, which in turn enhanced combustion [48].

4.3 Laser-Induced Plasma Ignition

Laser-induced plasma ignition has the advantages of precise control of excitation energy, frequency, and ignition position, and does not disturb the flow field due to its non-invasive nature. The laser ignition time is of the order of nanoseconds and there is no bright and blinding light, making it more suitable for academic research and one of the current research hotspots in the field.

The location of the laser-induced point can have a major effect on the ignition characteristics, the common locations of the current induced point being inside the fuel nozzle and inside the cavity. Studies have shown that when the laser-induced point is located inside the fuel nozzle, the laser-induced blast wave interacts with the bow shock wave of the fuel nozzle to produce a localized high temperature, which temporarily forms a flame after ignition which is quickly extinguished and cannot be stabilized [106]. When the laser-induced point is located inside the cavity, the fuel concentration is critical to successful ignition, the optimal ignition conditions being provided by adjusting the ignition position equivalence ratio [57], in addition

to considering the position of the fire nucleus, the initial fire nucleus motion velocity, and the shear force applied [55]. When laser-induced ignition is performed at the front of the cavity, the initial fire nucleus first diffuses along the spreading direction before moving axially to the rear edge of the cavity, gradually igniting the entire cavity [56]; when laser-induced ignition is performed at the middle or rear of the cavity, the initial fire nucleus first moves upstream with the airflow in the cavity [60, 62] to establish the initial flame at its front edge [107], before diffusing from the front edge to the rear edge of the cavity through the shear layer, eventually filling the cavity. By contrast, laser-induced plasma ignition in the rear of the concave cavity is more reliable [59]. Cai et al. observed that under certain conditions, laser-induced plasma ignition in a concave cavity could be divided into weak and strong ignition modes [17], where the weak ignition mode existed only at low equivalent ratios—where the initial fire nucleus was unable to directly ignite the fuel at the rear of the cavity—and the strong ignition mode occurred at higher equivalent ratios—where the initial flame quickly reached stability. On a millisecond time scale, the entire process of laser-induced ignition of the concave cavity can be defined by five phases [58]—namely, the turbulent dissipation, quasi-steady state, combustion enhancement, recovery, and combustion stabilization phases. Additionally, the use of pulsed laser-induced ignition could reduce the total incident laser energy, which is more advantageous compared to single laser-induced ignition, although the larger pulse interval could lead to ignition failure [61]. Laser-induced plasma ignition has obvious advantages, but it also has weaknesses such as high minimum ignition energy, high energy loss due to laser transmission and scattering, and onerous laser requirements [108] only applicable to laboratory conditions at present, limiting its practical usefulness. To further improve its practicality, the system structure needs to be simplified, the costs reduced, and the laser energy and frequency optimized [109].

4.4 Microwave Discharge Plasma Ignition

Microwave discharges can remotely control plasma generation by adding electron beams to the flow field in a directional manner, creating large-volume space discharges [109] with large areas of action. Microwave discharges can also be focused in the supersonic gas stream to avoid the phenomenon of plasma energy diffusion [63]. Consequently, microwave discharge methods have specific application prospects in the field of scramjet ignition. There are several research teams working in this field at home and abroad. Shibkov's team at the Moscow State University have conducted experiments on propane-air ignition using free microwave and surface microwave discharge (Fig. 1i) [19, 63], both of which achieved reliable ignition. In the surface microwave discharge ignition experiments, the ignition occurrence process was recorded in detail, the ignition delay time decreasing from 1 ms to 5 μs as the approximate field strength E/N increased from 40 to 200 Td, the shorter ignition delay time and high flame propagation speed being indicative of its research value.

4.5 *Multi-point and Combined Plasma Ignition*

In early fundamental experiments, plasma multipoint ignition has been shown to shorten the ignition time and achieve stable combustion more rapidly than single-point ignition methods [110, 111], a combined scheme using dielectric barrier discharge plasma-assisted laser plasma ignition being shown to further broaden the ignition boundary [112]. Consequently, to enhance ignition performance and reduce the plasma power in supersonic incoming flow, multipoint plasma ignition and combined plasma ignition schemes in scramjets are being increasingly proposed, although they are still in the early stages of development. Macheret et al. [113] of Purdue University proposed the idea of multipoint ignition using subcritical microwave discharge and dual-laser pulse ignition. Yang et al. [60] also suggested that laser-induced plasma multipoint ignition had great potential for scramjet applications. Combined plasma ignition research has mainly focused on combined microwave-DC discharge [63], combined plasma jet-dielectric barrier discharge [38], and combined laser-microwave [113] applications, but there are fewer related reports which need to be explored in more depth.

In summary, plasma ignition in scramjets can effectively shorten ignition delays, improve ignition efficiency, and broaden the ignition range, although different forms of plasma exhibit different ignition performance, among which the plasma jet ignition system and related results are more mature, having achieved reliable ignition of liquid kerosene fuel in scramjets. However, in the choice of working gas for the plasma jet igniter, if nitrogen or argon is used, it could have a negative effect on ignition performance. Arc plasma and microwave discharge plasma can achieve reliable ignition, but the excitation power is extremely high compared with other methods, which is not conducive to energy saving and environmental protection. Gliding arc plasma ignition and laser-induced plasma ignition are the hot spots of current research, both of them producing initial fire nuclei able to move with the flow field, gradually developing to stable combustion. However, one needs to consider the appropriate ignition position, otherwise, ignition failure can easily occur. Multipoint and combined plasma ignition interaction mechanisms and flow field variations are more complex, but the diversity of discharge types can change the relationships between different plasma action mechanisms, allowing combined plasma discharges to produce better ignition performance. The actual scramjet combustor is mostly a high-pressure environment, the plasma ignition efficiency decreasing with increasing pressure [114]. Consequently, further research needs to be conducted on how to improve the plasma ignition performance under high pressure. Moreover, the problems of energy consumption and igniter ablation loss due to high plasma excitation power, and the complexity of the plasma ignition system, also needs to be explored in depth.

5 Plasma-Enhanced Combustion

During combustion, all three major effects of plasma enhance combustion—where the aerodynamic effect increases the degree of turbulent pulsation of airflow in the combustor—facilitate flame surface expansion; the activity effect can accelerate the combustion process, and oxygen atoms [115], hydrogen atoms [116], and OH* [117] generated by plasma in different gas mixtures have also been shown to enhance combustion; plasma can also enhance combustion through its thermal effect, since the flame heat release rate can be controlled by high-temperature chain branching processes, while the activation energy of this type of reaction also largely determines the overall activation energy [102]. However, there are many complex action mechanisms between the plasma and flame, these effects being coupled with one another, adding to the complexity of explaining the mechanism of plasma-enhanced combustion. Consequently, there is no unified opinion on the magnitude of the role of each plasma effect in enhanced combustion. Zhou et al. and Chen et al. of the Space Engineering University experimentally examined the effect of dielectric barrier discharge plasma on the flame characteristics of coaxial shear diffusion combustion under different combustion conditions and found that the plasma aerodynamic effect could significantly expand the jet angle [118], the activity effect could increase the downstream heat release rate and improve combustion efficiency [119], while the thermal effect caused a temperature increment not exceeding 50 K [120]. Consequently, the aerodynamic and chemical effects of the dielectric barrier discharge plasma can be said to simultaneously enhance and stabilize combustion, and the role of thermal effects can be neglected. The nature of plasma varies widely among different discharge forms, and the core mechanism of enhanced combustion may differ for arc plasma and microwave plasma with higher excitation power, which needs to be explored.

In scramjets, it has been shown that stable combustion cannot be achieved within a smooth-walled scramjet without a cavity structure [64, 121], which provides a high-temperature, low-velocity reflux zone in which the flame can develop stably. The concave cavity structure is by far the most common flame stabilizer, but it can generate reflux resistance, increasing pressure drop losses, and reducing engine thrust performance. Some experiments have confirmed that scramjets with and without concave cavity structures maintain similar combustion patterns during the combustion process [40, 122], providing a basis for further research to examine the use of plasma instead of concave cavity structures for better scramjet performance. In a scramjet without a concave cavity structure, the plasma increases the pressure in the combustion zone, leading to the separation of the attached layers at the walls and inducing the generation of compression waves and high-temperature and pressure zones to form a stable combustion region [37].

Currently, Leonov's team in the United States focuses on the effect of arc plasma-assisted combustion in scramjets with and without cavity structures; the Moscow State University (Russia) focuses on microwave plasma-assisted combustion; and Tohoku University (Japan) focuses on the field of combined plasma jet-dielectric

barrier discharge plasma-assisted combustion. Additionally, Stanford University (United States), the University of Arizona (United States), and the Korea Seoul National University have also conducted relevant research. Domestically, the Air Force Engineering University and National University of Defense Technology focus on gliding arc plasma-assisted combustion, the Harbin Institute of Technology focuses on the field of branched plate plasma jets; the University of Chinese Academy of Sciences is conducting research related to microwave plasma-assisted combustion, and the Space Engineering University has explored dielectric barrier discharge and gliding arc plasma-assisted combustion.

5.1 Plasma Jet Enhanced Combustion

Plasma jets have been investigated for auxiliary combustion in scramjets using backward steps [6], cavity stabilizers [123, 124], and cavity-free cavities [37]. Li et al. [37] used strut plasma jets to achieve stable combustion in a cavity-free scramjet, and based on their experimental results, four flame-retention modes—that is, partial oxidation, weak flame, strong flame, and conical pillar flame—were proposed for enhanced combustion using plasma jets. They found that the flame front exothermic rate and flame temperature were the key factors affecting the flame retention mode, which could be controlled using the equivalent ratio and plasma jet flow pressure. Naito et al. [38] and Matsubara et al. [39] investigated enhanced supersonic combustion under the combined effect of plasma jet and dielectric barrier discharge, and showed that the addition of dielectric barrier discharge plasma resulted in a more stable flame for plasma jet-assisted hydrogen combustion and also greatly enhanced the relatively weaker flame, but had less effect on flame enhancement for stable combustion.

5.2 Arc/Gliding Arc Plasma-Enhanced Combustion

The use of arc and gliding arc plasma-assisted supersonic combustion is a hot area of interest in the field and has been studied by many teams in China and abroad. Depending on the combustor configuration, two main types of combustors can be distinguished—that is, those with and without cavities.

In the classical cavity combustor environment, the DC arc plasma in the cavity combustor can enhance the cavity mass exchange rate by more than an order of magnitude, effectively promoting fuel mixing and improving the flame retention capacity of the cavity combustor [125, 126]. In their enhanced combustion process, Leonov et al. [14, 41] suggested that there were two states of "cold" and normal combustion, and only a small volume of fuel was oxidized when "cold" combustion occurred. To further control the flow pattern and pressure distribution in the cavity, Leonov et al. [54] also designed an orbital discharge plasma exciter, as shown in
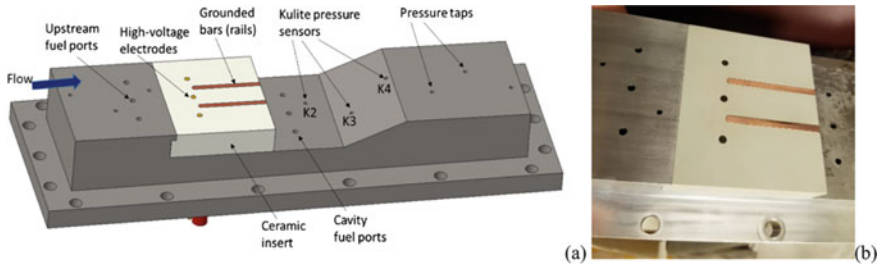
Fig. 6 Combustor structure diagram (**a**) and electrode system physical diagram (**b**) [54]

Fig. 6, the exciter comprising three high-voltage point electrodes and two grounded orbital copper electrodes, the orbital electrodes being used for initial breakdown and guiding the arc connection to the back side of the cavity. Experiments show that the orbital discharge initiation power threshold is lower than that of the DC arc discharge, which is more suitable for cavity ignition and flame retention. However, the effect of gliding arc plasma-enhanced supersonic combustion is not yet fully understood. Feng et al. proposed [52] that the gliding arc plasma in the cavity had certain combustion-assisting and partial flame stabilization effects, but Zhang et al. [50] and Wang et al. [51] both found that it had no combustion-assisting effect or even weakened flame intensity when it was depleted under roughly similar experimental conditions, the reasons for which remain to be investigated. After comparison, the gliding arc plasma excitation powers in the literature [50, 52], and [51] were 1199, 625, and 192 w, respectively, the large differences suggesting that the gliding arc plasma had a more stable enhanced combustion effect at higher excitation powers. Finally, the multi-channel gliding arc plasma could suppress the large-scale oscillations and combustion mode shifts in the cavity under different combustion modes [49].

Stable combustion was also achieved using pulsed DC arc plasma in a smooth-walled combustor environment without a cavity structure [46], with a combustion efficiency of up to 95% [45]. In terms of mechanism studies, Do et al. [46] suggested that it was the free radical source in the plasma that effectively stabilized the flame on the windward and leeward sides of the fuel nozzle on the smooth wall, while Parent et al. [127] suggested that the presence of a reflux zone near the plasma electrode to be the main reason for maintaining the flame. Both attributed the core mechanism of plasma-driven stable combustion to its chemical effect or flow control effect, respectively, giving differing explanations. Regarding combustion modes, Leonov et al. [42, 43] observed three different modes of arc plasma interaction with air and fuel— that is, strong combustion, which leads to a stable flame zone; weak combustion, characterized by a moderate increase in wall pressure, with combustion occurring mainly in the downstream region; and partial oxidation, with a slight increase in wall pressure. The transition between the various modes depends on factors such as plasma power, gas pressure, air temperature and fuel mass flow rate.

5.3 *Microwave Plasma-Enhanced Combustion*

Microwave discharge plasma can enhance the activity and concentration of OH*, CO, and other substances to increase the chemical reaction and combustion rates [128]. Among other things, free microwave discharge plasma can also change the fuel combustion characteristics and flame structure during enhanced combustion [65], so that the flame onset position during combustion is shifted forward to the jet region and the high-intensity flame is concentrated in the jet-stabilized flame region—presumably the plasma affects the flame boundary and turbulent vortex cluster, increasing the turbulent flame speed and resulting in an increase in the overall flame speed. It is evident that the main mechanism of plasma-stabilized enhanced combustion could also contain both its chemical and flow control effects. Additionally, a combination of microwave discharge plasma and gliding arc plasma could be considered for further power reduction [18]. As for surface microwave discharge plasma, it effectively excites molecules and atoms at high energy levels, producing ultraviolet radiation, and causing photoionization of impurity molecules, which can play an important role in enhancing the supersonic combustion of hydrocarbon fuels [19, 129]. However, it has not yet succeeded in stabilizing combustion in experiments without a cavity combustor [64]. Taken together, free microwave discharge plasma performs better in enhanced combustion applications.

In summary, it can be extremely complicated to investigate the plasma-enhanced combustion phenomenon in scramjets under the coupling influence of multiple plasma action mechanisms with high-speed flow fields and high-temperature flames. Preliminary studies have been conducted on the stable plasma flame-retention mode with and without a cavity, as well as the effects of different discharge modes and experimental parameters on combustion performance. It has been shown that plasma can achieve stable and enhanced combustion, improve combustion efficiency by increasing flame propagation speed, increasing flame intensity, and expanding the combustion reaction area, while also suppressing large-scale oscillations in different combustion modes and combustion mode shift. However, the mechanism and enhanced combustion mode of action need to be further explored—such as whether the core mechanism of plasma-induced combustion stabilization is its chemical effect, its flow control effect, or the result of a combination of both—as there is still disagreement which needs to be clarified by decoupling experiments. Additionally, as the research progresses, the negative effects of the gliding arc plasma on combustion under lean combustion conditions have also emerged, making it worth paying attention to the causes.

6 Conclusions

This paper summarizes the main research progress of plasma technology applications in scramjets in recent years, briefly reviews the mechanism of plasma action and its role in fuel mixing, ignition, and the enhanced combustion process, and compares the main research results of plasma ignition and combustion based on the discharge form. It can be difficult to conduct continuous experimental research due to the complexity and variability of the research object, the extreme conditions of the research environment, the high requirements for experimental instrumentation and measurement means, and the interdisciplinary integration of the research content. However, the existing research results confirm the enormous potential and application prospects of plasma applications in scramjets, which could play a positive role in the fuel mixing, ignition, and enhanced combustion stages.

In the fuel mixing stage, the plasma relies on properties such as initiating aerodynamic disturbances, promoting the generation of vortex structures, interacting with shock waves, controlling the flow structure near the reaction zone, and thermal effects to effectively mitigate the inadequate mixing caused by the short fuel residence time. In the ignition phase, the most prominent advantage of plasma is the considerable reduction in ignition delay time, which is of particular importance in supersonic and even hypersonic flight conditions. Additional advantages in ignition efficiency, ignition range, and flameout limits also make plasma ignition an increasingly attractive option. In the combustion stage, the core mechanism of plasma-enhanced combustion could include chemical and flow control effects. The properties of flame stabilization, improved combustion efficiency, and suppression of flame oscillation have made plasma-enhanced combustion a hot spot of interest in scramjet research, although the progress of such research has yet to advance much. Overall, the application of plasma technology could improve the operational stability of scramjets, broadening the range of flight conditions, and enabling them to operate under better conditions.

However, there are still many problems that have not yet been clarified. (1) The performance of plasma-enhanced combustion is a comprehensive result of the strong coupling of multiple mechanisms, although a detailed mechanism of action remains to be clarified. For example, in the process of enhanced combustion, how do the three main mechanisms of plasma action affect the combustion process? What is the contribution of each of them? Consequently, to gain more insight into how a certain plasma characteristic works at supersonic velocities, more ingenious ways of decoupling combustion phenomena need to be considered, and more detailed measurement methods need to be developed. The limitations of experimentally obtained data lead to a lack of comprehensive and reliable verification of the current plasma-enhanced combustion mechanisms and numerical simulation results. (2) In experimental studies, plasma exhibits better performance at low temperatures and low pressures, while its chemical kinetic effect weakens at high-temperatures. Moreover, in high-pressure environments, the discharge tends to be non-uniform. Consequently, there is a need to find a better way to generate stable and uniform plasma under high-pressure and high-temperature conditions in an actual combustor for optimal

operation. (3) The fuels studied so far are mostly hydrogen or small-molecule hydrocarbons, there being little experimental data or numerical simulation results related to large-molecule hydrocarbon fuels or even liquid kerosene. The combustor environment is more complicated after a liquid phase is added, and it is not clear whether there is a new mechanism of action. (4) There is a need to consider the too high a plasma power, excessive energy consumption in high-speed flow, ablation, cooling and other issues. Moreover, the introduction of plasma increases the complexity of the system, and whether its excitation method and structure can be implemented in engineering applications or achieve the control accuracy requirements also needs to be considered in depth. The miniaturization and lightweight nature of the plasma power supply is also a research topic requiring attention.

References

1. Das N, Pandey KM, Sharma KK (2021) A brief review on the recent advancement in the field of jet engine—scramjet engine. Materials Today: Proceedings 45(7):6857–6863
2. Seleznev RK, Surzhikov ST, Shang JS (2019) A review of the scramjet experimental data base. Prog Aerosp Sci 106(2019):43–70
3. Yan L, Liao L, Huang W, Li LQ (2018) Nonlinear process in the mode transition in typical strut-based and cavity-strut based scramjet combustors. Acta Astronaut 145(2018):250–262
4. Techer A, Moule Y, Lehnasch G, Mura A (2018) Mixing of fuel jet in supersonic crossflow: estimation of subgrid-scale scalar fluctuations. AIAA J 56(2):465–481
5. Wei BX, Gang Q, Zhang Y, Liu RJ, Tian L, Xu X (2013) A Study on performance comparison of integrated aerodynamic-ramp-injector/ gas-portfire flame holder with cavity. Appl Mech Mater 390(2013):8–11
6. Kim CH, Jeung IS, Choi B, Kouchi T, Takita K, Masuya G (2011) Effect of fuel injection location on a plasma jet assisted combustion with a backward-facing step. Proc Combust Inst 33(2):2375–2382
7. Lakka S, Randive P, Pandey KM (2021) Implication of geometrical configuration of cavity on combustion performance in a strut-based scramjet combustor. Acta Astronaut 178(2021):793–804
8. Wang YH, Song WY, Shi DY (2017) Investigation of flameholding characteristics in a kerosene-fueled scramjet combustor with tandem dual-cavity. Acta Astronaut 140(2017):126–132
9. Kimura I, Aoki H, Kato M (1981) Use of a plasma jet for flame stabilization and promotion of combustion in supersonic air flows. Combust Flame 42(1981):297–305
10. Zhou SY (2018) Studies of non-equilibrium plasma assisted combustion and its applications in aerospace propulsion systems. Space Engineering University (in Chinese)
11. Liu Y, Dou ZG, Yang B, Zhang P (2017) Experimental investigation on ignition of ethylene/air by plasma jet in supersonic combustor. Journal of propulsion technology 38(07):1532–1538 (in Chinese)
12. Tang JF, Xiang AD, Li J, Xie ZQ, Bao W, Yu DR (2021) Experimental study on plasma jet enhanced ignition in no-cavity supersonic combustor. Journal of propulsion Technology 42(11):2531–2537 (in Chinese)

13. Leonov SB, Houpt A, Hedlund B (2017) Experimental demonstration of plasma-based flame-holder in a model scramjet. In: AIAA (ed) 21st AIAA international space planes and hyper-sonics technologies conference. American Institute of Aeronautics and Astronautics Inc., AIAA, Xiamen, China

14. Leonov S, Savelkin C, Yarantsev D, Carter C, Sermanov V, Starodubtsev M (2008) Experiments on plasma-assisted combustion in M = 2 hot test-bed PWT-50H. In: AIAA (ed) 46th AIAA aerospace sciences meeting and exhibit. AIAA International, Reno, Nevada

15. Feng R, Zhu JJ, Wang ZG, Sun MB, Wang HB, Cai Z, Yan W (2020) Dynamic characteristics of a gliding arc plasma-assisted ignition in a cavity-based scramjet combustor. Acta Astronaut 171(20):238–244

16. Che XK, Li XQ, Li J, Ning YJ, Chen QY, Chen C, Wang HT (2021) Experimental investigation on improving mixing performance of two-rectangle jet by SDBD plasma. Physics of Gases 6(02):53–63 (in Chinese)

17. Cai Z, Zhu JJ, Sun MB, Wang ZG, Bai XS (2018) Ignition processes and modes excited by laser-induced plasma in a cavity-based supersonic combustor. Appl Energy 228(2018):1777–1782

18. Meng Y, Gu HB, Sun WM, Zhang XY (2020) Microwave enhanced gliding arc plasma assisted supersonic combustion. Acta Aeronautica et Astronautica Sinica 41(02):124–131 (in Chinese)

19. Shibkov VM, Shibkova LV, Gromov VG, Karachev AA, Konstantinovskii RS (2011) Influence of surface microwave discharge on ignition of high-speed propane-air flows. High Temp 49(2):155–167

20. Fedorov AV, Krivtsov VM, Soloviev VR, Soudakov VG (2011) Modeling of Aerodynamic forcing induced by surface dielectric barrier discharge. In: 49th AIAA aerospace sciences meeting including the new horizons forum and aerospace exposition

21. Li Y H, Wu Y, Song H M, Zhang P (2006) Research progress and mechanism of plasma flow control. In: Proceedings of the sixth annual power conference (in Chinese)

22. Che XK (2018) Plasma flow control and assisted combustion. Science Press, Beijing (in Chinese)

23. Cheng YF, Nie WS, Che XK, Tian XH, Hou ZY, Hui ZP (2013) Experimental investigation on the evolution of dielectric barrier discharge plasma induced flow at different operating pressures. Acta Phys Sin 62(10):295–302 (in Chinese)

24. Yun W, Hong LY, Min J (2010) Experimental investigation into characteristics of plasma aero-dynamic actuation generated by dielectric barrier discharge. Chin J Aeronaut 23(2010):39–45

25. Thomas FO, Corke TC, Duong A, Midya S, Yates K (2019) Turbulent drag reduction using pulsed-DC plasma actuation. J Phys D Appl Phys 52(43):434001

26. Che XK, Shao T, Nie WS, Yan P (2012) Numerical simulation on a nanosecond-pulse surface dielectric barrier discharge actuator in near space. J Phys D Appl Phys 45(14):145201

27. Bölke O, Lacoste DA, Moeck JP (2018) Low-frequency sound generation by modulated repetitively pulsed nanosecond plasma discharges. J Phys D Appl Phys 51(30):305203

28. Starikovskiy A (2015) Physics and chemistry of plasma-assisted combustion. Philosophical Transactions of the Royal Society A: Mathematical, Physical and Engineering Sciences 373(2048):20150074

29. Jacobsen LS, Carter CD, Jackson TA, Williams S, Barnett J, Bivolaru D, Kuo S, Tam C-J, Baurle RA (2008) Plasma-assisted ignition in scramjets. J Propul Power 24(4):641–654

30. Starikovskaia S, Lacoste DA, Colonna G (2021) Non-equilibrium plasma for ignition and combustion enhancement. The European Physical Journal D 75(8)

31. Ban YY, Zhang F, Zhong SH, Zhu JJ (2022) Numerical simulation of AC discharge plasma assisted ethylene/air combustion. Chinese Internal Combustion Engine Engineering 43(01):58–66 (in Chinese)

32. Zheng Z, Nie WS, Wu HL, Che XK (2019) Influence of plasma chemical kinetic effects on hydrogen combustion in a scramjet combustor. Journal of Propulsion Technology 40(01):151–157 (in Chinese)

33. Lacoste DA, Moeck JP, Durox D, Laux CO, Schuller T (2013) Effect of nanosecond repetitively pulsed discharges on the dynamics of a swirl-stabilized lean premixed flame. J Eng Gas Turbines Power 135(10):1–7

34. Moeck J, Lacoste D, Laux C, Paschereit C (2013) Control of combustion dynamics in a swirl-stabilized combustor with nanosecond repetitively pulsed discharges. In: AIAA (ed) 51st AIAA aerospace sciences meeting including the new horizons forum and aerospace exposition. American Institute of Aeronautics and Astronautics Inc., Grapevine, Texas

35. Barbosa S, Pilla G, Lacoste DA, Scouflaire P, Ducruix S, Laux CO, Veynante D (2015) Influence of nanosecond repetitively pulsed discharges on the stability of a swirled propane/air burner representative of an aeronautical combustor. Philos Trans A Math Phys Eng Sci 373(2048)

36. Pilla G, Galley D, Lacoste DA, Lacas F, Veynante D, Laux CO (2006) Stabilization of a turbulent premixed flame using a nanosecond repetitively pulsed plasma. IEEE Trans Plasma Sci 34(6):2471–2477

37. Li J, Tang JF, Zhang JL, Zhu XM, Zhang HR, Bao W, Yu DR (2021) Flame establishment and flameholding modes spontaneous transformation in kerosene axisymmetric supersonic combustor with a plasma igniter. Aerospace Science and Technology 119(2021)

38. Naito M, Matsubara Y (2012) Ignition of hydrogen and hydrocarbon in a supersonic flow by simultaneous operation of DBD and PJ. In: 18th AIAA/3AF international space planes and hypersonic systems and technologies conference

39. Matsubara Y, Takita K, Masuya G (2013) Combustion enhancement in a supersonic flow by simultaneous operation of DBD and plasma jet. Proc Combust Inst 34(2):3287–3294

40. Houpt A, Elliott S, Leonov SB (2019) Cold start-up and plasma-based flameholding in model scramjet. In: AIAA (ed) AIAA propulsion and energy 2019 forum. American Institute of Aeronautics and Astronautics Inc., AIAA, Indianapolis, IN

41. Leonov SB, Yarantsev DA, Napartovich AP, Kochetov IV (2007) Plasma-assisted chemistry in high-speed flow. Plasma Sci Technol 9(6):760–765

42. Leonov S, Yarantsev D, Sabelnikov V (2011) Electrically driven combustion near the plane wall in a supersonic duct. Progress in Propulsion Physics 2(2011):519–530

43. Leonov S, Houpt A, Elliott S, Hedlund B (2018) Ethylene ignition and flameholding by electrical discharge in supersonic combustor. J Propul Power 34(2):499–509

44. Firsov AA, Kolosov NS (2021) Combustion in a supersonic flow using a pylon equipped with a plasma actuator. J Phys: Conf Ser 2100(2021):012017

45. Shibkov VM, Shibkova LV, Kopyl PV, Logunov AA (2019) Stabilization of supersonic combustion of propane in an expanding aerodynamic channel with the use of low-temperature plasma. High Temp 57(2):164–176

46. Do H, Im S-K, Cappelli MA, Mungal MG (2010) Plasma assisted flame ignition of supersonic flows over a flat wall. Combustion and Flame 157(12):2298–2305

47. Feng R, Zhu JJ, Wang ZG, Sun MB, Wang HB, Cai Z, An B, Li L (2021) Ignition modes of a cavity-based scramjet combustor by a gliding arc plasma. Energy 214(2021):118875

48. Feng R, Huang YH, Zhu JJ, Wang ZG, Sun MB, Wang HB, Cai Z (2021) Ignition and combustion enhancement in a cavity-based supersonic combustor by a multi-channel gliding arc plasma. Experimental Thermal and Fluid Science 120(2021):110248

49. Feng R, Zhu JJ, Wang ZG, Zhang F, Ban YY, Zhao GY, Tian YF, Wang CL, Wang HB, Cai Z et al (2022) Suppression of combustion mode transitions in a hydrogen-fueled scramjet combustor by a multi-channel gliding arc plasma. Combust Flame 237(2022):111843

50. Zhang CY, Feng R, Zhu JJ, Sun MB, Wang HB, Cai Z (2021) Experimental investigation on gliding arc plasma-assisted combustion in the supersonic flow. Journal of Solid Rocket Technology 44(02):160–165 (in Chinese)

51. Wang WZ, Jia M, Feng R, Zhu JJ (2020) Experimental investigation on the gliding arc plasma supported combustion in the scramjet combustor. Acta Astronaut 177(2020):133–141

52. Feng R, Li J, Wu Y, Zhu JJ, Song XL, Li XP (2018) Experimental investigation on gliding arc discharge plasma ignition and flame stabilization in scramjet combustor. Aerosp Sci Technol 79(2018):145–153

53. Huang S, Wu Y, Song H, Zhu J, Zhang Z, Song X, Li Y (2018) Experimental investigation of multichannel plasma igniter in a supersonic model combustor. Exp Thermal Fluid Sci 99(2018):315–323

54. Leonov SB, Elliott S, Carter C, Houpt A, Lax P, Ombrello T (2021) Modes of plasma-stabilized combustion in cavity-based M = 2 configuration. Exp Thermal Fluid Sci 124(2021):110355

55. Ombrello T, Carter CD, McGann B, Do H, Peterson DM (2016) Establishing the controlling parameters of ignition in high-speed flow. In: AIAA (ed) AIAA SciTech Forum. San Diego, California, USA

56. Hassan E, Ombrello TM, Peterson DM (2021) Computational and experimental investigation of ignition in a Mach 2 cavity-based flameholder. Aerosp Sci Technol 115(2021):106756

57. McGann B, Carter CD, Ombrello TM, Hammack S, Lee T, Do H (2017) Gas property measurements in a supersonic combustor using nanosecond gated laser-induced breakdown spectroscopy with direct spectrum matching. Proc Combust Inst 36(2):2857–2864

58. Li XP, Liu WD, Pan Y, Yang LC, An B, Zhu JJ (2018) Characterization of ignition transient processes in kerosene-fueled model scramjet engine by dual-pulse laser-induced plasma. Acta Astronaut 144(17):23–29

59. Cai Z, Zhu JJ, Sun MB, Wang ZG, Bai XS (2018) Laser-induced plasma ignition in a cavity-based scramjet combustor. AIAA J 56(12):4884–4892

60. Yang LC, Li XH, Liang JH, Yu X, Li XP (2016) Perspective of laser-induced plasma ignition of hydrocarbon fuel in Scramjet engine. In: Engineering Doiae (ed) Seminar on laser fusion detection and drive energy technology, 979621. Department of Information and Electronic Engineering, Chinese Academy of Engineering, Chengdu, China

61. Yang LC, An B, Li XP, Yu Y, Li XH, Liang JH, Wang Q (2017) Characterization of successive laser induced plasma ignition in an ethylene fuelled model scramjet engine. In: AIAA (ed) International space planes and hypersonic systems and technologies conferences. American Institute of Aeronautics and Astronautics Inc., Xiamen, China

62. Li XP, Liu WD, Pan Y, Yang LC, An B (2017) Experimental investigation on laser-induced plasma ignition of hydrocarbon fuel in scramjet engine at takeover flight conditions. Acta Astronaut 138(2017):79–84

63. Shibkov VM, Aleksandrov AF, Chernikov VA, Ershov AP, Shibkova LV (2009) Microwave and direct-current discharges in high-speed flow: fundamentals and application to ignition. J Propul Power 25(1):123–137

64. Shibkov VM (2019) Ignition and combustion stabilization of multicomponent supersonic chemically active flows in low-temperature plasma conditions. J Phys: Conf Ser 1394(1)

65. Meng Y, Gu HB, Zhang XY (2019) Influence of microwave on structure of supersonic combustion flame. Acta Aeronautica et Astronautica Sinica 40(12):83–91 (in Chinese)

66. Zhang Y, Li CX, Wei BX, Xu X (2014) Review of fuel injection scheme for scramjet. Journal of Propulsion Technology 2014(02):61–67 (in Chinese)

67. Xu ZZ, Wu JP, Huang W, Wang JH, Yan L (2021) Research progress of jet mixing enhancement technology in scramjet engine. Tactical Missile Technology 2021(04):83–102+135 (in Chinese)

68. Houpt AW, Leonov SB, Ombrello T, Carter CD (202) Supersonic cavity flow control by upstream filamentary plasma. In: AIAA (ed) AIAA SciTech forum. American Institute of Aeronautics and Astronautics Inc., Orlando, FL

69. Elliott S, Lax P, Leonov SB (2022) Control of shock positions in a supersonic duct by plasma array. In: AIAA (ed) AIAA SciTech forum. American Institute of Aeronautics and Astronautics Inc, San Diego, CA

70. Savelkin KV, Yarantsev DA, Adamovich IV, Leonov SB (2015) Ignition and flameholding in a supersonic combustor by an electrical discharge combined with a fuel injector. Combust Flame 162(3):825–835

71. Huang W, Wu H, Du ZB, Yan L, Choubey G (2021) Design exploration on the mixing augmentation induced by the oblique shock wave and a novel step in a supersonic flow. Acta Astronaut 180(2021):622–629

72. Shekarian AA, Tabejamaat S, Shoraka Y (2014) Effects of incident shock wave on mixing and flame holding of hydrogen in supersonic air flow. Int J Hydrogen Energy 39(19):10284–10292

73. Schetz JA, Maddalena L, Burger SK (2010) Molecular weight and shock-wave effects on transverse injection in supersonic flow. J Propul Power 26(5):1102–1113

74. Zhou SY, Nie WS, Feng W, Cheng YF (2013) Effect of the arc plasma at upstream of the jet on scramjet combustor's performance. Missiles and Space Vehicles 2013(04):52–55 (in Chinese)

75. Houpt A, Leonov S, Ombrello T, Carter C, Leiweke RJ (2019) Flow control in supersonic-cavity-based airflow by quasi-direct-current electric discharge. AIAA J 57(7):2881–2891

76. Zheltovodov AA, Pimonov EA (2013) Intensification of mixing of parallel compressible flows using a localized pulse-periodic energy supply. Tech Phys Lett 39(11):1016–1018

77. Leonov S, Isaenkov Y, Firsov A, Shurupov M, Yarantsev D, Shneider M (2011) Plasma-based fast mixing and ignition in supersonic combustor. In: AIAA (ed) 17th AIAA international space planes and hypersonic systems and technologies conference. American Institute of Aeronautics and Astronautics Inc., San Francisco, California

78. Firsov AA, Dolgov E, Rakhimov R, Shurupov M, Leonov SB (2018) Mixing enhancement by electrical discharge in supersonic airflow. AIAA Paper

79. Shurupov MA, Leonov SB, Firsov AA, Yarantsev DA, Isaenkov YI (2014) Gasdynamic instabilities during decay of the submicrosecond spark discharge channel. High Temp 52(2):169–178

80. Elliott S, Houpt AW, Leonov SB (2019) Application of optical sensors for flame blow-off prediction in a plasma stabilized scramjet combustor. In: AIAA (ed) AIAA SciTech forum. American Institute of Aeronautics and Astronautics Inc., San Diego, California

81. Firsov A, Savelkin KV, Yarantsev DA, Leonov SB (2015) Plasma-enhanced mixing and flameholding in supersonic flow. Philos Trans A Math Phys Eng Sci 373(2048)

82. Elliott S, Lax P, Leonov SB (2022) Acetone PLIF visualization of mixing processes in a plasma stabilized supersonic combustor. In: AIAA (ed) AIAA SciTech forum. American Institute of Aeronautics and Astronautics Inc., San Diego, CA

83. Leonov SB, Yarantsev DA (2008) Near-surface electrical discharge in supersonic airflow: properties and flow control. J Propul Power 24(6):1168–1181

84. Zhou Y, Luo ZB, Wang L, Xia ZX (2022) Plasma synthetic jet actuator for flow control: review. Acta Aeronautica et Astronautica Sinica 43(03):98–140 (in Chinese)

85. Zhong WL, Xi WX, Duan LW, Xu QY, Li Q (2015) Experimental investigation on plasma torch for supersonic flowfield ignition and combustion. Journal of Propulsion Technology 36(10):1528–1532 (in Chinese)

86. Wang P, Shen CB (2019) Characteristics of mixing enhancement achieved using a pulsed plasma synthetic jet in a supersonic flow. J Zhejiang Univ Sci A 20(9):701–713

87. Liu F, Yan H, Pimonov EA, Zheltovodov AA (2018) Supersonic mixing control by localized pulse-periodic energy deposition. AIP Conf Proc 2036(1):030031–030035

88. Liu F, Yan H, Cao ZY (2022) Study on mixing after supersonic helium jet/shock wave interaction controlled by high frequency laser plasma. In: Sixth joint conference on space dynamics, pp 13–27

89. Liu F, Yan H (2019) Control of supersonic jet interacting with oblique shock by pulsed energy deposition. Journal of Propulsion Technology 40(06):1220–1230 (in Chinese)

90. Li L, Li XQ, Che XK, Zheng TK, Li JL, Nie WS (2018) Study on the influence of incentive parameters on plasma-enhanced jet mixing. Journal of Experiments in Fluid Mechanics 32(5):41–47 (in Chinese)

91. Li L (2018) Study on mechanism of plasma for rectangular turbulent jet, Space Engineering University (in Chinese)

92. Li JL (2017) Study on plasma enhanced jet mixing, Space Engineering University (in Chinese)

93. Chen QY (2020) Studies of non-equilibrium plasma assisted combustion and its applications in rocket combustion chamber, Space Engineering University (in Chinese)

94. Chen C (2020) Experimental study of non-equilibrium plasma controlled methane air counter-diffusion flame, Space Engineering University (in Chinese)

95. Zhou SY, Che XK, Nie WS (2014) Influence of nanosecond pulse dielectric barrier discharge plasma on the cavity performance in scramjet combustor. High Voltage Engineering 40(10):3032–3037 (in Chinese)

96. Wang SB, Yu JL, Cheng WD, Ma Y, Zheng RZ, Huang DQ, Wei QQ (2019) Chemical kinetic analysis of plasma excited methane combustion. Chemical Physics Letters 730:399–406
97. Do H, Cappelli MA, Mungal MG (2010) Plasma assisted cavity flame ignition in supersonic flows. Combust Flame 157(9):1783–1794
98. Wagner TC, O'Brien WF, Northam GB, Eggers JM (1989) Plasma torch igniter for scramjets. J Propul Power 5(5):548–554
99. Bonanos AM, Schetz JA, O'Brien WF, Goyne CP (2008) Dual-mode combustion experiments with an integrated aeroramp-injector/plasma-torch igniter. J Propul Power 24(2):267–273
100. Song ZX, He LM, Zhang JB, Zhao B, Lan YD, Liu XJ (2012) 3D numerical simulation of supersonic plasma ignition process. High Power Laser and Particle Beams 24(11):2746–2750 (in Chinese)
101. Cai Z, Wang TY, Sun MB (2019) Review of cavity ignition in supersonic flows. Acta Astronaut 165(2019):268–286
102. Ju Y, Sun W (2015) Plasma assisted combustion: dynamics and chemistry. Prog Energy Combust Sci 48(2015):21–83
103. Firsov AA, Dolgov EV, Kolosov NS, Yarantsev DA (2020) CFD analysis of pylon equipped by plasma module for combustion in supersonic airflow. J Phys: Conf Ser 1698(1):012014
104. Huang S-F, Song H-M, Wu Y, Jia M, Jin D, Zhang Z-B, Lin B-X (2018) Experimental investigation on electrical characteristics and ignition performance of multichannel plasma igniter. Chin Phys B 27(3):035203
105. Li YH, Wu Y (2020) Research progress and outlook of flow control and combustion control using plasma actuation. SCIENTIA SINICA Technologica 50(10):1252–1273
106. Gibbons N, Gehre R, Brieschenk S, Wheatley V (2018) Simulation of laser-induced plasma ignition in a hypersonic crossflow. AIAA J 56(8):3047–3059
107. Liu CY, Sun MB, Wang HB, Yang LC, An B, Pan Y (2020) Ignition and flame stabilization characteristics in an ethylene-fueled scramjet combustor. Aerosp Sci Technol 106(2020):106186
108. Chen M, Dou ZG, Xi WX (2018) Advances in methods of laser-induced plasma ignition. Laser & Optoelectronics Progress 55(03):030010 (in Chinese)
109. Hong YJ, Xi WX, Li L, Zhang P (2018) Comments on researches of mechanism for plasma assisted combustion and applications in high speed flow-field. Journal of Propulsion Technology 39(10):2274–2288 (in Chinese)
110. Morsy MH, Chung SH (2003) Laser-induced multi-point ignition with a single-shot laser using two conical cavities for hydrogen/air mixture. Exp Thermal Fluid Sci 27(4):491–497
111. Ryu SK, Won SH, Chung SH (2009) Laser-induced multi-point ignition with single-shot laser using conical cavities and prechamber with jet holes. Proc Combust Inst 32(2):3189–3196
112. Massa L, Freund JB (2017) Plasma-combustion coupling in a dielectric-barrier discharge actuated fuel jet. Combust Flame 184(2017):208–232
113. Macheret SO, Shneider MN, Miles RB (2020) Plasma-assisted fuel atomization and multipoint ignition for scramjet engines. J Propul Power 36(3):357–362
114. Deak N, Bellemans A, Bisetti F (2021) Plasma-assisted ignition of methane/air and ethylene/air mixtures: efficiency at low and high pressures. Proc Combust Inst 38(4):6551–6558
115. Ding P, Ruchkina M, Cont-Bernard DD, Ehn A, Lacoste DA, Bood J (2019) Detection of atomic oxygen in a plasma-assisted flame via a backward lasing technique. Opt Lett 44(22):5477–5480
116. Che XK, Zhou S, Nie W, Lin ZY (2015) Discharge simulation in mixtures of hydrogen and oxygen for plasma assisted combustion. High Voltage Engineering 41(06):2054–2059 (in Chinese)
117. Hakstege JP (2022) Comparative OH PLIF study for dye and OPO laser systems its application to optical diagnostics of plasma assisted combustion. Eindhoven University of Technology (in Chinese)
118. Chen QY, Che XK, Tong YH, Chen C, Zhu YZ, Nie WS (2021) Influence of surface dielectric barrier discharge on diffusion flame combustion characteristics. Journal of Beijing University of Aeronautics and Astronautics 47(05):1015–1024 (in Chinese)

119. Zhou SY, Nie WS, Che XK, Tong YH, Zheng TK (2019) Experiment study of effect of nonequilibrium plasma on methane-oxygen diffusive flame. Chinese Journal of Theoretical and Applied Mechanics 51(5):1336–1349 (in Chinese)
120. Zhou SY, Su LY, Shi TY, Zheng TK, Tong YH, Nie WS, Che XK, Zhao JF (2019) Experimental study on the diffusive flame stabilization mechanism of plasma injector driven by AC dielectric barrier discharge. Journal of Physics D: Applied Physics 52(26)
121. Wang HB, Wang ZG, Sun MB, Wu HY (2013) Combustion modes of hydrogen jet combustion in a cavity-based supersonic combustor. Int J Hydrogen Energy 38(27):12078–12089
122. Nozomu K, Seong-kyun I (2021) Flame dynamics under various backpressures in a model scramjet with and without a cavity flameholder. Proc Combust Inst 38(3):3861–3868
123. Dou ZG, Liu Y, Zhang P, Yang B (2017) Effect of equivalence ratio on flow field and combustion characteristics of plasma ignition in supersonic combustor. High Voltage Engineering 43(12):3981–3987 (in Chinese)
124. Zhang Z, Jin X, Xi WX (2019) Numerical study on combustion characteristics of supersonic strut combustor under plasma-assisted combustion. Journal of Propulsion Technology 40(09):2075–2083
125. Zhou SY, Nie WS, Che XK (2016) Numerical modeling of quasi-DC plasma-assisted combustion for flame holding cavity. Combust Sci Technol 188(10):1640–1654
126. Zhou SY, Che XK, Nie WS, Cheng YF (2013) Numerical study of effects of plasma on performance of scramjet combustor cavity. Journal of propulsion technology 34(7):950–955 (in Chinese)
127. Parent B, Hanquist KM, Omprakas A (2020) Fully-coupled simulation of plasma discharges, turbulence, and combustion in a scramjet combustor. In: AIAA (ed) AIAA AVIATION forum. American Institute of Aeronautics and Astronautics Inc., VIRTUAL EVENT
128. Rao X, Hemawan K, Wichman I, Carter C, Grotjohn T, Asmussen J, Lee T (2011) Combustion dynamics for energetically enhanced flames using direct microwave energy coupling. Proc Combust Inst 33(2):3233–3240
129. Shibkov VM (2019) Microwave discharges and their application. I. Surface microwave discharge. Moscow University Physics Bulletin 74(5):421–437

Investigation on Intelligent Drone-Mounted Mobile Vehicle for Power Transmission Line Inspection

Feng Wang, Libo Yang, Fuli Wan, Jiani Yang, Jie Yuan, Danhua Chen, and Lei Huang

Abstract To address the problem of low efficiency of real-time data transmission in areas without signals in the process of transmission lines inspection, the drone-mounted mobile operation platform is investigated. A power supply scheme for the platform is developed. A communication system based on 5G plus BeiDou satellite and its deployment scheme are proposed, which turns from single communication method to dual communication method. When the 5G signal is good, the data transmission is achieved through the 5G network; when the 5G network link fails, the satellite communication system starts to work. The autonomous flight performance of drone on the mobile operating platform is tested. The results show that the drone has good take-off performance. The high-precision positioning of drone for transmission line inspection can be met using the real time kinematic (RTK) positioning technique. The landing accuracy of drone based on image recognition is high, and the flight stability of drone is good.

Keywords Drone · Mobile operation platform · Autonomous flight · BeiDou satellite · 5G communication · Real time kinematic (RTK) positioning technique

F. Wang
State Grid Hunan Electric Power Company Limited, Changsha 410100, China

L. Yang
Hunan Province Key Laboratory of Intelligent Live Working Technology and Equipment (Robot), Changsha 410100, China

F. Wan · J. Yang
Live Inspection and Intelligent Operation Technology State Grid Corporation Laboratory, Changsha 410004, China

J. Yuan · D. Chen · L. Huang (✉)
College of Electrical and Information Engineering, Hunan University, Changsha 410082, China
e-mail: hl98@hnu.edu.cn

J. Yuan
e-mail: yuanjie@hnu.edu.cn

D. Chen
e-mail: danielchen@hnu.edu.cn

1 Introduction

High-voltage transmission lines are the backbone of the power grid when it is the important link for the transmission of electricity. The stability and reliability of the power system is influenced by its operating condition including the complex structure of transmission lines and the wide range of line distribution. The area through which the lines pass is mostly located in a harsh environment [1]. Transmission lines are exposed to the free space for a long time. It not only bears a high electrical stress, but also suffers external damage such as lightning strike and fouling corrosion, which makes transmission lines having hidden defects such as insulator deterioration and wire breakage. Presently, the discovery of these hidden defects mainly uses a combination of manual inspection and manual operating drone patrol [2, 3]. However, the artificial inspection has blind spots and are low efficient. It is difficult to complete the assessment of power infrastructure damage as well as inspection targets on time. Hence, drone full-region autonomous flight inspection is increasingly popular and has become a mainstream for the transmission line inspection.

As the requirements of the power grid for inspection refinement and intelligence level increasingly, there is a strong demand for full-region autonomous flight of drones [4]. However, existing high-precision drone autonomous flight techniques rely mainly on RTK networks, and autonomous flight operations are not possible in areas without network signals [5]. There is only 1 K/s image transmission speed for existing 4G network [6]. The examination of fine targets cannot be met duo to link bandwidth, network delay, transmission distance, etc. Compared with 4G communication, 5G has the characteristics of high speed, low time delay and large connection. Taking advantages of large communication range, wide network coverage and unrestricted geographical location, the satellite communication overcomes the weakness of 5G network [7]. A power line extraction method was proposed by Zhao et al. [8] based on the graph model. The extracted transmission line images were transmitted back to the terminal via a wireless network to construct a power line segment model. It is then to determine the operating condition for transmission line. However, transmission problems of wireless networks in signal-free areas are ignored. Data transmission between drones and low earth orbit satellite networks were studied by [9]. The collected data is transmitted by the drone to a low-orbiting satellite and then back to a ground-based station. Though satellite communication is not limited by terrain factors, the data transmission is slow. For hundreds of billions of terabytes of image data, satellite communication is difficult to meet the demand. Defect intelligent identification algorithm is used in this paper to add satellite communication function in drone inspection operation vehicle that is also fully integrated with BeiDou satellite high precision positioning and 5G communication technique. The task of transferring data is handled by the communication system on the vehicle. The 5G network is used to transmitting through when it is work. On the contrary, the satellite communication system completes the communication link establishment when the 5G network has weak coverage or connects failed.

The drone flight control and image data transmission are undertaken by various types of antennas and other radio frequency equipment [10, 11]. These devices often need to be mixed with other equipment mounted on the roof, as in-vehicle video surveillance and lighting. However, there are interferences, blocking and other electromagnetic compatibility risks. The passing ability and driving stability of vehicle will be more affected by the roof equipment [12]. Accurate positioning of the drone during autonomous flight was investigated in [13]. A high-precision and ultra-bandwidth method for positioning drones is proposed and the two-way time-of-flight localization scheme is combined with the maximum likelihood estimation method in the above paper. Positioning accuracy has reached to the decimeter level. Drone positioning problems in extremely constrained environments can be solved by the method. An innovative relative navigation system based on a tether system is proposed in [14]. In the absence of global positioning system, the drone can land safely on static and dynamic platforms is achieved, and the positioning error is limited within 20 cm. Radio frequency electronic mast technique is added to the drone communication command platform in this paper. High-precision positioning augmentation device is added to the mobile operating platform, making it act as a reference station for carrier phase differential settlement. The correction data is transmitted to the drone terminal in real time. Precise positioning and take-off and landing of drones during mobile operations can be realized.

Moreover, both 5G mobile signal enhancement technique and satellite transmission technique are studied in this paper. The BeiDou satellite high-precision positioning and 5G communication technique are integrated together to resolve the problem of data transmission in areas without 5G signals. The front-end and light weight of inspection data processing are completed. Accurate positioning, take-off and landing of drones during mobile operations are achieved by the combination of radio frequency electronic mast technique and satellite high-precision positioning technique. Thus, the efficiency of transmission line inspection can be guaranteed.

2 Drone-Mounted Mobile Vehicle

The mobile operation platform has the advantages of ruggedness, high reliability, stable operation, and strong environmental adaptability. It is widely used in the field of transmission line drone inspection. The platform consists of a system layer, an access layer, and a device layer, as shown in Fig. 1.
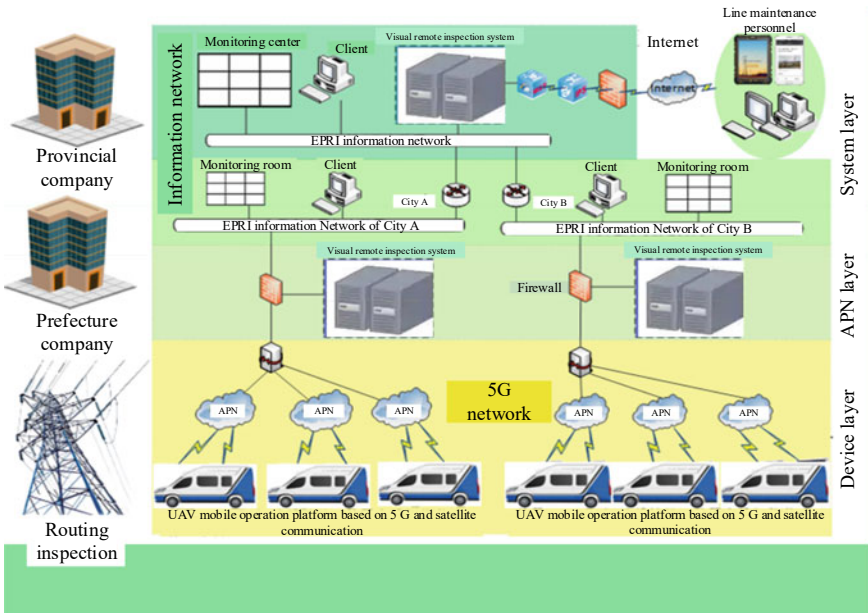
Fig. 1 Architecture of intelligent drone-mounted vehicle

3 Communication System

3.1 5G-BeiDou Satellite Communication System

5G technique is the latest generation of cellular mobile communication technique. It has great performance from the perspective of high data rates, reduced costs, increased system capacity, and massive device connectivity. Satellite communication is the ground radio communication station using artificial satellite to relay radio waves between two or more stations. It can realize long-distance voice, data, image, video transmission. A satellite communication network is a satellite system that allows real-time information processing, and it consists of a network of multiple satellites.

Currently, the mobile inspection platform is using 5G communication network as the only communication. In the absence of 5G signal, the only communication system of the mobile inspection operation platform is weak or even lost signal. This will cause that the data ahead cannot be transmitted back in time. The efficiency of mobile inspection work is severely impacted. The satellite communication function is added to the drone inspection vehicle to ensure the communication between the platform and the maintenance center. It enables the vehicle to have $1 + 1$ disaster-tolerant backup communication. An emergency communication function, which enables the communication of the drone inspection vehicle to be more secured, is added to the

(a)

(b)
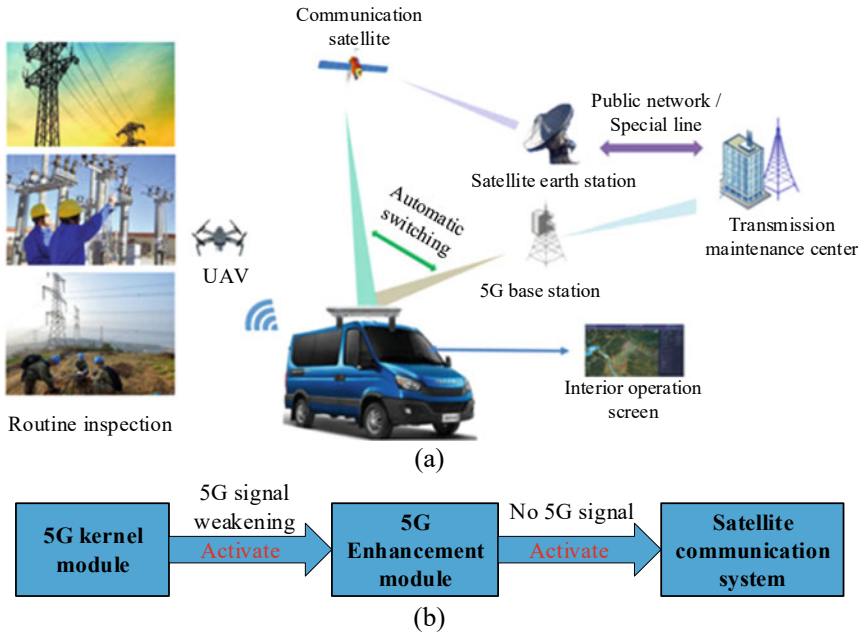
Fig. 2 Schematic of 5G-BeiDou satellite communication system and its deployment plan. **a** Communication system. **b** 5G system deployment plan

platform. The reliability and safety of mobile platforms are enhanced. Figure 2 is the schematic of 5G-BeiDou satellite communication system and deployment plan.

3.2 Phased Array Antenna

Satellite communication system mainly consists of satellite communication antenna terminal, supporting modem, and router. The satellite communication antenna is the main component to complete the satellite communication. It adopts the third-generation dynamic satellite antenna, as shown in Fig. 3. The moving antenna can ensure the communication connection whenever the carrier is stationary, even at high speed.

The phased array antenna is adopted, which has the advantages of low profile, quick satellite alignment, high dependability, good adaptability to low-orbit satellite networks, etc. [15]. The uniform linear array consists of multiple identical antenna elements arranged in a straight line according to the same element spacing [16]. Taking the uniform linear array composed of vibrator units as an example, two main ways of combining linear arrays are coaxial alignment and side-by-side arrangement, as shown in Fig. 4.

Fig. 3 Photo of phased array antenna
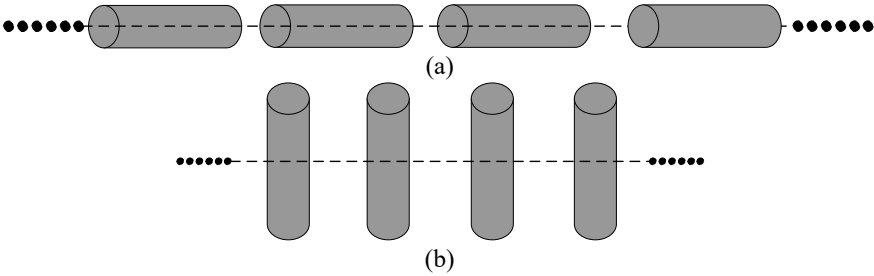
Fig. 4 Uniform linear arrays. **a** Coaxial alignment of linear arrays; **b** Array of lines side by side

If antenna elements are arranged in a linear array, there is the same array factor expression. Supposing that the number of array elements is N, the excitation of each array element is I_n, the phase shift constant is α, the angle between the ray and the array axis is β and the distribution of array element positions is d; we have

$$S(\beta) = \sum_{n=0}^{N-1} I_n e^{j(kd \cos \beta + n\alpha)} \tag{1}$$

Taking the rectangular grids plane array as an example, if each row or column of the plane array is regarded as a uniform linear array, the method for the linear array can be analogically used to the plane array. Supposing that the plane array has $N_x \times N_y$ array elements, the excitation of each element is I_{mn}, the array factor expression of the plane array can be derived as

$$S(\theta, \varphi) = \sum_{m=0}^{N_x-1} \sum_{n=0}^{N_y-1} I_{mn} e^{jk(md_x \cos \varphi + nd_y \sin \varphi) \sin \theta} \tag{2}$$

According to the mode of beam scanning, phased arrays can be divided into the one-dimensional phased array and the two-dimensional phased array, and the former means scanning in only vertical or horizontal orientation, the latter means scanning in both vertical and horizontal orientations.

(1) One-dimensional phased array

Supposing that a uniform linear array has N elements arranged at equal spacing d, as shown in Fig. 5, each array element is connected to a phase shifter, and each phase shifter controls the output excitation phase as $0, \alpha, 2\alpha, 3\alpha, \ldots, (N-1)\alpha$. By changing the magnitude of α through the phase shifter, the phase of each array element can be adjusted separately to control the wave velocity scanning, the radiated electric field in the far region is

$$E = C \frac{e^{-jkr}}{r} f(\theta, \varphi) S(\theta) \tag{3}$$

$$\begin{cases} S(\theta) = \sum_{n=0}^{N-1} I_n e^{jnu} \\ u = kd \sin\theta + \alpha = kd(\sin\theta - \sin\theta_0) \\ \sin\theta_0 = -\alpha/kd \end{cases} \tag{4}$$

where θ is the angle between the observation point and the antenna beam pointing, and θ_0 is the angle between the observation point and the side launch direction. Typically, the beam width of the array element pattern $f(\theta, \varphi)$ is relatively large. Let $f(\theta, \varphi) = 1$ and $I_n = 1$ in the condition of constant-amplitude feeding, the normalized array factor can be obtained as

Fig. 5 One-dimensional phased array
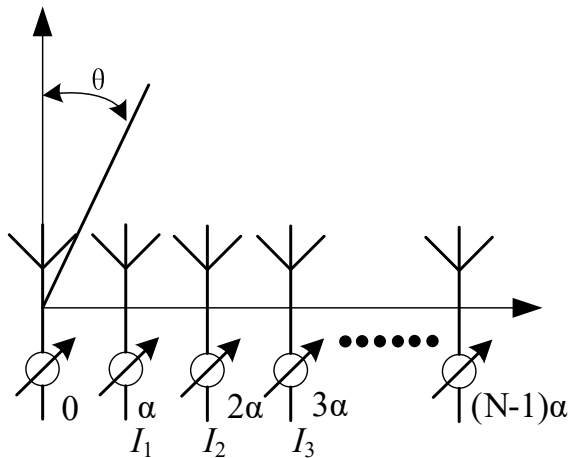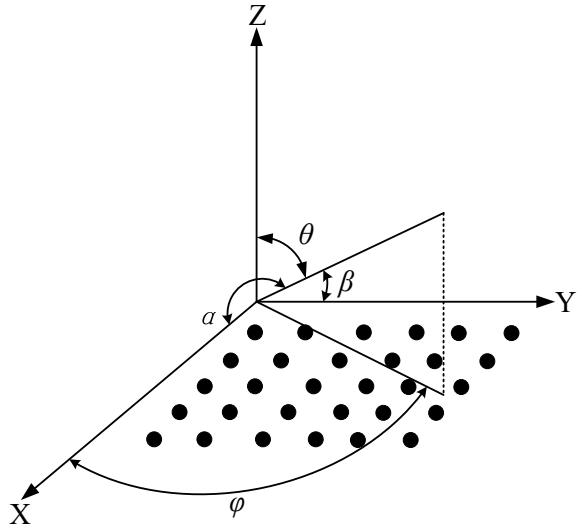
$$S_N(\theta) = \frac{\sin(Nu/2)}{N\sin(u/2)} \tag{5}$$

(2) Two-dimensional phased array

The two-dimensional phased array is generally implemented with planar arrays, as shown in Fig. 6, and its phase-control principle is consistent with the one-dimensional phased array. Considering a plane array with $N_x \times N_y$ array elements, the element spacing in the x- and y-axis are d_x and d_y, respectively, and the excitation phases of elements in the x- and y-directions are $\varphi_x = k_0 d_x \cos\alpha$ and $\varphi_y = k_0 d_y \cos\beta$, respectively. The array direction function is

$$F(\alpha, \beta) = \sum_{m=0}^{N_x} \sum_{n=0}^{N_y} \exp[jmk_0d_x(\cos\alpha - \cos\alpha_s) + jnk_0d_y(\cos\beta - \cos\beta_s)] \tag{6}$$

4 Autonomous Flight Test and Application

4.1 Precision Landing

A contrasting solid reference object is set at the landing point of the drone. The reference needs to have multiple layers of patterns, while the pattern cannot be symmetrical. The Quick Response Code (QR Code) shown in Fig. 7 is adopted in

Fig. 7 Drone precision landing sign

this paper. The advantage of the QR Code is that it can fuse a variety of information and has strong contrast.

The location and direction data of landing mark obtained by image processing algorithm needs to be converted into the actual physical distance from the pixel distance according to the projection model. For convenience, the landing mark is fixed on the wall, and the landing mark is obtained and identified at different distances between the camera and the landing mark. The projection models of pixel distances x, y, z and actual distances X, Y, and Z are established in Table 1.

The autonomous landing of the drone is mainly realized by drone flight control. The flight control receives the data obtained by the external sensors and then fuses the drone data. After being processed by flight control algorithm, it is converted to the motor speed so that the drone finally lands on the mobile platform. Twelve precision landing tests are conducted on the landing system in the outdoor. Landing locking distance is the maximum distance of a drone which can lock the landing position. If the actual horizontal distance between the center axis and the landing sign centroid of the platform is less than 5 cm after landing, it is considered that the landing accuracy is qualified.

It can be seen from Table 2 that the average locking distance of drone for precise landings is 18.5 m, the accuracy and flight stability of 12 landings are all qualified, and the flight time is about 6 min.

Table 1 Actual distance projection model of April tag

Signs direction	Tag16h5		Tag36h11	
	Expression	R^2	Expression	R^2
X axis	$X = 15x - 9.9$	0.9914	$X = 2.9x - 0.2$	0.9955
Y axis	$Y = 14.6y - 11.3$	0.9896	$Y = 2.6y$	0.9979
Z axis	$Z = -8.6z - 48.7$	0.9386	$Z = -1.2z - 6.4$	0.9731

Table 2 Precision landing test for drone

Test number	Flight hardware stability	Flight time (min)	Landing locking distance (m)	Landing accuracy
20220305-1	Qualified	6	19.1	Qualified
20220305-2	Qualified	6	18.3	Qualified
20220305-3	Qualified	6	19.2	Qualified
20220305-4	Qualified	6	20.1	Qualified
20220305-5	Qualified	6	18.1	Qualified
20220305-6	Qualified	6	17.8	Qualified
20220305-7	Qualified	6	19.3	Qualified
20220307-1	Qualified	6	17	Qualified
20220307-2	Qualified	6	21	Qualified
20220307-3	Qualified	6	17.6	Qualified
20220307-4	Qualified	6	18.3	Qualified
20220307-5	Qualified	6	16.2	Qualified

4.2 Take-Off Performance

RTK employs the carrier phase difference technique. RTK positioning can provide real-time three-dimensional positioning results of the station in the specified coordinate system and the accuracy can reach the centimeter level. RTK is based on the carrier phase for real-time positioning, the positioning system can be divided into two parts: the base station which is fixed at a specific position and remains stationary during a single measurement and the rover station which moves to the measured point. Its types can be divided into carrier phase difference and quasi carrier phase difference. The former, whose accuracy is centimeter-level, is the uncorrected observation value sent by the reference station; the latter, whose accuracy is decimeter-level, is the carrier phase correction value sent by the reference station. The schematic diagram for RTK positioning is shown in Fig. 8.

In RTK mode, the base station collects satellite data and transmits the data and site coordinate to the station. The station conducts the real-time carrier phase analysis on the collected satellite data and the received data link to obtain centimeter-level positioning results. The analysis time of real-time carrier phase is less than 1 s. The RTK has many advantages:

(1)   High positioning accuracy

For carrier difference and quasi-carrier difference, the positioning accuracy is at centimeter-level and decimeter-level, respectively, both of which are better than the general positioning system. The RTK can work normally within 15 km, and the latitude and longitude errors are very small.
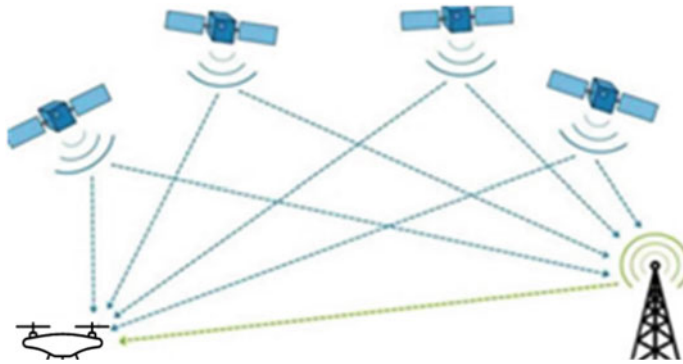
Fig. 8 Schematic diagram for RTK positioning

(2) High efficiency

Within the receiving range of RTK signal, one or more rover stations can be set up. When an accident occurs in one of the base stations, it can be switched to a nearby rover station. However, the rover stations are required to have an automatic frequency sweep function. At the same time, each rover station jointly performs a weighting on data of base station. This function requires high computation capability for rover station which needs to meet multi-channel reception.

(3) Fewer limitations

The application of drones not only saves cost and improves efficiency, but also guarantees the reliability of online inspections. In this paper, the high-precision positioning enhancement device, as shown in Fig. 9, is integrated with the system to realize the remote take-off and precise landing.

In this paper, a high-precision positioning enhancement device is installed on the vehicle. The platform become a base station for RTK signal to correct data and reduce

Fig. 9 Photos of take-off and landing module

errors. The corrected data are transmitted to the drone terminal in real-time. Through two differential observations of the interstellar station, it can be achieved:

(1) Eliminate the system deviation of satellite clock;
(2) Eliminate the influence of orbit error;
(3) Eliminate the clock error of receiver;
(4) Reduce the influence of atmospheric refraction on the observed data.

Through precise modeling, estimation and elimination of various errors from the observed values, the real-time centimeter-level accurate positioning can be realized, and the precise landing of the drone can be completed.

5 Conclusions

The conclusions are drawn as follows:

(1) In this paper, a mobile platform for drone transmission line inspection is designed, and several parts of platform can be customized and adjusted according to the different operation tasks. the solution of power supply is that lithium batteries power the drone charging cabinet and edge computing equipment, and generators power other body equipment.
(2) A 5G + BeiDou satellite communication scheme is proposed. When the 5G network is good, the data transmission is carried out through them; when the vehicle is located in the area with weak signal, the communication link are established by the BeiDou satellite, whose antenna adopts the 3rd satcom-on-the-move satellite antenna which are arranged in the two-dimensional phased array. The phase of each element of antenna array can be individually adjusted by software in order that the antenna realize beam scanning, and then align to the satellites in a specific direction.
(3) In this paper, the safe takeoff, precise landing and high-precision positioning performance of drone are tested. The results show that the average locking distance of drone precise landing is about 18.5 m, and the requirements for the landing accuracy and flight stability are met. Compared with GPS positioning technology, RTK-based high-precision positioning has higher positioning accuracy. Within the receiving range of RTK signals, one or more rover stations can be set up, dramatically improving the operation range and work efficiency of drones.

References

1. Yang L, Fan J, Liu Y et al (2020) A review on state-of-the-art power line inspection techniques. IEEE Trans Instrum Meas 69(12):9350–9366
2. Maharjan S, Zhu Q, Zhang Y et al (2013) Dependable demand response management in the smart grid: a Stackelberg game approach. IEEE Trans Smart Grid 4(01):120–132
3. Han J, Yang Z, Zhang Q et al (2019) A method of insulator faults detection in aerial images for high-voltage transmission lines inspection. Apply Science 9(10):2009
4. He T, Hu Z (2019) Research of multi-rotor UAVs detailed autonomous inspection technology of transmission lines based on route planning. IEEE Access 7:14955–114965
5. Um I, Park S, Kim HT et al (2020) Configuring RTK-GPS architecture for system redundancy in multi-drone operations. IEEE Access 8:76228–76242
6. Chang W, Yang G, Li E et al (2017) Toward a cluttered environment for learning-based multi-scale overhead ground wire recognition. Neural Process Lett 48(3):1789–1800
7. Zhou D, Sheng M, Wang X et al (2017) Mission aware contact plan design in resource-limited small satellite networks. IEEE Trans Commun 65(6):2451–2466
8. Zhao L, Wang X, Yao H et al (2019) Power line extraction from aerial images using object-based Markov random field with anisotropic weighted penalty. IEEE Access 7:125333–125356
9. Jia Z, Sheng M, Li J et al (2021) LEO-satellite-assisted UAV: joint trajectory and data collection for internet of remote things in 6G aerial access networks. IEEE Internet Things 8(12):9814–9827
10. Elnabty I, Fahmy Y, Kafafy M (2022) A survey on UAV placement optimization for UAV-assisted communication in 5G and beyond networks. Physical Communication
11. Zeng Y, Zhang R, Lim T (2016) Wireless communications with unmanned aerial vehicles: opportunities and challenges. IEEE Commun Mag 54(5):36–42
12. Zhou L, Zhao X, Guan X et al Robust trajectory planning for UAV communication systems in the presence of jammers. Chinese Journal of Aeronautics
13. Yang B, Yang E, Yu L (2022) High-precision UWB-based localisation for UAV in extremely confined environments. IEEE Sens J 22:1020–1029
14. Alarcon F, Santamaria D, Viguria A (2015) UAV helicopter relative state estimation for autonomous landing on moving platforms in a GPS-denied scenario. IFAC-Papers 48:37–42
15. Keshtkaran K, Ghalichechian N (2016) Suspended 60 GHz phased array antenna with high efficiency. In: 2016 international workshop on antenna technology (iWAT). Cocoa Beach, pp 37–39
16. Kim H, Park J, Lee S et al (2002) V-Band 2-b and 4-b low-loss and low-voltage distributed MEMS digital phase shifter using metal-air-metal capacitors. IEEE Trans Microw Theory Tech 50(12):2918–2923

Voltage Transformer Fault Diagnosis Based on Improved ResNet50

Zezhou Wang, Lun Chen, Yucheng Gan, Gang Chen, Yanfeng Lu, Hongyi Zhou, and Shuiqing Xu

Abstract In the modern power grid, the accuracy of power measurement and relay protection devices is critical for all parties involved in power supply, transmission, and utilization. The accuracy of the secondary current of the current transformer is of utmost importance in reflecting the primary current. To achieve this objective, we propose a fault diagnosis method for voltage transformers based on the ResNet50 network. This involves training the residual network with voltage fault signals to obtain an optimal fault diagnosis model with high recognition performance. By utilizing this model, we can accurately detect voltage transformer faults.

Keywords Voltage transformers · ResNet50 · Batch normalization · Troubleshooting

1 Introduction

Open-circuit fault diagnosis methods for inverters can be categorized into three types: signal-based processing methods, model-based processing methods, and data-driven methods. Signal-based methods analyze signal attributes such as amplitude, frequency, current average, and voltage ratio based on signals of current and voltage. However, these methods are prone to interference from external factors or internal system disturbances, resulting in high misdiagnosis rates. Model-based processing methods utilize mathematical models of the inverter, such as voltage residual models and current observers. However, these methods require a certain level of accuracy in

Z. Wang (✉) · G. Chen · H. Zhou
Haiyan Power Supply Company of State Grid Zhejiang Electric Power Co., Ltd., Haiyan, China
e-mail: 253557954@qq.com

L. Chen · Y. Gan · Y. Lu
Haiyan Nanyuan Electric Power Engineering Co., Ltd., Haiyan, China

S. Xu
Hefei University of Technology College of Electrical and Automation Engineering, Hefei, China

system modeling. Data-driven methods based on neural networks, expert systems, and support vector machines are also widely used. These methods do not require complex modeling but are more dependent on data.

To address the issues of harmonic interference in actual substation voltage transformers, the inaccurate simulation data, and the need for accurate system models in model-based fault diagnosis methods, this paper proposes a voltage transformer fault diagnosis method based on ResNet50. This method involves training voltage fault signals using the residual network to derive an optimal fault diagnosis model with high recognition performance. The model is then used to accurately identify faults in voltage transformers, enabling reliable fault diagnosis.

2 Voltage Transformer Fault Model Voltage Transformer Fault Model

According to the voltage transformer fault principle, there will always be errors between the measured value and the real value, as the voltage transformer is an infinite approximation. Additionally, when a transformer fails, there is a deviation in the fault. Thus, a mathematical model for voltage transformer faults can be obtained based on this principle:

$$V_t = kV + v_t + s_x + f_t \tag{1}$$

where V is the true value at a moment; t is the measured value at a moment; k is the transformer ratio.

2.1 Fixed Deviation Fault

The fixed deviation fault is characterized by a always present fixed deviation or fixed value between the measured and true values. In the mathematical model for this type of fault, the fixed deviation is represented by a fixed value 'b', as shown in the following equation:

$$V_t = kV + v_t + s_x + b \tag{2}$$

2.2 Drift Deviation Fault

The performance of electronic components in the voltage transformer's sensor head can be degraded due to its susceptibility to temperature changes. As a result, the measured value may experience drift deviation over time, which is known as drift deviation fault. The mathematical model for this type of fault can be expressed as follows:

$$V_t = kV + v_t + s_x + C(t - t_s) \tag{3}$$

2.3 Complete Failure Failure

When a hardware circuit failure or electronic component failure occurs in the voltage transformer, the measured value may not change with the actual value and instead remains at a fixed value (either zero value or the maximum range value). This type of failure is known as complete failure failure. The mathematical model for complete failure failure can be expressed as follows:

$$V_t = d \tag{4}$$

In order to study the three types of faults mentioned above, ten constants were set for each fault and twenty sets of data were collected for each constant. This resulted in a total of six hundred sets of data being collected for each type of fault constant as shown in Table 1.

Table 1 Fault deviation value

Fault deviation value	Fault deviation value									
Fixed deviation fault	3	5	7	9	12	−3	−5	−7	−9	−12
Drift deviation fault	3	5	7	9	12	−3	−5	−7	−9	−12
Complete failure	0	1	3	5	7	9	−1	−3	−5	−7

3 Residual Neural Network

3.1 Introduction to the Main Framework of Residual Neural Network

The ResNet50 residual network was selected as the backbone network for this study. The network comprises of α 7 × 7 convolutional kernel with 64 channels and α maximum pooling downsampling layer with a convolution kernel of size 3 × 3 and a step size of 2, denoted as β. Four groups of residual structures, named δ_1, δ_2, δ_3 and δ_4, are sequentially connected in series along the input–output direction of the network, followed by an average pooling layer ε and a fully connected layer ϕ. Group δ_1 consists of three identical residual structures 1 in series, group δ_2 consists of four identical residual structures 2 in series, group δ_3 consists of six identical residual structures 3 in series, and group δ_4 consists of three identical residual structures 4 in series.

3.2 Residual Block Structure

In mathematical statistics, a residual is defined as the difference between the actual observed value and the predicted or estimated value (fitted value). Residuals can provide important information about the underlying assumptions of a model. If the regression model is correct, we can treat the residual as the observed value of the error, which should be consistent with the assumptions of the model and have some properties of the error. By analyzing the residuals, we can examine the reasonableness of the model assumptions and the reliability of the data, which is referred to as residual analysis (Fig. 1).
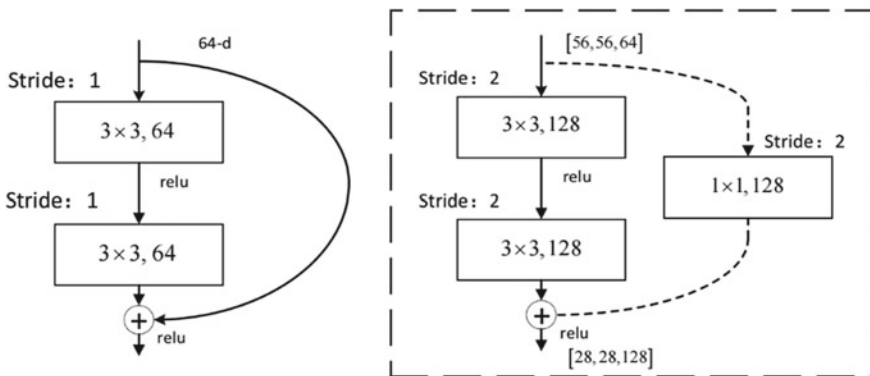
Fig. 1 Residual structure

Fig. 2 Residual structure with multiple convolution layers
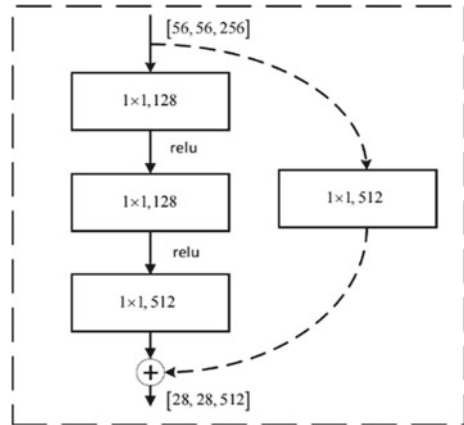
The input feature matrix is convolved through two 3 × 3 layers to obtain the main branch output. The curve on the right indicates that the input is directly connected to the output. Since the residual structure input feature matrix and output feature matrix are of the same shape, the feature matrix obtained from the main branch is added to the input feature matrix. The output feature matrix of this residual block is then obtained using the ReLU activation function.

When it is necessary to retrain the dataset and change the input and output shape, a dashed residual structure on the right is used. In this structure, the step stride of the first convolutional layer in the main branch is changed, and the height and width of the convolutional layer are reduced from 56 to 28, while the depth is changed from 64 to 128. The shortcut branch of this structure also uses a step of 2, and the depth of the input feature matrix is changed from 64 to 128, while the height and width are changed from 56 to 28 (Fig. 2).

In the aforementioned residual structure, the input feature matrix with a shape of [56, 56, 256] is downscaled when passed through the first convolutional layer of the main branch. The depth of the input feature matrix is reduced from 256 to 128, and the step stride remains the same. The third convolutional layer acts as a dimensional increase, increasing the depth of the input feature matrix from 128 to 512.

The shortcut branch in the residual structure uses a step stride of 2. Thus, the width and height of the input feature matrix are reduced from 56 to 28. This convolution layer increases the width of the input feature matrix from 256 to 512 and changes the shape of the initial input feature matrix to [28, 28, 512]. This shape is consistent with the shape of the output feature matrix on the main branch and thus, can be added to the output feature matrix on the main branch. The output of the residual structure is obtained by adding the ReLU activation function to this sum.

Fig. 3 Principle of batch normalization

3.3 Principle of Batch Normalization

Batch Normalization is a technique used in deep neural networks to prevent overfitting and accelerate training. This is achieved by normalizing the data for each input batch, which helps the network to converge better and reduces the need for additional regularization techniques such as Dropout. The principle of batch normalization is shown in Fig. 3.

The input to each layer in the convolutional kernel is the feature matrix output from the previous layer. It is required that the feature matrix output from each layer conforms to the distribution law of mean 0 and variance 1. For an input x with d dimensions, the feature matrix of each batch data is calculated, and then each of its dimensions is normalized. Firstly, the mean value of each dimension of the feature matrix is obtained as μ_B. The operation formula for this process is as follows:

$$\mu_B = \frac{1}{m} \sum_{i=1}^{m} x_i \tag{5}$$

where m represents the number of all vectors in one dimension of the feature matrix; μ_B is a vector in which each element represents the mean value of one dimension.

The variance of the output eigenmatrix σ_B^2 is obtained by the following equation:

$$\sigma_B^2 = \frac{1}{m} \sum_{i=1}^{m} (x_i - \mu_B)^2 \tag{6}$$

Here, the variable σ_B^2 represents the variance of each dimension of the feature matrix we calculate, and each element of the μ_B vector represents the mean of a dimension. To normalize the input feature matrix "x" for each dimension, we calculate the standard deviation using the mean μ_B and variance σ_B^2 formula. The standard deviation is calculated as follows:

$$\widehat{x_i} = \frac{x_i - \mu_B}{\sqrt{\sigma_B^2 + \varepsilon}} \tag{7}$$

During the training process, the mean and variance of each set of voltage fault signals are continuously calculated, and the statistical means and variances are recorded using the moving average method.

4 Experimental Results

To train a neural network, a complete dataset needs to be passed through the network once and returned once. For the ResNet50 model, we define an epoch as consisting of 100 iterations over the entire training dataset. Each epoch in this model consists of 45 batches, with each batch using the Batch Gradient Descent learning algorithm.

We numerically classify the three types of faults, fixed deviation, drift deviation, and complete failure faults, into three categories: 0, 1, and 2. The fault data set in the control group contains 450 voltage signals containing faults, and each fault data set in the conventional group contains 200 fault data, totaling 600 fault data.

We use the voltage signal as the network input, with a batch size of 20, an initial learning rate of 1e-4, and a reduction in learning rate after reaching a certain loss. The parameters are initialized with an open normal and normal distribution, and the model is updated with the Adam optimizer during training. The validation results are depicted in Fig. 4.

We use the 600 sets of fault data as the input for the neural network for iterative learning. After 100 epoch training, the validation set accuracy reaches 92.5%, which is not the optimal prediction result. This is because the fixed deviation and drift deviation voltage signals are more similar, leading to less than optimal recognition results. For instance, category 0 fixed deviation is easily classified as drift deviation, producing less than accurate classification results, as shown in Fig. 5.

To help the network better identify drift bias and fixed bias, 100 drift bias samples and 100 fixed bias samples are added in addition to the original 600 fault data sets. This updates the number of fault data sets to 800, of which 720 are used as training
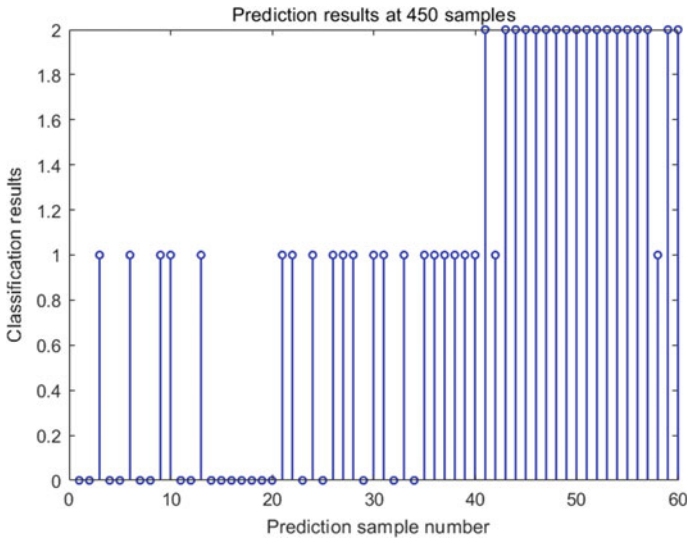
Fig. 4 Initial prediction results
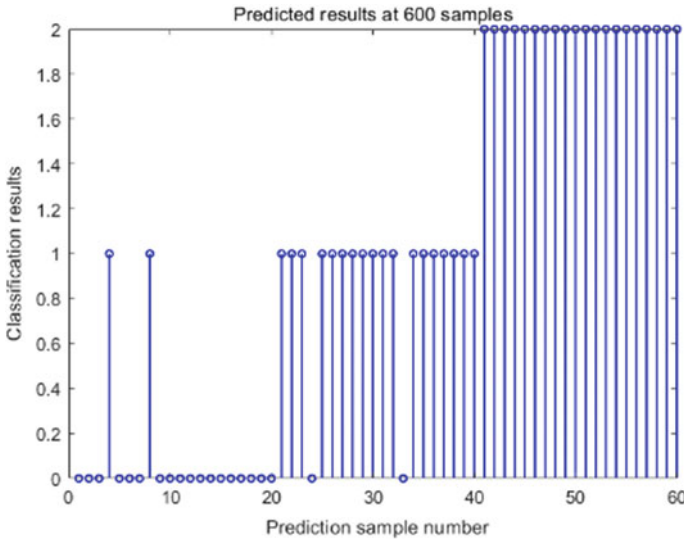
Fig. 5 Initial prediction results

set samples, 80 are used as validation set samples, and 60 additional fault data are added as test set samples.

After adding the 100 sets of drift deviation and 100 sets of fixed deviation data, the training results have significantly improved. The accuracy of the validation set has increased from 92.5 to 98.3%, which is a great training effect (Fig. 6).

The three training sets contain different sample data, and thus, their training results differ significantly. The training accuracy and validation accuracy of each training set are shown in Table 2.

An analysis of the application of convolutional neural network in fault diagnosis reveals that with a greater amount of test set data, the accuracy rate of fault recognition can be improved. The voltage transformer fault identification system based on convolutional neural network not only recognizes faults faster, but also has higher self-adaptation ability and can analyze fault types with greater resolution.
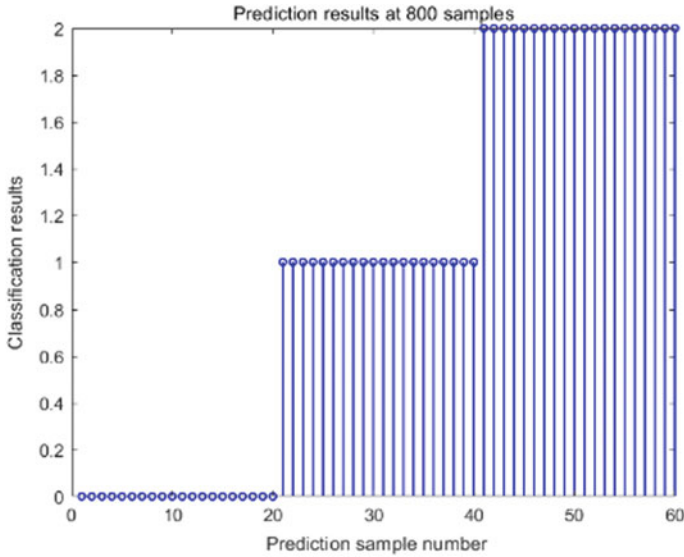
Fig. 6 Improved prediction results

Table 2 Classification effect under different training sets

Number of test set samples	450	600	800
Training accuracy (%)	83.6	92.5	98.3
Validation accuracy (%)	80	93.3	100

References

1. Tziouvaras DA, McLaren P, Alexander G et al (2000) Mathematical models for current, voltage, and coupling capacitor voltage transformers. IEEE Trans Power Delivery 15(1):62–72
2. Hou D, Roberts J (1996) Capacitive voltage transformer: transient overreach concerns and solutions for distance relaying. In: Proceedings of 1996 Canadian conference on electrical and computer engineering. IEEE, vol 1, pp 119–125
3. Dalessandro L, da Silveira CF, Kolar JW (2007) Self-capacitance of high-voltage transformers. IEEE Trans Power Electron 22(5):2081–2092
4. Lucas R, McLaren PG, Keerthipala WWL et al (1992) Improved simulation models for current and voltage transformers in relay studies. IEEE Trans Power Delivery 7(1):152–159
5. Christensen LH (1995) Design, construction, and test of a passive optical prototype high voltage instrument transformer. IEEE Trans Power Delivery 10(3):1332–1337
6. Parfomak PW (2014) Physical security of the US power grid: high-voltage transformer substations

7. Lyutikova MN, Korobeynikov SM, Rao UM et al (2022) Mixed insulating liquids with mineral oil for high-voltage transformer applications: a review. IEEE Trans Dielectr Electr Insul 29(2):454–461

8. Dujic D, Zhao C, Mester A et al (2013) Power electronic traction transformer-low voltage prototype. IEEE Trans Power Electron 28(12):5522–5534

9. Zhao C, Dujic D, Mester A et al (2013) Power electronic traction transformer—medium voltage prototype. IEEE Trans Industr Electron 61(7):3257–3268

10. Harada K, Anan F, Yamasaki K et al (1996) Intelligent transformer. PESC Record. In: 27th annual IEEE power electronics specialists conference. IEEE, vol 2, pp 1337–1341

11. Filiatrault A, Matt H (2005) Experimental seismic response of high-voltage transformer-bushing systems. Earthq Spectra 21(4):1009–1025

12. Ziomek W, Vijayan K, Boyd D et al (2011) High voltage power transformer insulation design. In: 2011 electrical insulation conference (EIC). IEEE, pp 211–215

13. Lai JS, Maitra A, Mansoor A et al (2005) Multilevel intelligent universal transformer for medium voltage applications. In: Fortieth IAS annual meeting. conference record of the 2005 industry applications conference, 2005. IEEE, vol 3, pp 1893–1899

Fuzzy Logic Approach for Life Time Estimation of Polyimide (PI) Insulations Used at High-Frequency

Bilal Iqbal Ayubi, Zhang Li, Wang Yiwei, Zhou Shengrui, and Zou Liang

Abstract The critical role of insulation system quality in the proper functioning of solid-state transformers (SST) is very important. To ensure that the SST is maintained properly and estimate its lifespan, certain parameters must be measured, reflecting the degradation rate of the transformer dielectric insulation. However, the complexity of the insulation structure and degradation process can make this task difficult. To address this issue, the paper proposes a new approach using fuzzy logic to create a reliable insulation life model that predicts the life of an SST based on experimental tests. The validity of this fuzzy logic model is confirmed by experimental data collected under various parameters, including voltage magnitude, frequency, and temperature. The results show that the proposed model is effective and can assist in making timely decisions to protect equipment.

Keywords Fuzzy logic · Polyimide (PI) insulation · Solid state transformer SST

1 Introduction

Modern power systems are increasingly relying on power electronic converters, which leverage advancements in high power electronic devices and control technologies. These converters are utilized to power various electrical equipment, including high frequency transformers found in solid-state transformers and rotating machines that are connected to adjustable speed drives. The high frequency voltage generated by these converters has unique characteristics such as a high repetition rate, large

B. I. Ayubi · Z. Li (✉) · W. Yiwei · Z. Shengrui · Z. Liang
Shandong University, Jinan 250100, China
e-mail: zhleee@sdu.edu.cn

B. I. Ayubi
e-mail: d2019065@mail.sdu.edu.cn

Z. Liang
e-mail: zouliang@sdu.edu.cn

instantaneous value, and short rise time, resulting in a high slew rate. However, the frequency of the voltage also causes power loss in ferromagnetic material, conductors, and dielectrics to increase considerably, leading to intense electro-thermal stress [1–5]. To address this issue, polyimide (PI) is commonly used as insulation in high frequency applications. Nevertheless, the normal operating temperature of HF electrical equipment can exceed 150 °C, accelerating the aging process of insulation materials and potentially leading to premature insulation failure [6–8]. A literature proposed fuzzy logic approach for insulation life estimation of power transformer based on different parameters [9, 10].

In order to evaluate the influence of various factors, such as electrical, thermal, or mechanical stress, on insulation material for HF electrical equipment, reliable conclusions require the assessment of multiple factors. These factors can have a synergistic effect on each other, making lifetime prediction of insulation material even more complex. This paper proposes a fuzzy logic approach that utilizes data collected mainly from polyimide insulation experiments under different voltages, frequency and temperature in create life time of insulation.

2 Experiment Setup

In the experiment, a 75 μm thick Polyimide (PI) film was utilized. To ensure accurate results, the film's surface was cleaned with alcohol and dried in a 60 °C oven for 2 h to eliminate the effects of moisture and external pollution that could alter the PI film's dielectric properties. The use of alcohol during the cleaning process reduces the dispersion of external factors on the results. The ball-plate electrode was employed in the experiment to simulate the electric field of high-frequency transformer gas–solid insulation distribution characteristics. This electrode has normal tangential electric field components. The ball electrode has a diameter of 20 mm, while the plate electrode's diameter is 75 mm, and the thickness is 10 mm, as shown in Fig. 1.

3 Fuzzy Logics

Fuzzy logic is a type of mathematical logic that allows for reasoning with uncertain or vague information. It is particularly useful in situations where precise measurements or definitions are difficult to obtain, as it allows for a more flexible approach to decision-making. One area where fuzzy logic has been applied is in the estimation of insulation life in electrical systems. Insulation is a critical component in any electrical system, as it prevents electrical current from flowing where it is not intended to, and it also protects the system from external factors such as moisture, temperature changes, and physical stress.
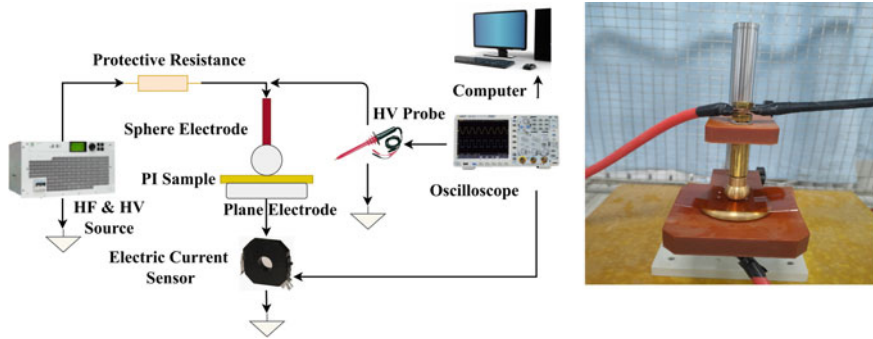
Fig. 1 Ball-plate electrode structured-based experimental setup

However, over time, insulation can degrade due to a variety of factors, including voltage parameters and environmental conditions. It is therefore important to estimate the remaining life of insulation in order to prevent failures and ensure the continued safe and efficient operation of the electrical system.

Fuzzy logic can be used in insulation life estimation by taking into account a range of factors that may affect the remaining life of the insulation. These factors may include the age of the insulation, the operating conditions of the system and the level of stress on the insulation. Similar to artificial neural networks, fuzzy logic is a knowledge-based AI technique that involves three fundamental steps: fuzzification, inference, and defuzzification, as illustrated in Fig. 2. By transforming input data into dimensionless variables between zero and one, fuzzy logic insulation life models can be developed from measured data. This is achieved by normalizing the data using limits that characterize their normal and extreme values.

By considering these factors in a fuzzy logic system, an estimate of the life time of the insulation can be calculated. This estimate can then be used to plan for future maintenance and replacement of the insulation, ensuring that the electrical system remains safe and reliable.
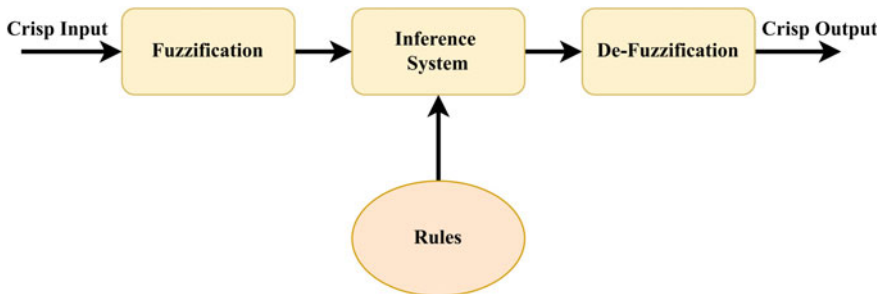
Fig. 2 Fuzzy logic structure

Table 1 Insulation life obtained by aging tests

Amplitude	Frequency	Temperature	Life time (min)
1500	5000	13	270
1500	5000	180	170
3000	5000	13	38
3000	5000	180	28
1500	30,000	13	40
1500	30,000	180	25
3000	30,000	13	8
3000	30,000	180	6

One advantage of using fuzzy logic for insulation life estimation is its ability to handle uncertain and imprecise information. In many cases, precise measurements of the factors that affect insulation life may be difficult to obtain, or the relationship between these factors and insulation life may be complex and difficult to model. Fuzzy logic allows for a more flexible approach that can take into account a wide range of inputs and produce an estimate of insulation life that is more accurate and reliable than traditional methods.

4 Experimental Results Analysis

In this study, accelerated aging experiments were conducted on polyimide (PI) films using a range of voltage frequencies 5–30 kHz, amplitudes 1.5–3.0 kV, and temperatures 13–180 °C [11]. Finally, the reliability of the lifetime prediction model was assessed through an additional experiment (Table 1).

5 Fuzzy Logic Life Time Estimation Model

During the lifespan of a transformer insulation, various factors contribute to its ageing, and their effects combine in intricate ways, resulting in a complex ageing process. Due to this complexity, creating an accurate model to predict insulation system degradation behavior is not feasible. However, this paper proposes the implementation of a fuzzy inference system to estimate insulation life using three parameters voltage magnitude, frequency and temperature resulting in more precise model output.

5.1 Membership Functions

This paper used Gaussian membership function which is given by Eq. (1),

$$f(x; \sigma, c) = e^{\frac{-(x-c)^2}{2\sigma^2}}$$ (1)

where the σ is the shape of curve and c is center.

Figures 3, 4, 5 showing input variable membership function for voltage, frequency and temperature. The model's output variable MFs based on three factors are developed and measured based on life time, Fig. 6. Based on insulation test data, fuzzy rules are developed for life time model, Fig. 7.
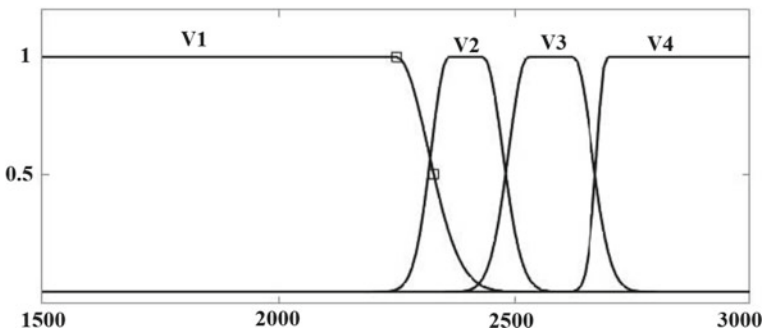
Fig. 3 Input MF for voltages
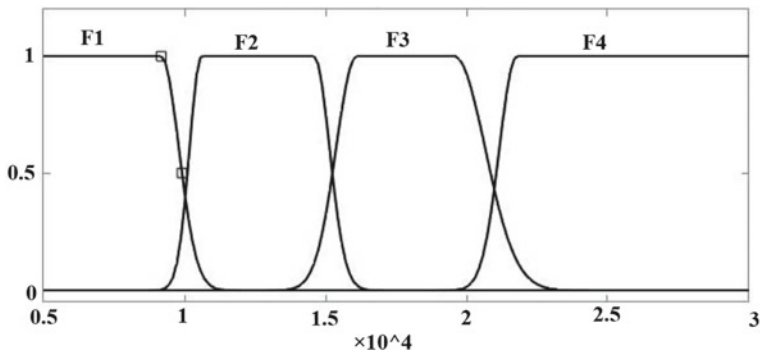
Fig. 4 Input MF for frequency
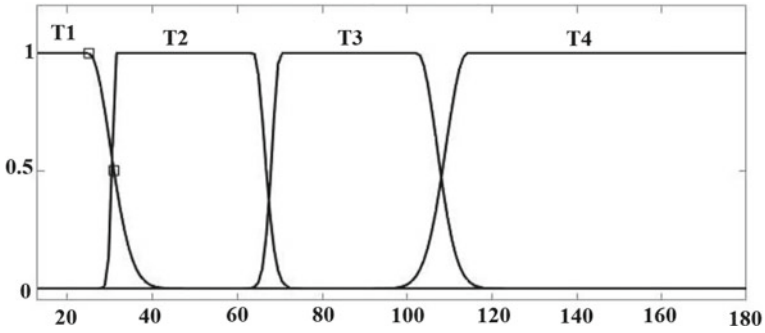
Fig. 5 Input MF for temperature
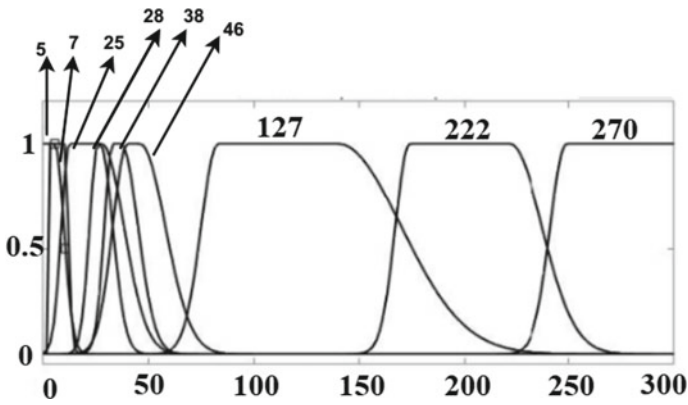
Fig. 6 Output MF for life time (min)

6   Interaction Between Parameters

When the voltage applied to the insulation is increased, the electric field strength within the insulation also increases. This leads to an increase in the probability of partial discharge (PD) events, which can cause insulation degradation and ultimately reduce the lifespan of the insulation. Therefore, it is important to operate electrical systems at the rated voltage or below to minimize the risk of PD events and prolong the life of the solid insulation.

Frequency can greatly affect the solid insulation. As the frequency increases, the polarization of the insulation materials also increases, leading to an increase in the temperature and the likelihood of PD events and premature aging of the solid insulation occurs.

Temperature is a crucial factor that affects the solid insulation. High temperatures can cause thermal degradation, which can lead to cracks, oxidation, and embrittlement of the insulation materials. On the other hand, low temperatures can cause
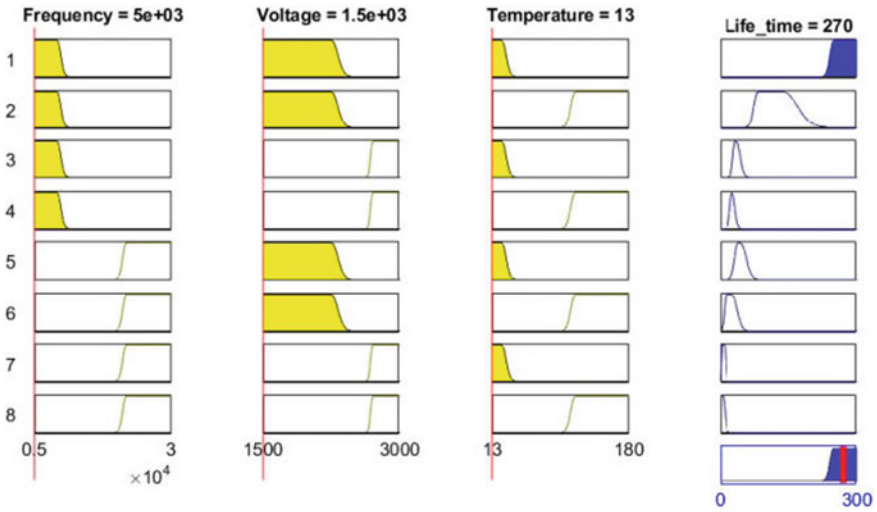
Fig. 7 Fuzzy rules for model

mechanical stress, such as contraction and expansion of the materials, which can lead to cracks and mechanical failure of the insulation. The proposed fuzzy logic model for life time estimation is shown in Fig. 8.

Based on the influence coefficients, it has been observed that the frequency and temperature exhibit the strongest interaction. The next strongest interaction is between the amplitude and frequency, while the interaction between voltage and temperature is the weakest. Surface Graph of interaction between three factors is shown in Figs. 9, 10 and 11.
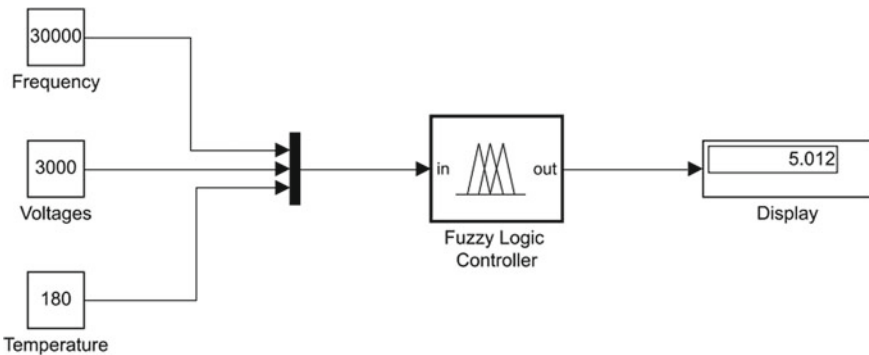
Fig. 8 Proposed Fuzzy logic model for life time
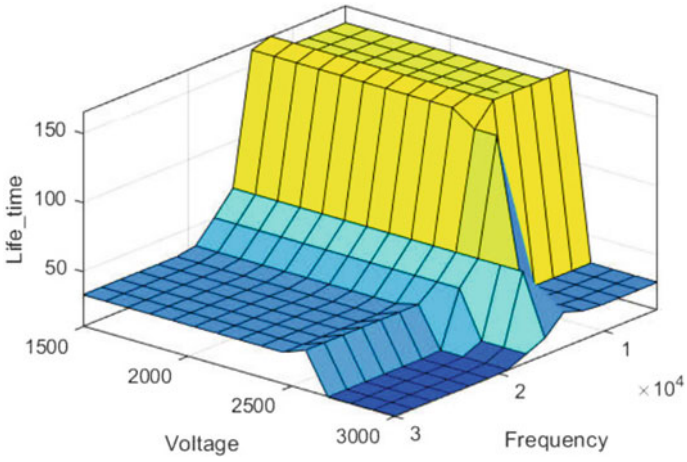
Fig. 9 Surface graph of voltage and frequency effects on life time
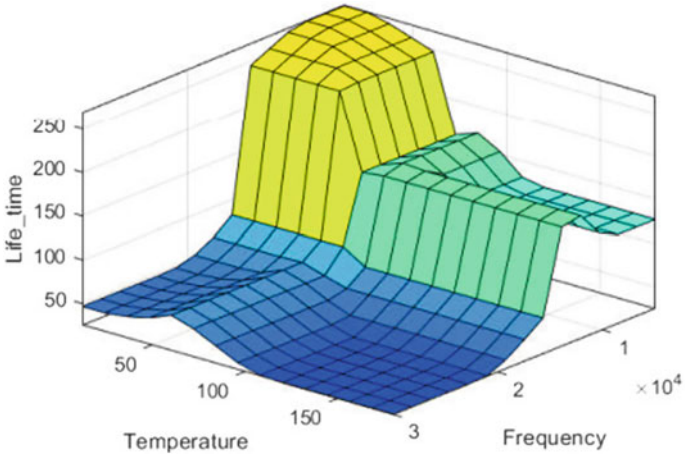
Fig. 10 Surface graph of temperature and frequency effects on life time
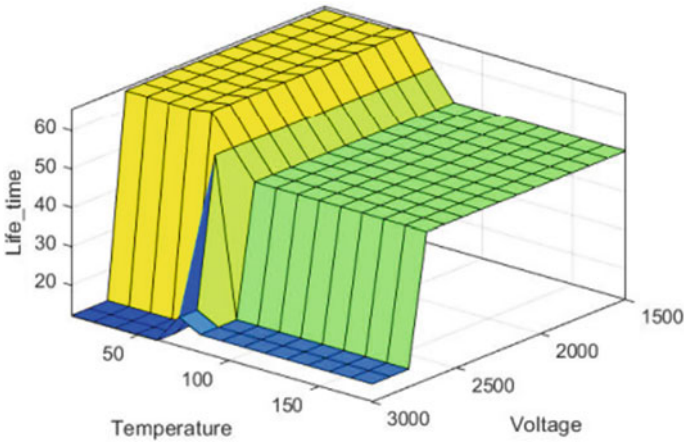
Fig. 11 Surface graph of voltage and temperature effects on life time

7 Conclusion

A life estimation model using a fuzzy logic approach was suggested to assess the insulation life of PI films under various experimental conditions, such as voltage frequency, amplitude, temperature, and their interactions. The experimental results indicate that an increase in voltage frequency, amplitude, or temperature leads to an acceleration in the aging rate of PI insulation. Moreover, the interaction between frequency and temperature shows the largest impact and with frequency and amplitude having a greater influence coefficient also. Voltage and temperature have the weakest impact on PI insulation. The proposed model is believed to be useful for insulation condition assessment.

References

1. Chen H et al (2016) A 50-kVA three-phase solid-state transformer based on the minimal topology: Dyna-C. IEEE Trans Power Electron 31:8126–8137
2. She X, Huang AQ, Burgos R (2013) Review of solid-state transformer technologies and their application in power distribution systems. IEEE Journal of Emerging and Selected Topics in Power Electronics 1(3):186–198
3. Wang D et al (2016) A 10-kV/400-V 500-kVA electronic power transformer. IEEE Trans Industr Electron 63(11):6653–6663
4. Cavallini A, Fabiani D, Montanari GC (2010) Power electronics and electrical insulation systems Part 1: phenomenology overview. IEEE Electrical Insulation Magazine 26(3):7–15

5. Liu T, Li Q, Huang X, Lu Y, Asif M, Wang Z (2018) Partial discharge behavior and ground insulation life expectancy under different voltage frequencies. IEEE Trans Dielectr Electr Insul 25(2):603–613
6. Akram S, Gao G, Liu Y, Zhu J, Wu G, Zhou K (2015) Degradation mechanism of Al_2O_3 nano filled polyimide film due to surface discharge under square impulse voltage. IEEE Trans Dielectr Electr Insul 22(6):3341–3349
7. Haq SU, Jayaram SH, Cherney EA (2008) Insulation problems in medium-voltage stator coils under fast repetitive voltage pulses. IEEE Trans Ind Appl 44(4):1004–1012
8. Bonnett AH (1994) Analysis of the impact of pulse-width modulated inverter voltage waveforms on AC induction motors. In: Proceedings of IEEE pulp and paper industry conference, Nashville, TN, USA, pp 68–75
9. Forouhari S, Abu-Siada A (2018) Application of adaptive neuro fuzzy inference system to support power transformer life estimation and asset management decision. IEEE Trans Dielectr Electr Insul 25(3):845–852
10. Bakar NA, Abu-Siada A (2016) Fuzzy logic approach for transformer remnant life prediction and asset management decision. IEEE Trans Dielectr Electr Insul 23(5):3199–3208
11. Liu T et al (2019) Multi-factor model for lifetime prediction of polymers used as insulation material in high frequency electrical equipment. Polym Testing 73:193–199

Quantum Mechanism of Insulation Degradation Induced by Charge Relaxation in Silicone Gel Under the Ultrafast Pulsed Electric Field

Teng Gao and **Dongxin He**

Abstract For the problem of insulation deterioration under ultra-fast pulsed electric field, we study the charge characteristics of organic insulating materials from the quantum point of view. It is found that due to the strong interaction between the electrons and the nucleus in organic molecules, the electrons exist in the trap energy level in the form of local states when there are defects in the material. Based on Marcus' theory, the local space charge transition is different from the free electrons, and it will be not only related to trap distance, trap depth, temperature, and other factors, but also closely related to the soft properties of polymer materials. Therefore, the relative speed between the space charge relaxation time and the mutation time of ultra-fast pulsed electric field is the premise to reveal the insulation failure caused by trapping and detrapping.

Keywords Space charge · Ultra-fast pulsed electric field · Relaxation time

1 Introduction

Silicon carbide (SiC) as a typical representative of the third generation semiconductor, its devices and modules have higher operating voltage (more than 10 kV), higher operating temperature (more than 250 °C), faster switching frequency (more than 30 kHz) and lower working loss, which is conducive to the power electronic equipment to high efficiency, miniaturization development [1, 2]. In order to give full play to these excellent properties of SiC materials, it is necessary to realize efficient and reliable connection of power and signal through packaging. Because of silicone gel with good insulation, high temperature resistance, good adhesion to most

T. Gao · D. He (✉)

Shandong Provincial Key Laboratory of UHV Transmission Technology and Equipment, School of Electrical Engineering, Shandong University, Jinan, China
e-mail: hdx@sdu.edu.cn

T. Gao
e-mail: gt@sdu.edu.cn

materials after curing, and strong self-healing ability, it can meet the requirements of insulation and waterproof, shock-proof and moisture-proof for device packaging, and become the first choice of insulation materials for power electronic equipment packaging [3]. However, the faster switching speed (up to 5 kV/μs) makes the silicone gel withstand high frequency and high amplitude pulse electric field with extremely steep voltage rise rate, leading to rapid deterioration and early failure, which brings severe challenges to the reliability of equipment operation [4].

The macroscopic insulating properties of silicon gels under conventional electric fields have been studied extensively. Dodd et al. found that the electrical trees of silicone gel contained fibrous parts and bubble parts, showing that treeing behavior that includes features typical of both liquids and solids [5]. Sato et al. studied the surface discharge characteristics of the interface between silicone gel and substrate. They believed that the cavity diameter was affected by electrostatic force generated by partial discharge, and the surface charge accumulation and temperature would affect the cavity propagation [6, 7]. For insulation deterioration in pulsed electric fields, researchers usually infer the motion of space charges from electrical branches. Liu et al. found that the initial voltage of the crosslinked polyethylene electrical branch under the action of DC superimposed pulsed electric field was much lower than the initial voltage of the electrical branch under the simple application of DC electric field. They believed that the injected space charge would be accelerated by the pulsed voltage and collide with the polymer, triggering the electrical branch [8]. Du et al. studied the effect of pulse duration on the growth characteristics of electric tree at low temperature, and found that the longer the pulse duration, the faster the growth rate of electric branches. Therefore, it is inferred that with the extension of pulse duration, more high-energy charges may be injected into the polymer and collide with the molecular chain, accelerating the degradation of dielectric materials [9]. Liu et al. studied the initiation, growth, extension and other microscopic processes of the composite insulated strip under repeated pulse voltage, and concluded that there were two reasons for the faster initiation of the branch under repeated pulse voltage: First, when the voltage rise rate exceeds 5 kV/μs, the charge carriers generated at the tips of the rising and falling edges may obtain enough energy to directly affect the molecular chain, causing it to split into low molecular products and gases, and finally forming the electrical branch channel. Second, the charge carriers produced by the tip of the needle recombine after acceleration, generating ultraviolet radiation and promoting the photodegradation of insulating materials [10]. Zhou et al. studied the electrical tree behavior of silicon rubber (SIR) under high temperature pulse voltage, and found that with the increase of pulse frequency, more frequent partial discharge occurred in the channel, and made a similar inference about this phenomenon: the extremely steep rising edge of pulse voltage would aggravate the charge motion [11]. More recently, Sato et al. investigated the electrical branch behavior under repeated pulsed electric fields and found that the cavity length increases with frequency [12]. At present, it is believed that the ultra-fast pulsed electric field will accelerate the movement of space charge, resulting in collision, radiation recombination and other processes, damaging molecular chains, and thus leading to the deterioration of insulating materials.

In theory, some scholars have carried out researches on charge trapping and detrapping behaviors [13–17], but little attention has been paid to the time scale of dynamic behavior processes such as space charge trapping and detrapping under ultra-fast pulsed electric field, namely relaxation time. For rigid materials, electrons are extended states and respond very quickly to the external field. However, for polymer materials, electrons generally exist in the form of local states, and their relaxation time is closely related to molecular properties, trap properties, temperature and other factors. In addition, the electric field mutation time and charge relaxation time (ns ~ μs) reach the same order of magnitude under the ultra-fast pulsed electric field, the relaxation time of space charge becomes an important factor affecting charge detrapping and trapping[18–21]. From the perspective of force analysis (as shown in Fig. 1), the force on the space charge includes electric field force and material stress caused by potential fields such as nucleus and impurities. Under constant electric field, electric field force and material stress reach equilibrium state easily. Once the nanosecond pulsed electric field is applied, the electric field force suddenly increased at the time of rising edge. When the relaxation time of space charge is larger than the nanosecond scale (i.e. $\tau_e > ns$), the charge has no time to react, the material stress on the charge remains unchanged, and the electric field force suddenly increases, which results in the charge detrapping with the pulsed electric field, triggering the electrical branching and even breakdown behavior; When the relaxation time of space charge is less than the nanosecond scale (i.e. $\tau_e < ns$), in order to overcome the external electric field stimulation, the space charge rapidly shifts to overcome the external electric field stimulation, the material stress and electric field force increase at the same time, and it is still in a state of equilibrium, which can effectively slow down the insulation failure. Therefore, the relative speed of relaxation time of space charge and mutation time of ultra-fast pulsed electric field is the premise to reveal the insulation failure caused by trapping and detrapping. However, there is a lack of quantitative characterization of the space charge relaxation time at the edge time of the ultra-fast pulse, especially the dependence on the molecular properties and trap properties.

In this paper, we attempt to reveal the insulation deterioration mechanism induced by space charge trapping and detrapping from the perspective of quantum. Based on Marcus theory, the relationship between charge relaxation time and trap properties is quantified. Our results reveal the effect of space charge relaxation on insulation deterioration the perspective of time and space, and provide guidance for insulation deterioration protection at ultra-fast time scale.
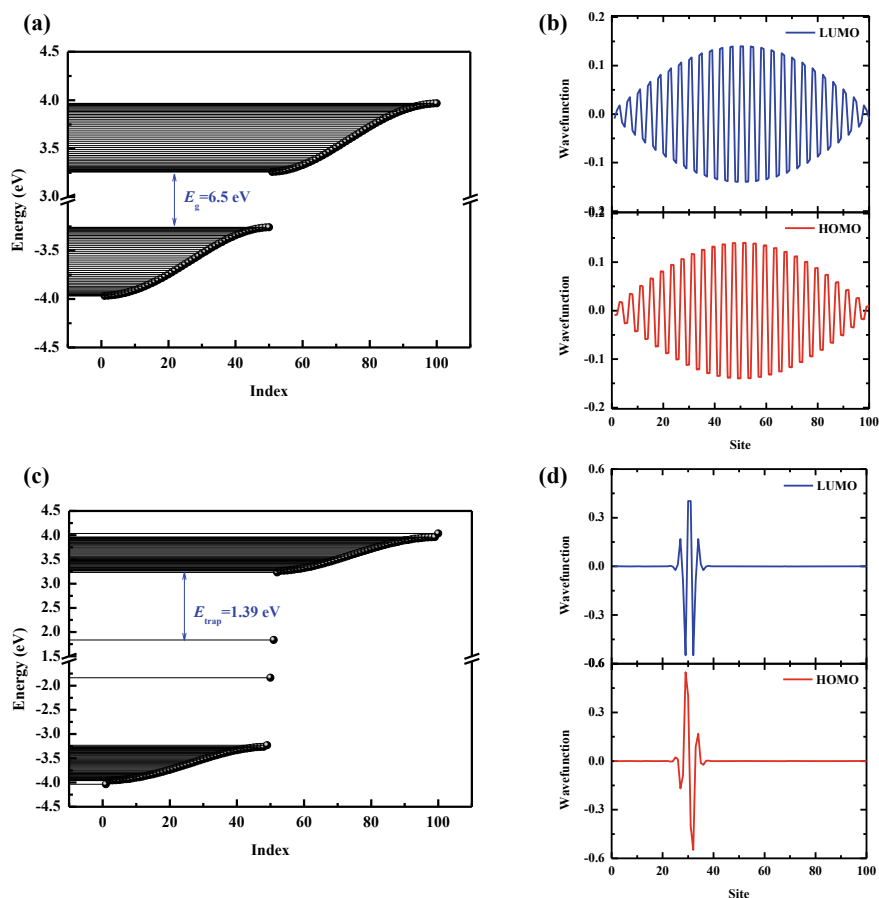
Fig. 1 Distributions of the energy levels (**a** and **c**) and electron wavefunction (**b** and **d**)

2 Theory and Methods

2.1 *Tight-Binding Su–Schrieffer–Heeger (SSH) Model*

Organic silicone gel with the long molecular chain is a quasi-one-dimensional structure. Carriers will polarize surrounding electrons, atoms, or the whole molecule during transport, and move with the polarized field, that is, the organic silicone gel molecule has the strong electron–phonon coupling. In order to describe this property, we adopt the quantum tight-binding Su–Schrieffer–Heeger (SSH) model to study the behavior of the space charge.

The poly-siloxane molecule is regarded as a one-dimensional atomic chain composed of Si–O groups, and the action potential of each group on electrons is

$V(\vec{r} - \vec{R})$, then the Hamiltonian of the system can be written as:

$$H = \sum_i [-\frac{\hbar^2}{2m}\nabla_i^2 + \sum_n V(\vec{r}_i - \vec{R}_n)] + \frac{1}{2}K(\vec{R}_{n+1} - \vec{R}_n)^2. \tag{1}$$

In Eq. (1), i and n denote the indicators of electron and atom, respectively. The first term is the electron Hamiltonian, including the kinetic energy of the electron and the interaction of the electron with the nucleus, where m and V represent the electron mass and atomic potential field. The second term is the elastic energy between atoms, and K is the elastic constant. $\vec{R}$ and $\vec{r}$ are the atom displacement and electron displacement.

As the electron is near the group l, the potential energy acting on the electron mainly comes from $V(\vec{r}_i - \vec{R}_l)$, and the potential energy of other groups is much smaller, which can be regarded as perturbation, i.e. tight bound approximation. Therefore, the electron Hamiltonian can be written as the sum of the isolated atomic Hamiltonian,

$$H_e = \sum_i [-\frac{\hbar^2}{2m}\nabla_i^2 + V(\vec{r}_i - \vec{R}_l)] + \sum_{n \neq l} V(\vec{r}_i - \vec{R}_n). \tag{2}$$

The eigenfunction $|\varphi_l(\vec{r})\rangle$ of the isolated atomic Hamiltonian can be used as the zero-order approximate wavefunction of the system. According to degenerate perturbation theory, the electronic wave function $\psi(\vec{r})$ of the whole system can be written as a linear superposition of $|\varphi_l(\vec{r})\rangle$, namely, $\psi(\vec{r}) = \sum_l C_l |\varphi_l(\vec{r})\rangle$.

For a multi-electron system, we need to quantize the electron Hamiltonian twice, and obtain its secondary quantized form,

$$H_e = E_0 \sum_n C_n^\dagger C_n - \sum_n t_{n,n+1}(C_{n+1}^\dagger C_n + C_n^\dagger C_{n+1}). \tag{3}$$

where $C_n^\dagger(C_n)$ denotes the creation (annihilation) operator of an electron at site n. The first term of Eq. (3) means the on-site energy with intensity E_0. The second term of Eq. (3) means electron transfer between the nearest-neighbor sites along the chain, and the transfer integral $t_{n,n+1}$ between sites n and $n+1$ is written as $t_{n,n+1} = t_0 - \alpha(u_{n+1} - u_n) - (-1)^n t_e$. t_0 is the transfer integral in a uniformly arranged lattice. α is the electron–phonon coupling constant. t_e is the symmetry-breaking term. u_n means the lattice displacement.

We suppose that electrons can always response the lattice potential instantly and take the adiabatic approximation. The electronic eigenstate and eigenenergy ε_μ are obtained by solving the eigenequation of the electronic Hamiltonian, which can be expressed as

$$-t_{n,n+1}|\varphi_{\mu,n+1}\rangle - t_{n,n-1}|\varphi_{\mu,n-1}\rangle = \varepsilon_\mu|\varphi_{\mu,n}\rangle. \tag{4}$$

According to the principle of minimum energy, atomic displacement can be obtained by the following equation,

$$u_{n+1} - u_n = \frac{2\alpha}{NK} \sum_{\mu,n} \rho_{n,n+1} - \frac{2\alpha}{K} \sum_{\mu} \rho_{n,n+1},$$ (5)

where the density matrix $\rho_{n,m}$ is defined as $\rho_{n,m} = \sum_{\mu} \varphi^*_{\mu,n} f_{\mu} \varphi_{\mu,m}$ with f_{μ} being the Fermi–Dirac distribution for μth energy level. Equations (4) and (5) are solved by self-consistent iterative calculation, from which the atom displacement and the electronic states are obtained.

2.2 Marcus Theory

Consider an important property of organic polymers, that is, the strong electron–phonon coupling. Because of this property, the space charge exists in the form of a local state, which means that the motion of the charge is coupled to the molecule. The charge transfer between trap i and trap j takes place via hopping with a rate ω_{ji}, which is usually expressed by semiclassical Marcus formula,

$$\omega_{ji}(t) = \frac{t_{ji}^2}{\hbar} \left[\frac{\pi}{k_B T \lambda} \right]^{1/2} \exp\left[-\frac{(\lambda + \Delta E_{ji})^2}{4k_B T \lambda} \right],$$ (6)

where $t_{ji} = t_0 e^{-2\gamma R_{ij}}$ represents the space charge transfer integral between trap i and trap j. t_0 is the maximum transfer integral between the traps. γ is the reciprocal of the local wave function, reflecting the localization of the space charge. $R_{ij} = |R_j - R_i|$ is the space distance between the two traps. $\Delta E_{ji} = (\varepsilon_j - \varepsilon_i) - eE(t)R_{ij}$ denotes the energy difference between the two traps, which includes the contribution of the electric potential generated by the external electric field. λ is the reorganization energy and represents the vibration of molecular energy caused by the relaxation of the geometric structure after charge trapping (detrapping), which is calculated by optimizing the structure of neutral state and anionic state. We obtain the energy E_0 and E_c^* before and after doping in neutral configuration, and the energy E_0^* and E_c before and after doping in charged configuration. The reorganization energy λ is determined as

$$\lambda = (E_c^* - E_c) + (E_0^* - E_0)$$ (7)

Therefore, the transition rate of carriers not only related to trap distance, trap depth, temperature, and other factors, but also closely related to the soft properties of polymer materials, which are often ignored in previous work. $\tau_i = 1/\sum_j \omega_{ji}$ represents the time the charge stays on trap i, i.e., the charge relaxation time.

3   Results and Discussion

We construct the model with a molecular chain of 100 groups, as shown in Fig. 1. Based on the tight-binding SSH model, the band structure of the electron and the electronic state at the edge of the band gap were calculated. It was found that the band gap of organic siloxane was about 6.5 eV, as shown in Fig. 1a, and the electrons in the ground state were extended states distributed throughout the molecular chain, as shown in Fig. 1b.

Once a defect exists in the chain where we set a defect with a distortion in the chain at the 30th group, the charge will be localized at the defect. We calculate the energy levels and find that the conduction band and the valence band split into two local energy levels appearing in the forbidden band, and the corresponding wavefunction is localized near the defect, as shown in Fig. 1c and d. In addition, we can obtain the energy of the trap $E_{\text{trap}} = 1.39$ eV.

Analysis that due to the electron–phonon coupling in organic polymers, the space charge is localized as a polaron by its surrounded molecular distortions. Thus, molecular structure is closely related to electronic properties. In different molecular defect structures, the electron energy level changes with the type of the defect. Next, we construct three different defect types: molecular distortion, molecular bond breaking, and heavy metal doping, and calculate the depth of trap energy levels, as shown in Fig. 2.

Due to the strong coupling between the electron and the molecule, when the electron transition or transport occurs, the energy of the electron and the energy of the molecule will be converted to each other. Based on Marcus theory, the transition
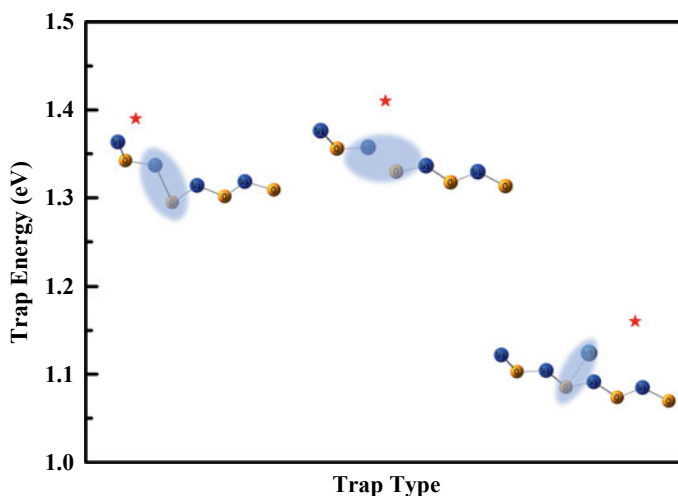
Fig. 2   Schematic diagram of the different defects and trap energy
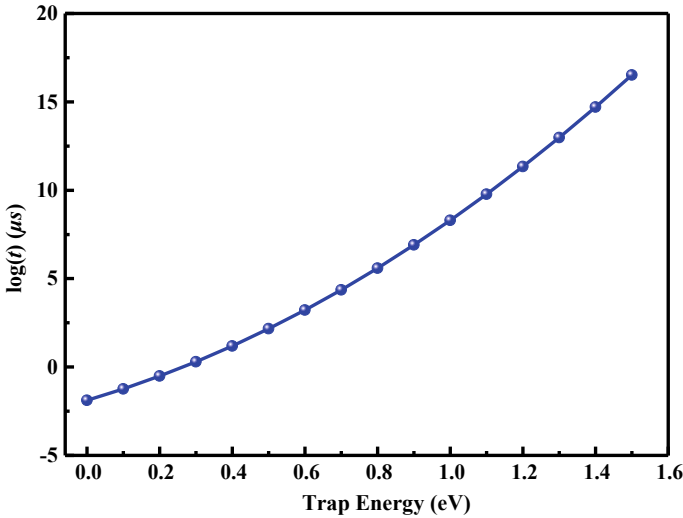
Fig. 3 Exponential relationship between space charge detrapping and trap depth

of charge between traps is not only related to trap distance, trap depth, temperature, and other factors, but also closely related to the electron–phonon coupling of polymer materials. The relaxation time of space charge is closely related to molecular properties, while the molecular structure of silicone gel is easy to be affected by the environment, such as cross-linking reaction, group drop, etc., so the relaxation process of space charge will be more complicated.

Based on Marcus theory, we calculate the relationship between space charge detrapping and trap depth, and the results are shown in Fig. 3. We find that the detrapping time increases exponentially with the trap depth. When the trap energy level is shallow, the detrapping time of space charge may reach the nanosecond level, which is comparable to the mutation time of ultra-fast pulsed electric field. At this time, according to the force analysis of space charge, charge is more likely to detrapping and lead to molecular deterioration, resulting in insulation failure.

4 Conclusion

In conclusion, we proposed a quantum theory to reveal the mechanism of insulation deterioration. We found that the charge in silicone gel materials exists in the trap in the form of local states when there are defects in the material. Based on Marcus' theory, the local space charge transition is different from the free electrons, and it will be not only related to trap distance, trap depth, temperature, and other factors, but also closely related to the soft properties of polymer materials. In addition, when the trap energy level is shallow, the detrapping time of space charge may reach the nanosecond

level, and the relaxation time of space charge is an important factor affecting charge detrapping. Our model provides a microscopic quantum understanding of insulation deterioration induced by the space charge and opens a route to improve insulation performance by regulating molecular properties.

References

1. Qian Z, Zhang J, Sheng K (2014) Status and development of power semiconductor devices and its applications. Proceedings of the Chinese Society of Electrical Engineering 34(29):5149–5161 (in Chinese)
2. Khazaka R, Mendizabal L, Henry D et al (2015) Survey of high-temperature reliability of power electronics packaging components. IEEE Trans Power Electron 30(5):2456–2464
3. Sato M, Kumada A, Hidaka K et al (2014) On the nature of surface discharges in silicone-gel: prebreakdown discharges in cavities. In: 2014 IEEE conference on electrical insulation and dielectric phenomena (CEIDP). Des Monies, IA, USA: IEEE, pp 19–22
4. Yao Y, Lu G, Boroyevich D et al (2015) Survey of high-temperature polymeric encapsulants for power electronics packaging. IEEE Transactions on Components, Packaging and Manufacturing Technology 5(2):168–181
5. Salvatierra LM et al (2016) Self-healing during electrical treeing: a feature of the two-phase liquid-solid nature of silicone gels. IEEE Trans Dielectr Electr Insul 23(2):757–767
6. Sato M, Kumada A, Hidaka K et al (2016) Surface discharges in silicone gel on AlN substrate. IEEE Trans Dielectr Electr Insul 23(1):494–500
7. Nakamura S et al (2021) Effect of temperature on electrical Treeingin silicone gel for power modules. In: 2021 IEEE conference on electrical insulation and dielectric phenomena-Vancouver-Canada
8. Liu Y, Cao X (2013) Electrical tree initiation in XLPE cable insulation by application of DC and impulse voltage. IEEE Trans Dielectr Electr Insul 20(5):1691–1698
9. Du BX, Xue JS, Zhang MM (2017) Effect of pulse duration on electrical tree and breakdown process of epoxy resin in LN2. IEEE Trans Dielectr Electr Insul 24(1):359–366
10. Liu X, Wang J, Zhang R, Xue C, Chen H, Li Y (2020) Electrical tree characteristics under AC and repetitive pulse voltages in wind turbine generator composite insulation. IEEE Trans Dielectr Electr Insul 27(3):1007–1014
11. Zhang Y, Zhou Y, Zhang L et al (2018) Electrical treeing behaviors in silicone rubber under an impulse voltage considering high temperature. Plasma Sci Technol 20(5):054012
12. Nakamura S, Kumada A, Hidaka K et al (2019) Electrical treeing in silicone gel under repetitive voltage impulses. IEEE Trans Dielectr Electr Insul 26(6):1919–1925
13. Li W, Liao R, Yuan X, Huang J, Cao D, Hao J (2012) Effects of thermal aging on space charge and trap characteristics of cellulose insulation papers. Proceedings of the CSEE 32(07):145–153 (in Chinese)
14. Chen G, Xu Z (2009) Charge trapping and detrapping in polymeric materials. J Appl Phys 106:123707
15. Zhou T et al (2011) Charge trapping and detrapping in polymeric materials: trapping parameters. J Appl Phys 110:043724
16. Wang W et al (2017) Trap-controlled charged decay and quantum chemical analysis of charge transfer and trapping in XLPE. IEEE Trans Dielectr Electr Insul 24(5):3144–3153
17. Meunier M, Quirke N, Aslanides A (2001) Molecular modeling of electron traps in polymer insulators: chemical defects and impurities. J Chem Phys 115:2876

18. Haq SU, Jayaram SH, Cherney EA (2007) Evaluation of medium voltage enameled wire exposed to fast repetitive voltage pulses. IEEE Trans Dielectr Electr Insul 14(1):194–203
19. Zhou K, Wu G, Gao B, Cao K, Zhou L (2008) Space charge effects on partial discharge activities under pulse voltage. Transactions of China Electrotechnical Society 23(10):11–17 (in Chinese)
20. He D, Zhang T, Meng F, Li Q, Wang W, Liu H, Teyssedre G (2021) Space charge behaviors in cable insulation under a direct current-superimposed pulsed electric field. High Voltage 6(3):426–434
21. Zhang T, He D, Wei J, Liu H, Li Q, Teyssedre G (2022) Charge vibration behaviour in polyimide under the pulse voltage with different rise and fall times. High Voltage 7(1):64–74

Multi-objective Optimization of Permanent Magnet Actuator Based on Surrogate Model

Ke Danyang and Zheng Xin

Abstract In order to solve the problem that the performance parameters of permanent magnet actuators are difficult to be identified and by computers and the multi-objective optimization problem, this paper proposes a multi-objective optimization method based on the surrogate model. Firstly, a surrogate model based on orthogonal least squares radial basis functions (OLS-RBF) is proposed to solve the problem of identifying the performance parameters of permanent magnet actuators. Then, for the multi-objective optimization problem, a novel elimination mechanism is proposed for NSGA-III to take the place of the original selection mechanism, which improves the diversity of the Pareto solution sets and reduces the running time of the algorithm. And combine it with the fitted surrogate model for multi-objective optimization. Finally, taking the electromagnetic needle selector with permanent magnets as an example, the feasibility of the method and the accuracy of the improved NSGA-III algorithm are verified by simulation, which lays the foundation for the general optimization design scheme of permanent magnet actuators.

Keywords Permanent magnet actuator · Permanent magnet · Improved NSGA-III · Surrogate model · Multi-objective optimization

1 Introduction

Permanent magnets actuators have the characteristics of high coercive force, high remanence, and fast response speed, so they are widely used in industry, medical, military and other fields, so the optimization work for them is of great significance. Due to the close correlation between the performances of permanent magnets and

K. Danyang (✉) · Z. Xin
College of Electrical Engineering and Automotion, Fuzhou University, Fuzhou 350000, Fujian, China
e-mail: 782553095@qq.com

Fujian Key Laboratory of New Energy Generation and Power Conversion, Fuzhou 350000, Fujian, China

503

the actuators [1], which includes electromagnetic force, magnetic flux, magnetic flux density, and economic indicators and so on, the optimization of permanent magnet actuators should focus on the size of the permanent magnet while considering multiple different optimization objective functions. These functions usually conflict with each other, so the optimization of the actuators is a typical multi-objective optimization problem. Pareto-based multi-objective optimization, such as NSGA-II [2] and SPEA2 [3], performs well when solving two or three-objective optimization problems, but it faces great difficulties when dealing with multi-objective optimization problems. Based on NSGA-II, Deb et al. proposed NSGA-III [4] for solving multi-objective optimization problems. However it was found that NSGA-III had the problem of increase of selection times.

In addition, the complexity and nonlinearity of the relationship between optimization factors and objectives is difficult to express through mathematical expressions. The surrogate model is based on the idea of low computational time and cost through the fitting methods to replace finite element calculations and then approach the target functions. References [5] and [6] analyze the scope of application of different surrogate models in engineering practice such as motor optimization, sky wheel design, and lower pipeline design. In recent years, surrogate models such as response surface model [7], radial basis model [8, 9], and Kriging model [10, 11] have been widely used in multi-objective optimization. However, the fitting error of the surrogate model to the data is difficult to control and is prone to overfitting or underfitting.

In order to solve the multi-objective optimization problem of permanent magnet actuators, this paper proposes an orthogonal least squares radial basis function (OLS-RBF) surrogate model. Firstly, build a preliminary surrogate model, and improve the model to speed up the relationship between the approximation optimization factor and goal, while reducing the possibility of overfitting and underfitting; After that, the trained surrogate model is used as the objective function of the improved NSGA-III for iterative optimization to obtain Pareto solution set. Finally, taking the electromagnetic needle selector with permanent magnets as an example, the three objectives of the average suction force of No. 2 and No. 3 needle pieces, the electromagnetic attraction force of No. 1 needle piece and the cost of the needle selector are optimized under the condition of 11 needle pieces. After the optimal solution is obtained, the feasibility of this method on the electromagnetic actuator with permanent magnets is verified by simulation, which lays the foundation for the design of optimization software in the future.

2 OLS-RBF Surrogate Model

The OLS-RBF surrogate model is a surrogate model based on ridge regression and RBF neural network. The RBF surrogate model is a local approximation of the neural network which is represented as Eq. (1), where ϕ_i is the basis function of the i-th hidden layer neuron, c_i the center point of that, and σ_i the center point width of that, $\|x\text{-}c_i\|$ represents the Euclidean distance between the sample point and the center

point. OLS is represented as formula (2), and the surrogate model selects the center point of the RBF neural network through the least squares method. If each sample point is chosen, the error ε between the true value y and the predicted value ^y is reduced.

$$\phi_i(||x - c_i||) = \exp\left(-\frac{||x - c_i||}{2\sigma_i^2}\right)$$ (1)

$$y = \hat{y} + \varepsilon = \sum_{i=1}^{n} \lambda_i \phi_i(||x - c_i||) + \varepsilon$$ (2)

In the above formula, λ_i is the output weight of the radial basis function.

When the OLS-RBF surrogate model is performing model training, it is necessary to adjust the hidden node expansion constant according to different samples. The larger the hidden node expansion constant, the easier it is for the neural network to learn complex nonlinear functions, but at the same time there is also the possibility of overfitting. In order to reduce the occurrence of overfitting and underfitting, this paper introduces the gradient descent operator ω to improve the selection of the center point width of the OLS-RBF neural network through formula (3). Gradient descent is performed on the width of the center, which effectively reduces the number of neurons in the hidden layer when selecting the center of the radial basis function each time. Figure 1 is a flowchart of the improved OLS-RBF neural network.

$$\sigma^* = \sigma - \omega \triangle \sigma$$ (3)

In the above formula, σ^* and σ are the center widths of the new and old basis functions respectively. $\triangle\sigma$ is the difference between the center widths of the new and old basis functions. ω is the gradient descent operator.
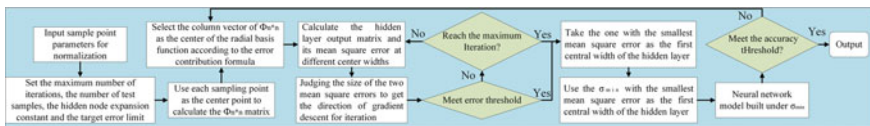
Fig. 1 OLS-RBF surrogate model flow chart
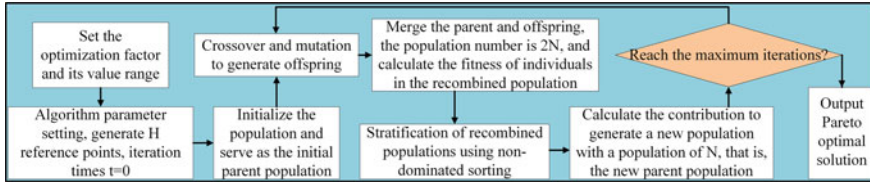
Fig. 2 NSGA-III flow chart

3   Introduction of Improved NSGA-III

3.1   Overview of NSGA-III

Based on the NSGA-II, the NSGA-III introduces a reference point to guide the diversity of the population close to the Pareto optimal solution. In NSGA-III, a novel environment selection method based on reference points and Euclidean distance is proposed.

NSGA-III first normalizes the individual optimization factors and objectives, so that all individuals are on the same hyperplane as the reference point. The H structure reference point is constructed according to the individual and the reference line. The parent population P_t is randomly initialized according to the value range of the optimized variable, and the offspring Q_t is generated through genetic variation. Both P_t and Q_t are with the population numbers of N, and they are recombined together to form the population R_t. The population is hierarchically clustered by sorting non-dominated classes, and duplicate individuals are eliminated. If the number of populations is greater than N, associate the population individual with the nearest reference point. For reference points with few associations, find out the closest solution associated with the reference point in the critical layer to supplement. Then Re-hierarchical clustering, select the non-dominated subset with high priority, keep the number of populations as N, and the new population as the new parent. Repeat genetic and optimization operations until the maximum number of iterations is met. The flowchart of NSGA-III is shown in Fig. 2.

3.2   Improvements of the Selection Mechanism

The original NSGA-III is widely used to solve many engineering optimization problems, but there are still some problems with the original NSGA-III. For example, the number of non-dominated solutions increases dramatically with the number of targets, leading to an increase in the number of executions of the selection mechanism.

Aiming at the above problems, this paper proposes an improved NSGA-III. The original NSGA-III recombinant population performs non-dominated sorting. If the sorting has only 1 layer, only one judgment is required. But when the number of
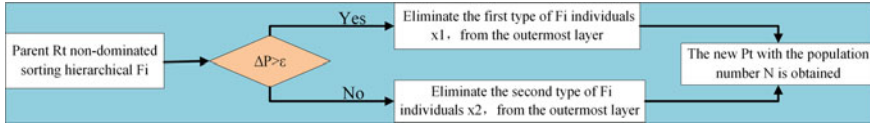
Fig. 3 Flowchart of the elimination mechanism

iterations and the objective function increase, the ranking of non-dominated solutions will also increase dramatically. When it is necessary to select N individuals, it is necessary to perform N judgments. The improved NSGA-III adopts a new elimination mechanism to replace the old selection mechanism that improves the efficiency of selection. After the non-dominated class is sorted, a new elimination mechanism is adopted when selecting the offspring Pt, and the steps are shown in Fig. 3. After the non-dominated sorting of the population Rt, individuals are eliminated from high to the low. Introduce the self-convergence factor ΔP. If it is greater than the self-convergence factor, it means that the convergence is poor, choose to eliminate the first type of individual x_1, otherwise eliminate the second type of individual x_2. The first type eliminates x_1 with the farthest Euclidean distance from the origin, and the second type is x_2 with the smallest distribution density. The long distance indicates that the convergence of individuals is poor and the low density indicates that the diversity of individuals is poor.

4 Simulation and Verification of Multi-objective Optimization Based on Surrogate Model

4.1 Surrogate Model Training of Electromagnetic Needle Selector with Permanent Magnet

In order to verify the feasibility of the multi-objective optimization method based on the surrogate model, this paper takes an electromagnetic needle selector with permanent magnets from a flat knitting machine as an example. In the textile industry, needle selectors play an important role in realizing automated textiles.

The three-dimensional model of the needle selector built by Solidworks is shown in Fig. 4. The material of the needle pieces, the iron core and the yoke is electrical pure iron, and the permanent magnet material is N35. There are four work locations on the needle selector, and there is an excitation coil under each work location. The main working circuit is composed of a permanent magnet, a coil and an iron core. There is a reaction force spring on the needle piece. When there is no need for needle pieces selection, the permanent magnet provides electromagnetic force which is greater than the maximum reaction force of the spring that is 1 N. And then the spring is compressed and the needle pieces are adsorbed on the surface of the selector. When the needle piece needs to be selected, an electric current is passed to
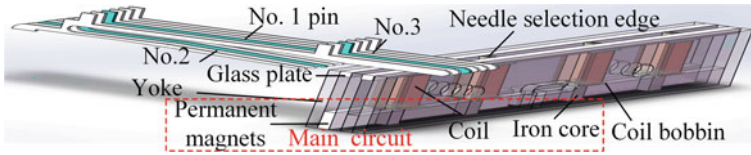
Fig. 4 3D model of the needle selector

the electromagnetic coil under the work location to counteract the permanent magnet suction force. When the suction force of the needle piece is less than 1 N, the needle is piece selected.

The upper part of the work location is designated as No. 1 needle piece, and the adjacent sides are respectively designated as No. 2 and No. 3 needle pieces, and so on. When the number of needle pieces is different, the simulation results are shown in Table 1. When the force on the needle piece is less than 1N, it is selected. When the number of needle pieces is too large, there will be wrong selection. Therefore, it is necessary to perform multi-objective optimization on the needle selector to improve performance.

Because the needle selector contains permanent magnets, it has a great influence on the performance of the needle selector. And according to the various factors of range analysis and variance analysis, after comparing each factor, the optimal factors are selected as permanent magnet width (D_m), height (L_m), iron core width (D_z), air gap length between needle selector and the work location (L_g), coil ampere-turns (A). The value range of each parameter is shown in Table 2.

Table 1 The relationship between the force on the needle pieces and the number of needle pieces before optimization	Number of needle pieces	The needle piece force/N		
		No. 2	No. 1	No. 3
	1		0.464	
	3	1.305	0.525	1.308
	5	0.875	0.601	0.845
	7	0.698	0.640	0.706
	9	0.612	0.653	0.628
	11	0.559	0.604	0.556

Table 2 Value range of needle selector parameters	Optimization factor	Ranges
	Dm/mm	[2.3, 2.7]
	Dz/mm	[2.3, 2.7]
	Lg/mm	[0.08, 0.12]
	Lm/mm	[8.1, 8.9]
	Turns/A	[600, 1000]

In maxwell, a three-dimensional simulation model of the needle selector is established for parametric modeling. In order to save simulation calculation memory, non-magnetic materials are not considered in this paper. The sample parameters are designed according to Taguchi algorithm, orthogonal test and central composite test, and the performance sample parameters are obtained by finite element simulation. The average suction force (F_{23}) of No. 2 and No. 3 needle pieces, the suction force (F_1) of No. 1 needle piece and the production price (W) of the needle selector under the working condition of 11 needle pieces are selected as the optimization objectives.

By training the OLS-RBF surrogate model on the obtained sample set, a predictable surrogate model is obtained. After fitting, the fitting rates of the average suction force of No. 2 and No. 3 needle pieces and the suction force of No. 1 needle piece were 98.28 and 93.42%. The production price of the needle selector can be obtained through material volume and price calculation without fitting.

4.2 Multi-objective Optimization Results

The two objective functions obtained by fitting the above surrogate model and the production cost are used as the objective functions of the NSGA-III. Set the number of populations to 100, the maximum number of iterations to 100, and the crossover and mutation probabilities to 0.9 and 0.1 for multi-objective optimization. To avoid the influence of the randomness of the genetic algorithm on the results, the Pareto frontier after running the multi-objective optimization program five times is shown in Fig. 5.

In this paper, four parameters commonly used in the literature are selected to compare the algorithm before and after optimization. The spacing (SPC) parameter measures the distance between the solutions in the Pareto front, and a large interval value indicates that the distribution of the solutions is relatively uniform. The Diversity (DIV) parameter indicates the degree of difference between the solutions in the Pareto front, and a larger DIV value indicates that the solution is more uniform. The difference is relatively large. The MSI parameter indicates the maximum distance of the solution in the Pareto front. The TIME parameter indicates the optimization time.

It can be seen from Table 3 that the MSI has increased by 22.7%, indicating that the distribution of the improved Pareto solution set is more dispersed. The time is saved by 8%, and the DIV and SPC are increased by 31.89% and 11.87%, indicating that the diversity of the solution set has been significantly improved after the improvement.

The compromise solution is selected through the fuzzy membership degree, and the optimal parameters of the needle selector are obtained. The size comparison and cost of the needle selector before and after optimization are shown in Table 4. At the same time, through the calculation of the material cost, it can be seen that the production cost has been saved by 6.73%.

The optimized performance parameters obtained through maxwell software simulation are shown in Table 5. It can be seen that under different working conditions,
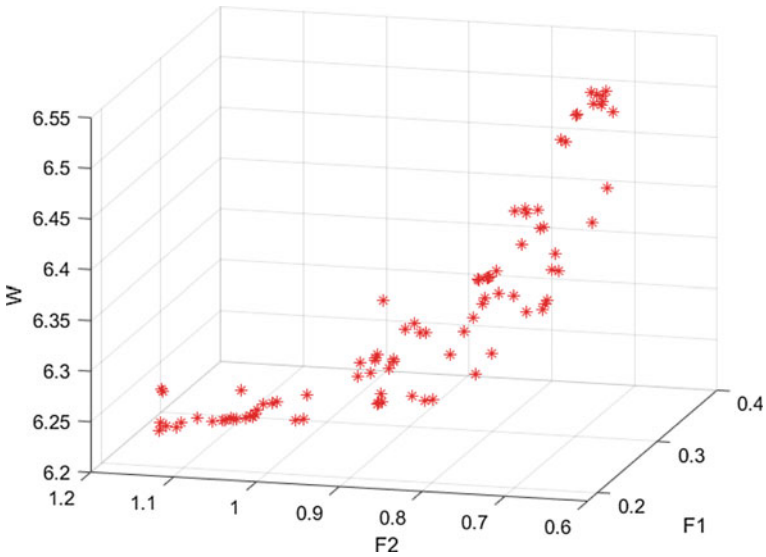
Fig. 5 Pareto frontier graph obtained by multi-objective optimization

Table 3 Comparison of NSGA-III algorithm parameters before and after improvement

Parameter	MSI	TIME/s	DIV	SPC
Before optimization	0.21105	1915.22	4.5492	0.5808
Optimized	0.27315	1760.95	6.0329	0.6590

Table 4 Comparison of needle selector size and cost before and after optimization

Parameter	Dz/mm	Lm/mm	Dm/mm	Lg/mm	Turns /A
Before optimization	2.50	8.50	2.50	0.10	1440
Optimized	2.70	8.13	2.30	0.08	960

F23 is larger than 1N and F1 is smaller than 1N, which achieves the optimal design of the needle selector.

5 Conclusions

Aiming at the problem that the performance parameters of the permanent magnet actuator are difficult to be identified by computer as well as to perform the optimization of multiple objectives, an improved NSGA-III optimization method for

Table 5 The relationship between the force on the needle pieces and the number of needle pieces after optimization

Number of selectors	Needle force/N		
	No. 2	No. 1	No. 3
1		0.7315	
3	1.8992	0.4095	1.8473
5	1.4631	0.3418	1.3535
7	1.2721	0.3123	1.2459
9	1.1898	0.3023	1.1254
11	1.0789	0.2642	1.1020

the permanent magnet actuator based on the surrogate model is proposed, and the following conclusions are derived.

(1) The gradient descent operator is used to improve the OLS-RBF neural network to make the sample fitting accuracy meet the actual needs.

(2) The selection mechanism of the NSGA-III is improved to increase the speed of the algorithm and the diversity of Pareto solution sets.

(3) Taking the electromagnetic needle selector with permanent magnet as an example, using the fitted neural network model for multi-objective optimization, the results show that 8% of the running time is saved and the diversity of Pareto solution sets is improved. At the same time, the performance parameters of the electromagnetic actuator with new parameters meet the design conditions and save 6.73% of the production cost.

The multi-objective method proposed in this paper is applied to the single-stage electromagnetic needle selector design of high-end flat knitting machines. The simulation results verify the feasibility of the method and lay the foundation for the design of general optimization software for permanent magnet actuators.

References

1. Wang XY, Gao P (2015) Optimal design of permanent magnets of in-wheel motor based on evolution strategy. Proceedings of the Chinese Society of Electrical Engineering 35(04):979–984 (in Chinese)

2. Deb K, Pratap A, Agarwal S, Meyarivan T (2002) A fast and elitist multiobjective genetic algorithm: NSGA-II. IEEE Trans Evol Comput 6:182–197

3. Yuan X, Zhang B, Wang P et al (2017) Multi-objective optimal power flow based on improved strength Pareto evolutionary algorithm. Energy 122:70–82

4. Deb K, Jain H (2014) An evolutionary many-objective optimization algorithm using reference-point-based nondominated sorting approach, Part I: solving problems with box constraints. IEEE Trans Evol Comput 18(4):577–601

5. Xie BC, Zhang Y, Xu ZY et al (2022) Review on multidisciplinary optimization key technology of electrical machine based on surrogate models. Transactions of China Electrotechnical Society 37(20):5117–5143 (in Chinese)
6. He X, Yang LL, Ran RJ et al (2022) Comparative studies of surrogate models based on multiple evaluation criteria. Journal of Mechanical Engineering 58(16):403–419 (in Chinese)
7. Rafiee V, Faiz J (2019) Robust design of an outer rotor permanent magnet motor through six-sigma methodology using response surface surrogate model. IEEE Trans Magn 55(10):1–10
8. Li RQ, Bian HD, Yang SB (2022) Permanent magnet synchronous motor control system based on RBF neural network. Light Industry Machinery 40(04):52–56 (in Chinese)
9. Hao JS, Suo SF et al (2020) Optimization of torque ripples in an interior permanent magnet synchronous motor based on the orthogonal experimental method and MIGA and RBF neural networks. IEEE Access 8:27202–27209
10. Tian ZR, Zhi PP, Yun GL (2023) Multi-objective robust optimization design method based on adaptive incremental kriging model. China Mechanical Engineering 1–10 (in Chinese)
11. Huang R, Zheng D (2020) Multi-objective optimization design of unequal-thickness permanent magnet motor based on kriging proxy model and particle swarm optimization. Small & Special Electrical Machines 48(07):19–23 (in Chinese)

Contact Defects Diagnosis and Load Capacity Estimation for Double-Fracture Disconnect Switchgear

Jieshuai Ren, Zifan Dong, Hongbin Li, Jun Chen, Jinbin Li, and Yunhao Qiu

Abstract At present, there is no effective ways to estimate the contact status and maximum load capacity of the double-fracture disconnect switchgear (DDS), which cause the contact defects cannot be excavated when the load is low. To this end, the heat transfer process inside the DDS is analyzed using a thermal network, and a varying-parameters state-space model is established, which takes the load current and ambient temperature as input variables, and key nodes temperature as state variables. On this basis, a real-time least square system estimation method for contact resistance is proposed, whose input are the on-line measurement results of contact temperature, shell temperature and load current. Then, an estimation method for maximum load capacity is proposed according to the estimated contact resistance and rated temperature rise. A DDS temperature rise experiment plat-form which takes a switchgear cabinet as an example is set up to verify the accuracy of the state-space model and the effectiveness of the contact resistance estimation under different contact resistance. The proposed method can diagnose the contact defect of the two contacts of DDS and estimate its maximum load capacity without any additional hardware, which provides timely guide for substation operation personnel and builds the physical layer, model layer and application layer of DDS digital twin.

Keywords Double-fracture disconnect switchgear (DDS) · Thermal network · Real-time system identification · Contact resistance estimation · Load capacity estimation · Digital twins

J. Ren (✉) · Z. Dong · J. Chen · J. Li · Y. Qiu
Equipment Technology Center, State Grid Hubei Electric Power Co., Ltd. Electric Power Research Institute, Wuhan 430077, China
e-mail: 591667076@qq.com

H. Li
Equipment Division, State Grid Hubei Electric Power, Wuhan 430077, China

1 Introduction

The DDS is widely used in power transmission and distribution, including 10 kV and 35 kV air-insulated handcart switchgear, as well as the 110 kV and 220 kV GIS DDS used for non-outage expansion of substations in recent years [1]. Poor contact of disconnect switchgears often cause overheating of the metal and insulation parts, which leads to melting of the contact, degradation of insulation, short-circuit, load loss and even fire [2–4]. Therefore, the temperature monitoring of the contacts has been widely used, and it is required to be installed according to the State Grid 2021 Guidelines for Modular Construction of Substations 2.0, and the relevant standards also limit the rated temperature of contacts [2].

However, thermal faults in switchgears usually occur under a sudden load increase, contact defects that causes thermal faults cannot be detected by temperature measurement under low load. Therefore, compared to monitoring the temperature of the contacts, it is more valuable for operation and maintenance personnel to diagnose contact defects in real-time and predict the maximum load current.

The value of contact resistance reflects the contact defects directly, but it cannot be directly measured in operation. In addition, for DDS, two contacts are in serial and there is no measuring point between them. So, it is impossible to measure the contact resistance of the two breaking points independently in on-site experiments.

Therefore, only indirect methods can be used to calculate the contact resistance. These methods are mainly based on multi-physics field simulation and thermal network model [3–5]. The multi-physics field simulation needs huge amount of calculation, which usually used for optimized design and offline defect tracing analysis of switching equipment, rather than real-time defect diagnosis. The thermal network model is the dual model of the circuit in terms of heat transfer, using thermal sources, thermal resistances, thermal capacitors and other components to construct simplified heat transfer systems. It is fast in calculation and is suitable for real-time analysis of the heat transfer process of equipment with a small number of internal temperature measuring points as inputs [6]. Literature [7] proposed a contact resistance calculation method based on temperature measurement of the contacts and fitting with a first-order transfer function model. This method can estimate the time constants of the heat transfer model of a single contact point under the input of a standard step current, and then estimate the contact resistance. Literatures [8, 9] also proposed a thermal defect diagnosis method based on steady-state temperature response. However, currently, these research methods cannot be used for actual on-site operation conditions with initial temperature rise values of contact points and arbitrary input currents, nor can they describe the mutual influence of heat transfer between the two contacts of double-fracture devices.

This paper analyses the heat transfer process of DDS based on the thermal network, constructs a state-space model with variable constants and estimates the contact resistance based on the least square method system identification. Experiment results show that the proposed method can diagnose contact defects and predict the actual maximum load capacity even if the load and contact temperature are low, and can be

used as the physical layer, model layer, and application layer of temperature part of the DDS digital twin.

2 Thermal Network Model for DDS

The schematic diagram of the gas-insulated DDS, such as switchgear cabinet and GIS DDS, is shown in Fig. 1. A unified simplified thermal network model can be constructed as shown in Fig. 2. In Fig. 2, the heat-generation and heat-transfer elements are characterized by three types: thermal source, thermal capacity, and thermal resistance.

   The heat sources in DDS include the heat generation of the two contacts and the adjacent conductors (Q_i in Eq. 1), as well as the eddy current heat generation at the metal shell (Q_s in Eq. 2). In Eqs. 1, 2, I represents the real-time RMS of the load current; r_i is the resistance at Q_i. The contacts resistance can be changed due to contact deterioration and closing failure, which need to be estimated in real time. In Eq. 2, f is the current frequency, B is the magnetic field strength and is in proportional
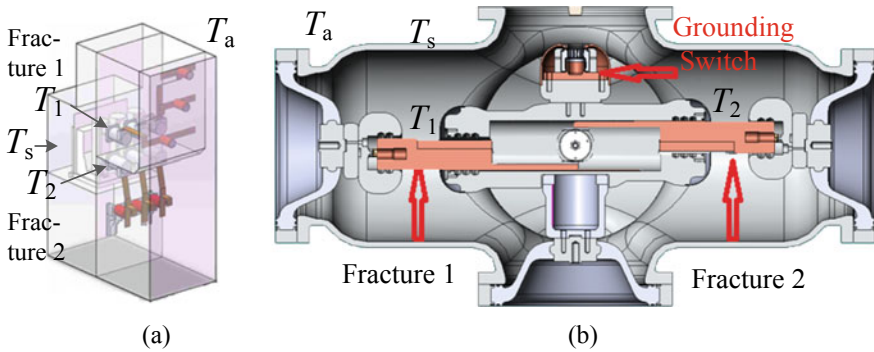
Fig.1 DDS schematic diagram. **a** Switchgear cabinet. **b** GIS DDS

Fig. 2 DDS thermal model
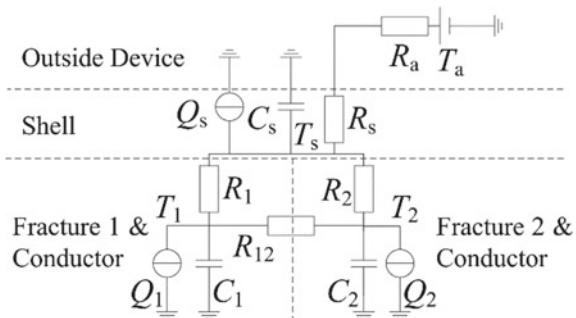
to I, d is the conductor thickness, and V is the conductor volume. It can be written as a simplified form on the right side of the equation, where r_s is the equivalent eddy current resistance. Because the eddy current loss in the shell of DDS cannot be measured in actual operation, an equivalent resistance r_s of the eddy current loss also needs to be estimated based on the average temperature of the shell. The change of resistance with temperature is taken into consideration, expressed as Eq. 3. The resistance value of the conductors can be calculated based on the dimensions in the design drawings of DDS.

$$Q_i = I^2 r_i \ (i = 1, 2) \tag{1}$$

$$Q_s \propto f B^2 d^2 V = I^2 r_s \tag{2}$$

$$r_i = r_{i0}(1 + \alpha T) \tag{3}$$

The thermal capacity C_1, C_2, and C_s characterize the rate of temperature rise of each part mentioned above. They are the product of specific heat capacity and mass of each part and can be calculated based on the design drawings.

The thermal resistance characterizes the heat transfer inside and outside of the. Within the range of ambient temperature to the highest allowable temperature rise of 75 K [2] considered in this paper, only conduction and convection need to be considered, while radiation can be ignored. R_{12} is the thermal resistance of the conductor between the two contacts, and Rs is the thermal resistance of the shell. The above thermal resistances are thermal conduction property, as shown in Eq. 4. R_1 and R_2 are the thermal resistances from the contacts and nearby conductors to the shell, and R_a is the thermal resistance from the shell to the ambient temperature T_a. The above thermal resistances are thermal convection property, as shown in Eq. 5. In Eqs. 4 and 5, A is the surface area of each part, k is the thermal conductivity, l is the length of the thermal conduction path, and h is the convective heat transfer coefficient on the surface.

$$R_{cd} = l/kA \tag{4}$$

$$R_{cv} = 1/hA \tag{5}$$

Based on the above thermal network model, a state-space equation (Eq. 6) can be formed with the contact temperatures T_1, T_2 and shell temperature T_s as the state variables and output variables, load current and ambient temperature as input variables. The state-space equation is a variable-parameter equation, and the variable parameters lies in the temperature-dependent part of each resistance in the input matrix **u**.

$$\begin{cases} \dot{x} = Ax + Bu \\ \quad\ y = Cx \end{cases}, x = \begin{bmatrix} T_1 & T_2 & T_s \end{bmatrix}^T,$$

$$u = \begin{bmatrix} I^2(1 + \alpha T_1) & I^2(1 + \alpha T_2) & I^2(1 + \alpha_s T_s) & T_a \end{bmatrix}^T$$

$$A = \begin{bmatrix} -\frac{1}{C_1}\left(\frac{1}{R_{12}} + \frac{1}{R_1}\right) & \frac{1}{C_1 R_{12}} & \frac{1}{C_1 R_1} \\ \frac{1}{C_2 R_{12}} & -\frac{1}{C_2}\left(\frac{1}{R_{12}} + \frac{1}{R_2}\right) & \frac{1}{C_2 R_2} \\ \frac{1}{C_s R_1} & \frac{1}{C_s R_2} & -\frac{1}{C_s}\left(\frac{1}{R_1} + \frac{1}{R_2} + \frac{1}{R_s + R_a}\right) \end{bmatrix}$$

$$B = \begin{bmatrix} \frac{r_{10}}{C_1} & 0 & 0 & 0 \\ 0 & \frac{r_{20}}{C_2} & 0 & 0 \\ 0 & 0 & \frac{r_{s0}}{C_s} & \frac{1}{C_s(R_s + R_a)} \end{bmatrix}$$

$$C = \begin{bmatrix} 1 & 0 & 0 \\ 0 & 1 & 0 \\ 0 & 0 & 1 \end{bmatrix} \tag{6}$$

The model is suitable for three-phase separated-box DDS or three-phase common-box DDS with almost equal contact resistances due to three-phase linkage.

3 Diagnosis of Contact Defects and Estimation of Load Capacity for DDS

3.1 Diagnosis of Contact Defects

The state-space equation (Eq. 6) is a high-order time-varying equation. In practical applications, the node temperatures and load currents that serve as input and state variables are discrete values sampled by sensors at predetermined sampling periods. Therefore, it is advisable to use a least square method for parameter identification that requires the discretization of the system. In this study, a time-discretized simulation model of Eq. 6 was constructed using Simulink in MATLAB, as shown in Fig. 3, and the "nlinfit" toolbox based on least-squares regression in MATLAB was used to identify the resistance values r_{10}, r_{20}, and r_{s0}.

The model in Fig. 3 is the objective function of least square regression analysis. The inputs and outputs of the function are the **x** and **y** matrices in Eq. 6. In each time step, the input matrix B is preprocessed to simulate the change in resistance with temperature.
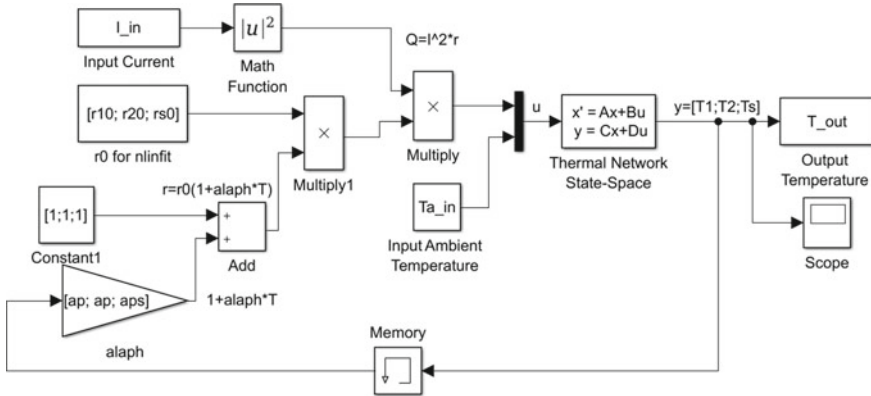
Fig. 3 A simulation model for the state space of thermal networks

3.2 Estimation of Load Capacity

The actual maximum load capacity of the DDS can be defined as the smaller value between its rated load current and the load current that causes its contact temperature to reach the specified maximum temperature rise $T_{r\max}$. Therefore, when a contact defect occurs in the DDS, its maximum load capacity is limited by the contact resistance at the location with the higher temperature. Based on the steady-state response obtained from the simulation model in Fig. 3 when t $= \infty$, the objective function Eq. 7 can be constructed, where f_1 and f_2 are the steady-state temperatures at contact 1 and 2, r_i represents the estimated values of the contact resistance at different locations, T_a is the ambient temperature, and ΔT_r is the preset temperature rise margin. By using numerical methods such as Newton's method, the maximum allowable load current of the DDS can be solved for achieving the contact temperature of the DDS to reach $T_{r\max} - \Delta T_r$.

$$\max(f_1(r_1, r_2, r_e, T_a), f_2(r_1, r_2, r_e, T_a)) = T_{r\max} - \Delta T_r \tag{7}$$

4 Experimental Verification

4.1 Experimental Configuration

To verify the proposed DDS contact defect diagnosis and load capacity estimation method, a DDS temperature rise experimental platform was constructed for a 10 kV switchgear cabinet, as shown in Fig. 4a. The experimental platform used a
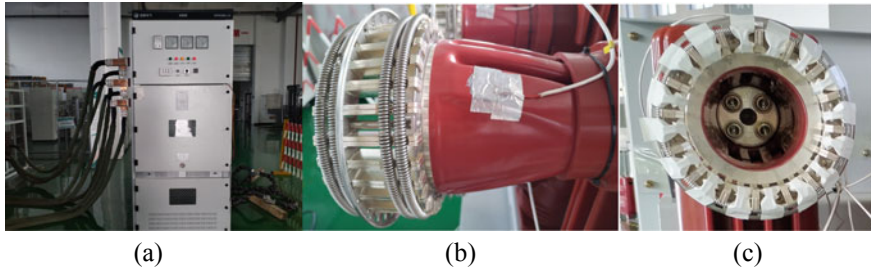
Fig. 4 DDS temperature rise experimental platform. **a** Experimental platform, **b** contact temperature measurement, **c** contact defect setting

switchgear with a rated current of 3000 A as the experimental subject and a three-phase current source as the current input. The temperature at the contacts and the shell were measured using thermocouples, as shown in Fig. 4b. The average temperature of the three phases at either contact in the DDS was taken as the temperature state variables T_1, T_2, and the average temperature of the shell was taken as the temperature state variable T_s.

To simulate contact defects, insulating tapes was attached on part of the contact fingers on the contacts to increase the contact resistance, as shown in Fig. 4c. The same number of covered contact fingers were used at the three-phase contact points of any break point to ensure that the contact resistance of each phase is approximately equal, thereby satisfying the conditions for using the thermal network model in Fig. 4.

The geometric and physical properties of the components in the experimental platform are shown in Table 1. The data at the two contacts include the data for the nearby conductors, and the thermal conduction distance between the contact points is half of the average length. Based on the values in Table 1, the thermal resistance and heat capacity values in the simplified thermal network model in Fig. 4 can be calculated as shown in Table 2.

Table 1 The geometric and physical properties of the components in the experimental platform

Properties	Contact 1	Contact 2	Shell
Material	Copper	Copper	Cast iron
Resistivity $\rho(\Omega\,m)$ (20 °C)	1.75×10^{-8}	1.75×10^{-8}	5×10^{-7}
Thermal conductivity k (W/m K)	386	386	81
Surface heat transfer coefficient h (W/m^2 K)	5	5	7
Specific heat capacity c (J/(kg K))	0.39×10^3	0.39×10^3	0.46×10^3
Thickness d (cm)	1.6	1.6	0.3
Average length l (cm)	83	72	l
Heat transfer area S (cm^2)	3984	3456	144,453
Mass m (kg)	28.4	24.6	380.4

Table 2 Values of physical quantities in thermal network model

Thermal capacity	Value (J/K)	Thermal resistance	Value (K/W)
C_1	1.11×10^4	R_1	0.0797
C_2	9.60×10^3	R_2	0.0691
C_s	1.75×10^5	R_{12}	1.045
		R_s	2.563×10^{-6}
		R_a	2.063

4.2 Experimental Results

This paper conducted 3 groups of dynamic temperature rise experiments using the DDS temperature field experimental platform, with contact resistances of 1 time, 2 times, and 8 times of the normal value. The load current, three-phase average temperature from each contact, average temperature of shell and ambient was collected in the experiment. The method in Sect. 3.1 was used to identify the system with the above data, and finally, the estimated total contact resistance values for 3 situations were obtained as shown in Table 3. Figure 5 shows the comparison between the measured contact temperature values of the 3 groups and the calculated results of the model. It can be seen that the thermal network model fitted by the least square method can accurately estimate the transient temperature values of the state variables.

In practical applications, the current curve and temperature rise curve of DDS in the factory test can be collected to identify the contact resistance values of the two contacts at normal state. This can be used as the reference for identifying the contact resistance of DDS equipment during the future operation.

Based on the contact resistance estimation results of the three groups of experiments, the load capacity verification method in Sect. 3.2 can be used to calculate the load current required to reach the rated maximum temperature rise $T_{r\max}$. The calculated results are shown in Table 4. From Table 4, it can be seen that when contact defect occurs, even if the contact resistance has reached 8 times the normal value, the maximum temperature at the contacts was not reach $T_{r\max}$ (75 K) to trigger the overheating alarm before the load reaches its maximum. However, the maximum load capacity of the DDS is much lower than the rated value. Therefore, if the scheduling planning of switchgears is still based on the rated value, there will be a risk of overheating. The proposed load capacity estimation method can guide the operation and maintenance personnel to schedule the load according to the actual contact status of the switchgear to avoid this risk.

Table 3 Estimated value of contact resistance with adjacent conductor

Preset contact resistance	1 times	2 times	8 times
Estimated contact resistance with adjacent conductor	1.00 times	1.22 times	2.70 times
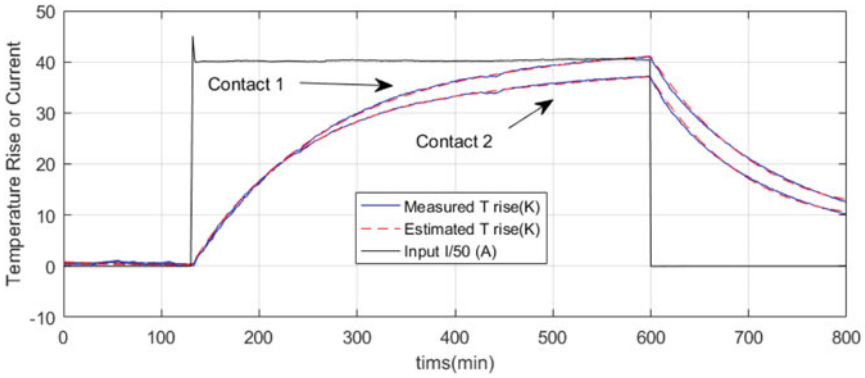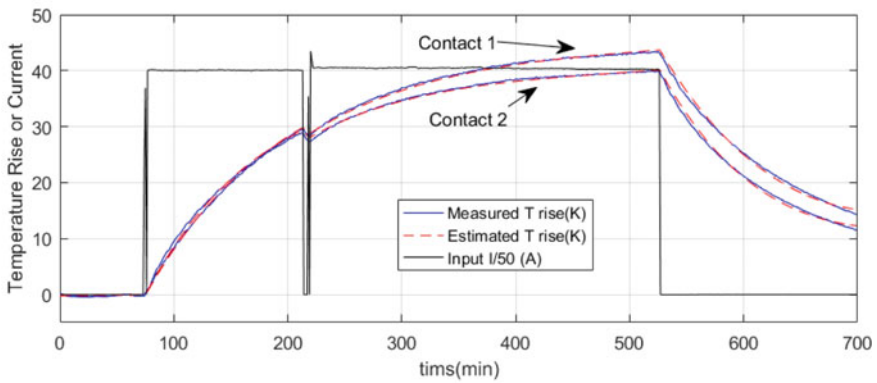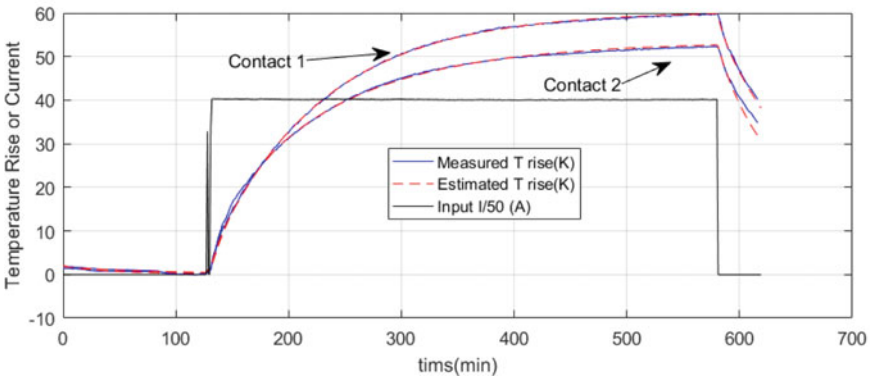
Fig. 5 Comparison between the contact temperature values of experiments and the calculated values of the model. Preset contact resistances: 1 time **a**, 2 times **b**, and 8 times **c**

Table 4 Estimated load capacity of the experiment

Preset contact resistance	1 times	2 times	8 times
Maximum load capacity	3000 A	2907 A	2452 A

5 Conclusion

The DDS thermal network model proposed in this paper provides a feasible solution for detecting contact defects and overheating risks in switchgear cabinets or GIS DDS even if the load is low. By a variable constant state space model and least square system identification, the calculation of the DDS contact status and the estimation of the maximum load capacity under the current contact status are realized. Temperature rise experiments under different contact resistances are conducted, proving the accuracy of the real-time contact defect diagnosis and the proposed load capacity estimation method. The proposed method does not require additional sensor installation inside the DDS equipped with contact temperature sensors, which is convenient for engineering applications and can quickly improve the efficiency of substation operation and maintenance. It can also serve as the basis for the temperature part of the DDS digital twin.

References

1. Cheng Z, Wu d, Zeng F et al (2020) Research on test method based on 220 kV GIS intervaldouble-fracture disconnector isolating switch technology. Hunan Electric Power 24:15–18
2. GB/T 11022-2020:Common technical requirements for high-voltage switchgear and control equipment standards
3. Su Y, Xie Z, Li L et al (2020) Temperature rise simulation analysis of air switchgear heating fault based on coupling of multi-physical field. High Voltage 56(11):1–7
4. Fjeld E, Rondeel W, Attar E et al (2021) Estimate the temperature rise of medium voltage metal enclosed switchgear by simplified heat transfer calculations. IEEE Transactions on Power Delivery 36(2):853–860
5. Nowak R, Duc J, Samul B et al (2021) Thermal network approach for a quick and accurate study of multiple connected switchgears. Heat Transfer Engineering 43(3–5):183–197
6. Stosur M, Szewczyk M, Sowa K et al (2016) Thermal behaviour analyses of gas-insulated switchgear compartment using thermal network method. IET Generation, Transmission & Distribution 10(12):2833–2841
7. Zhang Q, Duan J, Ye B et al (2014) Research of measuring contact resistance based on the electrical contact transient thermal circuit model. Power System Protection and Control 42(15):27–33
8. Zhao Z (2021) Study on loop resistance and temperature rise of contact spring system within relays. Harbin Institute of Technology

9. Huimin L, Li B, Shan J et al (2022) A steady-state thermal network analysis modeling method for hermetically sealed electromagnetic relay and its experimental verification. IEEE 67th Holm conference on electrical contacts (HLM), pp 265–271

SDBD Enhanced Supercombustion Chamber Blending Characteristics Simulation Studies

Jiaying Ge, Yongjian Ning, Kexue Che, Hao Jiang, and Xiuqian Li

Abstract In order to improve the fuel mixing efficiency of scramjet, combined with the research progress at home and abroad, the effect of surface dielectric barrier discharge plasma on the mixing of detached combustors was numerically simulated, and the impact of different positions and The results show that: positively excited plasma can increase fuel mixing length and reduce fuel penetration depth; and the effect of excitation forms on the fuel penetration depth and effect of blend length. The results show that: positively excited plasma can increase fuel mixing length and reduce fuel penetration depth; the effect of reversely excited plasma on fuel is related to the application position.

1 Introduction

The scramjet engine is an important part of the hypersonic air-breathing vehicle propulsion system, and is the research focus of the next generation of hypersonic flight and cruise [1–4]. Due to the short residence time (on the order of milliseconds) of the gas flow in the scramjet combustion chamber [5], efficient and rapid mixing of fuel and surrounding air is required to achieve supersonic combustion, and the mixing process is substantially affected by the geometry and injection strategy, is one of the key factors determining the combustion process. Therefore, a scramjet combustor requires an injection method with significant penetration and mixing efficiencies. In the past few decades, fuel mixing enhancement strategies in supersonic flow have received extensive attention from scholars [5–7].

J. Ge · Y. Ning · K. Che (✉) · H. Jiang · X. Li
Department of Aerospace Science and Technology, University of Aerospace Engineering, Beijing 101416, China
e-mail: 18843103828@163.com

As a new active flow control technology, plasma flow control uses plasma as a carrier of momentum, energy, etc., and acts on the excitation and boundary layer in the flow field to achieve the effect of flow control by changing the physical properties of the fluid near the excitation and boundary layer and the local structure of the flow field [8–10]. The effect of flow control is achieved by changing the physical properties of the fluid and the local structure of the flow field near the surge and boundary layer. The plasma flow control technology has the advantages of relatively low energy consumption, simple and lightweight structure, high control sensitivity and easy adjustment of the exciter response, etc. [11]. The plasma flow control technology has the advantages of relatively low energy consumption, simple and lightweight structure, high control sensitivity and easy adjustment of exciter response. The application of plasma flow control technology in supersonic flow has attracted much attention from scholars at home and abroad in the past decade or so, and has been widely and deeply discussed.

This paper designed a galloping test system for real overhead line conductors based on adaptive excitation. By the controllable periodic electromagnetic force, the vibration amplitude of the overhead wire can be controlled, and the vibration can last a long time. The adaptive action time required were studied based on dynamic finite element simulations. Considering the geometric nonlinearity, the finite element model of the system including the wire and insulators was built. Through controllable excitation force, the conductor vibration state can be controlled, and the motion characteristics during galloping can be reproduced. It can be used to analyze the bearing force of tower structure, bolt, insulator string and other subassembly of the whole transmission line system during galloping, evaluate the anti-galloping effect of interphase spacer, and provide a basis for the research of technology for fast suppression of transmission line galloping.

2 Simulation Model and Boundary Conditions

In this paper, a structured mesh is used for numerical simulation calculations, and local encryption is performed in the lower wall surface and the area near the spray hole, etc. The two-dimensional grid division is shown in Fig. 1. The coordinate origin is located at the right end of the nozzle with diameter d = 1 mm, the total length of the combustion chamber is 500 mm, the entrance of the combustion chamber is 176 mm from the coordinate origin, the entrance height is 60mm, the boundary of the concave cavity is 30 mm from the coordinate origin, the concave cavity L/D = 6, where D = 24 mm. The incoming flow conditions are typical supercombustion ramjet combustion chamber fluid parameters, the Mach number of incoming air is 1.6, the total pressure is 241 kPa, the total temperature is 295 K. The hydrogen is injected into the combustion chamber from the injection hole in the direction perpendicular to the bottom surface with Mach number 1, total pressure 476 kPa, and total temperature 300 K. The incoming flow and fuel are both pressure inlets, and the wall surface is a non-slip adiabatic solid boundary condition. In this paper, the SST k-ω model is
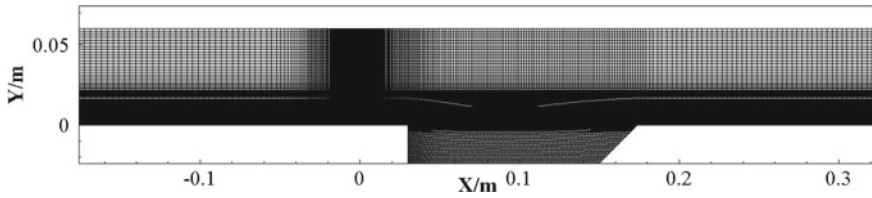
Fig. 1 Example of a two-dimensional grid
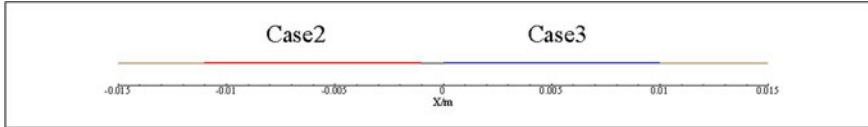
Fig. 2 Example of plasma position

used for numerical calculations, and the equations are solved using a density-based, implicit solver with the AUSM flux vector splitting format, second-order spatial windward format, and the Courant number is taken as 0.5.

The plasma position is set as shown in Fig. 2. Case1 indicates no plasma action condition. The plasma length is 10 mm, set in front of the spray hole and behind the spray hole position, respectively, indicated by Case2 and Case3, and the electrode length is 5 mm, with the tip aligned with the edge of the spray hole.

The plasma applied power supply is a high frequency AC power supply with a voltage amplitude of 30 kV and a discharge frequency of 5 kHz. the plasma volume force model is detailed in the literature [12].

3 Simulation Results and Analysis

For the purpose of analysis, some representative hydrogen mass fraction lines were selected for comparison, and the penetration depth and mixing length were used as blending effect evaluation parameters. The penetration depth of fuel is defined as the vertical height distance between the position of the fuel mass fraction isochrones and the bottom surface. The mixing length was defined as the distance between the position of the mass fraction contour and the spray hole after the fuel was ejected from the spray hole.

3.1 Effect of Excitation Position on Blending Effect

The effect of applying positive excitation plasma at different positions is shown in Fig. 3. Figure 3 shows the comparison of iso-mass fraction line distribution for hydrogen mass fractions of 0.5, 0.6, 0.7 and 0.8, respectively. Figure 3b shows the comparison of the distribution of equal mass fraction lines for hydrogen mass fractions of 0.2, 0.3, and 0.4, respectively. The overall trend of Case3 is similar to that of Case2, which is lower than the penetration depth of Case1 but higher than its mixing length, but with a slightly smaller variation compared to Case2. Case3 follows the same trend as Case2 and maintains the same trend as the high mass fraction line at mass fractions of 0.3 and 0.4, i.e., the penetration depth decreases but the mixing length increases, but the effect is weaker than that of high mass fraction of hydrogen is more weak and almost overlaps with Case1. It changes to a decreasing trend of both penetration depth and mixing length when the mass fraction decreases to 0.2. The reason for this phenomenon is mainly twofold, one is because the proportion of high mass fraction increases leading to the proportion of low mass fraction decreases under the same fuel mass condition, so the overall performance of mixing effect becomes worse at low mass fraction; on the other hand, the influence of flow field becomes gradually weaker with the flowing plasma.

The effect of applying reverse excitation plasma at different positions is shown in Fig. 4. Figure 4a shows the iso-mass fraction line distribution for hydrogen mass fractions of 0.5, 0.6, 0.7, and 0.8, respectively. Figure 3b shows the comparison of the distribution of iso-mass fraction lines for hydrogen mass fractions of 0.2, 0.3, and 0.4, respectively. From Fig. 4, the penetration depth of Case2 in the range of high mass fractions has increased to a certain extent, while the mixing length has decreased significantly, and the distribution area of high mass fraction hydrogen has also decreased significantly. the trend of Case3 is consistent with the positive excitation condition, and the penetration depth decreases but the mixing length increases with little trend compared with Case1. In the low mass fraction distribution range, Case2 still maintains the same trend as the high mass fraction range, with an increase in penetration depth but a decrease in mixing length compared to Case1. The trend of Case3 is still consistent with the forward excitation condition, where the penetration depth decreases but the mixing length increases at a mass fraction of 0.4, and both the penetration depth and mixing length decrease when the mass fraction decreases to 0.3. The trend of the blending effect under the reverse excitation discharge condition confirms the speculation that the blending effect under the forward excitation condition has an effect on the blending effect of the high mass fraction of the fuel on the blending effect of the low mass fraction.
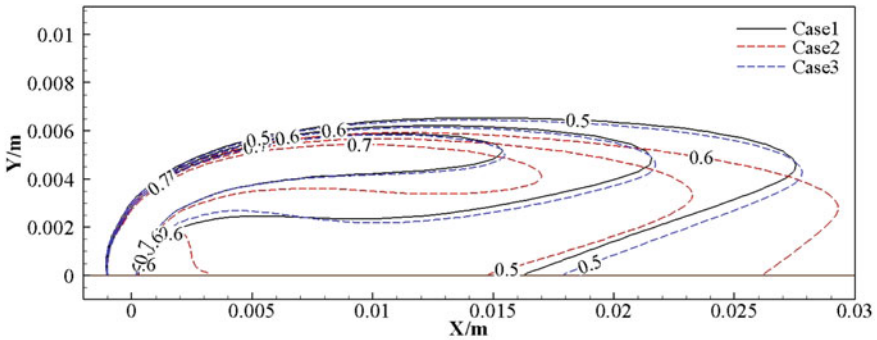
(a) Hydrogen mass fraction of 0.5-0.8
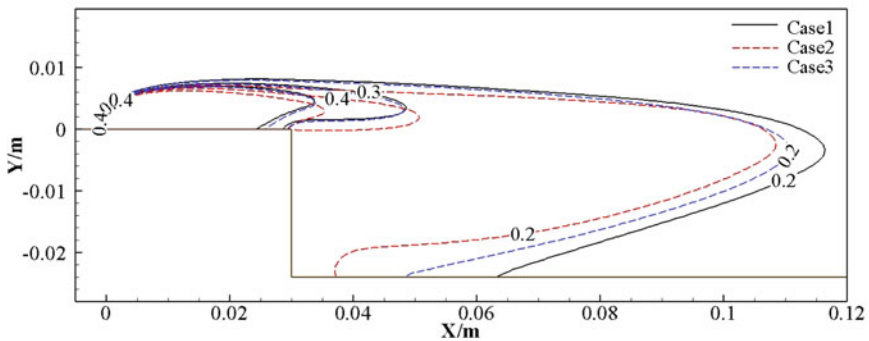
(b) Hydrogen mass fraction of 0.2-0.4

Fig. 3 Comparison of the effect of applying positive excitation plasma at different positions

3.2 The Effect of Incentive Form on Blending Effect

Case1 indicates no plasma action condition, Case2 and Case3 indicate the same position plasma forward excitation discharge form and reverse excitation discharge form respectively.

A comparison of the linear distribution of the mass fractions of different excitation forms of hydrogen at the position of the wall in front of the spray hole is shown in Fig. 5. From Fig. 5, Case2 shows a significant decrease in penetration depth and increase in mixing length relative to Case1 until the mass fraction drops to 0.2, and a decrease in penetration depth and mixing length relative to Case1 at a mass fraction of 0.2. The trend of Case3 is opposite to that of Case2, showing a significant increase in penetration depth and a significant decrease in mixing length relative to Case1 in the global range.
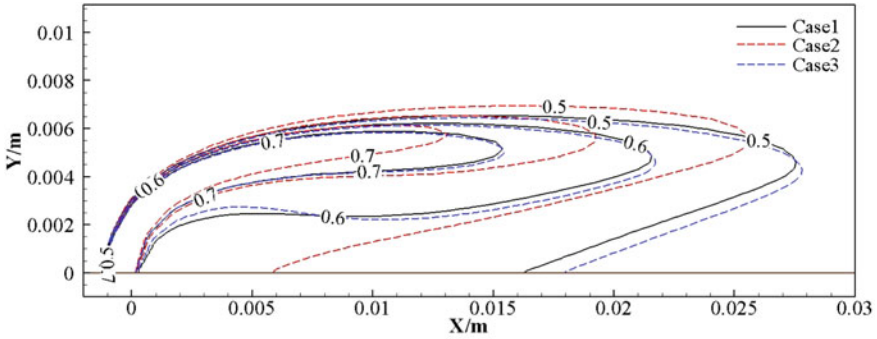
(a) Hydrogen mass fraction of 0.5-0.8
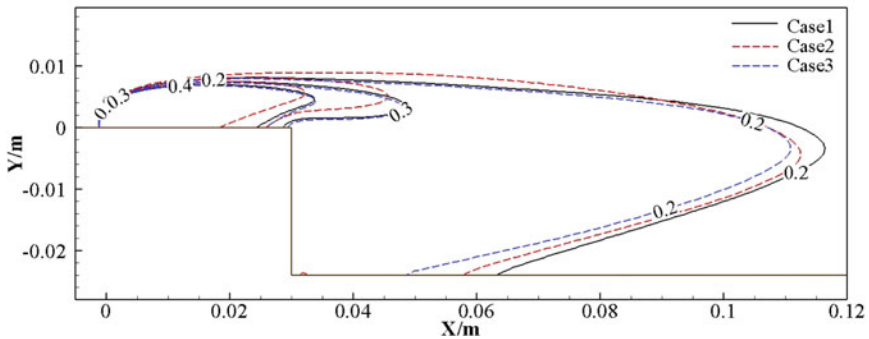
(b) Hydrogen mass fraction of 0.2-0.4

Fig. 4 Comparison of the effect of applying reverse-excitation plasma at different positions

A comparison of the line distribution of hydrogen iso-mass fraction for different excitation forms at the post-wall position of the spray hole is shown in Fig. 6. The difference between Case2 and Case1 is significantly higher than that between Case3 and Case2, while Case3 shows a lower penetration depth and mixing length compared to Case1 at a mass fraction of 0.2.
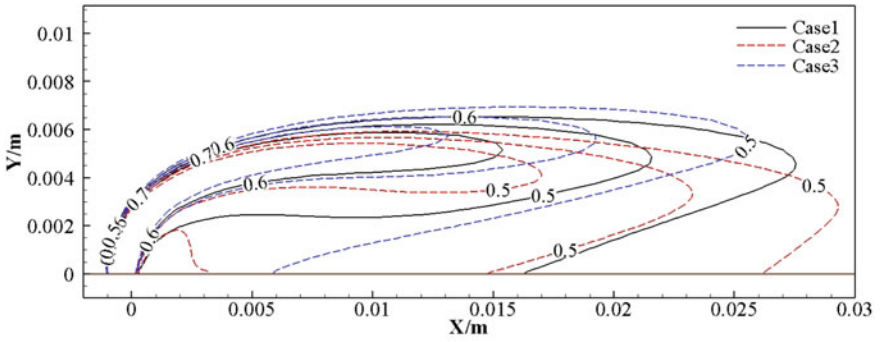
(a) Hydrogen mass fraction of 0.5-0.7
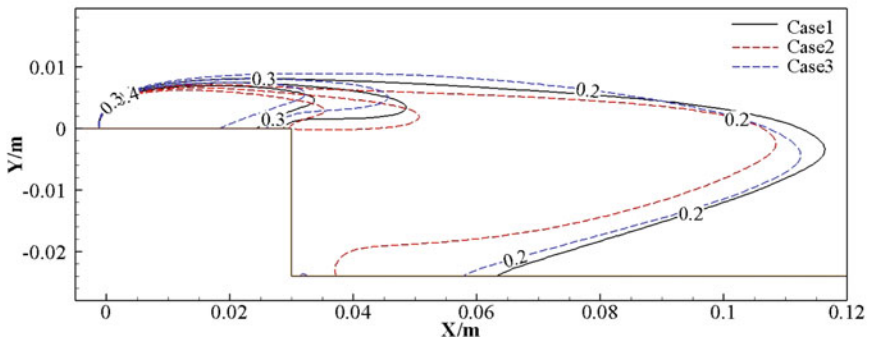
(b) Hydrogen mass fraction of 0.2-0.4

Fig. 5 Comparison of plasma effect of different excitation forms before spraying holes
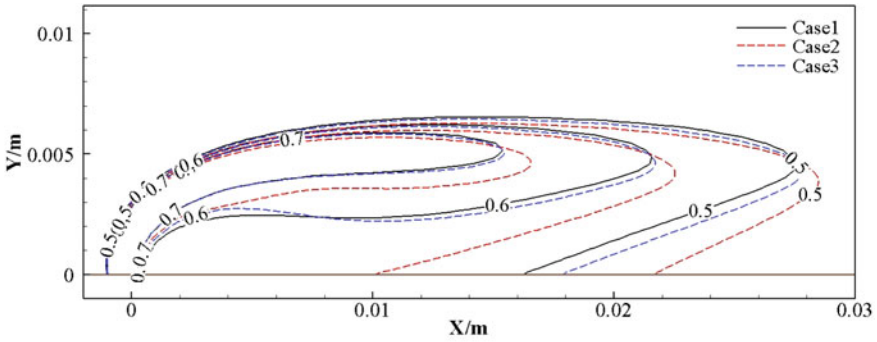
(a) Hydrogen mass fraction of 0.5-0.7
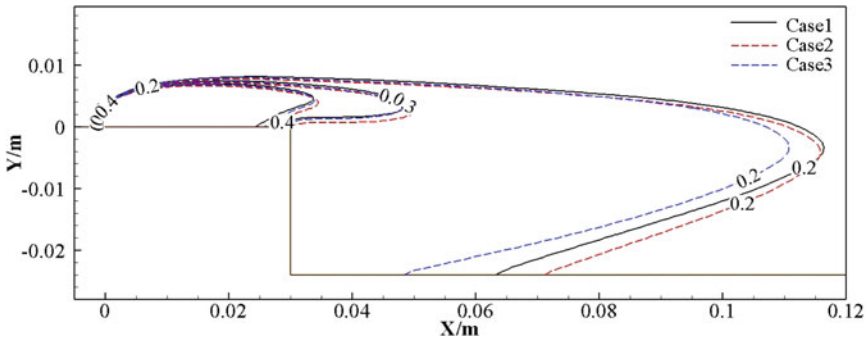
(b) Hydrogen mass fraction of 0.2-0.4

Fig. 6 Comparison of plasma effect of different excitation forms after spraying holes

4 Conclusion

In this chapter, the influence effects of different plasma control schemes are analyzed separately through two-dimensional model simulation calculations. The mixing length and penetration depth of the fuel are used as the evaluation parameters of the blending effect. The results demonstrate that the plasma has an effect on fuel blending for different control schemes, and the specific effects can be summarized as follows.

(a) In the higher range of hydrogen mass fractions, the effect of plasma on the blending effect follows the law of "the effect of mixing length and penetration depth", i.e., the penetration depth decreases when the mixing length increases and vice versa;

(b) The plasma effect is more sensitive to the location of application, with the effect of plasma applied at the lower wall location before the spray hole being more pronounced than the effect at the location after the spray hole;

(c) The law of the effect of different forms of discharge excitation is also location-dependent and cannot be analyzed independently;

(d) For the mixing length of fuel, the lifting effect of forward excitation form is significantly higher than that of reverse excitation; while for the penetration depth of fuel, the effect of reverse excitation is better than that of forward excitation, but the effect is weaker.

References

1. Huang W, Du ZB, Yan L et al (2019) Supersonic mixing in airbreathing propulsion systems for hypersonic flights. Progress in Aerospace Sciences 109:100545
2. Cai Z, Wang TY, Sun MB (2019) Review of cavity ignition in supersonic flows. Acta Astronautica 165:268–286
3. Zhang JC, Wang ZG, Sun MB et al (2020) Effect of the backward facing step on a transverse jet in supersonic crossflow. Energies 13(16):4170
4. Choubey G, Yuvarajan D, Huang W, Shafee A, Pandey KM (2020) Recent research progress on transverse injection technique for scramjet applications-a brief review. Int J Hydrogen Energy 45(51):27806–27827
5. Liang CH, Sun MB, Liu Y et al (2020) Numerical study of flow structures and mixing characteristics of a sonic jet in supersonic crossflow. Acta Astronautica 166:78–88
6. Sharma V, Eswaran V, Chakraborty D (2020) Effect of fuel-jet injection angle variation on the overall performance of a SCRAMJET engine. Aerospace Science and Technology 100:105786
7. Zhao M, Ye T (2019) URANS study of pulsed hydrogen jet characteristics and mixing enhancement in supersonic crossflow. International Journal of Hydrogen Energy 44(36):20493–20503
8. Li YC, Gerdroodbary MB, Moradi R et al (2020) The influence of the sinusoidal shock generator on the mixing rate of multi hydrogen jets at supersonic flow. Aerospace Science and Technology 96:105579
9. Manh TD, Nam ND, Cerdroodbary MB et al (2020) Numerical simulation of mixing of hydrogen jet at supersonic cross flow in presence of upstream wavy wall. International Journal of Hydrogen Energy 45(1):1096–1106
10. Xu Z, Wu J, Huang W et al (2020) Research progress of supercombustion ram engine jet mixing and enhancement technology. Tactical Missile Technology 4:83–102
11. Wan X (2020) Research status and development prospects of plasma flow control. Flying Missile 10:63–68
12. Zhou P (2013) Simulation and experimental study of plasma flow control in near space. Aerospace Engineering University, Beijing

Research on the Braking Characteristics of Electromagnetic Eddy Current Braking

Yuzhuo Wang, Peng Ma, Hao Wang, Jiliang Li, Zhen Lu, Xiang Li, Hongliang Zhang, and Hai Jin

Abstract With the aim of researching the braking characteristics of the electromagnetic eddy current brake and the influence of various factors on the braking performance, in this paper, a 3D transient field simulation model is established based on the finite element method with the DS-50 eddy current brake as an object, and verifies the reasonableness of the model by analyzing the change of the rotation angle of the rotor of the eddy current brake with time, so that this model to be used to simulate the electromagnetic characteristics of the eddy current brake as well as the influencing factors of the braking torque. The results show that when the speed is less than 50 rpm, the braking torque increases rapidly with the increase of speed, and after the speed reaches 75 rpm, the braking torque gradually shows a slow increase; as the excitation current is increased, the braking torque exhibits a gradually increasing trend and the peak torque increases according to a linear function.

Keywords Electromagnetic eddy current brake · Finite element method · Braking torque

1 Introduction

The rapid development of the oil platform industry has led to widespread attention being paid to the application of the brake system, as a guarantee of safe operation [1–3]. Friction brakes have obvious flaws such as rapid wear, short life expectancy, and difficult operation and maintenance under high-speed braking conditions, so traditional mechanical braking methods cannot meet the requirements for emergency braking requirements in drilling systems [4–6]. Eddy current brakes are one of the most popular braking systems, and in comparison to other braking devices, eddy

Y. Wang · P. Ma · H. Wang · J. Li · Z. Lu · X. Li · H. Zhang (✉) · H. Jin
College of Electrical and Information Engineering, Lanzhou University of Technology,
Lanzhou 730050, China
e-mail: zhanghl-518@qq.com

535

current brakes have been shown to significantly reduced maintenance costs at high speeds, lack of wear, and excellent braking performance [7–9].

The literature [10] gives a theoretical formula for the braking characteristics of eddy-current brakes using a magnetic circuit analysis model, and investigates the influence of the design parameters on the torque characteristics by means of a finite element model, which provides a benchmark for optimal brake design. The literature [11] has used 3D finite element analysis to verify the effectiveness of the theoretical modeling of the braking torque, and used finite element analysis to optimize the size and structure of the electromagnetic eddy-current brakes. The study of braking characteristics presented here lays the foundation for the full use of eddy current braking.

Firstly, this paper presents working principle of the electromagnetic eddy current brake; secondly, a three-dimensional model of the electromagnetic eddy current brake is established, and the electromagnetic performance of the electromagnetic eddy current brake is simulated and analyzed by finite element method. The curve of the braking torque of the electromagnetic eddy current brake with time is obtained; Finally, the factors affecting the braking torque of electromagnetic eddy current braking were investigated and analyzed, and plots of braking torque velocity characteristic diagrams were obtained under different excitation currents and different rotational rates.

2 Working Principle

During the operation of the electromagnetic eddy current brake, DC is applied to its excitation coil, and a phase chain of magnetic flux phase chain is formed between the rotor and the stator which results in the rotor being in a closed magnetic field circuit. The magnetic line of force produced by the magnetic field passes through the magnetic pole → air gap → armature → air gap → magnetic pole to form a closed circuit; Fig. 1 shows a schematic diagram of the working principle for the electromagnetic eddy current brake.

The law of electromagnetic induction states that an induced electromotive force is generated on the rotor and that the induced electromotive force generated by the eddy currents is:

$$E = BLV = BLR\omega \tag{1}$$

In the formula, B is the magnetic induction force of the air gap; L is the effective armature length; V is the linear circumferential speed of the magnetic force cutting the conductor; R is the effective radius of the armature.

The eddy currents generated in the armature due to the action of the induced electromotive force:
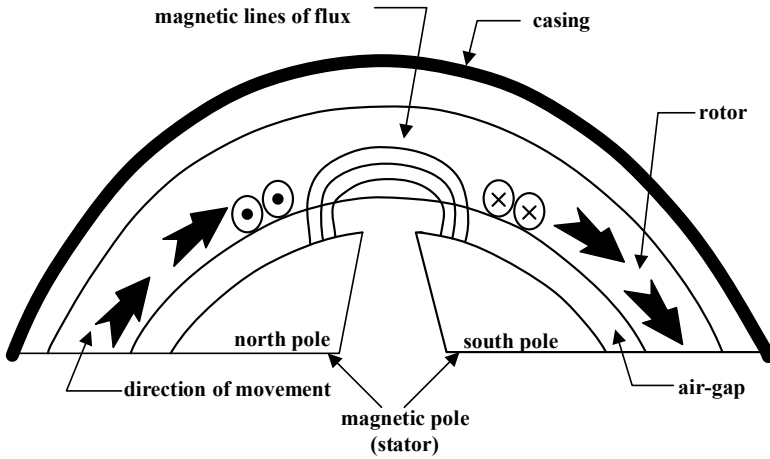
Fig. 1 Working principle diagram of electromagnetic eddy current brake

$$I = \frac{E}{2Z_a} = \frac{BLR\omega}{2Z_a} \tag{2}$$

In the formula, Z_a is the impedance in the eddy current circuit.

Eddy current and magnetic field induction generate electromagnetic forces:

$$F = BLI = BL \times \frac{BLRW}{2Z_a} = \frac{1}{2Z_a} B^2 L^2 R\omega \tag{3}$$

The total electromagnetic torque produced on the armature is:

$$M = 2ZFR = B^2 L^2 R^2 \frac{Z}{Z_a} \frac{\pi}{60} n = CnB^2 \tag{4}$$

In the formula, Z is the polar logarithm; $C = 2\pi Z L^2 R^2 / 60 Z_a$ is the electromagnetic eddy current braking torque coefficient. Torque M is used by the electromagnetic eddy current brakes to prevent the rotation of the drum.

From $M = CnB^2$, it can be concluded that a brake whose armature diameter, armature length, working air gap, and armature material geometry have been determined has a braking torque that is related to the speed and excitation current.
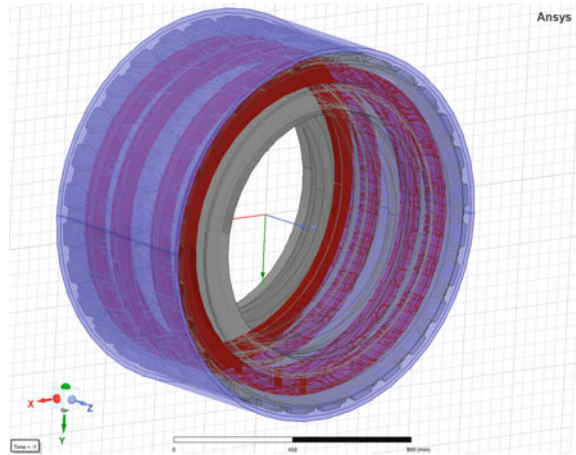
3   Finite Element Analysis of Transient Magnetic Field

3.1   Parameter Settings

The 3D finite element simulation model of an electromagnetic eddy current brake is
shown in Fig. 2. Set the number of coils turns as 413, rated current as 40 A, speed
as 50 rpm, termination time as 150 ms and step size as 5 ms. The material of rotor
and stator material are usually low-carbon steel.

3.2   Result Analysis

In 50 ms, the rotation speed n = 50 rpm, then the period T = 1.2 s, 1.2 s in the
rotation of 360°, so 1 ms rotation 0.3°, 50 ms should be rotated 15°. From the graph
of rotation angle versus time in Fig. 3, it can be seen that it is consistent with the
theory and verifies the reasonableness of the model.

The 3D finite element mesh dissection of the electromagnetic eddy current brake
is shown in Fig. 4. When the software adaptive mesh splitting, the air gap is denser
than other air gaps. When the electromagnetic field is stable, there is no eddy current
on the stator, so the magnetic field on the stator is non-rotating. Instead, the magnetic
field on the rotor is a rotating magnetic field because the rotor rotates and eddy
currents are created on the rotor. Because eddy currents is mainly generated on the
rotor surface, the grid of the rotor surface is refined.

The magnetic field distribution of the electromagnetic eddy current brake is shown
in Fig. 5. Each part of the electromagnetic eddy current brake has a magnetic density
distribution that is near saturation. The current in the coil is a direct current, while
the stator part is fixed and the size of its magnetic field does not vary with time. After

Fig. 3 Rotation angle versus time
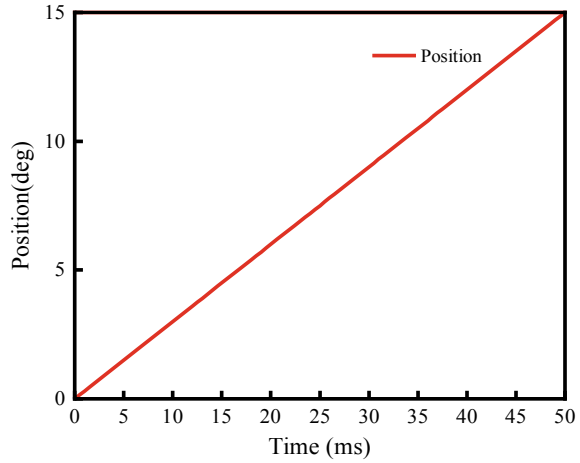
Fig. 4 Profile of 3D finite element mesh
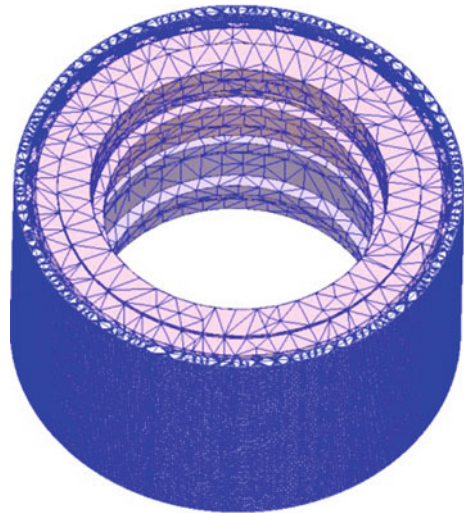
the rotor part starts, it cuts the magnetic induction line and generates eddy currents. The magnitude of the magnetic field in the rotor also changes as the size of the eddy current change.

The variation curve of electromagnetic eddy current brake braking torque with time is shown in Fig. 6. In the initial stage of applying excitation, the rotor suddenly moves into the magnetic field, and the torque size increases faster, which will produce vibration and the torque value is in a fluctuating state, with the passage of time, the movement gradually enters a stable state, and the fluctuation of the braking torque value becomes smaller and smaller, and gradually stabilizes. The simulation of this model results in a slight vibration around 60 KN m at the end.
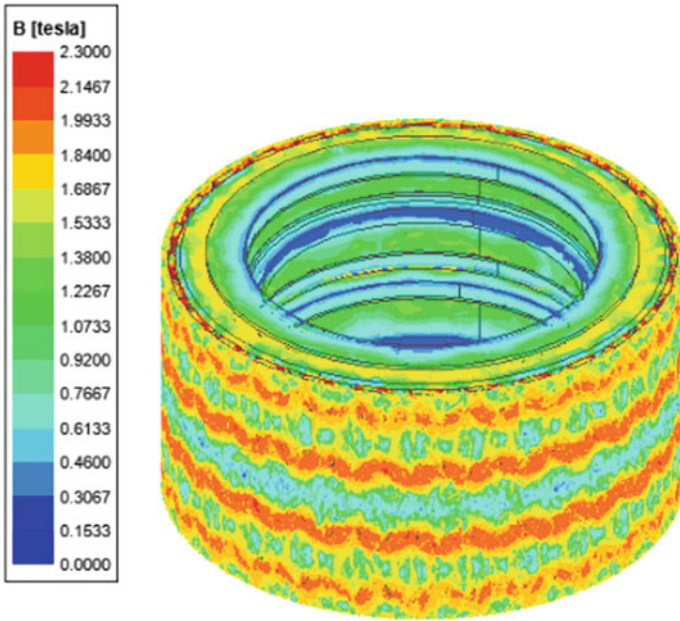
Fig. 5 Schematic of the magnetic field distribution

Fig. 6 Variation curve of braking torque over time
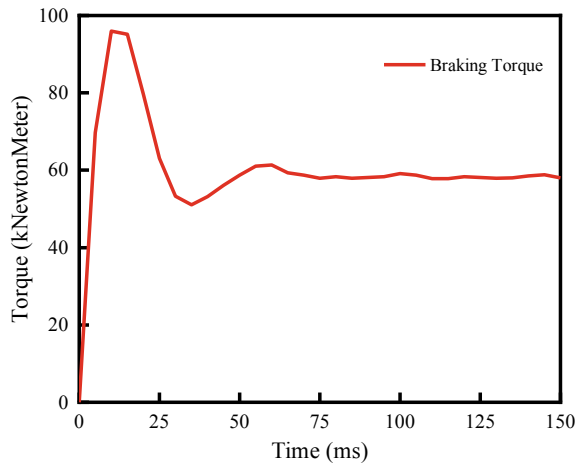
Fig. 7 Braking torque diagram at different rotational speeds
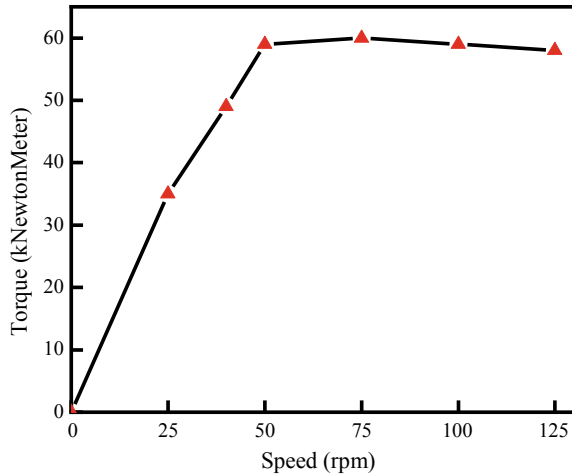
4   Research on the Influence of Various Factors on Torque

4.1   Research on the Influence of Rotational Speed on Torque

The variation of braking torque characteristics at 25, 50, 75, 100 and 125 rpm is shown in Fig. 7. If the rotational speed is low, below 50 rpm, then the braking torque generated by the electromagnetic braking of the eddy currents increases rapidly as the rotational speed increases. Once the speed reaches 75 rpm, the braking torque gradually shows a slow increase as the speed increases and even tends to decrease at higher speeds. The reason for this phenomenon is that, with the gradual acceleration of the speed, the antimagnetic potential generated by the eddy current in the stator also increases, weakening the excitation potential generated by the excitation current. The temperature of the stator and rotor increases as the running time becomes longer during the speed increase. Along with the temperature increase, the conductivity of the stator decreases and less eddy current power is dissipated, which also causes a decline in the braking torque.

4.2   Research on the Effect of Excitation Current on Torque

The variation of the braking torque characteristic for currents of 10, 20, 40 and 80 A is shown in Fig. 8. Brake torque increases with excitation current and peak torque is linear. The primary reason for this variation is that the electromagnet has a non-linear magnetic characteristic. The magnetic permeability decreases with the increase of the excitation current, the magnetic induction intensity growth trend nonlinear and the growth rate decreases.

Fig. 8 Braking torque speed
characteristic diagram under
different excitation current
conditions
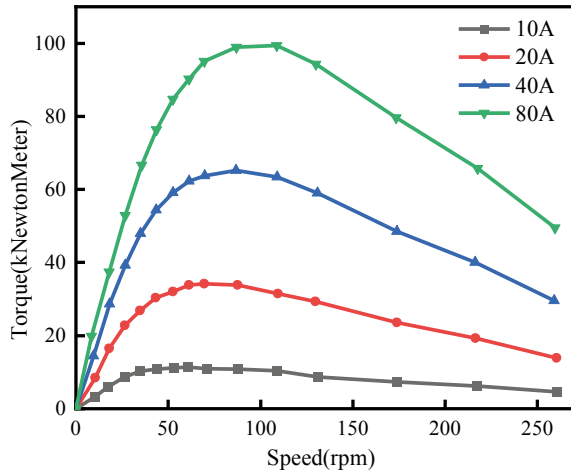
5 Conclusion

In this article, the DS-50 type electromagnetic eddy current brake is used as a research topic, introducing the working principle of the electromagnetic eddy current brake. The mesh profile, magnetic field distribution and the change curve of braking torque with time of the electromagnetic eddy current brake are analyzed by finite element simulation; the influence of the rotational speed and excitation current of the electromagnetic eddy current brake on the braking torque is studied. It can be observed that when the speed is less than 50 rpm the braking torque generated by the electromagnetic eddy current braking increases rapidly as the speed is increased; once the rotational speed reaches 75 rpm, the braking torque gradually shows a slow increase as the speed increases, and even has a tendency to decrease at higher speeds; with the increase in excitation current, the braking torque gradually increases and the peak torque increases as a linear function.

References

1. Ye L, Liu Y, Li D (2019) Performance analysis and optimization of liquid-cooled and flywheel-type eddy current retarder. IEEE Trans Magn 55(6):1–5
2. Li X, Ye L, Li M et al (2021) Research on temperature and braking performance of water-cooled eddy current retarder. IEEE Access 9:38991–38998
3. Ye L, Li D, Ma Y et al (2011) Designed performance of a water-cooled permanent magnet retarder for heavy vehicles. IEEE Trans Energy Convers 26(3):953–958

4. Cheng M, Wen H, Zeng Y, Jiang Y (2020) Analysis of airgap field modulation behavior and torque component in electric machines. Transactions of China Electrotechnical Society 35(5):921–930 (in Chinese)
5. Lubin T, Rezzoug A (2017) Improved 3-D analytical model for axial-flux eddy-current couplings with curvature effects. IEEE Trans Magn 53(9):1–9
6. Tian J, Li D, Ning K et al (2020) A timesaving transient magneto-thermal coupling model for the eddy current brake. IEEE Trans Veh Technol 69(10):10832–10841
7. Weijie W, Desheng L, Longxi Z et al (2017) Research on the influence of different stator materials on the braking torque of liquid-cooled eddy current retarder with dual salient poles. Australian Journal of Mechanical Engineering 15(2):84–92
8. Zhang LX, Li DS, Yin WL (2014) Study on influence factor of braking torque in liquid-cooled eddy current retarder with a structure of two salient poles. J Chem Pharm Res 6(5):1135–1141
9. Baoquan K, Yinxi J, Lu Z et al (2015) Characteristic analysis and control of a hybrid excitation linear eddy current brake. Energies 8(7):7441–7464
10. Ren Q, Zhang J, Luo J (2021) Characteristic analysis and control of a rotary electromagnetic eddy current brake. Appl Comput Electromagn Soc J 36(8):1065–1074
11. Ye L, Liu Y, Li D (2019) Optimization design and test of dual air-gaps and liquid-cooled eddy current retarder. Int J Appl Electromagnet Mech 61(6):1–14

Design and Simulation Analysis of a New Air-Core Permanent Magnet Compensated Pulsed Alternator with Segmental Squirrel-Cage

Yuan Cheng, Guanyu Guo, and Shuhan Hu

Abstract Compensated pulsed alternator (CPA) uses the flux compression effect of compensation elements to reduce transient inductance and release large current, and is used in the field of pulsed power with the advantages of high energy and power density. However, the traditional compensation elements are integral structures, such as compensation shield and short-circuit compensating winding. During the discharge process, especially at the highest current moment, the compensating potential directions are different under different poles, so the compensating eddy currents or compensating currents will be affected and weakened, which decreases the local compensation effect. To improve this disadvantage, this paper proposes a new air-core permanent magnet (PM) CPA with segmental squirrel-cage, which has the advantages of the PM excitation and air-core, small volume, light weight, compact structure and large output current. And at the highest current moment, the compensating current in each segment of the squirrel-cage will not be influenced by the compensating potential under different poles, thus the compensating effect is better. The simulation results verify that segmental squirrel-cage has more advantages than the conventional compensating elements. The research results are an important guide to the optimal design of compensating elements, and also provide a basis for the selection of the number of segments of the segmental squirrel-cage.

Keywords Air-core compensated pulse alternator · Finite-element simulation · Motor design · Harmonic analysis · Permanent excitation

Y. Cheng (✉) · G. Guo · S. Hu
School of Electrical Engineering and Automation, Hefei University of Technology, Hefei 230009, China
e-mail: 2012800015@hfut.edu.cn

G. Guo
e-mail: 2021170530@mail.hfut.edu.cn

S. Hu
e-mail: 2021170471@mail.hfut.edu.cn

1 Introduction

The pulsed power technology refers to the technology that releases stored energy in a short time to provide high-power pulse for a given load, and has important applications in both civil and military fields [1]. The key of pulsed power is pulsed power supplies, which can be divided into capacitors, rotating electrical machines, inductors and batteries according to different physical characteristics. Compensated pulsed alternator (CPA), one of the rotating electrical machines, with the integrated comprehensive advantages of energy density and power density [2]. At present, the CPA is commonly used in in fusion reactors, high-power pulsed lasers, and hypervelocity electromagnetic launchers [3].

CPA is a special type of synchronous alternator that differs from a normal synchronous alternator in that the CPA has a compensation element. The function of the compensation element is flux compression, which can reduce the transient inductance so as to release large current. There are four types of compensation: passive compensation, selective passive compensation, active compensation, and no compensation using the field coil as the compensating winding [4]. Active compensation can be used for laser flashlamp loads, and passive compensation or selective passive compensation can be used for electromagnetic emission loads [2]. The University of Texas at Austin Center for Electromechanics (UT-CEM) first began studying CPA, and has been leading the development of CPA. Up to now, CPA has experienced several generations of development. Not only air-core structure and multi-phase structure have been emerged, but also the performance has been constantly improved [5]. Air-core structure has been widely used in CPA because of its advantages of large current, light weight and no core loss. The discharge waveform of multi-phase structure is highly adjustable, which can meet the demands of various working conditions by controlling multi-phase. However, these structures usually use electric excitation, such as self excitation or pulse excitation. The field winding, brush and slip will lead to the problems of large size and heavy weight, and may reduce the reliability of operation. Permanent magnet (PM) removes field windings, brushes and slip rings, thus the alternator is smaller in a size, more compact and its operational reliability is robust. H. Wang researched and made a permanent magnet CPA (PM-CPA), studied its performance and demonstrated the feasibility of the PM-CPA [6]. Wu et al. also designed and analyzed PM-CPA based on Halbach array [7].

Many scholars have researched CPA, but they are basically based on traditional compensation elements, and there are few researches on the optimization of compensation elements. S. Wu and A. S. Kulkarni studied the effect of the compensation shield's thickness, which provided guidance for the selection of the thickness of the compensation [8, 9]. J. Li and C. Ye researched the two compensating windings and squirrel-cage rotor winding respectively, which provided ideas for the optimal design of compensating elements [10, 11]. However, the compensation shield and the short-circuit compensating winding are integral structures. During the discharge process, especially at the highest current moment, the direction of the compensating potential under the opposite pole is opposite, resulting in the compensating eddy

current or compensating current being affected and weakened, which reduces the local compensation effect. To solve this problem, this paper designs an air-core PM-CPA (APM-CPA) with segmental squirrel-cage. The designed APM-CPA not only has the advantages of air-core structure and PM excitation, but also can ensure that the compensating currents in different squirrel-cage's segments is not influenced by the compensating currents in other segments at the highest current moment, which can concentrate the compensating currents under one pole and has preferable compensating effect. It is verified through simulation that the segmental squirrel-cage has more advantages than the conventional compensating elements. And the results of the research are important for the optimization of the compensation element, and also provide a basis for the selection of the squirrel-cage's segments.

2 Design Basis and Scheme

2.1 Stator Design

The designed alternator is a two-phase and four-pole APM-CPA, and the schematic of designed APM-CPA is shown in Fig. 1. The field winding, brush and slip can be eliminates by the PM excitation, which reduces the processing difficulties and assembly costs. So the designed alternator is simple in structure and reliable in operation. And the unbalanced magnetic force can be effectively removed by the four-pole structure during the operation of the alternator, so the winding force is more uniform, which can reduce the vibration of the alternator.

There are 48 slots on the stator. Considering the waveform control of the CPA, the two-phase winding configuration is adopted. And the two-phase windings are identical and completely decoupled, that is, 90° electrical angle difference between two phases, which can facilitate the control of the two phases and can meet the needs of different loads. Two-phase windings are denoted as phase-A winding and phase-B winding. Considering the discharge performance of the CPA, the number of coil turns is 1, which can directly reduce the inductance and resistance of the armature winding

Fig. 1 Schematic diagram of designed APM-CPA
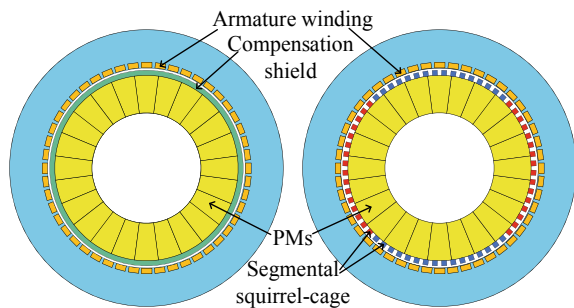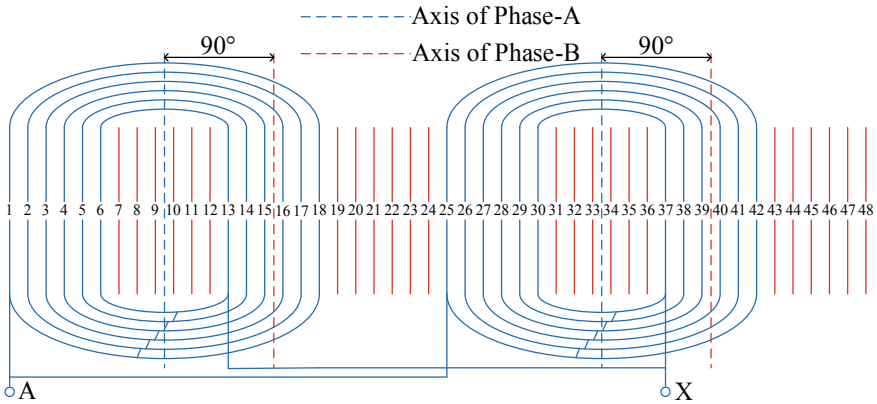
Fig. 2 Wiring diagram of the phase-A winding

and improve the discharge capacity of the CPA. Because of the large current flowing in the armature winding of the CPA, a parallel branch structure is also adopted, which not only can further reduce the inductance and resistance of the armature winding and improve the discharge capacity, but also can reduce the current density and improve the capability of a wire to withstand the highest current, playing a certain role in safety protection. In order to facilitate assembly, the concentric winding is used, and the specific wiring diagram is shown in Fig. 2. Because the two-phase winding structure is exactly the same, only the phase-A winding is provided.

2.2 Rotor Design

As shown in Fig. 1, the rotor structure with rotating magnetic poles is adopted, which can improve operational reliability and meet higher power requirements. In order to improve the flux density of the air-gap, the PMs are placed according to the Halback array. The Halback array can enhance the magnetic field on one side and cancel the magnetic field to near zero on the other side, so the magnetic direction setting of the Halback array is particularly important. The interval angle (θ) of magnetic direction between adjacent PMs can be expressed as:

$$\theta = 180°/pn \tag{1}$$

where p is the number of pole pairs, n is the number of the magnets each of magnetic pole. Thus, the specific magnetic direction of the PMs as shown in Fig. 3.

In addition, the magnetic field distribution of Halback array PM structure is almost standard sinusoidal distribution with little harmonic content, which can effectively reduce the harmonic content in no-load voltage. And a new compensation structure,

Fig. 3 Specific magnetic direction of PMs
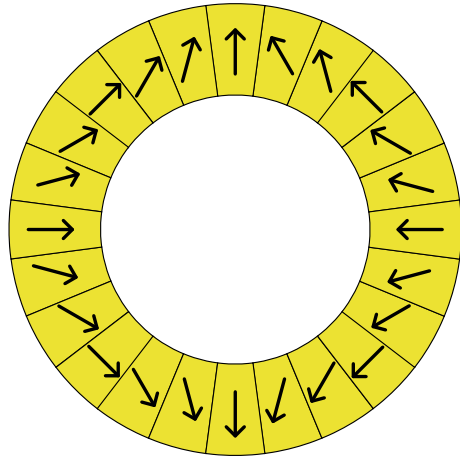
segmental squirrel-cage, is accepted. Due to the use of a four-pole construction, the squirrel-cage uses a four-segment structure. This selection can ensure that the compensating current is concentrated under the corresponding pole at the highest current moment, having preferable local compensating effect, that is, the discharge current peak value can be higher. And in the following research, it is proved that the selection of segments of squirrel-cage based on the number of pole pairs can achieve better results.

The high-strength and non-conductive composite materials are used to cast the segmental squirrel-cage and PMs as a whole to form the rotor. It can fix the segmental squirrel-cage and support the PM well. And the specific parameters of the relevant alternators are shown in Table 1.

Table 1 Specific parameters of the relevant alternators

Parameter	Value	Parameter	Value
Number of stator slots	48	Number of bars	64
Stator outer diameter	470 mm	Rotor outer diameter	389 mm
Stator inner diameter	390 mm	Rotor inner diameter	210 mm
Stator core length	500 mm	PMs' number	24
Effective air-gap length	0.85 mm	PM's outer diameter	372 mm
Thickness of shield	8 mm	PM's inner diameter	228 mm
Compensation shield	Copper	Magnetic steel	NdFe35

3 Simulation and Verification

The finite element model is established according to Fig. 1 and Table 1, and the simulations of no-load and discharge are conducted respectively. The results of no-load simulation prove the reasonableness of the alternator design. The results of discharge simulation show that the compensating effect of segmental squirrel-cage is preferable and is more advantageous than that of conventional compensating element. It also demonstrates that the selection of segments of squirrel-cage based on the number of pole pairs can achieve better results.

3.1 No-Load Characteristic Analysis

According to the alternator design above, the harmonic content in the no-load voltage can be effectively reduced. From the no-load voltage waveform and the spectrum analysis of the no-load voltage in Fig. 4, it can be seen that the no-load voltage amplitudes of phase-A and phase-B are both 409.31 V. And the waveform is sinusoidal, and only has the fundamental wave content. This is consistent with the theoretical analysis and also proves the rationality of the designed APM-CPA.

Meanwhile, it can be seen from the waveform of no-load voltage that the phase difference of two-phase is 90° electrical angle, which also proves that the two-phase windings are decoupled from each other. Therefore, the required waveform can be easily obtained through the coordination of the two phases, such as the two-phase in parallel and the two-phase in series. As there are many and complex waveform control strategies, for purpose of facilitating the verification of the advantages of segmental squirrel-cage compensation, diodes are selected to discharge in simulation. Figure 5 shows the discharge schematic diagrams of two-phase in parallel and two-phase in series, where R is the discharge resistor, D_1 and D_2 are the uncontrolled diodes.

(a)   (b)
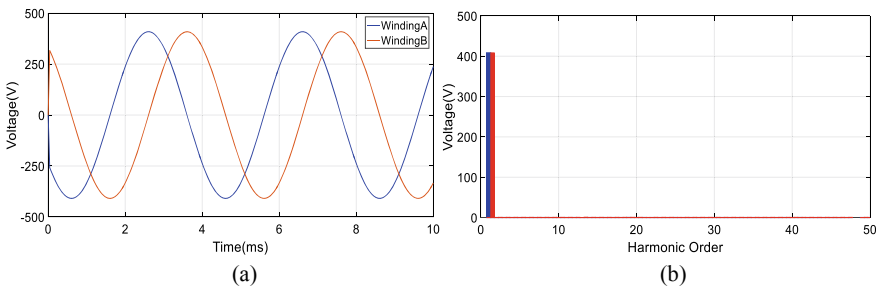
Fig. 4 Harmonic analysis of no-load voltage. **a** No-load voltage waveform. **b** Spectrum analysis of no-load voltage
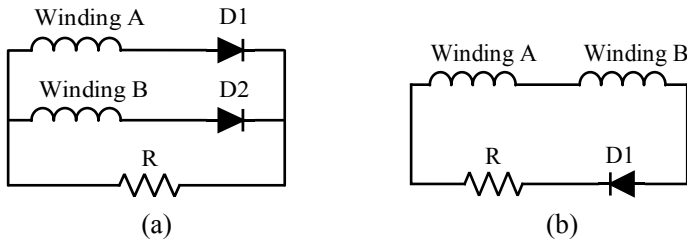
Fig. 5 Discharge schematic diagrams. **a** Two-phase in parallel. **b** Two-phase in series

3.2 Discharge Characteristic Analysis

The simulation of discharge is conducted at 7500 rpm based on Fig. 5, R is 10 mΩ. Meanwhile, in order to ensure the comparability of characteristics of discharge under various compensation ways, the remaining parameters of the alternator are kept the same except for the various compensating methods. Then, the discharge simulations are conducted in the cases of shield compensation (Shield.Comp.), full squirrel-cage compensation (Full.Comp.), four and eight segments compensation (Seg4.Comp. and Seg8.Comp.), and the discharge waveforms are shown in Fig. 6, and the results are included in Table 2 for comparison.
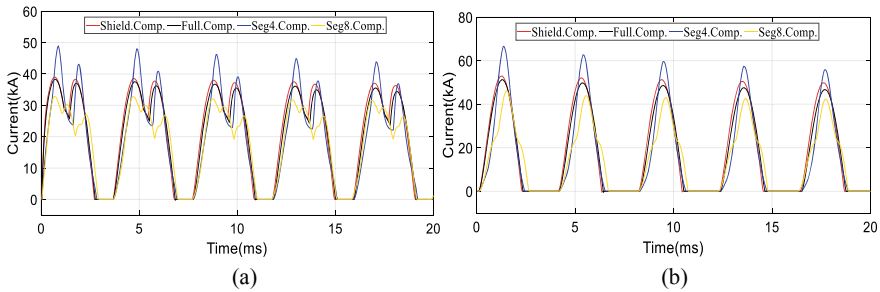
Fig. 6 Discharge waveforms of different compensation methods. **a** Two-phase in parallel. **b** Two-phase in series

Table 2 Pulse amplitude and pulse width under various compensation methods

Compensation methods	Discharge in parallel		Discharge in series	
	Pulse amplitude (kA)	Pulse width (ms)	Pulse amplitude (kA)	Pulse width (ms)
Shield.Comp	39.00	3.13	52.98	2.20
Full.Comp	38.30	3.17	51.27	2.24
Seg4.Comp	48.97	3.30	66.59	2.36
Seg8.Comp	32.85	3.32	46.19	2.56

It can be clearly seen from the results in Fig. 6 and Table 2 that the pulse amplitude of Seg4.Comp. is the highest, the pulse amplitudes of Shield.Comp. and Full.Comp. are high and their difference is not large, and the pulse amplitude of Seg8.Comp. is the lowest. When the two phases are connected in parallel, compared with the pulse amplitudes of Shield.Comp. and Full.Comp., the pulse amplitude of Seg4.Comp. increases by 25.6% and 27.9%, respectively; When the two phases are connected in series, compared with the pulse amplitudes of Shield.Comp. and Full.Comp., the pulse amplitude of Seg4.Comp. increases by 25.7% and 29.9%, respectively. So Seg4.Comp. has the best compensation effect. Although Seg8.Comp. has also been segmented, its compensation effect is not ideal. Because the eight segmental squirrel-cage is divided into two sections under one pole, so the compensating current under one pole is divided into two parts, that is, the compensating current is dispersed. This is equivalent to the reduction of compensation area, so the compensation effect is decreased. Therefore, the selection of the segments of the squirrel-cage based on the number of pole pairs can achieve better results. In addition, it can be seen that the pulse width is wider with two-phase in parallel, and the waveform is highly adjustable, but the current amplitude is sacrificed; The current amplitude is higher with two-phase in series, but the pulse width is sacrificed.

4 Conclusion

In this study, a new APM-CPA with segmental squirrel-cage is designed and simulated. The two-phase decoupled windings are adopted by the APM-CPA, which can meet the requirements of multiple tasks through the coordination between the two phases. The Halback array PM structure is used, which can effectively reduce the harmonic of the no-load voltage. The selection of the segments of the squirrel-cage based on the number of pole pairs, which can concentrate the compensating current under the corresponding pole at the highest current moment and have a preferable local compensating effect. It is verified through simulation that the segmental squirrel-cage compensation offers more benefits than conventional compensation. And the results of the research are important for the optimization of the compensation element, and also provide a basis for the selection of the segments of squirrel-cage.

References

1. Nguyen B, Yen W, Chao P, Wang S (2020) A new high-efficiency power management circuit for a novel two-phase compensated pulse alternator. IEEE Trans Plasma Sci 48(9):3176–3187
2. Wu S, Zhao W, Wang S, Cui S (2017) Overview of pulsed alternators. IEEE Trans Plasma Sci 45(7):1078–1085
3. Wang H, Liu K, Zhu B, Feng J, Ao P, Zhang Z (2015) Analytical investigation and scaled prototype tests of a novel permanent magnet compulsator. IEEE Trans Magn 51(8):1–9
4. Spann ML, Pratap SB, Werst MD, Walls WA, Fulcher CW (1989) Compulsator research at the University of Texas at Austin-an overview. IEEE Trans Magn 25(1):529–537
5. Kitzmiller JR, Pratap SB, Driga MD (2003) An application guide for compulsators. IEEE Trans Magn 39(1):285–288
6. Wang H, Liu K, Yu X, Ao P, Zhang Z (2015) Design, analysis, and testing of a novel permanent magnet compulsator. IEEE Trans Plasma Sci 43(4):1040–1048
7. Wu S, Wu S, Cui S, Zhao W (2017) Design and analysis of a high-speed permanent magnet compensated pulsed alternator. IEEE Trans Plasma Sci 45(7):1314–1320
8. Wu S, Cui S, Song L, Liu M (2008) Design, fabrication and experiment of iron-core passive compulsator. In: 2008 international conference on electrical machines and systems. pp 3544–3548
9. Kulkarni AS (2017) Performance analysis of passive compulsators used for EML application with different compensation shield thickness. In: 2017 IEEE 21st international conference on pulsed power (PPC), pp 1–4
10. Li J, Yan X, Lv L, Tan L, Tian J, Lou J (2012) Pulsed power regulation in selective passively compensated pulsed alternator. IEEE Trans Magn 48(11):3875–3878
11. Ye C, Li W, Yang J, Chang S, Zhi G, Xiang Y et al (2021) Development and analysis of a novel cascaded brushless self-excited air-core compensated pulsed alternator with squirrel-cage rotor winding. IEEE Trans Industr Electron 68(7):5571–5581

Influence of Insulating Cylinder on Electric Field Inside Cast-Resin Dry-Type Power Transformer

Xinhan Qiao , **Wei Li, Ke Xu, Yue Ming, Jiliang Yi, Xia Li, Xiaoquan Zhang, and Wenfeng Chen**

Abstract Insulating cylinders are important components in dry-type transformers. Placing an insulating cylinder in the main air channel can effectively reduce insulation distance between LV and HV winding. Therefore, to study the influence of insulating cylinders on the distribution of electric field in transformers is necessary. This paper built a CRDT cross-sectional model and the electric field was calculated by using finite element software COMSOL. This paper focused on the influence of the position, quantity, and relative permittivity of insulating cylinders on the electric field of transformers, especially on the electric field of HV winding. In addition, this paper also studied the influence of insulating cylinders on the electric field of the main air channel. The results show that, the insulating cylinders will increase the electric field strength of the transformer. The results also show that reducing the relative permittivity of the insulating cylinders can reduce the above impact.

Keywords Dry transformer · Insulating cylinder · Electric field

X. Qiao (✉) · W. Li
School of Electrical Engineering, China University of Mining and Technology, Xuzhou 221116, China
e-mail: qiaoxinhan@foxmail.com

K. Xu
State Key Laboratory of Environmental Adaptability for Industrial Products, China, National Electric Apparatus Research Institute Co., Ltd., Guangzhou 510663, China

Y. Ming
School of Mechanical and Electrical Engineering, Xuzhou University of Technology, Xuzhou 221018, China

X. Qiao · J. Yi · X. Li · X. Zhang · W. Chen
Sunten Electric Equipment Co., Ltd., Foshan 528300, China

1 Introduction

Transformers are important equipments in the power system. They play an important role in the generation, transmission, and distribution of electricity. The traditional transformer is oil-filled transformer. However, the ability of this type of transformer to resist short circuits is feeble and the transformer is prone to fire and explosion [1]. Then the SF6 transformer appeared, but its short-circuit resistance is still poor. It also has poor heat dissipation, cumbersome maintenance, and SF6 has environmental protection issues [2, 3]. By now, with the development of insulation materials, the application of dry-type transformers is increasing. Cast-resin dry-type power transformer (CRDT) is a kind of dry-type transformers which is used very widely. Its ability to resist short circuits has been enhanced [2]. Compared to traditional oil-filled transformers, dry type transformers are not flammable, which makes them suitable for use in residential areas, hospitals, and other areas that require high levels of fire and explosion prevention [1, 4]. In addition, the weight of dry-type transformers is lighter than oil-filled transformers, thereby reducing installation and cooling costs, as well as reducing downtime for maintenance and inspection [5].

Insulating cylinders are important components in dry-type transformers. In the dry-type transformers, the main air channel is the area with weak insulation, which is prone to happen discharge [6]. The use of insulating cylinders in the main air duct can reduce the insulation distance between high and low voltage windings, thereby reducing the net weight and production cost of the transformer [7]. Therefore, in order to use insulating cylinders more reasonably, to study the influence of insulating cylinders on the electric field of transformers is necessary. In existing research, researchers have found that the height and position of the insulating cylinder have little effect on the electric field of the main air channel [8]. This paper would comprehensively analyze the influence of insulating cylinders on the electric field.

2 Model Building

This model is built based on real transformer manufacturer drawing. In order to simplify the study, this paper made the following assumptions for the model.

(1) Considering the symmetry of the transformer, this paper only built the 1/2 cross-section of one phase in the three phases of the transformer. Also ignoring the influence of other phases on the local phase.
(2) The primary voltage of this transformer is 66 kV, and the secondary voltage is 1.14 kV. The influence of LV winding on the electric field which is near HV winding is very small. Therefore, this paper simplified the LV winding.
(3) This paper ignored the influence of other structural components near the HV winding in the transformer.
(4) The voltage remains unchanged throughout the entire study.

Based on the above assumptions, a CRDT model built using finite element software COMSOL is shown in Fig. 1a. In this transformer, the conductor of HV winding and LV winding is copper, and the surrounding insulation material is epoxy. The relative permittivities of materials in the transformer are shown in Table 1.

Refer to the literature [9], the solution domain of the model is shown in Fig. 1b. In Fig. 1b, ab, cd, and de represent the air boundary, and ea represents the ground. The iron core was applied with zero potential. The LV winding was applied with 1.14 kV. The HV winding was applied with different voltages as the number of turns increases.
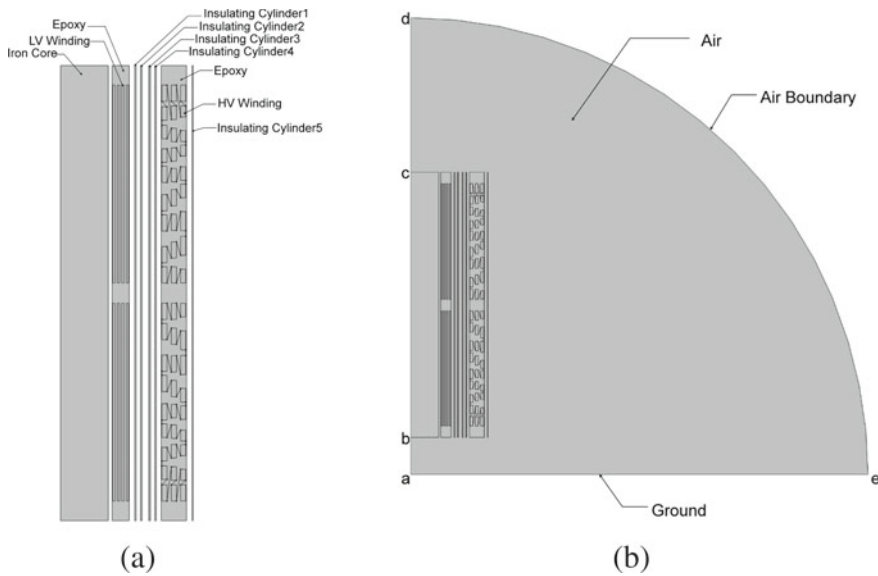
Fig. 1 The model of transformer

Table 1 The relative permittivities of materials in the transformer	Medium material	Relative permittivity
	Iron	8000
	Copper	8000
	Insulating cylinder	4.5
	Epoxy	3.5
	Air	1.0

3 Calculation Results and Analysis of Electric Field

3.1 Electric Field Distribution of Original Model

This study used finite element software to calculate the electric field of the original model. The result is shown in Fig. 2. Through research, it was found that the locations with high electric field strength are concentrated near the HV winding. Therefore, in subsequent studies, the main focus will be on the electric field of the HV winding.

3.2 Influence of the Insulating Cylinder's Position on the Electric Field

In this section of the study, only one insulating cylinder is reserved for the convenience of research. This study placed an insulating cylinder at distances of 50, 80, and 110 mm from the HV winding and calculated the electric field. The electric field strength on the surface of the HV winding under the above conditions is shown in Fig. 3.

From Fig. 3, it can be seen that there is only a slight difference in the electric field strength on the surface of the HV winding when the insulating cylinder is in different positions. The values of the maximum electric field strength of the HV winding are shown in Table 2.

From the above data, it can be observed that as the position of the insulating cylinder changes, there is an opposite trend in the maximum field strength inside the HV winding and the maximum field strength on the surface of the HV winding. The closer the insulating cylinder is to the HV winding, the smaller the maximum field strength inside the HV winding, and the greater the maximum field strength on the surface of the HV winding.

3.3 Influence of the Insulating Cylinder's Quantity on the Electric Field

This paper placed 1, 2, 3, and 4 insulation cylinders in the main air channel to calculate the electric field of transformer. The insulating cylinders were evenly placed. The electric field strength on the surface of the HV winding under the above conditions is shown in Fig. 4. The values of the maximum electric field strength on the surface and inside of the HV winding are shown in Table 3.

From the data, it can be found that as the number of insulating cylinders between HV and LV windings increases, the curve of electric field strength will rise upwards. The field strength increases significantly near the middle and end positions of each
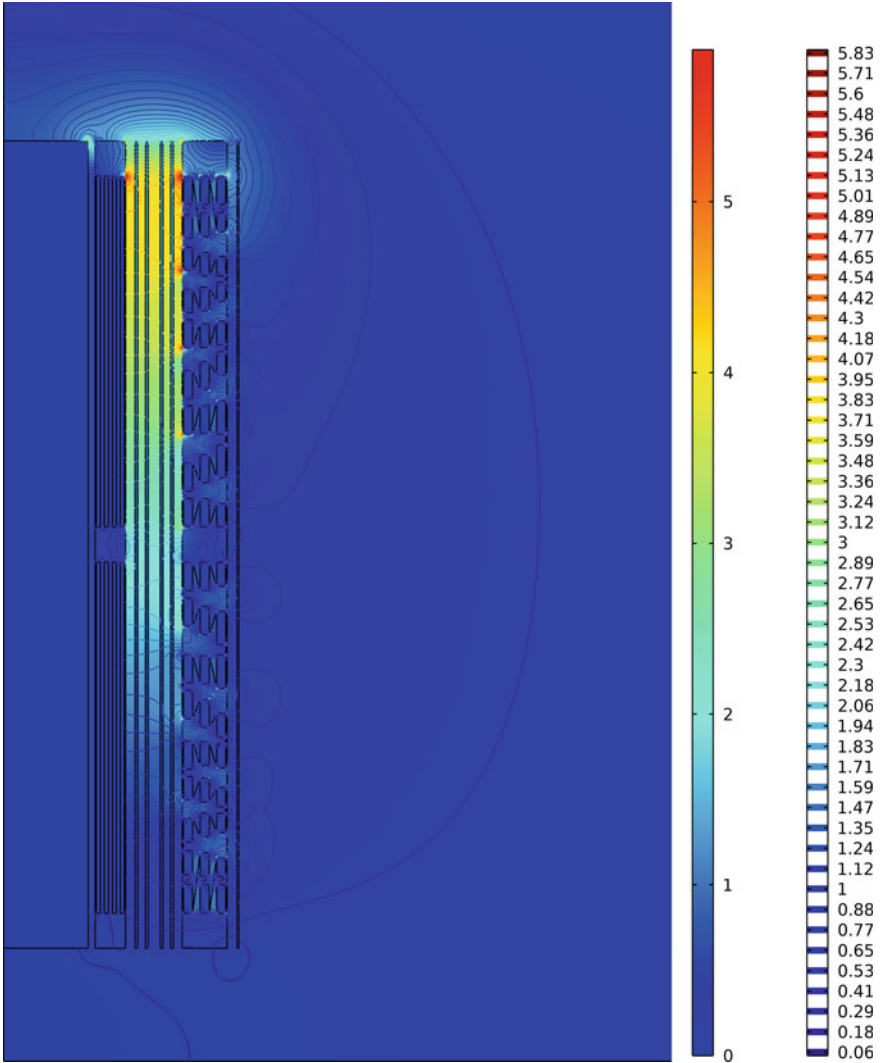
Fig. 2 Electric field distribution of original model

high-voltage coil section, as well as the middle position of the insulation between coil sections. As the number of insulating cylinders between HV and LV windings increases, the maximum electric field strength inside and on the surface of the HV winding increases. And the maximum field strength on the surface of the HV winding is more affected by the number of insulating cylinders.

Previous studies have found that the position of insulating cylinder has little effect on the electric field. Therefore, the differences in electric field studied in this section can be considered as the impact of the number of insulating cylinders.
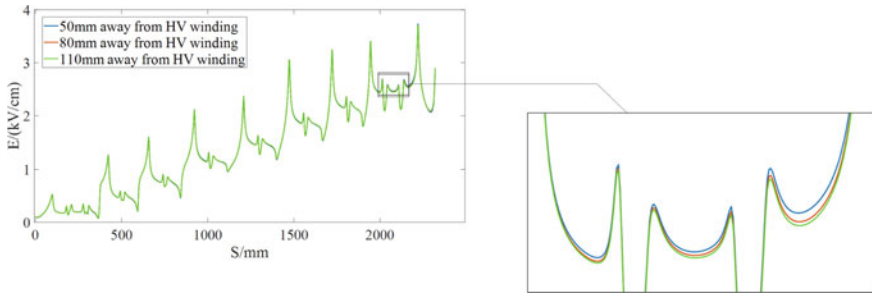
Fig. 3 Electric field strength on the surface of HV winding when the insulating cylinder is in different positions

Table 2 The maximum electric field strength of the HV winding

Location of insulating cylinder	The maximum electric field strength on the surface of the HV winding (kV/cm)	The maximum electric field strength inside the HV winding (kV/cm)
50 mm away from HV winding	3.7629	6.5053
80 mm away from HV winding	3.7400	6.5213
110 mm away from HV winding	3.7336	6.5327
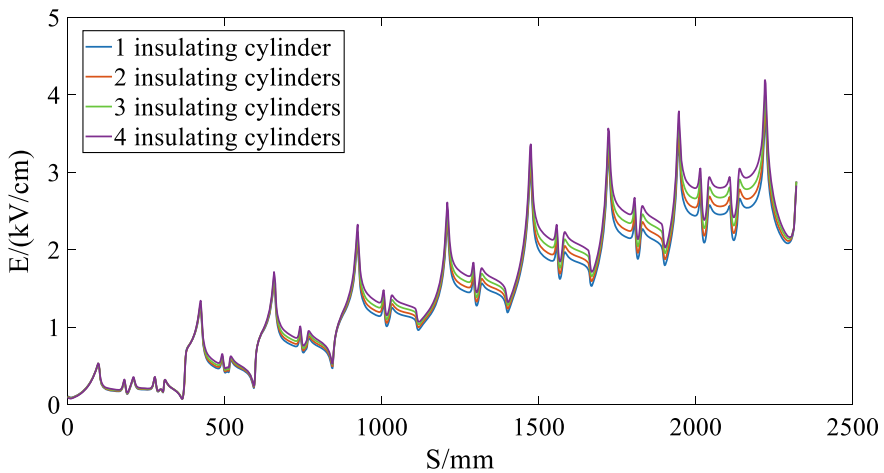
Fig. 4 Electric field strength on the surface of HV winding under different number of insulating cylinders

Table 3 The maximum electric field strength on the surface and inside of the HV winding

The number of insulating cylinders	The maximum electric field strength on the surface of the HV winding (kV/cm)	The maximum electric field strength inside the HV winding (kV/cm)
1 insulating cylinder	3.7400	6.5213
2 insulating cylinders	3.8764	6.5355
3 insulating cylinders	4.0309	6.5495
4 insulating cylinders	4.2159	6.5908

Table 4 The maximum electric field strength on the surface and inside of the HV winding

The number of insulating cylinders	The maximum electric field strength on the surface of the HV winding (kV/cm)	The maximum electric field strength inside the HV winding (kV/cm)
1 insulating cylinder	3.7156	6.4928
2 insulating cylinders	3.8144	6.5047
3 insulating cylinders	3.9237	6.5165
4 insulating cylinders	4.0479	6.5583

3.4 Influence of the Insulating Cylinder's Relative Permittivity on the Electric Field

Based on the previous research, which involved placing different numbers of insulating cylinders in the main air channel, in this section of research, the relative permittivity of the insulating cylinder was changed from 4.5 to 2.5. The electric field of the transformer was calculated. The maximum electric field strength on the surface and inside of the HV winding is shown in Table 4.

By comparing the data from Tables 3 and 4, it can be found that when the relative permittivity of the insulating cylinder decreases, the maximum electric field strength of the HV winding decrease.

3.5 Influence of the Insulating Cylinder on the Electric Field in the Main Air Channel

In order to further explore the influence of the insulating cylinder on the electric field, this section of research will compare the electric field of the main air channel with or without an insulating cylinder.

This study built two models, one with an insulating cylinder placed in the middle of the main air channel and the other without an insulating cylinder. This study selected several axial lines on the main air channel, compared and studied the electric field of

the same lines in two models. The lines are 40, 60, 100, 120 mm away from the HV winding. There is also a line on the surface of the insulating cylinder. The electric field strength is shown in Fig. 5.

From the above data, it can be found that using an insulating cylinder can reduce the electric field strength on the position of the insulating cylinder's surface, while in most air areas, the electric field strength will increase. In addition, as the distance from the HV winding increases, the influence of the HV winding decreases, the phenomenon shown is that the curve is becoming smoother.
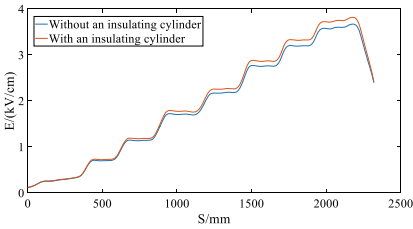
(a) The line which is 40mm away from the HV winding
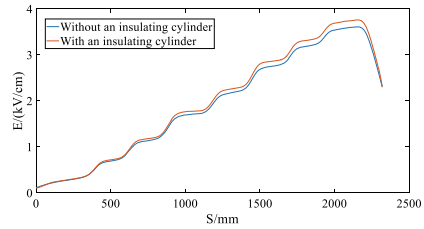
(b) The line which is 60mm away from the HV winding
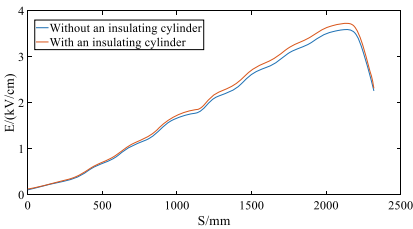
(c) The line which is 100mm away from the HV winding
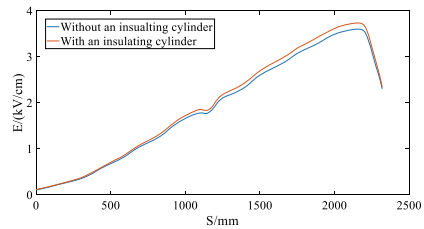
(d) The line which is 120mm away from the HV winding
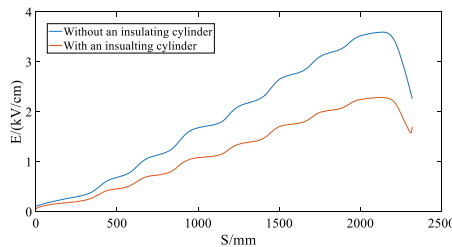
(e) Electric field strength on the surface of the insulating cylinder and the electric field strength of the same line in another model

Fig. 5 The electric field in the main air channel

4 Conclusions

This paper built a two-dimensional model of the CRDT transformer, studied the influence of insulating cylinder on the electric field. Finally, this paper has got some conclusions as follows.

(1) The position of the insulating cylinder has a slight effect on the electric field of the HV winding, which can be ignored in practical engineering.
(2) The increase in the number of insulating cylinders will increase the electric field strength of the HV winding, and the insulating cylinder will also increase the electric field strength of most of the air areas in the main air channel.
(3) Reducing the relative permittivity of the insulation cylinder can reduce the electric field strength of the HV winding.

References

1. Jaafar MJ, Muhamad NA, Jamil MKM, Rosle N (2021) Electric field and potential changes studies on cast-resin dry-type power transformer having misalignment. In: 2021 IEEE international conference on the properties and applications of dielectric materials (ICPADM), pp 37–40
2. Han J, Liu Z (2001) The development of 110 kV resin-cast dry-type transformers. In: Proceedings of the 5th international conference on electrical machines and systems (ICEMS), pp 236–238
3. Wang Z, Zhang Z, Zhang J, Zhao X, Pan Y (2020) Development of 110kV epoxy cast dry-type power transformer. Transformer 57(9):48–50+71 (in Chinese)
4. Eslamian M, Vahidi B, Hosseinian SH (2011) Analytical calculation of detailed model parameters of cast resin dry-type transformers. Energy Convers Manage 52(7):2565–2574
5. González VE, Gómez P, Espino-Cortés FP (2011) Design of the insulating supports in medium voltage dry-type transformers. In: 2011 electrical insulation conference (EIC), pp 45–48
6. Hu R et al (2019) Electric field optimization of cast resin dry-type transformer under lightning impulse. In: 2019 IEEE conference on electrical insulation and dielectric phenomena (CEIDP), pp 556–559
7. Saberi S, BigdeliM, Azizian D (2022) Insulation system optimization in dry-type transformer using finite element method. In: 2022 30th international conference on electrical engineering (ICEE), pp 518–523
8. Zhang X, Liu X, Xu Y et al (2017) Research on the electric field in the main air channel of 10kV dry-type transformer based on finite element software. Electric Engineering 443(3):7–9 (in Chinese)
9. Zhou K (2014) Electric field calculation and coil surface discharge restraining method research of casting dry type transformer. Hunan University (in Chinese)

Modeling and Application of Transformer Degradation Development Law Based on Degradation Track

Jing Shan, Mengjun Liu, Xiaoyi Ji, and Yangchun Cheng

Abstract Transformer fault will cause great harm to the grid reliability, but the current condition evaluation guidelines can only make threshold judgment on the current condition quantity, lacking early warning criteria. In addition, it is difficult to analyze the degradation process and the dispersion of the late degradation using the commonly used prediction methods because there are few transformer fault cases. For this reason, this paper collects a large amount of field fault data, proposes the analysis method of transformer deterioration development law based on degradation track, and lays the foundation for determining the early warning criterion of transformer condition evaluation. Firstly, the degradation-based reliability modeling method and analysis process are summarized, and the most suitable modeling method is selected by balancing the advantages and disadvantages of each aspect. Then the application of each degradation model is analyzed from the theoretical level, and the degradation track model is determined to describe the transformer degradation development law. Finally, according to the statistical distribution of the field data to determine the state quantity note value, combined with the collected fault data to establish the transformer degradation track model and estimate the model parameters, and describe the application methods of degradation track model.

Keywords Transformer · Degradation track · Degradation law · Reliability modeling

J. Shan (✉) · M. Liu · X. Ji
School of Electrical and Electronic Engineering, North China Electric Power University, Beijing 102206, China
e-mail: shanjingddd@163.com

Y. Cheng
Beijing Key Laboratory of High Voltage and EMC, North China Electric Power University, Beijing 102206, China

1   Introduction

Power transformer is the hub equipment of the power grid, not only expensive, but also the core equipment of power conversion, the good or bad state of the transformer has a vital role in the safe operation of the power grid. According to the data, there are more than 30,000 transformers of 110 kV and above in China, and transformer fault will cause great harm to the reliability of the power grid and bring huge economic loss. The role of transformers is so huge that the condition assessment of transformers is especially critical [1]. Once an abnormality is detected in a field transformer, the maintenance personnel will immediately shut down the transformer for maintenance, resulting in a lack of data on the development of the fault process, which is not conducive to the study of transformer degradation development law [2]. Therefore, there is an urgent need to study a suitable analysis method of transformer degradation development law.

The core of transformer degradation development law modeling is to analyze the equipment degradation process, and the analysis methods are mainly divided into four categories: based on fault physics, based on degradation track fitting, based on degradation amount distribution, and based on stochastic process [3].

The idea of modeling based on the distribution of degraded is to analyze the statistical characteristics of the random time variation of degraded quantities [4, 5]. However, the modeling method based on the distribution of degradation needs not only to determine the distribution model of degradation at each measurement moment, but also to determine the variation of model parameters with time and accelerated stress. The modeling method of performance degradation based on the distribution of degradation amounts is more complicated, not only to determine the distribution model of degradation amounts at each measurement moment, but also to determine the variation of model parameters with time and accelerated stress [6, 7]. Most of the modeling methods based on stochastic processes make assumptions based on subjective judgments or engineering experience, which may result in inaccurate reliability models extrapolated to rated stresses [8].

The method based on the degradation track fitting is to build the performance degradation model by fitting the degradation data of the device at each measurement moment. At present, there are two types of degradation track fitting methods: one is to fit the degradation track using linear, power, exponential functions [9], and the other is to fit the degradation track using intelligent algorithms such as neural networks, time series, and least-squares vector machines [10]. In this paper, we will use the degradation track fitting modeling method to model the degradation development law of transformer, whose main advantages are simple modeling process, easy parameter estimation, and convenient for engineering applications.

2 Degradation-Based Reliability Theory

2.1 Degradation-Based Reliability Modeling Approach

In the traditional reliability theory, fault is considered as an abstract random event. The state of the equipment is generally simplified into two discrete states, normal and fault. The fault-based reliability modeling method mainly uses the information when the equipment fault occurs, especially the fault time data, to establish the law of equipment fault occurrence time, and does not focus on the state evolution during the equipment fault process. In contrast, the degradation-based reliability modeling approach focuses first on the information of the equipment fault process. The fault process of the equipment is portrayed by selecting the reliability characteristic quantities that are highly correlated with the life and reliability of the equipment and describing their change laws over time using a quantitative mathematical model, called the performance degradation process model.

Degradation-based reliability techniques provide a feasible path to solve several difficult problems in modern reliability engineering. First, it provides a new way to solve the problem of modeling and evaluating the reliability of small-sample long-life equipment; second, it is highly adaptable to engineering and helps to overcome the phenomenon that reliability theory and practice are different; third, it bridges the quantitative relationship between quality and reliability and expands the scope of reliability research.

2.2 Degradation-Based Reliability Modeling Analysis Process

The degradation-based reliability modeling method is based on the description of the evolution law of the amount of equipment degradation, which mainly includes two parts: modeling and analysis of the degradation process and modeling and analysis of the life distribution of the degradation process and the fault threshold [11], as shown in Fig. 1.

First is the fault mechanism analysis, and on the basis of the fault mechanism analysis, the reliability characteristic quantity describing the equipment degradation and the fault criterion are determined. Secondly, the degradation data are obtained and pre-processed according to the actual situation in order to eliminate the abnormalities, pollution, noise, etc., and facilitate the subsequent modeling process. Then it is necessary to determine the type and structure of the degradation process model and the degradation process model identification by various means, including the estimation of model parameters and model goodness test. Finally, the fault threshold is determined, the fault probability is calculated and the remaining life is calculated.
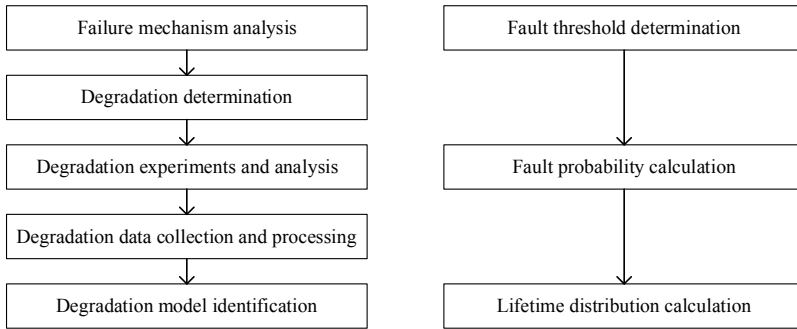
(a) Degradation process modeling and analysis (b) Lifetime distribution modeling and analysis

Fig. 1 Degradation-based reliability modeling process

3   Modeling of Transformer Degradation Development Law

In this paper, the oil chromatography gas content is used as the degradation quantity to analyze the development law of transformer degradation. According to the analysis in the previous section, the modeling method of degradation track fitting is used to establish the transformer degradation process model after collecting the field transformer fault data.

3.1   Transformer Degradation Process Model Selection

Degradation process models are generally complex, and when applying models for life prediction and reliability assessment, different models may lead to different results, and very small perturbations that deviate from the true model may lead to serious prediction deviations. Therefore, a combination of multiple tools is needed to determine the type and structure of degradation process models.

Since degradation track models, degradation models based on Wiener processes, degradation track models based on Gamma processes, and degradation models based on composite Poisson processes have been most extensively studied and are also capable of describing a wide range of known degradation mechanisms [12], appropriate models can be selected in the manner of Fig. 2.

In this paper, the degradation track model is chosen to analyze the transformer degradation process for the following two reasons:

1. The degradation track model is simple in form and can be cross-checked with the empirical models in national and IEC standards.
2. Based on the fault data collected in the field, the individual sample functions are determined by regression analysis techniques, and the individual differences in the degradation process are described by randomization of the model parameters.
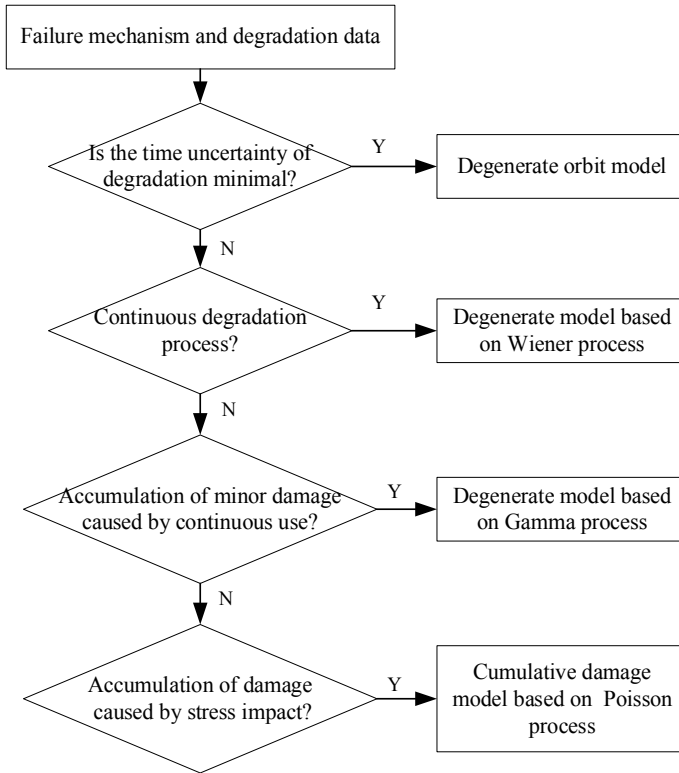
Fig. 2 Degradation process modeling

3.2 Determination of Oil Chromatography Attention Values

The different fault detection times of each transformer lead to different fault initiation chromatographic values, while the degradation tracks vary due to the dispersion of the equipment. In order to unify the starting point of each degradation track, the quantile point of the statistical distribution is taken as the starting point of transformer degradation, i.e., the transformer oil chromatographic gas content attention value.

The basic idea of oil chromatography attention value determination is to carry out stratified random sampling of the collected online monitoring data and non-parametric testing of the sampled data to obtain the attention value of the original data and the distribution function that can characterize the distribution law of the original data [13].

The following is an example of 110kV main substation chromatography H_2. Two sets of data were taken for each of 617, 110 kV transformers in operation to form a sample containing 1234 sets of data, and the data analysis was done for H_2 in the sample data, and the following results were obtained:

(a) H$_2$ Distribution fitting curve
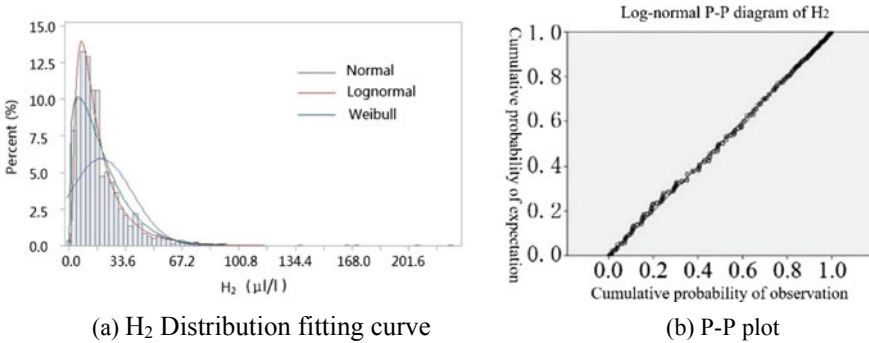
(b) P-P plot

Fig. 3 Probability density function fitting curve

From the fitted probability density function plot and its P-P plot, the fitted result of H$_2$ obeys the lognormal distribution, and its histogram, the fitted probability density function plot and the corresponding P-P plot are shown in Fig. 3, and the distribution parameters, the significance of the log distribution and the quantile of the log distribution are shown in Table 1, respectively.

The plot of the fitted probability density function shows that: the curve of the log–normal function fits best with the outer edge of the histogram; most of the points in the log-normal P-P plot are near the diagonal straight line in the plot, so it can be assumed that H$_2$ approximately obeys the log-normal distribution.

The observed and estimated values for the 90, 95 and 99% quantile points are given in Table 1. From the values given in the table, it can be seen that the observed and estimated values of the quantile values are very close to each other. Therefore, the estimated value of the quantile of the fitted distribution function can be used as the value of attention for the detection parameter. Comparing the national and IEC standards, the values of the gas quantile points are smaller than the attention values given in the national and IEC standards. Since the calculated attention values take into account the regional variability, the attention values are more relevant and more stringent. In this paper, the statistical obtained 90% quantile as the starting point of transformer degradation, i.e., the starting point of degradation track with H$_2$ as the degradation amount is concentrated near 39 µL/L.

Table 1 Quartiles of the logarithmic distribution

Percentage (%)	Quantile (µL/L)		IEC60599-2007	GB/T7252-2001
	Observations	Estimated value		
90	39	40.03	50–150	150
95	53	53.76		
99	133	112.21		

3.3　Transformer Degradation Track Modeling

In the process of degenerate orbit modeling, determining the degenerate function f is the first problem to be solved in building a degenerate orbit model. It is usually based on empirical or deterministic description of the degradation process, and then randomness is introduced into the parameters of the function. However, in the absence of degradation mechanisms or empirical formulas, the form of the degradation function f is usually determined by regression analysis. Typical degenerate orbit models include constant degenerate rate model, power degenerate rate model, inverse power degenerate rate model, exponential degenerate rate model, and hybrid model.

In this paper, we collected 100 transformer oil chromatographic data of high temperature overheating faults in the field, with voltage levels of 330 kV and below. The modeling analysis of the collected faulty transformer data is performed based on the modeling method of degenerate track fitting. The analysis results are as follows: the degenerate track model function is in exponential form, as shown in Eq. (1), and the parameters and model are shown in Table 2 and Fig. 4. As can be seen from the parameters in the table, the goodness of fit is close to 1, which indicates that the model function has a good fit for the sample data points.

$$f = ae^{bt} \tag{1}$$

As seen in Fig. 4, the initial values of the degraded tracks vary, and the differences in the initial conditions come from the manufacturing process of the transformer, the region, and the operating environment. Figure 5 shows the histogram of the initial values of the degraded track and the fitted probability density function curve, which is fitted to approximate a normal distribution with a mean μ of 30.7521 and a standard deviation σ of 61.7956.

Table 2 Parameters of the H_2 degenerate orbit model

Degradation orbit model parameters		Goodness-of-fit	
a	b	R-square	RMSE
40.46 (23.97, 56.95)	0.01585 (0.01209, 0.01962)	0.9718	17.15
34.49 (17.11, 51.87)	0.0196 (0.01233, 0.02686)	0.9753	9.529
17.21 (−0.6015, 35.02)	0.03432 (0.01762, 0.05101)	0.8415	23.97
25.69 (5.676, 45.71)	0.0307 (0.0208, 0.0406)	0.9625	28.28
32.26 (23.47, 41.06)	0.01951 (0.01458, 0.02444)	0.9954	2.821
33.8 (2.513, 65.27)	0.01849 (0.008065, 0.02892)	0.9133	7.811
34.41 (17.11, 51.87)	0.0227 (0.01233, 0.02686)	0.9644	4.515
31.42 (−1.114, 3.399)	0.05116 (0.03384, 0.06849)	0.9513	22.88
31.91 (30.59, 33.23)	0.01665 (0.01556, 0.01773)	0.9986	0.5208
19.33 (−13.25, 51.92)	0.02763 (0.0004734, 0.05479)	0.8363	11.12
37.93 (28.82, 47.05)	0.01219 (0.004655, 0.01973)	0.9053	4.123
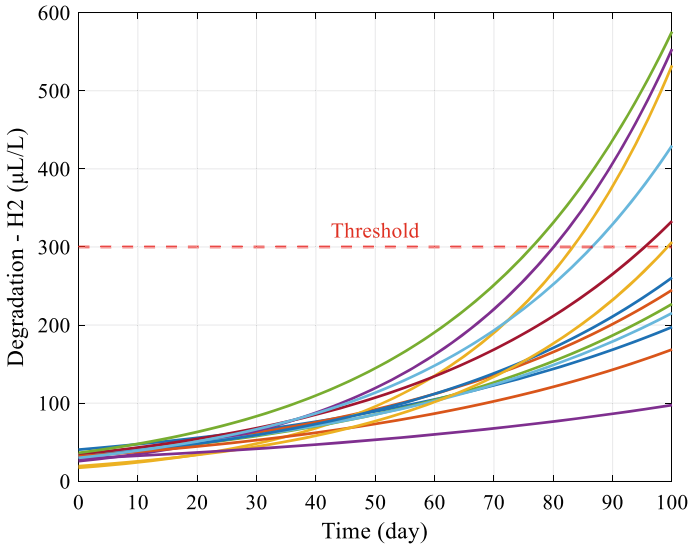
Fig. 4 H_2 degenerate orbit model
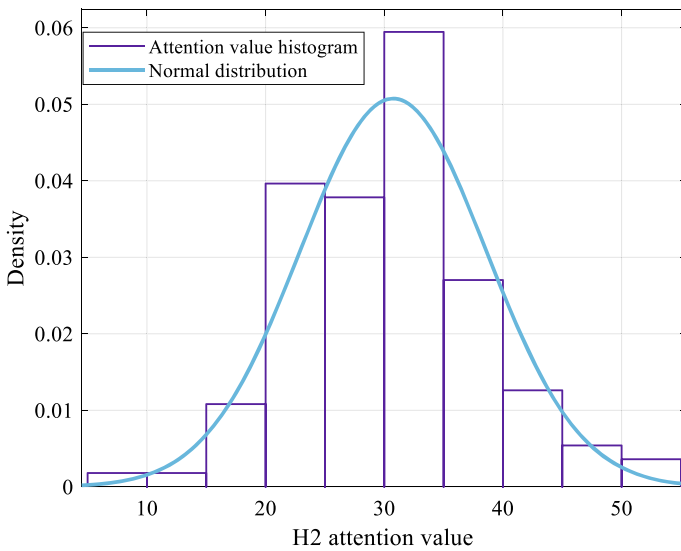
Fig. 5 Initial value distribution of degenerate orbit

3.4   Application Method of the Degradation Track

Early warning criterion determination. There are thousands of prediction algorithms, and the neural network, for example, is mainly divided into two parts: training

and prediction, of which training requires a large amount of online monitoring data as the basis. However, at present, there are few transformer fault cases, and 99% of the training set is normal data, so it is difficult to predict the trend of transformer degradation [14]. At the same time, the lack of transformer degradation process data makes it difficult to obtain the degradation development pattern and to determine the early warning criteria including the rate of change of state quantity. If the transformer degradation track is known, the above problems can be solved.

When the transformer has a deterioration trend, the prediction model of smooth trend will no longer be applicable, and it is necessary to use the deterioration track for prediction. The parameters are determined using the near-term monitoring volume and the degradation track model to achieve accurate long-term prediction of the transformer degradation trend. In addition, once the deterioration track model and parameters are obtained, early warning criteria can be determined, including graded deterioration warning thresholds, graded deterioration rate warning thresholds, etc.

Fault probability calculation. The current method of equipment state evaluation is mainly to judge the transformer state by comparing the state quantity with the standard threshold, which is macro and general, and can only qualitatively determine the impact of defects on the equipment, but lacks the reliability or the fault probability measurement. Based on the reliability theory, the fault probability of a transformer is calculated by combining the deterioration track to quantitatively describe the degree of defects of a transformer.

The strength-stress interference model in reliability theory is widely used in the reliability calculation of mechanical parts. Based on this theory, the strength S at the defect of the equipment is regarded as a random variable with probability density function $f(S)$, and the electrical stress s at the defect is also regarded as a random variable with probability density function $h(s)$, and the probability that the electrical stress is greater than the insulation strength is obtained through convolution operation (i.e., the probability that the insulation is broken down). $p(s)$ is the fault probability density distribution function, as shown in Eq. (2); the area under the $p(s)$ curve is numerically equal to the insulation fault probability F, as shown in Eq. (3).

$$p(s) = h(s) \int_0^s f(S) dS \tag{2}$$

$$F = \int_{-\infty}^{+\infty} h(s) \left[\int_{-\infty}^s f(S) dS \right] ds \tag{3}$$

For a specific device with defects, the interference model can be degraded to Eq. (4), where x_0 is the state quantity of the device, the integration function $f_D(y)$ is the fault threshold distribution function, and the result of the integration is the fault probability in that state.
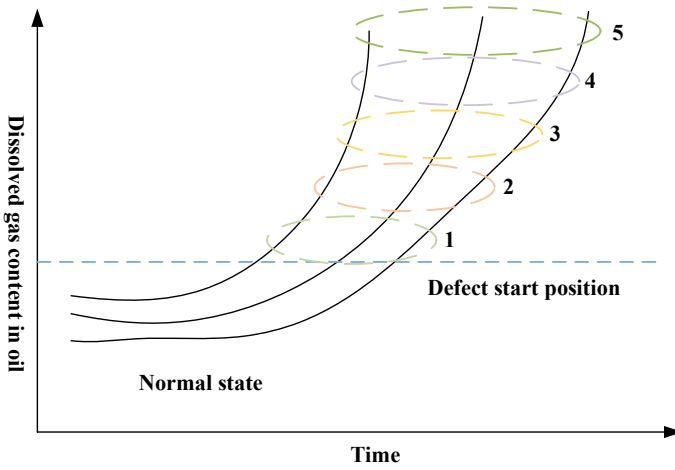
Fig. 6 Graded fault thresholds

$$F = \int_0^{x_0} f_D(y)dy \tag{4}$$

In this paper, it is considered that a fixed degradation threshold cannot characterize the individual differences of transformers, so it is more appropriate to describe the degradation threshold using a distribution function. This idea coincides with the strength-stress interference model, i.e., the fault threshold distribution function is determined from multiple degradation tracks, and then the fault probability is calculated according to Eq. (4). The fault probability defined in this paper is the probability of serious fault of the device after a number of years, and the fault probability threshold distribution functions from level 1 to 5 represented in Fig. 6 indicate the thresholds of serious fault of the device after different years, respectively.

4 Conclusion

In order to analyze the development process of transformer degradation, this paper collects a large amount of field data, establishes the degradation track model, and obtains the following results:

1. The degradation track model is formally simple, and the individual sample function can be determined by regression analysis technique, and the randomization of model parameters can describe the individual differences in the degradation process, so the degradation track model is used to describe the degradation process of transformers.

2. The degradation track model and estimated model parameters of transformer degradation track were determined by using the method of degradation track fitting, which is consistent with the exponential growth model, and the goodness of fit R^2 is above 0.9, which is a good fit.

3. The degradation track model of transformer can be used to predict the long-term degradation trend and determine the early warning criterion, which can solve the problem that the prediction model is not applicable due to small fault cases. In addition, the degradation track model can be used to obtain the fault threshold distribution function, so as to calculate the equipment fault probability and quantitatively determine the severity of equipment fault.

References

1. Jiang XC, Sheng GH (2018) Research and application of big data analysis of power equipment condition. High Voltage Engineering 44(04):1041–1050 (in Chinese)
2. Rajesh KNVPS, Rao UM, Fofana I et al (2023) Influence of data balancing on transformer DGA fault classification with machine learning algorithms. IEEE Trans Dielectr Electr Insul 30(1):385–392
3. Wang HW, Teng KN (2017) Review of reliability evaluation technology based on accelerated degradation data. Systems Engineering and Electronics 39(12):2877–2885 (in Chinese)
4. Gao JY, Qing C (2022) Research on the reliability of drum screen filter drive pinion gear in nuclear power plant based on fault physics. Nucl Sci Eng 42(06):1312–1316 (in Chinese)
5. Jing B, Cui ZB, Sun HD et al (2022) Online life prediction of the fuel pump based on fault physics and data-driven fusion. Chinese Journal of Scientific Instrument 43(03):68–76 (in Chinese)
6. Ma XH, Wang W, He C et al (2018) Reliability evaluation of high range MEMS accelerometer based on degradation distribution. Chinese Journal of Electron Devices 41(04):991–996 (in Chinese)
7. Jin TT, Yang ZJ, Wang DC et al (2020) Reliability modeling for hydraulic components of heavy duty machine tools in distribution of degradation amount for oil contamination profile. China Mechanical Engineering 31(13):1613–1620+1628 (in Chinese)
8. Li HR, Zhao GY, Yao HM (2022) Research on reliability modeling of bivariate correlation degradation based on nonlinear wiener process. In: 2022 13th international conference on reliability, maintainability, and safety (ICRMS). pp 223–227. IEEE. Hong Kong, China
9. Wang F, Chu T (2012) Lifetime prediction of LED-based light bars by accelerated degradation test. Microelectron Reliab 52(7):1332–1336
10. You Q, Zhao Y, Hu GP et al (2011) Reliability assessment using accelerated degradation data based on time series model. Systems Engineering-Theory & Practice 31(02):328–332 (in Chinese)
11. Jin G (2014) Reliability technology based on degradation. National Defence Industry Press, Beijing (in Chinese)
12. Shen LJ, Wang YD, Zhai QQ et al (2019) Degradation modeling using stochastic processes with random initial degradation. IEEE Trans Reliab 68(4):1320–1329

13. Zhao CZ, Bai HY, Cheng YC et al (2018) Statistic distribution of the chromatographic data of running transformer oil. High Voltage Apparatus 54(12):180–187 (in Chinese)
14. Yi GX, Li B, Li XS et al (2021) Research on prediction of turbine mechanical performance degradation based on attention LSTM. In: 2021 global reliability and prognostics and health management (PHM-Nanjing). pp 1–6. IEEE. Nanjing, China

Impact of Typical Structural Parameters on Hotspot Temperature Rise in Dry-Type Bridge-Arm Reactors: A Simulation Study

Li Yin, Wei Yang, Kun Wang, Jie Wang, Chong Zhang, Yun Chen, Jian Qiao, and Guangke Wang

Abstract The dry-type bridge arm reactor is an indispensable apparatus in flexible DC transmission systems, and it holds significant importance in promoting the intelligent development of power grids. This article focuses on the dry-type bridge arm reactor and establishes a numerical model for the coupling of fluid and temperature fields. It thoroughly investigates the impact of multiple typical structural parameters on the hotspot temperature rise of the reactor. Initially, a two-dimensional axisymmetric model for the dry-type bridge arm reactor is established, and the finite element simulation method is adopted to calculate the distribution of the temperature and flow fields within the reactor. Subsequently, the impact mechanism of structural parameters, such as encapsulation thickness, air duct width, and air duct height, on the temperature distribution and temperature rise of the reactor were investigated. Finally, a structural optimization design scheme for the reactor is proposed by comprehensively considering various factors. The results demonstrate that the optimized reactor's hotspot temperature rise is reduced from 83.33 °C to 76.07 °C, indicating a notable decrease in temperature rise. The optimization method is of significant guidance in improving the heat dissipation capacity of the reactor.

Keywords Dry-type bridge arm reactor · Multi-physics coupling · Hotspot temperature rise · Structural parameters · Optimization design

L. Yin · W. Yang (✉) · K. Wang · Y. Chen · J. Qiao · G. Wang
State Grid Smart Srid Research Institute Co., Ltd, Beijing 102209, China
e-mail: yinlibj@163.com

J. Wang · C. Zhang
Power Science Research Institute of State Grid, Sichuan Electric Power Company, Chengdu 610041, Sichuan, China

1 Introduction

The dry-type bridge arm reactor is an electrical component commonly used in high-voltage DC transmission systems and is capable of effectively controlling the system's current and voltage. However, traditional dry-type bridge arm reactors are susceptible to local overheating and can potentially cause fires in high voltage and high current operating environments, severely compromising the system's reliability and stability. Therefore, analyzing the temperature and flow field distribution of the dry-type bridge arm reactor under multi-physics coupling conditions, investigating the impact of structural parameters on its heat dissipation performance, and conducting optimization design based on this is of significant importance in further improving the stability and reliability of high-voltage DC transmission systems.

In recent years, domestic and foreign scholars have conducted numerous studies on the thermal field analysis and structural optimization of dry-type bridge arm reactors. The research methods for the temperature field of the reactor mainly include the average temperature rise method, the method of assigning convective heat transfer coefficients, and the method of fluid-temperature field coupling. The literature [1] introduced the method of calculating the average temperature rise of transformer windings, but this method has lower accuracy and cannot reflect the temperature rise distribution at different positions of the reactor. The literature [2] obtained the temperature variation on the winding height of the reactor by assigning different convective heat transfer coefficients to the surface of the reactor, but the determination of the convective heat transfer coefficient relies on empirical formulas, which may not be consistent with the actual situation. Compared with the average temperature rise and analytical calculation methods, the finite element method can obtain detailed temperature and flow field distributions, and it has been widely used in the temperature field calculation of reactors [3]. In terms of thermal optimization of reactor structures, reference [4] used the finite element method to lower the temperature rise of the reactor by adjusting the air duct width and coil thickness. The literature [5] proposed an idea to improve the heat dissipation capacity of coil-air passage units by adjusting the height of the coil's insulation layer in the thermal optimization of reactor structure, but it did not take into account the condition of using a rain cover device. Reference [6] conducted an optimization study on the hollow reactor rain cover, adjusting the parameters of the rain cover to improve the reactor's heat dissipation capability. However, the study did not consider the impact of the airflow on the flow field. In conclusion, the inherent complexity of the reactor's structure and the various structural parameters have complex effects on its heat dissipation ability. Existing studies have mostly focused on local optimization designs of the reactor's structure, which cannot achieve overall optimization of the reactor's heat dissipation performance, thereby limiting the practical application value of various methods.

According to the design parameters of the reactor, this paper establishes a two-dimensional axisymmetric finite element model of the fluid-temperature field coupling for a dry bridge-arm reactor based on the COMSOL simulation platform. The temperature and flow field distribution characteristics of the reactor during stable

operation are analyzed, and the influence of multiple structural parameters on the hot-spot temperature rise of the reactor is explored. Finally, taking into consideration both the safety and economic viability, a proposal for the structural optimization design of the reactor is presented, while ensuring its performance in terms of reactance.

2 Reactor Basic Structure and Model

2.1 The Basic Structure

This paper focuses on the RKGKL-10 kV-600A-20mH dry bridge arm reactor, which has a rated voltage of 10 kV, a rated current of 600 A, a winding height of 2715 mm, an inner diameter of 1300 mm, and an outer diameter of 1675.65 mm. The top of the reactor is equipped with a rain cover to reduce the influence of environmental factors such as rainwater. The body is composed of 6 coaxial parallel windings, and there is a star-shaped bracket at the upper and lower ends as the inlet and outlet line confluence, which also provides mechanical clamping force for the windings. Several fine polyester support rods are arranged radially between the winding packages of the reactor, and the air channels between the support rods form a heat dissipation channel between the winding packages. The coil in the package is made by parallel winding of multiple round aluminum wires, and the surface insulation material of the package is glass fiber reinforced epoxy resin. The simplified structure of the reactor is shown in Fig. 1.

2.2 Working Principle and Model

(1) Working principle of reactor

An inductor is composed of multiple encapsulations made by winding multi-layered aluminum wires in a spiral shape. In electromagnetic calculations, the non-magnetic materials such as the support bars, external insulation, and rain covers of the package are ignored. At the same time, the weak influence of the connection arm is neglected. As a result, the reactor can be equivalent to a two-dimensional axisymmetric structure. The various enclosures of the reactor are numbered from 1 to X radially, from the inside out, and the coil layers within each enclosure are numbered from 1 to Y, also from the inside out. Hence, the structure of the reactor can be regarded as a winding with W layers, and in the circuit, it can be regarded as W branches in parallel consisting of resistors and inductors. The principle of calculating the field-circuit coupling of the dry bridge arm reactor is shown in Fig. 2. The left side of Fig. 2 shows a schematic diagram of the equivalent circuit of the reactor, where R_W
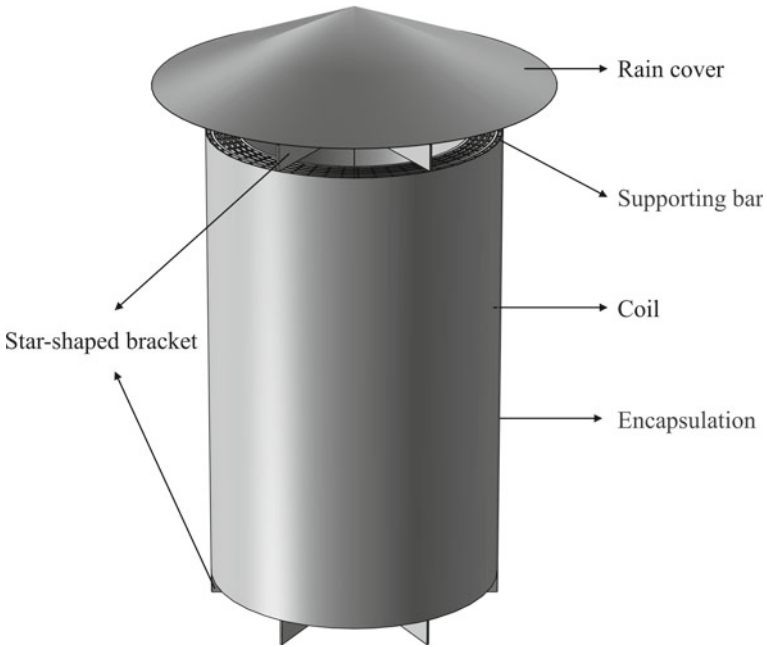
Fig. 1 The basic structure of a dry-type bridge-arm reactor
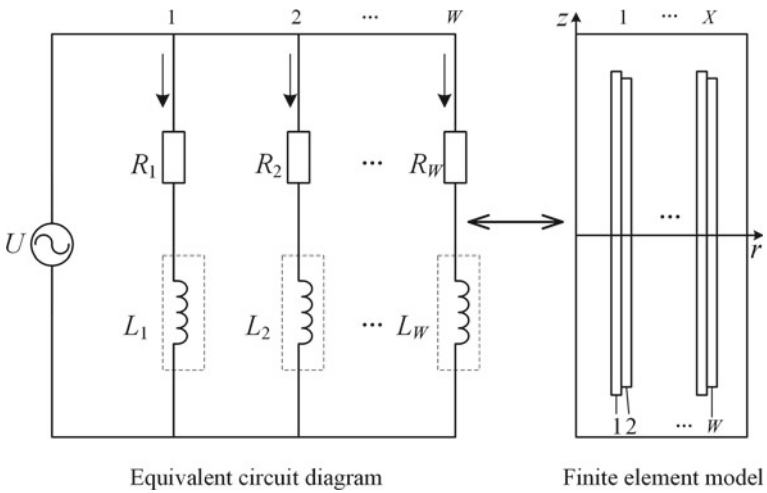
Fig. 2 The principle of coupling calculation of dry bridge armor

corresponds to the resistance of the Wth layer coil, and L_W is the self-inductance of the Wth layer coil, which can be equivalent to a two-dimensional rectangle on the right side of Fig. 2.

The windings of each layer of the reactor are subjected to alternating current voltages on both sides, and the field-circuit coupling analysis method follows the Maxwell equations, with the solution of the magnetic field inside and outside the domain also satisfying the Poisson equation [7], as shown in Eq. (1).

$$
\begin{cases}
\dfrac{\partial^2 A_\theta}{\partial r^2} + \dfrac{\partial A_\theta}{r \partial r} - \dfrac{A_\theta}{r^2} + \dfrac{\partial A_\theta}{\partial z^2} = -\mu J \\[2mm]
\dfrac{\partial^2 A_\theta}{\partial r^2} + \dfrac{\partial A_\theta}{r \partial r} - \dfrac{A_\theta}{r^2} + \dfrac{\partial A_\theta}{\partial z^2} = 0
\end{cases}
\tag{1}
$$

In the equation, A_θ represents the circumferential component of the vector magnetic flux density, while θ, z and r denote the angles, axial and radial coordinates in cylindrical coordinates. μ is the magnetic permeability of aluminum wire and J is the current density flowing through each layer of the winding.

The circuit equation satisfied by the ith layer winding is:

$$
U_i = I_i R_i + \frac{d\psi_i}{dt}
\tag{2}
$$

$$
\psi_i = n_i \int_{S_i} \nabla \times A_i \cdot dS = n_i \oint_{l_i} A_i \cdot dl
\tag{3}
$$

The variables Ψ_i and A_i represent the magnetic flux and magnetic potential of each layer of winding, respectively.

The main sources of heat in the reactor come from the resistance losses $P_R(i)$ and eddy current losses $P_E(i)$ of each layer of the winding. The aluminum wire cross-section is circular, and the calculation method [8] for the losses of the ith layer winding is:

$$
P_i = P_R(i) + P_E(i)
\tag{4}
$$

$$
P_R(i) = I_i^2 R_i = \frac{n_i D_i \pi^2 J_i^2 d_i^2}{4\gamma}
\tag{5}
$$

$$
P_E(i) = \frac{n_i \gamma D_i \pi^2 \omega^2 d_i^4}{64} \left(B_r^2(i) + B_h^2(i) \right)
\tag{6}
$$

In the equation, P_i represents the loss of each layer winding, I_i represents the current of each layer winding, R_i represents the resistance of each layer winding, γ represents the electrical conductivity of the aluminum conductor, n_i represents the number of turns of each layer winding, D_i represents the winding diameter of each layer winding, J_i represents the current density flowing through each layer winding, d_i represents the self-diameter of the aluminum wire of each layer winding, ω is the angular frequency of the current excitation, $B_r(i)$ and $B_h(i)$ are the radial and

axial components of the magnetic induction intensity at the center of the aluminum conductor, respectively.

By calculating the resistive loss $P_R(i)$ and eddy current loss $P_E(i)$, the volumetric heat density of each layer of the winding can be obtained, given by:

$$Q_i = \frac{P_i}{V_i} \tag{7}$$

where V_i is the volume of the ith layer winding.

(2) Coupling model of flow field and temperature field

The reactor exchanges heat with the ambient air through three forms of heat transfer: natural convection, radiation, and conduction [9]. In the process of calculating fluid-temperature coupling, in addition to the basic heat conduction equation, the fluid control equation is also followed, which includes the mass conservation equation, momentum conservation equation, and energy conservation equation [10]. The three-dimensional steady-state heat conduction equation of the reactor with the internal heat source of each winding is expressed as:

$$\frac{\partial T}{\partial t} = \alpha \left(\frac{\partial^2 T}{\partial x^2} + \frac{\partial^2 T}{\partial y^2} + \frac{\partial^2 T}{\partial z^2} \right) + f \tag{8}$$

In the given equation, $\alpha = k/c\rho$; $f = F/c\rho$; the variables T represent the temperature on the surface of each winding, k represents the thermal conductivity, c represents the specific heat capacity, ρ represents the material density, and F represents the heat source intensity.

Considering air as an incompressible fluid, it follows the law of conservation of mass during its flow process, as shown in Eq. (9).

$$\rho \left(\frac{\partial u}{\partial x} + \frac{\partial v}{\partial y} + \frac{\partial w}{\partial z} \right) = 0 \tag{9}$$

where ρ is the air density and u, v, w are the components of the fluid velocity field vector in the x, y and z coordinate axes.

The momentum conservation equation is

$$
\begin{aligned}
\rho \frac{du}{dt} &= \rho F_x + \frac{\partial \sigma_x}{\partial x} + \frac{\partial \tau_{yx}}{\partial y} + \frac{\partial \tau_{zx}}{\partial z} \\
\rho \frac{dv}{dt} &= \rho F_y + \frac{\partial \tau_{xy}}{\partial x} + \frac{\partial \sigma_y}{\partial y} + \frac{\partial \tau_{zy}}{\partial z} \\
\rho \frac{dw}{dt} &= \rho F_z + \frac{\partial \tau_{xz}}{\partial x} + \frac{\partial \tau_{yz}}{\partial y} + \frac{\partial \sigma_z}{\partial z}
\end{aligned}
\tag{10}
$$

In the given equation, F represents the volumetric force, σ denotes the normal stress, and τ represents the shear stress.

The law of energy conservation is a universal principle that is followed in nature. In an inductor, energy is propagated in the form of heat, and is based on the three laws of thermodynamics. The expression for this law is:

$$\rho \cdot \nabla(uT) = \frac{\lambda}{c} + \nabla^2 T_f + S \tag{11}$$

The fluid temperature and velocity vector are represented by T_f and , respectively. λ is the thermal conductivity coefficient of the fluid, and S represents the viscous dissipation term.

3 Multi-physical Field Coupling Analysis

3.1 Model Assumption

The Reynolds number of the innermost winding of the reactor is defined as $Re = 2Vr/v$, where the average air flow velocity V is taken as 0.87 m/s, the minimum winding radius r is 0.653 m, v is the kinematic viscosity of air, and $v=16.96 \times 10^{-6}$ m²/s. By calculation, it can be found that $Re>2320$, therefore, a turbulent flow model is selected.

When establishing a two-dimensional fluid-temperature coupled computational model, the following assumptions are made:

1. The model only considers the steady-state heat dissipation process of the encapsulated coils, while ignoring the influence of the spacers and insulating supports between the encapsulations on the temperature rise of the reactor.
2. The heat source within the reactor is composed of resistive and eddy current losses within each layer of the windings. The heat density per unit volume is used as the parameter for the applied heat source within the temperature field.
3. The insulation material of the reactor is considered to be isotropic, and its material properties are shown in Table 1 [11].

Table 1 Main material parameters of the reactor

Material	Thermal conductivity (W m⁻¹ K⁻¹)	Density (kg m⁻³)	Specific heat capacity (J kg⁻¹ K⁻¹)
GFRP	0.4	1500	871
Aluminum alloy	218	2731	881
Air	0.03	Change with temperature	1006.43

3.2   Model Boundary Condition

When performing the 2D magnetic circuit-electromagnetic field coupling calculation for the dry bridge arm reactor, the axial boundary of the solution domain is subjected to axisymmetric boundary conditions, which means the magnetic field normal component is zero, i.e. $A|\eta_1 = 0$. The surrounding boundary is subjected to far-field boundary conditions, i.e. $A|\eta_2 = 0$.

In addition to satisfying the boundary conditions of the governing equations, it is also necessary to meet the following requirements in the fluid-temperature field:

1. Specify the no-slip boundary condition on the interface between the calculation domain boundary, the solid of the reactor, and the air, that is, $V_x = V_y = V_z = 0$.
2. Set the surface emissivity to 0.9 [12].
3. Set the ambient temperature around the reactor to 300.15 K.
4. Set the gravitational acceleration to 9.81 m/s^2 in the negative direction of the z-axis.

3.3   Mesh Generation

The density of the mesh directly affects the accuracy of the temperature field simulation calculation. In order to balance the calculation accuracy and speed, a free meshing method is adopted. The mesh is dense near the envelope coil and the rain cover, and sparse away from the envelope coil. The meshing results are shown in Fig. 3.

3.4   Simulation Results of Temperature Field

In COMSOL, the unit volume heat density of each layer of the winding calculated was applied as a thermal source excitation to the reactor. The calculation was completed through material selection, boundary condition application, meshing, and solver settings. The reactor temperature field distribution was obtained through iteration and post-processing, as shown in Fig. 4.

From Fig. 4, it can be seen that the hot spot temperature of the dry bridge arm reactor under steady-state operation is 110.33 °C, with an ambient temperature of 27 °C, resulting in a temperature rise of 83.33 °C. The temperature rise distribution of the coil in the encapsulation of the reactor is basically the same, gradually increasing with height along the axial direction, and the highest temperature is located near the top position of the coil encapsulation. The temperature difference between the internal layers of the reactor is significant. Except for the outermost layer without a winding, the fifth layer has the highest hotspot temperature among all layers, followed by the innermost layer, while the temperatures of the middle three layers are similar.
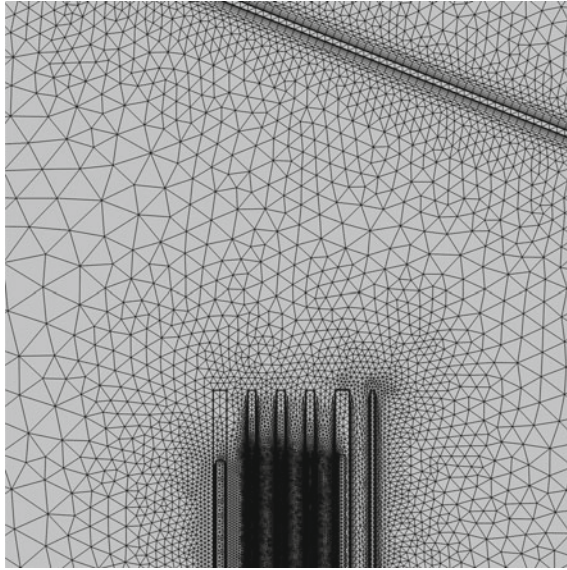
Fig. 3 Mesh generation results

To further investigate the temperature variation during the operation of the reactor, the temperature variation curves of each package are plotted, as shown in Fig. 5.

According to Fig. 5a, it can be inferred that the dry bridge arm reactor goes through three stages during operation: rapid heating (0–1.0 h), slow heating (1.0–4.5 h), and steady-state operation (4.5–5.5 h). Analysis suggests that during the initial operation of the reactor, the winding losses within the encapsulation produce a significant amount of thermal energy. This thermal energy cannot be dissipated rapidly, leading to a rapid increase in temperature. As the temperature of the winding insulation increases, the temperature difference between the insulation and surrounding air gradually increases, resulting in a greater amount of heat transfer. The air at the bottom of the duct absorbs the heat and accelerates upward under the effect of natural convection. The rise in fluid temperature typically results in a decrease in density, leading to an increase in the upward velocity of the air with the temperature rise. Thus, the airflow inside the reactor can be accelerated, resulting in further improvement in overall heat dissipation efficiency. As the fluid velocity gradually increases, the external radiation heat dissipation efficiency of the reactor surface also increases synchronously, and the temperature rise of the reactor gradually reaches a steady state. It is precisely the complex interaction between heat transfer and fluid flow described above that results in significant temperature differences among the various package seals inside the reactor, and the multiple stages experienced during stable operation. As shown in Fig. 5b, it can be inferred that the hot spot temperature of each package seal is almost proportional to the heat generation rate of the seal winding. Among them, package seal 1, as the innermost layer of the package seal, has a lower
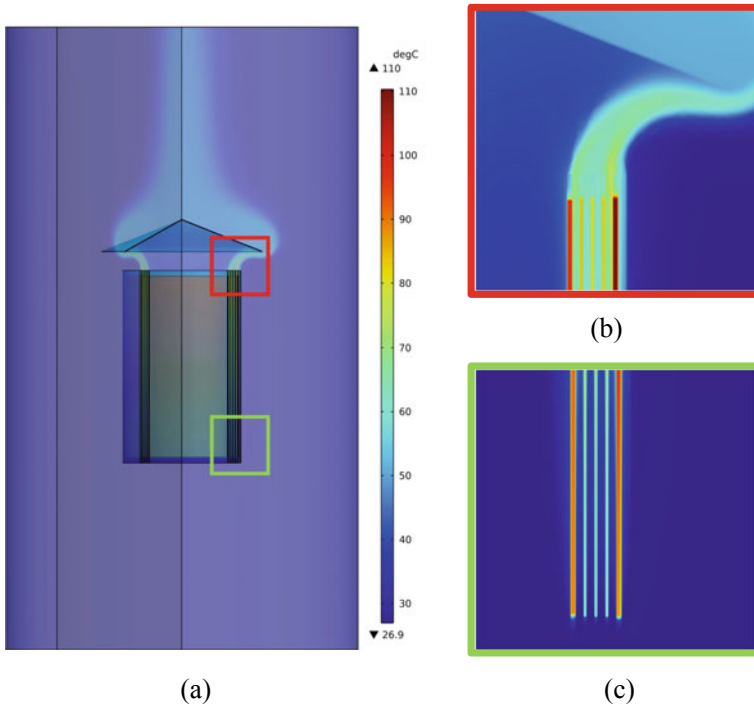
Fig. 4 Temperature distribution of dry bridge arm reactor. **a** 3D model temperature. **b** Top temperature field of 2D model. **c** Bottom temperature field of 2D model
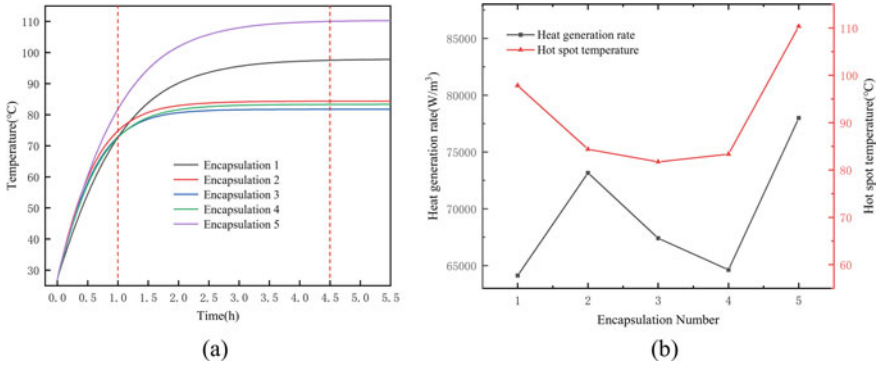
Fig. 5 Temperature curve of each package of reactor

heat generation rate than that of the seal winding in package seal 2. However, due to its location in the innermost part of the reactor and the restriction of the rain hood structure on the inner convection effect, its poor heat dissipation effect leads to a higher final hotspot temperature compared to package seal 2. Hence, it can be seen that the temperature distribution of the reactor is influenced by multiple factors, and the relationship between them is complex.

4 Influence Law of Structural Parameters

4.1 Experimental Design

The encapsulation material, due to its direct contact with the coil heat source, has become the most critical component for insulation and thermal insulation of the reactor.

Based on the above research, it can be inferred that the thickness of the encapsulation material, as well as the width and height of the air gap between adjacent encapsulation materials, will have a direct impact on the temperature and flow field distribution of the entire reactor. Therefore, further investigation is needed to explore the impact of the encapsulation material thickness d, air gap width w, and air gap height h on the hot spot temperature rise of the dry-type bridge arm reactor. Considering the actual insulation requirements and heat dissipation effects of the reactor, the research range of each typical structural parameter does not exceed 20% of the actual structural parameters. Specifically, the range of w is 20 ~ 30 mm, the range of d is 0.76 ~ 1.12 mm, and the range of h is 2215 ~ 3215 mm, as shown in Fig. 6.

4.2 Influence Law

The three structural variable parameters were interpolated and studied with five values each. The dry bridge arm reactor model was reconstructed and simulated using finite element method. The experimental results are shown in Table 2.

From Table 2, it can be inferred that the hotspot temperature of the reactor decreases with the increase of the air channel width and height, and increases with the increase of the encapsulation thickness. Specifically, with the increase of encapsulation height and air channel width, and the decrease of encapsulation thickness, the heat dissipation efficiency of the encapsulation-air channel unit is significantly improved. The analysis suggests that increasing the width of the duct can increase the effective heat dissipation surface area of the reactor, thereby improving the efficiency of natural convection heat transfer on the surface of the reactor. Moreover, increasing the width of the air channel can reduce the air resistance inside the package, enabling smoother air flow and enhancing the overall heat dissipation efficiency of
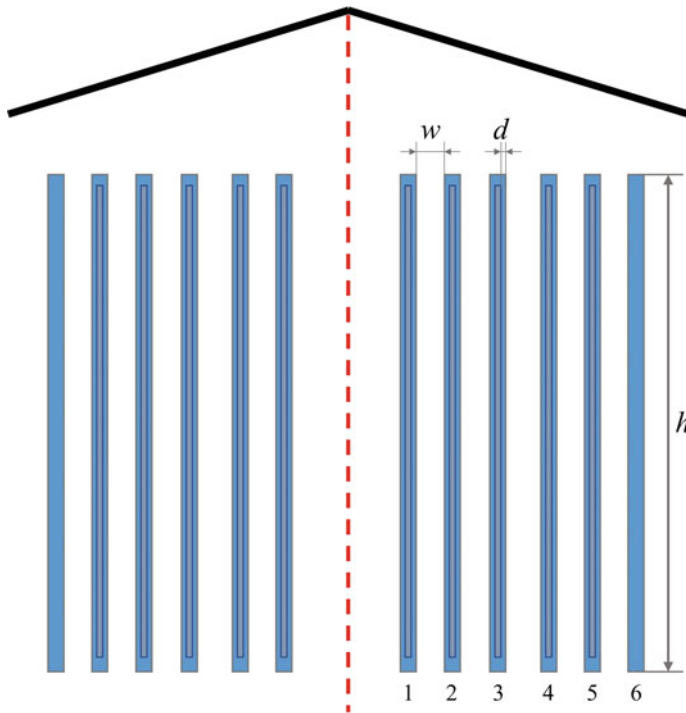
Fig. 6 Structure and parameter description

the reactor. As the height of the air passage increases, the distance of gas flow in the passage increases, which to a certain extent promotes the air flow inside the reactor, allowing heat to be more fully transferred to the gas. Moreover, increasing the height of the air duct can also reduce the temperature gradient inside the package, thereby lowering the hotspot temperature. As the main area for heat transfer between the winding heat source and external gas, the encapsulation plays an important role in heat transfer. Reducing the thickness of the insulation can effectively shorten the heat transfer distance, decrease the thermal resistance inside the insulation, and accelerate the heat transfer to the outside, while ensuring the insulation capacity of the reactor. This can achieve the effect of improving the heat dissipation efficiency of the reactor.

4.3 Structure Optimization

Based on the research results above, considering the impact mechanism of the three typical structural parameters on the heat dissipation performance of the reactor, while ensuring the reactor's own performance meets the operational requirements, the optimization objective function is set to reduce the hotspot temperature of the reactor, with

Table 2 Simulation calculation results of hot spot temperature

Structural parameters	Packet number	Hotspot temperature (°C)				
Air channel width (mm)		20	22.5	25	27.5	30
	1	99.657	98.345	97.792	97.495	97.314
	2	88.856	86.284	84.369	82.903	81.694
	3	85.760	83.659	81.740	80.271	79.233
	4	88.451	85.856	83.335	81.454	80.036
	5	113.25	111.76	110.33	109.33	108.58
Package thickness (mm)		0.76	0.85	0.94	1.03	1.12
	1	97.749	97.770	97.792	97.77	97.749
	2	83.533	83.950	84.369	84.745	85.119
	3	80.929	81.334	81.74	82.133	82.524
	4	82.696	83.015	83.335	83.74	84.145
	5	109.55	109.942	110.33	110.7	111.068
Air channel height (mm)		2215	2465	2715	2965	3215
	1	110.068	103.942	97.792	93.507	89.222
	2	92.11	88.243	84.369	81.648	78.928
	3	89.205	85.479	81.74	79.17	76.601
	4	90.385	86.867	83.335	80.91	78.485
	5	123.657	117.006	110.33	105.661	101.04

coil loss and unit heat dissipation cost as constraint functions, and the reactor's structural parameters are re-determined. An optimized new dry bridge arm reactor two-dimensional axisymmetric finite element simulation model is established on a finite element simulation platform, and the model is subjected to multi-physics coupling simulation again to calculate its temperature distribution and hotspot temperature.

Before analyzing and comparing the temperature field distribution of dry-type bridge arm reactors before and after structural optimization, it is necessary to first normalize the temperature spectrum calculated by simulation, in order to visually observe the high and low temperatures of the reactor before and after optimization. The comparison of the temperature field distribution of the reactor before and after optimization is shown in Fig. 7a. Upon comparison, it can be inferred that altering the structural parameters of the reactor did not affect the distribution pattern of the temperature field within it. The temperature variations in each encapsulation followed the same trend as before optimization. To better observe the specific effect of structural optimization on the hotspot temperature rise of the reactor, the temperature field distribution simulation results of the package where the hotspot temperature is located were presented together with its axial temperature change curve. This was done in order to show the corresponding relationship, as depicted in Fig. 7b. Upon observation, it is evident that structural optimization of the dry bridge

(a)   (b)
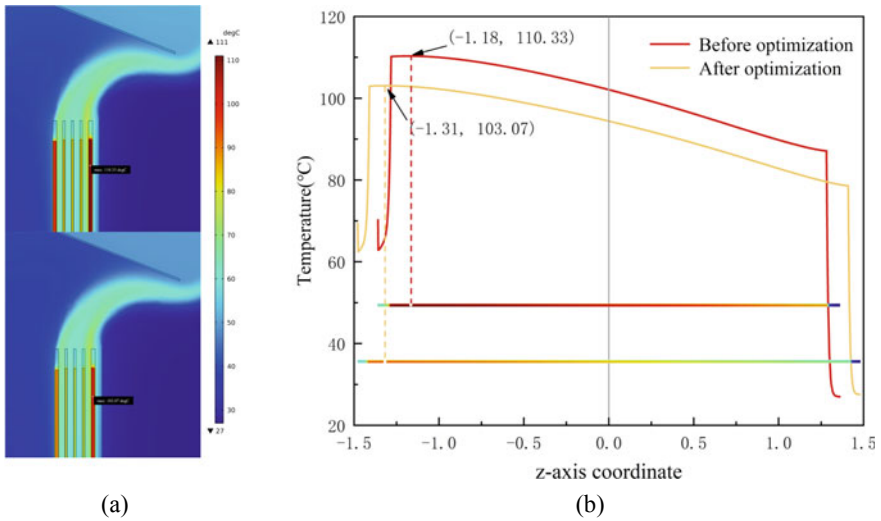
Fig. 7 Simulation results. **a** Comparison of local temperature distribution **b** Comparison of axial temperature distribution in the package where the hot spot is located

arm reactor operating in a 27 °C ambient temperature can significantly reduce its hotspot temperature. After optimization, the reactor's hotspot temperature decreased by 7.26–76.07 °C compared to the original temperature of 83.33 °C. In summary, by performing a rational optimization design on the structural parameters of the dry bridge arm reactor, it is possible to significantly reduce its hotspot temperature while ensuring insulation capability and controlling costs. This optimization can improve the reactor's heat dissipation performance, thereby enhancing the stability and reliability of the reactor. The comparison of the simulation results further confirms the feasibility of the optimization method, providing strong support for its practical application.

5   Conclusion

This article establishes a two-dimensional axisymmetric simulation model for the flow and temperature fields of dry bridge arm reactors. It analyzes the impact of several typical structural parameters on the temperature distribution and hotspot temperature rise of the reactor, and proposes an optimization scheme for the structural parameters of the reactor based on this analysis.

(1) The temperature variations and distribution characteristics of the dry-type bridge arm reactor have been obtained. The temperature rise process during the operation of the reactor can be divided into three stages: rapid temperature rise, slow

temperature rise, and steady state. The distribution of temperature field is influenced by multiple factors, including heat source losses, heat dissipation paths, and location.

(2) The specific analysis was conducted on the impact of structural parameters such as encapsulation thickness, air channel width, and air channel height on the hot spot temperature rise of dry bridge arm reactors. By comparing the results of the finite element simulation calculations, it can be concluded that the hot spot temperature of the reactor will decrease to varying degrees as the package height and duct width increase, and the package thickness decreases. Analysis suggests that changes in the three parameters mainly result in variations in the heat transfer pathways and natural convection heat dissipation effect, thereby altering the overall heat dissipation capacity of the reactor.

(3) Based on the impact of structural parameters, the design of the dry-type bridge arm reactor was optimized, taking into account the heat dissipation performance, insulation level, and production cost. The simulation results demonstrate that the optimized structure of the dry reactor can significantly improve its heat dissipation performance, as evidenced by a decrease in the hotspot temperature from 83.33 to 76.07 °C.

References

1. Ye ZG (1999) Temperature rise test of dry-type air-core reactor and calculation of its winding temperature rise. Transformer 36(9):7–11 (into Chinese)
2. An L, Wang Z, Tang G (2002) 3D-temperature field prediction by FEM and temperature-rise test for dry-type reactor. Journal of North China Electric Power University 29(3):75–78 (into Chinese)
3. Zhang M, Wang H, Sun G et al (2021) AC and DC temperature rise characteristics of large capacity dry-type air core reactors based on isothermal isobaric design method. Southern Power System Technology 13(12):74–78 (into Chinese)
4. Smolka J, Nowak AJ (2011) Shape optimization of coils and cooling ducts in dry-type transformers using computational fluid dynamics and genetic algorithm. IEEE Trans Magn 47(6):1726–1731
5. Yuan Z, He J, Pan Y et al (2015) Research on electromagnetic efficiency optimization in the design of air-core coils. International Transactions on Electrical Energy Systems 25(5):789–798
6. Yuan FT, Yang SW, Qin SH et al (2022) Thermal performance analysis and optimization design of dry type air core reactor with the double rain cover. Thermal Science 26(1 Part A):273–286
7. Yan X, Yu X, Shen M et al (2015) Research on calculating eddy-current losses in power transformer tank walls using finite-element method combined with analytical method. IEEE Trans Magn 52(3):1–4
8. Rodríguez DJ, Alonso Orcajo G, Cano JM et al (2020) Thermal analysis of dry-type air-core coils for the optimization of passive filtering systems. Energies 13(17):4540
9. Santisteban A, Piquero A, Ortiz F et al (2019) Thermal modelling of a power transformer disc type winding immersed in mineral and ester-based oils using network models and CFD. IEEE Access 7:174651–174661

10. Li C, Wang H, Luo C et al (2021) Numerical simulation and detection of dry-type air-core reactor temperature field based on laminar–turbulent model. AIP Adv 11(3):035002
11. Fan M (2021) Finite element simulation of dry resistance temperature field and measurement method based on optical fiber sensing. North China Electric Power University (into Chinese)
12. Pfeifer N, Kizilcay M, Malicki P (2023) Analytical and numerical study of an iron-core shunt-compensation reactor on a mixed transmission line. Electric Power Systems Research 220:109315

Multi-physics Based Temperature Distribution Simulation of HVAC Submarine Cable at Various Velocity

Zhen Zhang, Yuanxiang Zhou, Jianning Chen, Yuhang Li, and Yasong Dai

Abstract The temperature distribution of submarine cables is an important parameter reflecting its operation status. The acquisition of temperature distribution trends for submarine cables under varying seawater flow rates holds important engineering significance. In this paper, the geometric model is constructed using a 220 kV three-core AC armored submarine cable laid on the seabed. The simulation model of AC three-core submarine cable temperature field is proposed based on the coupling of electro-thermal-flow multi-physics field. Finally, the study investigates how the steady-state temperature distribution of submarine cables varies with different seawater flow velocities. The results show that the temperature is radially distributed at the seawater velocity of 0m/s, and the temperatures of different phase conductors are different by the relative position, which are 89.9 °C, 89.6 °C and 89.08 °C, respectively. As the seawater flow velocity increases, the heat taken away from the cable surface by convection increases. When the seawater flow velocity is 1×10^{-6}m/s, 0.0001 m/s, 0.001 m/s, 0.001 m/s and 0.001 m/s, the maximum conductor temperatures are 69.5 °C, 44.6 °C, 38.5 °C, 33.6 °C and 32.7 °C, and the ampacity is 871.7 A, 1216 A, 1382.8 A, 1590.7 A and 1640.9 A, respectively. The simulation results can provide reference for submarine cable transmission engineering design.

Keywords Submarine cable · Multi-physics · Temperature distribution · Ampacity · Velocity

Z. Zhang · Y. Zhou (✉) · Y. Dai
The Wind Solar Storage Division of State Key Laboratory of Power System and Generation Equipment, School of Electrical Engineering, Xinjiang University, Urumqi 830047, China
e-mail: zhou-yx@tsinghua.edu.cn

Y. Zhou · J. Chen · Y. Li
State Key Laboratory of Control and Simulation of Power System and Generation Equipment, Department of Electrical Engineering, Tsinghua University, Beijing 100084, China
e-mail: chen-jn18@mails.tsinghua.edu.cn

Y. Li
e-mail: yh-li20@mails.tsinghua.edu.cn

1   Introduction

In September 2020, China put forward a major strategic decision to achieve carbon peaking by 2023 and carbon neutrality by 2060. Under the guidance of the 'emission peak, carbon neutrality' target, China needs to speed up the low-carbon transition and build a new power system based on new energy. Due to China's long coastline and abundant offshore wind resources, wind power is one of the large scale and competitive forms of new energy power generation [1–3].

At present, submarine cable with cross-linked polyethylene (XPLE) as the main insulation has been widely used [4]. Conductor temperature is an important index to evaluate the safety of cables [5]. So scholars at home and abroad have carried out extensive research on the calculation of cable temperature and capacity. Taskin et al. examined how the temperature distribution of a cable is affected by the temperatures in different environments, namely air and water [6]. Czapp et al. studied the influence of solar radiation on the temperature field of cables exposed to air [7]. Verschaffel-Drefke et al. studied the influence of four different backfill substances on cable temperature field through experiments [8]. Zhang et al. took the power–frequency AC single-core cable HJQF41-110 kV as an example, and analyzed the temperature field and ampacity of the cable buried in the landing section by analytical method, finite element simulation and experimental study [9]. Xia et al. calculated the steady-state ampacity of ± 500 kV HVDC submarine cable in J-tube environment [10]. Zhang et al. analyzed the influence law of different laying sections, laying methods, ambient temperatures and burying depths on cable temperature distribution and ampacity [11]. At present, there is still a lack of research on the temperature field of high-voltage AC three-core submarine cable under different seawater velocity.

In this paper, a simulation model based on the coupling of electro-thermal-flow is built, and the steady-state temperature field distribution law is studied when the sea water velocity is static. Finally, the influence law and mechanism of different seawater velocity on steady-state temperature distribution of three-core submarine cable are analyzed. It can provide reference for submarine cable transmission engineering.

2   The Simulation Model

This study takes 220 kV AC three-core XPLE submarine cable as the research object, establishes a coupled simulation model. Commercial finite element software is used for modeling, meshing and solving.

2.1 Geometric Model

The AC three-core XPLE submarine cable is mainly composed of copper conductor, XPLE, screen layer, sheath, armor, etc. The typical structure is shown in Fig. 1, and the specific parameters are provided in Table 1 [12].

The 'laid' method is adopted for the arrangement of the XPLE submarine cable, that is, the cable is placed horizontally on the seabed. Since the axial laying length of the submarine cable is much larger than the cable diameter, and the current density at different sections is basically equal, only radial heat transfer of the cable is considered in this paper. Figure 2b is the geometric model of submarine cable amplification with the three phases A, B and C as shown in the figure.
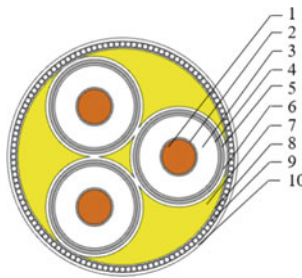
1-Wate-resisting Copper Conductor, 2- Conductor Screen, 3-XPLE, 4-Insulation Screen, 5-Lead Sheath, 6-PE Sheath, 7-Filled Part, 8-Inner Sheath, 9-Armour, 10-Outer Sheath

Fig. 1 Schematic diagram of submarine cable structure

Table 1 The typical parameters of submarine cable

Structure	Outer diameter (mm)	Thermal conductivity (W m^{-1} k^{-1})
Conductor	38.0	400
Conductor screen	2.0	10
XPLE insulation	24.0	0.2857
Insulation screen	2.8	10
Lead sheath	3.7	34.8
PE sheath	3.4	0.2857
Inner sheath	1.8	0.2857
Steel wire armor	6.0	44.5
Outer sheath	4.0	0.1667

(a) Laying section (b) Geometric model of cable
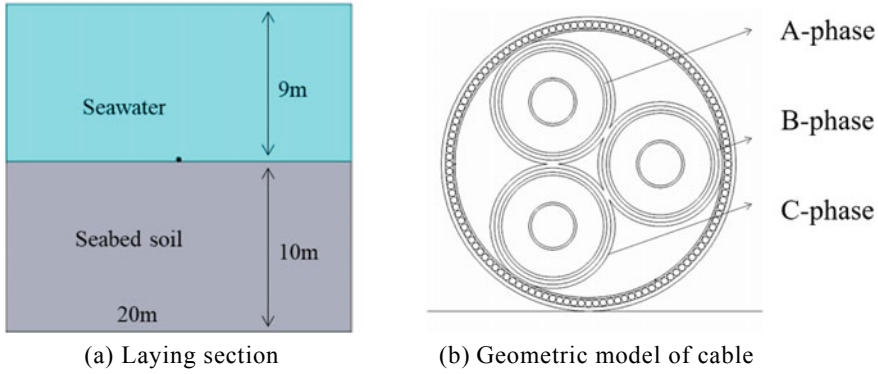
Fig. 2 Sub-sea laying

2.2 Control Equations

Maxwell equations are used to calculate the electromagnetic distribution of the three-core submarine cable. The hydrodynamic equations are used to calculate the flow of seawater, and the heat convection and diffusion equations are used to calculate the temperature of solid and fluid.

Electromagnetic field equations

$$
\begin{cases}
\nabla \times H = J \\
B = \nabla \times A \\
J = \sigma E + j\omega D + \sigma v \times B + J_e \\
E = -j\omega A
\end{cases}
\tag{1}
$$

where, H is magnetic field strength, A/m; J is a current density vector, A/m^3; B is magnetic flux density, T; A is extra-surface magnetic potential, Wb/m; σ is conductivity, S/m; E is electric field strength, V/m; J_e is external injection current density, A/m^3; v is speed (Lorenz), m/s.

Laminar flow field equations

$$
\begin{cases}
\rho(u \cdot \nabla)u = \nabla \cdot [-pI + \mu(\nabla u + (\nabla u)^T)] \\
\rho \nabla u = 0
\end{cases}
\tag{2}
$$

where, ρ is the density of the fluid, kg/m^3; u is an velocity vector of fluid, m/s; p is fluid pressure, Pa; I is an unit matrix; μ is power viscosity, Pa·s; T is the temperature of fluid material, K.

Solid heat transfer equations:

$$
\begin{cases}
\nabla \cdot q + \rho_1 C_{\rho_1} \frac{\partial T}{\partial t} = Q \\
q = -k\nabla T
\end{cases}
\tag{3}
$$

where, ρ_1 is the density of the material, kg/m^3; $C_{\rho 1}$ is solid constant pressure heat capacity, J/(kg k); q is local heat flux density, W/m^2; k is thermal conductivity, W/(m k); Q is the heat source in solid materials, W/m.

Fluid heat transfer equation:

$$\rho C_\rho u \cdot \nabla T + \nabla \cdot q + \rho C_\rho \frac{\partial T}{\partial t} = Q \tag{4}$$

where, C_ρ is fluid constant pressure heat capacity, J/(kg k); u is speed of fluid, m/s.

Electromagnetic thermal coupling equations:

$$\begin{cases} \rho C_\rho u \cdot \nabla T = \nabla \cdot q + Q_e \\ Q_e = J \cdot E \end{cases} \tag{5}$$

where, Q_e is the heat source in materials, W/m.

2.3   The Boundary Conditions

Electromagnetic field boundary conditions are as follows. Set the load current of a three-phase copper conductor with a phase difference of 120°.

Fluid field boundary conditions are as follows. In Fig. 2a, seawater flows in from the left and out from the right. The left is the inlet, whose velocity is u, and the right is the outlet, whose pressure is 0 Pa.

Temperature field boundary conditions are as follows. The boundary conditions for the solution of the steady-state heat transfer partial differential equation for submarine cables is summarized into three types. The temperature of the first category of boundary stays constant, i.e. the bottom of Fig. 2a, which is considered to be far enough away from the cable to be unaffected by the cable temperature. The second type of boundary defines the heat flux value. In Fig. 2a, the heat flux on the left and right sides is 0. The third type of boundary condition is the upper of seawater area in Fig. 2(a), where convective heat flux is set to simulate the heat dissipation of upper seawater. The convective coefficient h is 6.5 W/(m^2 K), and the reference temperature is T_{ref}. And a constant pressure point constraint is set on the boundary:

$$\begin{cases} n \cdot (-\lambda \nabla T) = h(T - T_{ref}) \\ P = P_0 \end{cases} \tag{6}$$

2.4 Solution Method

For the solution model, the denser the meshing, the more accurate the result, and the higher the computational complexity. In general, meshing should be as simple as possible with a certain degree of accuracy. In the case of submarine cable laying, the submarine cable and the part in contact with the seabed are divided into dense grids, and the soil and seawater are divided into relatively coarse grids.

Establish an algebraic equation group based on the grid division results and control equations, solve the temperature at each element node, and form the temperature matrix in the entire solution domain. Obtain the temperature distribution of the entire domain through interpolation.

3 Results and Discussion

3.1 Temperature Field Distribution Under Static Seawater

It is adopted that the load current of cable is 740 A, seawater temperature is 20 °C, seawater velocity is 0 m/s, and soil thermal conductivity is 1.0 W/(m k).

The temperature distribution of the submarine cable environment under static seawater is shown in Fig. 3. In Fig. 3a, The submarine cable has the highest temperature. When the seawater is 0 m/s, there is almost only heat conduction. Figure 3b shows the temperature of the submarine cable section. The highest temperature is on the three-phase conductor, which reaches 89.9 °C.

(a) The temperature field distribution of surroundings

(b) The temperature field distribution of submarine cable
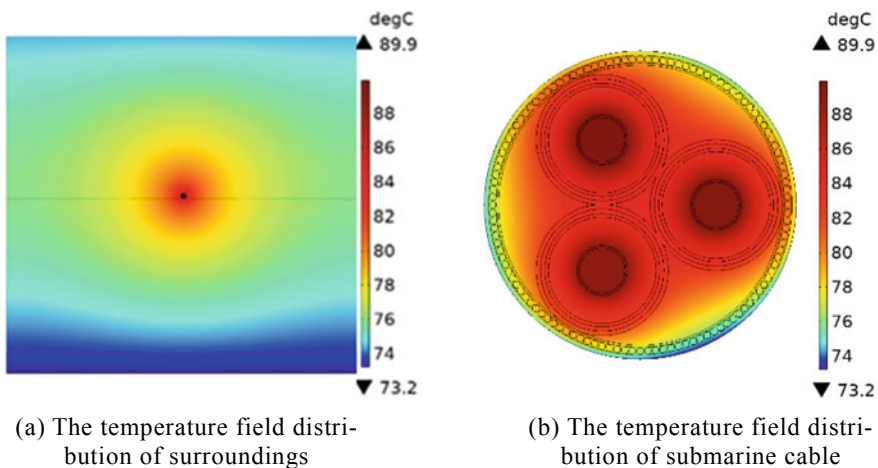
Fig. 3 The temperature field distribution of $u = 0$ m/s
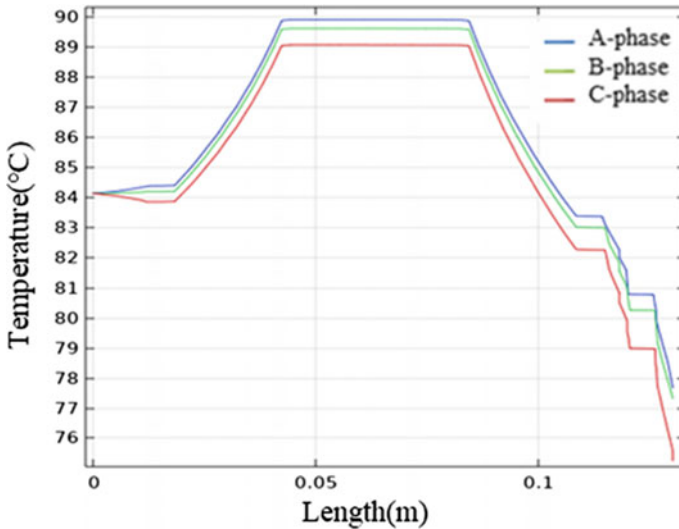
Fig. 4 Radial temperature distribution of submarine cable

Figure 4 shows the radial temperature curve of the different phase conductor, and the A, B and C phases are shown in Fig. 2b. The temperature distribution is not uniform in the multilayer structure of the submarine cable. Copper conductors have a relatively high heat coefficient, so temperature is evenly distributed. The insulation layer is the thickest, with the lowest thermal conductivity and the greatest temperature drop. The conductor screen and insulation screen is very thin, so it is believed that their temperature is roughly equivalent to the temperature of the adjacent layer. The metal sheathed layer is composed of lead metal, the armored layer is made of thin steel wire, which has a high thermal conductivity in these regions and maintains a nearly constant temperature. Moreover, the temperature distribution of the three-phase conductors is different, the conductor temperatures of phase A, B and C are 89.9 °C, 89.6 °C and 89.08 °C, respectively. The temperature distribution of the lowest and highest phase conductors differs by 0.9 °C. The temperature of the insulation layer of the three-phase conductor drops by about 6.5 °C.

3.2 Effects of Seawater Velocity

Submarine cable load current, seawater temperature and soil thermal conductivity are the same as Sect. 2.1. Seawater velocity is 1×10^{-6} m/s, 0.0001 m/s, 0.001 m/s, 0.1 m/s and 1 m/s, respectively.

Figure 5 illustrates the contour map of velocity distribution during submarine laying when the seawater velocity is 0.1 m/s. The ends of the submarine cable exhibit
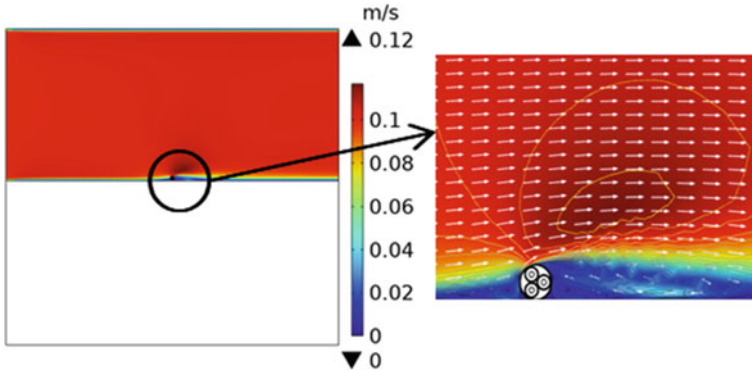
Fig. 5 The map of seawater velocity distribution ($u = 0.1$ m/s)

low velocities, resulting in a backflow effect. At the upper end of the submarine cable, a swirl flow is generated with a velocity of 0.12 m/s.

Figure 6 shows the temperature distribution at different flow rates. In Fig. 6, different seawater velocity has a great influence on the temperature distribution in the environment where the submarine cable is laid. When the flow rate is 0 m/s, the radial temperature change is relatively small. When the velocity is 1×10^{-6} m/s, the temperature of the cable has a great heat conduction to the soil. In seawater area, the temperature distribution is reduced because the flow of seawater carries away some of the heat. As the velocity increases, the heat conduction decreases. There is almost no heat conduction when the velocity reaches 1 m/s. This is because the velocity of the backflow formed at both ends of the cable increases with the increase of the velocity, which accelerates the heat convection. Figure 7 shows the relationship between different seawater velocity and A-phase temperature of the submarine cable. As the velocity increases from 0 to 1m/s, the A-phase temperature decreases. When the velocity is higher than 0.1 m/s, the temperature is relatively evenly distributed along the A-phase radial direction, and the temperature tends to be constant.

The changes of ampacity and maximum temperature under different seawater velocity are shown in Table 2. The ampacity and temperature of the submarine cable vary greatly when the seawater from still to flowing. At 0 m/s, the temperature is 89.9 °C and the ampacity is 740 A. When the flow rate of seawater is 1m/s, the temperature drops to 32.7 °C, a decrease of about 63.86%. The ampacity increased to 1640 A, an increase of about 121.4%. Conductor temperature and ampacity rise with the increase of velocity and finally tend to be flat. When the velocity is 1×10^{-6} m/s, 0.0001m/s, 0.001m/s, 0.1m/s and 1m/s, the temperature is 69.5 °C, 44.6 °C, 38.5 °C, 33.6 °C and 32.7 °C, the ampacity is 871.7A, 1216A, 1382.8A, 1590.7A and 1640.9A, respectively.

Figure 8 shows conducted heat flux and convective heat flux of 1×10^{-6} m/s and 0.1 m/s. There is little difference between convective heat flux and conduction heat flux at 1×10^{-6} m/s. At 0.1 m/s, the convective heat flux is much larger than
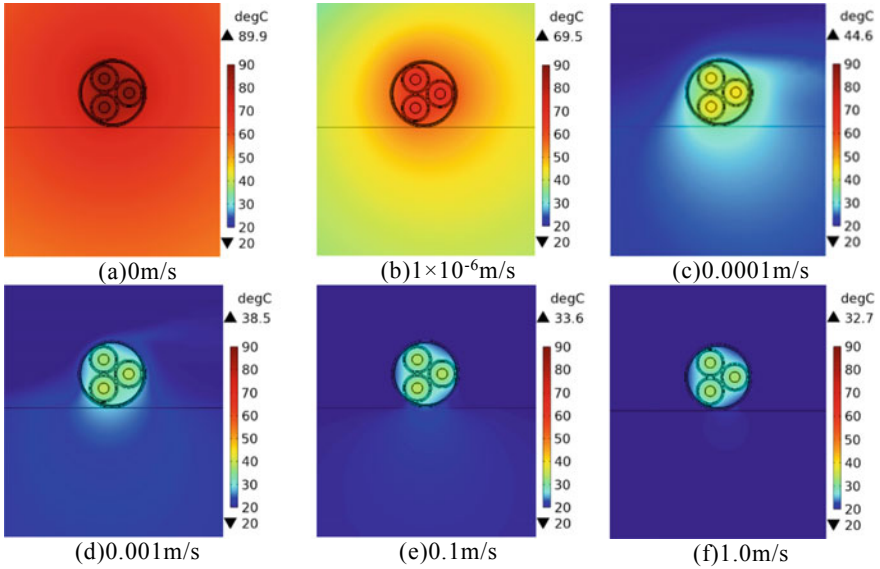
Fig. 6 Submarine cable temperature distribution of 0 m/s, 1×10^{-6} m/s, 0.001 m/s, 0.001 m/s, 0.1 m/s, 1 m/s
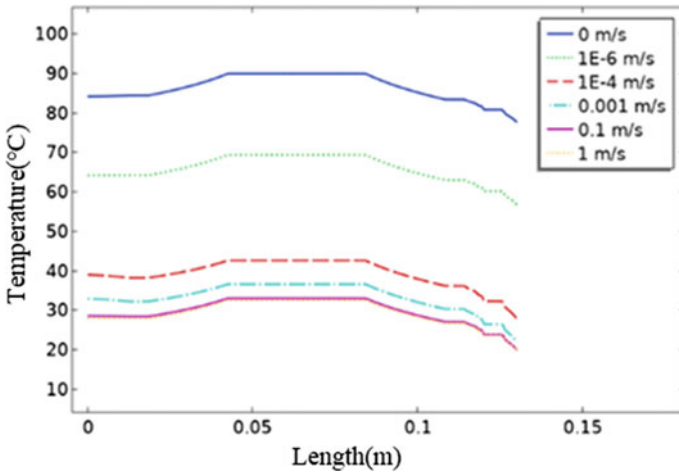
Fig. 7 Radial temperature of A phase of submarine cable at different flow rates

the conduction heat flux. Therefore, when the water velocity increases, it will carry away a lot of heat, making the cable temperature drop significantly.

Table 2 Conductor temperature and ampacity of submarine cable under different velocity

Seawater velocity (m/s)	Conductor temperature (°C)	Ampacity (A)
0	89.9	740
1×10^{-6}	69.5	871.7
0.0001	44.6	1216
0.001	38.5	1382.8
0.1	33.6	1590.7
1	32.7	1640.9

(a) conducted heat flux of
1×10^{-6}m/s

(b) convective heat flux of
1×10^{-6}m/s

(c) conducted heat flux of
0.1m/s

(d) conducted heat flux of
0.1m/s
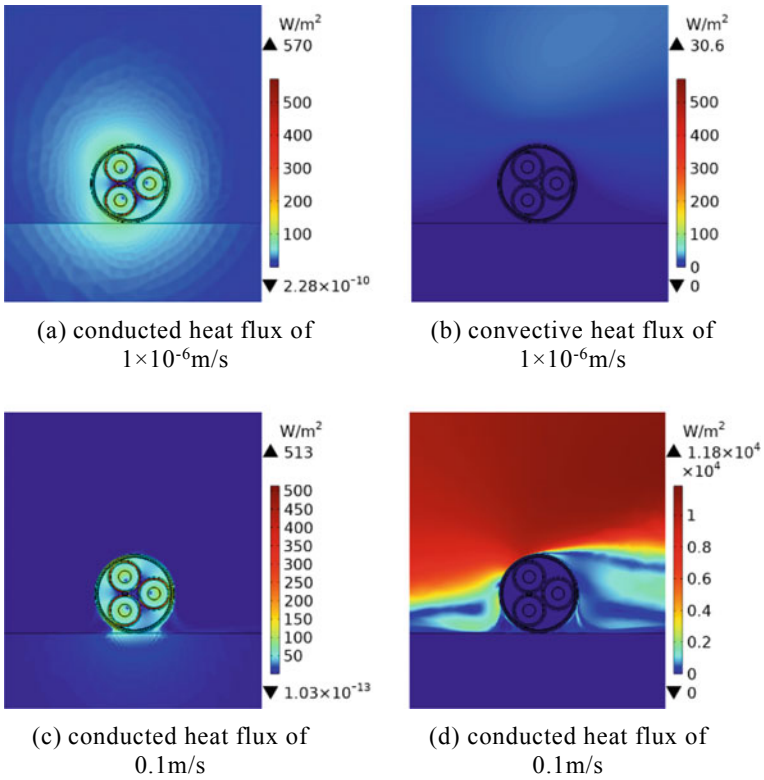
Fig. 8 Heat flux distribution of 1×10^{-6} m/s and 0.1 m/s

4 Conclusions

The text analyzed the temperature distribution of a three-core submarine cable laid in a sea water environment using the finite element method.

(1) When the velocity is 0 m/s, the heat dissipation environment is poor and the conductor temperature reaches 89.9 °C. In the spatial distribution of the submarine cable, the temperature of different conductors is also different. The conductor temperature of phase A, B and C is 89.9 °C, 89.6 °C and 89.08 °C, respectively.

(2) When the seawater is flowing, the cable temperature drops significantly compared to still. When the velocity is from 0 m/s to 1m/s, the convection heat transfer effect is obvious, resulting in the decrease of cable temperature and ampacity, which decrease by 63.86% and 121.4%, respectively.

References

1. Xu W (2023) Analysis and discussion on the development trend of offshore wind power. Resources Economization & Environmental 1:140–143 (in Chinese)
2. Chen Y (2023) The current situation, trend and policy recommendations of China's power structure transformation under the carbon peak and neutrality goals. The World of Survey and Research 3:71–78 (in Chinese)
3. Yang K (2021) Promote the realization of "carbon peak, carbon neutrality" and accelerate the construction of a new type of power system with new energy as the main. China Power Enterprise Management 13:50–53 (in Chinese)
4. Cheng B, Xu Z et al (2014) Economic comparison of AC/DC power transmission system for submarine cables. Electric Power Construction 35(12):31–136 (in Chinese)
5. Pilgrim J, Lewin P, Gorwadia A, Waite F, Payne D (2013) Quantifying possible transmission network benefits from higher cable conductor temperatures. IET Gener Transm Distrib 7(6):636–644
6. Taskin S, Seker S, Kalenderli O (2014) Coherence analysis on thermal effect for power cables under different environmental conditions. Turkish Journal of Electrical Engineering and Computer Sciences, Ankara: Tubitak Scientific & Technical Research Council Turkey 22(1):25–33
7. Czapp S, Szultka S, Tomaszewski A (2020) Design of power cable lines partially exposed to direct solar radiation-special aspects. Energies 13(10):2650
8. Verschaffel-Drefke C, Schedel M, Balzer C et al (2021) Heat dissipation in variable underground power cable beddings: experiences from a real scale field experiment. Energies 14(21):7189
9. Zhang L, Xuan Y, Le Y et al (2016) Ampacity calculation, temperature simulation and thermal cycling experiment for 110 kV submarine cable. High Voltage Apparatus 52(6):135–140+146 (in Chinese)
10. Xia Y et al (2022) Simulation study on steady-state ampacity of ±500 kV DC submarine cable under J-tube laying environment. Proceedings of the CSEE 1–11 (in Chinese)
11. Zhang H et al (2022) Ampacity analysis of extra-high voltage XLPE submarine cable in typical layout environments. Electric Power Engineering Technology 41(6):154–162 (in Chinese)
12. Guo Y, Wei X et al (2020) Electrical parameters calculation of 220 kV optical fiber composited three-core submarine cable. Shandong Electric Power 47(11):28–33 (in Chinese)

Rapid Recovery of Voltage Sag in Distribution Network Based on Dq Transformation

Yifan Zhang, Xiaoming Xiang, Xun Sun, Fenglinzi Dan, Linjia He, Jin Chen, Min Shen, Yuyang Qiao, and Zhiwei Chen

Abstract This paper proposes a real-time voltage compensation method based on dq transformation by simulating three-phase voltage. With A, B and C phases as reference, the phase locking method of second order generalized integrator is used to measure the three-phase voltage phase. The three phase alternating current is established respectively, and the corresponding U_d and U_q are obtained by abc-dq transformation. When the voltage dropping, the U_d corresponding to the single phase voltage will drop, so that keeping the U_d value at the rated value (U_d at the rated voltage of the grid), and the voltage drop can be quickly recovered. The energy of the DC unit of the inverter is rectified by the auxiliary winding of the transformer. When the voltage sag occurring, the corresponding voltage compensation is given by the single-phase inverter, which can keep the original amplitude of the grid voltage. The simulation model of the circuit is established by MATLAB/SIMULINK. The three-phase voltage drop is simulated in the simulation circuit, and the load voltage waveform and the output voltage waveform of the inverter are simulated in the case of the drop. The effectiveness of the proposed method is verified by observing the load voltage waveform after compensation.

Keywords Second order generalized integrator · Voltage sag · Compensation · Dq transformation

Y. Zhang · X. Xiang · X. Sun · F. Dan · L. He · J. Chen
State Grid Anhui Electric Power Co., LTD. Dangtu County Power Supply Company, Maanshan, China

M. Shen
Qilu Institute of Technology, Jinan, China

Y. Qiao · Z. Chen (✉)
Hefei University of Technology, Hefei, China
e-mail: 15656985985@126.com

1 Introduction

With the increase of nonlinear load and the failure of the power system itself, the problems such as voltage fluctuation and current harmonics will occur in the power grid, which may lead to the failure of precision instruments and greatly affect the social and economic benefits [1]. Based on the analysis of the voltage sag compensation methods of domestic and foreign scholars, this paper puts forward the research of real-time voltage compensation topology based on hybrid transformer based on single-phase voltage to simulate three-phase voltage with dq transformation, which is of great significance to solve the voltage sag, distortion and other problems in the power grid.

At present, the research schemes of power grid sag mainly include the following: the single-phase voltage signal is delayed for several cycles to construct its orthogonal signal, and the depth of voltage sag can be rapidly detected by using dq transform [2]. The dual-loop vector decoupling control strategy can improve the dynamic performance of DVR in compensation [3]. On the basis of fuzzy control, the incremental parameter fuzzy adaptive PID control is designed. By realizing adaptive PID parameters control, the DVR system can achieve rapid and stable compensation voltage [4]. The topology design of bridge current limiting voltage restorer can well solve the problem that dynamic voltage restorer is vulnerable to short-circuit current impact [5].

2 Compensation Strategy of Dynamic Voltage Restorer

At present, the compensation strategies of dynamic voltage restorer mainly include complete voltage compensation, in-phase voltage compensation and minimum energy compensation. The in-phase voltage compensation method requires that the compensated voltage output by the inverter should be in the same phase as the grid voltage after the temporary drop. This method can minimize the compensation voltage and can reduce the DC energy storage capacity [6, 7]. When the grid voltage after the temporary drop lags behind the original grid voltage, the grid voltage after compensation will also lag behind the original grid voltage. This method is not applicable to loads with high requirements for network quality. The schematic diagram of in-phase voltage compensation is shown in Fig. 1. U is the power grid voltage before the fault, U_s is the power grid voltage after the fault, U_{dvr} is the voltage compensated by the dynamic restorer, I_l is the load current, and U_l is the load voltage after the compensation.

The complete voltage compensation strategy requires that the voltage before the voltage drop is taken as the reference, and the voltage phase and amplitude after the voltage drop are restored to the level before the voltage drop, so as to ensure the continuity of voltage and current [8]. The advantage of this method is to ensure that the power grid can recover to the voltage amplitude and phase before the power grid

Fig. 1 Schematic diagram of in-phase voltage compensation
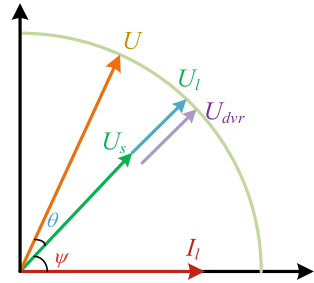
Fig. 2 Schematic diagram of complete voltage compensation method
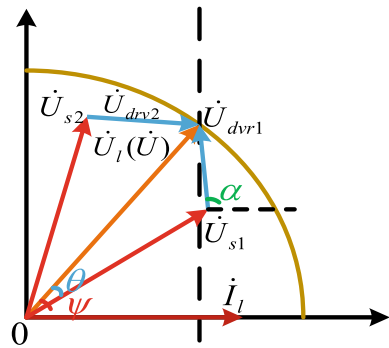
sag, but the disadvantage is that the compensating voltage amplitude of the output of the dynamic voltage restorer is large, and there is power exchange between the system, so the economy is poor. U_l is the voltage before the power grid drop, U_{s1} is the voltage after the power grid drop, and U_{dvr1} is the voltage compensated by the dynamic restorer. The schematic diagram of the complete voltage compensation method is shown in Fig. 2.

The minimum energy compensation strategy requires that the load voltage after compensation has the same amplitude as the voltage before sag. By controlling the voltage output of the dynamic voltage restorer to be perpendicular to the load current of the power grid, the active energy exchange between the dynamic restorer and the power grid can be reduced [9]. The minimum energy compensation strategy can compensate the voltage sag for a long time, and the grid voltage amplitude before and after the compensation is unchanged. Therefore, the grid voltage amplitude before and after the compensation is very deep can also be well compensated. Although the grid voltage amplitude before and after the compensation is unchanged, there is nothing to be done about the lagged phase Angle, which will lead to the voltage waveform discontinuity, as shown in Fig. 3. U is the power grid voltage before the voltage dip, U_{s2} is the power grid voltage when point B is running, U_{dvr2} is the voltage of the dynamic voltage restorer, and U_l is the load voltage.

When the A-phase voltage drops, the A-phase load voltage after the drop is taken as the reference, the three-phase voltage [10] with the same amplitude as the A-phase

Fig. 3 Schematic diagram of minimum energy compensation
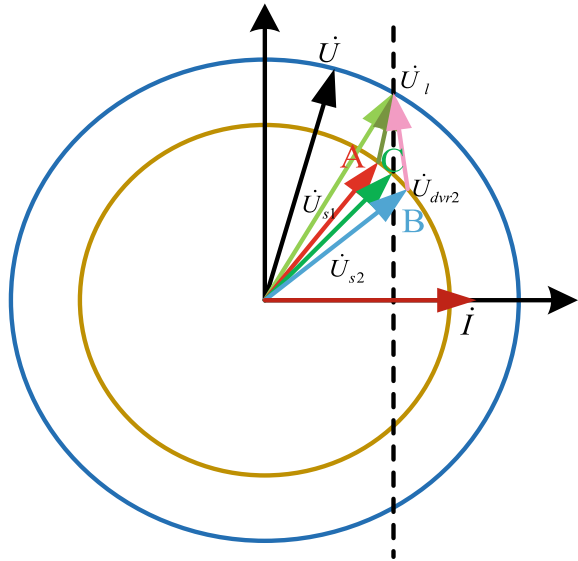
voltage and A phase difference of 120° is constructed. After the dq transformation, the corresponding U_d [11] after the A-phase drop can be obtained. The rated voltage corresponds to U_D under the dq transformation. The difference between U_D and U_d by PI and sine function product to form the modulation signal, and the control signal can be obtained by comparing the modulated signal with the triangular wave. The control signal is input to the inverter, and the inverter output compensates the A-phase sag voltage in real time, so that the voltage of the A-phase load is almost equal to the voltage before the sag. The principle of this method is illustrated only with A-phase voltage sag as an example. The voltage compensation of phase B and C is similar to that of phase A, which will not be introduced here. The principle diagram of A-phase voltage sag compensation is shown in Fig. 4.

3 Emulation Proof

This paper uses Matlab/Simulink to simulate single-phase voltage sag and three-phase voltage sag respectively.

The maximum value of the three-phase voltage is 311 V and the frequency is 50 Hz. When set between 0.5–0.6 s, the three-phase voltage will drop by 50%, accompanied by a certain phase Angle jump. Grid side voltage waveform is shown in Fig. 5.

The three-phase load voltage after compensation is shown in Fig. 6. At this time, the amplitude of the three-phase load voltage is close to the amplitude before sag. The compensated voltage output of the dynamic voltage restorer is shown in Fig. 7.
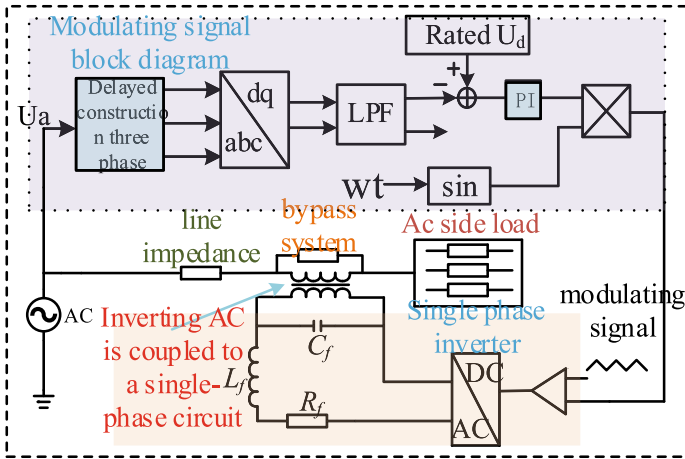
Fig. 4 A-phase dq detection schematic diagram
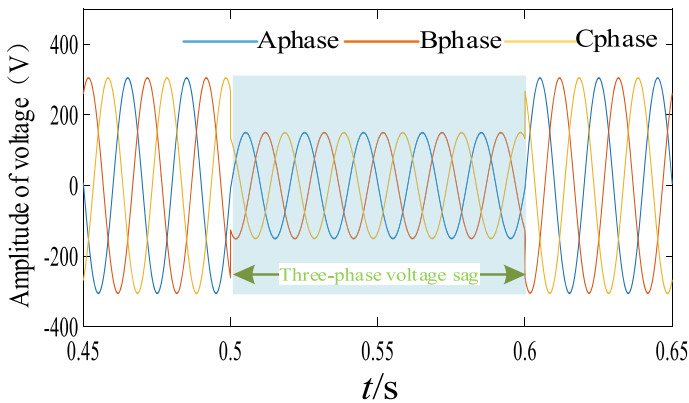
Fig. 5 Three-phase network side voltage

The maximum value of three-phase voltage is 311 V and the frequency is 50 Hz. We take phase A as an example, 50% single-phase voltage drop occurs between 0.5 and 0.6 s, accompanied by a certain phase angle jump. The variation of voltage waveform on the three-phase network side is shown in Fig. 8.

The three-phase load voltage waveform is shown in Fig. 9. At this time, the voltage amplitudes of phase B and C remain unchanged, while the voltage amplitudes of phase A are compensated, and the compensated A-phase voltage amplitudes are close to the voltage amplitudes before the voltage amplitudes drop. When the A-phase voltage sag occurring, the compensated voltage of the dynamic voltage restorer is shown in Fig. 10. At this time, the compensated voltage of B and C phases is 0.
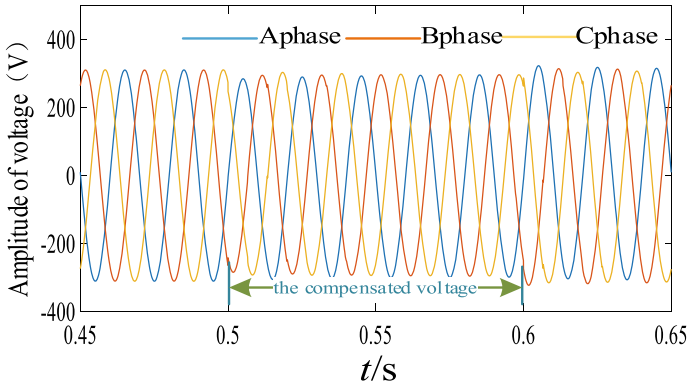
Fig. 6 Three-phase load voltage
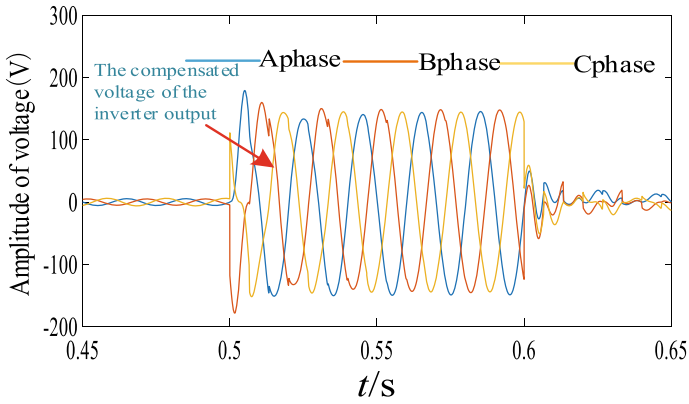
Fig. 7 Compensating voltage of inverter output
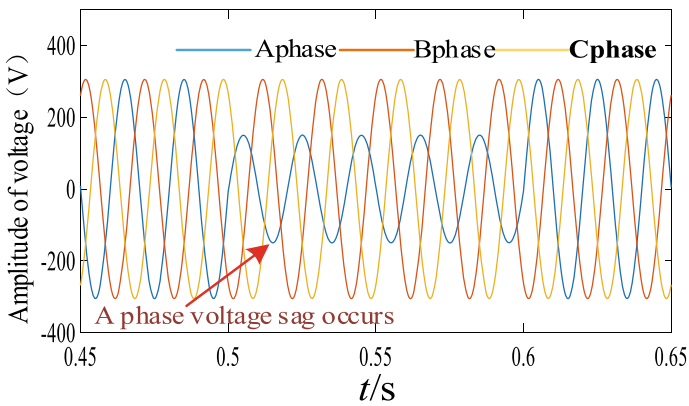
Fig. 8 Three-phase grid side voltage
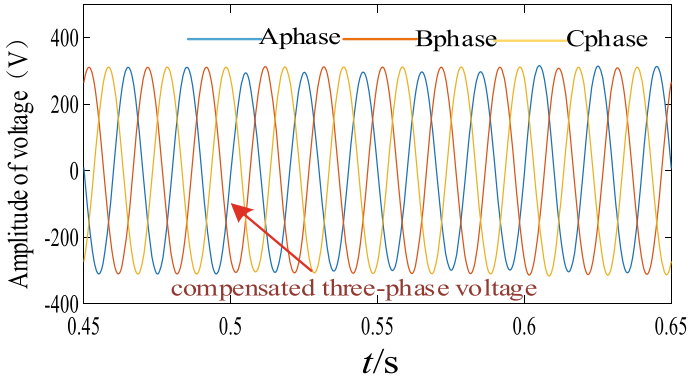
Fig. 9 Three-phase load voltage
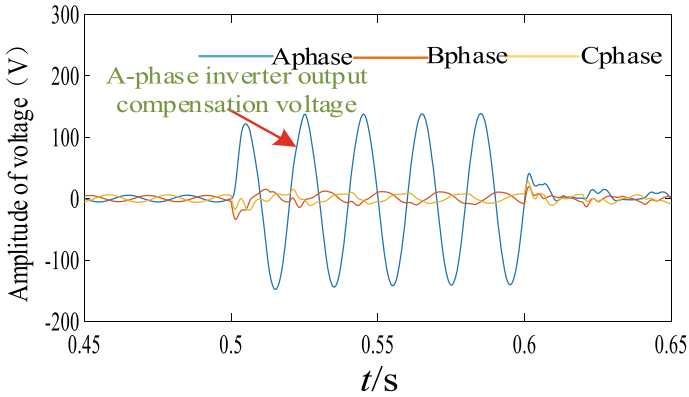
Fig. 10 Compensating voltage of inverter output

After the A-phase voltage compensation, the load voltage amplitude of A phase is approximately equal to the voltage amplitude before the sag.

4 Experimental Verification

At 0.5 s, the three-phase voltage drops by 40%, and the waveform of the three-phase voltage is shown in Fig. 11. Three dynamic voltage restorers work at the same time, and the compensated voltage waveform is shown in Fig. 12. The three-phase load voltage after compensation is shown in Fig. 13, and the amplitude of the load voltage after compensation is almost the same as that before the sag.

At 0.5 s, A phase of the three-phase voltage drops by 40%, and the waveform of the three-phase voltage is shown in Fig. 14. Among the three dynamic voltage
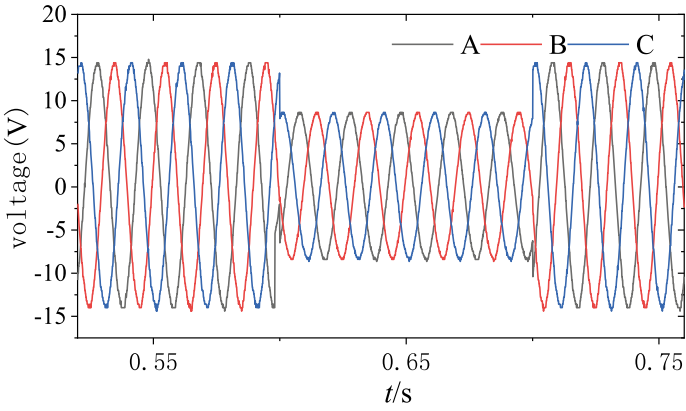
Fig. 11 Three-phase network side transient voltage drop
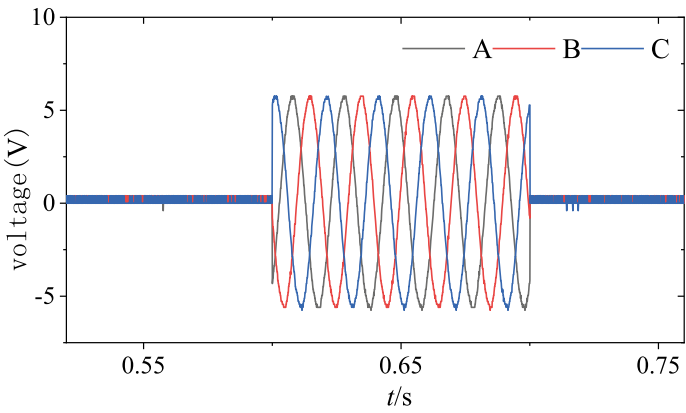
Fig. 12 Compensating voltage of inverter output
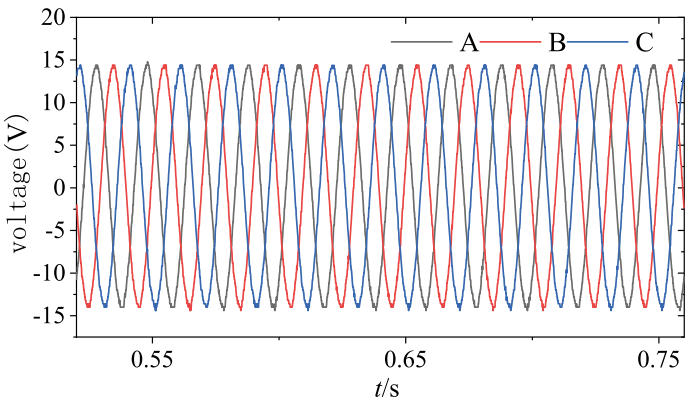
Fig. 13 Voltage after three-phase load compensation
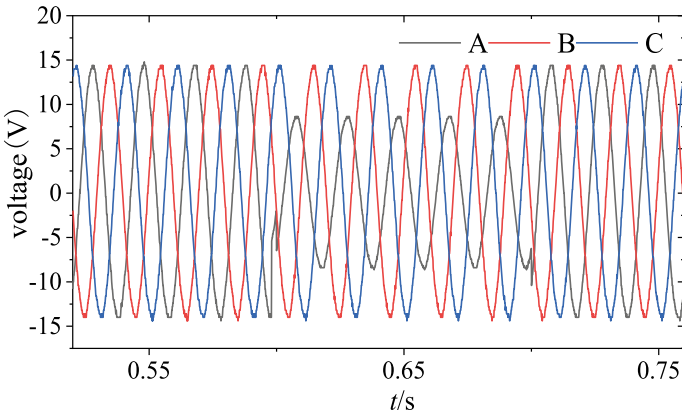
Fig. 14 Single-phase voltage sag
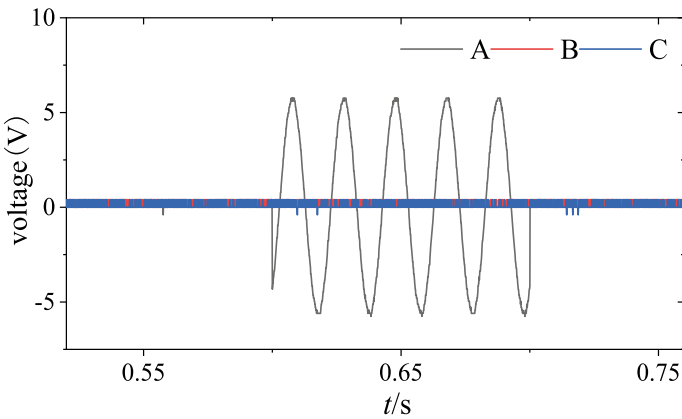
Fig. 15 Compensating voltage of inverter output

restorers, only the A-phase inverter works, and the compensated voltage waveform is shown in Fig. 15. The three-phase load voltage after compensation is shown in Fig. 16, and the amplitude of the load voltage after compensation is almost the same as that before the sag.
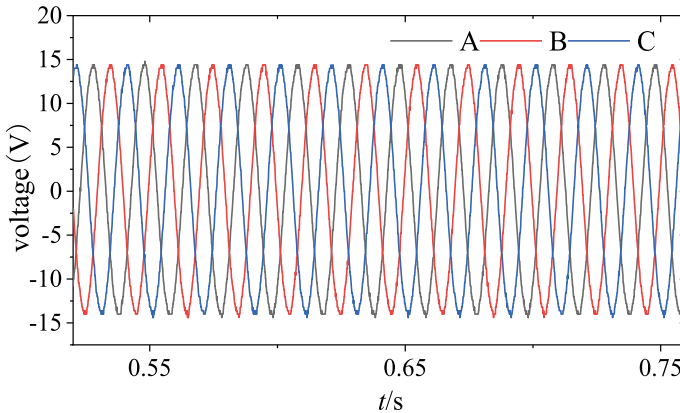
Fig. 16 Voltage after single-phase load compensation

5 Conclusion

In this paper, single-phase voltage is used to construct three-phase voltage. When one of the three-phase voltage drops temporarily, the three-phase voltage formed by the phase voltage corresponds to a direct flow after dq transformation. The direct flow deviates from the given value, and the control signal is obtained through PI, so that the dynamic voltage restorer outputs the voltage to be compensated.

The phase-locked loop in this paper adopts the phase-locked method of second-order generalized integrator to realize the station-free tracking control of the phase of the three-phase grid side voltage. When the voltage distortion occurs in the grid, there are positive sequence, negative sequence and zero sequence components. This method can detect the positive sequence fundamental frequency component of the voltage as the voltage input of the phase-locked loop.

References

1. Wang Y, Cai G, Liu C et al (2020) Single-phase dynamic voltage restorer based on bi-polar direct AC/AC conversion. Power Automation Equipment 44(06):171–177
2. Li J, Chen J, Yang B et al (2020) Single phase voltage sag detection method based on signal short time delay algorithm. IEEE Sensors 21:27–30+4 (in Chinese)
3. Yang H, Shen Y (2019) Research on dynamic performance of DVR based on dual-loop vector decoupling control strategy. Journal of Jianghan University (Natural Science Edition) 47(05):416–423 (in Chinese)
4. He Z, Guo X (2019) Dynamic voltage restorer based on fuzzy neural network PID. Journal of Qiqihar University (Natural Science Edition) 35(03):23–27 (in Chinese)
5. Tu C, Li Q, Guo Q et al (2020) Design and control method of bridge current limiting and dynamic voltage restorer fusion. IEEE Sens J 35(20):4384–4396 (in Chinese)
6. Yang B (2019) Research on the key technology of multi-function hybrid power electronic transformer. Southeast University, Nanjing (in Chinese)

7. Sun H (2019) Research on key technology of hybrid power quality control device based on multi-winding transformer. Southeast University, Nanjing (in Chinese)
8. Xia X (2012) Design and implementation of large capacity multi-level dynamic voltage restorer (DVR). Hebei University of Technology, Tianjin (in Chinese)
9. Tu C, Lu B, Guo Q et al (2020) Operation characteristics analysis of series capacitance coupled dynamic voltage restorer based on minimum energy compensation method. IEEE Sens J 35(17):3727–3738 (in Chinese)
10. Hu B, Zhao X (2020) Research on dynamic voltage restorer of microgrid based on hybrid energy storage. Chinese Journal of Electrical Engineering 15(04):99–105 (in Chinese)
11. Huang L (2019) Research on simulation and application of delay locking virtual three-phase DQ0 transform method in DVR. IEEE Sensors 01:16–17+23 (in Chinese)

Metering Fault Diagnosis Model Based on Deep Feature Fitting Network with Mixture of Experts

Lingyu Liang, Wenqi Huang, Xiangyu Zhao, Xiaotao Jiang, Shang Cao, Huanming Zhang, Jiaxuan Hou, and Xin Wang

Abstract In the field of power metering, automatic monitoring and analysis of equipment alarm events are essential for stable operation of the metering system. To address the problem of fault diagnosis for metering equipment, a mixed-expert model based on deep neural networks is proposed. The proposed model combines the advantages of mixture-of-experts (MoE) and Deep feature fitting networks (DFFN). The MoE system can divide the measurement warning problem into several sub-problems for processing, which greatly improves the system's ability to recognize and predict warning problems. On the other hand, the DFFNs can be used to analyze measurement data, fit complex features, and better analyze fault problems.

Keywords Mixture of experts · Deep feature fitting network · Fault diagnosis · Power metering

L. Liang · W. Huang · X. Zhao · S. Cao · H. Zhang · J. Hou
China Southern Power Grid Digital Grid Research Institute Co., Ltd., Guangzhou 510663, China
e-mail: liangly1@csg.cn

W. Huang
e-mail: huangwq@csg.cn

X. Zhao
e-mail: zhaoxy1@csg.cn

S. Cao
e-mail: caoshang@csg.cn

H. Zhang
e-mail: zhanghm@csg.cn

J. Hou
e-mail: houjx@csg.cn

X. Jiang · X. Wang (✉)
Zhejiang University-China Southern Power Grid Joint Research Centre On AI, Zhejiang University, Hangzhou 310000, China
e-mail: wangxin2009@zju.edu.cn

X. Jiang
e-mail: jkbasara@qq.com

1   Introduction

The power metering system is crucial for power grid operation, affecting economic efficiency and safety. Abnormalities in metering equipment, due to installation quality, operation failure, or electricity theft, can result in increased unspecified electricity losses, infringing national interests. Therefore, intelligent and accurate fault detection is crucial for efficient power metering equipment operation.

There are many existing studies on fault diagnosis for metering equipment, in which we mainly discuss the two types more related with our work that fault diagnosis based on expert system and fault diagnosis based on learning.

1.1   Fault Diagnosis Based on Expert System

Fault diagnosis based on expert system mainly uses an expert knowledge base to diagnose faults. During diagnosis, the system will apply the existing rule base to reason and make judgment based on the real-time data collected, and finally obtain the fault diagnosis results. Zhu et al. [1] proposed an expert system to locate faults and connect this system to the SCADA monitoring system to achieve early warning of potential faults in wind turbines. However, the expert system also has certain limitations, the accuracy and reliability of the expert system receives the limitation of expert knowledge, it is difficult to adapt to the emergence of new fault types, and the scalability is poor.

1.2   Fault Diagnosis Based on Learning

Deep learning can transform the low-level features of input data into high-level features, simulate complex functions, and obtain the intrinsic patterns of sample data. So compared with the traditional fault diagnosis, the fault diagnosis method based on deep learning greatly improves the efficiency and accuracy of fault diagnosis. Wang et al. [2] introduces the basic theory, research status and challenges of fault diagnosis technology based on deep learning, and expounds the great application prospect of fault diagnosis technology based on deep learning.

As deep learning continues to deepen, deep learning-based fault diagnosis gradually becomes a research hotspot. Teng et al. [3] proposed a fault diagnosis method based on deep learning theory. The deep learning diagnosis model is constructed by extracting the features of historical fault samples, and the probability value of the faulty device tripping is evaluated when the system detects the risk, which improves the accuracy of fault identification. Feng et al. [4] proposed a mechanical fault diagnosis method based on deep learning and knowledge graph, which achieves more accurate and reliable fault diagnosis results by combining traditional time-series data

analysis and knowledge graph. Li et al. [5] proposed an intelligent rotating machinery fault diagnosis method based on deep learning and data augmentation to improve the accuracy and robustness of fault diagnosis.

1.3 Mixture of Experts and Feature Fitting Networks

Mixture of Experts (MoE) has significant advantages in addressing issues such as high data complexity and difficulties in modeling with a single model. Due to its strong modeling and generalization abilities, MoE has achieved good application effects in many fields such as computer vision, natural language processing, speech recognition, etc. Chen et al. [6] proposed an overview and insights into the Mixture of Experts (MoE) model and its applications in deep learning. Zhang et al. [7] proposed a mixture of experts (MoE) approach to customize deep neural networks (DNNs) for low-cost applications. Wang et al. [8] proposed a deep mixture of experts model that uses shallow embedding techniques to address the issues of high-dimensional input spaces and large-scale datasets.

Li et al. [9] proposed the concept of Feature fitting networks in 2016, which aims to automatically extract relevant features from the original data using neural networks to map the input data into a low-dimensional feature space while retaining key information in the data. Gao et al. [10] used the feature-fitting network to experiment with the dataset, and the results are obvious.

The main contribution of this paper is to carry out research work on the fault diagnosis of electric power metering equipment combined with deep learning framework. Using the excellent feature extraction ability of deep neural network and the selection ability of MoE (Mixture of Experts) structure for different data types, this paper propose a deep neural network model (Gated Neural Network) based on MoE to complete the diagnosis of power metering equipment faults.

2 Metering Fault Diagnosis GNN Model

The general process of metering equipment fault diagnosis is as follows: In the case of metering equipment fault, the fault phenomenon data is firstly obtained by monitoring system or sensor, then the fault data is analyzed and processed, and the fault type and prediction are derived by combining with relevant technical means.

Therefore, in this paper, we analyzes the problem in terms of fault type classification and fault data prediction and propose a deep neural network model Gated Neural Network (hereinafter referred to as GNN) for metering equipment fault diagnosis. The model is structured as a mixture of experts (MoE) with deep feature fitting networks (DFFN) as the main structure.

Table 1 Fault type of metering equipment

Alarm level / Fault type	Level I	Level II	Level III
Power consumption abnormal	Missing watch codes	Watch code backwards Total split time watch code not equal	Watch code flies away Watch code stops walking Watch code zero and being frozen
Voltage abnormal	Voltage disconnection	Missing voltage pass rate	Voltage loss
Load abnormal		Load overload Current unbalance	Voltage imbalance
Clock abnormal			Energy meter clock anomaly
Acquisition abnormal		Collection terminal offline	Low automatic meter reading rate

2.1 Types of Metering Equipment Failures

Common metering equipment fault types are shown in Table 1. From the user type perspective, metering equipment fault types is divided into dedicated user metering equipment, public user metering equipment, low-voltage metering equipment, substation metering equipment and power plant user metering equipment. And from the alarm level perspective, it is further divided into four alarm levels. For the consideration of information security, Table 1 only lists subsection of the metering equipment fault types for illustration, and does not explain the fault corresponding to a user type, but only lists the common fault names and corresponding fault characteristics.

Different user groups have similar fault types, e.g., dedicated and public users have similar characteristics in voltage anomalies. Similarities and correlations exist in physical electrical quantities between different fault types, e.g., voltage anomalies and power consumption anomalies may occur simultaneously and be distributed in the same moment in voltage, current, inductance, and other electrical quantity values. Faults have regular changes in time that can be referred from the faults history. In this paper, these complex factors are analyzed and incorporated into the sample features when analyzing intelligent fault diagnosis schemes and building deep neural networks.

2.2 GNN Model for Fault Diagnosis of Metering Equipment

The fault sample data has a certain dimensionality and can be fitted using deep neural networks. MoE units are used to process different fault types separately, and change
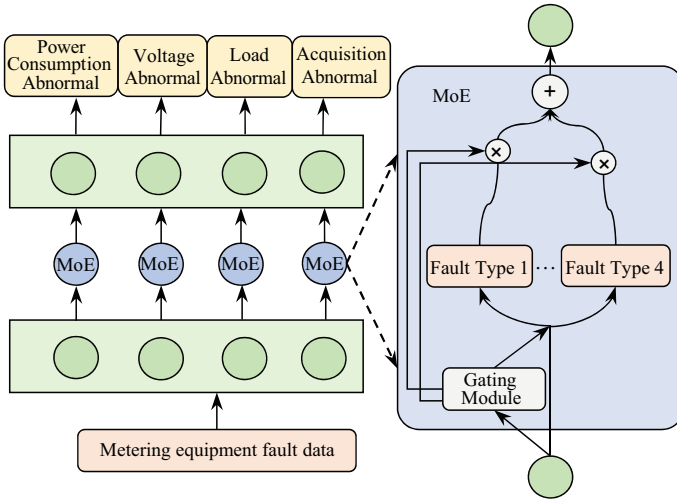
Fig. 1 The MoE for metering fault diagnosis

the weights of the feature fitting network dynamically, improving the response speed. The combination of MoE and deep feature extraction network can process time-based metering equipment fault collection data as a time series.

The GNN model proposed in this paper for fault detection of metering equipment mainly consists of two parts: hybrid expert component and a feature fitting networks.

Hybrid expert components for fault problems. In this paper, the hybrid expert module is used to complete the classification and identification of features, and the feature fitting process is changed from being implemented with one neural network to having the MoE unit control the feature identification and selection, and then the resulting weights are given to the subsequent network for feature calculation. The detailed structure of the MoE component is shown in Fig. 1.

The hybrid expert component divides the fault types into multiple sub-regions, each expert specializing in one type of fault problem. Although there exist a lots of metering equipment fault types as shown in Table 1, each type actually only has low complexity. That leads to the execution efficiency with multiple MoEs is acceptable although it increases the size of the model.

This paper trains a MoE model for fault diagnosis using a combination of data from different sources and feature distributions. Experts are developed for each type of fault, and a gating module selects the corresponding expert to process the data. The model needs to train both the experts and gating module for the MoE component. The MoE component of this model is shown on the left side of Fig. 1, and its internal structure is shown in detail on the right side of the figure.

Hybrid expert systems include Competitive MoE and Cooperative MoE. For Competitive MoE, the feature distribution regions of the data are discrete distributed on a feature dimensional space. It is suitable to use Competitive MoE for sample data with large feature differences and a long spatial distance. Considering that the

individual feature values of the collected data of the metering equipment are correlated and coupled in spatial distribution, it is not desirable to distinguish them strictly (it is impossible to strictly distinguish the electrical feature values between different faults), so Cooperative MoE is used in this paper to deal with the fault problem.

Define the dimension of the input data x as d and the feature dimension of the output value y as c. In the presence of k experts, set the learning rate of MoE as λ. The output of MoE is defined as

$$V_{ik} = \omega_{ik}x, \text{ for } jin(0\ldots(d-1)) \text{ and } i \text{ in}(0\ldots(c-1)) \tag{1}$$

where V_{ik} denotes the prediction of expert k for the ith column and ω_{ik} is the output weight of expert k for the ith column.

The weights and output means for the Cooperative MoE are defined by the following equation:

$$\Delta\omega_{ik} = \lambda(y_i - \widehat{y_i})g_k x \tag{2}$$

$$\Delta m_k = \lambda(y_i - \widehat{y_i})(v_{ik} - \widehat{y_i})g_k x \tag{3}$$

In the definition formula, m_k represents the output mean value of the kth expert, and g_k represents the output value of the gating module of the kth expert.

Each "expert" analyzes and handles one type of fault regardless of other types, and finally the "experts" corresponding to all fault types fuse their outputs with the output of the gating module. In this paper, multiple "experts" are defined to deal with different fault types because in addition to electrical faults (power consumption, current, load), there are also non-electrical faults (meter code anomalies, acquisition anomalies, coverage problems due to offline terminals, etc.).

Feature Fitting Network for Predicting Fault Data. The final step of feature fitting for the input data is accomplished through the fault data prediction and fault type classification network. The input training samples are used partially to train the MoE unit and partially to train the prediction and classification network in the entire GNN model. This also applies to model validation. As shown in Fig. 2, for the entire fault data prediction and fault type classification network, its weight matrix is obtained by parameter fusion of weight matrix 1 and weight matrix 2. The weight values corresponding to data prediction are completed by this part itself, while the weight values corresponding to fault type analysis are transmitted from the MoE unit to this part.

The structure of the fault data prediction and fault type classification network is defined as having an input layer, an output layer, and two hidden layers. The input parameter is the metering data mentioned above, and the output layer is a column vector composed of predicted fault data and fault types. The hidden layers calculate the feature distribution mapping of the metering data with temporal characteristics at two time points, $t - 1$ and t. (as shown in Fig. 3).

Fig. 2 The prediction and classified network for metering fault data
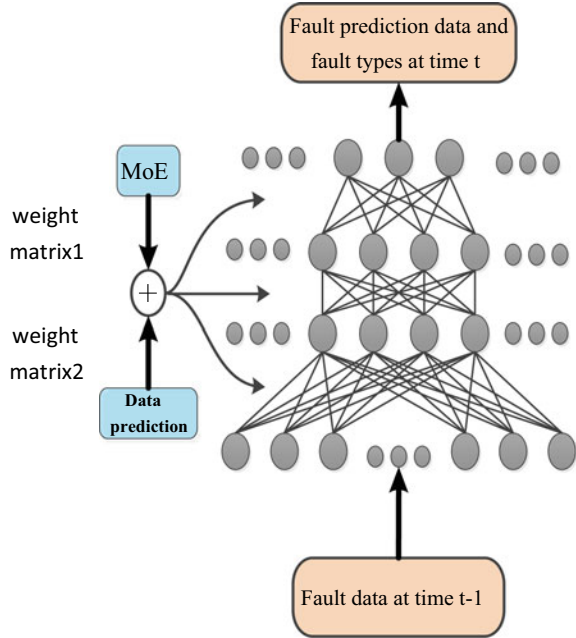
Fig. 3 The relationship between input and output of metering data
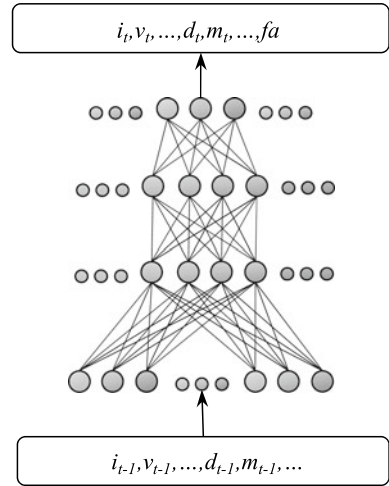
Here the input data vector consists of various data from the metering side such as electrical acquisitions (current, voltage, primary and secondary voltage status, clock status, etc.), equipment statistics (meter code status, online/offline status, etc.), etc., which are defined in Fig. 3 by the variables i, v, d, m in combination with the time subscript $t - 1$. The output then contains the predicted non-real metering characteristics (time subscript t) with the corresponding fault type (fa).

The neural network structure of the fault data prediction and fault type classification network proposed in this paper is defined as follows.

(1) Define the fault classification function as Ω. Let the input vector be X, then Ω can be expressed as

$$\Omega(X|\mu) = \sigma(\omega_2 \cdot \varphi(\omega_1 \cdot \varphi(\omega_0 \cdot X + b_0) + b_1) + b_2) \tag{4}$$

where φ represents the activation function ReLU for each layer, the input parameter X is the feature vector in the data collected from the metering equipment as described above, σ expresses the output function as a Softmax classification function, and the parameter μ represents the parameters of the hidden layer of the fault classification network, $\mu = \{\omega_0, \omega_1, \omega_2, b_0, b_1, b_2\}$, where the weight matrix ω is obtained from the MoE output.

(2) Define the fault data prediction function as θ and the input vector as X, then θ can be expressed as

$$\theta(X|v) = \omega_2 \cdot ELU(\omega_1 \cdot ELU(\omega_0 \cdot X + b_0) + b_1) + b_2 \tag{5}$$

where ELU is the activation function of each layer, the output parameters are the same as in Eq. (4), and the parameter v denotes the parameters of the hidden layer of the fault data prediction network, $v = \{\omega_2, \omega_1, \omega_0, b_2, b_1, b_0\}$, whose parameters are obtained from the training of this model.

3 Experiment

3.1 Experiment Analysis

After completing the GNN, this paper makes an evaluation of fault detection. The quantitative statistics of fault diagnosis accuracy in the experiments of this paper are shown in Table 2.

In the experiments of this paper, we use the DAE model and the CNN model as comparative models, which have been widely used in fault diagnosis business and have achieved good results in the combination of deep learning and fault diagnosis. In this paper, we propose a new GNN model to improve the accuracy by separating

Table 2 Accuracy analysis of GNN

Model	Accuracy
Stand-alone DAE	0.934
Stand-alone CNN	0.952
GNN	0.960

Table 3 Comparison of training time between DAE, CNN, and GNN

Data size (unit: pieces)	Batch size	DAE convergence time	CNN convergence time	GNN convergence time
About 60,000	1000	10 h	10 h	10 h

fault type determination and fault feature fitting into two tasks. We further refine the temporal granularity of data samples and use MoE units to handle real-time dynamic classification and prediction problems, while reducing the size of the feature fitting network. We also add MoE units to select and update weights in the front-end, thus improving real-time performance and accuracy, although the relative training process becomes complicated. Experimental results show that our proposed GNN model exhibits superior performance in fault diagnosis.

We also compare the time overhead of training the model in this paper with the DAE model and the CNN model. As shown in Table 3. The model training time is almost the same with the same number of samples and training batches.

4 Conclusion

The use of deep learning techniques in metering equipment fault diagnosis has been growing due to their ability to handle high-dimensional data and capture complex features. In this article, we provide a comprehensive analysis of a deep learning-based fault diagnosis model for metering equipment and introduce a GNN model that incorporates MoE and a deep feature fitting network to enhance performance. The main work of this paper is summarized as follows.

(1) Analysis of metering equipment fault types
(2) Design a hybrid model based on MoE and feature fitting network. The MoE unit is designed to detect different fault types, and the weights of the feature fitting network are updated in real time based on the results of the MoE unit.

There are several areas where the gated neural network proposed in this paper for fault diagnosis of metering equipment could be enhanced and improved. For instance, there is a need to address the issues related to collecting comprehensive data while ensuring data security. Additionally, further research is required to investigate how to effectively combine different types of neural network models with the MoE framework.

References

1. Zhu G, Chen S, Ren N et al (2021) Fault diagnosis and warning design of wind turbines based on expert system. In: IEEE 4th international conference on automation, electronics and electrical engineering (AUTEEE). IEEE, pp 755–758
2. Wang H, Wei J, Li P (2022) Research on fault diagnosis technology based on deep learning. J Phys: Conf Ser 2187(1):012041
3. Teng S, Li J, He S, Fan B, Hu S (2021) On-line fault diagnosis technology and application based on deep learning of fault characteristic of power grid. J Phys: Conf Ser 2023(1):012023
4. Feng F, Wu C, Zhu J et al (2020) Research on multitask fault diagnosis and weight visualization of rotating machinery based on convolutional neural network. J Braz Soc Mech Sci Eng 42(11):603
5. Li X, Zhang W, Ding Q et al (2020) Intelligent rotating machinery fault diagnosis based on deep learning using data augmentation. J Intell Manuf 31:433–452
6. Chen Z, Deng Y, Wu Y et al (2022) Towards understanding mixture of experts in deep learning. arXiv preprint arXiv:2208.02813
7. Zhang B, Davoodi A, Hu Y (2020) A mixture of experts approach for low-cost DNN customization. IEEE Design & Test 38(4):52–59
8. Wang X, Yu F, Dunlap L et al (2020) Deep mixture of experts via shallow embedding. Uncertainty in artificial intelligence. PMLR 552–562
9. Li Y, Chen C, Wasserman WW (2016) Deep feature selection: theory and application to identify enhancers and promoters. J Comput Biol 23(5):322–336
10. Gao Z, Sun J, Yang H et al (2020) Exploration and research of human identification scheme based on inertial data. Sensors 20(12):3444

Calculation and Measurement of Sequence Parameters of Three-Core Submarine Cable with Semi-conductive Sheaths

Tao Huang, Shuangzhi Zhao, Xuancheng Huang, Zhicheng Lei, Xuwei Zhou, and Hailiang Lu

Abstract As the scale of offshore wind power continues to expand, more and more three-core AC submarine cables have been put into construction. Submarine cables are the only way of offshore wind power transmission. The accurate acquisition of their sequence parameters is an important basis for planning, designing and analyzing offshore wind power systems. In view of the fact that the existing IEC standards do not have a formula corresponding to the parameters of submarine cables with semi-conductive sheaths, this paper uses a simulation method to calculate the sequence parameters of a 220 kV three-core AC semi-conductive submarine cable. Considering the semi-conductive layer of the cable and its more structures and laying environment, the sequence parameters are deduced and calculated taking into account the semi-conductive sheaths through the multi-conductor system modeling of cables and the application of the symmetrical component principle, and compared with the measured values. The results show that the sequence parameters can reflect the unknown material parameters and the submarine environment, and the simulation results are more accurate, which can provide reference for engineering designers.

Keywords Three-core AC submarine cable · Sequence parameter · Semi-conductive sheath · Multi-conductor system · Symmetrical component method

T. Huang (✉) · S. Zhao · X. Huang · Z. Lei
Jiangsu Frontier Electric Technology Co. Ltd, Nanjing 211102, China
e-mail: 510152265@qq.com

X. Zhou · H. Lu
School of Electrical Engineering and Automation, Wuhan University, Wuhan 430072, China

1 Introduction

In recent years, in response to the national "dual carbon" policy, offshore wind farms are continuously developing from small to large and from shallow to deep. The construction of offshore power transmission and transformation projects has been continuously promoted. Submarine cables, as the only way to transmit offshore wind power, are the core equipment of offshore power transmission and transformation projects. When planning the integration of wind farms into the power system, the line sequence parameters are an important basis for system electrical characteristic analysis, power flow distribution and short-circuit current calculation, relay protection setting and other work [1].

There are generally two methods for obtaining cable sequence parameters: the measurement method and calculation method [2]. Due to the fact that submarine cables are laid on the seabed, the complex laying environment on the seabed cannot be fully considered in theoretical calculations. Therefore, the measurement method is the most accurate method to reflect the on-site submarine cable sequence parameters. However, for long-distance high voltage and ultra-high voltage submarine cables, the measurement equipment costs a lot, and large circulating currents and induced voltages will be generated on the metal sheaths and armor, which will interfere with the accurate measurement of power frequency parameters and pose a certain threat to the safety of testing personnel and instruments.

The calculation methods mainly use the IEC formulas or the simulation based on the principle of symmetrical components, which both require the knowledge of numerous parameters such as the size, material, arrangement, and laying conditions of cables. Different specifications and models of cables have different parameters, making it difficult to accurately obtain all parameters. The international standard IEC 60909 (the same as the national standard GB/T 15544) provides the most commonly used formulas for calculating the sequence impedance of cables. The general factory parameters of cables are based on these formulas. But unlike land cables, submarine cables need to be equipped with armor layers to ensure mechanical strength. The IEC formula does not consider the impact of armor layers on sequence impedance, and cannot fully consider the impact of the grounding environment, either [3]. Compared with the formula method, the simulation method for calculating the sequence impedance of cables can consider structures such as armor layers and semi-conductive layers, as well as different grounding modes. But it requires more actual parameters and the numerical calculation process is more complex [4]. With the continuous development of electromagnetic transient simulation software, the simulation of electrical parameters of single-core cables has received some research and application [5–8]. Due to continuous expansion of the offshore wind power scale, more and more high voltage three-core AC submarine cables are being put into engineering [9–11], especially the three-core semi-conductive submarine cables have more applications. However, for calculating the sequence parameters of three-core submarine cables with the semi-conductive structure, there is currently no corresponding formula in the IEC standard and the research on simulation methods is not

sufficient. The calculation in reference [12] only analyzed the sequence parameters of a three-core submarine cable line containing fiber optic units, but ignored the cable resistance and did not consider the semi-conductive structure. The calculated results were not compared with the measured results, and the calculation parameters were rarely explained.

This paper takes a 220 kV three-core AC submarine cable with the semi-conductive sheath structure used in a certain offshore wind power project as an example. Firstly, based on the calculation principle of multi-conductor systems and the symmetrical component method, the solving process of the cable sequence parameters is derived. Then, based on the structure, materials, and environment of the submarine cable, a three-core submarine cable simulation model considering semi-conductive sheaths is established, and the simulation values of its sequence parameters are given. To illustrate the necessity of considering the semi-conductive sheaths for calculating the sequence parameters of the semi-conductive submarine cables, this article compares the estimated results of IEC formulas, the calculated results without considering the semi-conductive sheaths, and the on-site measured results, verifying the feasibility of the proposed method.

2 Structure and Material Parameters of the Three-Core Submarine Cable

This paper uses an HYJQF41-F-127/220-3 × 500 AC three-core submarine opto-electronic composite cable as the research object. The specific structural diagram of the submarine cable with semi-conductive sheaths is shown in Fig. 1.

According to the function and material type of each layer structure of the submarine cable, some layered structures can be equivalent to one layer to appropriately simplify the cable structure. Because the radial water barrier and insulation shield both use semi-conductive materials and have similar effects, they can be equivalent to one layer of main insulation shield. Similarly, the filler, wrapping tape, and PP inner

Fig. 1 Schematic diagram of 220 kV three-core semi-conductive submarine cable

1 Copper conductor
2 Conductor shield
3 Insulation
4 Insulation shield
5 Radial water barrier
6 Metal sheath
7 Semi-conductive PE sheath
8 Filler
9 Wrapping tape
10 PP inner cushion layer
11 Galvanized steel wire
12 Asphalt
13 Optical fiber unit
14 PP outer covering layer
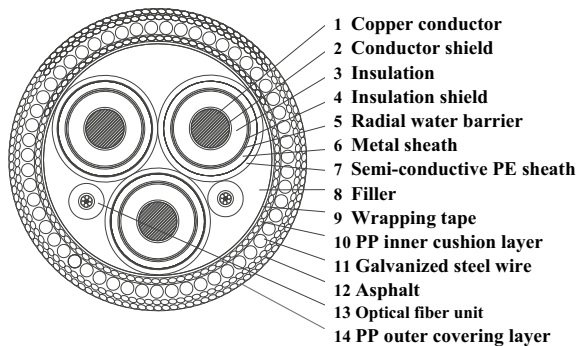
cushion layer are simplified and equivalent to one filling layer, while the asphalt and PP outer covering layer are equivalent to one layer of the armor insulation sheaths. The size parameters and simplified structure of each part of the submarine cable are shown in Table 1. When simplifying the structure, it is necessary to calculate the equivalent dielectric constant or equivalent resistivity of different materials based on their characteristics [13].

Based on the parameters provided by the manufacturer and relevant standards [14], unknown material parameters are selected based on literature and engineering characteristics. The final material parameters for each part of the submarine cable are shown in Table 2. Among them, the filling part of the submarine cable is subject to long-term immersion in seawater, and its dielectric constant is taken as the dielectric constant of seawater. It is difficult to obtain accurate values for the resistivity of the semi-conductive sheaths in practice. Based on the technical requirements of the semi-conductive sheath material for submarine cables and the range of values in reference [15], and considering the advantages of reducing the circulating current and induced voltage in the metal sheaths of long-distance three-core submarine cables, the resistivity of the semi-conductive layer is set to 2.57×10^{-6} ($\Omega \cdot$ m).

Table 1 Dimension parameters and simplified structure of the submarine cable

Original structure	Nominal thickness (mm)	Approximate outer diameter (mm)	Simplified structure
Copper conductor	/	26.5	Core conductor
Conductor shield	2.6	31.7	Conductor shield
Insulation	27.0	85.7	Main insulation
Insulation shield	1.2	88.1	Main insulation shield
Radial water barrier	2×0.5	90.1	
Metal sheath	3.5	97.1	Metal sheath
Semi-conductive PE sheath	3.3	103.7	Semi-conductive sheath
Filler	/	/	Filling layer
Wrapping tape	2×0.3	224.0	
PP inner cushion layer	1.5	227.0	
Galvanized steel wire	$6.0 \times 113 \pm 3$ pieces	239.0	Armor
Asphalt	0.2	/	Armor insulation sheath
PP outer covering layer	4.0	246.6	

Table 2 Material parameters of the 220 kV three-core submarine cable

Simplified structure	Resistivity at 20 °C($\Omega \cdot$ m)	Relative permeability	Relative dielectric constant
Core conductor	1.724×10^{-8}	1	—
Conductor shield	—	—	—
Main insulation	—	1	2.5
Main insulation shield	—	—	—
Metal sheath	2.14×10^{-7}	1	—
Semi-conductive sheath	2.57×10^{-6}	1	—
Filling layer	—	1	81
Armor	1.38×10^{-7}	300	—
Armor insulation sheath	—	1	1.5329

3 Sequence Parameter Calculation for the Three-Core Submarine Cables

3.1 Simulation Based on Multi-conductor System Modeling

A three-core submarine cable with semi-conductive sheaths can be regarded as a multi-conductor system consisting of the cores, sheaths and armor, which includes the following 10 conductor structures: three-phase cores, three-phase metal sheaths, three-phase semi-conductive sheaths, and an armor, with significant electromagnetic coupling between each conductor. Therefore, the impedance matrix of a three-core submarine cable is a 10th order matrix.

According to the meaning of each element in the impedance matrix [16], it can be written in the form of a block matrix as follows:

$$\mathbf{Z_f} = \begin{bmatrix} \mathbf{Z_C} & \mathbf{Z_{CS}} & \mathbf{Z_{CB}} & \mathbf{Z_{CP}} \\ \mathbf{Z_{CS}} & \mathbf{Z_S} & \mathbf{Z_{SB}} & \mathbf{Z_{SP}} \\ \mathbf{Z_{CB}} & \mathbf{Z_{SB}} & \mathbf{Z_B} & \mathbf{Z_{BP}} \\ \mathbf{Z_{PC}} & \mathbf{Z_{PS}} & \mathbf{Z_{PB}} & \mathbf{Z_P} \end{bmatrix} \tag{1}$$

where, $\mathbf{Z_C}$ is a 3×3 impedance matrix of the three-phase cores; $\mathbf{Z_S}$ is a 3×3 impedance matrix of the three-phase metal sheaths; $\mathbf{Z_B}$ is a 3×3 impedance matrix of the three-phase semi-conductive sheaths; $\mathbf{Z_P}$ is a 1×1 impedance matrix of the armor; $\mathbf{Z_{CS}}$ is a 3×3 mutual impedance matrix between the cores and metal sheaths; $\mathbf{Z_{CB}}$ is a 3×3 mutual impedance matrix between the cores and semi-conductive sheaths; $\mathbf{Z_{SB}}$ is a 3×3 mutual impedance matrix between the metal sheaths and semi-conductive sheaths; $\mathbf{Z_{CP}} = \mathbf{Z_{PC}^T}$ is a 3×1 mutual impedance matrix between

the cores and armor; $\mathbf{Z}_{SP} = \mathbf{Z}_{PS}^T$ is a 3×1 mutual impedance matrix between the metal sheaths and armor; $\mathbf{Z}_{BP} = \mathbf{Z}_{PB}^T$ is a 3×1 mutual impedance matrix between the semi-conductive sheaths and armor.

Therefore, the transmission equation of a three-core submarine cable can be expressed in the following form:

$$
-\frac{d}{dx}\begin{bmatrix} \mathbf{U}_C \\ \mathbf{U}_S \\ \mathbf{U}_B \\ \mathbf{U}_P \end{bmatrix} = \begin{bmatrix} \mathbf{Z}_C & \mathbf{Z}_{CS} & \mathbf{Z}_{CB} & \mathbf{Z}_{CP} \\ \mathbf{Z}_{CS} & \mathbf{Z}_S & \mathbf{Z}_{SB} & \mathbf{Z}_{SP} \\ \mathbf{Z}_{CB} & \mathbf{Z}_{SB} & \mathbf{Z}_B & \mathbf{Z}_{BP} \\ \mathbf{Z}_{PC} & \mathbf{Z}_{PS} & \mathbf{Z}_{PB} & \mathbf{Z}_P \end{bmatrix}\begin{bmatrix} \mathbf{I}_C \\ \mathbf{I}_S \\ \mathbf{I}_B \\ \mathbf{I}_P \end{bmatrix}
\tag{2}
$$

where, $\mathbf{U}_C = [u_{Ca}\ u_{Cb}\ u_{Cc}]^T$ is the voltage of the three-phase cores; $\mathbf{U}_S = [u_{Sa}\ u_{Sb}\ u_{Sc}]^T$ is the voltage of the three-phase metal sheaths; $\mathbf{U}_B = [u_{Ba}\ u_{Bb}\ u_{Bc}]^T$ is the voltage of the three-phase semi-conductive sheaths; $\mathbf{U}_P = [u_P]$ is the voltage of the armor; $\mathbf{I}_C = [i_{Ca}\ i_{Cb}\ i_{Cc}]^T$ is the current of the three-phase cores; $\mathbf{I}_S = [i_{Sa}\ i_{Sb}\ i_{Sc}]^T$ is the current of the three-phase metal sheaths; $\mathbf{I}_B = [i_{Ba}\ i_{Bb}\ i_{Bc}]^T$ is the current of the three-phase semi-conductive sheaths; $\mathbf{I}_P = [i_P]$ is the current of the armor.

In engineering, the metal sheaths and armor are usually interconnected and grounded at both ends of the submarine cable line, and the semi-conductive sheaths is used to replace the insulation sheaths between the metal sheaths and armor. Therefore, it can be considered that the entire submarine cable is grounded. Let $d\mathbf{U}_S = \mathbf{O}_{3\times1}$, $d\mathbf{U}_B = \mathbf{O}_{3\times1}$, and $d\mathbf{U}_P = \mathbf{O}_{1\times1}$, and then Eq. (2) can be simplified to the following formula:

$$
\begin{cases}
-\dfrac{d}{dx}\begin{bmatrix} \mathbf{U}_C \\ \mathbf{O}_{7\times1} \end{bmatrix} = \begin{bmatrix} \mathbf{Z}_C & \mathbf{Z}_{CSBP} \\ \mathbf{Z}_{SBPC} & \mathbf{Z}_{SBP} \end{bmatrix}\begin{bmatrix} \mathbf{I}_C \\ \mathbf{I}_{SBP} \end{bmatrix} \\[6pt]
\mathbf{Z}_{CSBP} = \begin{bmatrix} \mathbf{Z}_{CS} & \mathbf{Z}_{CB} & \mathbf{Z}_{CP} \end{bmatrix} \\[6pt]
\mathbf{Z}_{SBPC} = \begin{bmatrix} \mathbf{Z}_{CS} & \mathbf{Z}_{CB} & \mathbf{Z}_{PC} \end{bmatrix}^T \\[6pt]
\mathbf{Z}_{SBP} = \begin{bmatrix} \mathbf{Z}_S & \mathbf{Z}_{SB} & \mathbf{Z}_{SP} \\ \mathbf{Z}_{SB} & \mathbf{Z}_B & \mathbf{Z}_{BP} \\ \mathbf{Z}_{PS} & \mathbf{Z}_{PB} & \mathbf{Z}_P \end{bmatrix} \\[6pt]
\mathbf{I}_{SBP} = \begin{bmatrix} \mathbf{I}_S & \mathbf{I}_B & \mathbf{I}_P \end{bmatrix}^T
\end{cases}
\tag{3}
$$

Further elimination of the sheaths and armor parameterization leads to:

$$
\begin{cases}
-\dfrac{d\mathbf{U}_C}{dx} = \mathbf{Z}_F\mathbf{I}_C \\[6pt]
\mathbf{Z}_F = \mathbf{Z}_C - \mathbf{Z}_{CSBP}\mathbf{Z}_{SBP}^{-1}\mathbf{Z}_{SBPC}
\end{cases}
\tag{4}
$$

where, $\mathbf{Z}_F$ is a 3×3 equivalent three-phase impedance matrix of the submarine cable line.

The sequence impedance matrix $\mathbf{Z}_{sq}$ can be obtained by performing the following transformation on $\mathbf{Z}_F$ based on the principle of symmetric components.

$$
\begin{cases}
\mathbf{Z}_{sq} = \mathbf{T}^{-1}\mathbf{Z}_F\mathbf{T} \\
\mathbf{T} = \dfrac{1}{\sqrt{3}}\begin{bmatrix} 1 & 1 & 1 \\ 1 & a^2 & a \\ 1 & a & a^2 \end{bmatrix}, \ a = e^{j120°}
\end{cases}
\tag{5}
$$

The diagonal elements in $\mathbf{Z}_{sq}$ refer to the zero sequence impedance, positive sequence impedance, and negative sequence impedance of the three-core submarine cable line. The calculation method for the sequence admittance parameter is the same as above.

According to the above calculation principle, accurately obtaining the impedance matrix and admittance matrix of a three-core submarine cable is a prerequisite for calculating the sequence parameters. Based on the known submarine cable structure and material parameters, a simulation model of a three-core submarine cable as shown in Fig. 2 is established in PSCAD to calculate the impedance and admittance matrices of the cable considering the semi-conductive grounding structure. Among them, the burial depth is the distance between the submarine cable position and sea level, set as 50 m. Considering the impact of the seawater on seabed soil [17], the environmental resistivity is set to 10 $\Omega \cdot$ m. The cable armor has been soaked in seawater for a long time, so it can be considered as continuous grounding. Therefore, the insulation sheath structure of the armor is ignored in the simulation.

To illustrate the impact of the semi-conductive sheaths on the calculated results of sequence parameters, this paper also builds a submarine cable simulation model without semi-conductive sheaths. The comparison results of the sequence parameter simulation between the two models are shown in Table 3.

Fig. 2 Schematic diagram of three-core submarine cable simulation structure
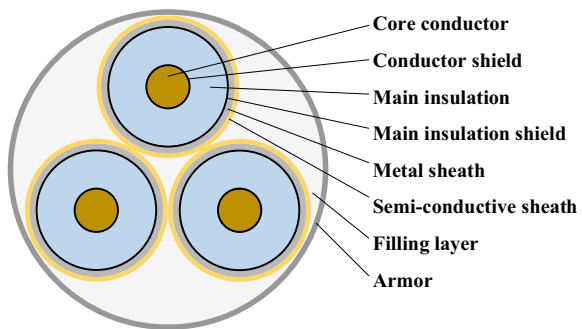
Table 3 Simulation results of sequence parameters

Sequence parameter	Without semi-conductive sheaths		With semi-conductive sheaths	
	Positive sequence	Zero sequence	Positive sequence	Zero sequence
Resistance (Ω/km)	0.0612	0.1968	0.0621	0.1874
Reactance (Ω/km)	0.1535	0.1322	0.1524	0.1281
Susceptance (S/km)	4.42×10^{-5}	4.42×10^{-5}	4.42×10^{-5}	4.42×10^{-5}

3.2 Estimation of Sequence Parameters Based on IEC Formulas

There is no calculation formula for the sequence parameters of submarine cables with semi-conductive sheaths and armor in the IEC standard. So currently the formulas for the sequence parameters of ordinary insulated cables in standard are often used in engineering design for the approximate estimation.

For this example of the submarine cable, the capacitance C per unit length of the cable is:

$$C = \frac{\varepsilon}{18 \ln\left(\frac{D_i}{d_{cs}}\right)} \times 10^{-9} \text{ (F/m)} \tag{6}$$

where, D_i is the diameter of the main insulation; d_{cs} is the diameter of the conductor shield; ε is the relative dielectric constant of the main insulation.

The capacitance B per unit length of the cable is:

$$B = 2\pi f C \text{ (S/m)} \tag{7}$$

where, f is power frequency.

According to the above formula, the admittance per kilometer of the submarine cable in this calculation example is $B_{IEC} = 4.387 \times 10^{-5}$ (S/km).

The AC resistance of the conductor at 20 °C is:

$$R = R_0(1 + y_s + y_p) \tag{8}$$

where, R_0 is the conductor DC resistance at 20 °C; according to relevant standards, $R_0 = 3.66 \times 10^{-5}$ (Ω/m); y_s is the skin effect coefficient; y_p is the proximity effect coefficient. The calculated AC resistance of the submarine cable core conductor at 20 °C is $R = 3.925 \times 10^{-5}$ (Ω/m).

For cables with metal sheaths grounded at both ends, the positive sequence impedance can be calculated as follows [18]:

$$Z_1 = R + j\mu_0 f\left(\frac{1}{4} + \ln\frac{2GMD}{d_c}\right) + \frac{\left(\mu_0 f \ln\frac{GMD}{r_{Sm}}\right)^2}{R_s + j\mu_0 f \ln\frac{GMD}{r_{Sm}}} \text{ (Ω/m)} \tag{9}$$

where, μ_0 is vacuum permeability; GMD is the geometric mutual distance among three-phase conductors; $r_{Sm} = (r_{Si} + r_{So})/2$ is the middle radius of the metal sheaths; r_{Si} is the inner radius of metal sheaths; r_{So} is the outer radius of metal sheaths; R_s is sheath resistance per unit length.

According to the above formula, the positive sequence impedance of each kilometer in this calculation example is $Z_{1-IEC} = 0.0506 + j0.1423 (\Omega/\text{km})$.

For cables with metal sheaths grounded at both ends, the zero sequence impedance can be calculated as follows [18]:

$$Z_0 = R + 3\pi f \frac{\mu_0}{4} + j\mu_0 f \left(\frac{1}{4} + 3 \ln \frac{660\sqrt{\rho_e/f}}{\sqrt[3]{d_c GMD^2/2}} \right)$$
$$- \frac{\left(3\pi f \frac{\mu_0}{4} + j3\mu_0 f \ln \frac{660\sqrt{\rho_e/f}}{\sqrt[3]{r_{Sm}GMD^2}} \right)^2}{R_S + 3\pi f \frac{\mu_0}{4} + j3\mu_0 f \ln \frac{660\sqrt{\rho_e/f}}{\sqrt[3]{r_{Sm}GMD^2}}} (\Omega/\text{m}) \qquad (10)$$

where, ρ_e is the soil resistivity, taken as $10\,\Omega \cdot \text{m}$.

According to the above formula, the zero sequence impedance of each kilometer in this calculation example is $Z_{0-IEC} = 0.2411 + j0.1215 (\Omega/\text{km})$.

4 Measurement of Sequence Parameters of the Three-Core Submarine Cable

In this paper, the YTLP transmission line power frequency parameter test system is used to measure the sequence parameters of the submarine cable. During the test, both ends of the sheaths and armor are directly grounded, and then different excitations are applied to the core to obtain positive sequence and zero sequence parameters.

The measurement test wiring methods of different sequence parameters are as follows:

(1) Positive Sequence Impedance: the three-phase cores are short-circuited and not grounded at the end of the submarine cable line, and a three-phase power frequency power supply is applied at the head of the line.
(2) Zero Sequence Impedance: the three-phase cores are short-circuited to ground at the end of the submarine cable line; and short-circuited at the head of the line with a single-phase power frequency power supply applied.
(3) Positive Sequence Capacitance: the three-phase cores are set to open circuits at the end of the submarine cable line, and a three-phase power frequency power supply is applied to the head of the line.
(4) Zero Sequence Capacitance: the three-phase cores are short-circuited and not grounded at the end of the submarine cable line, and short-circuited at the head of the line with a single-phase power frequency power supply applied.

Table 4 Measured results of submarine cable sequence parameters

Measurement	Positive sequence	Zero sequence
Resistance (Ω/km)	0.0688	0.1585
Reactance (Ω/km)	0.1510	0.1464
Susceptance (S/km)	4.43×10^{-5}	4.44×10^{-5}

The length of the submarine cable tested in this paper is 68 km. The measured results of the above-mentioned recording instruments are the sequence parameters of the entire length of the line. The results of sequence parameters converted to unit length are shown in Table 4.

5   Comparison and Analysis of Calculated and Measured Results

There are some factors affecting the measurement accuracy of the sequence parameters in the measurement test of the submarine cable, such as the influence of power frequency interference voltage on the zero sequence parameters, the technical problems of the test personnel, and the sequence parameters measured at different temperatures will also be different. However, compared with formula estimation and simulation modeling, the measurement method can best reflect the actual situation of the submarine cable. Therefore, taking the actual measured value as the true value, the errors of the IEC formula estimation results and the simulation results and the measured value are shown in Table 5. In Table 5, the formula estimation error E_{IEC} and simulation error E_{PSC} are calculated by Eqs. (11) and (12).

$$E_{\text{IEC}} = \frac{x_{\text{mea}} - x_{\text{IEC}}}{x_{\text{mea}}} \times 100\% \tag{11}$$

$$E_{\text{PSC}} = \frac{x_{\text{mea}} - x_{\text{PSC}}}{x_{\text{mea}}} \times 100\% \tag{12}$$

where, $x_{\text{mea}}, x_{\text{IEC}}, x_{\text{PSC}}$ are measured values, formula estimated values, and simulation values, respectively.

Generally speaking, the errors of the formula estimation, simulation and actual measurement results of positive sequence susceptance and zero sequence susceptance are very small, because there are few factors that affect the susceptance calculated results. As long as the dimensions of the main insulation and conductor shield can be obtained accurately, the correct susceptance can be obtained. The simulation results of positive sequence impedance and zero sequence impedance are more accurate than the formula estimation, and the simulation results considering the semi-conductive sheaths are closer to the measured values than those without the semi-conductive sheaths. This shows that compared with the IEC formulas, the simulation

Table 5 Errors of calculated and measured results of sequence parameters

Sequence parameters	Formula estimation error (%)	Simulation errors (%)	
		Without semi-conductive sheaths	With semi-conductive sheaths
Positive sequence resistance (Ω/km)	26.453	11.047	9.782
Positive sequence reactance (Ω/km)	5.737	−1.683	−0.974
Positive sequence admittance (S/km)	0.901	0.127	0.126
Zero sequence resistance (Ω/km)	−52.142	−24.188	−18.237
Zero sequence reactance (Ω/km)	17.020	9.780	12.505
Zero sequence admittance (S/km)	1.127	0.354	0.354

can take the structure of the submarine cable and laying environment into consideration more fully, and can obtain more accurate results. Neglecting the semi-conductive sheaths during simulation modeling will result in certain errors. Reasonable setting of the structure and parameters of the semiconductive sheaths is indispensable for the simulation of the sequence parameters of the semi-conductive submarine cable.

Further analysis shows that the error of the positive sequence impedance mainly comes from the structure and temperature of the submarine cable. The armor and semi-conductive structure of the three-core submarine cable are not considered in the formula estimation, and the coupling relationship between the armor, semi-conductive structure and other conductors is not considered, either. Therefore, the formulas for positive sequence resistance and positive sequence reactance have bigger errors in estimation. Although the simulation results are better than the formula estimation, there is still a certain error between the positive sequence resistance calculated by simulation and the measured value. This is because the temperature of the submarine cable conductor is difficult to obtain accurately during measurement, and the resistivity of the conductor is easily affected by temperature. In this simulation example, the resistivity of the cores, sheaths and armored conductor of the submarine cable is set to the resistivity at 20 °C, which is somewhat different from the field situation.

Due to the difficulty in fully expressing the grounding structure of the three-core submarine cable in the formulas or simulation, it brings errors to the calculation of the zero sequence impedance. When measuring zero sequence impedance, all paths connected between the head and end grounding points of the cable are zero sequence current circuits. The main circuit branches include the metal sheaths, semi-conductive structures, and armor. The IEC formulas do not consider semi-conductive structures, which is equivalent to reducing one branch of the parallel circuit of zero

sequence current, resulting in a significant increase in zero sequence resistance. The simulation takes into account the influence of the semi-conductive sheaths, which is more accurate than the formula estimation. However, due to long-term immersion in seawater, the cable filling parts actually also has semi-conductivity. Therefore, compared to the actual situation, the cable simulation model is equivalent to having an additional parallel branch in the zero sequence current circuit, so the simulated zero sequence resistance is larger than the measured value. Similarly, the special semi-conductive grounding structure is also one of the reasons for the error of the zero sequence reactance calculation. In addition, the difficulty in obtaining actual soil resistivity and burial depth can also affect the accurate calculation of zero sequence impedance.

In summary, the simulation model of the submarine cable considering semi-conductive sheaths in this paper is more accurate than the IEC formulas for calculating the sequence parameters. But due to the complex structure and environment of the three-core submarine cable, it is necessary to carry out on-site measurement tests on the sequence parameters in order to reflect the actual situation of the cable more comprehensively.

6   Conclusion

In this paper, for a 220 kV three-core AC semi-conductive submarine cable, the calculation process of its sequence parameters is derived based on the multi-conductor system modeling method and the principle of symmetrical components. Then the simulation model of the sequence parameters is established, and the on-site measurement test of the sequence parameters is carried out. By comparing the results of the simulation, IEC formula estimation and field measurement, and analyzing the errors and causes of errors, the following conclusions can be drawn:

(1) The submarine cable simulation model established in this paper considering the semi-conductive sheaths is generally more suitable for the actual situation than the model without the semi-conductive sheaths, which effectively improves the calculation accuracy of the positive sequence resistance, positive sequence reactance and zero sequence resistance. Compared with the IEC formula estimation, the sequence parameter simulation takes into account more structure and environmental conditions of the submarine cable, and the simulation results are closer to the actual measurement. It can provide reference for engineering designers.

(2) There is a certain error between the simulation results and the measured values, because the measured values can more truly reflect the unknown material parameters and the seabed environment than the simulation model, so the measured values of submarine cable sequence parameters can provide more reliable line data for power system safety analysis.

References

1. Ma C, Li JT, Zhang BY, Yan ZX, Sun ZH (2022) Calculation of high frequency electrical parameters of buried cable based on electromagnetic mode analysis. Electr Mach Control 26(7):1–9 (in Chinese)
2. Wang XT, Xiang ZT, Ban LG et al (2013) Calculation and analysis on power-frequency parameters for 500 kV cable lines. Power Syst Technol 37(8):2310–2315 (in Chinese)
3. Benato R, Caciolli L (2012) Sequence impedances of insulated cables: measurements versus computation. IEEE PES transmission and distribution conference and exposition. IEEE Press, Florida, USA, pp 1–7
4. Xu Z, Qian J (2013) Comparison of different methods for calculating electrical parameters of power cables. High Voltage Eng 39(3):689–697 (in Chinese)
5. Ren HT, Zheng SS (2021) Study on parameter unbalance of 500 kV double circuit cable line considering different arrangement. 4th International conference on energy, electrical and power engineering (CEEPE). IEEE Press, Chongqing, China, pp 611–615
6. Zhou ZQ, Liu XZ, Wang SH et al (2018) Simulation calculation of transient voltages on insulation and sheath along 500 kV XLPE submarine cable. High Voltage Eng 44(8):2725–2731 (in Chinese)
7. Zhang HM, Zhang HJ, Zhao YQ et al (2022) Field-circuit coupled modelling of superconducting cable for positive and zero sequence impedance analysis. In: IEEE 5th International electrical and energy conference (CIEEC). IEEE Press, Nanjing, China, pp 4629–4632
8. Tian SJ, Liu XZ, Liu H et al (2017) Simulating calculations of transient voltages and insulation coordination on 500 kV AC XLPE sub-marine cable line. In: Proceedings of 2017 International conference on high voltage engineering and power system. IEEE Press, Bali, Indonesia, pp 484–487
9. Zhang JM, Zhang HL, Xie SH et al (2017) Typical application and development prospect of XLPE insulated submarine cable for offshore wind farm in China. Southern Power Syst Technol 11(8):25–33 (in Chinese)
10. Shao SA, Ma X, Feng RN et al (2020) Review of researches on submarine cables at home and abroad. Southern Power Syst Technol 14(11):81–88 (in Chinese)
11. Huang XW, Li XJ, Zuo GQ (2023) Application status and prospect of submarine cable projects at home and abroad. Wire Cable 1:1–6 (in Chinese)
12. Guo YG, Wei X, Yu QY et al (2020) Electrical parameters calculation of 220 kV optical fiber composited three-core submarine cable. Shandong Electr Power 47(11):28–33 (in Chinese)
13. Gustavsen B (2001) Panel session on data for modeling system transients insulated cables. IEEE power engineering society winter meeting. IEEE Press, Columbus, United States, pp 718–723
14. International Electrotechnical Commission (2014) Electric cables—calculation of the current rating Part 1–1: current rating equations (100% load factor) and calculation of losses: IEC 60287-1-1. Switzerland, Geneva
15. Liu Y, Xiao Y, Su Y et al (2018) Loss calculation and influence on ampacity of single-core AC sub-marine cable under different grounding modes. High Voltage Apparatus 54(10):56–62 (in Chinese)
16. Peng N, Zhang P, Liang R (2021) Fault sensing and location of the three-core armored cables in distribution network based on the analysis of the fault-featured transient moduli. Proc CSEE 41(16):5767–5779 (in Chinese)

17. Li JT, Zhang Z, Fang CY et al (2015) Feasibility study on using jacket structure as natural grounding electrode for offshore wind turbines. Insulators Surge Attesters 6:148–153 (in Chinese)
18. International Electrotechnical Commission (2008) Short-circuit currents in three-phase AC systems—Part 2: data of electrical equipment for short-circuit current calculations: IEC 60909-2. Geneva, Switzerland

Finite Element Equivalent Heat Transfer Coefficient Solution for Transformer Windings Based on Asymptotic Homogenization Method

He Zhang, Yadong Liu, Si Chen, Yingjie Yan, and Xiuchen Jiang

Abstract In order to reduce the complexity of calculating the temperature field of a transformer by finite elements analysis software, this paper establishes a method for predicting the winding heat transfer coefficient based on the asymptotic homogenization theory, writes a solution code by matlab, and calculates the equivalent heat transfer coefficient of the winding with temperature. The winding model is simplified by this coefficient, and the temperature field simulation is carried out for the original complex model and the simplified model. The simulation results of the simplified model match with the simulation results of the complex model, which proves that the method can be used for transformer winding finite element model simplification.

Keywords Heat transfer coefficient · Transformer temperature field · Asymptotic homogenization · Transformer windings

H. Zhang · Y. Liu (✉) · S. Chen · Y. Yan · X. Jiang
Department of Electrical Engineering, Shanghai Jiao Tong University, Shanghai 200240, China
e-mail: lyd@sjtu.edu.cn

H. Zhang
e-mail: zhang_he@sjtu.edu.cn

S. Chen
e-mail: chensi_425@sjtu.edu.cn

Y. Yan
e-mail: yanyingjie@sjtu.edu.cn

X. Jiang
e-mail: xcjiang@sjtu.edu.cn

1 Introduction

Power transformer is an important equipment in power system. Accurate acquisition of hot spot temperature of winding can provide important reference for guiding transformer load control and ensuring safe and efficient operation of transformer equipment [1–3].

At present, finite element simulation has been more and more widely used in transformer temperature calculation [3–8]. However, the mesh division is required to perform finite element analysis, and the insulation layer of winding is very thin. The mesh size needs to be small when modeling the dissection of transformer winding, resulting in a large number of overall dissection meshes, which increases the calculation volume and calculation time [9]. The heat transfer coefficient is a key physical parameter in the temperature field calculation. In the winding modeling, the winding is considered as a whole and the equivalent heat transfer coefficient of the insulation layer is solved. However, the existing winding equivalent parameter solution process does not consider the insulating oil in the gap between the winding conductors and between the conductors and the insulating paper. The large difference between the thermal conductivity of the insulating oil and the thermal conductivity of the copper conductor as well as the large influence of the thermal conductivity of the insulating oil by the temperature lead to the winding solution equivalent must consider the influence caused by the insulating oil and temperature in the gap.

The winding interior can be considered as a periodic composite structure, and the winding can also be considered as a composite material consisting of insulating paper, enameled wire, and insulating oil. The current methods for predicting periodic composites are roughly divided into two categories: analytical and numerical methods, and the numerical method contains the representative cell method and the asymptotic homogenization method, among which the numerical method can consider the internal structural changes and is more universal. Among the numerical methods, the asymptotic homogenization method is based on strict mathematical derivation, and its calculation accuracy is higher than that of the representative unit method, so the asymptotic homogenization method is chosen to calculate the equivalent heat transfer coefficient of the winding.

2 Asymptotic Homogenization Equivalent Heat Transfer Coefficient Solution

The asymptotic homogenization method is a multiscale approach to solving the problem using strictly mathematical methods. The specific implementation of this method for solving the thermal conductivity of periodic composites is as follows [10–12]:

(1) Expansion of the material temperature field into an asymptotic expression containing macroscopic and microscopic scales using small parameters as a bridge, based on the scaling characteristics of materials with periodicity at the fine scale;

The temperature representation $T_{(x)}$ contains the macroscopic quantity x, the microscopic quantity y and the small parameter ε.

$$T_{(x)} = T_0(\mathbf{x}, \mathbf{y}) + \varepsilon T_1(\mathbf{x}, \mathbf{y}) + \varepsilon^2 T_2(\mathbf{x}, \mathbf{y}) + \cdots$$

(1)

The equation linking the macroscopic quantity x, the microscopic quantity y and the small parameter ε is shown in Eq. (2).

$$y = \frac{x}{\varepsilon}$$

(2)

(2) Substitute the temperature expression into the macroscopic heat transfer equation and simplify the equation

$$\int_\Omega K_{ij} \frac{\partial T}{\partial x_i} \cdot \frac{\partial \delta T}{\partial x_j} d\Omega + \int_{\Gamma_1} \alpha(T - T_f) \delta T ds$$

$$+ \int_{\Gamma_2} q \delta T ds = 0, \forall T \in T_\Omega$$

(3)

Simplify to get Eq. (4)

$$\int_\Omega K_{ij}^\varepsilon \left[\frac{\partial T_0}{\partial x_i} + \varepsilon \cdot \frac{\partial T_1}{\partial x_i} + \frac{\partial T_1}{\partial y_i} + \varepsilon^2 \cdot \frac{\partial T_2}{\partial x_i} + \varepsilon \cdot \frac{\partial T_2}{\partial y_i} + \cdots \right] \left(\frac{\partial \delta T}{\partial x_j} + \frac{1}{\varepsilon} \frac{\partial \delta T}{\partial y_j} \right) d\Omega$$

$$+ \int_{\Gamma_1} \alpha(T_0 + \varepsilon T_1 + \varepsilon^2 T_2 + \cdots - T_f) \delta T \, dS + \int_{\Gamma_2} q \delta T \, dS = 0, \ \forall \delta T \in T_{a \times Y}$$

(4)

(3) Considering ε as the independent variable, the equation is constant.

Compare each order of the equation left and right ε.
ε^0:

$$\int K_{ij}^\varepsilon \left(\frac{\partial T_0}{\partial x_i} \frac{\partial \delta T}{\partial x} + \frac{\partial T_1}{\partial y_1} \frac{\partial \delta T}{\partial x} + \frac{\partial T_1}{\partial x_1} \frac{\partial \delta T}{\partial y_j} + \frac{\partial T_2}{\partial y_1} \frac{\partial \delta T}{\partial y_1} \right) d\Omega$$

$$+ \int_{\Gamma_1} \alpha T_0 \delta T \, dS + \int_{\Gamma_2} \overline{q} \delta T \, dS = 0, \forall \delta T \in T_{\Omega \times Y}$$

(5)

ε^{-1}:

$$\int_\Omega K_{ij}^\varepsilon \left(\frac{\partial T_0}{\partial x_i} + \frac{\partial T_1}{\partial y_i} \right) \frac{\partial \delta T}{\partial y_i} \mathrm{d}\Omega = 0, \quad \forall \delta T \in T_{\Omega \times Y} \tag{6}$$

By Eq. (6) then we further obtain:

$$T_1(\boldsymbol{x}, \boldsymbol{y}) = -N(\boldsymbol{y}) \frac{\partial T_0}{\partial x_i} \tag{7}$$

N($\boldsymbol{y}$) is the characteristic temperature field.

(4) The expression is simplified and combined with the macroscopic equation to obtain the equivalent coefficients.

Substitute Eq. (7) into Eq. (6) and simplify to obtain Eq. (8).

$$\int_\Omega \left[\frac{1}{|Y|} \int_Y K_{ij}^\varepsilon \left(\frac{\partial \mathrm{T}_0}{\partial x_i} + \frac{\partial T_1}{\partial y_i} \right) \mathrm{d}Y \right] \frac{\partial \delta T}{\partial x} d\Omega$$
$$+ \int_{\Gamma_1} \alpha (T_0 - T_f) \delta T \, dS + \int_{\Gamma_2} \overline{q} \delta T \, dS = 0, \ \forall \delta T \in T_\Omega \tag{8}$$

Matching Eq. (8) and the macroscopic heat transfer Eq. (3), the equivalent heat transfer coefficient calculation expression can be obtained.

C_{ij}: Equivalent heat transfer coefficient

$$C_{ij} = \frac{1}{|Y|} \int_Y K_{ij}^\varepsilon \left(1 + \frac{\partial \mathrm{N}}{\partial y_i} \right) dY \tag{9}$$

3   Simulation Simplification Example Analysis

3.1   Transformer Winding Simulation Model and Unit Cell Model

A two-dimensional model of the winding cross section is constructed in comsol, and a suitable single cell is selected as the calculation model for the progressive homogenization method. The comsol model and the single cell model are shown in Fig. 1. The overall model is 17 mm high and 7.1 mm wide, the diameter of copper conductor in the single cell is 0.71 mm, the insulating cardboard is 1.42 mm long and 0.14 mm wide, and the rest of the gap between copper conductor and copper conductor is filled by insulating oil.
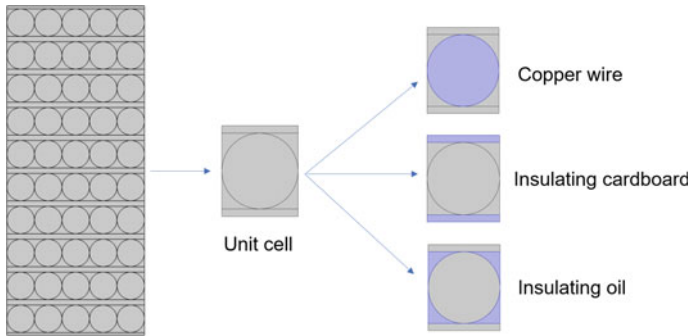
Fig. 1 Transformer winding simulation model and unit cell model

Table 1 Thermal conductivity of various materials of winding [8, 13]

Material	Copper	Insulating cardboard	Insulating oil
Heat transfer coefficient W/ (m K)	400	0.19	$0.1509 - 7.101 \times 10^{-5}$ T

The thermal conductivity of each type of material is shown in Table 1.

3.2 Calculation of Equivalent Heat Transfer Parameters for Windings

Write the progressive homogenization calculation code in matlab to calculate the equivalent heat transfer coefficient of the winding in the operating temperature interval variation value, the calculation results are fitted as shown in Fig. 2.

3.3 Simplified Model of Winding and Temperature Field Calculation

In this paper, the simplification process by the progressive homogenization method is shown in Fig. 3. The simplified model is transformed into a homogeneous material with the same length and width as the original model, and the heat transfer coefficient is solved by the progressive homogenization method.

The same boundary conditions are imposed on the original complex model and the simplified model: the bottom end is a constant 400 k thermostatic plate, the upper end and the left and right sides are set with convective heat transfer, the heat transfer coefficient is set to 10 W/(m^2 K), observe the temperature distribution in the
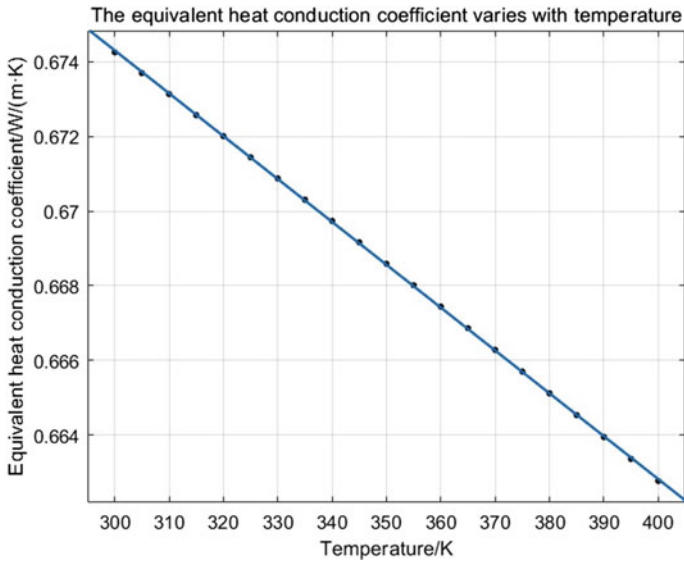
Fig. 2 Equivalent heat transfer coefficient with temperature
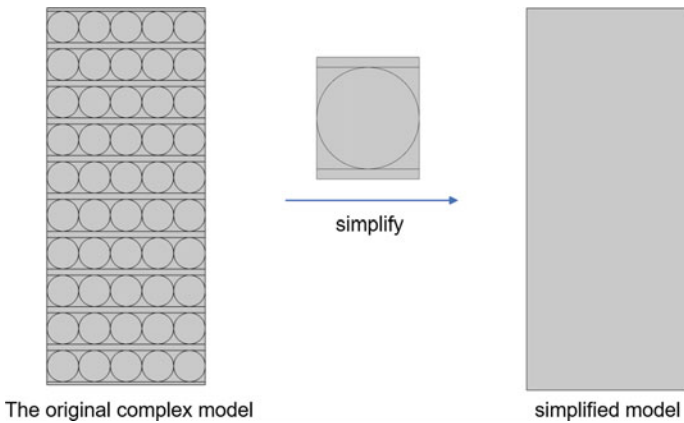
Fig. 3 Simplified model process diagram by asymptotic homogenization method

rightmost y-direction of the original model and the simplified model, and the results are shown in Fig. 4. The simplified model replaces the complex model with good effect and can meet the engineering needs.
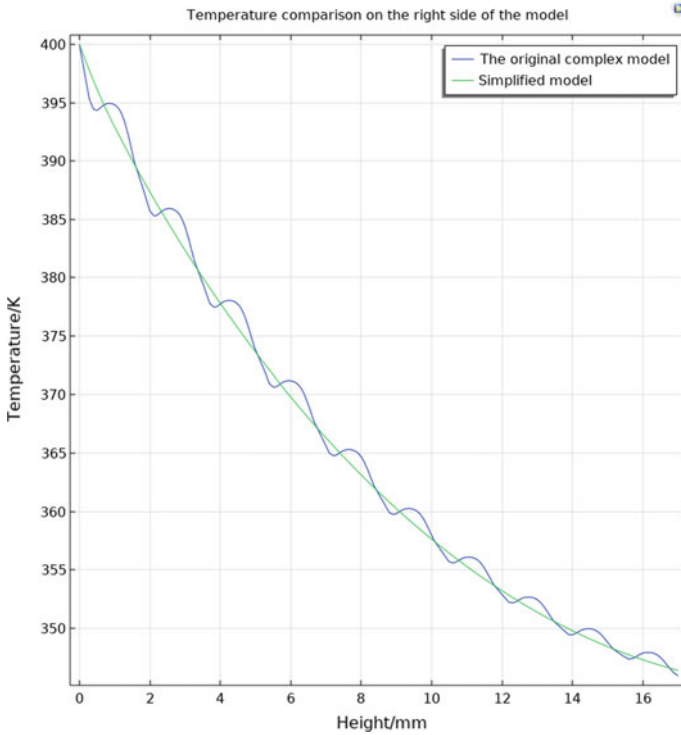
Fig. 4 Temperature comparison chart on the right side of the model

4   Conclusion

This paper calculates the equivalent heat transfer coefficient of winding containing transformer insulating oil based on the asymptotic homogenization method, and uses this coefficient to simplify the model and compare it with the original complex model to verify its effectiveness in simplifying the finite element model of the winding. The results show that:

(1) Variation of the heat conduction coefficient of transformer insulating oil with temperature leads to variation of the overall equivalent parameters with temperature;

(2) It is reliable to use the asymptotic homogenization method to calculate the equivalent heat transfer coefficient of winding containing transformer insulating oil to simplify the original complex model of transformer.

References

1. Ruan J, Deng Y, Huang D, Duan C, Gong R, Quan Y, Hu Y, Rong Q (2020) HST calculation of a 10 kV oil-immersed transformer with 3D coupled-field method. IET Electr Power Appl 14:921–928. https://doi.org/10.1049/iet-epa.2019.0469
2. Tu Y, Chen J, Wang S et al (2016) Moisture migration in oil-impregnated film insulation under thermal ageing. IEEE Trans Dielectr Electr Insul 23(2):1135–1141
3. Li Y, Shen W, An G et al (2023) Comparison of heat transfer characteristics between natural ester oil and mineral oil in large oil-immersed transformer. Heat Mass Transfer 59(4):729–739. https://doi.org/10.1007/s00231-022-03289-w
4. Chen S et al (2022) Inversion and localization of turn-to-turn short-circuit faults in 10 kV oil-immersed transformers. High Voltage Engineering 1–13 (in Chinese)
5. Zhou L et al (2018) Simulation on three-dimensional temperature field and oil flow field of oil-immersed transformer based on polyhedral mesh. High Voltage Engineering 44(11):3524–3531 (in Chinese)
6. Diaz EMG et al (2022) CFD analysis of an 800 kV HVDC transformer using rapeseed oil as the cooling fluid. CSEE Journal of Power and Energy Systems 8(5):1508–1518
7. Li L et al (2019) Prediction of oil flow and temperature distribution of transformer winding based on multi-field coupled approach. Journal of Engineering 16:2007–2012
8. Liu Y et al (2022) Framework and application prospect of internal state inversion and reconstruction of power equipment. High Voltage Engineering 48(8):2883–2896 (in Chinese)
9. Deng Y et al (2021) Three dimensional thermal fluid field simulation of 10 kV transformer based on parameter thermal equivalence. Electric Power Automation Equipment 41(4):212–218 (in Chinese)
10. Hasssani B, Hinton E (1998) A review of homogenization and topology optimization I-homogenization theory for media with periodic structure. Comput Struct 69:707–717
11. Hasssani B, Hinton E (1998) A review of homogenization and topology optimization II-analytical and numerical solution of homogenizaitoin equation. Comput Struct 69:719–738
12. Zhang R et al (2014) Realization methods of computational homogenization for thermal conductivity coefficient of composites. Acta Materiae Compositae Sinica 31(6):1581–1587 (in Chinese)
13. Xie Y et al (2016) Multi-physical field coupled method for temperature rise of winding in oil-immersed power transformer. Proceedings of the Chinese Society of Electrical Engineering 36(21):5957–5965 (in Chinese)

Partial Discharge Location Method for Oil-Impregnated Pressboards Based on PSO Algorithm

Ziqi Yang, Ronghao Cao, Dezhao Wu, and Yangchun Cheng

Abstract Before the breakdown of the insulation material, the growth and aging of electrical trees is an important factor leading to the material's final breakdown. The morphology and growth law of electrical trees in insulating materials are the theoretical basis for diagnosing the severity of defects in power equipment and timely warning. Therefore, the study of the method of observing the morphology of electrical trees is of great engineering significance for improving the long-term operation of electrical equipment. However, due to the opacity of the pressboard material, there is no effective observation method for the electrical trees generating inside it. In this paper, it is proposed to model the measurement system, establish a mathematical model for solving inverse problem in the electrostatic field, and combine PSO (particle swarm optimization) to solve the inverse problem to achieve partial discharge location. In addition, the objective function of the optimization algorithm is analyzed, and the methods to improve the accuracy of partial discharge location are explored. On the basis of the previous one-dimensional measurement system, a two-dimensional measurement system is proposed to improve the positioning accuracy in the y direction.

Keywords Electrical trees · Inverse problem · PSO · Partial discharge location

Z. Yang (✉) · R. Cao · D. Wu
School of Electrical and Electronic Engineering, North China Electric Power University,
Beijing 102206, China
e-mail: 120212201439@ncepu.edu.cn

Y. Cheng
Beijing Key Laboratory of High Voltage and EMC, North China Electric Power University,
Beijing 102206, China

1 Introduction

The growth process of electric branches is an important window period for diagnosis and early warning of faults. Most of the power transformers use oil-paper insulation system. However, most scholars at home and abroad focus on the research of electrical trees in transparent materials such as XLPE [1–3].

Due to the opacity of insulating cardboard, there is currently a lack of effective observation means for its internal electrical trees, which limits the intelligent operation and maintenance level of power transformers and restricts the reduction of its failure rate. In recent years, Cheng Yangchun and others have proposed a distributed electric field measurement system [4–10], which can realize the observation of electrical trees in insulating pressboard, which is a breakthrough in the measurement technology of electrical trees in opaque insulating materials. However, the measurement accuracy and the reconstruction accuracy of electric branches need to be improved.

2 Simplification of Electrostatic Field Models for Measurement Systems

The physical diagram of the one-dimensional electric field measurement system is shown in Fig. 1, the measuring system is composed of transformer oil, oil-impregnated pressboard, PCB (printed circuit board), quartz glass, and their dielectric constants are respectively 2.2, 4.5, 3.0–4.0, and 4.4. This model is a needle plate electrode model, oil-impregnated pressboard, PCB and quartz glass were placed between the needle and the plate, as shown in Fig. 1.

Since the dielectric constant of transformer oil is relatively small compared with the other three layers of medium, the measurement system is equivalent to two layers of medium in the calculation, that is, transformer oil is the first layer, oil-impregnated cardboard, PCB, and quartz glass belong to the second layer. The equivalent model is shown in Fig. 2.The relative permittivity of medium 1 is set to 2, and that of medium 2 is set to 4. The thickness of medium 2 is 4.35 mm. The coordinate origin is located

Fig. 1 Needle-plate high-voltage PD test platform

(a) Profile sketch (unit:mm)   **(b) Overall view**
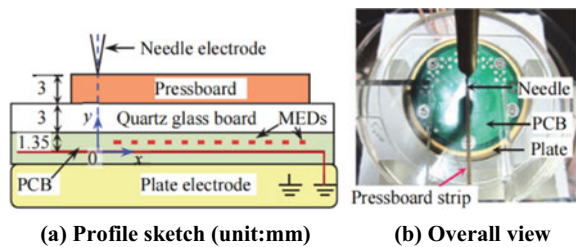
Fig. 2 Point charge equivalent model
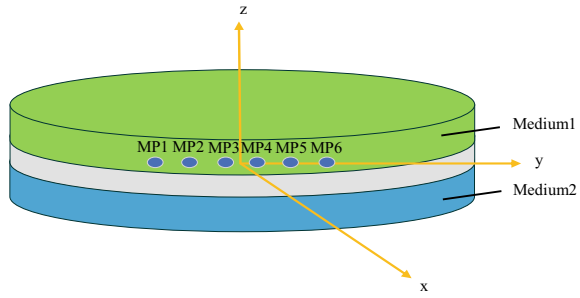
in the center of the model, and the x–y plane is located on the plane between medium 2 and the ground.

3 Mathematical Models for Solving Inverse Problem

3.1 Multi-layer Media Mirroring

Based on the equivalent model in Fig. 2, the mirror method is used to establish the relationship between the position of point charge and the boundary electric field. Theoretically, the two-layer dielectric model requires infinite secondary mirror images in the calculation, which will generate an infinite number of mirror image charges. However, infinite mirror charges are too complicated to calculate. Through theoretical settlement, the error between the five-time mirror image and the infinite mirror image is only 0.01% [10], so the five-time mirror image is sufficient to meet the requirements of the inverse problem calculation of the simulated multi-layer media mirror method. The position relationship between the mirrored charges are shown in Fig. 3, and the electric field strength after substituting the amount of mirror charges at MP1 ~ MP6 E_i is shown in Eq. 1.

$$
E_{iy} = \frac{1}{2\pi\varepsilon_2}\left\{\sum_{j=1}^{2}\frac{(-k_{12})^j q_0(0.00035 + (2ja - y_0))}{\left[(x_i - x_0)^2 + (y_i + (2ja - y_0))^2\right]^{\frac{3}{2}}}\right.
$$
$$
+ \sum_{j=1}^{3}\frac{-(-k_{12})^j q_0(0.00035 - (2ja - y_0))}{\left[(x_i - x_0)^2 + (y_i - (2ja - y_0))^2\right]^{\frac{3}{2}}}
$$
$$
+ \sum_{j=0}^{2}\frac{-(-k_{12})^j q_0(0.00035 + (2ja + y_0))}{\left[(x_i - x_0)^2 + (y_i + (2ja + y_0))^2\right]^{\frac{3}{2}}}
$$
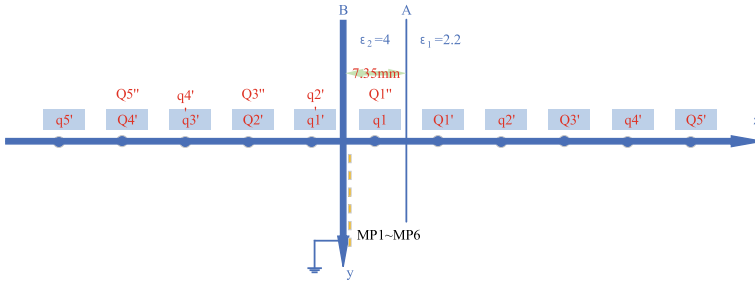
Fig. 3 Location of image charges

$$+ \sum_{j=1}^{2} \frac{(-k_{12})^j q_0 (0.00035 - (2ja + y_0))}{\left[(x_i - x_0)^2 + (y_i - (2na + y_0))^2 \right]^{\frac{3}{2}}} \Bigg\} \tag{1}$$

3.2 Characterization of Electrostatic Field Inverse Problems

The Eq. 1 gives an expression of the electric field strength for the six measurement points $E_i (i = 1, 2, \ldots, 6)$, and by putting them in pairs, the amount of charge q in the formula can be eliminated, then the equation system will reduce a independent variable, as shown in Eq. 2.

$$\frac{E_{(i+1)y}}{E_{iy}} = m_j(x_0, y_0); \ (i = 1, 3, 5 \ j = 1, 2, 3) \tag{2}$$

It can be seen from the formula that the equation system has three unknowns x_0, y_0, z_0, E_{iy} is the electric field strength at the measurement electrode of the measurement system, f_j represents the error between the ratio of the electric field measurement value and the ratio of the value calculated by the electric field formula. The equation system of the inverse problem is established with f_j. This system of equations is too complex and difficult to be solved directly, so this paper uses PSO [11] to solve it. The objective function of the optimization issue is the sum of squares of the error f_j.

$$f_j = m_j(x_0, y_0, z_0) - \frac{E_{iy}}{E_{(i+1)y}} \tag{3}$$

$$F(X) = f_1^2 + f_2^2 + f_3^2 \tag{4}$$

where, $X = [x_0, y_0](x_0 \in (-0.006, 0.012); \ y_0 \in (0.000, 0.01); \ )$.
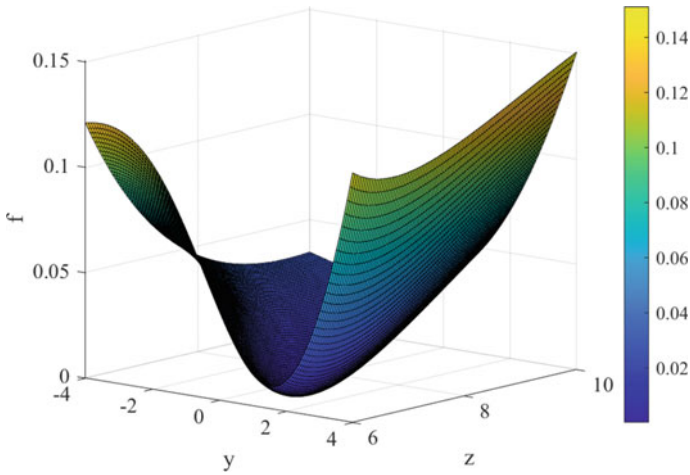
Fig. 4 Objective function image

The correlation determination theorem 1 of functions is used to analyze the independence of the subfunction f_j. According to the theorem, the equations of each subfunction f_1, f_2, and f_3 are independent of each other, so the objective function of Eq. 4 is feasible.

3.3 Objective Function Characterization

Draw the objective function image shown in Fig. 4 with the help of the MATLAB, and analyze the sensitivity of the objective function to explore the function characteristics.

In the range of independent variables, a binary equation system consisting of the electric field strength of measurement points and containing three equations of the form Eq. 3 only has one solution, that is, the objective function constructed based on this equation system only has one point whose function value equal to 0. It is also clear from the objective function image that the objective function constructed based on the electrostatic field inverse problem model has only one minimum point. The sensitivity coefficient around the minimum point of the objective function is relatively large, indicating that the model is easy to solve. At the same time, when using optimization algorithms such as PSO algorithm to solve the objective function, the global optimal solution can be easily found.

4 Data Processing

As shown in Fig. 5 is a distributed measurement system that measures the potential U at the measurement point near the ground electrode. The circuit of the distributed measurement system is described in [9], as shown in Fig. 5.

In the electric field of a single-point charge, the field strength is a fractional power function of the variables x and x_i, as shown in Eq. 1. Therefore, the Taylor expansion of the electric field function should be a higher-order polynomial. Then, the fourth-order polynomial is used to fit the side face data, and the ratio k of the fitted data to the measurement data of each measuring electrode is obtained, and these ratios are the correction coefficients of each measurement electrode.

The measurement system used in this article can measure six voltage signals simultaneously. To simplify the calculation process, the variable V_i is introduced to eliminate fractional powers from the formula.

$$V_i = \Delta U_i^{-\frac{2}{3}} \approx k_2(qy_0)^{-\frac{2}{3}}\left[(x_0 - x_i)^2 + y_0^2\right] \tag{5}$$

It can be seen from the above equation that V_i is about the second-order polynomial function of x_i, so the second-order polynomial fitting curve is used to reduce the error, and the fitting curve is shown in Fig. 6.

(a) profile of PCB

(b) Equivalent

(c) MED array

(d) overall view of PCB
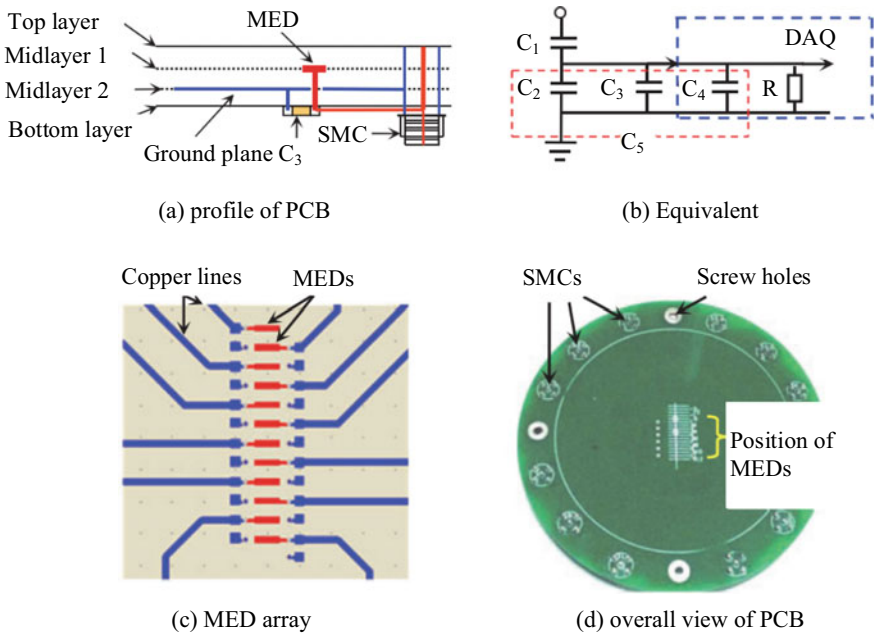
Fig. 5 Distributed potential measurement circuit

Fig. 6 Fitting curve of V_i
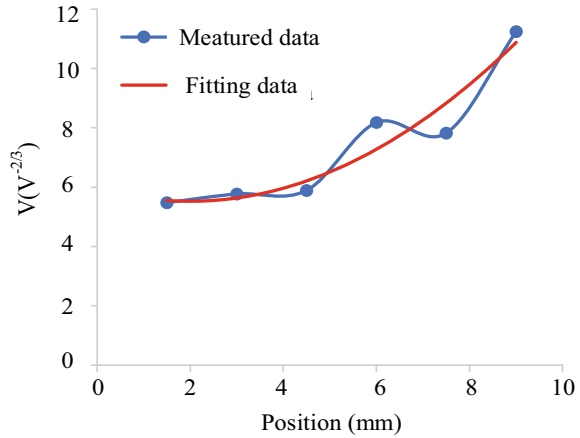
The original experimental measurement data is not accurate, so correction and noise cancellation were important experimental processing steps. First, the correction coefficient k was used to correct the measurement data, and then according to the characteristics of Eq. 5 to fit the data, finally, process the data and backward to obtain the processed experimental data, and then substitute them into the PSO optimization algorithm to solve the inverse problem, the data processing process is shown in Eq. 6.

$$u_i \rightarrow U_i = k_1 u_i = k_1 \Delta y E_i \rightarrow V_i = \Delta U_i^{-\frac{2}{3}} \rightarrow V_i^{'} \rightarrow \Delta U_i^{'} = V_i^{'-\frac{3}{2}} \qquad (6)$$

5　Results and Analysis

The above method is used to solve the inverse problem of obtaining the field source charge position with the known boundary electric field strength, and PD location is drawn in Fig. 7. Fig. 8 shows the PD location diagram calculated by the previous single-layer dielectric equivalent model [9].

Comparing the two sets of diagrams, it can be found that the partial discharge position obtained by the equivalent model of the two layers of medium has stronger aggregation, and the outline of the electric branches is clearer.

Especially in the z direction, the positioning results obtained by the PSO algorithm are more accurate. In this paper, the transformer oil is regarded as an independent layer of medium in the simplified model, and the number of dielectric layers in the calculation is increased, so that the model is closer to the actual measurement system in the z direction, and the accuracy of the positioning results in the z direction is improved. At the same time, compared with the previous calculation, the multilayer

(a) 54th minute   **(b) All partial discharge location**
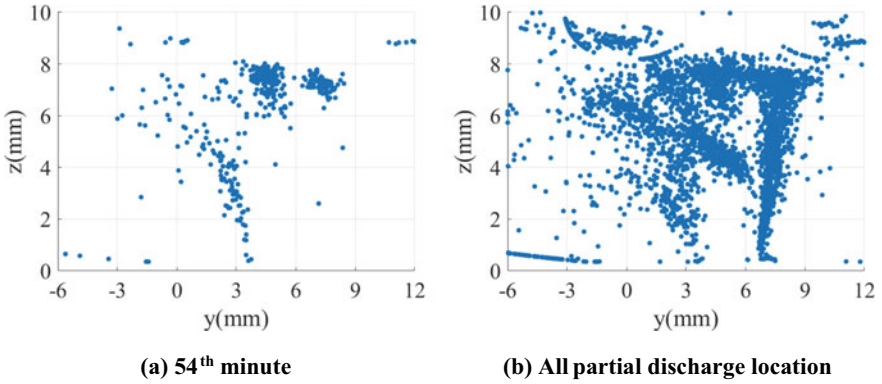
Fig. 7 PD location of two-layer media equivalent model

(a) 54th minute   **(b) All partial discharge location**
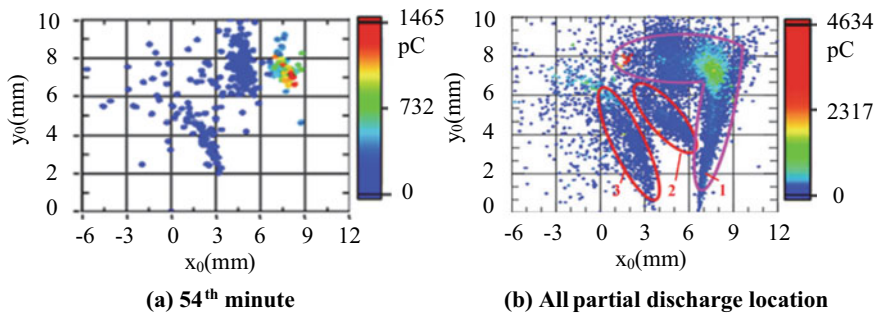
Fig. 8 PD location of single-layer media equivalent model

media mirroring is also considered, which further improves the accuracy of the partial discharge positioning results.

6 Conclusion

In this paper, the PSO algorithm is used to solve the electrostatic field inverse problem, and the boundary electric field strength is used to reverse the field source charge position. The equation system of this inverse problem is very complex, and difficult to decouple, thus cannot be solved directly, but the PSO algorithm solves this problem by solving the optimal solution of the objective function. The distributed measurement system consists of a multilayer medium, and this paper considers the multilayer medium in the calculation to improve the accuracy of partial discharge positioning.

To further improve the accuracy of partial discharge positioning, we consider to use a two-dimensional distributed measurement system, that is, the measuring electrodes are distributed in the x–y plane rather than just along the y-axis. In addition, the two-dimensional distributed measurement system is also helpful for realizing the three-dimensional reconstruction of electrical trees. In the calculation process, using the three-layer medium or four-layer medium is also important to improve the positioning accuracy in the z direction. At present, only the mirror image of the different medium planes is considered, in practice, the mirror image of the needle also needs to be considered.

References

1. Wu S, Zheng S, Zhang Z et al (2021) The relationship between electrical tree growth and partial discharge characteristics in XLPE. In: 2021 IEEE electrical insulation conference (EIC). Denver, CO, USA, pp 461–464
2. Zhang Z, Zheng S, Wu S, Liu D, Guan A, Zhong A (2021) Analysis of electrical tree growth and partial discharge stagnation in epoxy resin. In: 2021 international conference on advanced electrical equipment and reliable operation (AEERO). Beijing, China, pp 1–4
3. Zhang Y, Zhou Y, Zhang L, Teng C, Hu D, Liu R (2020) Electrical tree growth and its partial discharge pattern in silicone rubber under AC voltages. In: 2020 IEEE international conference on high voltage engineering and application (ICHVE). Beijing, China, pp 1–4
4. Cheng Y, Duan B, Tan X, Song H, Zhao C (2016) A novel method of measuring length and location of single channel carbonized trees in oil-impregnated pressboard. In: 2016 IEEE conference on electrical insulation and dielectric phenomena (CEIDP). Toronto, pp 1003–1006
5. Duan B, Cheng Y, Bai H et al (2016) A method for on-line monitoring of electric tree growth in press-board of transformers. In: 2016 IEEE international conference on high voltage engineering and application (ICHVE). Chengdu, China, pp 1–4
6. Meng H, Cheng Y, Li G et al (2017) The one-dimensional potential measurement system for the carbonization trace detection in oil-impregnated pressboard. In: 19th international conference on dielectric liquids (ICDL). Manchester, UK, pp 1–4
7. Cheng Y, Diao C, Liu S (2013) Development law of partial discharge of oil-paper insulation and diagnosis of defect state under constant voltage. High Voltage 39(05):1061–1068 (in Chinese)
8. Cheng Y, Wei J, Li C et al (2015) Accelerated deterioration of oil-paper insulation between turns of transformer under partial discharge. Transactions of China Electrotechnical Society 30(18):203–212 (in Chinese)

9. Cheng Y, Duan B, Li F (2020) Electrical tree reconstruction method for oil-impregnated press-boards based on the inverse problem for the electrostatic field. IEEE Trans Dielectr Electr Insul 27(1):94–102
10. Zhang S, Cheng Y, Yu H (2020) Three-dimensional reconstruction of the electric tree in oil-impregnated pressboard based on partial discharge location. In: 2020 IEEE international conference on high voltage engineering and application (ICHVE). Beijing, China, pp 1–4
11. Robinson J, Rahmat-Samii Y (2004) Particle swarm optimization in electromagnetics. IEEE Trans Antennas Propag 52(2):397–407

Hot Spot Temperature Prediction of Transformer Windings Naturally Cooled by Internal Oil Based on Thermoelectric Analogy Principle

Hetong Lan, Jinchao Lv, Lingfeng Jin, Yiming Zheng, Gang Liu, and Yunpeng Liu

Abstract Aiming at the problem that the hot spot temperature of oil-immersed power transformer with natural oil cooling is affected by oil temperature and oil time constant, a prediction model of hot spot temperature of transformer winding based on thermoelectric analogy principle is proposed in this paper. Firstly, based on the principle of thermoelectric analogy, considering the change of time constant of top oil affected by oil temperature, the Susa thermal model is improved, and the thermal model of power transformer with natural cooling of internal oil is established. Secondly, based on the top oil temperature, the fourth-order Runge–Kutta method is used to calculate the winding hot spot temperature. Then, the research group used the model SFSZ7-31500/110 transformer for temperature rise test. Finally, the proposed algorithm is verified by simulation experiment and compared with Susa's temperature rise algorithm. The results show that the proposed algorithm has less error, which verifies the effectiveness of the proposed method.

Keywords Transformer · Thermal model · Hot-spot temperature · Oil time constant

1 Introduction

Transformer is the core of energy conversion and transmission in the power system components. In the present study, limited by sensor point, unable to obtain winding temperature distribution in detail, to a detailed study on the mechanism of its internal

H. Lan (✉) · J. Lv · G. Liu · Y. Liu
Hebei Provincial Key Laboratory of Power Transmission Equipment Security Defense, North China Electric Power University, Baoding 071003, China
e-mail: 3110765687@qq.com

L. Jin · Y. Zheng
State Grid Zhejiang Electric Power Company, Electric Power Research Institute, Hangzhou 310000, China

heat. Local overheating of the transformer winding may cause damage to the transformer insulation and reduce the insulation life [1]. GB/T 15164-1994 "Load Guidelines for Oil-immersed Power Transformers" states: "The temperature of the hot spot of the transformer winding is an important limiting factor for the size of its load value, and every effort should be made to accurately determine the temperature value [2–4]".

The calculation methods of transformer internal temperature mainly include thermal simulation measurement method, temperature rise guidelines and algorithms, neural network calculation method, numerical calculation method, and thermal model method. The thermal simulation measurement method uses the sum of the product of top oil temperature, hot spot coefficient and the temperature difference between copper and oil to calculate hot spot temperature, which has a simple principle and large error [5]. The calculation method of temperature rise guideline assumes that although the oil temperature rises linearly in height, the winding temperature distribution line and the oil temperature distribution line are two parallel lines, as shown in Fig. 1. The neural network method takes the ambient temperature around the transformer and load value as the input value, and the top oil temperature as the output value. By comparing the measured value of the neural network and the linear regression model, the American research team concluded that the random neural network could predict the temperature more accurately and presented the RNN model for forecasting the top oil temperature [6, 7].

Finite element method or finite volume method is often used in numerical simulation. Liu et al. [8] used finite element theory to compare and analyze the temperature field distribution under the condition of average heat source and non-average heat source. Numerical simulation method has high precision and accurate positioning. However, because there's a lot of computation involved, the calculation time is longer and the real-time performance is poor. The thermal model is a model that simulates the heat distribution inside the transformer by using the thermal circuit diagram. At present, many scholars have done research work on transformer thermal model. Thinking about the effect of winding temperature rise on load loss and oil temperature on oil viscosity, Susa introduced nonlinear thermal resistance to build the top-oil

Fig. 1 Hot spot calculation formula schematic diagram
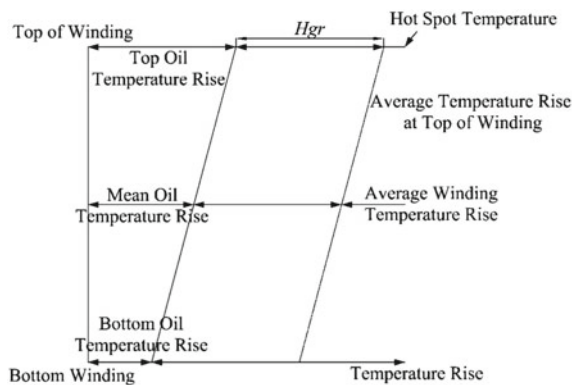
temperature model as well as winding hot-spot temperature model. The findings show that the Susa's model is more accurate than the formula recommended in Appendix G of IEEE Std C57.91 [9, 10]. Li et al. [11] introduced solar radiation to improve the thermal model for calculating the top oil temperature. Zhou et al. [12] corrected the nonlinear thermal conductivity by considering the change of oil viscosity with temperature. Jin et al. [13] considered the influence of pie thermal resistance, built an experimental platform through steady-state heat flow method to obtain thermal resistance, and built a distributed parameter thermal model based on thermoelectric analogy theory to prove the accuracy of calculation consequence. The oil viscosity correction factor proposed by Luc Paulhiac takes into account the working state of fan and oil pump, and builds a thermal model for the forced guide oil circulation air-cooled structure transformer [14]. Alvarez used the extended Kalman filter to fit the parameters of a simple equivalent thermal loop to consider ambient cooling conditions and to correct the heat capacity value of cooling oil [15]. Experts and scholars refined the thermal model from different angles, further modified the centralized parameters, and made outstanding contributions to the improvement of the accuracy of the calculation of temperature rise in the transformer thermal model.

It can be seen from the above studies that accurate calculation of the viscosity, heat capacity and nonlinear thermal resistance of transformer oil is very important for the computational accuracy of hot spot temperature. The product of heat resistance and heat capacity is the oil time constant, which changes with the transformer working condition and oil temperature. Therefore, considering the time variation of load rate and oil viscosity, this paper revises the oil time constant under different working conditions, and proposes an improved thermal model. In addition, the thermal model proposed revises the winding time constant according to the hot spot temperature, also considers the variation of load loss with winding's temperature. The hot spot temperature is calculated from the top oil temperature, and the fourth order Runge–Kutta method was used. In order to verify the effectiveness of the model, the members of the research group carried out temperature rise tests on the transformer model SFSZ7-31500/110 under overload, rated load and underload. The transformer was operated in ONAN cooling mode and thermocouple was used to measure the internal temperature. The simulation results were used to compare and analyze the characteristic temperature of the improved thermal circuit model and Susa thermal circuit model, and the error was analyzed with the measured data.

2 Calculation Method of Transformer Hot-Spot Temperature

2.1 Calculation Model of Top Oil Temperature of ONAN Cooling Mode Transformer

For by the low temperature heat the liquid through a wall of one side wall to the other side of the fluid in the process is called heat transfer process, the process includes three links: from the thermal fluid flow to the side of the wall of high temperature heat transfer for the convective heat transfer way. High temperature side from the wall to the side of the wall of low temperature heat transfer for thermal conductive heat transfer way. The heat transfer from the low temperature side of the wall to the cold fluid is also convective heat transfer mode. This heat transfer process can be likened to a simple resistance series circuit.

Based on the flat-wall heat transfer process, the temperature conduction process inside the transformer is described below. Coil core and other components are good conductors of heat. Under overload conditions, the temperature of the core and winding rises very quick, and the heat flow is transmitted to the surface of the good conductor. Under the action of transformer oil circulation, heat exchange is carried out in the form of heat convection between high temperature good conductor surface and low temperature transformer oil surface. As the temperature rises, the density of transformer oil decreases and rises to the top of the mailbox. After the heat is transferred to the tank wall, the temperature decreases and again flows into the bottom of the tank, forming a natural circulation of oil flow. Under the action of convective heat transfer, the temperature of the tank wall and the heat pipe wall rises, and the heat is transferred from the inner wall to the outer wall in the form of heat conduction. Owing to the external environmental temperature of transformer tank and the outer wall temperature, in the form of thermal radiation and convection heat to the surrounding environment [13]. The heat loss process is shown in Fig. 2.

Pictured above the oil-immersed transformer cooling process ignores the clip pieces parts involved in the process of heat transfer. For winding and cooling liquid, of course, in terms of the parameters of the thermal resistance and the heat capacity of fine calculation such as pieces of clamp parts considerations can be ignored no hurry. From the heat dissipation process inside the transformer, it can be seen that the winding temperature is of great importance for the calculation of the hot spot of the transformer, and in this process, the determination of the thermal resistance and heat capacity of the transformer oil is the research difficulty. Based on heat transfer theory and thermoelectric analogy, the top oil temperature model of transformer as shown in Fig. 3 is given.

In Fig. 3, q_{fe}(W) is the heat generated by no-load loss, q_l(W) is the heat generated by load loss of the transformer, q_{tot}(W) is the heat generated by total loss of the transformer, $C_{th\text{-}oil}$(J/K) is the equivalent heat capacity of transformer oil, θ_{oil}(K) is the

Fig. 2 Heat loss process of transformer
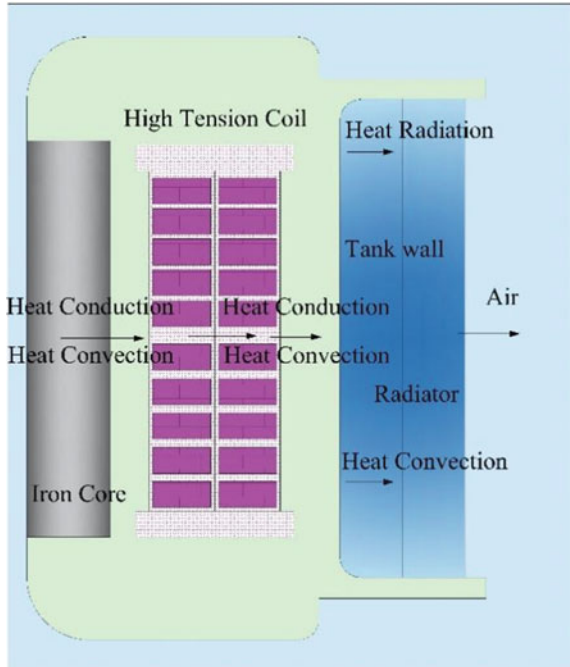
Fig. 3 The top-oil temperature model of transformer
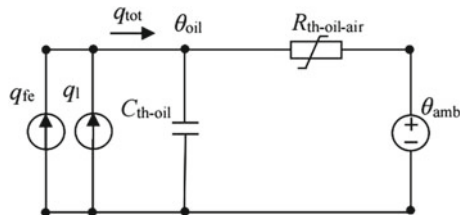
oil temperature at the top of the transformer, $R_{\text{th-oil-air}}$(K/W) is the nonlinear thermal resistance of oil to air, θ_{amb}(K) is the ambient temperature around the transformer.

If the heat capacity is expressed as the ability to store heat, then the thermal resistance can be described as the ability to hinder the conduction of temperature. Nonlinear thermal resistance is inversely proportional to the heat transfer coefficient, heat transfer coefficient changes along with the change of oil viscosity. Therefore, the variation of oil viscosity with temperature is considered, and then the nonlinear thermal resistance is considered [8]. The thermal resistance between air and oil can be expressed as:

$$R_{\text{th - oil - air}} = \frac{1}{A_{\text{rad}} h_{\text{rad}}} \tag{1}$$

where, A_{rad} is the equivalent contact area or surface area of the heat sink, m^2; h_{rad} for heat transfer coefficient, $W/(m^2 K)$.

According to thermodynamic theory, the expression of Nusselt number, Prandtl number and Glashof number is as follows [14]:

$$\begin{cases} Nu = \dfrac{h \times L}{k} \\ Pr = \dfrac{c_{oil} \times \mu}{k} \\ Gr = \dfrac{L^3 \times \rho_{oil}^2 \times g \times \beta \times \Delta\theta_{oil}}{\mu^2} \end{cases} \quad (2)$$

Thus, heat transfer coefficient is:

$$h = \left(\frac{\Delta\theta_{oil}}{\mu}\right)^n \times C \times \left(\rho_{oil}^2 \times g \times \beta \times k^{\frac{1-n}{n}} \times L^{3-\frac{1}{n}} \times c_{oil}\right)^n = C_1 \times \left(\frac{\Delta\theta_{oil}}{\mu}\right)^n \quad (3)$$

where C_1 is a constant.

When operating under rated load conditions:

$$R_{th\text{-}oil\text{-}air\text{-}r} = \frac{1}{A_{rad} C_1} \left(\frac{\mu_r}{\Delta\theta_{or}}\right)^n \quad (4)$$

where $R_{th\text{-}oil\text{-}air\text{-}r}$ (K/W) is the thermal resistance between air and oil under rated conditions; μ_r is rated the top oil temperature of oil viscosity, kg/(ms); n is an empirical constant, the value of which is determined by the transformer cooling mode, cold start or hot start. The n value in ONAN cooling mode is 0.25. The value of this empirical constant requires several field tests and a large amount of data analysis. Due to the limited working environment of the author, the corresponding research content cannot be completed, so the empirical coefficient recommended by Susa is used here for calculation and analysis [9]. For different types of transformers, the empirical parameters will change, but the range of change is not large, readers in order to accurately the value of this empirical parameter can be studied and analyzed for specific transformer data.

According to circuit theory, the time constant $\tau_{oil,rated}$ (min) under rated load is:

$$\tau_{oil,rated} = R_{th\text{-}oil\text{-}air\text{-}r} C_o = \frac{C_o}{A_{rad} C_1} \left(\frac{\mu_r}{\Delta\theta_{or}}\right)^n \quad (5)$$

The steady-state oil temperature rise is:

$$\Delta\theta_{ou} = \Delta\theta_{or} \left(\frac{1 + R K^2}{1 + R}\right)^x \quad (6)$$

where, R is the ratio of load loss to no-load loss under rated current, K is the load factor, and x is the oil index.

Therefore, oil time constant correction factor K_d under arbitrary load can be introduced:

$$k_d = \frac{\tau_o}{\tau_{or}} = \left(\frac{\mu_{ou}\Delta\theta_{or}}{\mu_r\Delta\theta_{ou}}\right)^n = \left(\frac{\mu_{ou}}{\mu_r}\left(\frac{1+RK^2}{1+R}\right)^{-x}\right)^n \tag{7}$$

Because $K = 0$ in the cooling process of the transformer, the correction factor k_d will become infinite, which makes the calculation error. In order to eliminate this outlier, the driving force of the oil flow in the running process is considered in addition to the heating effect of the loss of the load represented by the equivalent load rate term on the oil flow, and the cooling effect of the external heat sink on the oil. So add a in type for a smaller load rate constant η to describe the cooling effect of cooling fin, turning it into:

$$k_d == \left(\frac{\mu_{ou}}{\mu_r}\left(\frac{1+RK^2}{1+R}+\eta\right)^{-x}\right)^n \tag{8}$$

The dependence of oil viscosity on temperature is expressed as follows:

$$\mu = 0.13573 \times 10^{-5} \times e^{\left[\frac{2797.3}{\theta_{oil}+273}\right]} \tag{9}$$

The temperature dependence of load loss $P_{l,pu}(\theta_e)(W)$ is also considered as follows:

$$P_{l,pu(\theta e)} = P_{dc,pu} \times \left(\frac{\theta_e + \theta_k}{\theta_{e,rated} + \theta_k}\right) + P_{a,pu} \times \left(\frac{\theta_{e,rated} + \theta_k}{\theta_e + \theta_k}\right) \tag{10}$$

where, θ_e (K) is the temperature at which the loss is estimated; $P_{dc,pu}$ (W) is DC loss per unit value; $P_{a,pu}$ (W) is the additional losses per unit value;θ_k (K) is the temperature coefficient of loss correction.

Consider that the viscosity of oil is affected by the temperature of each part of the oil, the temperature of the loss estimate is equal to the average hot spot temperature value:

$$\theta_e = \frac{\theta_{hs,lv} + \theta_{hs,hv}}{2} \tag{11}$$

where, $\theta_{hs,lv}$ (K) is the hot spot temperature of low voltage winding; $\theta_{hs,hv}$ (K) is the hot spot temperature of the high voltage winding.

According to the thermal circuit diagram, the formula for calculating the top oil temperature can be obtained:

Fig. 4 The hot-spot
temperature model of
transformer
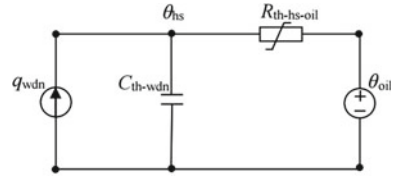
$$\frac{1 + R \times P_{l,pu}(\theta_e) \times K^2}{1 + R} \times \mu_{pu}^n \times \Delta\theta_{oil,rated}$$

$$= \mu_{pu}^n \times \tau_{oil,rated} \times k_d \times \frac{d\theta_{oil}}{dt} + \frac{(\theta_{oil} - \theta_{amb})^{1+n}}{\Delta\theta_{oil,rated}^n} \tag{12}$$

The above formula is the basic calculation model of top oil temperature. The variation of oil time constant and oil viscosity with temperature is considered.

2.2 Hot Spot Temperature Calculation Model of ONAN Cooling Mode Transformer

The hot spot temperature model of transformer is shown in Fig. 4.

Where $C_{th\text{-}wdn}$ (W·h/ºC) is the heat capacity of the transformer winding, q_{wdn} (W) is the heat generated by the loss of the transformer winding, θ_{hs} (K) is the hot spot temperature of the winding, θ_{oil} (K) is the top oil temperature calculated by the oil temperature model at the top of the transformer winding, $R_{th\text{-}hs\text{-}oil}$ (K/W) is the nonlinear thermal resistance of the winding to oil,.

Taking the top oil temperature as the temperature source and the winding loss as the ideal heat source, after deducing and simplifying the formula, the equation of winding hot spot temperature can be written:

$$\left\{ K^2 \times P_{wdn,pu}(\theta_{hs}) \right\} \times \mu_{pu}^n \times \Delta\theta_{hs,rated} = \mu_{pu}^n \times \tau_{wdn,rated} \times \frac{d\theta_{hs}}{dt} + \frac{(\theta_{hs} - \theta_{oil})^{n+1}}{\Delta\theta_{hs,rated}^n} \tag{13}$$

where, $P_{wdn,pu}(\theta_{hs})$ is:

$$P_{wdn,pu}(\theta_{hs}) = P_{dc,pu} \times \left(\frac{\theta_{hs} + \theta_k}{\theta_{hs,rated} + \theta_k} \right) + P_{eddy,pu} \times \left(\frac{\theta_{hs,rated} + \theta_k}{\theta_{hs} + \theta_k} \right) \tag{14}$$

where, $P_{dc,pu}(\theta_{hs})$ and $P_{eddy,pu}(\theta_{hs})$ are the unit values of DC loss and eddy current loss.

3 Example Verification and Result Analysis of Thermal Model

Depending on the operation state of the transformer fan, the machine can be operated in ONAN/ONAF two ways. The whole temperature rise test of our research group was run under ONAN cooling mode. The temperature rise test is carried out in accordance with the short-circuit method required in IEC 60076–2, with all windings at their rated tap. There are three load levels in the extended temperature rise test. The rated load test (100%) is carried out on the first day, the underload test (70%) is carried out on the second day, and the overload test (125%) is carried out on the third day. After the end of the test every day, the transformer is naturally cooled until the next day to continue loading. The average temperature of multiple thermocouples at each position was taken as the recorded value of the measuring point here. Here I would like to thank the members of the research group who participated in the experiment for their efforts and hard dedication during the experiment. The basic parameters of the transformer are shown in Table 1.

In this cooling mode, the maximum allowable current is 63% of the rated current, and this current is used as the reference of the rated current to calculate the load rate and other parameters. The test process is shown in Fig. 5.

The two models proposed in the previous section are solved in cascade, The four-order Runge–Kutta method is used to calculate the top oil temperature and winding hot spot temperature according to the formula derived above, and the least square optimization of the transformer top oil temperature model is carried out using the continuous data of temperature rise test. The optimization result is $\eta = 0.06$. The calculation results of the improved model are compared with the thermal model proposed by Susa, and the error analysis is carried out according to the test results.

The comparison of top oil temperature is shown in Fig. 6, and the comparison of winding hot spot temperature is shown in Fig. 7.

According to the test data, the error analysis is carried out. It can be seen from the above figure that the calculation results of the thermal model are in good agreement with the experimental measurement results. For more accurate comparison, the mean absolute error *MAE* is defined as follows:

Table 1 Basic parameters of 110 kV test transformer

Item	Value	Font size and style	Value
Model	SFSZ7-31500/110	No-load loss	37.9
Rated capacity (MVA)	31.5/31.5/31.5	Load loss	151.5(HM)/189.1(HL)/ 121.9(ML)
Rated Voltage (kV)	$(110 \pm 3 \times 2.5\%)/(38.5 \pm 2 \times 2.5\%)/10.5$	Rated current	165/472/1653
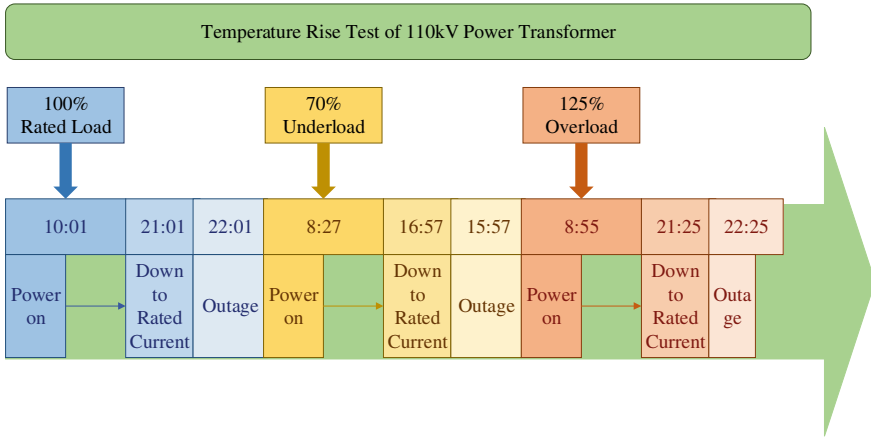
Fig. 5 Temperature rise test flow of 110 kV power transformer

Fig. 6 Calculation results of top oil temperature of 31.5/31.5/31.5 MVA-ONAN transformer
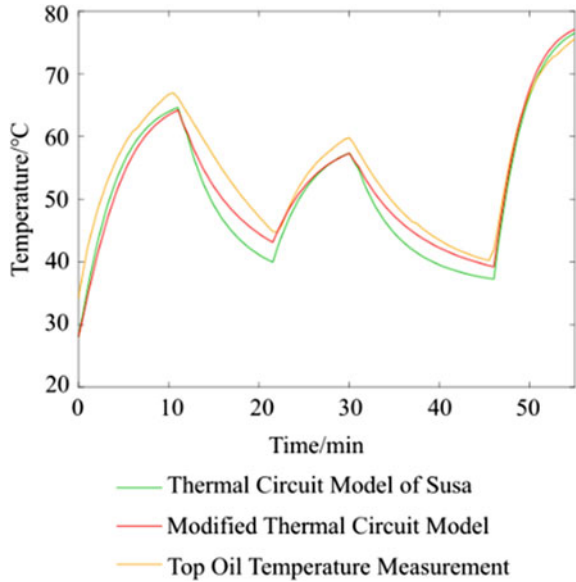
$$MAE = \frac{\sum\limits_{n=1}^{N} \left| \theta_{n,\text{calculated value}} - \theta_{n,\text{measureded value}} \right|}{N} \qquad (15)$$

According to the calculation results of top oil temperature, the average absolute error calculated by Susa thermal model is 5.68 °C, and the average absolute error calculated by improved thermal model is 4.67 °C, which increases the accuracy by 17.6%. According to the calculation results of hot spot temperature, the average

Fig. 7. 31.5/31.5/
31.5MVA-ONAN
transformer winding hot spot
temperature calculation
results
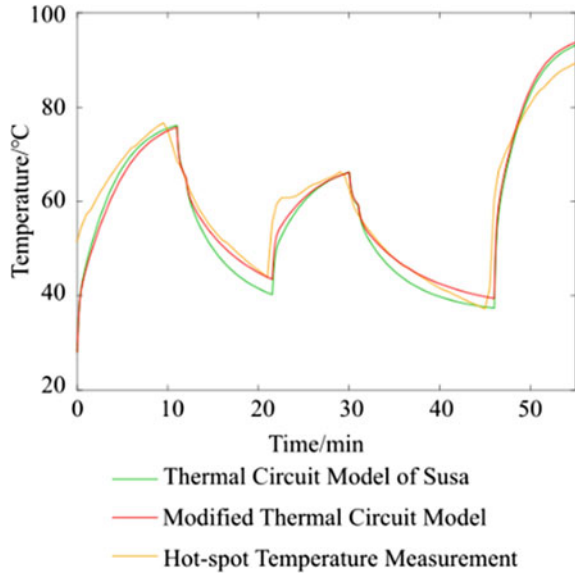
absolute error calculated by Susa thermal model is 6.17 °C, and the average absolute error calculated by improved thermal model is 5.33 °C, which increases the accuracy by 13.6%. It can be seen from the calculation results that the improved thermal model is more accurate. It can be seen from the research results that it is necessary to consider the influence of heat capacity on oil temperature and load rate. If the objective conditions permit, the heat capacity value should be corrected in time to improve the calculation accuracy and provide reliable data support for the transformer load capacity. One of the reasons why the error is not small enough is that the empirical parameters of the model are not calculated by the data of the test transformer, but by the recommended empirical parameters. In the subsequent research, the empirical parameters can be calculated to improve the calculation accuracy of the model.

4 Conclusion

In this paper, considering the time variability of oil time constant, the introduction of correction factor, considering the influence of winding temperature rise on load loss and oil temperature on oil viscosity, the introduction of nonlinear thermal resistance to build the top oil temperature model and winding hot spot temperature model, and compared with Susa hot circuit model. Error analysis was made according to the results of temperature rise test and the calculation results of the thermal model of the transformer naturally cooled by internal oil, and the conclusions were as follows:

(1) In different working conditions, the viscosity of transformer oil varies with oil temperature, and the heat capacity value and nonlinear thermal resistance of oil are also time-varying. Therefore, it is very important to correct the time constant of transformer oil in the process of calculating the top oil temperature and hot spot temperature according to the thermal model.

(2) The improved thermal model has modified the time constant of transformer oil, which is more accurate than the calculation results of top oil temperature and hot spot temperature of the thermal model of Susa.

Transformer is the core component of energy conversion and transmission in power system. In the present study, limited by sensor points, unable to obtain winding temperature distribution in detail, and then can't detailed study on the mechanism of its internal heat. Oil-immersed transformer internal structure is complex, this paper made some approximation in the process of research, such as ignoring the clip pieces and insulation parts structure on the influence of heat transfer. And the premise condition is obtained by using the lumped parameter, that is, when the heat transfer heat resistance compared with thermal resistance can be ignored. Although the improved model is proposed in this paper, it still needs to be further improved in many aspects, the research content is still insufficient, the innovation performance needs to be further improved, and the future needs to be further studied in the determination of concentrated parameters and refined model.

References

1. Quan Y, Chen J, Li W et al (2011) Methodology of forecasting the oil-immersed transformer over-hot fault tendency based on catastrophe theory. Proc CSEE 31(18):100–106 (in Chinese)
2. General Administration of Quality Supervision, Inspection and Quarantine of the People's Republic of China, Standardization Administration of the People's Republic of China (2009) GB/T 1094.7—2008 power transformers-Part 7: loading guide for oil-immersed power transformer. China Standard Press, Beijing (in Chinese)
3. Dong X, Zhang C, Ruan J et al (2021) Research and practices of dynamic thermal rating for oil-immersed power transformer. High Voltage Eng 47(6):1959–1968
4. Taheri AA, Abdali A, Taghilou M et al (2021) Investigation of mineral oil-based nanofluids effect on oil temperature reduction and loading capacity increment of distribution transformers. Energy Rep 7:4325–4334
5. Liu X (2010) Calculation model of hot-spot temperature in oil-immersed transformers based on thermal-electrical analogy theory. College of Electrical Engineering of Chongqing University (in Chinese)
6. Tylavsky DJ et al (2000) Transformer top-oil temperature model and simulation. IEEE Trans Ind Appl 36(5):1219–1225
7. He Q et al (2000) Prediction of top-oil temperature for transformers using neural networks. IEEE Trans Power Delivery 25(4):1205–1211

8. Liu G, Jin Y, Ma Y et al (2017) Two-dimensional temperature field analysis of oil-immersed transformer based on non-uniformly heat source. High Voltage Eng 43(10):3361–3370 (in Chinese)
9. Susa D (2005) Dynamic thermal modelling of power transformers. Department of Electrical and Communications Engineering, Helsinki University of Technology
10. IEEE Std C57.91-1995. IEEE guide for loading mineral-oil-immersed transformers
11. Yuan L, Ning L, Yu L (2018) A model of load capacity assessment for oil-immersed transformer by using temperature rise characteristics. Proc CSEE 38(22):6737–6745
12. Zhou Z, Chen B, Li Y (2021) Transformer load capacity assessment model based on thermoelectric analogy. Guangdong Electr Power 34(4):101–106 (in Chinese)
13. Jin N, Xu X, Wen H et al (2019) Thermal behavior calculation model of oil-immersed transformer winding based on thermoelectric analogy theory. Control Instrum Chem Ind 46(9):725–730 (in Chinese)
14. Paulhiac L, Desquiens R (2022) Dynamic thermal model for oil directed air forced power transformers with cooling stage representation. IEEE Trans Power Delivery 37(5):4235–4244
15. David L (2019) Transformer thermal capacity estimation and prediction using dynamic rating monitoring. IEEE Trans Power Delivery 34(4):1695–1705

Study on Thermal Stability of OPGW in Distribution Line During Lightning Striking and Grounding Short Circuit Faults

Lu Qu, Minchuan Liao, Ruihan Qi, Ruifa Feng, Gang Liu, Lei Jia, and Xiao Sha

Abstract In order to study the thermal stability and its influencing factors of OPGW under power frequency short circuit fault and lightning fault, a three-dimensional transient temperature finite element simulation model is established in this paper, and the temperature simulation of 8 different types of OPGW is carried out. The results show that the temperature rise of OPGW is low when the single-phase power frequency short-circuit fault occurs in the transmission line. When the two-phase power frequency short-circuit fault occurs in the transmission line, the OPGW produces a higher temperature rise. When the fault time is 100 ms, the aluminum layer temperature reaches 380.39 °C, which exceeds the maximum tolerated temperature of aluminum in OPGW, which may cause the aluminum layer to overheat and melt and fall off, affecting the mechanical and electrical properties of OPGW. When OPGW is subjected to a single lightning stroke, its temperature rise rate is less than that of the two-phase power frequency short circuit fault.

Keywords OPGW · Finite element · Thermal stability · Lightning strike · Power frequency short circuit

1 Introduction

The southern part of China is located in the tropical and subtropical monsoon region, and thunderstorms are frequent all year round. Lightning strike is one of the most important causes of distribution network failure and equipment damage. At present,

L. Qu · M. Liao · R. Qi · R. Feng · G. Liu · L. Jia
Electric Power Research Institute, China Southern Power Grid, Guangzhou 510663, China

National Engineering Research Center of UHV Technology and New Electrical Equipment, Kunming 651701, China

X. Sha (✉)
Shandong University of Technology, Zibo 25500, China
e-mail: Shaxiao1123@163.com

most of the distribution automation equipment in the distribution network generally adopts wireless communication mode. In many communication signals covering weak mountainous areas, the communication of distribution automation equipment is unstable, and even seriously affects the normal operation of the distribution network. The optical fiber composite over-head ground wires (OPGW) is set up on the top of the power line tower, which has two functions of lightning conductor and communication channel. It is an important component of the power network communication system [1–4]. Its application in the distribution network is conducive to improving the reliability of the lightning protection communication performance of the distribution network.

At present, OPGW has been widely used in transmission lines in China, but its application in distribution lines is not yet mature. The operation experience of transmission lines shows that when the transmission line is struck by lightning and power frequency short circuit fault, the fault current will flow through the OPGW to produce temperature rise, which will damage the outer layer of OPGW, and even damage the communication fiber, resulting in communication blocking, which poses a great threat to the safety of power system [5–7].

This paper combines the fault current characteristics of distribution network, and establishes the finite element simulation model of temperature rise characteristics of typical distribution network OPGW under the condition of power frequency short circuit and lightning stroke. Considering single-phase short circuit fault, two-phase short circuit fault, single lightning stroke, the influence of OPGW section size and aluminum layer conductivity of outer aluminum clad steel wire on the temperature rise characteristics of distribution network OPGW under different working conditions is compared and analyzed. The research work has certain guiding significance for the selection, operation and maintenance of distribution network OPGW.

2 Distribution Network OPGW Temperature Distribution Calculation Model and Typical Parameters

2.1 Distribution Network OPGW Temperature Rise Distribution Calculation Equation and Parameters

When the distribution line is struck by lightning or short circuit fault, high amplitude lightning current or power frequency short circuit current will appear on the OPGW above the distribution line, which can cause the OPGW temperature to rise. The temperature rise distribution characteristics of OPGW in distribution network obey the basic laws of constant electric field, Joule heat law and heat transfer, and satisfy the temperature field control equation of Eq. (1):

$$\lambda \left(\frac{\partial^2 T}{\partial x^2} + \frac{\partial^2 T}{\partial y^2} + \frac{\partial^2 T}{\partial z^2} \right) + q = \rho c \frac{\partial T}{\partial t}$$

$$q = |J|^2 \cdot \sigma \tag{1}$$

where λ is the thermal conductivity of the material; ρ is the density of the contact end material; c is the specific heat capacity of the contact end face material; j is the current density; σ is the resistivity of the material; q is the thermal power per unit volume of the contact end caused by the current flowing through the material conductor resistance and the contact resistance between the materials.

The interface Γ_3 between OPGW and air satisfies the convective heat transfer condition, as shown in Eq. (2).

$$-\lambda \left(\frac{\partial^2 T}{\partial u} \right)_{\Gamma_3} = h \left(T_W - T_f \right) \tag{2}$$

where λ is the thermal conductivity of the material; T_f is the air temperature around OPGW, and the initial temperature is 40 °C. T_w is the surface temperature of OPGW, and the initial temperature is 40 °C. h is the thermal convection coefficient between OPGW and air, and the natural thermal convection coefficient is 5 W/mm^2 °C.

The distribution network belongs to the small current grounding system. The short-circuit current flowing through the OPGW is generally only a few amperes, but the duration is long. When a two-phase grounding fault occurs, a loop is formed between the two phases, and the short-circuit current flowing through the OPGW may be as high as thousands of amperes, but usually the relay protection will trip quickly, so the current duration is generally only a few ms. The energy of single lightning stroke is generally small, which will not cause strong temperature rise of OPGW. In recent years, the power grid has suffered many multiple lightning strike accidents. Under the action of multiple lightning strikes, the OPGW of the distribution network may experience strong temperature rise changes. Therefore, considering the characteristics of single-phase grounding fault, two-phase short-circuit fault and lightning fault in distribution network, this paper determines the current loading method of OPGW end face in temperature rise calculation.

3 Analysis of the Influence of Temperature Rise Characteristics of Distribution Network OPGW Under the Condition of 2 Short Circuit Fault

3.1 Analysis of Temperature Rise Characteristics of OPGW Under Single-Phase Grounding Fault

When a single-phase power frequency short-circuit fault occurs in the distribution line, the short-circuit current flowing through the OPGW is small. Therefore, this paper selects 2 A, 4 A, 6 A, 8 A and 10 A as single-phase short-circuit current, and the current duration is 30 min.

Under the action of 2 A single-phase short-circuit current, the current density distribution and temperature distribution on the OPGW section with a cross-sectional area of 40 mm^2 and a conductivity of 20% are shown in Fig. 1. Since the conductivity of aluminum is better than that of steel, the current density on the aluminum layer is higher. The maximum current density and the highest temperature rise of OPGW in the distribution network are both at the outermost aluminum layer of the aluminum-clad steel pipe. The temperature of the aluminum-clad steel pipe gradually decreases from the outside to the inside, and the contact point between steel and aluminum also has a certain temperature rise. In addition, the single-phase short-circuit current is small and the heat production is less. There is a thermal convection process between OPGW and air, and the heat is dissipated quickly. Therefore, the temperature rise of OPGW is small under single-phase short-circuit current.

Under the action of different single-phase short-circuit currents, the maximum temperature calculation of OPGW in 4 types of distribution networks is shown in Table 1. From Table 1, it can be seen that under the single-phase short-circuit fault, the temperature rise of each type of OPGW is low, and as the single-phase short-circuit current increases from 2 to 10 A, the temperature increase of OPGW is small, and the maximum temperature only increases by 4.22 °C. It can be seen that the single-phase short circuit has little effect on the thermal stability of OPGW.
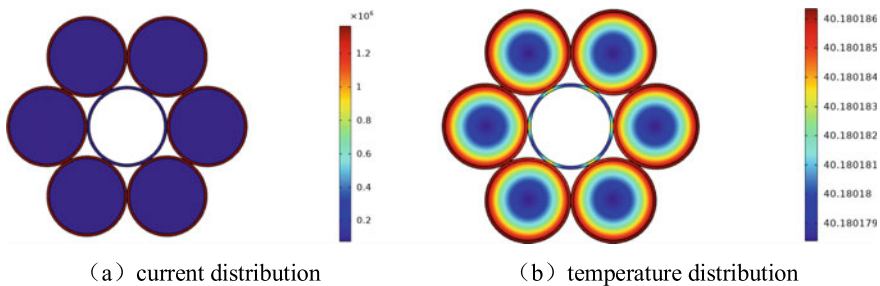

（a）current distribution （b）temperature distribution

Fig. 1 OPGW simulation results for single-phase faults

Table 1 The highest temperature rise of OPGW under different single-phase power frequency short-circuit current amplitudes

OPGW model	Maximum temperature of OPGW/°C				
	2 A	4 A	6 A	8 A	10 A
OPGW-40-24-1-1	40.18	40.72	41.62	42.88	44.40
OPGW-40-24-1-4	40.11	40.42	40.94	41.67	42.61
OPGW-50-36-1-1	40.12	40.49	41.11	41.97	43.08
OPGW-50-36-1-4	40.07	40.29	40.65	41.15	41.80

Under the condition that the amplitude of single-phase short-circuit current and the conductivity of aluminum-clad steel wire are constant, the maximum temperature rise of OPGW decreases with the increase of conductive cross-sectional area. Under the condition of constant cross-sectional area of OPGW, as the conductivity of aluminum-clad steel wire increases from 20 to 40%, the area proportion of aluminum increases, the area proportion of steel decreases, and the maximum temperature rise of OPGW decreases.

3.2 Analysis of Temperature Rise Characteristics of OPGW Under Two-Phase Short Circuit Fault

The two-phase short-circuit fault current of the distribution network can be as high as several kA, but the relay protection device will quickly remove the fault line, and the duration is generally short. In order to analyze the temperature rise characteristics of OPGW in distribution network under two-phase short-circuit fault, the two-phase short-circuit currents in this section are 2 kA, 4 kA, 6 kA, 8 kA and 10 kA respectively, and the current duration is 100 ms. Under the action of 4 kA short-circuit current, the temperature rise distribution of OPGW in distribution network is shown in Fig. 2.

As the cross-sectional area of OPGW increases, the temperature rise of OPGW gradually decreases. The conductivity of aluminum layer in aluminum clad steel wire increases, which can reduce the temperature rise of OPGW. Under the action of 2–10 kA two-phase short-circuit current, this paper selects 8 kinds of distribution network OPGW temperature rise curve changes as shown in Fig. 3.

When OPGW flows through single-phase power frequency short-circuit current, the maximum temperature rise of OPGW is much lower than the maximum temperature rise of 300 °C allowed by the aluminum layer of aluminum clad steel tube. The maximum temperature of OPGW-40-24-1-1 is 380.39 °C when t = 100 ms and the two-phase short-circuit current is 10 kA, which exceeds the allowable temperature of the aluminum layer by 300 °C. It may cause the aluminum layer to melt and fall off, which will affect the mechanical properties of OPGW. Figure 4 shows the variation curve of the maximum temperature rise of OPGW with time under the

(a) S=40mm^2，σ=20%   (b) S=40mm^2，σ=40%

(c) S=50mm^2，σ=20%   (d) S=50mm^2，σ=40%
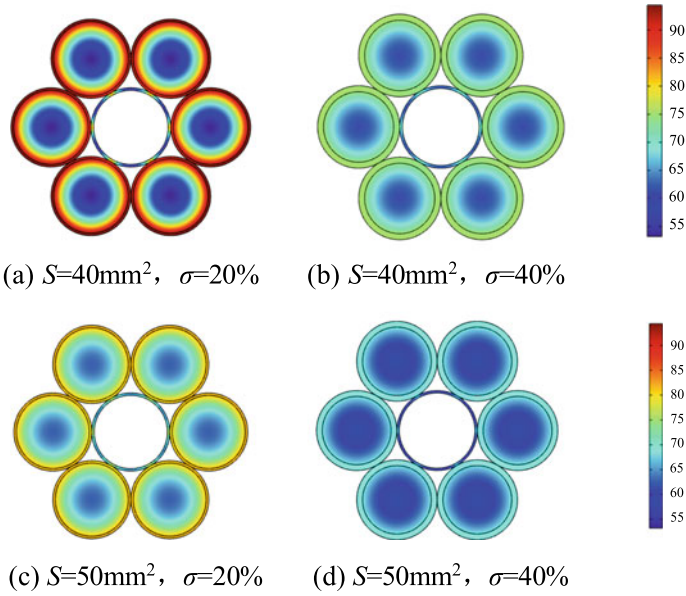
Fig. 2 Temperature distribution of different OPGW sections at short-circuit current 4 kA
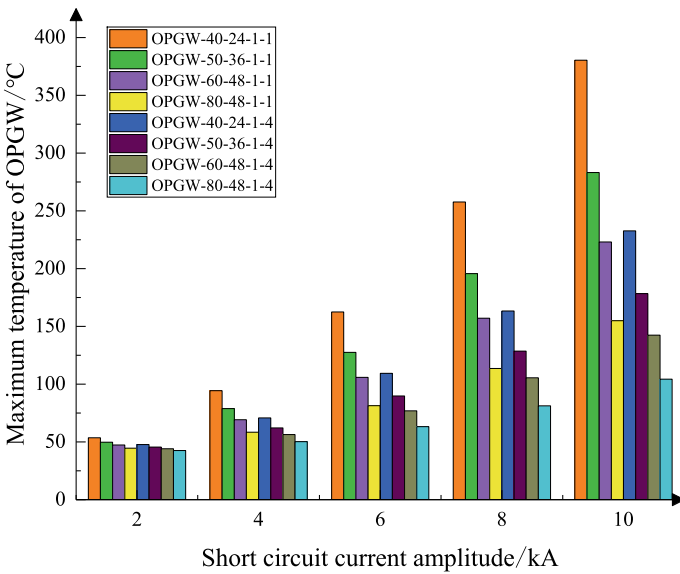
Fig. 3 Temperature rise change of OPGW in distribution network during two-phase short circuit fault
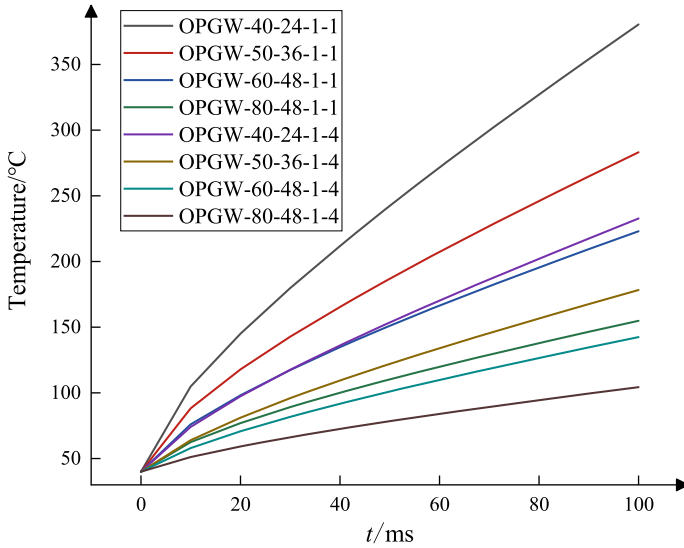
Fig. 4 The temperature rise trend of OPGW under 10 kA power frequency short circuit current

action of 10 kA short-circuit current. The highest temperature rise of OPGW with cross-sectional area of 40 mm^2 and conductivity of 20% has reached 300 °C at 70 ms.

4 Analysis on the Influence of Temperature Rise Characteristics of OPGW Under Lightning Strike Fault

4.1 Analysis of Temperature Rise Characteristics Under Single Lightning Strike Condition

The distribution network OPGW may be subjected to natural lightning discharge during operation. This section studies the temperature rise characteristics of the distribution network OPGW during a single lightning discharge. The lightning current waveform is 2.6/50 µs, and the lightning current amplitudes are 20 kA, 40 kA, 60 kA, 80 kA, and 100 kA, respectively. When T = 300 µs, the maximum temperature rise of OPGW in different distribution networks is shown in Fig. 5.

When the lightning current amplitude is 20 kA, the temperature rise of each type of OPGW is not much different, not more than 4 °C. With the increase of lightning current amplitude, the maximum temperature of OPGW decreases with the increase of its cross-sectional area, but it shows a certain saturation trend. The conductivity of aluminum clad steel wire increases from 20 to 40%, and the maximum temperature
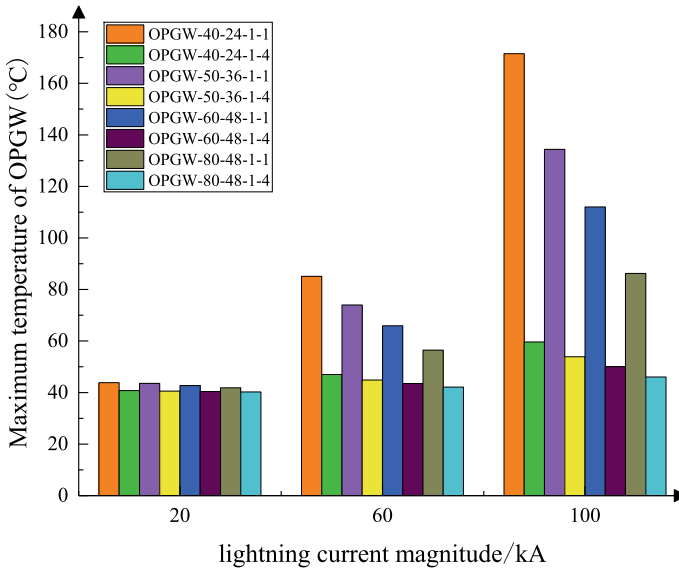
Fig. 5 The maximum temperature rise of OPGW under single lightning strike

Table 2 The highest temperature rise of different types of OPGW under lightning strike failure

OPGW model	Maximum temperature of OPGW/°C				
	20 kA	40 kA	60 kA	80 kA	100 kA
OPGW-40-24-1-1	43.82	57.62	85.13	124.33	171.49
OPGW-40-24-1-4	40.78	43.06	47.04	52.54	59.67
OPGW-50-36-1-1	43.58	54.58	73.98	100.39	134.41
OPGW-50-36-1-4	40.55	42.14	44.89	48.87	53.91
OPGW-60-48-1-1	42.73	51.53	65.95	86.11	112.05
OPGW-60-48-1-4	40.40	41.56	43.55	46.44	50.10
OPGW-80-48-1-1	41.86	47.05	56.50	69.09	86.23
OPGW-80-48-1-4	40.24	40.98	42.14	43.81	46.07

of OPGW decreases obviously under the same lightning current. The increase of conductivity of aluminum clad steel wire can effectively improve the thermal stability of OPGW under single lightning strike (Table 2).

5   Conclusion

In this paper, the thermal stability of 8 different types of OPGW under lightning strike and power frequency short circuit fault is simulated, and the following conclusions are drawn:

(1)   When OPGW suffers from single-phase power frequency short-circuit fault, OPGW produces a small temperature rise, and the maximum temperature rise of OPGW increases with the increase of current amplitude, but the influence is small, and the temperature of each type of OPGW is not much different; when the two-phase power frequency short-circuit current flows through, OPGW generates a large temperature rise. When the short-circuit current of OPGW-40-24-1-1 is 10 kA and the time is 100 ms, the temperature rise will exceed the maximum tolerance temperature of the aluminum layer of the aluminum-clad steel tube in OPGW, which may lead to overheating of the aluminum layer, resulting in melting and shedding, affecting the mechanical properties of OPGW.

(2)   When OPGW is struck by a single lightning stroke, OPGW will also produce a large temperature rise, and its temperature rise rate is greater than that of single-phase short-circuit fault, but less than that of two-phase short-circuit fault.

(3)   Under the condition that the current amplitude is the same as the conductivity of aluminum clad steel wire, when the cross-sectional area of OPGW increases from 40 to 80 mm^2, the maximum temperature rise of OPGW decreases with the increase of the outer diameter of stainless steel tube. When the cross-sectional area of OPGW is constant, the maximum temperature rise of OPGW decreases with the increase of the conductivity of aluminum clad steel wire, and the increase of the conductivity of aluminum clad steel tube can effectively reduce the maximum temperature rise of OPGW.

References

1. Li T, Li M, Xiang T et al (2017) Analysis of high voltage insulator flashover characteristics based on OPGW optical sensor. Insulators Surge Arresters 278(4):147–151. (in Chinese)
2. Ogiso M, Komori S, Yasui S, Yamamoto T, Kobayashi H (2020) Consideration of generating mechanism of the overvoltage between the ground wires in a building struck directly by lightning. IEEJ Trans Power Energy 140(3)
3. Masato O, Syunya K, Shinji Y, Tatsuya Y, Hiroshi K (2020) Consideration of generating mechanism of the overvoltage between the ground wires in a building struck directly by lightning. Electr Eng Japan 212(1–4)
4. Stracqualursi E, Araneo R, Faria JB, Andreotti A (2022) Protection of distribution overhead power lines against direct lightning strokes by means of underbuilt ground wires. Electric Power Systems Res 202
5. Deng Y, Fan S, Gong Y et al (2020) Study on induced voltage after insulation reconstruction of 500 kV transmission line overhead ground wire and OPGW. Insulators Surge Arresters 298(6):15–21. (in Chinese)

6. Deng H, Zhang R, Chen J et al (2018) Research on principles and methods of lightning strike location based on OPGW light polarization state. Insulators Surge Arresters 281(1):148–153. (in Chinese)
7. Fang Y, Xiaoliang T, Wenkuo Y et al (2022) Analysis of transmission line wind vibration monitoring based on a multi parameter distributed optical fiber sensor. Power Syst Protect Control 50(11):169–177 (in Chinese)

Effect of Humidity on Negative Streamer Discharge in Short Air Gap

Yueguang Yang, Lu Qu, Yuqin Liao, Minchuan Liao, Haodong Qin, Ruifa Feng, Ruihan Qi, and Qingchen Wang

Abstract Humidity affects the microscopic process of negative streamer discharge in air gap. Considering the influence of humidity on ionization, attachment and recombination in the discharge process, a fluid model of negative streamer discharge in rod-plane air gap is established. The initiation, development and breakdown process of negative streamer discharge in air gap are simulated under the conditions of relative air humidity of 0, 30, 60 and 90%. In this study, humidity promotes negative streamer discharge. It is found that humidity promotes negative streamer discharge, and humidity is positively correlated with the average development speed of negative streamer discharge, the electric field intensity of streamer head and the peak value of electron concentration.

Keywords Humidity · Streamer discharge · Fluid model · Velocity of streamer propagation · Simulation research

1 Introduction

The corridor of high voltage transmission line is far away, and the climatic conditions along the line are complex. Rain, fog and other weather will increase the air humidity around the transmission line and affect the discharge characteristics of the external insulation of the transmission line [1, 2]. As an important form of air gap discharge, streamer discharge is a very complex nonlinear discharge process, which is

Y. Yang (✉) · Y. Liao · H. Qin
Electric Power Research Institute of UHV Power Transmission Corporation of CSG,
Guangzhou 510000, China
e-mail: 393217467@qq.com

L. Qu · M. Liao · R. Feng · R. Qi · Q. Wang
Electric Power Research Institute, China Southern Power Grid, Guangzhou 510663, China

L. Qu · M. Liao · R. Feng · R. Qi
National Engineering Research Center of UHV Technology and New Electrical Equipment,
Kunming 651701, China

affected by many factors such as temperature [3], air humidity, atmospheric pressure [4]. As the air humidity increases, the internal water molecule content increases. Water molecules are polar molecules with certain electronegativity, affecting the movement of charged particles in the air gap. Therefore, studying the comprehensive influence of humidity on air streamer discharge is helpful to further study the discharge characteristics of external insulation of transmission lines under different humidity conditions.

Due to the extremely short discharge time of air gap streamer, its microscopic physical process is difficult to observe. Allen and other scholars have numerically simulated the influence of humidity on the generation of electron avalanches and the development of streamers in the air. It is found that the number of electrons in the electron avalanche and the average radius of streamer development increase with the increase of humidity. And under different humidity conditions, for every 1 g/m^3 increase in absolute humidity, the corona current of positive streamer increases by about 1.4% [5, 6]. Starikovskiy and other scholars have analyzed the increase of humidity and air pressure on positive streamer discharge under the 9–12 cm parallel plate electrode structure. From the perspective of particle vibration and energy transfer, the increase of humidity is negatively correlated with the development of positive streamer [7]. Jiang et al. simulated the influence of humidity on the positive streamer discharge process under strong electric field conditions, and obtained that humidity was positively correlated with peak electron concentration, average development speed and development radius during the development of positive streamer [8, 9].

In summary, scholars' are little research on the influence of air humidity on negative streamer discharge. In order to study this factor on the negative streamer discharge in view of microscopic, this study establish a two-dimensional axisymmetric fluid model of negative streamer discharge with needle-plate in air gap. The development process of negative streamer discharge in air under four humidity conditions is simulated. The influence of air humidity on the streamer development speed, charged particle concentration and field strength during the development of negative streamer is analyzed. From the perspective of microscopic particle movement, the mechanism of humidity affecting the movement of charged particles in the air and the difference in the influence of humidity on streamer discharge under different conditions are analyzed.

2 Mathematical Model and Parameters of Streamer Discharge Process

2.1 Mathematical Equations of Charged Particle Development and Space Electric Field Coupling

The fluid mechanics model used in the simulation uses the electron and positive and negative ion continuity equations that calculate the space charge development to couple and calculate the Poisson equation of the space electric field change caused by the space charge change. The particle continuity equation in simulation is as follows [10]:

$$\frac{\partial N_p}{\partial t} + \nabla \cdot \left(N_p \mu_p \boldsymbol{E} - D_p \nabla N_p \right) = \alpha N_e |\mu_e \boldsymbol{E}| - \beta_{ep} N_e N_p - \beta_{np} N_n N_p + S \quad (1)$$

$$\frac{\partial N_p}{\partial t} + \nabla \cdot \left(N_p \mu_p \boldsymbol{E} - D_p \nabla N_p \right) = \alpha N_e |\mu_e \boldsymbol{E}| - \beta_{ep} N_e N_p - \beta_{np} N_n N_p + S \quad (2)$$

$$\frac{\partial N_n}{\partial t} + \nabla \cdot \left(-N_n \mu_n \boldsymbol{E} - D_n \nabla N_n \right) = \eta N_e |\mu_e \boldsymbol{E}| - \beta_{np} N_n N_p \quad (3)$$

where the e, p, n is the quantities respectively related to electrons, positive and negative ions. N is the particle number; μ is the particle mobility, m^2/Vs; $\boldsymbol{E}$ is the electric field strength vector; the product of mobility and electric field intensity vector is the migration velocity v of particles in the electric field. D is the particle diffusion coefficient, m^2/s; α is ionization coefficient, m^{-1}; η is the adhesion coefficient, m^{-1}, β_{ep} is the electron and cation composite coefficient, m^3/s; β_{np} is the composite coefficient of positive and negative ions, m^3/s; t is time, s; S is the change rate of background particle number density caused by simulated radiation ionization.

The (1)–(3) formula is calculated with Poisson equation of space electric field to describe the relationship between charged particles and electric field during discharge. Poisson equation is described as follows:

$$-\nabla \cdot (\varepsilon_0 \varepsilon_r \boldsymbol{E}) = -e(N_p - N_e - N_n) \quad (4)$$

where e is the electronic quantity; ε_0 is the vacuum dielectric constant; ε_r is the relative dielectric constant.

2.2 Correction Method of Discharge Parameters Considering Humidity Effect

In this paper, the parameter processing method of water vapor in air given by Abdel-Salam et al., namely Wieland approximation method [11], is adopted. The corresponding parameters (such as α) are decomposed into dry air component and water vapor component (represented by α_w and α_d respectively), and the remaining parameters are the same as those under dry air conditions. Since the discharge process is mainly affected by the ionization process and the attachment process, this paper decomposes the ionization coefficient α and the attachment coefficient η according to this method.

$$\alpha = H \frac{P_w}{P} \alpha_w + \frac{P_d}{P} \alpha_d \tag{5}$$

$$\eta = H \frac{P_w}{P} \eta_w + \frac{P_d}{P} \eta_d \tag{6}$$

where H represents absolute humidity, g/m^3; P_w denotes the partial pressure of saturated water vapor, kPa; P_d represents dry air partial pressure, kPa; P is the total pressure of humid air, $P = 101.3$ kPa.

The modified negative streamer reaction coefficient and transport parameters in dry air and wet air are shown in Table 1. The positive and negative ions diffusion rate is much smaller than electrons. So positive and negative ions are considered to have no diffusion process. N is the number of air molecules at atmosphere, N $= 2.6876 \times 10^{25}$ m^{-3}.

Table 1 Streamer discharge parameters

Parameter (unit)	Expression or specific value
α_d (m^{-1})	$2 \times 10^{-20} N \times e^{(-7.248 \times 10^{-19}/(E/N))}$
α_w (m^{-1})	$N \times e^{(-0.05 + 0.7297 \ln(E/N \times 10^{21}))} + 22.88/(E/N \times 10^{21})$
η_d (m^{-1})	$0.18N \times e^{(-44.96 - 0.9055 \ln(E/N \times 10^{21}))} - 73.35/(E/N \times 10^{21})$
η_w (m^{-1})	$N \times e^{(-41.56 - 1.351 \ln(E/N \times 10^{21}))} - 73.51/(E/N \times 10^{21})$
β_{ep} (m^3/s)	$2 \times 10^{-13}(1 + 0.36 \, h/100)$
β_{np} (m^3/s)	$2 \times 10^{-12}(1 + 14 \, h/100)$
μ_e (m^2/Vs)	3×10^{-2}
μ_p (m^2/Vs)	2.43×10^{-3}
μ_n (m^2/Vs)	2.7×10^{-4}
D_e (m^2/s)	0.18

2.3 Air Gap Geometry and Boundary Conditions

The simulation model selects the rod-plate electrode gap distance $d = 3$ mm, and the rod electrode is an ellipsoid with a radius of curvature of 0.16 mm at the end of the long axis. A negative step voltage of 9 kV is applied to the needle, and the plate electrode is grounded. The initial charged particle concentration is set at the head of the rod electrode, and its distribution satisfies the Gaussian equation shown in Eq. (7):

$$N_p = N_e = n_0 \exp\left\{ -\left(\frac{r}{s_0}\right)^2 - \left[\frac{(z - z_0)}{s_0}\right]^2 \right\} \tag{7}$$

In previous studies, it has been found that setting a certain initial charged particle concentration will only promote discharge generation and will not change the streamer discharge characteristics [12]. When the initial electron concentration is set to 1×10^{14} mol/m^3, the streamer can be generated immediately near the electrode after the initial electron avalanche is formed. The distribution shape feature S_0 of the initial electron concentration is determined by the geometric characteristics of the electrode.

The geometric model and the size of the calculation area used in the simulation are shown in Fig. 1. When the grid is divided, due to the drastic change of particle concentration during discharge, the streamer development area under the rod electrode needs to be regionally meshed. As shown in Fig. 1, the average unit mass of the solution domain is 0.9477.

In the negative streamer discharge, it is necessary to set reasonable boundary conditions for solving the particle continuity equation. In this model, all the boundary conditions set for solving the particle continuity equation are shown in Table 2.
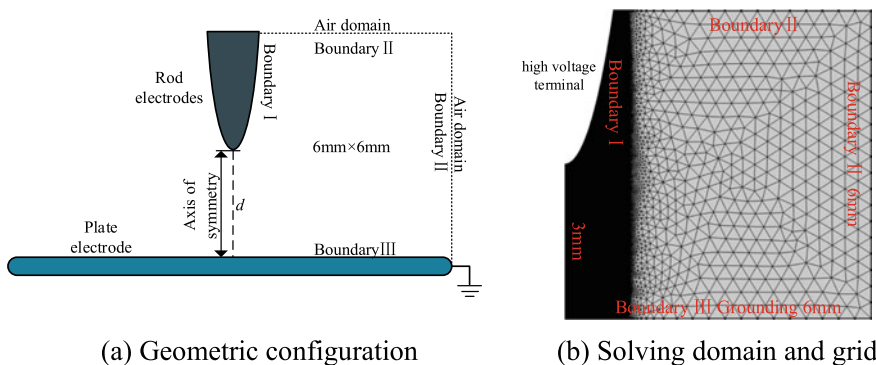

(a) Geometric configuration   (b) Solving domain and grid

Fig. 1 Geometric model and mesh generation

Table 2 Boundary conditions of continuity equations

Particle	Boundary I	Boundary II	Boundary III
Electron	$-\boldsymbol{n} \cdot (N_e \mu_e \boldsymbol{E} - D_e \nabla N_e) = \gamma N_p \lvert \mu_p \boldsymbol{E} \rvert$	$\boldsymbol{n} \cdot (-D_e \nabla N_e) = 0$	$\boldsymbol{n} \cdot (-D_e \nabla N_e) = 0$
Positive ion	$N_p = 0$	$\boldsymbol{n} \cdot \left(-D_p \nabla N_p\right) = 0$	$N_p = 0$
Negative ion	$N_n = 0$	$\boldsymbol{n} \cdot (-D_n \nabla N_n) = 0$	$\boldsymbol{n} \cdot (-D_n \nabla N_n) = 0$

3 Parameters and Model Feasibility Verification

In this section, according to the short gap negative streamer discharge process model in Sect. 1, the negative streamer discharge process in the 3 mm rod-plate gap under dry air conditions is calculated. Under dry air conditions, the electron concentration distribution and the axial electric field distribution in the gap are shown in Fig. 2.

As shown in Fig. 2a, under the applied voltage of $-9\,\text{kV}$, the electron concentration of the streamer head reaches 5.64×10^{20} mol/m^3 due to the intense ionization process after the streamer initiation of 0.48 ns, which is 100 times higher than the initial electron concentration of the rod electrode head. In the process of streamer development, the electron concentration in the axial direction is maintained between 10^{19} and 10^{21} mol/m^3, which is similar to the results of the streamer discharge of the negative rod in Ref. [13]. In the literature [14], the simulation of the streamer discharge process under dry air was studied. The maximum electron concentration of the streamer head in the development process was about 2×10^{20} to 3×10^{20} mol/m^3, and the maximum electron concentration of the streamer head in this model was 4×10^{20} to 6×10^{20} mol/m^3. The time required for the streamer to develop to the plate electrode is about 1.29 ns, and the average development speed is 2.32×10^6 m/s. The magnitude is consistent with the study of the negative streamer of the air gap needle-plate electrode structure in Ref. [15].

(a) Axial electron concentration distribution
(b) Axial electric field
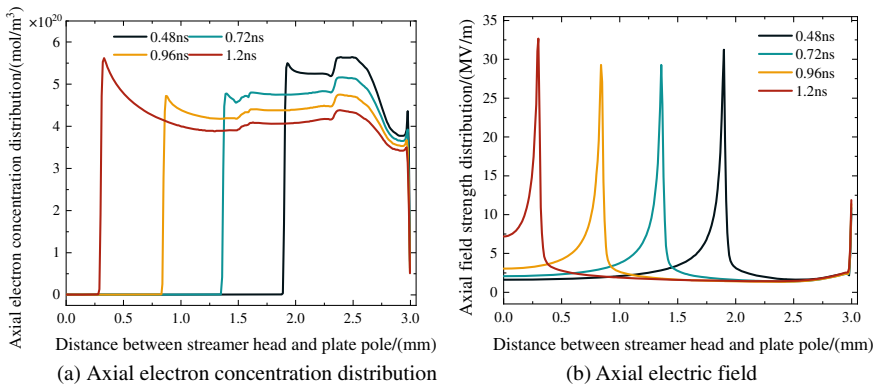
Fig. 2 The development process of negative streamer in dry and clean air

From Fig. 2b, the electric field distribution law meets the relevant research in the existing literature [15]: (1) The field strength value of the streamer head is between 10^6 and 10^7 V/m; (2) The electric field strength in the streamer development channel is within 5 MV/m.

4 Streamer Discharge Simulation Results and Analysis

In this paper, the simulation of negative streamer discharge is carried out in dry air without considering humidity and under four conditions of relative humidity of 30, 60 and 90%. The average velocity of streamer development under different conditions, the change of charged particle concentration with time in the channel during the development of streamer, and the axial electric field strength of the streamer development channel are compared.

4.1 The Influence of Humidity on the Average Development Speed of Streamer

Figure 3 shows the time taken when the streamer head develops to different positions under four kinds of humidity and the corresponding average speed in each development process.

When the relative humidity increases from 0 to 30%, the average development speed of streamer increases by about 60%, which shows that the influence of humidity on the development characteristics of streamer is significant. When the relative

Fig. 3 The average velocity of streamer development under different humidity conditions
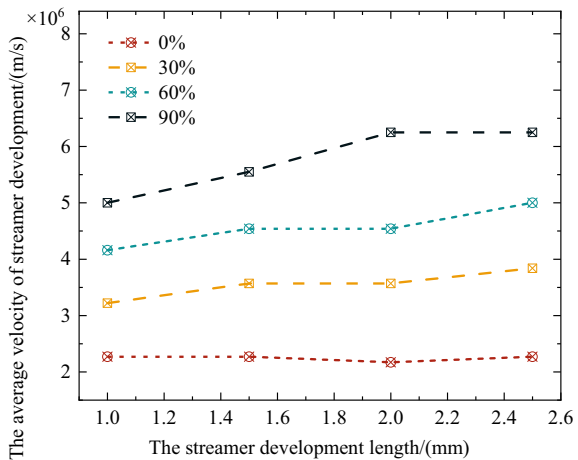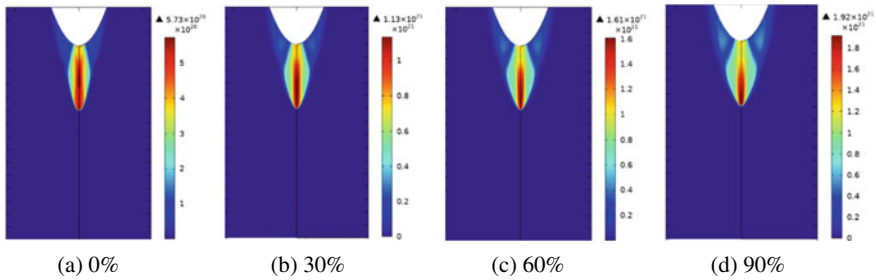
Fig. 4 The spatial distribution of electron concentration when streamer develops to 1 mm under different humidity conditions

humidity increases from 30 to 60% and from 60 to 90%, the average velocity of streamer development increases by about 20–30%.

4.2 Effect of Humidity on Charged Particle Concentration in Streamer Development Channel

Figure 4 shows the distribution of electron concentration in the gap with relative humidity of 0, 30, 60 and 90% when the streamer develops 1 mm downward.

It can be concluded from Fig. 4 that after the humidity increases, as the streamer develops downward, the area with higher electron concentration increases, and the streamer channel tends to expand radially.

4.3 Effect of Humidity on Electric Field Intensity During Streamer Development

The variation of the maximum electric field intensity of the streamer head with time is shown in Fig. 5. The change trend of the maximum electric field intensity of the streamer head with time is consistent in the four cases.

Compared with dry air conditions, the addition of humidity will increase the maximum field strength of the streamer head during the development of the streamer, but its effect on the electric field strength of the streamer head is not linear.

Fig. 5 The variation of field strength and position of flow injection head with time
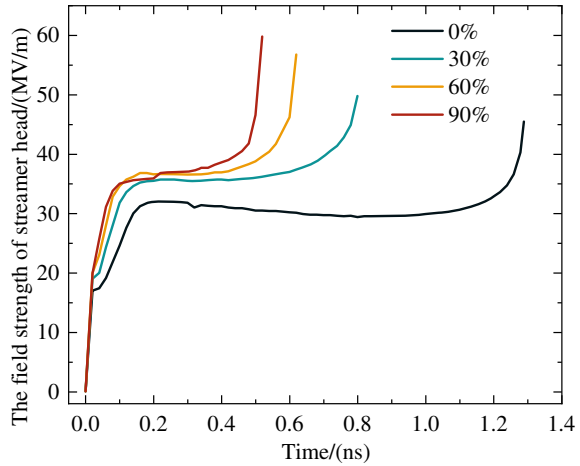
5 Conclusion

In this paper, a negative streamer discharge model with different humidity under atmospheric pressure is established based on fluid dynamics. The following four conclusions are obtained:

(1) As the humidity increases, the streamer development rate increases significantly. However, in the case of high humidity, the content of water molecules in the air is too high, and the adhesion process is greatly enhanced, which has a certain inhibitory effect on the development of the streamer and reduces the increase of the speed.

(2) When the humidity increases, the high-concentration electron region expands during the streamer development process, and the streamer development channel width increases. The addition of humidity will significantly increase the maximum field strength of the streamer head, but the effect of humidity on the head field strength is nonlinear.

References

1. Zhenya L (2013) Ultra-high voltage AC & DC grid. China Electric Power Press, Beijing
2. Wang L, Xu J, Sun T et al (2016) Optimizing the conductor's configuration in 1000 kV compact power transmission line. Electrical Meas Instrument 53(5):97–102
3. Zhang Z, Song H, Dai J et al (2021) Simulation research on the influences of temperature on streamer discharge of the needle plate air gap at atmospheric pressure. Proc CSEE 41(8):2929–2939
4. Pan M, Lv Y, Wang Q et al (2015) Simulation on streamer discharge of short air gap at low air pressure. Math Pract Theory 45(7):156–162

5. Allen NL (1985) The effect of humidity on avalanche growth and streamer initiation. J Phys D: Appl Phys 18(1):47–52
6. Boutlendj M, Allen NL (1991) Positive DC corona and spark over in short and long rod-plane gaps under variable humidity conditions. IEEE proceedings. A. Sci Meas Technol 138(1):31–36
7. Starikovskiy AY, Bazelyan EM, Aleksandrov NL (2022) The influence of humidity on positive streamer propagation in long air gap. Plasma Sour Sci Technol 31(11):1–19
8. Jiang X, Wu J, Ren X et al (2022) Effect of humidity on air gap streamer discharge and breakdown at atmospheric pressure. High Volt Eng 15:1–10
9. Ren X, Jiang X, Yang G, Huang Y, Wu J, Yang Z (2022) Effect of environmental parameters on streamer discharge in short air gap between rod and plate. Energies 15(3):817–817
10. Georghiou GE, Papadakis AP, Morrow R, Metaxas AC (2005) Numerical modelling of atmospheric pressure gas discharges leading to plasma production. J Phys D Appl Phys: A Europhys J 38(20):303–328
11. Abdel-Salam M (1985) Positive wire-to-plane coronas as influenced by atmospheric humidity. IEEE Trans Industry Appl IA-21(1):35–40
12. Peng Q, Sima W, Yang Q et al (2013) Influence of initial electron concentration on positive streamer discharge in pin-plane air gap. High Volt Eng 39(1):37–43
13. Cai P (2015) Effects of positive polarity and negative polarity rod-plate gap streamer evolution. Taiyuan University of Technology
14. Crichton BH (1996) Gas discharge physics, HV Technology (Digest No. 1996/173)/ IEE Colloquium on Advances in IET
15. Nijdam S, Teunissen J, Ebert U (2020) The physics of streamer discharge phenomena. Plasma Sources Sci Technol 29(10):1–49

Simulation Study on Potential Distribution Characteristics of Backfilling Water in Distribution Room

Zhongkui Feng, Chenyang Du, Xinghua Liu, Yang Yu, Yu Gao, Kai Li, and Qingchen Wang

Abstract Aiming at the problem of electrocution casualties of personnel in emergency repair after water flooding in underground distribution room caused by rainstorm weather, finite element simulation software was used to establish the water dispersion model in underground distribution room, calculate and analyze the influence of water medium and other factors on potential distribution, and obtain the potential distribution rule under the condition of water accumulation. The simulation results show that when connecting zones are installed around the distribution room, the water potential changes from 285.76 V without connecting zones to 48.14 V. With the water depth changing from 0.1 to 0.8 m, the water potential increased by 10.8%. The research results are of great significance for reducing electric shock casualty rate and ensuring underground production safety.

Keywords Underground water damage · Distribution system · Safety · Leakage of electricity · Hydrostatic potential

1 Introduction

China's regional extreme climate is complex, and extreme weather such as rainstorm and typhoon is frequent [1]. In some areas, the power supply and distribution equipment will have a large fault or even leakage risk under the condition of waterlogging in the rainy season, and the maintenance personnel and social pedestrians have frequent electric shock accidents. The occurrence of urban waterlogging has caused

Z. Feng · C. Du · X. Liu · Y. Yu · Y. Gao · K. Li
State Grid Zibo Power Supply Company, Shandong Electric Power Corporation, Zibo 255000, China

C. Du · X. Liu · Q. Wang (✉)
School of Electrical and Electronic Engineering, Shandong University of Technology, Zibo 255000, China
e-mail: up173712021@163.com

great losses to society, and also put forward higher requirements for the defense ability of society and power grid to cope with extreme weather conditions [2]. As far as the water electric shock accident is concerned, the current anti-electric shock measures for rainstorm weather are mostly passive measures, such as publicity of anti-electric shock knowledge to the public, placement of warning signs at locations prone to accidents, etc., which cannot effectively reduce the occurrence of electric shock casualties in rainy days. Leakage-proof electric shock has become a major safety hazard in rainstorm weather [3].

In view of such problems, domestic and foreign scholars have carried out in-depth research. Zhang et al. [4] studied the conductivity of water and the distribution of voltage and potential difference of charged water through experiments. Yuan et al. [5] established a solid-state transformer model and analyzed the distribution of steady-state electric field and local electric field. Deng et al. [6] used the finite element method to solve the casing electric field during rain flashover through the coupling of fluid field and electric field. In Refs. [7, 8], a three-dimensional model of insulators under water accumulation conditions was established, and the electric field distribution around insulators under different rainfall intensity and water conductivity was simulated by finite element method. In [9], three-dimensional models of electrodes with different shapes and structures were established, and the current density distribution near the electrode was analyzed by finite element simulation. Tian [10] established a three-dimensional model of AC overhead transmission lines, and calculated the distribution of power frequency electric field and human induced current near the lines. Li [11] and Zhang [12] studied the influence of the change of contact layer resistivity and contact layer thickness on the ground current and step voltage when the single-phase disconnection grounding fault occurs in the distribution network.

The current research mostly focuses on the power frequency electric field near the line and the induced electric analysis of metal objects. There are few simulations of actual working conditions, and there is a lack of in-depth research on the distribution characteristics of water potential. In this paper, the water dispersion model of the underground distribution room is established in the finite element simulation software, and the influence of different grounding methods, water depth on the potential distribution is analyzed. The potential distribution law under different conditions is obtained, so as to take preventive measures to effectively ensure the personal safety of power operators and power users and reduce the rate of electric shock casualties.

2 Human Safety Potential Threshold Under Water Immersion Condition

2.1 Human Current Safety Threshold

When a human or animal touches the accessible part of a faulty device or device, the current flowing through its body is called the contact current. The current effect of the human body caused by the contact current is affected by the current type (DC, AC), current size, current duration, current path in the human body and other factors.

Figure 1 shows the relationship between the duration of the current on the human effect and the current size given in the standard GB/T 13870.1, and the current path is from the left hand to the feet [13]. On the left side of a, that is, region 1, the human body has the probability to sense the current, but usually there is no startling response; in the middle of a and b, that is, region 2, the human body is likely to perceive the current and may experience involuntary muscle contraction, but does not produce harmful physiological effects; in the middle of b and c, that is, region 3, people experience muscle contraction, poor breathing, and cardiac function is affected; on the right side of curve c1, physiological effects such as cardiac arrest and respiratory arrest may occur in the human body. The probability of ventricular fibrillation in regions IV-1, IV-2 and IV-3 is about 5%, about 50% and more than 50%, respectively.

For the current path from the left hand to the feet, the current above the c2 curve (that is, when the current duration exceeds 5000 ms) in Fig. 1 corresponds to the
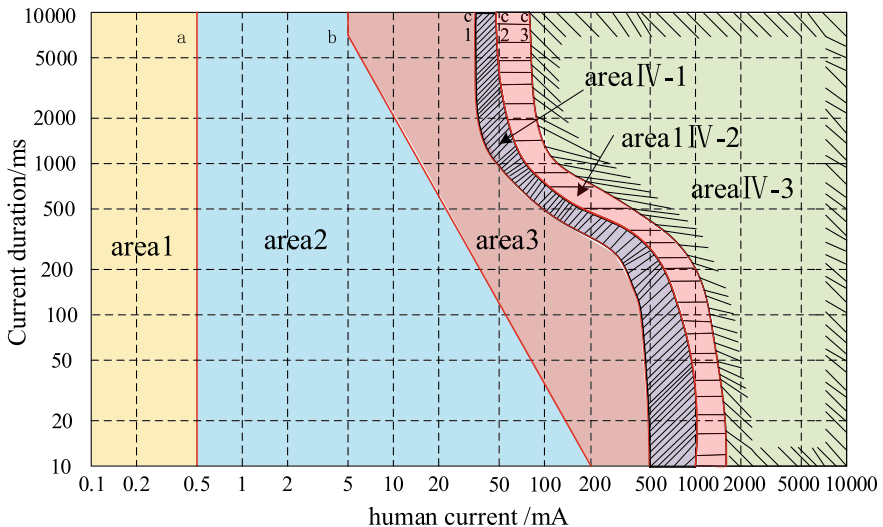
Fig. 1 The relationship between the duration of the current on the human effect and the current size when the current path is left hand to both feet

current size of 50 mA. In general, the current size is selected as the current size that causes human ventricular fibrillation. According to Fig. 1, when the human body current is 50 mA, the probability of ventricular fibrillation is 5%, which generally does not occur. In other words, 95% of people will not have ventricular fibrillation, which can be used as the current safety threshold of the human body.

2.2 Human Voltage Safety Threshold

There are two necessary conditions for the generation of current, one is the existence of closed loop, and the other is the existence of potential difference. When there is a potential difference between two different parts of the human body, a current path will be formed in the human body, resulting in a current [14]. When a direct current or power frequency alternating current passes through the human body, the human body can be equivalently regarded as a combination of resistance and capacitance [15, 16].

Analyzing the relationship between the current effect and the current size in Fig. 1, it is concluded that the current safety threshold of the human body is 50 mA when the current path is from the left hand to the feet, and the human body resistance is 1000 Ω. At this time, the current value is multiplied by the resistance value, and the voltage safety threshold of the human body can be obtained. The rated values of safety voltage in China are 42, 36, 24, 12 and 6 V. The industry stipulates that the safety voltage is 36 and 24 V for long-term contact. Due to the uncertainty of human body impedance and the influence of many factors such as external conditions, the safety voltage is not absolutely safe. The anti-shock measures formulated according to the voltage safety limit can only ensure the relative safety of electric shock.

3 Simulation Model and Parameters of Water Dispersion in Underground Distribution Room

The three-dimensional model of the distribution room under water immersion conditions is established by finite element simulation software.

In the simulation model shown in Fig. 2, the length of the three-dimensional model of the underground distribution room is 20 m, the width is 10 m, and the height is 3.8 m. The wall of the power distribution room model is set as concrete material, the thickness of each surface is 0.1 m, and the water depth is 0.35 m. The material of the distribution cabinet is galvanized steel, and the socket and the safety exit indicator shell material is polyvinyl chloride. The surrounding 0.1–0.15 m of the model is out of the installation zone, and the diagonal of the four connection zones is installed with two down leads. The material of the connection zone and the down lead is flat

steel. The conductivity and relative dielectric constant of the materials involved in the three-dimensional model of the underground distribution room are shown in Table 1.
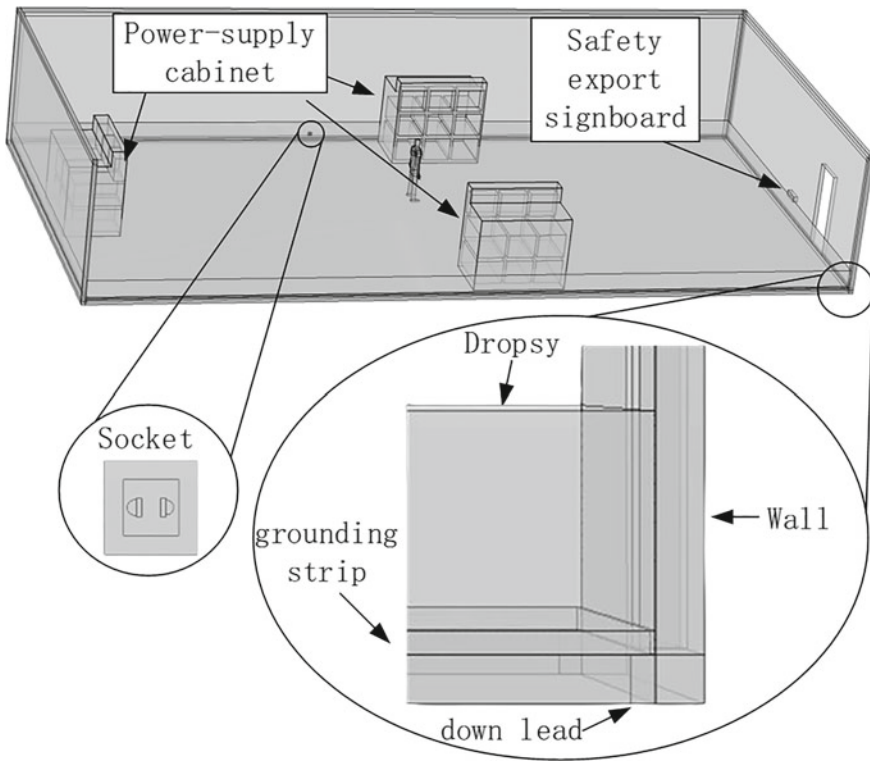
Fig. 2 Three-dimensional model of distribution room

Table 1 Model-related material parameters

Material name	Conductivity (S/m)	Relative dielectric constant
Concrete	$1e^{-4}$	5
Dropsy	0.2	81
Flat steel	$5.89e^{6}$	1
Polyvinyl chloride	$1e^{-7}$	5.5
Air	0	1
Galvanized steel	$5.2e^{5}$	1

4 Simulation Calculation of Water Flow Potential Distribution in Distribution Room

4.1 Simulation Calculation of Water Flow Potential Distribution

The finite element simulation software can take any waveform as the excitation source. In order to accurately simulate the actual leakage current, this paper uses a sinusoidal AC current waveform with a frequency of 50 Hz and an effective value of 220 V when setting the input conditions, and the leakage point is set at the bottom of the distribution cabinet. In order to analyze the potential distribution characteristics of the backflow water, all the potential distribution maps and electric field distribution maps in this paper are t = 5 ms, that is, the simulation results when the current is at the maximum value.

Figure 3a is the potential distribution map of the horizontal plane at 0.15 m when the power distribution cabinet in the urban underground power distribution room is leaking. Figure 3b is the contour map of the surface potential distribution at 0.15 m. It can be seen from the diagram that the value of the water surface potential decreases with the increase of the distance from the leakage conductor, and the speed of the potential reduction is basically unchanged. In the range of 5 m from the distribution cabinet, the value of the water surface potential is greater than 36 V, exceeding the human safety voltage, and there is a greater possibility of electric shock accidents when contacting water without protective measures.
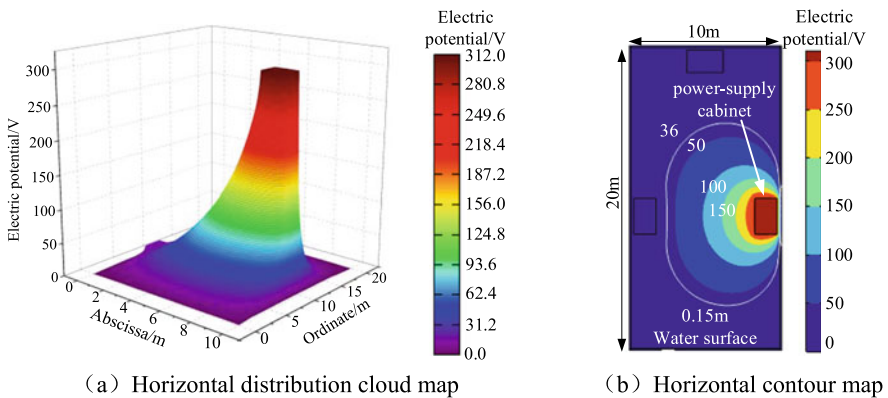

（a）Horizontal distribution cloud map   （b）Horizontal contour map

Fig. 3 Water potential distribution cloud and contour map

## 4.2 Calculation and Analysis of Influencing Factors of Water Charged Potential in Distribution Room

Influence of grounding mode on potential distribution. Different grounding modes will affect the potential distribution. In the simulation model set up in this paper, the grounding mode in the distribution room model is to set zero potential on the contact strip and down lead with a width of 50 mm and a thickness of 5 mm to simulate the grounding. The installation position of the connection zone is from 0.1 to 0.15 m near the ground. The influence of water surface potential change on potential distribution under different grounding modes is analyzed.

The average value of 0.125 m water surface potential of different grounding modes is simulated, and the results are shown in Fig. 4. When there is no contact zone, the average potential of the water surface is 285.76 V. Based on this potential, the potential reduction efficiency under different grounding modes is calculated. The average water surface potential is reduced by 37.8% compared with the non-contact zone. When the two roots are connected, the reduction is 68.5%; when three roots are connected, the decrease is 75.0%; when four roots are connected, the decrease is 83.2%. Considering the efficiency, economy and construction difficulty of potential reduction, an appropriate number of grounding zones can be selected according to the needs of the site.

Effect of inverted irrigation water medium on potential distribution. Keeping the other parameters of the basement model unchanged, the maximum potential of the water body at 0.5 m from the distribution cabinet under different water depth is simulated and analyzed. The calculation results are shown in Table 2.

From Table 2, it can be seen that with the increase of the depth of water accumulation, the maximum value of the potential around the distribution cabinet increases significantly. When the depth of water accumulation is 0.8 m, the potential increases by 14.6% compared with that without water accumulation. This is because the

Fig. 4 Average water surface potential and potential reduction efficiency under different grounding modes
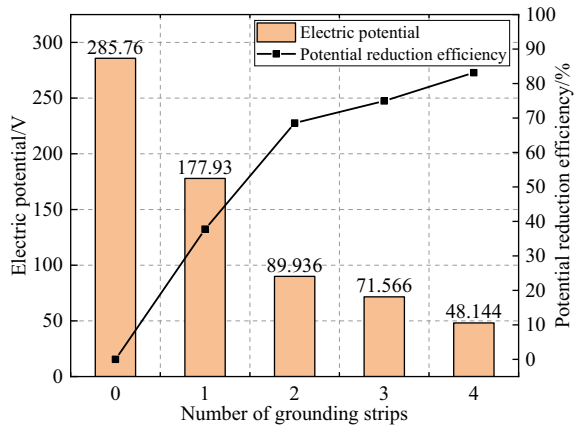
Table 2 Maximum potential at different water depths

Water depth (m)	Maximum potential (V)	Potential growth percentage (%)
0	209.43	/
0.1	216.59	3.4
0.2	219.77	4.9
0.3	223.23	6.6
0.4	226.78	8.3
0.5	230.24	9.9
0.6	233.29	11.4
0.7	236.27	12.8
0.8	239.98	14.6

increase of water depth leads to the increase of the total contact area between the water and the power distribution cabinet. The power distribution cabinet is an equipotential body, and the shell potential value is basically the same as the leakage point potential, so that the water potential around the power distribution cabinet increases.

4.3 Conservatory Measure

In order to reduce the occurrence of electric shock accidents and better protect personal safety, when reaching the accident site, the power supply should be cut off first, and measures should be taken to drain the water to reduce the probability of electric shock accidents. Under the premise of safety, the electric potential on the water surface or equipment is measured as much as possible by the electric rod, and the body is avoided by wearing protective clothing, wearing insulating gloves, insulating shoes and other measures to avoid direct contact with the equipment or water body.

5 Conclusion

In this paper, the potential distribution law of underground distribution room is simulated and calculated. In order to protect the personal safety of distribution system operators, the following three conclusions are put forward. First, by establishing a three-dimensional simulation model of the underground power distribution room, the distribution of the water potential in the event of a leakage accident is simulated. The results show that the potential in the 5 m range of the distribution cabinet is higher than the 36 V human safety voltage under the condition of surrounding grounding. Second, through the finite element analysis of the simulation model under different

leakage conductors, grounding modes and water medium, the results show that the grounding mode has a great influence on the water surface potential. When the grounding strip is installed all around, the average potential of 0.125 m water surface is 48.14 V, which is 83.2% lower than 285.76 V without grounding strip. The surface potential increases with the increase of water depth. Finally, power operators should cut off the power supply, wear protective clothing and wear insulating gloves when the accident occurs, and measure the water potential before contacting the water, so as to effectively ensure personal safety and reduce the rate of electric shock casualties.

References

1. Song Y, Gao X, Huo F (2022) Research on the site selection of urban emergency shelter considering the risk of flooding. China Saf Prod Sci Technol 18(06):31–37 (in Chinese)
2. Leng H, Chen T, Zhai G (2021) Reflections in the context of extreme climate: urban and rural construction and water management. Southern Arch 206(6):1–9. (in Chinese)
3. Chen L (2022) Real-world exploration and reflection of fire rescue teams in flood rescue and drainage. Fire Sci Technol 41(07):982–985 (in Chinese)
4. Zhang L, Li Y, Yang B (2005) Analysis of the risk of electric shock in water and its countermeasures. China Saf Sci J 15(5):5. (in Chinese)
5. Yuan N, Wu J, Leng Z (2022) Optimal design of insulation structure at high voltage connection of solid state transformer. High Volt Electr Apparatus 58(05):143–148 (in Chinese)
6. Deng W, Zhang B, Wang T (2017) Analysis of rain flash fault of flat resistance DC casing based on rain mixture model. Trans China Electrotech Soc 32(21):211–217 (in Chinese)
7. Dong B, Song J, Li T (2023) Lightning impulse arc development process and flashover characteristics of 110 kV silicone rubber insulators under strong rainstorm conditions. High Volt Technol 49(2):11. (in Chinese)
8. Ma J, Wang X, Qi Z (2022) Analysis of dry and wet flashing characteristics of silicon rubber composite insulator on the roof of EMU. High Volt Electr Equipment 58(06):171–177 (in Chinese)
9. Krasteva VTZ (2002) Estimation of current density distribution under electrodes for external defibrillation. Biomed Eng OnLine
10. Tian Z (2013) Calculation of power frequency electric field near AC overhead transmission lines and its induced current in human body. Chongqing University, 2013. (in Chinese)
11. Li G (2011) Single-phase short-circuit current calculation and step voltage finite element analysis of 10 kV distribution network. Hunan University, 2011. (in Chinese)
12. Zhang J (2021) Analysis method and technology development of single-phase grounding characteristics of distribution network combined with physical and simulation. Southwest Jiaotong University, 2021. (in Chinese)
13. GB/T 13870.1-2022, Effects of electric current on human and livestock Part 1: General part [S]. (in Chinese)
14. Misbah NR, Kadir M, Gomes C (2011) Modelling and analysis of different aspect of mechanisms in lightning injury. In: 2011 4th International conference on modeling, simulation and applied optimization, ICMSAO 2011. IEEE
15. Dias G, Gazzana DS, Bretas AS (2014) The need for standardization of human tolerability levels for lightning currents and voltages. In: Lightning protection. IEEE

16. Nescolarde L (2023) Comments on "Influence of the type of electrodes in the assessment of body composition by bioelectrical impedance analysis in the supine position." Clin Nutr (Edinburgh, Scotland) 42(3):253–254

Study on Temperature Rise Characteristics of Tower Grounding Electrode Under Lightning Strike and Power Frequency Short-Circuit Conditions

Huiqing Mao, Haipeng Tian, Yuanchao Hu, Tao Gao, Yi Chen, and Mingliang Mu

Abstract In order to study the temperature rise characteristics of tower grounding under lightning strike and power frequency short circuit conditions, this paper first calculates the current flowing into the tower grounding device under lightning strike and power frequency short circuit conditions. The calculated current flowing into the underground is taken as the terminal condition of the finite element simulation model of the tower grounding electrode. Low carbon steel and graphite wire and graphite belt are used as simulation grounding materials to analyze the temperature rise characteristics and influencing factors of the grounding electrode under lightning strike and power frequency short circuit conditions. The results show that when the lightning current and power frequency short circuit current flow into the grounding electrode, the temperature rise at the down lead of the grounding electrode is significantly higher than that at other positions of the grounding electrode, and the temperature rise of the down lead exposed to the air is the highest. The temperature rise of grounding electrode increases with the increase of current amplitude. The temperature rise of flexible graphite grounding material under power frequency short-circuit current may exceed its temperature tolerance limit, while the temperature rise of grounding electrode caused by lightning current is small.

Keywords Lightning strike · Power frequency short-circuit · Thermal stability · Flexible graphite

H. Mao · T. Gao · Y. Chen · M. Mu
State Grid Binzhou Power Supply Company, Shandong Electric Power Corporation, Binzhou 256600, China
e-mail: 13906498108@163.com

H. Tian (✉) · Y. Hu
School of Electrical and Electronic Engineering, Shandong University of Technology, Zibo 255000, China
e-mail: 1173936184@qq.com

1 Introduction

1.1 A Subsection Sample

Tower grounding electrode is an important part of lightning protection and grounding of transmission lines, which affects the safe and stable operation of power system [1–3]. Low carbon steel, copper and other metal materials are widely used as grounding materials because of their excellent electrical conductivity. Copper is mainly used as grounding material in foreign countries. However, in view of the lack of copper resources in China, low carbon steel and other metal materials are mainly used as transmission line tower grounding bodies [4, 5]. However, these metal grounding materials are very easy to corrode in the soil, and there are hidden dangers such as poor grounding of the grounding electrode, which brings great economic and financial losses [6, 7].

In view of the defects of traditional metal grounding materials, flexible graphite grounding materials and some non-metallic grounding materials have been widely used as grounding bodies. Literature [8, 9] found that flexible graphite grounding material has low permeability, no obvious skin effect, and high utilization rate compared with metal grounding materia. And has good corrosion resistance. Zhang Guofeng et al. [10] found that the resistivity of flexible graphite grounding material is larger than that of metal grounding material, and the temperature rise is higher when the fault current passes. Therefore, the thermal stability of flexible graphite composite grounding material under fault current is an important index to evaluate its application feasibility. Li et al. [11] proposed a finite element numerical calculation method of electrothermal dynamic coupling based on thin shell theory, and verified the feasibility of this model. Based on the current research literature, there are few studies on the thermal stability of the epitaxial grounding electrode.

In this paper, aiming at the thermal stability of tower grounding electrode under the condition of lightning strike and power frequency short circuit current, ATP-EMTP is used to build a simulation calculation model of lightning strike transmission line, and the current flowing into tower grounding electrode under the condition of lightning strike and power frequency short circuit current is calculated. Then, the finite element software is used to build the thermal stability simulation model of the grounding electrode of the transmission line tower. The low carbon steel with a diameter of 16 mm, the graphite wire with a diameter of 28 mm and the graphite belt with a diameter of 40×5 mm are selected as the simulated grounding materials. The thermal stability of different grounding electrode under lightning strike and power frequency short-circuit current are studied.

2 Simulation Model and Parameters

According to the research work of literature [12], the simulation calculation model of 500 kV transmission line is built by ATP-EMTP. The total length of the line is 20 km, with a total of 40 gears and a span of 500 m. The ground wire is insulated in the whole line. The relevant parameters of the line model are shown in Table 1.

Traditional metal grounding materials such as galvanized steel and copper clad steel are only coated with a very thin metal film on the surface of low carbon steel to prevent corrosion of grounding electrode. Compared with low carbon steel, there are only differences in corrosion characteristics. Therefore, this paper selects low carbon steel with a diameter of 8 mm, cable flexible graphite with a diameter of 28 mm and flat flexible graphite with a width of 40 mm and a thickness of 5 mm as the research objects. A 500 kV transmission line grounding simulation model is built in the finite element software. The buried depth of the grounding grid is 0.6 m, the length of the grounding grid frame is 15 m, and the extension of the grounding grid is 30 m.

According to the research work of literature, the electrothermal parameters of grounding material in simulation are set as shown in Table 2.

As the temperature of the grounding material changes, the resistivity of the grounding material also changes. In the finite element software, the resistivity of the grounding material changes with temperature by setting the linear resistivity. The resistivity temperature coefficients of low carbon steel and flexible graphite grounding materials are $5.77 \times 10^{-3}/°C$ and $-5.31 \times 10^{-4}/°C$, respectively.

Table 1 Route model parameters

Model	Outside diameter/(mm)	DC resistance at 20 °C/ $(\Omega \cdot km^{-1})$	Intrabundle spacing/(mm)
JLB40-150	15.75	0.2952	—
4xLGJ-630/45	33.6	0.04633	500

Table 2 Electrothermal parameters of grounding materials

Grounding material	Resistivity/$(\Omega \cdot m)$	Specific heat capacity/ $(J \cdot (kg \cdot K)^{-1})$	Thermal conductivity/ $(W \cdot (m \cdot K)^{-1})$	Density/$(kg \cdot m^{-3})$
Low carbon steel	$1.92e^{-6}$	450	50	7800
Flexible graphite	$3.25e^{-5}$	710	127	2000
Soil	100	1500	0.42	2000

Table 3 The maximum lightning current injected into the grounding device

Lightning current magnitude/kA	Current amplitude injected into the grounding device/kA
40	38.98
60	58.47
80	77.96
100	83.09
120	97.24

3 Lightning and Power Frequency Short Circuit Current Simulation Calculation

3.1 Lightning Strike Current Simulation Calculation

The 20th base tower is selected as the lightning fault point, and the grounding resistance is set to 1 Ω. The maximum lightning current flowing into the grounding device is calculated when the lightning current amplitude is 40 kA, 60 kA, 80 kA, 100 kA and 120 kA respectively. The results are shown in Table 3.

3.2 Power Frequency Short Circuit Current into the Ground Current Simulation Calculation

The grounding resistance is set to 1 Ω, 5 Ω, 10 Ω, 15 Ω and 20 Ω respectively, and the power frequency short-circuit current into the ground current under different grounding resistances is calculated. The results are shown in Table 4.

Table 4 Power frequency freewheeling injected into the grounding device

Earth resistance/Ω	Current amplitude injected into the grounding device/kA
1	9.9
5	7.0
10	5.3
15	4.2
20	3.5

4 Thermal Stability Calculation of Tower Grounding Electrode

4.1 Temperature Field Distribution Calculation Mathematical Model and Boundary Conditions

The electric field intensity, electric field and current density around the grounding electrode satisfy the following mathematical relationship:

$$E = -\nabla \varphi \tag{1}$$

$$J = \gamma \cdot E \tag{2}$$

Among them, the parameters ∇ in Eqs. (1) and (2) are Hamiltonian operators; γ the conductivity, S/m.

The heat conduction equation of the grounding electrode during the current dispersion process is as follows:

$$k \cdot \nabla^2 T + Q - C_v \frac{\partial T}{\partial t} = 0 \tag{3}$$

In formula (3), the thermal conductivity k (unit: W/(m·°C)) and the volumetric heat capacity C_v (unit: J/(m³·°C)) are the quantities that change with temperature. T is the temperature of each point around the field, °C; Q is the heat source density, calculated by the following formula:

$$Q = \rho \cdot J^2 \tag{4}$$

In Eq. (4), ρ is the resistivity of soil, Ω·m; J is the current density, A/m².

The heat conduction equation of the grounding electrode in the process of current dispersion is in the form of Cartesian coordinate system:

$$k_x \left(\frac{\partial T^2}{\partial x^2} \right) + ky \left(\frac{\partial T^2}{\partial y^2} \right) + kz \left(\frac{\partial T^2}{\partial z^2} \right) + Q - C_v \frac{\partial T}{\partial t} = 0 \tag{5}$$

In Eq. (5), k_x, k_y and k_z are the thermal conductivity in x, y and z directions, respectively, W/(m·°C).

In order to make Eq. (5) have a unique solution, heat transfer generally divides the boundary conditions into three categories: the boundary and the environment at infinity are set to the same temperature, and the boundary temperature is the initial temperature of 20 °C; the interface between the grounding electrode and the external environment satisfies the second boundary condition; the interface between soil and ambient air satisfies the third boundary condition, and the heat flux h is 5W/(m²·K).
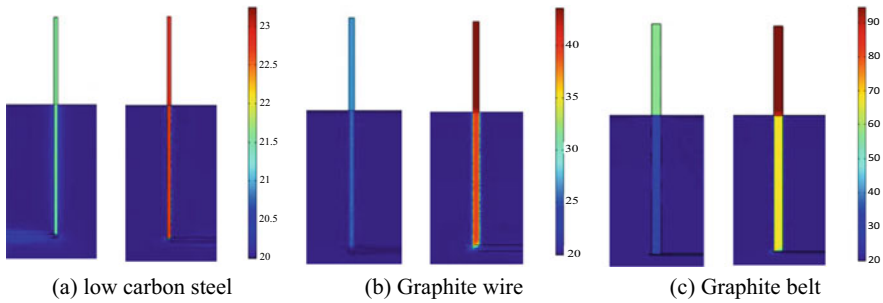
Fig. 1 The temperature distribution of the grounding lead-down line and the first and last ends of the epitaxial lead of lightning strike and power frequency follow current

4.2 Influence of Grounding Material

Through the analysis of the results of the thermal stability simulation model of the tower grounding electrode, it is found that the overall temperature rise of the grounding grid is low, but there is obvious temperature rise at the down lead. Figure 1 shows the temperature distribution of the down lead wire of different materials under the conditions of lightning strike (left) and power frequency short circuit (right). Among them, the power frequency short circuit current is 3.5 kA, and the temperature rise calculation time is 0.54 s; the lightning current amplitude is 97.24 kA, and the temperature rise calculation time is 300 μs.

It can be concluded from Fig. 1 that the temperature rise of the grounding conductor is the highest, and the temperature of the grounding conductor exposed to the air is higher than that buried in the soil. Comparing the three grounding materials, when subjected to the same amplitude lightning current and power frequency short-circuit current, the temperature rise rate of graphite-based flexible grounding material is higher than that of low-carbon steel grounding material, and because the sectional area of graphite belt is smaller than that of graphite wire, and the sectional area is an important factor affecting the temperature rise. The smaller the sectional area, the higher the temperature rise. Therefore, the temperature rise rate of graphite belt is higher than that of graphite wire.

4.3 The Influence of Current Amplitude

The calculation results in Table 1 are used as the terminal boundary conditions of the thermal stability simulation model of the tower grounding electrode to study the influence of the lightning current amplitude on the thermal stability of the grounding electrode. The maximum temperature rise curve of the grounding lead-down line under different lightning current amplitudes in Fig. 2.
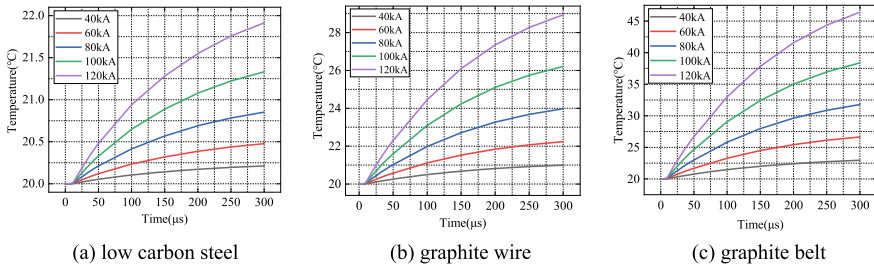
(a) low carbon steel (b) graphite wire (c) graphite belt

Fig. 2 The maximum temperature rise curve of the grounding lead-down line under different lightning current amplitudes

(a) low carbon steel (b) graphite wire (c) graphite belt
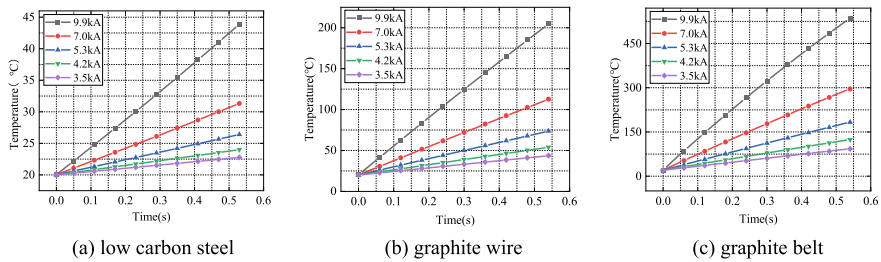
Fig. 3 The maximum temperature rise curve of the grounding lead-down line under different power frequency short-circuit

The calculation results of Table 2 are used as the terminal boundary conditions of the thermal stability simulation model of tower grounding electrode, and the influence of power frequency short-circuit current amplitude on the thermal stability of grounding electrode is studied. The temperature rise curve of the down lead under different power frequency short-circuit current amplitudes is shown in Fig. 3.

It can be seen that the temperature rise caused by the power frequency short-circuit current is greater than that caused by the lightning current, which indicates that the discharge time under the power frequency current significantly affects the temperature rise of the grounding electrode.

From Figs. 2 and 3, it can also be seen that the temperature rise of low carbon steel grounding electrode is lower than that of flexible graphite grounding electrode under both lightning strike and power frequency short circuit current conditions. When the amplitude of power frequency short circuit current is 9.9 kA, the maximum temperature of low carbon steel grounding electrode is 44.38 °C, which is far lower than the maximum temperature rise of 400 °C allowed by it. The maximum temperature of the graphite wire and graphite belt grounding electrode reaches 204.51 °C and 535.43 °C, respectively. When the temperature of graphite grounding material exceeds 320 °C, the mechanical properties of graphite-based flexible grounding material will be affected, resulting in loose grounding and broken strands. It can be seen that when the amplitude of the power frequency short-circuit current is 9.9 kA,

the temperature of the graphite belt grounding electrode has exceeded the maximum temperature rise allowed by the graphite grounding material, while the maximum temperature rise of the cable-shaped flexible graphite grounding electrode does not reach 320 °C, but it also produces a large temperature rise. When the amplitude of the power frequency short-circuit current continues to increase to 13 kA, the maximum temperature of the graphite wire grounding electrode reaches 322.12 °C, exceeding its allowable maximum temperature rise. The above shows that the thermal stability of low carbon steel is better than that of graphite based flexible grounding material, and under the condition of power frequency short circuit current, it may exceed the maximum temperature rise allowed by flexible graphite grounding electrode.

5   Conclusion

In this paper, the thermal stability and influencing factors of tower grounding electrode under lightning strike and power frequency short circuit current are simulated, and the following conclusions are drawn:

(1) When the tower grounding electrode is subjected to lightning current and power frequency short-circuit current, the temperature rise at the downlead of the grounding electrode is the highest, and the temperature rise of the downlead exposed to the air is greater than that buried in the soil. When the grounding electrode flows through the same amplitude of lightning current and power frequency short-circuit current, the temperature rise of flat strip flexible graphite grounding electrode is the highest, followed by cable flexible graphite grounding electrode, and the temperature rise of low carbon steel grounding electrode is the smallest.

(2) The temperature of grounding electrode is affected by the amplitude of lightning current and power frequency short-circuit current. The higher the current amplitude, the higher the temperature rise. Compared with the lightning current, the power frequency short circuit current causes higher temperature rise and greater harm to the grounding electrode. The flexible graphite grounding electrode may exceed its maximum allowable use temperature when subjected to power frequency short-circuit current, which affects the mechanical properties of graphite-based flexible grounding materials.

References

1. Caijiang L, Linfeng L, Zixuan L et al (2022) Location and corrosion detection of tower grounding conductors based on electromagnetic measurement. Measurement 199
2. Bhosale MJ, Karandikar PB, Kulkarni NR (2023) An optimal design for grounding grid configuration with unequal conductor spacing. Adv Eng Softw 176
3. Zhang Y, Cai H, Qi R, Hu T, Jia L, Liu G, Wu Y, Hu S (2022) Measurement and analysis of impulse grounding impedance of tower grounding device subjected to artificial lightning M-component. IET Gener Trans Distrib 17(1)
4. Li W, Hu Y, Zhao W et al (2020) Study on the current dispersion characteristics of grounding electrode based on expanded graphite composite grounding material. Insulators and Surge Arresters 4:68–74+79. (in Chinese)
5. Zhang G, Yu F, Yin L et al (2021) Impact grounding characteristics of flexible graphite grounding body based on finite element method. Insulators and Surge Arresters 303(5):128–134. (in Chinese)
6. Liu H, Zhang L, Xiong J et al (2017) Composite grounding application of transmission line tower with flexible graphite grounding material. IOP Conf Ser: Mater Sci Eng 220(1)
7. Lu Y (2022) Study on galvanic corrosion characteristics of the ground grid with different metal conductors in the converter station. J Phys: Con Ser 2213(1). (in Chinese)
8. Feng J, An Y, Jiang Z et al (2021) Study on inductance effect and spark discharge effect of flexible graphite composite grounding conductors. Insulators and Surge Arresters 3:112–118. (in Chinese)
9. Yuanchao H, Wenlong Z, Yunzhu A et al (2020) Research on grounding characteristics of flexible graphite composite grounding module. Insulators Surge Arresters 03:21–27 (in Chinese)
10. Guofeng Z, Kunyang L, Minglei Z et al (2020) Experimental study on dynamic and thermal performance optimization of graphite based flexible grounding electrode. Electron Meas Technol 43(16):17–21 (in Chinese)
11. Li J, Guo L, Hu P et al (2017) Finite element DC grounding electrode model of dynamic electric-thermal coupling based on shell theory. Power Syst Technol 41(9):3074–3082. (in Chinese)
12. Xia J (2019) Study on the grounding characteristics of the flexible graphite-copper composite grounding material. Wuhan University. (in Chinese)

Study on Dissipative Characteristics and Thermal Stability of Typical Grounding Materials in Substation

Huiqing Mao, Jianwei Zhang, Yunzhu An, Tao Gao, Yi Chen, Mingliang Mu, and Yinghui Jiang

Abstract Substation grounding network in the substation to ensure the reliable operation of substation and personnel safety plays a vital role, flexible graphite composite grounding material as a non-metallic anti-corrosion grounding material has been good performance in transmission line tower grounding applications, but there are certain problems in the application of substations. In this paper, the effects of current amplitude, soil characteristics and ground position on the ground dispersion and temperature rise characteristics of flexible graphite grounding grid and traditional metal grounding grid are compared and analyzed by COMSOL Multiphysics simulation software. The simulation results show that under the action of intrusion lightning, the scattering effect of flexible graphite grounding grid and metal grounding grid is similar, the surface potential is mainly concentrated near the entry point, and the temperature rise of the grounding grid is low and there is no fusing risk. Under the action of power frequency short circuit, the maximum temperature rise of flexible graphite grounding grid is very high, which does not meet the thermal stability requirements of flexible graphite materials, and the influence of soil characteristics on the temperature rise of flexible graphite grounding grid is not obvious, and the closer the entry point is to the edge of the grounding grid, the higher the temperature rise, so in order to ensure the safe and stable operation of the grounding grid, it is necessary to improve the down conductor. The research conclusion of this paper can provide a theoretical reference for the application of non-metallic flexible graphite composite grounding materials in substation grounding networks.

Keywords Transformer substation · Grounding grid · Flexible graphite materials · Diffusion characteristics · Thermal stability

H. Mao · T. Gao · Y. Chen · M. Mu · Y. Jiang
State Grid Binzhou Power Supply Company, Shandong Electric Power Corporation, Binzhou 256600, China

J. Zhang (✉) · Y. An
School of Electrical and Electronic Engineering, Shandong University of Technology, Zibo 255000, China
e-mail: 13906498108@163.com

1   Introduction

As a fault current and lightning current into the ground channel, the grounding network of substation plays a self-evident role in the safe and stable operation of the power system and the safety of staff [1]. The current power system grounding network materials often use flat steel, zinc-clad steel, copper-clad steel, copper and other metal materials, among which other metal materials other than copper grounding materials are susceptible to soil corrosion [2]. In view of the corrosion problem of grounding materials, non-metallic grounding materials have been studied, among which flexible graphite materials have received widespread attention due to their many advantages [3, 4].

The grounding characteristics and temperature rise of the substation are studied by simulation and simulation in the case of intrusion lightning and power frequency short-circuit current, and the grounding dispersion characteristics of the flexible graphite grounding grid are analyzed and the maximum temperature rise during grounding dispersion is calculated, so as to analyze the feasibility of its application in the substation grounding network and provide reference for its application in practical engineering later.

2   Simulation Models and Parameters

2.1   Dynamic and Thermal Stability of the Grounding Body

In the substation lightning strike or short circuit fault, the current into the grounding grid is generally in a few thousand amperes to tens of thousands of kiloamperes, the duration is generally only a few tenths of a second, the heat generated in a short time does not have time to disperse into the surrounding soil medium, almost all the heat is used to heat the grounding body, which may cause the temperature of the grounding body to exceed the allowable value, and even fusing [5, 6].

2.2   Substation Intrusion Lightning Current Waveform and Parameters

The lightning intrusion wave generated by the counterattack of the line tower of the lightning strike near the station is simulated as the input current. A schematic diagram of lightning strike near-pole tower intrusion into the substation is shown in Fig. 1.

According to Fig. 1, the ATP-EMTP simulation software is used to build the substation intrusion lightning current simulation model [7]. The simulated ground
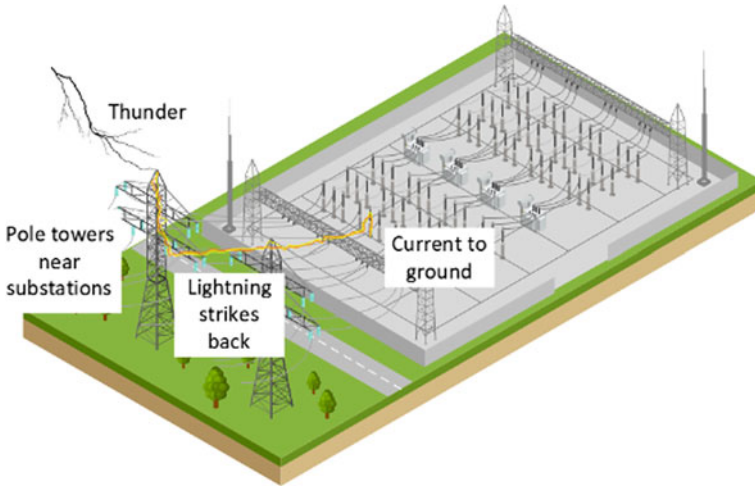
Fig. 1 Schematic diagram of lightning strike near the tower intrusion into the substation

current waveform with an amplitude of 100 kA ingress lightning current is shown in Fig. 2.

From Fig. 2, it can be obtained that the amplitude of the ground current at the entry point of the circuit breaker is higher, and with the change of the amplitude of the lightning current, the amplitude of the ground current will change accordingly, and the amplitude of the fitting curve can be obtained by the fitting function in the range of 10–30 kA.

Fig. 2 Waveform characteristics of intrusive lightning current
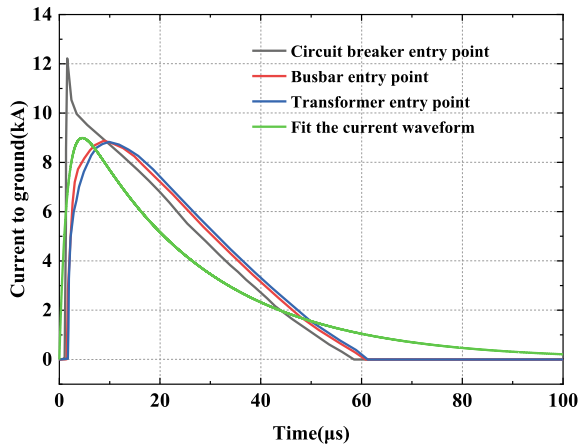
Table 1 Short-circuit current simulation results (kA)

Short circuit point	Single-phase short circuit		Two-phase short circuit		Three-phase short circuit	
	Total short-circuit current	Short-circuit current into ground	Total short-circuit current	Short-circuit current into ground	Total short-circuit current	Short-circuit current into ground
d_1	21.65	11.39	21.12	13.7	20.22	0
d_2	13.77	2.94	13.63	3.29	12.40	0

2.3 Power Frequency Short-Circuit Current and Parameters

The ATP-EMTP software is used to build the substation short circuit calculation model, in which the short circuit point of the 500 kV high-voltage side is set to d_1, the short-circuit point of the low-voltage side of 220 kV is set to d_2, and the short-circuit current size is calculated by simulation as shown in Table 1.

2.4 Substation Grounding Network Simulation Model and Parameters

The grounding dispersion characteristics and temperature rise characteristics of flexible graphite material grounding grid relative to copper grounding grid and galvanized steel grounding grid were analyzed by substation grounding network simulation, and then the thermal stability of flexible graphite grounding was verified.

According to the waveform characteristics of the ground current obtained by simulation, the grounding grid simulation model built by using flat steel grounding material, flat copper grounding material and flexible graphite grounding material is used by COMSOL Multiphysics simulation software, and the grounding grid simulation model is shown in Fig. 3.

3 Ground Dispersion and Thermal Stability Analysis Under the Action of Intrusion Lightning Current

In order to more intuitively clarify the influence of different grounding materials on the scattering characteristics of the grounding grid, the shunt coefficient introduced into the grounding grid is η as follows:

$$\eta = \frac{I_r}{I_s} \times 100\% = \frac{J_r \times S}{J_s \times S} \times 100\% \qquad (1)$$
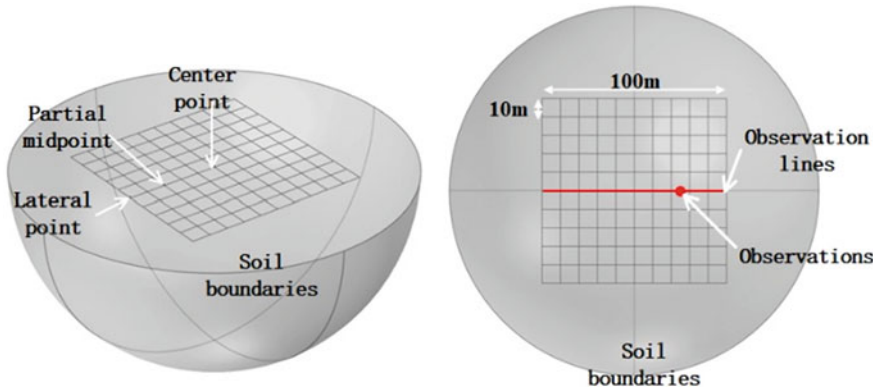
**Fig. 3** Schematic diagram of a short circuit in a substation

In Eq. (1), I_r is the current going into the grounding grid, I_s is the sum of the current entering the grounding grid, J_r is the density of the current entering the grounding grid, J_s is the current density entering the down conductor of the grounding grid, and S is the cross-sectional area of the grounding grid material.

## 3.1 The Effect of the Amplitude of the Lightning Current

In order to analyze the influence of lightning current amplitude on the scattering characteristics and thermal stability of the grounding grid, the resistivity of the fixed soil was 200 $\Omega \cdot$m, the entry point was the center of the grounding grid, and the duration was set to 300 μs. The variation law of the shunt coefficient along the observation line within the range of 0–50 m from the center point is shown in Fig. 4. The variation law of the maximum temperature of the three materials grounding grid with the amplitude of the lightning current is shown in Fig. 5.

The flexible graphite grounding grid, flat steel grounding grid, and flat copper grounding grid all have essentially the same shunt coefficient variation laws throughout the observation line, according to the simulation findings shown in Fig. 4. According to the simulation results shown in Fig. 5, the maximum temperature of the grounding grid of the three materials rises with an increase in lightning current amplitude, with the temperature rise of the flexible graphite grounding grid being very small and essentially unchanged while being higher than that of the metal grounding mesh.

Fig. 4 Distribution of shunt coefficients of observation lines
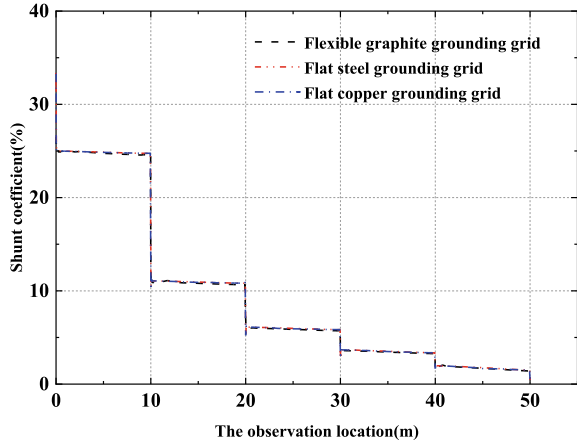
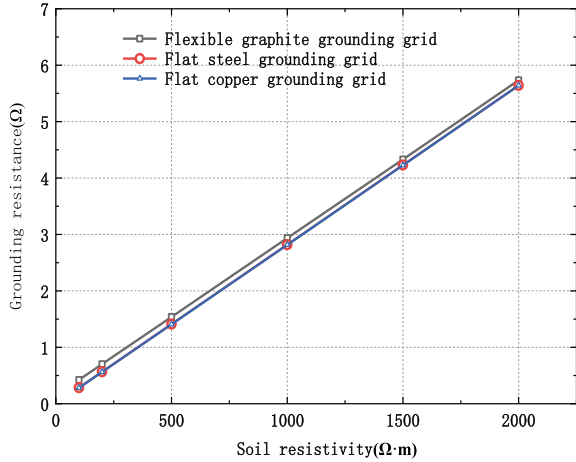**Fig. 5** The maximum temperature variation law of the grounding grid
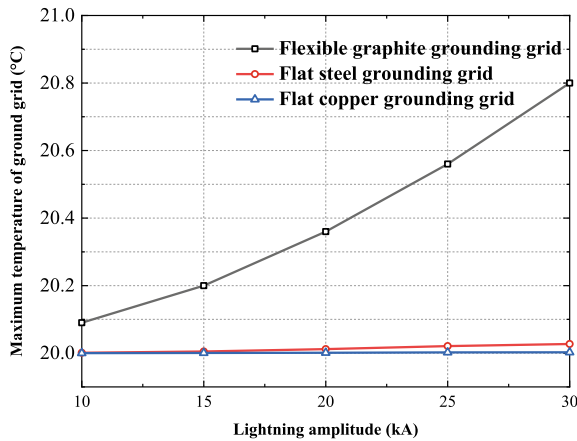
3.2 Influence of Soil Parameters

Other variables are held constant while analyzing the impact of soil resistivity on the grounding grid's dispersion characteristics; as soil resistivity changes, the grounding grid's grounding resistance change law is shown in Fig. 6, and the change in the diversion coefficient at the observation point is shown in Fig. 7.

Figure 6 shows that the grounding resistance of the grounding grid made of the three materials increases as soil resistivity increases, and that there is roughly a linear relationship between the two. Flexible graphite grounding mesh's grounding resistance, when subjected to the same soil resistivity, is not significantly different from that of metal grounding mesh, such as flat steel and flat copper, and the change in resistance trend is identical.

Fig. 6 Grounding resistance change law of grounding grid

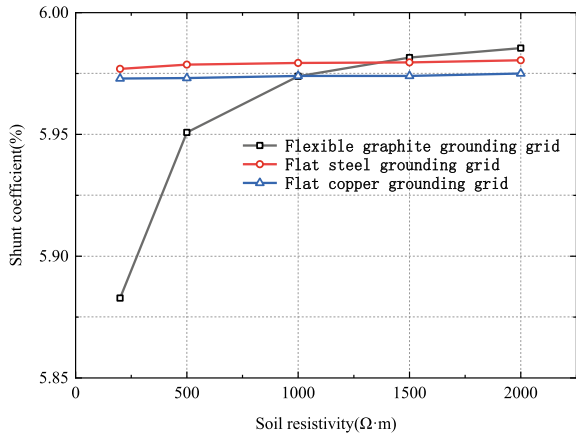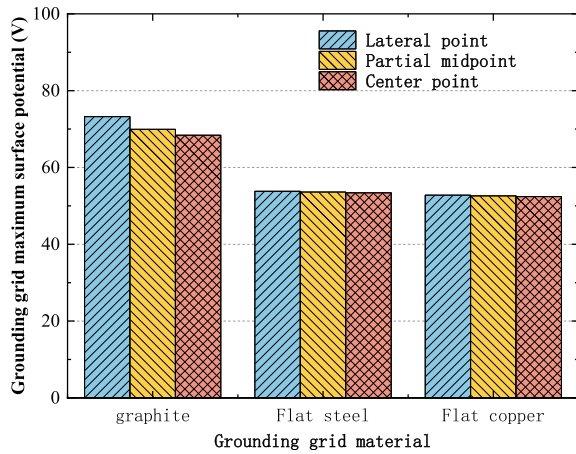**Fig. 7** The maximum temperature variation law of the grounding grid

Figure 7 shows that as soil resistivity increases, the shunt coefficient of flexible graphite grounding grid increases, and when it exceeds 1000 m, it tends to be stable and slightly higher than the shunt coefficient of metal grounding grid. This is primarily due to the effective length of flexible graphite material grounding net being longer than effective length of metal grounding mesh, the relative skin effect being weak, and the effective utilization area being large [8], so the diffusion effect at low soil resistivity is better and is greatly affected by soil resistivity.

3.3 The Effect of the Current Entering the Location

Figure 8 depicts the amplitude of the current into the ground, the soil resistivity, and the changes in potential of the grounding grid at various entry points in order to analyze the impact of the current entering the ground position on the scattering characteristics of the grounding grid.

According to the simulation results shown in Fig. 8, the highest surface potential of the flexible graphite material grounding net is consistently higher than highest surface potential of the metal grounding grid at the same current entry point, whereas the highest surface potentials of the flat steel grounding grid and the flat copper grounding grid are essentially the same. The highest surface potential of the flat steel and flat copper grounding grids barely changes as the current ingress point moves from the center to the edge of the grounding grid, but the maximum surface potential of the flexible graphite material grounding net rises, reaching up to 73.5 V, concentrated near the ground down conductor.

4 Simulation Analysis of Thermal Stability Under Power Frequency Short Circuit

4.1 The Effect of Short-Circuit Current Amplitude

Fixed soil resistivity and short-circuit current duration, the initial temperature is set to 20 °C, with the change of short-circuit current amplitude, the maximum temperature change curve of the grounding grid of the three materials is shown in Fig. 9.

It can be obtained from Fig. 9 that with the increase of the amplitude of the power frequency short-circuit current, the maximum temperature of the grounding grid of

Fig. 9 The maximum temperature variation of the grounding grid
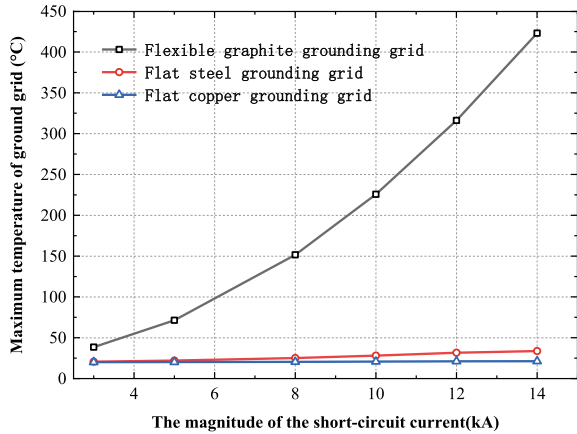
the three materials of flexible graphite increases, among which the temperature rise of metal grounding grids such as flat copper and flat steel is relatively low, and the temperature rise of flexible graphite grounding grids is much higher than temperature rise of metal grounding grids.

The results of the literature [9, 10] show that in the short-circuit shock resistance test, after the multiple impacts of the short-circuit current with a peak value of about 26 kA and a wavelength time of about 23 ms, the temperature of the grounding body reaches 210 °C, which has affected the original compactness of the grounding body to a certain extent.

4.2 The Effect of the Current Entering the Location

The size of the secured short-circuit current into the ground is 10 kA, the soil resistivity is 200 m, and the maximum temperature of the grounding simulation model at the three current entry points of the grounding grid center point, partial center point, and outer point is shown in Fig. 10 in order to analyze the relationship between the position of the short-circuit current entry point and the maximum temperature of the grounding simulation model.

Figure 10 shows that when the current entry point is the same, the maximum temperature of the non-metallic graphite grounding grid is significantly higher than the maximum temperature of the metal grounding grid, and as the current entry point gets closer to the grounding grid's edge, the temperature of the non-metallic composite grounding grid increases while remaining essentially constant for flat steel and flat copper.

Fig. 10 Maximum
temperature of the ground
grid at different entry points
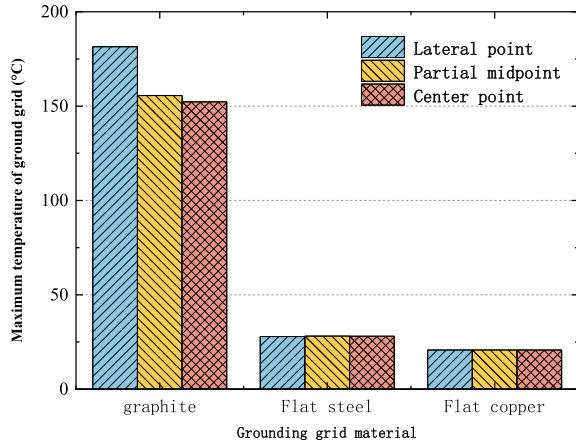
5 Conclusion

Through the simulation analysis of the dispersion characteristics and thermal stability of the substation grounding grid by COMSOL Multiphysics simulation software, the following conclusions can be drawn:

(1) The grounding diffusion effect of Φ40 mm flexible graphite grounding grid is similar to that of common flat steel and flat copper grounding mesh, and the grounding resistance of flexible graphite grounding grid has little difference from that of metal grounding grid, and the scattering performance is better under low soil resistivity.

(2) Compared with the metal grounding grid, the surface potential of the flexible graphite grounding grid is mainly concentrated near the entry point, but the potential distribution changes are not obvious.

(3) The maximum temperature of the grounding down conductor of the flexible graphite grounding grid is significantly higher than the maximum temperature of the metal grounding grid under the action of short-circuit current, and the temperature of the conductor does not meet the thermal stability requirements of flexible graphite.

(4) As the current entry point approaches the edge of the grounding grid, the maximum temperature of the grounding grid increases, so the temperature of the grounding grid edge ingress point should be used as a reference when judging the thermal stability.

The simulation results of this paper can provide a reference for the application of flexible graphite materials in the grounding network of substations.

References

1. Qian L, Xishan W (2018) Voltage grading optimization strategy for large grounding grid based on security. High Volt Apparat 54(6):177–183 (in Chinese)
2. Tao H, ZhiFeng D, Xiaolong Z et al (2018) Corrosion resistance of grounding materials used in electric system. Electroplating & Poll Control 38(05):52–55 (in Chinese)
3. Guofeng Z, Jingli L, Meng L (2021) Study on contact corrosion characteristics of metal down lead and flexible graphite. Electron Meas Technol 44(03):16–21 (in Chinese)
4. Bhosale MJ, Karandikar PB, Kulkarni NR (2023) An optimal design for grounding grid configuration with unequal conductor spacing. Adv Eng Softw 176
5. Li M, Cao S, Niu W et al (2022) A novel grid corrosion detection and two-dimensional imaging approach for a grounding substation. Am J Electr Comp Eng 6(2)
6. Yuanchao H, Tao H, Yunzhu A et al (2022) Simulation study on lightning impulse characteristics of flexible graphite composite grounding materials applied to grounding grid of power system. Front Energy Res
7. Jinliang H, Rong Z (2007) Grounding technology of power system. Science Press, Beijing (in Chinese)
8. Jinhu T, Yugen L, Junguang Z (2021) Calculation and influence factors analysis of lightning intruding overvoltage in GIS step-up station. High Volt Apparatus 57(12):74–82 (in Chinese)
9. Shijun H, Tao H, Yong Z et al (2016) Research of typical grounding material current release characteristic in transmission tower grounding grid. Water Resour Power 34(09):178–182 (in Chinese)
10. Yuanchao H, Jiangjun R, Wei X et al (2016) Study on flexible graphite composite material for electrical grounding and its correlation experimentations. High Volt Eng 42(06):1879–1889 (in Chinese)

Study on Mechanism and Protection of Lightning Overvoltage of Anticorrosive Layer of Buried Oil and Gas Pipeline Adjacent to Power Line

Lei Jia, Jian Yang, Shangmao Hu, Bo Gao, Gang Liu, and Yongcong Wu

Abstract With the continuous construction of social integrated energy lines, the intersection and proximity of power overhead lines and natural gas pipelines are becoming more and more frequent. The problem of lightning overvoltage in the case of adjacent crossing has attracted wide attention. Aiming at the problem of lightning overvoltage protection of anticorrosive coating of natural gas pipeline near high voltage line, firstly, ATP-EMTP software is used to calculate the characteristics of lightning current into the ground of tower near natural gas pipeline. Combined with COMSOL Multiphysics finite element software, the calculation model of lightning overvoltage of natural gas pipeline and its anticorrosive coating is established to clarify the output mechanism of pipeline body potential and anticorrosive coating potential difference. Secondly, the influence of lightning current amplitude, soil resistivity and "pipeline-line" spacing on pipeline overvoltage is analyzed by simulation. Finally, the lightning breakdown protection method of pipeline anticorrosive coating under the action of grounding current dispersion is proposed. The voltage limiting effect is verified by simulation examples and the construction suggestions of actual reconstruction project are put forward. The conclusion of this paper can provide reference for the design, construction and safe operation and maintenance of oil and gas pipelines.

Keywords Natural gas pipeline · Cross proximity · Lightning overvoltage · Anticorrosive coating

L. Jia (✉) · S. Hu · G. Liu · Y. Wu
Electric Power Research Institute, China Southern Power Grid, Guangzhou 510000, China
e-mail: jialei@csg.cn

National Engineering Research Center for UHV Power Technology and New Electrical Equipment Foundation, Guangzhou 510000, China

J. Yang · B. Gao
Electrical and Electronic Engineering College, Shandong University of Technology, Zibo 255000, China

1   Introduction

In recent years, the demand for comprehensive energy such as fossil energy and electric energy has been increasing, and the demand for natural gas resources in the international community has become more and more urgent. Natural gas energy and electric energy have become important factors in the international situation [1]. With the continuous construction of Sino-Russian transnational ultra-long natural gas pipelines, the Sino-Russian Eastern Gas Pipeline Project and the Sino-Russian Far East Natural Gas Pipeline Project are becoming more and more perfect. The maximum total gas supply will reach 48 billion cubic meters/year, which will become an important part of China's social energy supply [2]. With the establishment of the national pipeline network group, the natural gas pipeline projects such as the south and west trunk lines of Shandong pipeline network are under construction. It can be predicted that with the continuous advancement of the "double carbon" strategy, China's oil and gas pipeline project will usher in a period of high-speed construction during the "14th Five-Year Plan" period. With the increasing demand for comprehensive energy in society, multiple energy transmission lines such as electricity and natural gas are inevitably faced with "two lines and one place" working conditions such as proximity and cross-crossing [3].

2   Lightning Scattering Process of Pipeline Adjacent Power Line

Restricted by public land resources, power line construction and oil and gas industry site selection generally use a common "energy corridor". Therefore, power overhead lines and buried oil and gas pipelines often share "energy corridor" conditions. The vertical distance between the power line and the oil and gas pipeline is even within 10 m, as shown in Fig. 1. If the grounding grid of the tower is buried, the minimum distance between the underground dispersion point of the tower and the pipeline is even several meters. In addition to the influence of the coupling voltage of the power line on the pipeline on the cathodic protection potential under normal operating conditions, the potential risk of lightning strike transmission lines on oil and gas pipelines is often concerned in the operation and maintenance of oil and gas pipelines.

Because the transmission line is above the surface, its tower top and lightning conductor are often struck by lightning. Most of the tower ground current components will disperse through the "lightning conductor (or tower top)-hit tower-buried grounding body". On the one hand, the grounding current of the tower exists in the buried horizontal grounding body, on the other hand, the grounding current is dispersed by the steel structure inside the concrete pile foundation of the tower [4]. The physical process of "lightning line (or tower top)-hit tower-buried grounding body" shown in Fig. 1 shows that when the oil and gas pipeline is embedded around the concrete pile foundation of the tower, the lightning current will generate a higher

Fig. 1 Schematic diagram of "two lines and one ground"
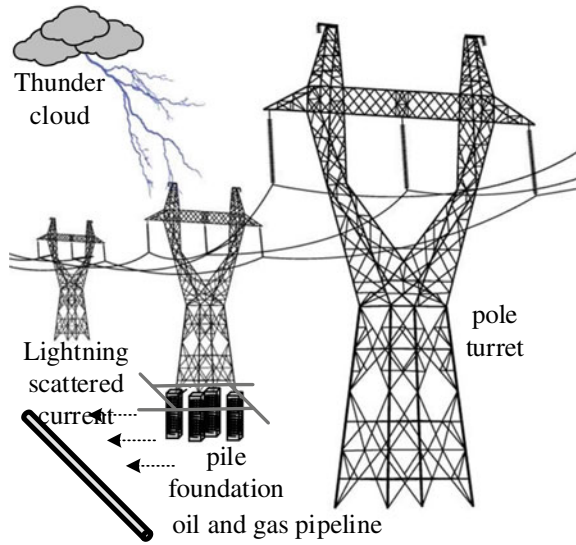
potential in the soil. Due to the direct contact between the oil and gas pipeline and the soil, the lightning current near the pile foundation of the tower will inevitably generate a certain amplitude of overvoltage on the pipeline body.

When lightning strikes the top of the power line tower or the lightning line, the potential on the adjacent oil and gas pipeline contains two parts: resistive coupling component and inductive coupling component. On the one hand, the lightning current shunts along the lightning line to both ends, and discharges in the adjacent towers on both sides. The high-frequency lightning current flowing through the lightning line causes the surrounding space (air and soil) to generate alternating electromagnetic field, and the voltage is coupled on the pipeline through electromagnetic induction. Although the pipeline potential rise caused by the inductive coupling component is not directly related to the tower, the size of the inductive coupling component is related to the grounding resistance of a single tower [5]. On the other hand, the tower discharges the lightning current into the soil medium along the metal tower body and the grounding down lead, and a high-amplitude high potential is generated in the soil. Because there is no insulation between the buried oil and gas pipeline and the soil medium [6], the outer layer of the pipeline in the soil adjacent to the tower pile foundation is in a high potential state.

The overhead transmission and distribution lines of 35 kV and above in the power sector are generally equipped with single or multiple lightning wires. When the natural lightning cloud discharges the lightning wire, in addition to the discharge along the nearest tower, a part of the lightning current will be shunted to the distance through the lightning wire, and the current will be dispersed through the grounding point set by the distant tower or overhead power line. The lightning current shunt process is shown in Fig. 2.

（a）Dispersing process　　　　　（b）Line and tower parameters
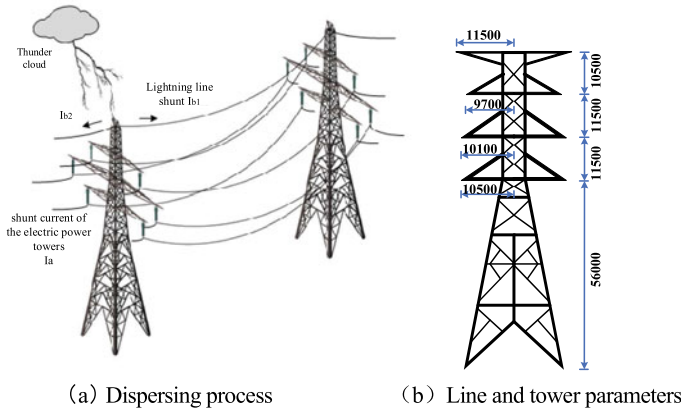
Fig. 2 Lightning strike and scatter process of power line

In addition to the coupling voltage of the normal operation line, the overvoltage protection of the natural gas pipeline coating near the power line mainly focuses on the influence of the lightning current flowing into the soil along the tower on the over-voltage potential. The diversion coefficient β of the tower is taken as the proportion coefficient of the lightning current scattered into the ground by the adjacent natural gas pipeline tower. Its physical meaning is: the ratio of the peak value of the lightning current I_a of the power tower and its grounding device with the nearest natural gas pipeline [7] spacing to the total lightning current hitting the tower, that is:

$$\beta = \frac{Ia}{Ia + Ib1 + Ib2} \times 100\% \tag{1}$$

In order to analyze the influence of lightning current amplitude on the shunt coefficient β of the tower, according to the actual design and construction conditions of the power system transmission line, the tower span is 450 m, and the tower body parameters are shown in Fig. 2b. Because the soil parameters inevitably affect the diversion coefficient β of the tower, the soil resistivity ρ is set to 300 Ω·m, and the tower grounding resistance R is 10 Ω. On this basis, the lightning current amplitude is selected to be 5–60 kA for simulation calculation. The influence of lightning current amplitude on the ground current amplitude and the tower shunt coefficient β is shown in Fig. 3.

From the simulation results shown in Fig. 3, it can be seen that with the increase of the lightning current amplitude I_m, the ground current I_a shows a gradual increase trend, and the increase is gradually increasing. From Fig. 3b, it can be seen that with the increase of lightning current amplitude I_m, the tower diversion coefficient β basically does not change. When the lightning current amplitude is 40 kA, the tower shunt coefficient is the smallest, which is 91.02%. When the lightning current amplitude is 5 kA, the tower shunt coefficient is the largest, which is 91.06%, and the maximum change range is 0.04%. This is because the change of the lightning
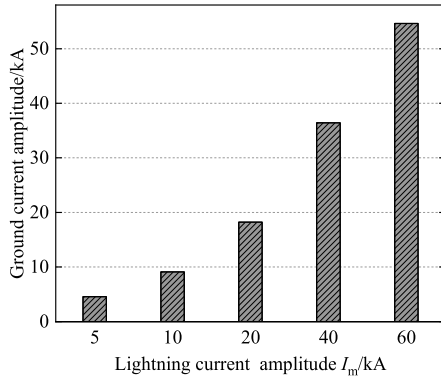
(a) The influence of natural lightning current on the tower grounding current
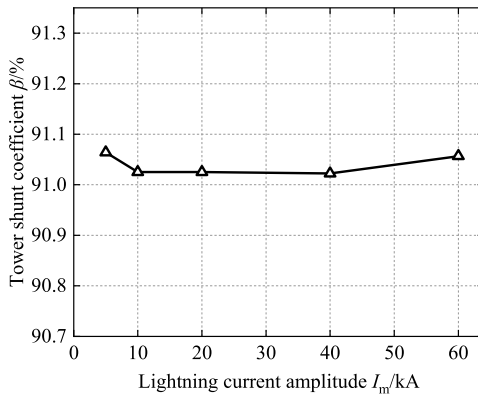
(b) The influence of lightning current amplitude on tower shunt coefficient
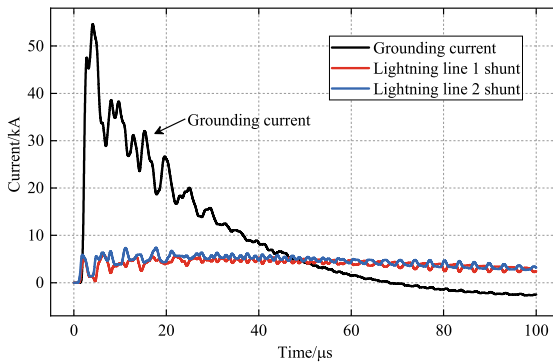
(c) Lightning conductor shunt calculation ($Im = 60$kA)

Fig. 3 Effect of natural lightning current on tower entry current and shunt coefficient

current amplitude I_m does not change the structure of the counterattack shunt circuit of the whole power line without considering the insulation erection of the lightning conductor. This makes although the increase of the lightning current amplitude I_m will increase the ground current I_a accordingly, but the tower shunt coefficient β remains unchanged. The lightning current shunt curve when the lightning current amplitude I_m is 60 kA can be drawn by ATP-EMTP software as shown in Fig. 3c. According to the simulation results, it can be seen that with the increase of the action time of the lightning current, the lightning current component of the struck tower increases first, and then decreases in a long period of time. This is due to the lightning current of the struck tower is set to 2.6/50 μs standard lightning current waveform, the wave head time is 2.6 μs, and its rising time is very short.

From the simulation results, it can be seen that with the increase of the tower grounding resistance R, the tower shunt coefficient β gradually decreases. When the tower grounding resistance R is 5 Ω, the tower shunt coefficient is the largest, 94.94%; when the grounding resistance R of the tower is 30 Ω, the shunt coefficient of the tower is the smallest, which is 78.30%, and the maximum change range is 16.64%. It can be seen that the change of the grounding resistance R of the tower has a significant effect on the shunt coefficient β of the tower.

3 Pipeline Overvoltage

3.1 Generation Mechanism of Pipeline Overvoltage

Because the grounding resistance of the power industry tower is generally maintained within 10 Ω, and the shunt ratio of the lightning conductor is small, the research generally believes that the resistive coupling component under lightning strike is the main factor. In addition, the insulation withstand voltage of the pipeline insulation coating is an important index to measure the lightning overvoltage problem when the power line and the oil and gas pipeline are adjacent to each other, and the damage degree of the insulation layer is related to the integrity of the pipeline surface and the pipeline structure. If there are damage points or metal flanges in the coating around the pipeline, the ground potential on the pipeline is high and the withstand potential of the coating is the potential difference on both sides. If the anticorrosive coating around the pipeline is intact and has no damage point, the metal pipeline body is grounded through the distal end. At this time, the tolerance potential difference of the pipeline anticorrosive coating is high, and there is a risk of insulation breakdown.

3.2 Influencing Factors of Pipeline Overvoltage

The simulation results show that the transient potential of the pipeline metal body and the insulation layer increases during the lightning flow to the soil medium around the tower, and the peak value reaches tens of kV. When the lightning current amplitude increases from 10 to 60 kA, the potential on the outer side of the coating and the potential on the metal conductor of the pipeline basically show a linear increase trend. Due to the greater increase of the potential on the outer side of the coating, the difference between the inner and outer sides of the pipeline increases accordingly. When the lightning current amplitude is 60 kA, the withstand voltage difference of the anticorrosive coating is 21.99 kV, and the transient voltage value is generally less than the withstand voltage value of 3LPE material 109 kV. If there is a damage point in the pipeline, the leakage current of this amplitude is easy to cause the further increase of the damage gap. Because the metal body of the pipeline is a good conductor, there is a potential risk of electric shock to pedestrians or operation and maintenance personnel at the far end of the pipeline in a few cases.

With the increase of "pipe-line" spacing d_{pg1}, the withstand voltage of the pipeline metal body and the anticorrosive coating began to decrease. The increase of the distance between the pipeline and the end of the grounding body will make more soil media participate in the dispersion, and the potential on the pipeline side will decay rapidly. When the distance increases from 30 to 70 m, the withstand voltage of the coating decreases by about 71.95%. When the natural gas pipeline and the power tower are adjacent or crossed, the pipeline or line project that has been put into operation generally has a large amount of relocation. Increasing the distance between the two is beneficial to the peak value of the limit pipeline overvoltage, and it is also necessary to take into account the technical economy of the overvoltage limitation method.

4 Overvoltage Protection Method of Pipeline

In the actual project, when the power line and the oil and gas pipeline are adjacent or crossed, the pipeline overvoltage is mainly restricted by the distance between the tower leakage grounding body and the pipeline and the lightning current amplitude. Since the latter is generally difficult to intervene manually as an objective natural factor, it is undoubtedly feasible to minimize the distance between power lines and oil and gas pipelines under the condition of "two lines and one place" in the design or operation and maintenance of power or oil and gas pipelines. Considering that the scattered flow cost of the power tower or oil and gas pipeline that has been put into operation is high in the vertical dimension, it is feasible to reduce the scattered flow component on the pipeline side of the tower through manual transformation and optimization.

For oil and gas pipelines or power lines that have been put into operation, large-scale relocation projects cost a lot of cost and construction. When oil and gas pipelines are close to power lines, the over-voltage of pipelines is mainly restricted by the relative distance between the tower discharge grounding body and the pipeline and the lightning current amplitude conditions. By changing the distance between the oil and gas pipeline and the tower discharge grounding body, it can effectively reduce the difference between the pipeline body point and the anti-corrosion layer withstand potential, and play a better protective effect.

5   Conclusion

Aiming at the problem of lightning overvoltage protection of oil and gas pipelines near power lines, a method of pipeline overvoltage protection considering the current dissipation of tower grounding grid is proposed. The mechanism of pipeline over-voltage is analyzed by simulation model and the application value of the optimization scheme is verified. The main research conclusions include:

(1) The lightning strike of the tower near the pipeline diffuses through the tower body and the bilateral lightning lines. The smaller the grounding resistance is, the larger the shunt coefficient is. The overvoltage amplitude of the pipeline is related to the lightning current amplitude and the "pipe-line" spacing.
(2) Optimizing the length of the grounding grid and the number of branches can limit the overvoltage of the pipeline, and realize the breakdown protection of the pipeline anticorrosive coating under the condition of ensuring the lightning protection requirements of the grounding resistance.

The conclusions of this paper can provide reference for the design and safe operation of power transmission and oil and gas pipelines.

References

1. Shi W (2016) Comparison between Kazakhstan's СНРК 2.04–29–2005 and China's GB 50057-2010. Oil & Gas Storage Transp 35(10):1122–1126. (in Chinese)
2. Guomin CAO (2022) Evalution of the interference of stray current of HVDC grounding electrode on newly-built crude oil pipeline and its protection method. Corr Protect 43(07):109–116 (in Chinese)
3. Cao F, Bai F, Li B et al (2021) Effect of output of cathodic protection power supply on potential distribution of pipeline under DC grounding electrode current interference. Corr Protect 42(8):63–68+75. (in Chinese)

4. Gao X, Hu Y, Jiang Z et al (2022) Safety protection measures of lightning strike at the intersection of overhead line and pipeline. Insul Surge Arresters 1:22–28. (in Chinese)
5. An N, Peng Y, Xiancang A et al (2012) Electromagnetic effects on underground oil/gas pipeline of the lightning strike on EHV AC transmission line. High Volt Eng 38(11):2881–2888 (in Chinese)
6. Dey PK, Ogunlana SO, Naksuksakul S (2004) Risk-based maintenance model for offshore oil and gas pipelines: a case study. J Qual Maintenance Eng 10(3):169–183
7. Zhao M, Luo L (2019) Analysis of safety early warning technology for the Myanmar-china oil and gas pipeline (Myanmar section). IOP Conf Ser: Earth Environ Sci 300:022024
8. Cheng S, Yuan W (2021) Corrosion mechanism and anticorrosion technology of oil and gas gathering and transportation pipeline. IOP Conf Ser: Earth Environ Sci 859:012115
9. Xie Y, Zuo P, Zhou X, Chen B, Zhou P, Feng C (2021) Analysis on material defects of circuit breaker oil and gas pipelines. IOP Conf Ser: Earth Environ Sci 621:012012

Research on Concrete Installation Grounding Scattering Characteristics and External Application Resistance Reduction Strategy

Yinlong Wang, Hao Li, Chengwei Jiang, Jie Zhang, Ting Li, Hui Zhang, and Qingchen Wang

Abstract In order to research the problems of grounding dispersion characteristics and resistance reduction efficiency of concrete foundation for wind turbine, this study uses COMSOL Multiphysics simulation software to build a model of concrete foundation for wind turbine, to study the effects of concrete resistivity and soil conditions on the dispersion characteristics of concrete foundation and spark breakdown characteristics of soil, and to propose structural optimization measures for external application of flexible graphite composite electrical grounding material. The results show that: the concrete foundation grounding resistance increases with the increase of concrete (soil) resistivity; the influence of soil resistivity on the concrete foundation dispersion characteristics is more obvious than that of concrete resistivity; the spark breakdown volume of the soil around the concrete foundation increases with the increase of concrete (soil) resistivity, while the soil resistivity has a greater effect on it; the external flexible graphite composite electrical grounding material can influence the concrete foundation dissipation characteristics and increase the spark breakdown volume of the soil around it. The results of the study can provide a reference for the design of concrete pile foundations for actual wind turbines.

Keywords Wind turbine · Concrete foundation · Grounding dispersion characteristic · Spark breakthrough · Flexible graphite composite electrical grounding material

Y. Wang · J. Zhang · T. Li
State Grid Anhui Electric Power Co., Ltd., Tongling Power Supply Company, Tongling 244000, China

H. Li · H. Zhang
State Grid Anhui Electric Power Co., Ltd., Construction Company, Hefei 230071, China

C. Jiang (✉) · Q. Wang
School of Electrical and Electronic Engineering, Shandong University of Technology, Zibo 255000, China
e-mail: daboozz2020@126.com

1   Introduction

Wind turbines are towering and mostly deployed in open areas such as plains and hills, which are vulnerable to lightning strikes [1]. When the lightning current is transmitted to the incoming ground, its dissipation will be hindered by the influence of the surrounding complex soil conditions, resulting in a sharp increase in the ground and wind turbine potential, which endangers the safety of the insulation of the turbine equipment [2]. Therefore, it is crucial to maintain the reliable operation of turbines by minimizing the grounding resistance of wind turbines under the limited grounding construction area and thus achieving rapid dissipation to the soil after lightning strikes the blades [3].

Numerous studies have been conducted by experts and scholars to the research of lightning protection and grounding of wind turbines. Deng et al. [4] conducted impact characteristic simulation tests on the typical wind turbine grounding device for different soil conditions. To solve the problem of insufficient safety of the wind farm grounding system during lightning strikes, the literature [5] interconnected the wind turbine grounding network. Sima et al. [6] proposed a new method for frequency domain analysis of impact characteristics. In the literature [7], the effect of the natural grounding grid structure of wind turbines on the lightning strike transient process was analyzed by establishing a lightning strike transient model. In addition, the literature [8] used CDEGS simulation software to build an offshore wind turbine grounding model. Furthermore, the use of flexible graphite composite electrical grounding materials has emerged as a new hotspot [9, 10]. However, most of the existing studies on the grounding device of wind turbine have not considered the influence of concrete foundation.

This paper simulates the grounding dissipation characteristics of a wind turbine's concrete foundation during a lightning strike and optimizes the structure. Firstly, the formula for calculating the grounding resistance of wind turbine concrete foundation is explained; then the model of wind turbine concrete foundation is built, and the effects of different factors on the grounding resistance and current dissipation characteristics of wind turbine concrete foundation are analyzed, and the soil breakdown field strength around it is also calculated; finally, the flexible graphite composite electrical grounding material is applied to the concrete foundation of wind turbine.

2   Model Construction and Simplification

2.1   *The Dispersion Calculation of Vertical Grounding Grid*

The main research of this paper is about the grounding characteristics of concrete pile foundation when lightning strikes wind turbine. Among them, the calculation of the grounding resistance of the concrete foundation of wind turbine can be referred

to the vertical grounding pole. Then the grounding resistance of concrete base when laid in concrete and soil is:

$$R_{DM} = F(\rho, S_1, G) - F(\rho_c, S_1, G) \tag{1}$$

where S_1 is the intersection area of concrete and soil, m^2; G is the geometric factor considering the shape of electrode; ρ_C is the concrete resistivity; ρ is the soil resistivity. Equation (1) can be used to calculate the resistance value of the grounding resistance when the electrode wrapped outsourced concrete is in the soil.

According to the formula proposed by E. J. Fagan and R. H. Lee for calculating the grounding resistance of outsourced concrete, the grounding resistance R_C of electrodes in concrete can be calculated using the following equation:

$$R_C = (1/2\pi L_r)\{\rho_C \ln(D/d) + \rho[\ln(8L_r/D) - 1]\} \tag{2}$$

where L_r is the total length of the reinforcement in the concrete foundation, m; D is the diameter of the concrete shell with outsourced reinforcement, m; d is the diameter of the reinforcement, m. In addition, considering the discontinuity of the steel skeleton in the concrete foundation, the resistivity correction factor K_1 and the discontinuity correction factor K_2 are introduced, Where, $K_1 = 1.1$ and $K_2 = 1.05$:

$$R = (K_1 K_2 \rho/2\pi L_r)\ln(4L_r/d) \tag{3}$$

2.2 Modeling and Parameters of the Simulation

Diagram of concrete foundation construction of wind turbine can be seen as Figs. 1, and 2 shows the Model of wind turbine concrete foundation. The steel reinforcement material was selected as Φ16 mm galvanized round steel with resistivity of $1.92 \times 10^{-6}\Omega/m$ and relative magnetic permeability of 636. The concrete thickness is 50 mm, the concrete is 200 mm from the bottom rebar, and the relative magnetic permeability is 1.
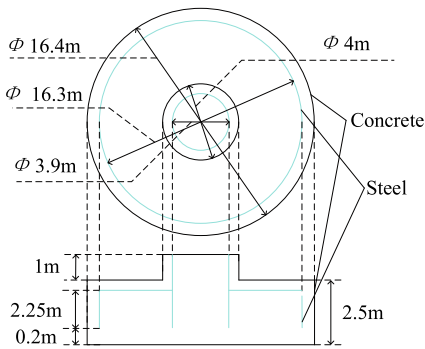
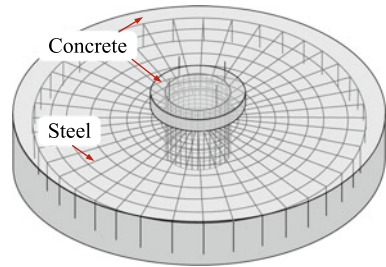(a) Actual construction drawing   (b) Diagram of concrete foundation

Fig. 1 Diagram of concrete foundation construction of wind turbine

(a) Form of concrete foundation   (b) simulation specific model

Fig. 2 Model of wind turbine concrete foundation

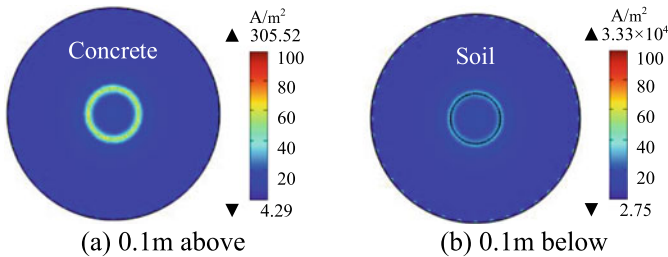# 3 Dispersion Characteristic of Wind Turbine Concrete Foundation

3.1 Effect of Concrete Resistivity on Dispersion Characteristics

The soil resistivity ρ is fixed at 500 $\Omega{\cdot}$m and the concrete resistivity ρ_C is changed. The grounding resistance values of wind turbine concrete pile foundation under different concrete resistivity conditions are shown in Table 1.

As can be seen from Table 1, the grounding resistance of wind turbine concrete foundation increases with the increase of concrete resistivity ρ_C under the condition of constant soil resistivity ρ. To illustrate this phenomenon, setting $\rho = 500$ $\Omega{\cdot}$m, $\rho_C = 10,000$ $\Omega{\cdot}$m, and observation surfaces of current density were constructed at 0.1 m above (in concrete) and 0.1 m below (in soil) from the bottom of the concrete base of wind turbine, respectively, as shown in Fig. 3.

Table 1 Grounding resistance of wind turbine foundation under different concrete resistivity

Soil resistivity ρ (Ω·m)	Concrete resistivity ρ_C (Ω·m)	Grounding resistance R_n (Ω)
500	5000	12.84
	8000	13.08
	10,000	13.17
	20,000	13.35
	50,000	13.47

(a) 0.1m above   (b) 0.1m below

Fig. 3 Current density at two different positions

According to the current density at different observation surfaces shown in Fig. 3, it is known that: when the observation surface is located in concrete, the solution can be obtained the maximum leakage current density is 305.52 A/m^2, and when the observation surface When the observation surface is located in the soil, the maximum leakage current density is 3.33×104 A/m^2, which means that under the action of high-frequency impressed lightning current, the current tends to drain through the steel reinforcement to the soil around the concrete foundation with less resistivity, while the concrete has a higher resistivity and smaller thickness, so the effect on the dispersed current of the concrete foundation of wind turbine is not obvious.

3.2 Effect of Concrete Resistivity on Dispersion Characteristics

The concrete resistivity ρ_C is fixed at 1000 Ω·m, and the soil resistivity ρ is changed to obtain the grounding resistance of wind turbine concrete pile foundation under different soil resistivities as shown in Table 2.

As can be seen from Table 2, with the increase of soil resistivity ρ, the concrete pile foundation grounding resistance of wind turbine increases under the condition that the concrete resistivity ρ_C of wind turbine grounding device remains unchanged. In addition, compared with the concrete resistivity, the soil resistivity has a greater influence on the grounding resistance of the concrete foundation of wind turbine. This is due to the effect of lightning inrush current, the current tends to drain to the

Table 2 Grounding resistance of wind turbine foundation under different soil resistivity

Concrete resistivity ρ_C ($\Omega \cdot$m)	Soil resistivity ρ ($\Omega \cdot$m)	Grounding resistance R_n (Ω)
10,000	200	6.99
	500	13.17
	1000	20.37
	1500	24.86
	2000	27.71

lower resistivity of the soil, when the soil resistivity increases, the current is more difficult to drain to the surrounding soil.

3.3 Soil Spark Breakdown Calculation in the Vicinity of the Foundation

To study the spark breakdown characteristics of the soil near the concrete foundation of wind turbine under the action of high amplitude impact lightning current, the critical soil breakdown field strength E_c was set to 100 kV/m [11], and the spark breakdown volume of the soil around the concrete pile foundation of wind turbine under different concrete resistivity and different soil resistivity was shown in Fig. 4.

According to Fig. 4, it can be seen that the spark breakdown volume of soil around the concrete pile foundation of wind turbine gradually increases as the concrete resistivity (soil resistivity) increases. This is due to the fact that as the soil resistivity increases, the electric field strength in the soil around the concrete foundation increases after applying the impact lightning current amplitude, and the volume of

(a) Influence of soil resistivity

(b) Influence of concrete resistivity
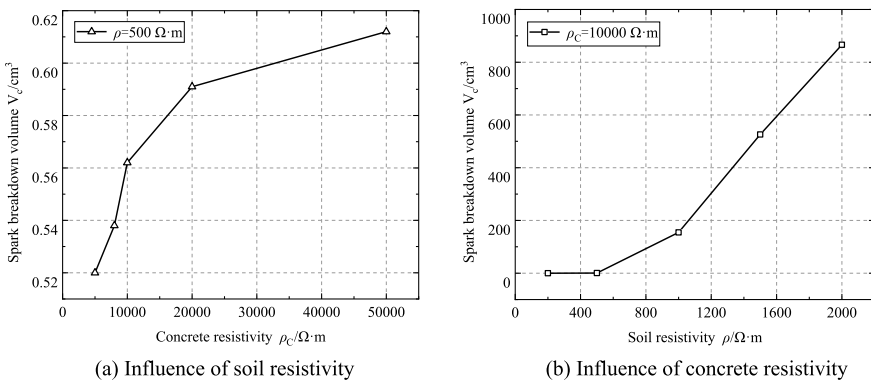
Fig. 4 Spark breakdown volume of soil around the foundation under different conditions

(a)   (b)
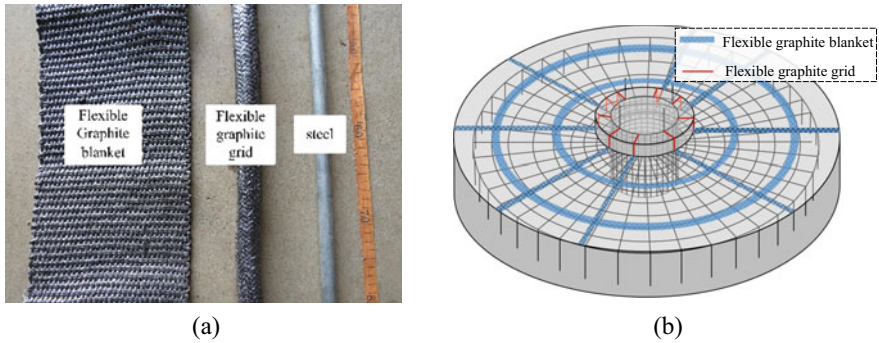
Fig. 5 External flexible graphite composite electrical grounding material for foundation

the area in the soil that can reach the critical breakdown field strength E_c is larger. The optimization of wind turbine concrete foundation grounding dispersion structure.

## 3.4 External Structure of Wind Turbine Concrete Foundation

The traditional resistance reduction scheme with long outreach may not achieve the expected resistance reduction effect due to construction problems. To solve this problem, this paper uses flexible graphite composite grounding material externally applied to the concrete pile foundation of wind turbine, as shown in Fig. 5.

3.5 Effect of External Materials on the Dispersion in Concrete Foundations

In order to analyze the effect of the flexible graphite composite grounding material on the grounding resistance of wind turbine concrete foundation after its external application, the resistance reduction efficiency μ is introduced, defined as:

$$\mu = (R_n - R_g/R_n) \times 100\% \tag{4}$$

where R_n is the natural grounding resistance of pile foundation before applying flexible graphite composite grounding material, Ω; R_g is the grounding resistance of pile foundation after applying flexible graphite composite grounding material, Ω. The resistance value and resistance reduction efficiency of concrete pile foundation of wind turbine after applying flexible graphite composite grounding material under different soil resistivity are shown in Fig. 6.
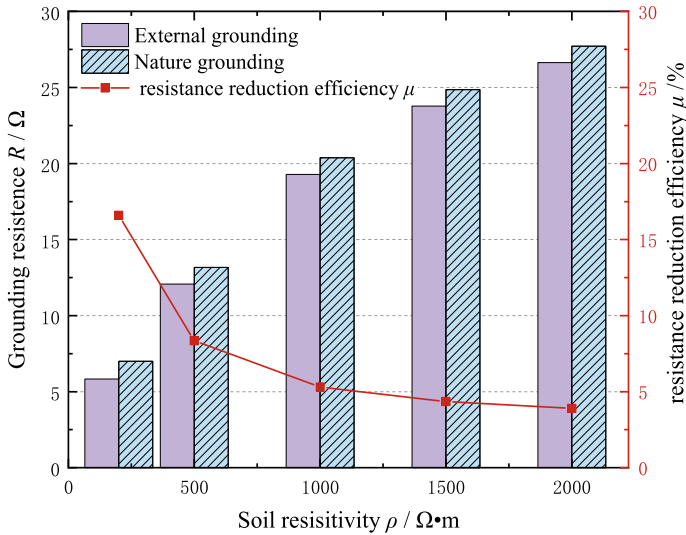
Fig. 6 Grounding resistance and resistance reduction efficiency of concrete foundation after external laying

As can be seen from Fig. 6, compared with natural grounding, the wind turbine concrete pile foundation with external flexible graphite composite grounding material grounding can better reduce grounding resistance and has higher resistance reduction efficiency. In addition, with the increase of soil resistivity around the concrete foundation of wind turbine, the more difficult it is for the current to drain into the surrounding soil, so the more difficult it is for the pile foundation to reduce resistance, and the resistance reduction efficiency decreases. This is because part of the injected current will be diverted along the flexible graphite cable body and the flexible graphite blanket material, the external material can effectively reduce the internal reinforcement of the wind turbine concrete pile foundation dissipation component, more current through the external material discharge to the soil. It can be seen that the external flexible graphite composite grounding material can effectively assist the concrete pile foundation of wind turbine to drain current into the surrounding soil while reducing its grounding resistance.

3.6 Effect of External Material on Soil Breakdown Area

In order to study the effect of external flexible graphite composite grounding material on the soil breakdown area near the concrete base of wind turbine, the critical breakdown field strength E_c of soil is set to 100 kV/m, and the spark breakdown volume of soil around the soil pile base under different soil resistivity is shown in Fig. 7.

Fig. 7 Spark breakdown volume of soil around concrete foundation after external flexible graphite composite electrical grounding material
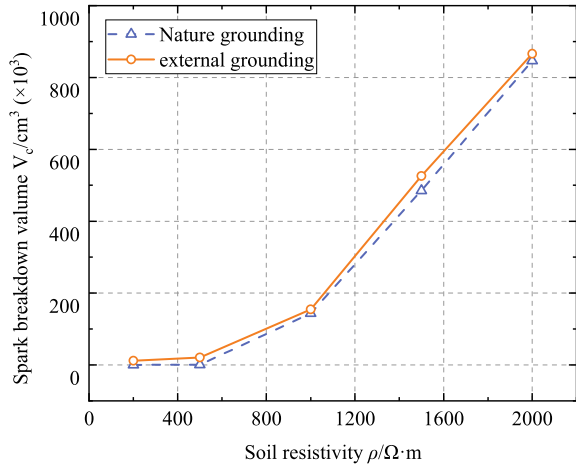
Compared with the natural grounding, the external grounding of the concrete foundation with flexible graphite composite grounding material will increase the spark breakdown volume of the soil around it, which is due to the action of the impact lightning current, part of the current component will drain along the flexible graphite composite grounding material to the soil, making the pile foundation to the surrounding soil leakage current increased, the electric field strength generated in the soil is more likely to reach the soil critical breakdown field strength E_c (100 kV/m), which makes the spark breakdown volume in the surrounding soil increase, more conducive to the dissipation of the wind turbine concrete pile foundation and resistance reduction.

4 Conclusion

(1) the grounding resistance of pile foundation increases with the increase of soil (concrete) resistivity, but the effect of soil resistivity is more obvious.
(2) As the soil resistivity increases, the spark breakdown volume of the soil (concrete) around the concrete foundation of wind turbine gradually increases, and when the soil resistivity increases to 500 $\Omega \cdot$m, the rate of increase of the spark breakdown volume of the soil around it tends to level off.
(3) When the flexible graphite composite electrical grounding material is applied to the concrete foundation of wind turbine, more current component is discharged to the soil through the external material, thus reducing the grounding resistance of the concrete foundation.

(4) The external flexible graphite electrical composite grounding material can increase the electric field strength of the soil around the concrete foundation of wind turbine and the spark breakdown volume, which is more conducive to the resistance reduction of the concrete foundation.

References

1. Sekioka S (2016) Discussion of current dependent grounding resistance using an equivalent circuit considering frequency-dependent soil parameters. In: 33rd International conference on lightning protection (ICLP). IEEE, Estoril, pp 25–30
2. Kontargyri VT, Gonos IF, Stathopulos IA (2015) Study on wind farm grounding system. IEEE Trans Industry Appl 51:4969–4977
3. Guo Z, Zhang X (2021) Calculation of wind turbines grounding resistances by simulation current algorithm. Insul Surge Arresters 6:5. (in Chinese)
4. Deng C, Peng Y, Qiu L (2017) Impulse test study on decreasing resistance measures of typical grounding devices of wind turbine generators. High Volt Apparatus 53:158–163 in Chinese
5. Esmaeilian A, Akmal A, Naderi MS (2012) Wind farm grounding systems design regarding the maximum permissible touch & step voltage. In: 11th International conference on environment and electrical engineering (EEEIC). IEEE, Venice, pp 74–79
6. Sima W, Li X, Yuan T (2009) Analysis of grounding grid impulse characteristics in frequency domain in consideration of soil non-linear characteristic. Proc CSEE 29:127–132 in Chinese
7. Sun T, Li W, Zhang B (2022) Analysis of lightning transient process at the base of wind turbine tower considering the influence of natural grounding bod. Insul Surge Arresters 1:29–35 in Chinese
8. Li W, Wang S, Shen W (2022) Feasibility study on TLP floating offshore wind turbine using mooring system as grounding body. Insul Surge Arresters 3:142–147 in Chinese
9. Feng J, Jiang Z, An Y, Hu Y, Gao X (2021) Study on inductance effect and spark discharge effect of flexible graphite composite grounding conductors. Insul Surge Arresters 3:112–118 in Chinese
10. Wang X, An Y, Hu Y (2022) Protection effect of oil and gas pipeline insulation layer based on low-inductive graphite composite grounding material. Corr Protect 43:33–39 in Chinese
11. Liew AC, Darveniza M (1974) Dynamic model of impulse characteristics of concentrated earths. Proc Inst Electr Eng 121:123–135

Study on Overvoltage and Protection of Buried Pipeline Near Lightning Strike Line Considering Soil Grounding Scatter

Jie Zhang, Ning Xiu, Bo Gao, Yinlong Wang, Ting Li, and Yongnai Zhang

Abstract At present, the cross-adjacent conditions of oil and gas pipelines and power lines are more and more frequent. The lightning overvoltage problem under the condition of "two lines—one ground" cross-adjacent to each other has attracted the attention of different industries. Aiming at the lightning overvoltage protection problem of oil and gas pipelines near power lines, firstly, COMSOL Multiphysics software was used to establish the calculation model of lightning overvoltage under the condition of "two lines—one ground" cross adjacent to each other, to clarify the production mechanism of pipeline potential and potential difference of anticorrosive layer. Secondly, the influence law of soil resistivity and soil stratification on the amplitude of pipeline overvoltage is analyzed by simulation calculation, and the method of pipe-line overvoltage protection considering the scatter flow of tower grounding grid is proposed. Finally, the pipeline pressure limiting effect of the optimized transformation scheme is verified by a simulation example and its engineering application value is demonstrated. The conclusions of this paper can provide a reference for the design, construction and safety operation and maintenance of oil and gas pipelines.

Keywords Oil and gas pipelines · Cross and proximity · Lightning overvoltage · Soil current dispersion

J. Zhang (✉) · Y. Wang · T. Li
State Grid Anhui Electric Power Co., Ltd., Tongling Power Supply Company, Tongling 244000, China
e-mail: jiezhang_1985@163.com

N. Xiu · Y. Zhang
State Grid Anhui Electric Power Company, Hefei 230000, Anhui, China

B. Gao
School of Electrical and Electronic Engineering, Shandong University of Technology, Zibo 255000, China

1 Introduction

Due to the great difference between power and oil–gas energy transmission, the former mainly adopts the structure of overhead lines in non-urban areas, while oil–gas pipelines are usually buried in underground soil. Whether it is the power industry or the oil–gas industry, more and more attention has been paid to the safe and stable operation of the two energy transmission pipelines under the condition of "two lines and one ground" crossing each other [1]. For a long time, there have been many studies on electromagnetic compatibility between power lines and oil–gas pipelines in academia. The main research results focus on the induced voltage generated on buried oil–gas pipelines during the normal operation of AC/DC transmission lines, especially the influence of induced potential on pipelines, valve chambers, cathodic protection devices, etc. Some electromagnetic compatibility protection measures have been piloted in the "two lines and one ground" cross-neighboring project [2–5]. In addition to the impact of power lines on oil–gas pipelines under normal operating conditions, some studies have found that the current entering the ground along the tower after the lightning strike of the power line may cause a certain overvoltage risk to the adjacent pipeline. This is an earlier research report in this field in China. Reference [6] proposed that the lightning overvoltage of pipeline anticorrosive coating can be reduced by installing drainage belt and changing the structure of tower grounding device. In reference [7], the potential risk of pipeline lightning strike under the condition of "two lines and one ground" cross and adjacent is analyzed by the simulation calculation software CDEGS theory. The above research shows that in order to avoid the problem of lightning overvoltage in the case of "two lines and one ground" crossing and adjacent between power lines and oil–gas pipelines, clarify the mechanism of overvoltage generation on adjacent pipelines, and propose overvoltage protection measures with small engineering operation surface and low construction cost. It has high engineering application value in the design, operation and maintenance of oil–gas industry and power sector.

In this paper, aiming at the problem of lightning overvoltage in the case of "two lines and one ground" crossing and adjacent between power lines and oil–gas pipelines, a method of pipeline pressure limiting and drainage considering the dispersion effect of tower grounding grid is proposed to reduce the overvoltage amplitude on adjacent oil–gas pipelines. The overvoltage protection effect of this method is verified by simulation examples. This method does not change the structure of oil–gas pipelines. The overall engineering quantity and construction cost are low, and it has high feasibility.

2 Overvoltage Generation Mechanism and Simulation Model

2.1 Overvoltage Generation Mechanism of Adjacent Pipeline

Subject to the constraints of public land resources, the construction of power lines and the location of oil–gas industries generally adopt a common "energy corridor". Therefore, power overhead transmission lines and buried oil–gas pipelines often share a common "energy corridor". As shown in Fig. 1, the vertical distance between the power line and the oil–gas pipeline is even within ten meters. If the grounding grid of the tower is buried, the minimum distance between the underground scattered point of the tower and the pipeline even reaches several meters. Because the transmission line is above the surface, its tower top and lightning conductor are often struck by lightning. Most of the tower ground current components will disperse through the "lightning conductor (or tower top)-hit tower-buried grounding grid". Due to the grounding current dispersion of the tower, on the one hand, it exists in the buried horizontal grounding grid, on the other hand, it relies on the reinforced structure inside the concrete pile foundation of the tower to carry out the grounding current dispersion [8]. Due to the direct contact between the oil–gas pipeline and the soil, the lightning current near the pile foundation of the tower will inevitably generate a certain amplitude overvoltage on the pipeline body [9]. Because the pipeline is a good conductor, if there is no insulation flange, the potential generated on the pipeline will have a greater impact on the outer insulation coating, and in some cases, there is a potential risk of electric shock to the remote pipeline operation and maintenance personnel.

Because the grounding resistance of the power industry tower is generally maintained within 10 Ω, and the shunt ratio of the lightning conductor is small, it is

Fig. 1 Schematic diagram of "two lines and one ground"

power circuit

Oil and gas pipelines to be buried
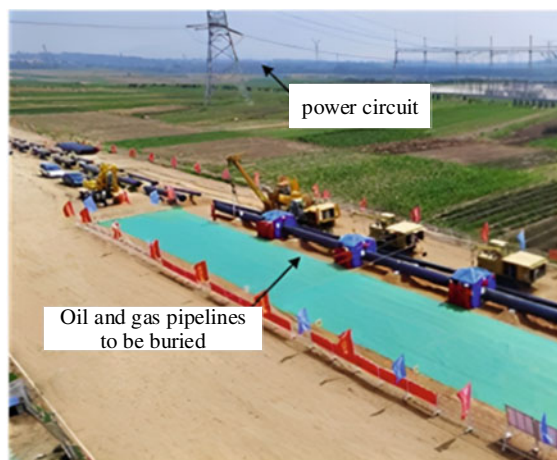
generally considered that the resistive coupling component is the main factor in the case of lightning strike [10]. In addition, the insulation withstand voltage of the pipeline insulation coating is an important index to measure the lightning overvoltage problem when the power line and the oil–gas pipeline are adjacent to each other, and the damage degree of the insulation layer is related to the integrity of the pipeline surface and the pipeline structure: If there are damage points or metal flanges in the coating around the pipeline, the ground potential on the pipeline is high and the withstand potential of the coating is the potential difference on both sides. If the anticorrosive coating around the pipeline is intact and has no damage point, the metal pipeline body is grounded through the distal end. At this time, the tolerance potential difference of the pipeline anticorrosive coating is high, and there is a risk of insulation breakdown.

2.2 Simulation Model and Parameter Setting

Through COMSOL Multiphysics finite element simulation software, the calculation model of lightning overvoltage under the condition of "two lines and one ground" crossing and adjacent between power lines and oil–gas pipelines is established. The finite element simulation calculation can calculate the potential, current and electric field components of any point in the soil medium, and can solve the withstand voltage on the pipeline body and insulation coating. In the simulation model shown in Fig. 2, the distance between the tower and the natural gas pipeline is $d_{pg1} = 40$ m, and the vertical distance between the extension end of the $\Phi12$ mm galvanized steel grounding grid and the pipeline is d_{pg2}. According to the standard construction specification, the buried depth of galvanized steel grounding conductor and pipeline is 0.8 m and 1.5 m respectively, and the frame and extension of grounding grid are l_{g1} = 16 m and $l_{g2} = 20$ m respectively. The length l_p of the oil–gas pipeline is 500 m, the outer diameter is $\Phi530$ mm, and the wall thickness of the steel pipe is 13 mm. Three layers of polyethylene material (3LPE) are used as the anticorrosion layer of the pipeline. The thickness of the insulation anticorrosion layer is 3 mm, and the surface resistivity ρ_F is 10^5 $\Omega\cdot$m.

The finite element simulation software can take any waveform as the excitation source. In order to accurately simulate the actual lightning current, this paper uses the wave front and half-wave length of 2.6/50 µs standard lightning current waveform recommended by the power industry test regulations when setting the input conditions. The standard lightning current double exponential function waveform is established in COMSOL Multiphysics finite element simulation software:

$$i(t) = 1.0474 I_m (e^{-14790.18t} - e^{-1877833t}) \tag{1}$$

According to the simulation calculation model shown in Fig. 2, the soil resistivity ρ under typical soil conditions is taken as 300 $\Omega\cdot$m, and the pipeline potential and the

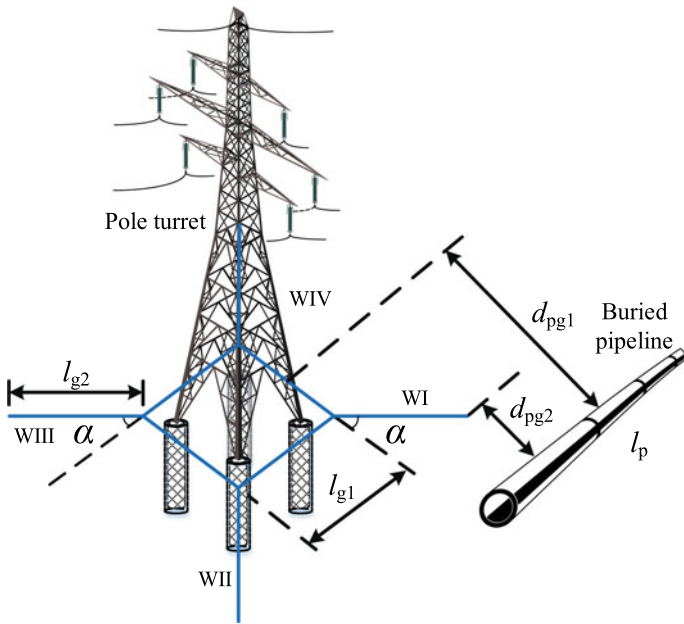**Fig. 2** Finite element model of "two lines and one ground"

corrosion resistance voltage difference under different lightning current amplitudes are shown in Fig. 3.

According to the simulation results of Fig. 3, it can be seen that the transient potential of the pipeline metal body and the insulation layer increases during the lightning flow to the soil medium around the tower, and the peak value reaches

Fig. 3 The potential of the pipeline body and the outer side of the anticorrosive coating
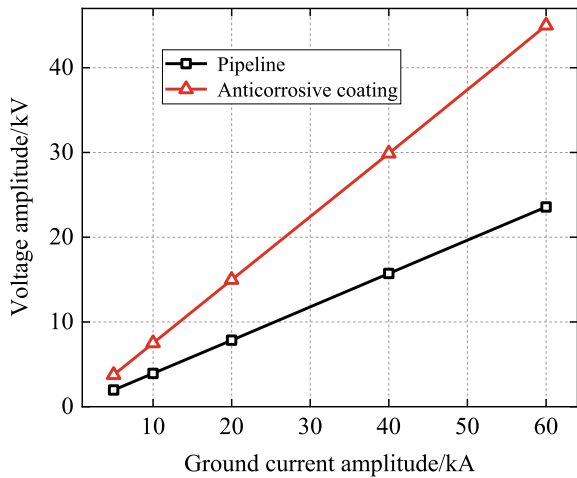
tens of kV. When the lightning current amplitude increases from 10 to 60 kA, the potential on the outer side of the coating and the potential on the metal conductor of the pipeline basically show a linear increase trend. Because the potential on the outer side of the coating increases more, the difference between the inner and outer sides of the pipeline increases accordingly. When the lightning current amplitude is 60 kA, the withstand voltage difference of the coating is 21.99 kV, and the transient voltage value is generally less than 109 kV of the 3LPE material [7, 11]. If there is a damage point in the pipeline, the leakage current of this amplitude is likely to further increase the damage gap. Because the metal body of the pipeline is a good conductor, there is a potential risk of electric shock to pedestrians or operation and maintenance personnel at the far end of the pipeline in a few cases.
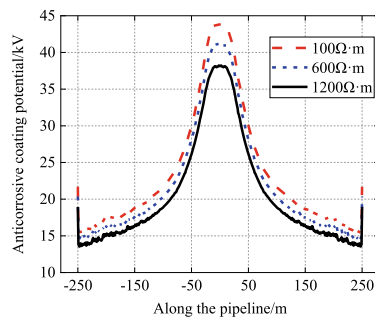
3   Effects of Soil Conditions

In order to further analyze the influence of grounding current on the pipeline potential and the withstand voltage difference of the anticorrosive coating, considering that the actual pipeline laying soil and terrain conditions are different, the simulation parameters under different terrain conditions are different. Therefore, the finite element simulation software COMSOL Multiphysics is used to establish the lightning overvoltage calculation model of "two lines and one ground" of power lines and oil–gas pipelines under different soil conditions. The calculation results of the double exponential lightning current peak of 60 kA and the soil resistivity ρ in the range of 100–1200 Ω·m are shown in Fig. 4.

From the simulation results shown in Fig. 4a, b, it can be seen that the change of soil resistivity basically shows a linear change law on the potential of the pipeline body and the surface anticorrosive layer: when the soil resistivity is low, the lightning is released into the soil medium near the tower, and the dispersion flow can be completed
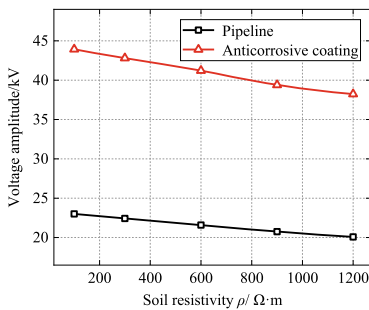
(a) External potential of pipeline body and coating.

(b) The potential distribution along the pipeline outside the coating.

**Fig. 4**   Influence of soil conditions on pipeline overvoltage

within a limited construction area, and the pulse current component to the far end, that is, the pipeline side, is less. When the soil resistivity increases from 100 to 1200 $\Omega\cdot$m, the pulse lightning current needs to be dispersed through the far end, which makes the current component on the side of the adjacent pipeline increase significantly, which will have an adverse effect on the potential on the side of the pipeline. From the simulation results, the withstand voltage difference of the pipeline coating under different soil conditions is still below 18.6 kV, and the withstand voltage difference does not exceed the limit withstand voltage (generally, the limit withstand voltage of the 3PE coating in uniform medium is about 109 kV). If the pipeline itself includes multiple layers, it can be considered not enough to break through the 3PE coating on the outside of the pipeline.

4　Effect of Grounding Structure on Pipeline Potential

The tower grounding grid is the main channel for lightning current discharge. The absolute distance between the grounding grid terminal and the pipeline is an effective way to achieve pipeline voltage suppression. Considering the actual power system lightning protection project, the structure of the general grounding grid has requirements for grounding resistance, and the grounding resistance of the tower needs to be limited within a certain range. Too many tower grounding bodies make the grounding resistance increase greatly, and the risk of power frequency freewheeling after lightning strikes the tower increases. The power frequency freewheeling problem caused by the lightning counterattack of the tower will cause the pipeline insulation layer to withstand milliseconds or even seconds of short-circuit impulse current.

Considering the actual lightning protection requirements of power towers, this paper proposes a corresponding structural optimization method for the tower grounding grid adjacent to oil–gas pipelines. By changing the angle and relative position between the epitaxial grounding grid and the pipeline, the structure of the grounding grid is optimized under the premise of maintaining the grounding resistance limit of the grounding grid, and the overvoltage protection of adjacent pipelines is realized. In the calculation model shown in Fig. 2, the angle between the epitaxial grounding grid and the vertical line of the pipeline is α, and the horizontal interval between the buried oil–gas pipeline and the tower grounding grid is consistent with Fig. 2. The distance between the center of the square galvanized steel grounding grid of the tower and the pipeline is $d_{\mathrm{pg1}} = 40$ m. The buried depth of the galvanized steel grounding conductor and the pipeline is 0.8 m and 1.5 m respectively. The peak current of the mine is set to 60 kA. The uniform soil resistivity ρ is 300 $\Omega\cdot$m, and the simulation results of α between 0° and 90° are shown in Fig. 5.

From the simulation results of Fig. 5a, b, it can be seen that as the angle α increases, the potential of the pipeline metal body and the outer side of the anti-corrosive coating shows a certain trend: before the optimization and transformation of the tower grounding grid, the overvoltage amplitude of the pipeline metal body reaches 20.84 kV, the potential in the soil outside the anticorrosive coating is about
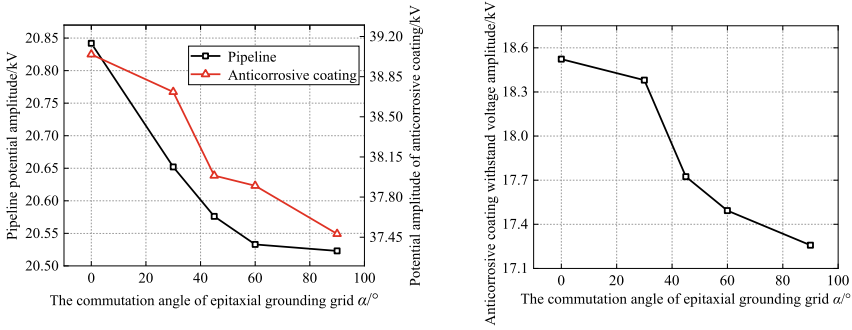
(a) Radial potential distribution of different α
angle pipeline and coating outside.

(b) The withstand voltage distribution of anti-
corrosion coatings with different α angles.

Fig. 5 Influence of grounding grid structure optimization on potential distribution

39.36 kV, and the withstand potential difference $\Delta U_{\alpha 0}$ of the anticorrosive coating is about 18.52 kV. When α increases from 0° to 90°, the overvoltage amplitude of the pipeline metal body is about 20.52 kV and decreases to a certain extent. Due to the change of the dispersion direction of the grounding grid, the calculated value of the potential outside the anticorrosion layer is 37.78 kV. At this time, the withstand potential difference $\Delta U_{\alpha 90}$ of the anticorrosion layer is about 17.26 kV. The change of α limits the component flowing to the pipeline side, which limits the overvoltage peak value of the pipeline and the outer side of the anticorrosion layer to a certain extent.

5   Conclusion

Aiming at the problem of lightning overvoltage protection of oil–gas pipelines near power lines, a method of pipeline overvoltage protection considering the current dissipation of tower grounding grid is proposed. The mechanism of pipeline overvoltage is analyzed by simulation model and the application value of the optimization scheme is verified. The main research conclusions include:

(1) The potential of the pipeline body and the withstand voltage difference of the coating are greatly affected by the direction of the grounding body, and the two show a symmetrical distribution on both sides. The tolerance potential difference of the pipeline anticorrosive coating at the center point has zero crossing or even "reverse". The axial potential of the pipeline is related to the distal grounding drainage point and the anticorrosive coating damage point.

(2) The withstand voltage difference of the pipeline coating under typical soil resistivity conditions does not exceed the limit value, and a single lightning discharge is not enough to break through the 3PE coating on the outside of the pipeline.

(3) By changing the angle and relative distance between the oil–gas pipelines and the tower discharge grounding grid, the tolerance potential difference between the pipeline body point and the anticorrosive coating can be effectively reduced.

The conclusions of this paper can provide reference for the design and safe operation of power transmission and oil–gas pipelines.

References

1. Dong H, Su J, Bi W, Zhang J, Xue Z (2015) Protection and reformation of stray current in valve chamber for gas transmission pipeline. Oil & Gas Storage and Transp 34(11):1246–1249 in Chinese
2. Gao X, Liu Q, Liu B, Hu H, Bi X, Jiang H (2013) Lightning potential distribution for internal floating roof tanks and its hazards. Oil & Gas Storage Transp 32(03):325–328 in Chinese
3. Dawalibi FP, Southey RD (1989) Analysis of electrical interference from power lines to gas pipelines Part I: computation methods. IEEE Trans Power Deliv 4(3):1840–1846
4. Dawalibi FP, Southey RD (1990) Analysis of electrical interference from power lines to gas pipelines Part II: parametric analysis. IEEE Trans Power Deliv 5(1):415–421
5. Kioupis N (2003) Study of the effect of AC-interference and AC-mitigation on the cathodic protection of a gas pipeline
6. Kou X, Li C, Li Y, Wen X, Lu H, Zhang K, Dong M, Guo L (2022) Influencing factors and protective measures of induced voltage of buried pipeline when lightning strikes transmission tower. Insul Surge Arresters 04:99–105 in Chinese
7. Kou X, Li C, Chen J, Wen X, Lu H, Zhang K, Guo L, Dong M (2022) Effect of frequency variation of soil resistivity on induced voltage of buried pipelines when lightning strikes transmission tower. Insul Surge Arresters 03:68–73 in Chinese
8. Liu L, Hu Y, Li X, Jiang Z, An Y, Lv Q (2021) Influence of power tower grounding on adjacent oil and gas pipelines. Oil & Gas Storage Transp 40(06):708–714 in Chinese
9. Wakelin RG (2004) Canada. Investigation and mitigation of corrosion on a 300 mm diameter natural gas pipeline. Corrosion 2004, Paper No. 04205
10. Gao X, Hu Y, Jiang Z, Ke F, Zhou Q, Duan Z, Zhou L (2022) Safety protection measures of lightning strike at the intersection of overhead line and pipeline. Insul Surge Arresters 01:22–28 in Chinese
11. An N, Peng Y, Ai X, Huang G, Shi Y, Zhang M (2012) Electromagnetic effects on underground oil/gas pipeline of the lightning strike on EHV AC transmission line. High Volt Eng 38(11):2881–2888 in Chinese